THERMAL HISTORY OF THE LABRADOR RIFTED MARGIN: INSIGHTS FROM APATITE AND ZIRCON (U-TH)/HE AND APATITE FISSION TRACK THERMOCHRONOLOGY

by

Kara A. Vogler

Submitted in partial fulfillment of the requirements
for the degree of Master of Science

at

Dalhousie University,
Halifax, Nova Scotia
April 2021

TABLE OF CONTENTS

CHAPTER 4: APATITE FISSION TRACK DATING – THEORY, METHODS AND RESULTS………. 123

LIST OF TABLES

LIST OF FIGURES

ABSTRACT

The Labrador margin, Eastern Canada formed from Mesozoic rifting, breakup and seafloor spreading between eastern Labrador and southwest Greenland, producing the Labrador Sea. This study aims to quantify the thermal rift-related history of the upper continental crust of Hopedale and Saglek blocks of the Labrador margin using apatite and zircon (U-Th)/He (AHe and ZHe) and apatite fission track (AFT) dating methods sensitive to closure temperatures between ~40–200 ^{o}C. This study presents new AHe, ZHe and AFT data from 32 bedrock samples distributed along four transects perpendicular to the coast at the latitudes of Saglek, Nain, Hopedale, and Makkovik. Cooling ages range from 18.0–937.5 Ma (AHe), 99.9–258.9 Ma (AFT), and 5.4 – 1612.75 Ma (ZHe). Temperature-time paths produced in *HeFTy* modelling software indicate episodes of rapid cooling initiating between 211.23–111.71 Ma, continuous cooling initiating between 100–150 Ma and cooling initiating between 19 – 66 Ma in northern transects.

LIST OF ABBREVIATIONS USED

AHe – apatite (U-Th)/He
ZHe – zircon (U-Th)/He
AFT – apatite fission track
FT – fission track
ODM – Overburden Drilling Management
NAC – North Atlantic Craton
SFZ – Snorri Fracture Zone
CFZ – Cartwright Fracture Zone
KSS – Kanairiktok Shear-Snorri Shear
HePRZ – Helium partial retention zone
RDAAM – radiation damage accumulation and annealing model
ADAM – α-damage annealing model
LMT – lithium metatungstate
LST – lithium heteropolytungstate
ICP-MS – inductively coupled plasma mass spectrometer
HERC – Health and Environments Research Centre
STD or SD – standard deviation
ESR – effective spherical ratio
PAZ – partial annealing zone
PRZ – partial retention zone
EDM – external detector method
Wt% - weight percent
MI – diiodomethane
TL – track length
MTL – mean track length
OT – oldest track
GOF – goodness of fit

ACKNOWLEDGEMENTS

I would like to acknowledge the Geological Survey of Canada for their funding of this project and recognize the people of Nunatsiavut for allowing us to conduct this research on their land.

A dissertation is not completed by the efforts of one person, but with the help, insights, ideas, and support of many. This dissertation is no exception - I could not have completed this project without the help of supervisors, mentors, colleagues, peers, family and friends.

I would like to express my deep and sincere gratitude to my supervisors, Dr. Isabelle Coutand and Dr. Deanne van Rooyen, for their insightful reviews, unwavering support, and grounding advice. I thank my committee members Dr. Djordje Grujic and Dr. John Gosse for their valuable guidance, and Dr. Roman Kislitsyn for his guidance, willingness to teach and assistance with lab analyses.

I would like to thank Dr. Étienne Girard for his support and patience both during and after the field season and Dr. David Corrigan for his time in the field and help sifting through archived rock samples. I am appreciative of those who engaged in helpful and insightful conversation regarding this research, including Dr. Scott Jess, Dr. Charlotte Keen, Dr. Kate Dickie, Dr. Lynn Dafoe, Dr. Alexander Peace, and Dr. Robert Ketcham.

I would like to thank Dr. Chris Greene and Jennifer Strang who talked me through hours of GIS dilemmas, and other students in the Earth Science department for their support, input and making long lab days tolerable, including Sarima, Sydney, Bryan, Phil, Kim, Max, Sean and Sherif. Finally, I am grateful to my parents, brothers and really my extended family for their supportive phone calls, pep-talks and care packages, and my friends and climbing partners for their moral support and persistent encouragement.

CHAPTER 1: INTRODUCTION

Stretching and thinning of the lithosphere can cause the breakup of a continent or craton to create new tectonic plate boundaries, which is followed by seafloor spreading, where new oceanic crust is produced, forming an ocean basin bordered by two rifted continental margins (e.g. Péron-Pinvidic and Manatschal 2019; Eldholm and Sundvor 1979). The extended continental lithospheric plates on either side of the new ocean basin are referred to as conjugate margins, experiencing cooling, exhumation, uplift, erosion, and input of sediment to offshore depotcentres (Braun 2018).

1.1 STATEMENT OF PROBLEM

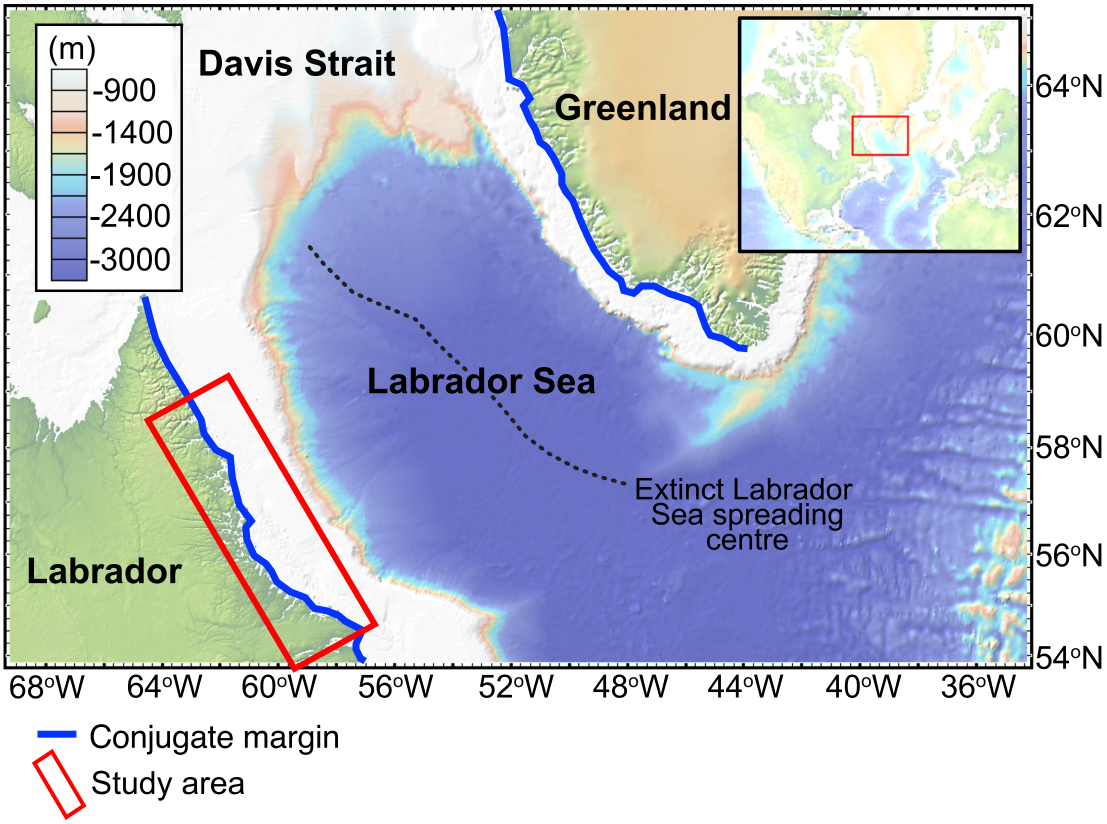

Figure 1.1 Labrador and Greenland conjugate margins (red dotted line) and their orientations to the extinct spreading centre in the Labrador Sea.

The Labrador Sea is a narrow (~900 km wide) ocean basin, formed following late Permian-Mesozoic rifting of the North American Craton (Balkwill and McMillan 1990), resulting in the separation of Labrador and southwest Greenland as conjugate margins of the extinct

Labrador Sea spreading centre (Roest and Srivastava 1989) (Figure 1.1). The Labrador Sea is bordered by the Newfoundland-Iberia margins in the south and the Davis Strait and Baffin Bay margins in the north (Gouiza and Paton 2019). The early stages of rifting in the Labrador Sea are characterized as simple shear rifting (Peace et al. 2016; Chian et al. 1995a), which describes asymmetric, magma-poor rifting resulting from large scale detachment faulting (Wernicke 1981, 1985; Lister et al. 1986). The rift evolved similar to other magma-poor margins, involving crustal thinning and hyperextension with the development of half-graben structures, steep normal faulting of the upper continental crust, a transition zone consisting of serpentinized mantle, and finally production of oceanic crust (Chian et al. 1995a; Keen et al. 1994) (Figure 1.2(A)). The rift migrated to its present-day location in the Labrador Sea (Dickie et al. 2011) and breakup occurred closer to southwestern Greenland than Labrador (Srivastava and Roest 1999) in the Late Cretaceous (Chian et al. 1995a; Keen et al. 2018).

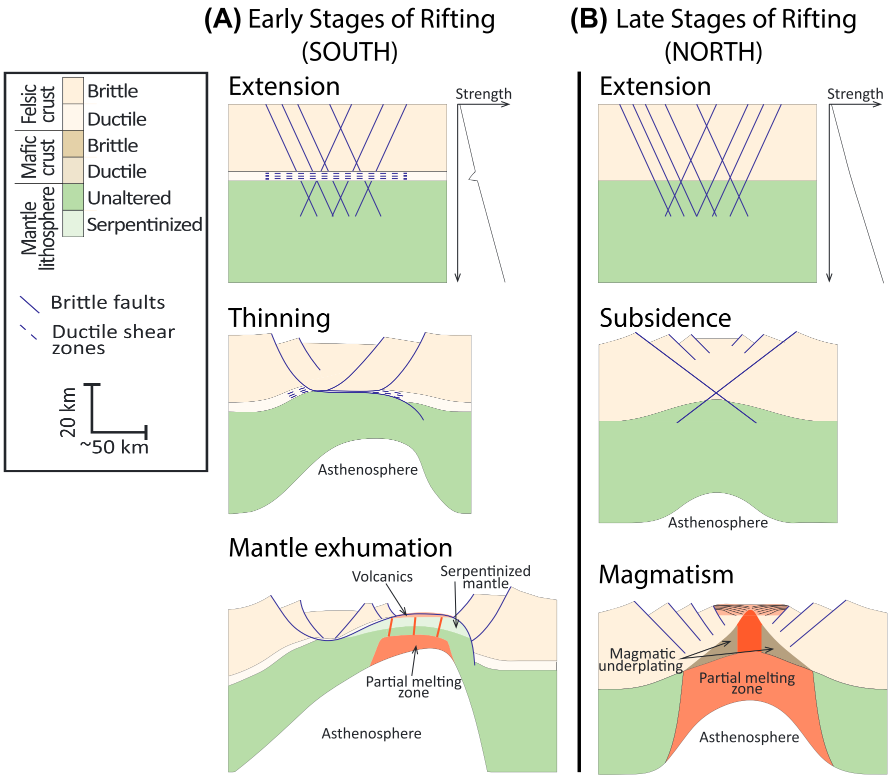

Figure 1.2 Schematic example of (A) simple-shear style asymmetric rifting showing the extension, thinning and mantle exhumation phases representative of early Labrador Sea rifting, as observed in structures along the southern region offshore of the Labrador margin, and (B) pure-shear style symmetric rifting with subsidence and late-rift magmatism, as observed in the later stages of rifting along the northern region offshore of the Labrador margin. Strength profiles indicate the rheological strength of the lithosphere, showing a strong, decoupled crust in the south and a strong, coupled crust in the north (modified from Gouiza and Paton 2019).

The rift opened from south to north following a diachronous continental breakup (Gouiza and Paton 2019; Peace et al. 2016; DeSilva 1999), transitioning from magma-poor in the south to magma-rich in the northern regions (Gouiza and Paton 2019; Keen et al. 2012; 2018 and references therein) (Figure 1.3), which overprinted existing rift structures (Dickie et al. 2011 and references therein). The source of the magmatism is disputed, and either resulting from excess magmatism associated with the Davis Strait hotspot at ~61 Ma (Gouiza and Paton 2019; Keen et al. 2012; 2018 and references therein) or plate-related interactions (Clarke and Beutel 2019; Peace et al. 2017). Rifting in the later stages is accommodated by pure-shear extension (Gouiza and Paton 2019), which describes a symmetrical rift with a brittle upper crust and a ductile lower crust (McKenzie 1978) (Figure 1.2(B)). Seafloor spreading, which follows breakup, indicates the end of tectonic activity along a margin (Liao and Gerya 2014), although the timing of onset seafloor spreading is disputed in the literature.

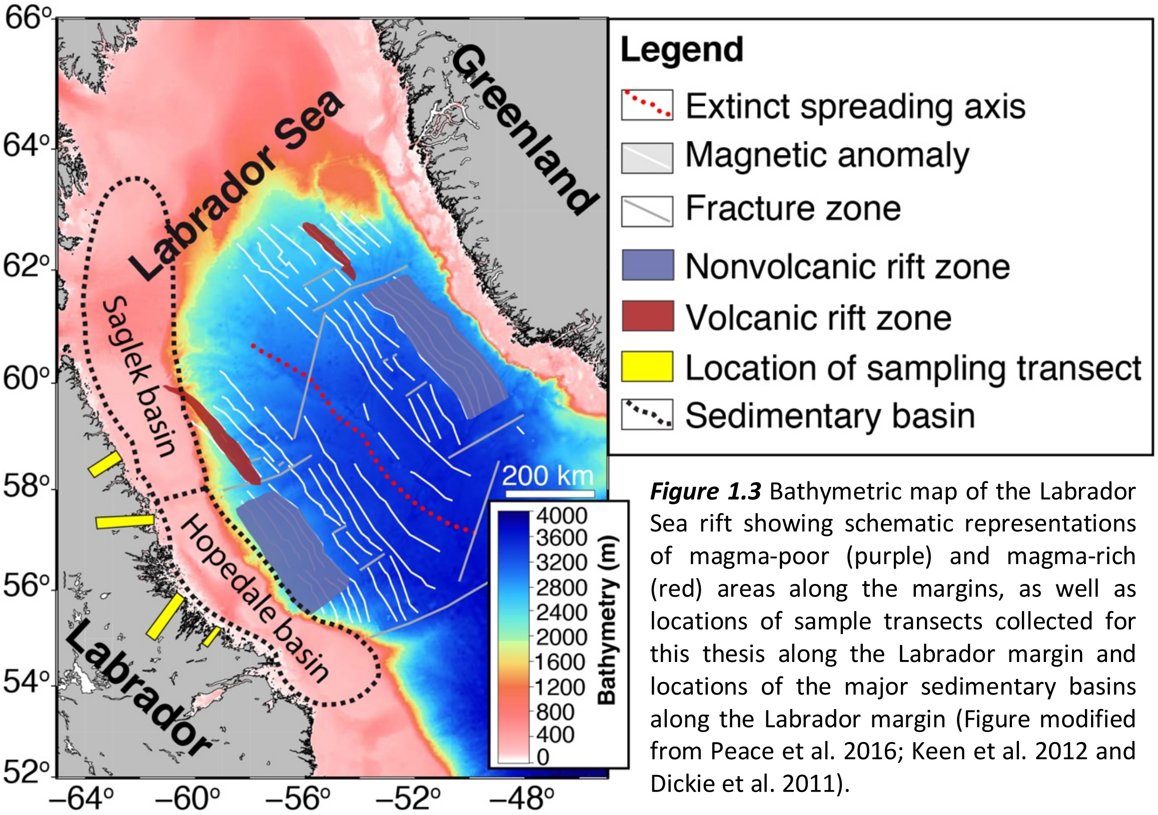

Figure 1.3 Bathymetric map of the Labrador Sea rift showing schematic representations of magma-poor (purple) and magma-rich (red) areas along the margins, as well as locations of sample transects collected for this thesis along the Labrador margin and locations of the major sedimentary basins along the Labrador margin (Figure modified from Peace et al. 2016; Keen et al. 2012 and Dickie et al. 2011).

The Labrador margin today is occupied by the Hopedale basin along the south-central part of the margin, the Saglek basin along the northern margin (Figure 1.3) (Keen et al. 2018) and the Chidley basin further offshore (e.g. Le Guerroué et al. 2018). Sedimentary basins along the Labrador margin contain 8–11 km thicknesses of syn-rift and post-rift sedimentary sequences with thicker packages at the northern end of the margin compared to the south (Peace et al. 2016). Sedimentation extends ~50–300 km offshore where sediment infill is ~3–6 km thick (Peace et al. 2016).

There are a few outstanding scientific questions regarding the thermal state of the continental crust of the Labrador–Greenland conjugate margins during rifting, such as:

1) What is the timing of onset and duration of intracratonic rifting and its spatial distribution according to the Labrador margin? (e.g. Peace et al. 2018; Japsen et al. 2016; 2014, Green 2013). When rifting occurs, continental crust becomes tectonically deformed, which should be recorded in the thermal evolution of the crust as displacement on normal faults bring crustal material in their footwall upwards, inducing crustal cooling (e.g. Malusá and Fitzgerald 2019; Campani et al. 2010).
2) What is the onset and time-space evolution of seafloor spreading? Seafloor spreading has a thermal effect on the margin. When a spreading center is nucleated and developed, localized tectonic activity along the margin quiets and there is a final cooling of the margin as compressed isotherms relax (e.g. Malusá and Fitzgerald 2019; Malusá 2016; Braun 2016, 2002).
3) How might a transition from magma-poor to magma-rich rifting have affected the rifting process (e.g. Gouiza and Paton 2019; Keen et al. 2018)? The Labrador Sea rift transitions from magma-poor rifting in the early stages along the southern part of the margin, to magma-rich rifting along the northern part of the margin in the late stages of breakup, where magmatism may have had an impact on rift processes such as crustal thinning (e.g. Gouiza and Paton 2019; Keen et al. 2018, 2012; Peace et al. 2016; Chalmers 1997).

1.2 OBJECTIVES, STUDY DESIGN, AND SCIENTIFIC CONTRIBUTION

There is inconsistent information on the timing and rates of rifting and post-rift processes regarding the Labrador Sea rift. While the southwestern Greenland margin has been extensively studied using low-temperature thermochronology (e.g. Jess et al. 2020, 2019; Green et al. 2016, 2013; Japsen et al. 2006, 2009; Larsen et al. 2009; Tappe et al. 2009; Kristofferson and Talwani 1977) the Labrador margin is devoid of such datasets except for a study by Centeno (2005), on the Torngat Mountain and Ungava Peninsula regions at the northern tip of Labrador. The objective of this study is to constrain and quantify the thermal history of the upper continental crust of Hopedale and Saglek blocks of the Labrador margin with regards to Mesozoic rifting using low-temperature thermochronology including apatite and zircon (U-Th)/He dating (AHe and ZHe, respectively) and apatite fission track (AFT) dating methods. These thermochronometers are sensitive to temperatures between ~40–200 ^{o}C, which makes them useful for studying the impact of tectonic and surface processes occurring within the upper 8–10 km of the Earth's crust (Reiners et al. 2005). Samples were collected from Labrador along four 32 – 132 km long horizontal transects perpendicular to the coastline (Figure 1.3), including: 7 samples at the approximate latitude of Makkovik; 9 samples at the latitude of Hopedale; 9 samples at the latitude of Nain; and 7 samples at the latitude of Saglek. This thesis provides cooling age data from multiple thermochronometers and presents a thermal history of rifting and post-rift landscape evolution from the entire margin and to add to the understanding of rifting and existing data, including AHe data from the Torngat mountains in Northern Labrador, geophysical studies, and age data from the Greenland margin.

First order questions answered by this study include:

1) What it the timing of onset of rifting and its duration? How does low-temperature thermochronology data from the Labrador margin compare to previous studies and data from the Labrador margin?
2) What is the spatial and temporal distribution of nucleation and propagation of seafloor spreading?

3) Is it possible to identify episodes of erosion, transport of sediments to offshore basins and, or landscape evolution?

Specific objectives for this project, to address the first order questions are outlined and were achieved as follows:

1) Acquire a multi-thermochronometric dataset comprised of AHe, ZHe, and AFT data to quantify thermal history of the upper continental crust of northern Labrador. Samples along the Hopedale transect were collected during a fieldwork in July 2018, while samples from all other transects were obtained from the Geological Survey of Canada (GSC) archives, collected between 1967 and 1971 during Opération Torngat. For mineral separation, samples from the 2018 field season were processed in the Crystal Isolation Facility at Dalhousie University in Halifax, NS, Canada while samples from the GSC archives were processed at Overburden Drilling Management (ODM) in Ottawa. All samples were cleaned, and grains were picked in the Low-Temperature Thermochronology Labs at Dalhousie and dated in the Noble Gas and Laser Ablation ICP-MS Labs also at Dalhousie.
2) Use thermal history data to constrain spatial and temporal cooling history, including spatial propagation of intracontinental rifting and post-rift landscape evolution of the Labrador margin. This was achieved by analyzing thermochronological data, including ZHe, AHe and AFT data in Excel and processing data in *HeFTy* (Ketcham 2016) thermal modelling software to calculate thermal inversions and evaluate temperature-time paths for each sample.
3) Interpret data using the models produced by *HeFTy*, GIS mapping of the data, and Excel graphing to identify processes responsible for the thermal history, or other processes possibly captured in thermochronology data. This objective will be useful for addressing the first order questions and to infer the timing of rifting processes and seafloor spreading between Labrador and Greenland.

CHAPTER 2: GEOLOGICAL AND GEODYNAMIC SETTING OF THE LABRADOR RIFTED MARGIN AND SURROUNDING AREA

2.1 PRE-MESOZOIC GEOLOGIC AND GEODYNAMICAL HISTORY

Northeastern Labrador, located in Newfoundland and Labrador and in the semi-autonomous Inuit territory Nunatsiavut, is a part of the North Atlantic Craton (NAC), a primarily Archean craton exposed in Greenland, Scotland, and Labrador (Hall et al. 2002). Since crustal structures from previous geological events can influence rift propagation and localization of deformation (Schiffer et al. 2020 and references therein), it is relevant to summarize previous tectonic events in the region. The major tectonic events affecting northern Labrador prior to Labrador Sea rifting include the Torngat orogeny (1.91 – 1.85 Ga), the Makkovikian orogeny (1.90 – 1.78 Ga) (Hinchey et al. 2020 and references therein), Labradorian orogeny (1.72–1.60 Ga) and Grenville orogeny (1.25–0.98 Ga) (Tollo et al. 2004), followed by the opening (570 – 470 Ma) of the Iapetus Ocean, and the closing of the Iapetus Ocean (Hammer et al. 2010). As a result of these tectonic events, Labrador is made up of a number of geologic provinces, each with different orogenic histories and crustal structures, including: the Nain Province; the Torngat Orogen; the Southeastern Churchill Province, known as the Core Zone; the Grenville Province; and the Makkovik Province (Figure 2.1, Figure 2.2).

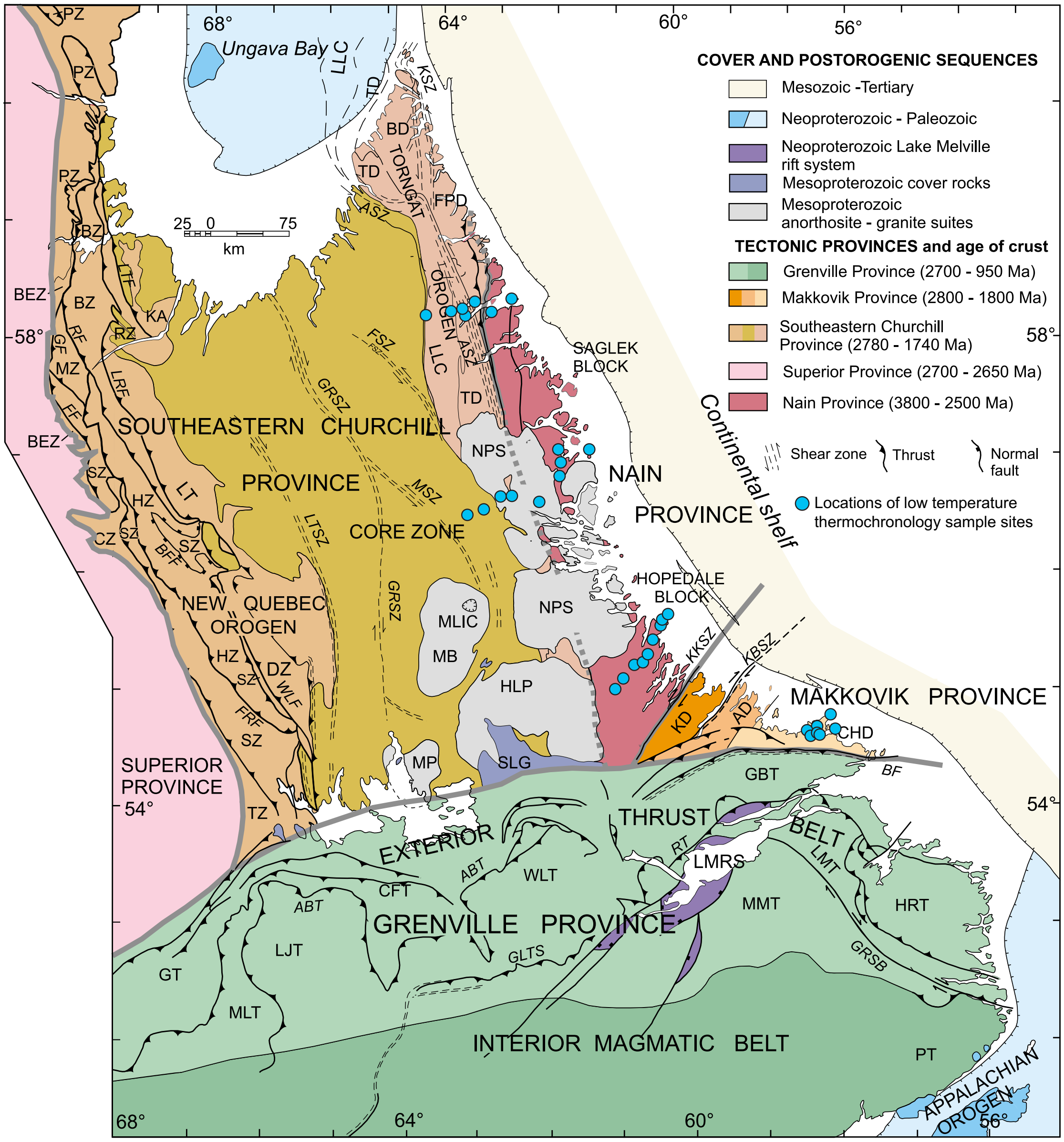

Figure 2.1 Regional map of the geologic provinces of northern Labrador. Blue dots indicate sample sites for (U-Th)/He and AFT data acquisition. Modified from Hall et al. (2002). Structural subdivisions are: (1) Southeastern Churchill Province: ASZ, Abloviak shear zone; BD, Burwell domain; BEZ, Berard zone; BFF, Bertin fault; BZ, Baby zone; CZ, Cambrian zone; DZ, Doublet zone; FF, Forbes fault; FPD, Four Peaks domain; FRF, Ferrum River fault; FSZ, Falcoz shear zone; GF, Garique fault; GRSZ, George River shear zone; HZ, Howse zone; KA, Kuujjuaq Arc; KSZ, Komaktorvik shear zone; LLC, Lac Lomier Complex; LRF, Lac Rachel fault; LT, Laporte terrane; LTF, Lac Turcotte fault; LTSZ, Lac Tudor shear zone; MSZ, Moonbase shear zone; MZ, Melezez zone; PZ, Payne zone; RF, Robelin fault; RZ, Rachel zone; SZ, Schefferville zone; TD, Tasiuyak domain; TZ, Tamarack River zone; WLF, Wade Lake fault. (2) Makkovik Province: ABT, allochthon boundary thrust; AD, Aillik domain; BF, Benedict fault; CHD, Cape Harrison domain; KBSZ, Kaipokok Bay shear zone; KD, Kaipokok domain; KKSZ, Kanairiktok shear zone. (3) Grenville Province: CFT, Churchill Falls terrane; GBT, Groswater Bay terrane; GLTS, Grand Lake thrust zone; GRSB, Gilbert River shear belt; GT, Gagnon terrane; HRT, Hawke River terrane; LJT, Lac Joseph terrane; LMT, Lake Melville terrane; MLT, Molson Lake terrane; MMT, Mealy Mountains terrane; PT, Pinware terrane; RT, Rigolet thrust; WLT, Wilson Lake terrane. (4) Postorogenic assemblages: HLP, Harp Lake pluton; LMRS, Lake Melville rift system; MB, Mistastin batholith; MLIC, Mistastin Lake impact crater; MP, Michikamau pluton; NPS, Nain Plutonic Suite; SLG, Seal Lake Group.

2.1.1 NAIN PROVINCE

The Nain Province is part of the NAC which extends from northeastern Canada through Greenland to northern Scotland (Figure 2.1) (Hall et al. 2002). The Nain Province comprises upper amphibolite to granulite facies gneiss aged 3.8–2.8 Ga (Bridgwater and Schiotte 1990) intruded by basaltic dyke swarms (2.2–2.0 Ga) and anorthosite-granite suites (2.1–2.0 Ga) (Wardle et al. 2002 and references therein). Archean gneisses and plutonic rocks are unconformably overlain by Paleoproterozoic aged sedimentary rocks (Wardle et al. 2002). The Nain Province is subdivided into the Saglek block (3.8–3.3 Ga) in the north, the Hopedale block (3.1–2.8 Ga) in the south (Wardle et al. 2002) and the Nain Plutonic Suite, which intrudes both Archean blocks (Funck and Louden 1998) (Figure 2.1). The Saglek block includes Early Archean (3.8–3.3 Ga) amphibolite to granulite facies orthogneisses and intercalated supracrustal belts, which range in age from 3.9 – 2.5 Ga and correlate to rocks in central Greenland (Louden and Fan 1998). The Hopedale block includes Meso-Neoarchean (3.3–2.8 Ga) metavolcanics, amphibolite facies orthogneiss assemblages (Hammer et al. 2010), and anorthosite-granite suites (2.1–2.0 Ga) (Wardle et al. 2002). The Nain Plutonic Suite includes anorogenic plutonic intrusions emplaced in the Archean and Early Proterozoic crust (Hall et al. 2002), ranging in age from 1.35–1.29 Ga (Ryan 2000). Based on seismic reflection data the Saglek block has a crustal thickness of 35 – 40km and the Hopedale block has an average crustal thickness of 35km (Hall et al. 2002).

2.1.2 SOUTHEASTERN CHURCHILL PROVINCE (CORE ZONE)

The Southeastern Churchill Province, now referred to as the Core Zone, was amalgamated into its current configuration collision of the Superior craton and the NAC (Corrigan et al. 2018). The Core Zone is bordered by the Torngat orogen to the east and New Quebec orogen to the west (Figure 2.1) (Wardle et al. 2002). It consists of at least three Archean crustal blocks; the George River Block, Mistinibi-Raude Block and Falcoz River Block, which are separated by steeply-dipping, crustal-scale shear zones (Corrigan et al. 2018). The eastern edge of the Core Zone, where samples for the Nain transect are located, is the Falcoz River Block, composed of ca. 2.89–2.80 Ga orthogneiss intruded by ca. 2.74–2.70 granite, tonalite, and granodiorite (Corrigan et al. 2018). Common lithologies include meta-plutonic rocks and upper-amphibolite facies orthogneiss and migmatite (Corrigan et al. 2018). The crustal thickness of the Core Zone is 34–38 km (Hall et al. 2002).

2.1.3 TORNGAT OROGEN

The Torngat Orogen is represented by a narrow zone of juvenile crust between the Archean Nain craton and the Core Zone (Figure 2.1). The Torngat orogeny occurred when the NAC collided with the Falcoz River Block of the Core Zone (1.87–1.85 Ga) (Figure 2.2), doubling its crustal thickness (Wardle et al. 2002). The Torngat orogen evolved over three tectonic events with different pressure-temperature conditions. The first event (1.87–1.86 Ga) is associated with peak granulite facies metamorphism, marking initial collision of the Nain craton to the Core Zone (Wardle et al. 2002). The second event (1.85–1.82 Ga) indicates peak granulite-facies conditions in areas associated with the development of the sinistral Abloviak shear zone, but amphibolite-facies metamorphism further north (Wardle et al. 2002). The third tectonic event (1.80–1.74 Ga) is associated with retrogression of granulite-facies assemblages from the previous events, as well as east-verging ultramylonite zones along the contact between the Tasiuyak domain ("TD" in Figure 2.1) and Nain craton (Wardle et al. 2002). The axial part of the orogen, the Tasiuyak domain, extending from the southern limit of the orogen to eastern Baffin Island is characterized by homogeneous, straight-layered gneiss (Tasiuyak gneiss) (Wardle et al. 2002). U-Pb titanite dates extending to 1.63 Ga indicate an intermittent period of cooling and uplift following deformation in the eastern part of the orogen (Scott 1998, from Wardle et al. 2002).

The Torngat root was formed during the Torngat Orogen from early oblique convergence of the Core Zone and Nain Province as the Core Zone was thrust beneath the Nain Province (Figure 2.1, Figure 2.2) (Hammer et al. 2010). According to normal-incidence and wide-angle seismic profiles, the crustal thickness of the Torngat root is up to ~55 km thick (Hall et al. 2002). Interpretations indicate that the root was preserved by transpressional motions along the Torngat Orogen (Hall et al. 2002). Although orogenic roots usually collapse, it is thought that the Torngat root was able to survive post-orogenic collapse because there was little post-orogenic magmatism (Hall et al. 2002).

2.1.4 MAKKOVIK PROVINCE

The Makkovik Province is the smallest structural province of Eastern Canada (Figure 2.1). It formed during the Makkovikian orogeny (1.90 – 1.78 Ma, Hinchey et al. 2020 and references therein), known as the Ketilidian orogen in southwestern Greenland, as juvenile crust was accreted to the NAC, involving collisional events, subduction and transpressive tectonic activity, arc magmatism, and structural reworking of the NAC (Hinchey et al. 2020; Ketchum et al. 2002). The Makkovik Province has been divided into three major tectonic units based on tectonic history and/or lithologic variation, including (from northwest to southeast) the Kaipokok domain, the Aillik domain, and the Cape Harrison domain (Figure 2.1) (Hinchey et al. 2020; Ketchum et al. 2002). The Kaipokok domain consists of structurally reworked Archean gneisses of the Nain Province at greenschist- to amphibolite-facies pressure-temperature conditions (Louden and Fan 1998), intruded by tonalitic-trondhjemitic and calcalkaline plutonic rocks (Hall et al. 1995), and overlain by Paleoproterozoic metavolcanic and metasedimentary strata, as well as granitoid rocks (Ketchum et al. 2002). The Aillik domain consists of Paleproterozoic metavolcanic and metasedimentary strata (Hinchey et al. 2020; Louden and Fan 1998) and intrusive suites (Kerr et al. 1996; Hall et al. 1995). The Cape Harrison domain is dominated syn- and post-tectonic intrusive plutonic rocks of Paleoproterozoic age, reworked orthogneiss, and including isolated enclaves of gneissic rocks preserved in younger granitoid plutons (Hinchey et al. 2020; Hall et al. 2002; Louden and Fan 1998). The crustal thickness of the Makkovik Province is ~35 km (Hall et al. 2002). Collision between juvenile, warm Makkovik Province arcs with the cold buttress of the old Nain Province caused delamination of the Archean Nain lithosphere at the Moho. Delamination resulted in an asymmetrical orogen with outwardly verging shear zones in the young, warm crust that are narrow to the north (25 km across) and wider to the south (200 km across) (Hall et al. 2002).

2.1.5 GRENVILLE PROVINCE

The Grenville Province in Labrador is the southernmost geographic province (Figure 2.1). It formed from Labradorian and Grenville orogenies. Archean crust is present along the northern margin of the Grenville Province (Hall et al. 1995), while the remainder of its crust was formed from tectonically stacked slices of Neoarchean, Paleoproterozoic, and Mesoproterozic crust (Hammer et al. 2010), prior to and during the Labradorian orogeny (1.72–1.60 Ga) (Ketchum et al. 2002). Labradorian orogeny resulted in accretion of multiple terranes influencing the architecture of the southeastern Grenville Province, resulting in thrusts verging outwards from an intracrustal detachment point (Beaumont et al. 1994). The Labradorian orogeny is also associated with mafic dyke injection, migmatization, emplacement of the Trans-Labrador batholith (1.65 Ga, Hall et al. 2002), and post-collisional magmatism (Gower et al. 1992). The Labradorian orogeny resulted in high-grade, granulite facies metamorphism. In geophysical studies, crust affected by the Labradorian orogeny is characterized by an easily identifiable Moho except where it is crossed by shear zones (Hall et al. 2002). The crust is up to 50 km thick, a result of coalescing shear zones (Hall et al. 2002). The Grenville orogeny (1.08–0.97 Ga) (Ketchum et al. 2002) involved an arc–back arc system existing from 1.5–1.2 Ga, multiple collisions, granitoid magmatism, and the Grenville Orogen, then its collapse (Hammer et al. 2010). The Grenville orogeny is associated with widespread granitoid plutonism (Louden and Fan 1998). Rocks in this region of the Grenville Province show metamorphism becoming progressively higher grade from north to south, which is interpreted as exhumation of increasingly deep level crust from the Labradorian orogeny (Louden and Fan 1998).

There is very little activity documented or preserved in this area following the end of the Grenville orogeny and the assembly of Rodinia. The next major phase of tectonic activity started with the rifting of the Iapetus Ocean (570 – 470 Ma) (Hammer et al. 2010) which formed the Lake Melville rift system within the Grenville Province. Rifting resulted in other structures including the Cartwright Arch, indicating an extensional basin with basalt fill (Gower et al. 1997), and the Long Range dykes (615 Ma) (Hammer et al. 2010). The Appalachian orogeny in Newfoundland (470 – 280 Ma) (Hammer et al. 2010) closed the Iapetus Ocean

(Funck et al. 2001) and completed the assembly of eastern North America (Hammer et al. 2010).

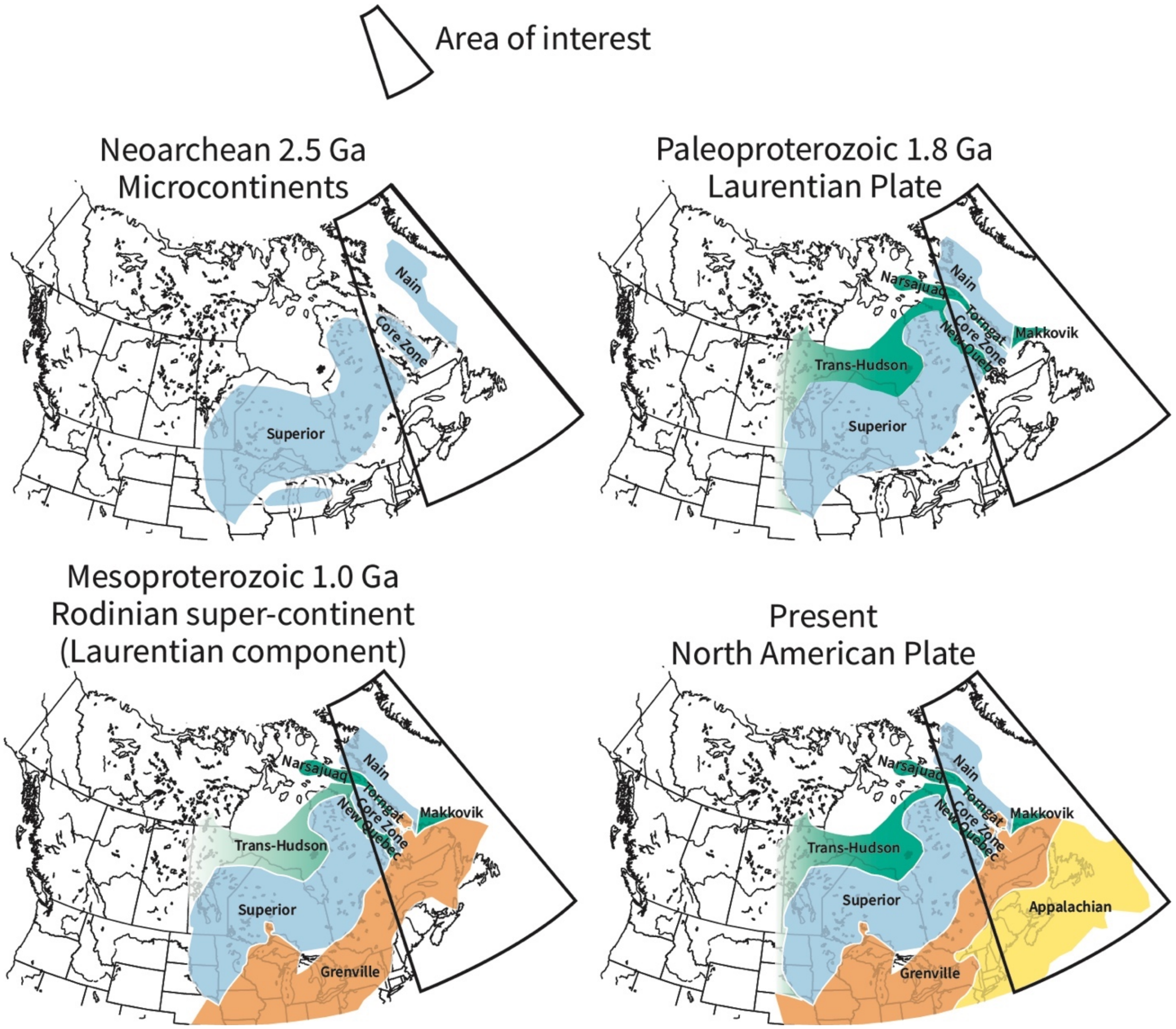

Figure 2.2 Reconstruction of the movement and timing of the cratonic terranes involved in this study and surrounding area coming together to form the present-day geographical geologic provinces (modelled after Hammer et al. 2010).

2.2 MESOZOIC-CENOZOIC RIFTING AND EVOLUTION OF THE LABRADOR MARGIN

2.2.1 HYPEREXTENDED RIFTING

A hyperextended rift is one where stretching of the crust causes coupling and embrittlement of the upper and lower crust, allowing major faults to reach the mantle, which causes serpentinization, or partial hydration of the upper mantle (Doré and Lundin 2015).

Hyperextended rift margins are generally asymmetric, which means that margins show structural, magmatic and sedimentary differences (Peace et al. 2016). They are characterized by slow extension rates of (e.g. 12 – 20 mm/yr, Dick et al. 2003), are magma-poor, with no igneous continental crust formed during breakup (Manatschal 2004) and show highly thinned continental crust (Doré and Lundin 2015) of ≤10 km thick (Péron-Pinvidic et al. 2013). Rifting is a dynamic process where the type of deformation experienced by the craton evolves in both space and time. Spatial deformation occurs both laterally and vertically, as the rheology of the materials and thermal influences affect resulting structures (Doré and Lundin 2015).

The rifting process is divided into three phases, each with characteristic deformation, that overprint each other, including a stretching phase, a thinning phase, and an exhumation phase (Figure 2.3) (Lavier and Manatschal 2006). The stretching phase is dominated by distributed deformation in the form of listric faulting, where hyperextension is accommodated by decoupling of crust and mantle (Lavier and Manatschal 2006). The thinning phase is characterized by the localization of strain in the form of detachment faulting and the development of major ductile shear zones, which weaken the lithosphere to further accommodate hyperextension (Lavier and Manatschal 2006). During the exhumation phase, the upper and lower crust are coupled during stretching creating major ductile shear zones and allowing prominent detachment faults to reach the mantle and cause partial hydration (serpentinization) of the upper mantle (Péron-Pinvidic et al. 2013) as a weakening mechanism, as well as exhumation of the mantle (Lavier and Manatschal 2006). Structures resulting from each rifting phase are observed at the surface, providing a lateral expression of the three rifting phases (Figure 2.3). Exhumation is followed by seafloor spreading and passive margin formation.

As a result of these phases, all rifted margins have similar crustal frameworks (Gouiza and Paton 2019), including the following domains (Figure 2.3) (Chenin et al. 2017): (1) The proximal margin, containing products of the stretching phase, including moderate stretching and thinning of the continental crust (to ~30 km thick), high-angle listric faults and graben and half-graben sedimentary basins filled by wedge-shaped syn-tectonic sediments (Gouiza et al.

2019; Péron-Pinvidic et al. 2013; Mohn et al. 2012; Manatschal 2004). (2) The necking zone, a narrow (50–60 km wide) area between the proximal and distal margins containing products of the thinning phase, where crustal thickness drastically decreases from ~30 km to less than 10 km and the Moho dips up to 35° (Mohn et al. 2012). (3) The distal margin, containing products of the exhumation phase, including hyperextended crust and exhumed, serpentinized mantle (Péron-Pinvidic et al. 2013). (4) The outer domain, which is located between the basement of the distal margin and oceanic crust, and (5) the oceanic domain, composed of homogenous oceanic crust ~6–7 km thick (Chenin et al. 2017) as the location of seafloor spreading.

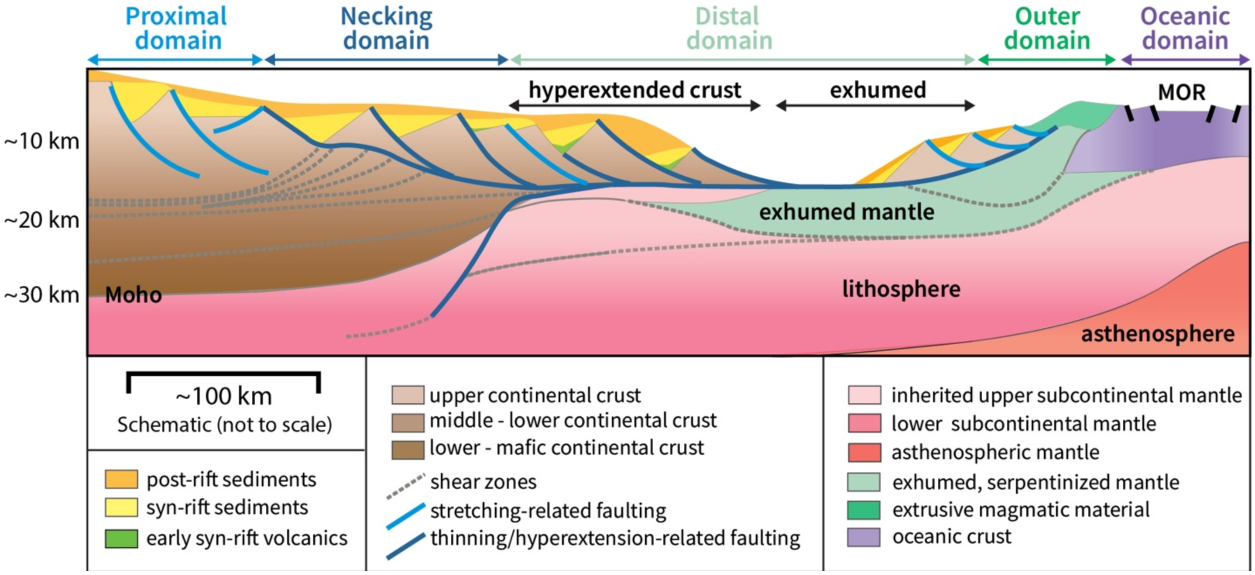

Figure 2.3 Schematic diagram of the rifting process, including the different domains of rifting, faulting associated with the different rifting phases (e.g. stretching and thinning) and locations of syn- and post-rift sediments (modelled after Peron-Pinvidic et al. 2013 and Peace et al. 2016).

The Labrador margin shows expressions of the three rifting phases and rifting domains that have been well-studied and characterized offshore Labrador during the 1990s in geophysical studies (e.g. Chian and Louden 1994; Chian et al. 1995a; Keen et al. 1994) using multichannel seismic reflection data and wide-angle seismic reflection and refraction data (Figure 2.4). The phases of rifting were imprinted in the crustal structures along the Labrador margin, which were divided into three zones (Figure 2.3) (Chian et al. 1995a; Keen et al. 1994): (1) extended continental crust in the proximal margin, comprised of hyperextended crust with sequential normal faults cutting the upper crust and younging toward the ocean with little evidence of syn-rift sedimentation; (2) exhumed, serpentinized mantle in the distal margin, with deeply penetrating faults causing serpentinization where continental crust is less than 5 km thick, which is observed in geophysical data as incoherent reflectors and basement ridges without any distinct Moho reflector; (3) and oceanic crust in the oceanic domain, with a clearly imaged and semi-continuous Moho, an inner section defined by considerable topography that does not correlate with top basement topography, and an outer section consisting of well-organized, linear magnetic anomalies with oceanic character and no evidence of basement faulting (Keen et al. 2018; Delescluse et al. 2015; Chian et al. 1995a). The oceanic crust is slightly thicker towards the north, which may be related to its proximity to magmatism associated with late-stage rifting (Keen et al. 2012; 2018).

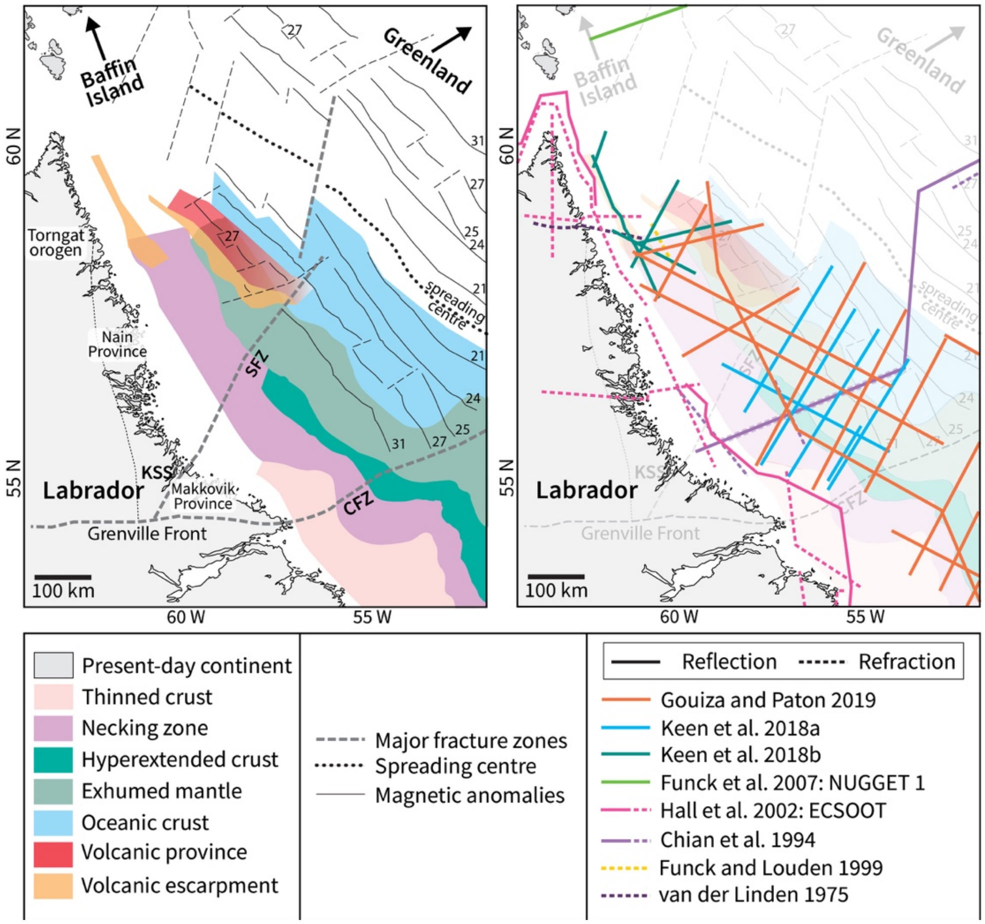

Figure 2.4 (Left) Locations of the zones of rifting, regions of magmatism, magnetic anomalies, and major shear zones that divide the crustal segments. (Right) Locations of geophysical transects indicating seismic reflection and refraction lines and their references. SFZ: Snorri Fracture Zone, CFZ: Cartwright Fracture Zone, KSS: Kanairiktok Shear-Snorri Shear. Types of crust data is interpreted from 2D gravity modelling in Gouiza and Paton (2019), magnetic anomalies and fracture zones from Dickie et al. (2011), extent of magmatism from Keen et al (2018).

More recent studies (e.g. Keen et al. 2018, Gouiza and Paton 2019) have defined boundaries between these regions and identified characteristic crustal structures using higher quality 2D multichannel seismic reflection data (Figure 2.4). Crustal geometries along the Labrador margin vary from north to south as a result of rheological differences of the pre-rift basement (e.g. Gouiza and Paton 2019). Rheology influences the thickness of the decoupling ductile crust that determines when the upper and lower crust become coupled and lithospheric deformation occurs (e.g. a delay of coupling delays when faults reach the mantle, causing breakup to occur later) (Gouiza and Paton 2019; Péron-Pinvidic et al. 2013). Crustal segments are separated by inherited Precambrian structures including the Kanairiktok Shear-Snorri Shear (KSS) (or the SFZ offshore), and Grenville Front or Grenville Suture (GS) (or the CFZ offshore) (Figure 2.4) (Gouiza and Paton 2019). North of the KSS, there is no hyperextended continental crust in the distal domain, rather a wide necking zone and wedges of Early Paleocene and Early Eocene aged flood basalts typical of magma-rich margins (Gouiza and Paton 2019 and references therein). Pre-rift basement is composed of Archean aged rock with a 35 km thick crust and a 200 km thick cold lithosphere that was strong and coupled (Gouiza and Paton 2019), resulting in a more symmetrical rifting style. Between the KSS and Grenville front, the crust contains the typical phases and zones of hyperextended rifting, including extended continental crust, exhumed, serpentinized mantle, and oceanic crust zones, with volcanic rocks, sills, and dykes. There was less crustal stretching in the northern segment than in the south and continental breakup was facilitated by a thermal anomaly associated with the passing proto-Icelandic plume at around 65.8 – 64.4 Ma (Gouiza and Paton 2019; Peace et al. 2017; Dickie et al. 2011; Srivastava and Roest 1999).

As a result of the complex rifting history, the Labrador and Greenland conjugate margins exhibit structural, magmatic and sedimentary asymmetry (Peace et al. 2016). The continental shelf on the Labrador margin is ~150 km wide, but <50 km wide on the Greenland margin (Figure 2.5(A, B)) (Peace et al. 2016). Sedimentary basins along the Labrador margin contain 8–11 km thicknesses of syn-rift and post-rift sedimentary sequences, with thicker packages at the northern end of the margin compared to the south (Peace et al. 2016). Sedimentation extends

~50–300 km offshore where sediment infill is ~3–6 km thick. Along the southwestern Greenland margin, basins are <2–4 km thick and don't extend more than 100 km offshore (Figure 2.5 (C, D)) (Peace et al. 2016). Although syn-rift magmatism appears on both rifted margins, the Labrador margin contains only minor Mesozoic igneous intrusions and primarily in the Aillik domain of the Makkovik province, while the southwest Greenland margin has extensive rift-related diking and Jurassic to Cretaceous igneous outcrops (Gouiza and Paton 2019; Larsen et al. 2009; Peace et al. 2016; Tappe et al. 2007).

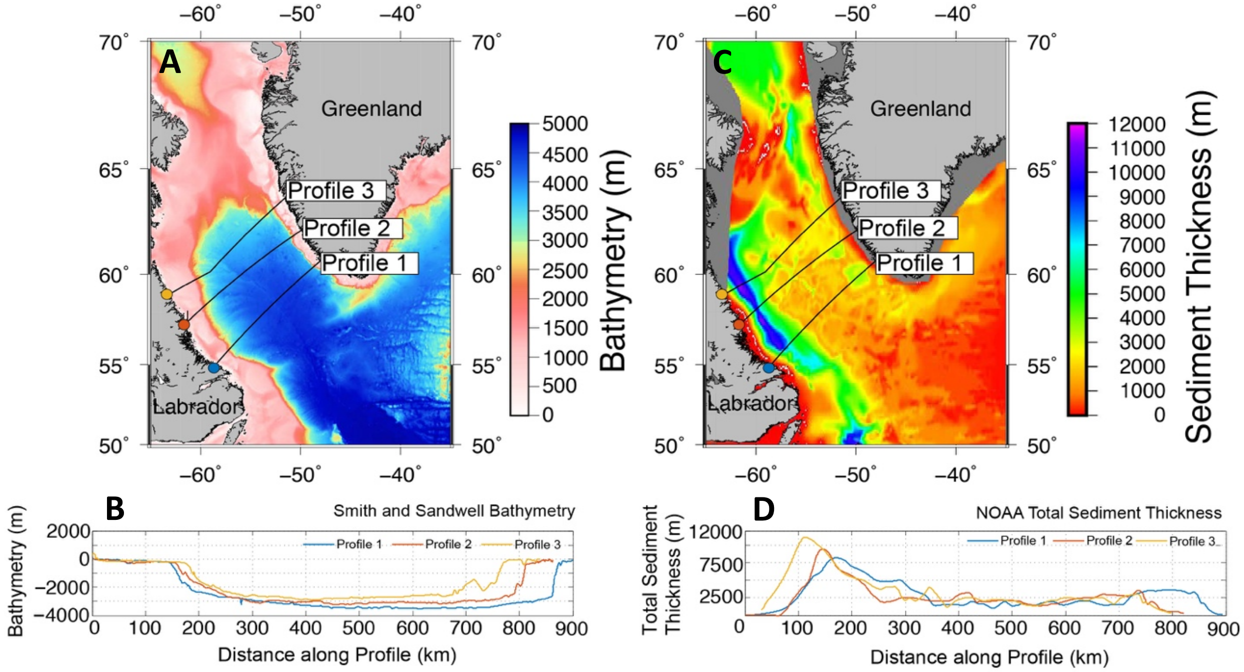

Figure 2.5 (A) Bathymetry of the Labrador Sea from Smith and Sandwell (1997) global bathymetry data. (B) Bathymetry along profiles 1, 2, and 3. (C) Total sedimentary thickness in the Labrador Sea from the National Oceanic and Atmospheric Administration (NOAA) world's oceans and marginal seas total sedimentary thickness (version 2; Whittaker et al., 2013). (D) Total sedimentary thickness along profiles 1, 2, and 3. For C and D, the Labrador 0 km and the west Greenland at 900 km (Modified from Peace et al. 2016).

2.2.2 EXISTING DATA FROM THE LABRADOR SEA RIFT: SOUTHWEST GREENLAND

As a result of extensive rift-related magmatism along the Greenland margin, numerous studies have dated igneous intrusions using ^{40}Ar/^{39}Ar, Rb-Sr and U-Pb methods to determine timing of emplacement and characterized their source and relationship to Mesozoic rifting based on chemical composition (e.g. Japsen et al. 2009, 2006; Larsen et al. 2009; Secher et al. 2009; Tappe et al. 2009, 2007; Frei et al. 2008; Bizzarro et al. 2002). Larsen et al. (2009) dated dykes and dyke swarms from different locations along the west coast of Greenland obtaining ages ranging from ~28 – 186 Ma, with Paleogene ages occurring north of Uummannaq Fjord and Triassic-Cretaceous ages occurring south of Uummannaq Fjord (except for Qaqqarsuk-Fossilik) (Figure 2.6) (Larsen et al. 2009).

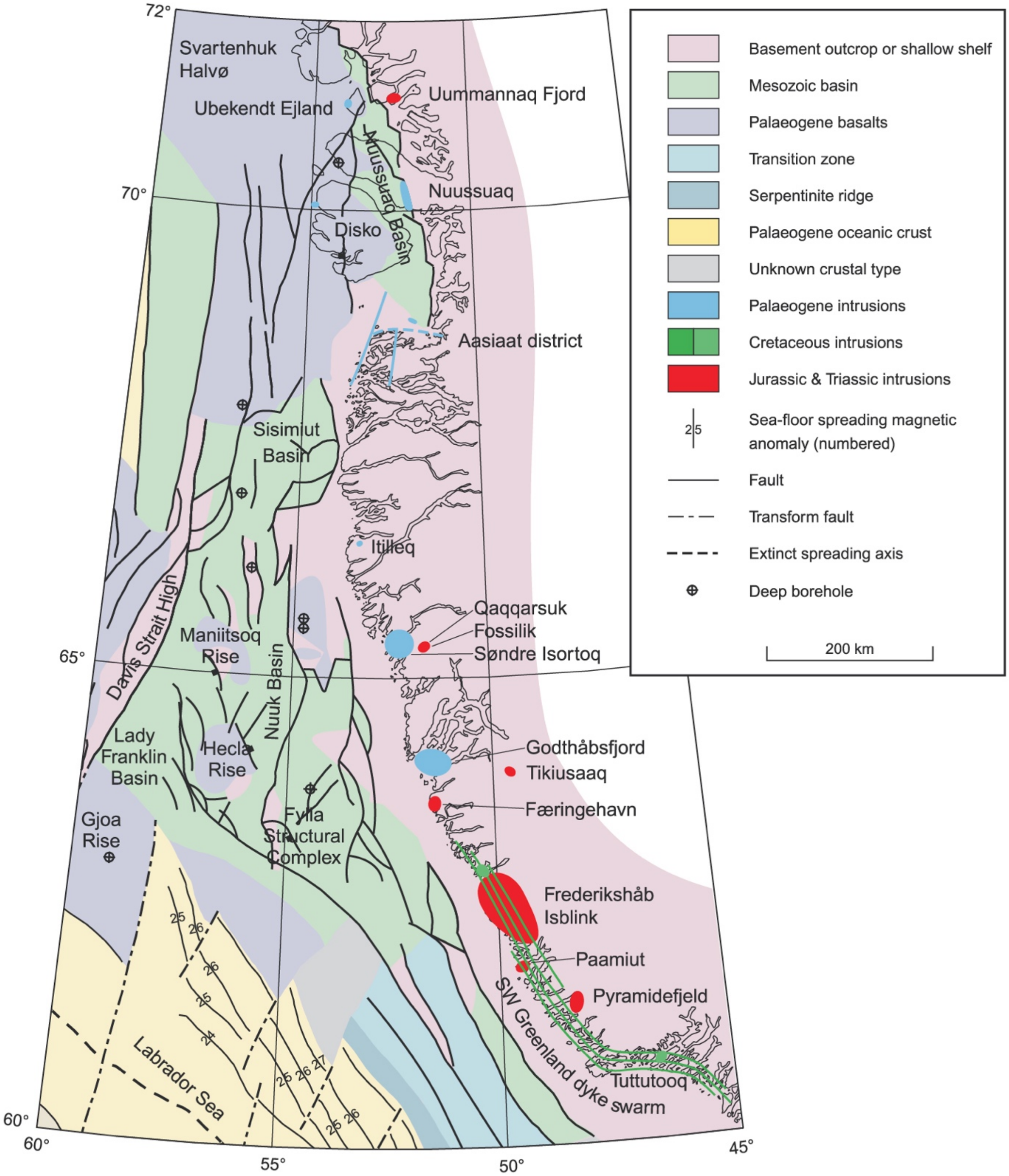

Figure 2.6 Map of the coastline of Southwest Greenland and nearby offshore areas including locations of Mesozoic – Paleogene igneous rocks sampled and dated in Larsen et al. (2009).

The composition of an igneous intrusion can be used to deduce when it was emplaced during the rifting process, making it possible to connect age with rift progress (Larsen et al. 2009; Tappe et al. 2009). For example, the composition of melt depends on the composition of the melting mantle and the pressure and temperature at which melting takes place. A thick (e.g. where lithosphere is 200-230 km, Larsen et al. 2009 and references therein) Archaean craton such as the North Atlantic craton exposed in West Greenland is thick, cold, and does not melt unless the lithosphere is stretched, pressure changes and/or heat is added as the hot asthenosphere rises beneath the thinned region (Larsen et al. 2009). As systematic tectonic development of rifting evolves with time, including a gradually thinning lithosphere and asthenospheric upwelling to shallower levels, a systematic development of melt compositions occurs, whereby melts change composition from volatile-rich and SiO_2-poor to volatile-poor and SiO_2-rich with decreasing pressure and increasing degrees of melting (Larsen et al. 2009). Therefore, ages of ~223 – 150 Ma from aillikite, alnöite and carbonatite dikes representative of small volumes of magma at great depths, would be related to the start of extension, while ages of 140 – 133 Ma, from basaltic alkaline to enriched tholeiitic dikes representative of large degrees of melting at shallower depths, would be related to regional rifting between Labrador and Greenland. The rifting process in southwest Greenland was divided into the following periods according to the compositions of the dykes (Larsen et al. 2009): early extension (223 – 150 Ma), increased extension (150 Ma), rifting (140 – 133 Ma), subsidence and sedimentation (130 – 120 Ma), renewed extension, subsidence and sedimentation (100 – 65 Ma), and breakup, seafloor spreading and magmatism (65 Ma onwards).

(U-Th)/He and AFT data has also been collected from the Greenland margin between Nuussuaq and Itilleq (Figure 2.6, Figure 2.7), although reports only discuss AFT data in the context of Mesozoic rifting and Cenozoic processes (Japsen et al. 2009; 2006). Japsen and co-workers (2006) defined five specific cooling episodes, initiating between 230 – 220 Ma, 160 – 150 Ma, 36 – 30 Ma, 11 – 10 Ma, and 7 – 2 Ma. The type of cooling was described as either continuous and monotonic, having long term exhumation, or episodic, with episodes of heating and cooling. Cooling between 160 and 150 Ma was attributed to exhumation of the margin, rock uplift and exhumation observed cooling prior to 61 Ma was attributed to magmatic activity and onset of seafloor spreading, rock uplift initiating between 36 and 30 Ma is related to the cessation of seafloor spreading in the Labrador Sea (Japsen et al. 2006; Chalmers and Pulvertaft 2001).

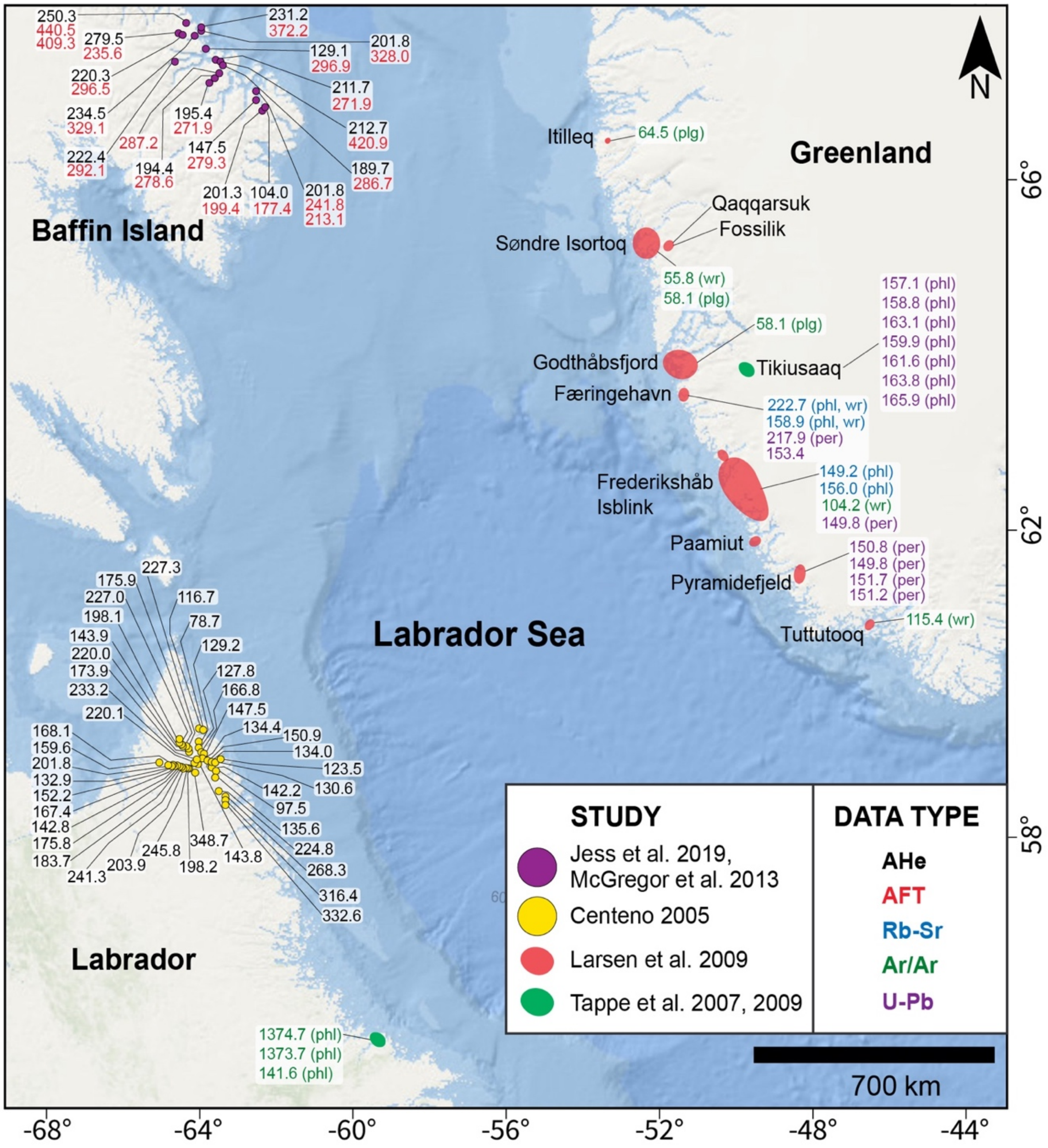

Figure 2.7 Existing age data from the surrounding margins of the Labrador Sea rift including Labrador, Greenland and Baffin Island. Dating method is indicated by font colour. Phl: phlogopite, plg: plagioclase, wr: whole rock, per: perovskite.

2.2.3 EXISTING DATA FROM THE LABRADOR SEA RIFT: LABRADOR

Since there is little magmatism expressed onshore in Labrador, collection of dyke emplacement data has been minimal compared to the Greenland margin. On Ford's Bight near Aillik Bay (Figure 2.7), an ultramafic lamprophyric breccia diatreme was dated using biostratigraphy of *Crepidolithus crassus* microfossils. This species was restricted to the early-upper Jurassic (197 – 145 Ma) and deposited in a proximal marine environment and the diatreme is inferred to have erupted through Jurassic and Lower Cretaceous marine sediments (King and McMillan 1975). Alkaline dykes from a nephelinite suite in Aillik Bay and Cape Strawberry produced Mesozoic rift-related $^{40}Ar/^{39}Ar$ phlogopite ages of 142 Ma and 141.6 ± 1.0 Ma (Figure 2.7) (Tappe et al. 2007) although these ages are disputed by Peace et al. (2016).

Centeno (2005) applied AHe dating methods to samples from the Torngat Orogen and Ungava Peninsula regions on the northern tip of Labrador to determine exhumational and tectonic history of the margin and to quantify topographic evolution of the Torngat Mountains. Results indicate the onset of rapid cooling affecting the Torngat Mountains at ~140 – 150 Ma, according to a vertical transect from Mt. D'Iberville (Figure 2.8). Ages near the Labrador coastline are as young as ~78 Ma, which is interpreted to suggest ~1-2 km of post-rift erosion or renewed rift-related exhumation in late Cretaceous to early Tertiary. Samples from a coast-perpendicular (east-west) transect extending ~180 km across the Ungava Peninsula at the latitude of the Nachvak Fiord produced AHe ages of 100 to 150 Ma near the modern-day coastline and ages >200 Ma in the core of the Torngat Mountains, likely from postulated westward tilting experienced by the Labrador margin during rifting. A north-south transect at 450 m elevation had older ages at its southern end (~268 – 332 Ma near the Saglek Fiord) and younger ages moving northward (e.g. ~80 – 130 Ma near the Kangalaksiorvik Fiord), possibly attributed to obliquity of the transect with respect to the coastline, or otherwise a diachronous rift propagation from south to north. Further inland, a north-south transect at 1000 m elevation had ages older than 200 Ma. Centeno (2005) suggested a protracted rifting history beginning as early as ~150 Ma, culminating in the initiation of seafloor spreading in the Labrador Sea and the break-up of the Greenland-Canadian craton at ~65 Ma.

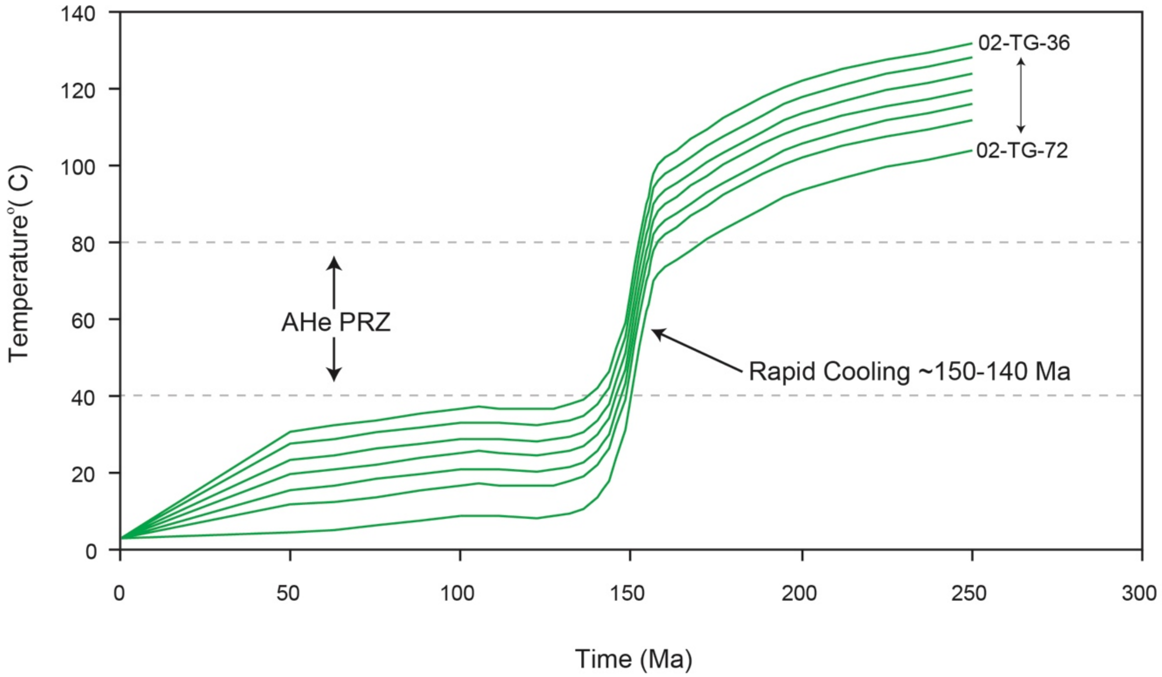

Figure 2.8 Best fit temperature-time paths for AHe data from five samples from a vertical transect collected at Mt. D'Iberville in the Torngat Mountains, indicating a cooling history with accelerated cooling between ~150-140 Ma (Centeno 2005). AHe PRZ: Apatite Helium Partial Retention Zone, the range of temperatures in which helium is neither fully retained, nor fully diffused out of the mineral phase.

Composition of the Hopedale and Saglek sedimentary basins offshore Labrador provide evidence of continental erosion, periods of deposition, and rift-related processes. The Chidley basin offshore the Hopedale basin is much less explored with regards to Mesozoic rifting and will not be discussed further (e.g. Le Guerroué et al. 2018). Based on analyses of offshore wells in the Hopedale and Saglek basins paired with seismic data, the formations on the Labrador shelf are divided into three mega-sequences according to deposition during successive tectonic regimes (Balkwill et al. 1990), including: intra-cratonic rifting, separation of Labrador and Greenland and seafloor spreading, and subsidence of the Labrador Sea oceanic crust. The onset of significant extension in the North Atlantic plate signifying the early rift phase is indicated in the sequence of intra-cratonic rifting by Alexis Formation volcanic rocks or Bjarni interbedded volcanics and sediments (Figure 2.9) dated 131±6 to 121±5 Ma (K-Ar whole rock, Umpleby, 1979), occurring at the base of syn-rift grabens, half-grabens and steeply dipping normal faults (Dickie et al. 2011).

Overlying the Alexis formation, the Bjarni Formation is composed of syn-rift coarse-grained arkose sandstones and deposited in a non-marine environment, which transitions to marginal marine, then lagoonal setting with rising sea level (Figure 2.9) (Balkwill et al. 1990; Dickie et al. 2011). The top of the Bjarni formation is marked by a deep erosional unconformity during the Cenomanian age (100 – 93.9 Ma) (Figure 2.9) indicating the end of large-scale growth faulting associated with the early rift phase (Dickie et al. 2011). There was a phase of uplift and erosion during the Coniacian (89.8 – 86.3 Ma), and possible adjustments between early and late rift phases before deposition of the Markland formation on an erosional unconformity at the top of the Bjarni Formation (Figure 2.9) post-rift subsidence and deposition were occurring on the proximal margin (Dickie et al. 2011). The Markland formation is associated with the onset of spreading in the southern Labrador Sea, a period of rapid transgression and cooling of the shelf region and Labrador margin (Dickie et al. 2011).

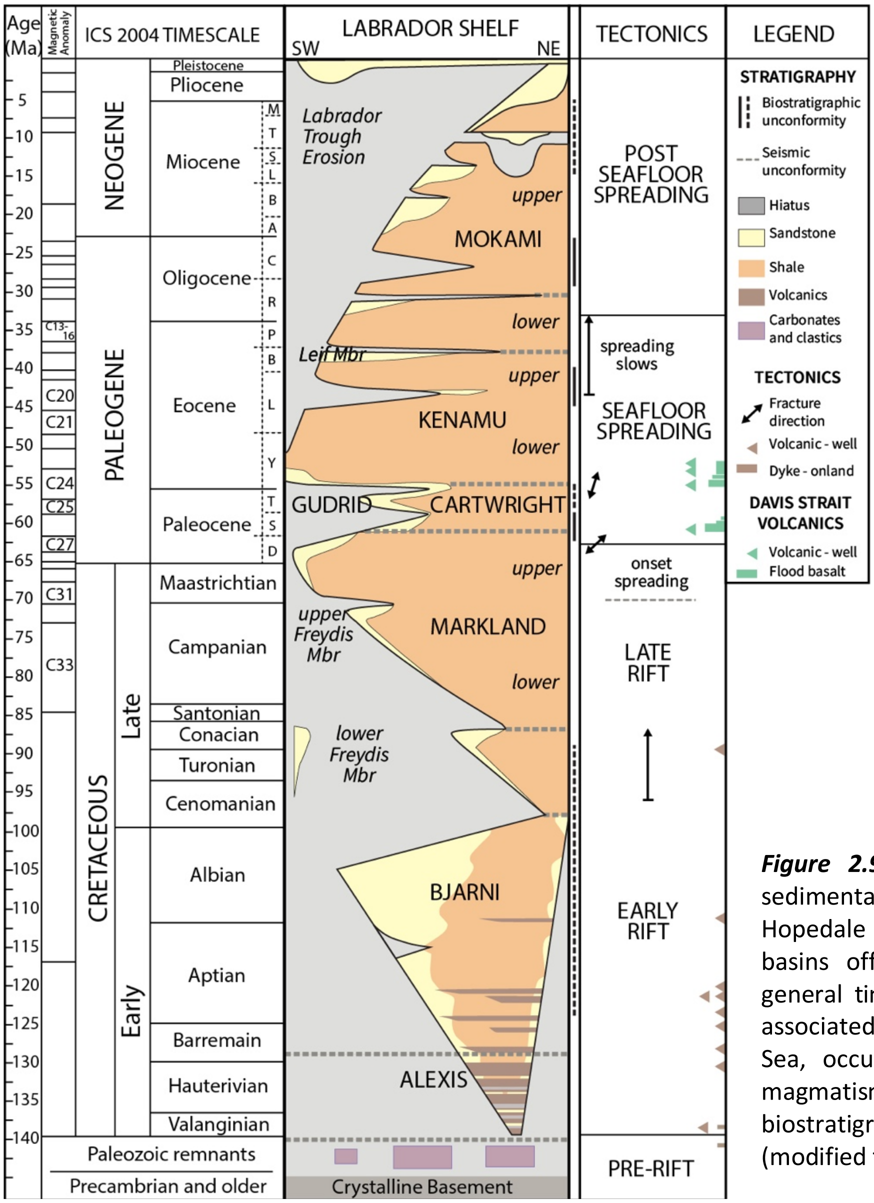

Figure 2.9 Stratigraphic column of sedimentary packages in the Hopedale and Saglek sedimentary basins offshore Labrador, including general timing of tectonic processes associated with rifting in the Labrador Sea, occurrences of volcanism and magmatism and the locations of biostratigraphic unconformities (modified from Dickie et al. 2011).

2.2.4 POST-RIFT HISTORY OF THE LABRADOR MARGIN

The end of the stretching and rifting process is marked by the onset of seafloor spreading, where oceanic crust is produced, and the Earth's magnetic anomaly is recorded in the forming seafloor (Lavier and Manatschal 2006). The timing of onset of seafloor spreading of the Labrador Sea is disputed but otherwise, spreading history has been studied and reported in detail using magnetic anomaly data (Srivastava 1978; Roest and Srivastava, 1989; Chalmers and Laursen 1995; and Oakey and Chalmers 2012), and Ocean Drilling Program wells (Srivastava et al. 1989). Proposed dates for the onset of spreading range from 120 – 63 Ma (C34 – C26), dates for a time of a major regional reorganization and change in spreading direction range from 58 – 53 Ma (C24 – C25) and dates for the cessation of spreading range from ~35 – 25 Ma (C13 – C7) (Figure 2.4) (reported by Seton et al. 2012 and Peace et al. 2016 and referenced therein). Production of oceanic crust seaward of the Hopedale Basin began as early as 90 – 92 Ma (C34, Gaina et al. 2002; and Srivastava 1989; Rowley and Lottes 1988). The oldest identified magnetic anomaly in the area is C33 (Seton at al. 2012), but the oldest, undisputed magnetic anomaly is C27 (66 – 63 Ma) (Chalmers and Larsen 1995), as seafloor spreading isochrons are well defined in crust younger than this time and poorly defined in crust older than this time (Chalmers and Larsen 1995, Srivastava and Roest 1995). According to reprocessed seismic data, C27 is the suggested onset of seafloor spreading (Chalmers, 1991; Chalmers and Laursen, 1995), but sedimentary-tectonic history of the basins does not coincide with this age (Seton et al. 2012). Spreading history following timing of onset is agreed upon relatively consistently, as summarized by Delescluse et al. (2015): Spreading rates between C27 and C25 were slow and opening occurred in a NE-SW direction, until C25 – C24, where Greenland began moving northward with respect to North America and spreading became ultraslow; C13 indicates a waning stage of accretion and possibly the extinction of spreading altogether, although spreading may have continued until C7 (Rowley and Lottes 1988).

The onset of seafloor spreading in the southern Labrador Sea occurred along with transgression and increased subsidence in the Hopedale Basin and lithospheric cooling of the shelf (Dickie et al. 2011). Tectonic uplift and flood basalts either associated with the arrival of the Proto-Icelandic plume in the Davis Strait region and the northern Labrador Sea (Dickie et al. 2011), or plate-tectonic interactions (Clarke & Beutel 2019) occurred at ~61.6 – 59.2 Ma and then again at ~56.0 – 52.0 Ma (Dickie et al. 2011). Evidence of these eruptions appear in the Vaigat Formation picrite (65.5 – 61 Ma), Maligât Formation (61 – 60 Ma) and Svartenhuk Formation (60 – 58 Ma) depleted basalts, and in the Naqerloq Formation enriched basalt (56 – 54 Ma) (Peace et al. 2017). A regression period occurred with the deposition of clastic sediments including the Cartwright and Gudrid Formations between ~61.6 – 59.2 Ma (Dickie et al. 2011). Volcanism occurred in association with a change in seafloor spreading direction from NE–SW to NNE–SSW between C24 – C25 (58 – 53 Ma) (Roest and Srivastava 1989), and corresponds to the timing of the opening of the northern North Atlantic, and unconformities at the tops of the Cartwright and Gudrid Formations (Dickie et al. 2011). An unconformity observed on both the Labrador and Greenland margins indicates that the rate of seafloor spreading slowed abruptly in the Lutetian (47.8 – 41.8 Ma), (Dickie et al. 2011).

A few other notable erosive events include (Dickie et al. 2011): a mass wasting event that was possibly related to a bolide impact (28 km diameter) onshore at Mistastin Lake occurred in the Late Eocene (38 +/- 4 Ma Mak et al. 1976; 36.4 +/- 4 Ma, Grieve 2006), resulting in large slump features in the Hopedale Basin and mass transport deposits further offshore indicating slope instability, along with an unconformity at the top of the Kenamu Formation (Dickie et al. 2011); global sea level decrease and a major cooling trend during the Oligocene, then another period of cooling in the mid-Miocene (Haq and Al- Qahtani 2005; Zachos et al. 2001); and an event that produced channels in the late Miocene that is possibly related to rock uplift and erosion in the Davis Strait (~11 Ma; Japsen et al. 2006).

CHAPTER 3: (U-Th)/He THERMOCHRONOLOGY - THEORY, METHODS AND RESULTS

3.1 INTRODUCTION TO LOW TEMPERATURE THERMOCHRONOLOGY

Thermochronology is a geological discipline that studies the thermal history of rocks. It is used to measure the timing and rate at which rocks are cooled following a heating event, making it possible to quantify the vertical motions of those rocks due to tectonic and geomorphic processes (Braun et al. 2006). In the context of this thesis, a thermochronometer is defined as a radioisotopic system involving three components (e.g. Reiners et al. 2005): (1) an unstable radioactive parent isotope, which breaks down according to the process of radioactive decay; (2) a radiogenic daughter product, which is the product of the decay; and (3) the mineral phase containing these isotopes. The daughter products can diffuse out of the mineral through thermally-activated diffusion until cooling below a threshold range of temperatures when they will be retained within the mineral phase – this is when the thermochronological clock starts (Figure 3.1).

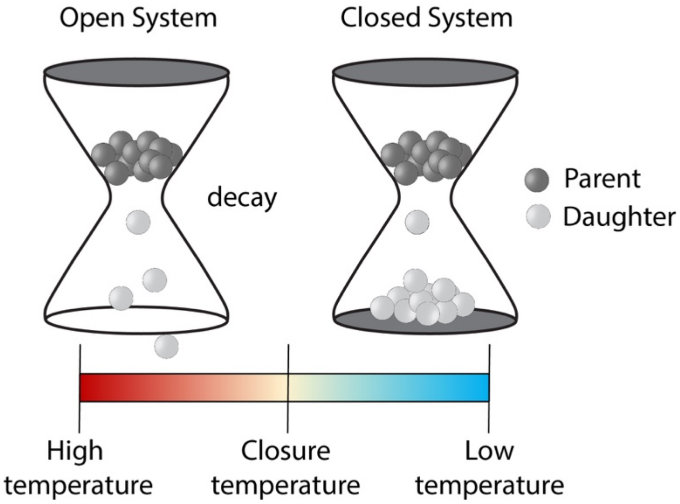

Figure 3.1 Schematic representation of the processes involved in producing ages within the phase, modelled after (Braun et al. 2006).

There are various thermochronometers that can quantify different earth processes over a large range of closure temperatures from 0–900 °C (e.g. Figure 3.3; Reiners et al. 2005). Low temperature thermochronometers are useful for quantifying the thermal history of the uppermost part of the continental crust for temperatures between ~25–250 °C (Ault et al.

2019), and therefore identifying the earth processes affecting the thermal field of the uppermost 8–10 km of the Earth's crust (Reiners et al. 2005) assuming an average continental crust geothermal gradient of ~20–30 °C/km (e.g. Gleadow et al. 2002) typical for a tectonically undisturbed 30 – 40 km thick continental crust. Reconstructing the thermal history of the upper continental crust can be used in a variety of applications, including: interpreting landscape evolution by estimating the timing and rate of near-surface tectonic and geomorphic processes (Figure 3.2) (e.g., Zeitler et al. 1987; Wolf et al. 1996a; Wolf et al. 1996b; House et al. 1997; House et al. 1998; Wolf et al. 1998; Reiners and Farley 1999; Reiners et al. 2000; Reiners and Farley 2001, Malusa and Fitzgerald 2019); inferring source-to-sink sediment budgeting (Malusa and Fitzgerald, 2019 and references therein); and locating natural resources (Brune et al. 2013).

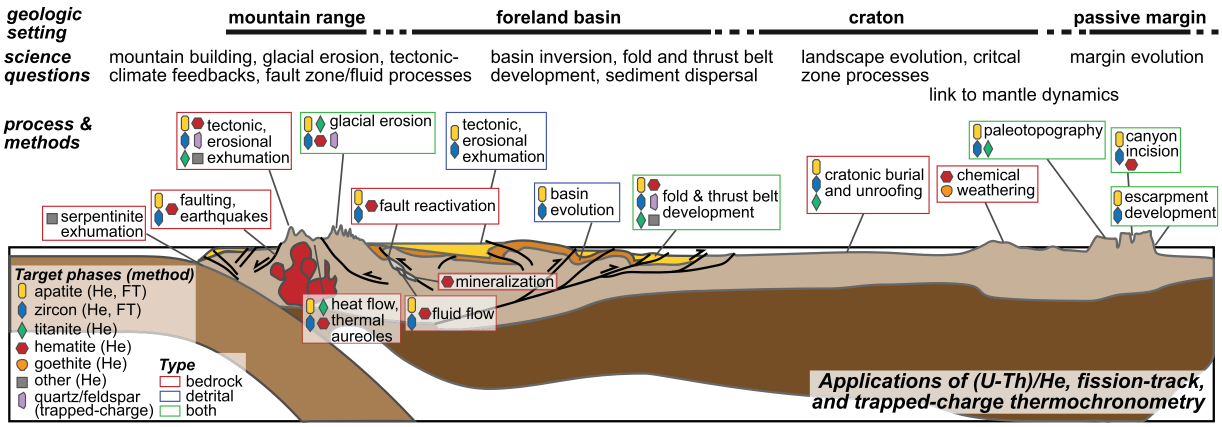

Figure 3.2 Schematic cross section of a continent illustrating how low temperature thermochronometry can be applied to a variety of Earth science questions through diverse geologic settings. Low temperature thermochronometers, including fission track, (U–Th)/He and trapped charge thermochronometry, are applied to target phases, such as zircon and apatite, from both bedrock and detrital systems (Ault et al. 2019).

In this study, we use three low temperature thermochronometers with closure temperatures between ~20–200 °C (e.g. Ault et al. 2019); apatite fission track (AFT), apatite (U-Th)/He (AHe) and zircon (U-Th)/He (ZHe) (Figure 3.3). (U-Th)/He dating involves measuring the production of ^{4}He from the decay of ^{238}U, ^{235}U, and ^{232}Th, and ^{147}Sm (Farley 2000), while AFT dating involves measuring the production of damage zones called fission tracks from the spontaneous nuclear fission of ^{238}U (Donelick et al. 2005). Using multiple low temperature thermochronometers makes it possible to quantify a rock's thermal history over a range of crustal depths (Ehlers and Farley 2003).

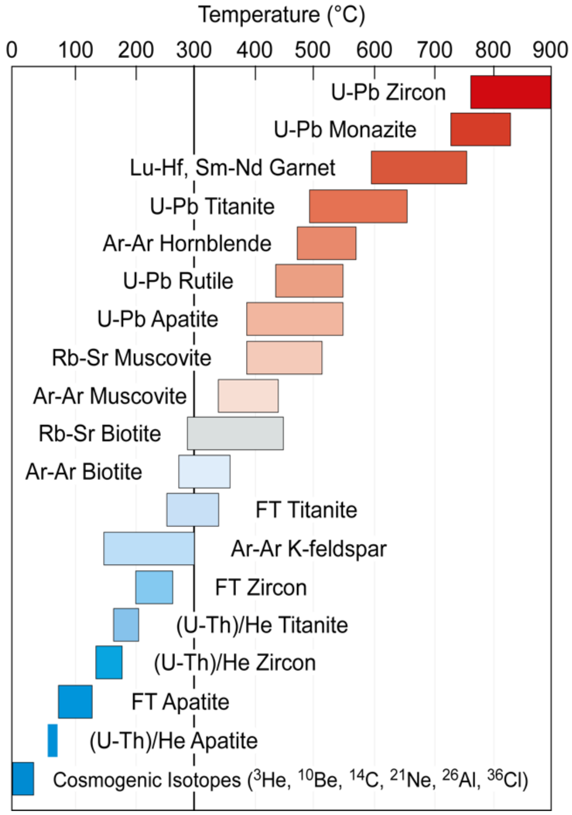

Figure 3.3 Closure temperature ranges for different thermochronometric systems and their mineral phases, where the vertical line separates low-temperature thermochronometers from high temperature thermochronometers (Reiners et al. 2005).

3.2 ISOTOPIC DECAY AND CLOSURE TEMPERATURES

Thermochronology relies on the radioactive decay of an unstable parent isotope at a known rate to produce a stable daughter isotope. The rate of decay is determined according to an element's half-life, defined by Ernest Rutherford (Rutherford at Soddy 1902) as the time required for half of the initial quantity of radioactive parent isotope (N_p) to undergo decay (Groch 1998, Braun et al. 2006):

$$\frac{\mathrm{d}N_p}{\mathrm{d}t} = -\lambda N_p \tag{3.1}$$

where λ (time^{-1}) is the decay constant of parent isotopes. Using this concept, the general age equation was developed as follows (e.g. Reiners and Shuster 2009):

$$N_d = N_{d,0} + N_p\left(e^{\lambda t} - 1\right) \quad \textbf{\textit{(3.2)}}$$

where N_d is the current number of daughter atoms, $N_{d,0}$ is the original number of daughter atoms (which is often negligible because it is assumed that the system was hot enough to be completely reset, such that previous daughters would have diffused out of the crystal), N_p is the current number of parent atoms, and *t* is the cooling age. Equation 3.2 assumes that the number of daughter atoms (N_d) before they are fully retained in the crystal is zero and that the system is closed. Equation 3.2 can be rearranged to calculate cooling age:

$$t = \frac{1}{\lambda ln\left(\frac{N_d}{N_p}+1\right)} \quad \textbf{\textit{(3.3)}}$$

As long as a parent isotope is present, daughter products are continually formed, but may be lost from the mineral through temperature-controlled diffusion processes (discussed in section 3.5) until the mineral cools below a specific temperature range defined for each radiometric system (Figure 3.3). The calculated age from Equation (3.3) is an ‘apparent age’, or a ‘cooling age’, recording time passed since a mineral cooled sufficiently for daughter products to be fully retained within the crystal lattice (Reiners and Brandon 2006; Reiners and Shuster, 2009). Closure temperature (T_c) is defined as the temperature at the time corresponding to the apparent age (Dodson 1973). At the T_c, diffusion becomes negligible and most daughter isotopes are not lost from the crystal lattice (Braun et al. 2006). T_C of a particular mineral system can be approximated using the Dodson equation (1973):

$$T_c = \frac{R}{\left\{E_a \times ln\left(\frac{A\tau D_0}{a^2}\right)\right\}} \quad \textbf{\textit{(3.4)}}$$

where *R* is the ideal gas constant (~8.314 J/K*mol), E_a is activation energy of the daughter product (kJ/mol), *A* is a dimensionless constant defined by the geometry and decay constant of the mineral (ranges from 55 for a sphere to 8.7 for a plane sheet), *a* is the radius of the diffusion domain, D_0 diminishes with time constant, τ, where D_0 is the diffusion coefficient at infinitely high temperature, given by the Arrhenius equation (Dodson 1973):

$$D = D_0 e^{-E/RT} \tag{3.5}$$

where D is the diffusion coefficient at absolute temperature T, R is the ideal gas constant, and E is the activation energy for the diffusion process. D_0, E_a and a are the diffusion parameters, which define T_c for different thermochronometers and vary for different isotopic species and mineral phases.

3.3 APATITE AND ZIRCON (U-Th)/He THERMOCHRONOLOGY

(U-Th)/He dating of apatite and zircon minerals, records thermal history at temperatures ranging from ~30–250 °C (Figure 3.3) (e.g. Ault et al. 2019 and references therein). Isotopes ^{238}U, ^{235}U, ^{232}Th, and ^{147}Sm are unstable and decay into daughter products to ultimately produce stable isotopes at the end of the decay chain (Figure 3.4). Daughter products and other products of the decay process include various isotopes (equations 3.6 – 3.9 or Figure 3.4), α particle or ^{4}He (a helium atom stripped of electrons), beta-particles (β) and decay energy (Q), energy released during the decay reaction. ^{4}He is the daughter product that is measured against parents in AHe and ZHe dating. Production of ^{4}He from ^{238}U, ^{235}U, ^{232}Th, and ^{147}Sm decay is outlined by the equations 3.6 – 3.9, which assume that daughters are preserved in a closed system (Farley 2000):

$$^{238}U \rightarrow {}^{206}Pb + 8\,{}^{4}He + 6\beta + Q \tag{3.6}$$
$$^{235}U \rightarrow {}^{207}Pb + 7\,{}^{4}He + 4\beta + Q \tag{3.7}$$
$$^{232}Th \rightarrow {}^{208}Pb + 6\,{}^{4}He + 4\beta + Q \tag{3.8}$$
$$^{147}Sm \rightarrow {}^{143}Nd + 1\,{}^{4}He + Q \tag{3.9}$$

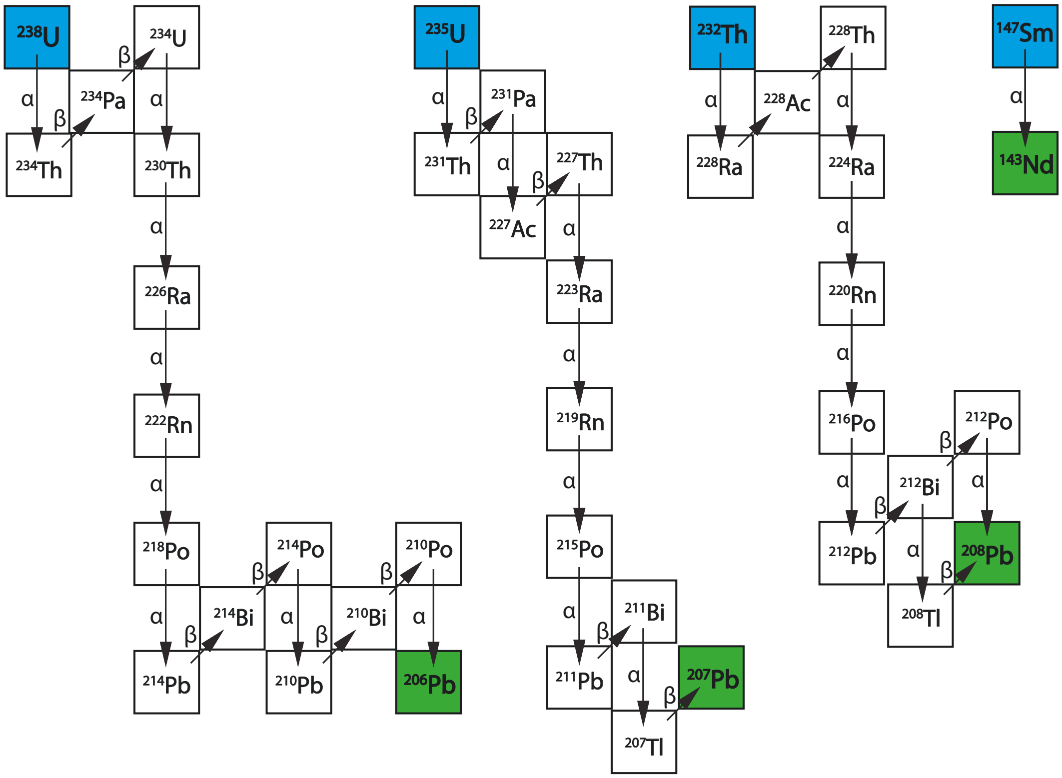

Figure 3.4 Decay chains for unstable parent isotopes ^{238}U, ^{235}U, ^{232}Th, and ^{147}Sm (blue) showing the series of decays to stable daughter products ^{206}Pb, ^{207}Pb, ^{208}Pb, ^{143}Nd (green) and the emission of α (or ^{4}He atoms stripped of their electrons) and β particles at each intermediate stage (modified from Macquarie University web page 2011).

Zircon ($ZrSiO_4$) is a valuable mineral for thermochronological studies (Jeong et al. 2018; Cherniak 2010; Wolfe and Stockli 2010; Bernet and Garver 2005; Reiners 2005; Cherniak and Watson 2003) because (1) it is a common and widely distributed mineral (Anthony et al. 1995) present in igneous and metamorphic rocks as a common accessory mineral and in clastic sedimentary rocks from erosion of pre-existing rocks; (2) it is very resistant to physical and chemical weathering (Wolfe and Stockli 2010) because of its high hardness of 7.5 (Anthony et al. 1995) and low solubility in crustal melts and fluids (Cherniak 2010); (3) zircon can be dated by various isotopic dating methods (Bernet and Garver 2005) because it retains minor and trace elements in high concentrations, including U, Th, and Sm (Jeong et al. 2018; Bernet and Garver 2005; Reiners 2005; Cherniak and Watson 2003), with U content of up to 100–1000 ppm (Jeong et al. 2018).

Apatite ($Ca_5(PO_4)_3(OH,F,Cl)$) is also a valuable mineral in thermochronology because it is the most common rock-forming phosphate mineral (Anthony et al. 1995) making it ubiquitous to various rock types (Wu et al. 2019). It can form as three end members, hydroxylapatite, fluorapatite, chlorapatite, but the most common end member is fluorapatite, which forms prismatic hexagonal crystals (Anthony et al. 1995). Apatite is found as an accessory mineral in most igneous rocks, including syenites, alkaline rocks, carbonatites, kimberlites and granite pegmatites; apatite is common in Ca-rich regional metamorphic and igneous rocks such as marbles and skarns. Apatite is also found in features of secondary processes, including Alpine-type fissures, and hydrothermal tin veins; and it is an essential component in sedimentary phosphorites, appearing as detrital or diagenetic components in shales, oolitic ironstones, and phosphatic carbonate rocks (Anthony et al. 1995). Apatite has even been studied as a potential storage mineral for nuclear waste elements, including U and Th, for the same reasons that make it useful in thermochronology, such as its ability to incorporate actinides into the crystalline structure (Emproto et al. 2020) and its low solubility and slow dissolution rate in geological fluids (Oelkers & Montel 2008). The concentration of natural uranium in apatite typically ranges from 1-200 ppm (Donelick et al. 2005).

3.4 HELIUM (^{4}He) INGROWTH AND AGE CALCULATION

A cooling age (*t*) is calculated using the helium ingrowth equation to determine the number of ^{4}He particles produced within a host mineral (Farley 2002):

$$^{4}He = 8\ {}^{238}U\left(e^{\lambda_{238}t}-1\right)+7\left({}^{238}U/137.88\right)\left(e^{\lambda_{235}t}-1\right)+6\ {}^{232}Th\left(e^{\lambda_{232}t}-1\right) \qquad \textbf{\textit{(3.10)}}$$

where the coefficients before *U* and *Th* correspond to the number of ^{4}He particles emitted in that decay series (Figure 3.4); ^{4}He, ^{238}U, ^{232}U and ^{232}Th are present-day concentrations of each isotope; *t* is accumulation time or the uncorrected cooling age, λ is the decay constant for the corresponding isotope ($\lambda_{238} = 1.551 \times 10^{-10} yr^{-1}$, $\lambda_{235} = 9.849 \times 10^{-10} yr^{-1}$, $\lambda_{232} = 4.948 \times 10^{-11} yr^{-1}$); and the value 1/137.88 is the present day ratio of ^{235}U/^{238}U (Steiger and Jäger 1977) (Table 3.1), which is used to that only ^{238}U must be measured. Equation 3.10 is sufficient for calculating ^{4}He in zircon, as Sm usually does not have a substantial contribution to total ^{4}He because ^{147}Sm has a very long half-life (Table 3.1), only produces one α particle per decay event, and only accounts for 14.99% of total Sm (Vermeesch 2018; Hourigan et al. 2005). Since apatite contains lower U and Th mass fractions than zircon (Wu et al. 2019), Sm decay has a greater effect on total ^{4}He (Reiners 2005) and is included in age calculations according to the following equation (Hourigan et al. 2005):

$$^{4}He = 8\ {}^{238}U\left(e^{\lambda_{238}t} - 1\right) + 7\left(\frac{^{238}U}{137.88}\right)\left(e^{\lambda_{235}t} - 1\right) + 6\ {}^{232}Th\left(e^{\lambda_{232}t} - 1\right) + {}^{147}Sm\left(e^{\lambda_{147}t} - 1\right) \quad \textbf{\textit{(3.11)}}$$

where $\lambda_{147} = 1.07(9)\ \times 10^{-11} yr^{-1}$ (Kossert et al. 2009). Equation 3.11 is the one used to calculate both ZHe and AHe ages at Dalhousie.

The variable *t* appears multiple times within the cooling age equation and must be approximated to calculate final cooling age. Helios software written by Dr. Roman Kislitsyn (2007, 2008, 2020; see Appendix B for more information) is used to conduct Taylor series expansion (Cooperdock et al. 2019) for approximating *t*. All errors on the ages were calculated by Dr. Roman Kislitsyn at Dalhousie University and they are all ~10 times lower than reproducibility on standards, including Durango apatites and Fish Canyon Tuff zircons. Standard deviation of repeated analyses of standard minerals is 2.8% for Durango apatites and 6.8% for Fish Canyon Tuff zircons.

Table 3.1 Radioisotope decay reactions used in (U-Th)/He cooling age calculations (Kossert et al. 2009; Steiger and Jäger 1977).

Decay Reaction	Decay Constant	# ^{4}He atoms produced
$^{238}U \rightarrow {}^{206}Pb + 8\ {}^{4}He + 6\beta + Q$	$\lambda = 1.55e^{-10}\ yr^{-1}$	8
$^{235}U \rightarrow {}^{207}Pb + 7\ {}^{4}He + 4\beta + Q$	$\lambda = 9.85e^{-10}\ yr^{-1}$	7
$^{232}Th \rightarrow {}^{208}Pb + 6\ {}^{4}He + 4\beta + Q$	$\lambda = 4.95e^{-11}\ yr^{-1}$	6
$^{147}Sm \rightarrow {}^{143}Nd + 1\ {}^{4}He + Q$	$\lambda = 1.07(9)e^{11}\ yr^{-1}$	1

The ^{4}He ingrowth equation assumes that there is no pre-existing ^{4}He in the grain being dated (Farley 2000). This assumption is acceptable for the following reasons: (1) ^{4}He inherited from a previous cooling history, due to incomplete degassing during reburial and metamorphism, is in most cases (although not always) unlikely because ^{4}He is highly diffusive at high temperatures in apatite and zircon, (2) the concentration of ^{4}He in the atmosphere is so low (5 ppm) that it would not make a critical contribution to ^{4}He in the grain, and (3) although it is possible for crustal or mantle ^{4}He to be incorporated within a grain in fluid inclusions, the concentration of ^{4}He in the fluids and/or the density of inclusions must be high to affect (U-Th)/He ages, except when ages are young (e.g. <120 Ma) (Farley 2000). Fluid inclusions hosting ^{4}He have been detected in apatites (Lippolt et al. 1994; Stockli et al. 2000), but this potential obstacle is remedied by selecting inclusion-free apatites (see section 3.10.2 Grain Selection).

Another assumption is secular equilibrium among all daughter products in the decay chain, which means the production of daughter product from the decay of a parent isotope equals the rate of decay of daughter product (Farley 2002). This is possible because the half-life of the daughter isotope is much shorter than the half-life of the initial parent isotope, such that the decay rate of parent and production of daughter becomes constant. For example, parent isotope ^{238}U has a half-life of ~4.47 Ga, while ^{230}Th, an intermediate daughter product within the ^{238}U decay chain (Figure 3.4), has a half-life of ~77 ka. Other intermediate isotopes within the ^{238}U decay chain have half-lives on the scale of minutes to days. Therefore, it takes approximately five half-lives, or 385 kyr for secular equilibrium between ^{238}U and ^{230}Th to be established (Reiners 2005) and the decay of intermediate isotopes is approximately equal to the decay of their initial parent. The effects of secular disequilibrium are only relative in (U-Th)/He thermochronometry when dating volcanic rocks younger than 10^3 –10^5 ka, or when (U-Th)/He dates reflect the age of rock formation, rather than a cooling age (Reiners 2005).

3.5 ^{4}He DIFFUSION IN ZIRCON AND APATITE

For any given mineral, solid-state diffusion processes are thermally activated (Dodson 1973) and the diffusion rate of ^{4}He is primarily temperature dependent. At temperatures higher than the T_c, radiogenic ^{4}He can diffuse in and out of a crystal lattice. The rate of ^{4}He diffusion also depends on the ^{4}He diffusivity properties of the mineral (Reiners and Brandon 2006;

Cherniak et al. 2009), including grain size (radius of the diffusion domain, *a*), grain geometry, chemical composition, and the density of lattice defects and/or radiation damage (Farley 2002). The grain is the diffusion domain (Wolfe and Stockli 2010) because diffusivity scales with grain size and the temperature dependence of diffusivity is characterized by the activation energy (E_a) (Farley 2000). Therefore, T_c can vary within a radiometric system as a function of grain size and cooling rate (Figure 3.5).

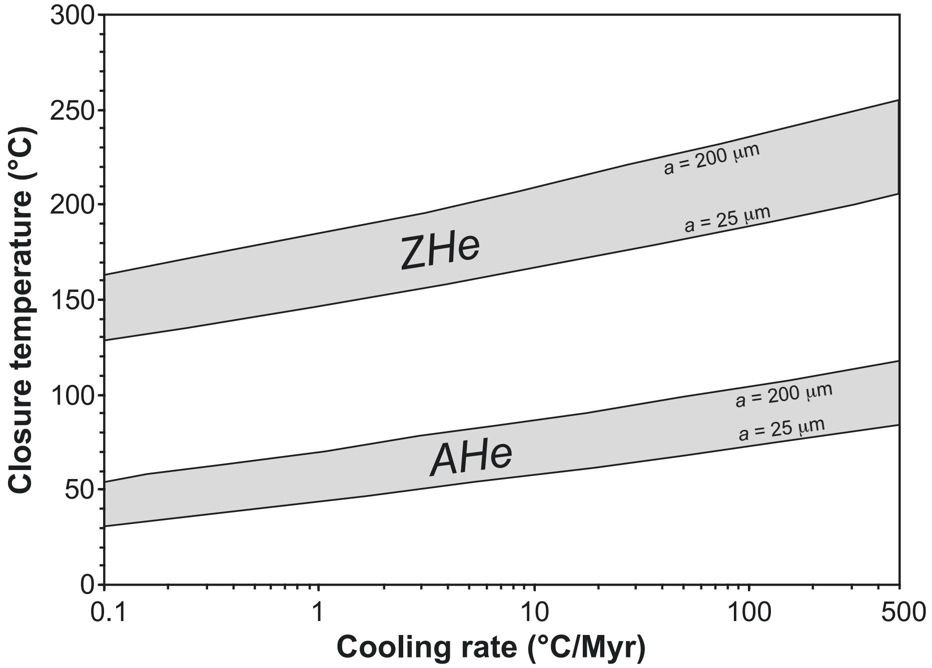

Figure 3.5 Closure temperatures calculated for AHe and ZHe systems (Dodson 1973) using a wide variety of reasonable grain sizes to account for different diffusion domain size (where *a* = diffusion domain size, roughly equal to the radius of a sphere) and different cooling rates (after Reiners 2005).

Diffusion increases at higher temperatures (Mancktelow 1997), following an Arrhenius relationship (e.g. Farley 2002; Reiners 2005; Reiners and Brandon 2006; Reiners and Shuster 2009). A linear relationship between diffusivity and temperatures on an Arrhenius plot suggests a simple ^{4}He diffusion pattern, where the slope is proportional to E_a and y intercept is $\ln(D_0/a^2)$ (e.g. Figure 3.6) (Farley 2000). Diffusion parallel to the *c*-axis is faster than diffusion perpendicular to it (Figure 3.6). To account for this discrepancy, the radius of the diffusion domain is modelled using a cylindrical geometry for the slow diffusion direction and a planar geometry for the fast diffusion direction (Cherniak et al. 2009).

Diffusivity of ^{4}He in zircon is determined in laboratory experiments by heating samples and measuring the incremental ^{4}He released (e.g., Farley et al. 1996; Wolf et al. 1996; House et al. 1997; Wolf et al. 1998; Reiners et al. 2000). Results of the step-heating experiments include ^{4}He diffusion and T_c for the ZHe system. Diffusion kinetics for zircon have activation energies (E_a) ranging from 163–173 kJ/mol and diffusivities at infinite temperature (D_o) ranging from 0.09–1.5 cm^2 s^{-1} (Reiners et al. 2002; Reiners et al. 2004; Reiners 2005). Equation 3.4 for the ZHe system yields T_c of ~130–250 °C for grains with 25–200 µm radius (Figure 3.6) (Reiners 2005), assuming a constant cooling rate of 10 °C/Myr (Reiners et al. 2002). T_c can be as low as ~20 °C for zircon grains that have severe radiation damage (Guenthner et al. 2013; Ault et al. 2018; Ault et al. 2019). Arrhenius plots can be helpful for analyzing the effect that temperature has on rate of diffusion. Except for in the very early stages of heating in the step-heating experiments, zircon displays a linear relationship between the logarithm of diffusion and the reciprocal of temperature in an Arrhenius plot (Reiners et al. 2005). A non-linear Arrhenius plot for zircon grains suggests a more complicated relationship, such as multiple diffusion mechanisms or diffusion domains (Farley 2002).

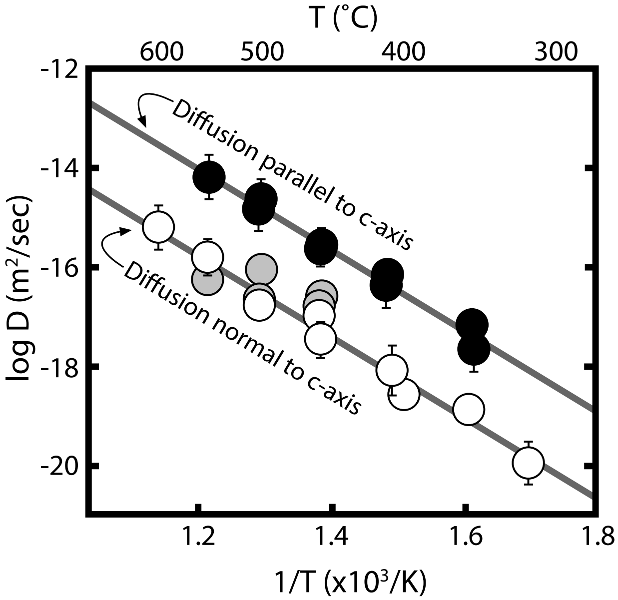

Figure 3.6 Arrhenius plot for helium diffusion in zircon (after Cherniak et al. 2009). Diffusion parallel to the c-axis (black circles) is faster than diffusion normal to the c-axis (white and grey circles).

Apatite crystals also follow a linear relationship on an Arrhenius plot, as diffusivity over a range of temperatures produces a line (Cherniak et al. 2009) (Figure 3.7). Since euhedral apatite crystals are prismatic or elongated along the *c*-axis, grain dimensions must be converted to an equivalent spherical radius (Wolf et al. 1996, 1998; Spiegel et al. 2007) to calculate the radius of the diffusion domain. ^{4}He diffusion and effective closure temperatures for the AHe system were also determined and calculated using step-heating experiments (Cherniak et al. 2009). For apatite crystals, diffusion kinetics have an activation energy (E_a) of 138 $\pm$ 2.1 kJ/mol, with log(D_0) = 1.5 $\pm$ 0.6 cm^{2}s$^-$. T_c range for the AHe system is ~30–120 °C (Ault et al. 2019; Farley 2000; Flowers et al. 2009; Gautheron et al. 2009; Shuster et al. 2006; Shuster & Farley 2009) for grains with 25–200 μm radius (Figure 3.7) (Reiners 2005), assuming a constant cooling rate of 10 °C/Myr (Farley 2000).

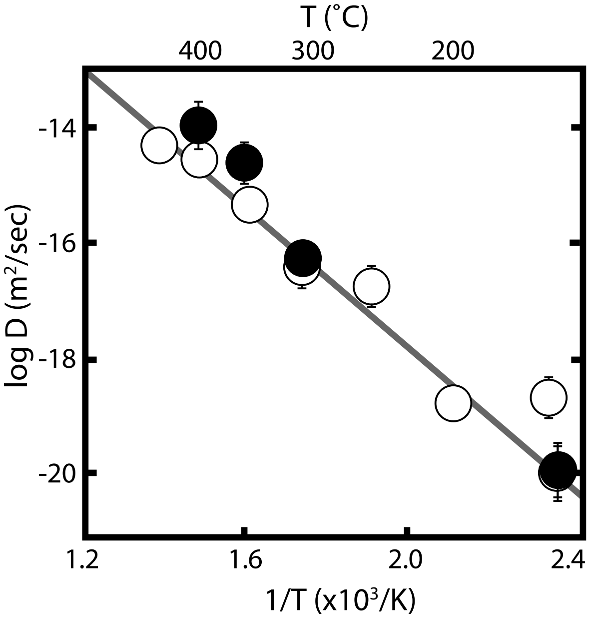

Figure 3.7 Arrhenius plot for helium diffusion in apatite (Cherniak et al. 2009). Diffusion normal to c-axis (white circles) is analogous to diffusion parallel to c-axis (black circles) with respective activation energies of 117±6 kJ/mol and 129±12 kJ/mol.

Several factors can cause an inhomogeneous distribution of ^{4}He in the mineral, including: the natural distribution of U, Th, and Sm in the grain; α ejection from the grain (see section 3.6.1); fluid inclusions (see section 3.10.2; and differential losses of ^{4}He from past thermal histories (e.g. Cherniak et al. 2009). Defects, such as dislocations, can affect diffusivity by altering the grain's crystalline structure and creating fast diffusion paths, influencing mobility and distribution of ^{4}He (Cherniak et al. 2009).

3.6 ALPHA-EJECTION

Kinetic energy released during radioactive decay of parent isotopes causes ^{4}He particles, also referred to as α-particles, to travel a 'stopping distance' (Ehlers and Farley 2003) from the decay site before coming to a halt. α-particle ejection occurs when α-particles produced within ~20 μm of the edge of the mineral are ejected out of the mineral and lost to the surrounding environment (Farley 2000). Conceptually, ejected α-particles will come to rest on the surface of a 20 μm sphere in some direction from the nucleus of the parent isotope (Figure 3.8). Stopping distances vary according to mineral and parent isotope as outlined in Table 3.2 (Ketcham et al. 2011), showing α-particle ejection distances of 5.39–22.25 μm in apatite and 4.76–18.43 μm in zircon. Since parent isotopes remain in the grain, the loss of α-particles causes an underestimation of the sample's age which is corrected in the age calculation.

Table 3.2 Mean α-particle stopping distances for parent isotopes in apatite and zircon crystals (Ketcham et al. 2011).

Mineral	Formula	Density (g/cm^3)	Mean stopping distance (μm)			
			^{238}U	^{235}U	^{232}Th	^{147}Sm
Apatite	$Ca_5(PO_4)_3F$	3.20	18.81	21.80	22.25	5.93
Zircon	$ZrSiO_4$	4.65	15.55	18.05	18.43	4.76

3.6.1 ALPHA-EJECTION AND AGE CORRECTION

Since α-ejection correction is calculated based on surface area to volume ratio (Farley at al. 1996), the magnitude and uncertainty of the correction is determined by the volume and geometry of a grain (Reiners 2005). The volume of the grain controls the probability of ejection, for example, in a large grain the outer 20 μm is a lesser percentage of the total volume, resulting in a smaller percentage of probable ejections and a smaller correction value. The smallest acceptable size for a grain to be dated is ~60 μm width for zircon (Reiners 2005) and 75 μm in width for apatite (Ehlers and Farley 2003). The geometry of a grain determines the surface area over which α-particles can be ejected. For example, it is more likely for α-particles to be ejected at the corner of a crystal (>50%) than along a flat face (~50%) (Farley 2002).

Anhedral grains with high surface area to volume ratios result in larger corrections compared to euhedral grains with smaller surface area to volume ratios (Reiners 2005). Therefore, ideal zircon grains are euhedral tetragonal prisms with well-preserved pyramidal terminations and ideal apatite grains are euhedral hexagonal prisms (Ehlers and Farley 2003).

The following equations were used to correct for α-ejection (Reiners 2005):

$$F_{He} = 1 + A_1\beta + A_2\beta^2 \tag{3.12}$$

where F_{He} is the correction factor, β is the surface-area-to-volume-ratio of the grain under analysis, and A_1 and A_2 are diffusion parameters specific to the isotope, mineral, and geometry calculated by Hourigan et al. (2005). Since U and Th have different ejection distances, a correction factor must be calculated for each isotope, then combined to calculate a bulk correction value, F_{BHe}, with weighted ratios of U and Th (Reiners 2005):

$$F_{BHe} = a_{238}\,{}^{238U}F_{He} + (1 - a_{238})\,{}^{232Th}F_{He} \tag{3.13}$$

where,

$$a_{238} = \left(1.04 + 0.245\left(\frac{[Th]}{[U]}\right)\right)^{-1} \tag{3.14}$$

The raw age is corrected by applying bulk correction (Farley et al. 1996):

$$t_{corrected} = \frac{t_{uncorrected}}{F_{BHe}} \tag{3.15}$$

Assumptions for α-ejection equations are: (1) implantation from surrounding grains is insignificant, and (2) there is homogeneous spatial distribution of U and Th within the mineral (Spiegel et al. 2009).

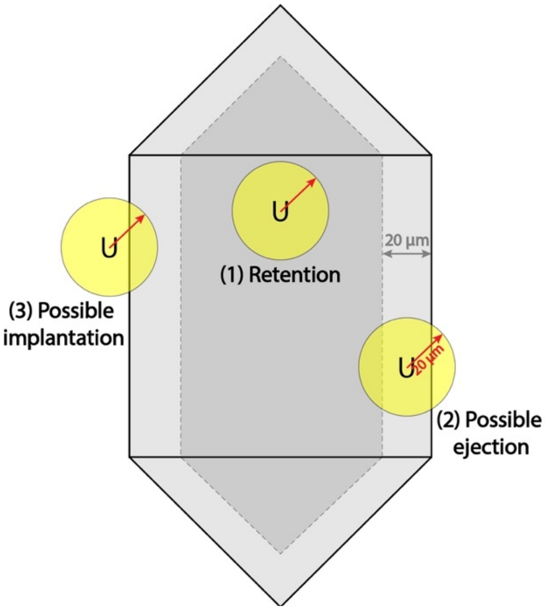

Figure 3.8 Possible outcomes of α-ejection including (1) retention of the α particle within the grain if the parent nucleus is located more than the stopping distance away from the edge of the crystal, or the α particle travels away from the grain edge towards the centre of the grain, (2) ejection of the α particle out of the grain if the parent nucleus is located within one stopping distance of the crystal boundary and the α particle travels towards the grain edge, and (3) implantation of an α particle ejected from a neighbouring grain, affecting only the outermost 20 μm of the grain under study (modified from Farley 2002).

3.6.2 IMPLANTATION OF ALPHA PARTICLES

A process called implantation may occur, where α-particles ejected from one grain are implanted in a neighbouring grain during decay, possibly affecting the outermost 20 µm of a crystal (Figure 3.8) (Farley 2002). For this to occur, two grains essentially must be in contact with one another. Implantation is rare because the concentration of the mineral being dated is usually very small within the host rock (Farley 2002), such that it is unlikely for two grains to be in contact. Therefore, implantation is statistically insignificant and is not considered in age calculations (Ehlers and Farley 2003).

3.7 HELIUM PARTIAL RETENTION ZONE (HePRZ)

The partial retention zone (PRZ) or helium partial retention zone (HePRZ) is defined as the range of temperatures or depths where decay products, such as ^{4}He, are only partially retained due to thermally activated diffusion (Reiners and Brandon 2006). Theoretically, the crust can be separated into three zones (Figure 3.9): (1) A lower limit at great depth and high temperature, referred to as the zone of full loss, where ^{4}He completely diffuses out of the mineral and is lost to the environment. The mineral is considered an ‘open system’ (Braun et al.

2006) and resulting ages are null (Farley 2002). (2) An upper limit at relatively shallow depths referred to as the ‘blocking temperature’, which is also the onset of closed-system behaviour (Braun et al. 2006). At this temperature, ^{4}He is fully retained and ages are finite, reflecting the rate of, or time since cooling below the blocking temperature (Farley 2002). (3) A middle limit between upper and lower limits known as the HePRZ, where daughters are neither fully retained nor fully lost (Reiners and Brandon 2006). The T_c lies within the boundaries of the HePRZ where there is some retention of daughters (Figure 3.9) (Braun et al. 2006).

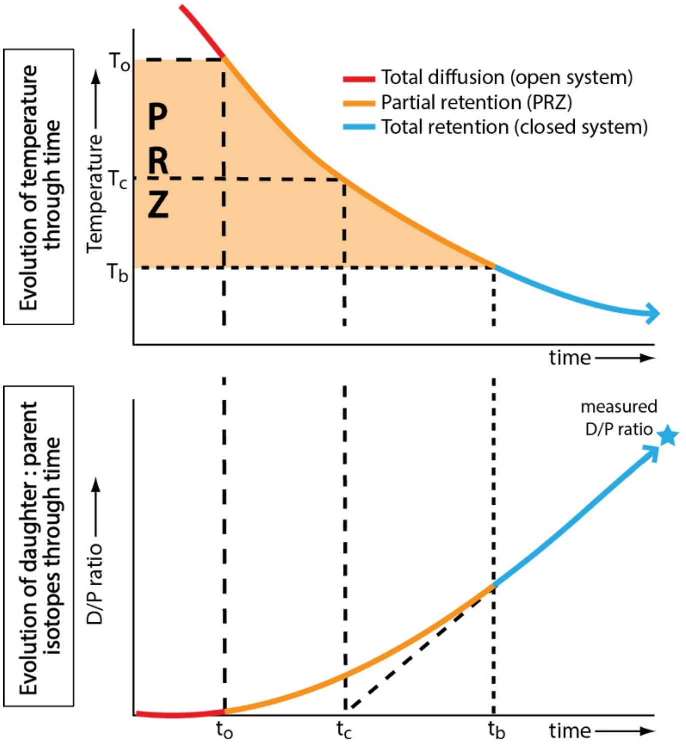

Figure 3.9 Schematic representations of (top graph) the evolution of temperature, showing the temperature at open system (T_o), closure temperature (T_c), blocking temperature (T_b), and location of the PRZ, and (bottom graph) the evolution of daughter to parent isotopes, compared to time (x-axis), including the timing of apparent thermochronological age of the system (t_c), time of initial partial retention (t_o), and time of blocking when the system fully closes (t_b) (modified from Braun et al. 2006).

The upper and lower boundaries of the HePRZ correspond to the temperatures at which 10% and 90%, respectively, of ^{4}He is retained within the crystal lattice (Wolf et al. 1998). (U-Th)/He ages vary with temperature/depth and time a sample may have spent in the HePRZ. The amount of ^{4}He lost depends on the rate at which the sample cooled through the HePRZ. Samples that cool rapidly lose little ^{4}He, whereas samples that cool slowly spent more time in the HePRZ and lose more ^{4}He. The slower a grain cools increases its susceptibility to other factors that can affect age, including zoning (section 3.8), grain size, and variability of kinematic parameters (Ehlers and Farley 2003). It should be noted that the specific temperature defining these zones can fluctuate because T_c can vary as a function of grain size, cooling rate (Figure 3.5) (Lisker et al. 2009), radiation damage (Guenthner et al. 2013; Ault et al. 2018; Ault et al. 2019) and geothermal gradient (Ehlers & Farley 2003). The following depths apply to a typical geothermal gradient of 20–30 °C/km. For apatites, the lower limit of the crust ranges from depths ~1.5 km (40 °C to surface temperatures), the upper limit corresponds to depths of 4 km (> 80 °C) (Farley 2002) and the middle zone, the HePRZ, corresponds to depths between~2–3 km (~40–80 °C) (Farley et al. 1996; Farley 2000; Stockli et al. 2000). For zircon, the lower limit of the crust ranges from depths of ~4 km (~130 °C to surface temperatures), the upper limit corresponds to depths ~8 km (>200 °C), and the middle zone, the HePRZ, corresponds to depths between ~5–8 km (~130–200 °C) (Stockli and Wolfe 2009).

3.8 ZONING OF PARENT ISOTOPES

It is possible for parent isotopes to be zoned within grains. Assuming that the distribution of U-Th is homogeneous can result in errors of up to ∼30% in α-ejection corrections (Hourigan et al. 2005). Zoning is more common and better documented in zircons than in apatites – any magmatic zircons, or zircons that underwent high grade metamorphism likely have zoning (e.g. Guenthner et al. 2013; Hourigan et al. 2005; Meesters and Dunai 2002). Zoned zircons can have U-rich cores, resulting in high ^{4}He retention and overestimated ages; or U-rich rims, which experience more α-ejection and produce underestimated ages (Hourigan et al. 2005). Models using spherical grain shapes provide retentivity values (α-ejection correction factors) that are accurate to within ~2.5%, while models using tetragonal prisms with pyramidal terminations, which is more comparable to actual zircon grain morphologies, provide values that are accurate to ~1% (Hourigan et al. 2005). Hourigan and coworkers (2005) introduced a new parameter known as the bulk ^{4}He retentivity for an entire grain, which estimates the effect of zoning for grain morphologies using a weighted average from integration over a 3-dimensional grid, then by relating bulk ^{4}He retentivity of a grain to its surface-area-to-volume ratio. Models focus on quickly cooled samples and therefore do not address the combined effect of α-ejection and ^{4}He diffusion.

3.9 RADIATION DAMAGE

Radioactive decay of unstable elements, such as U and Th, can damage the crystal structure of apatite or zircon, which alters ^{4}He diffusion and annealing properties of the mineral (Guenthner et al. 2013; Reiners et al. 2005). Radiation damage appears in the form of isolated defects and vacancies within the crystal structure (Reiners et al. 2005). The main cause of radiation damage is α-decay (e.g. Shuster et al. 2006; Flowers et al. 2009), but damages are also produced by: (1) ionization from β and γ decay; (2) displacement of atoms due to heavy nuclide recoil during α decay; (3) atomic stopping of α particles; and (4) formation of nuclear fission tracks (Ault et al. 2018; Rios et al. 2000; Trachenko et al. 2002; Donelick et al. 2005). The amount of radiation damage in a crystal will increase with time at a rate proportional to the parent nuclide concentration but will also decrease in response to heating (Shuster and Farley 2009).

Radiation damage in zircon is a physical alteration of the crystal structure as a result of high parent nuclide concentration (Wolfe and Stockli 2010). Damage can reduce the ^{4}He retentivity of the crystal lattice (Reiners 2005), causing ^{4}He loss (Farley 2002; Nasdala et al. 2004; Reiners 2005) and underestimated ages (Figure 3.10). A low α dose of ~1 x 10^{16} to 5 x 10^{17} α/g has little impact on diffusion overall and can actually decrease diffusivity where damage zones block diffusion pathways along the c-axis (Reiners 2005; Reiners et al. 2004; Ault et al. 2019). An α dose greater than ~2 x 10^{18} α/g damages the crystal structure so much that damage zones become interconnected, forming pathways for ^{4}He to be transported and diffuse rapidly (Nasdala et al. 2004; Reiners 2005; Guenthner et al. 2013; Ault et al. 2019). Radiation damage accumulates in grains with old ages of 100s of Ma (Wolfe and Stockli 2010), grains that experienced slow cooling (Ault et al. 2019), and grains with relatively high U and Th concentrations (Reiners 2005).

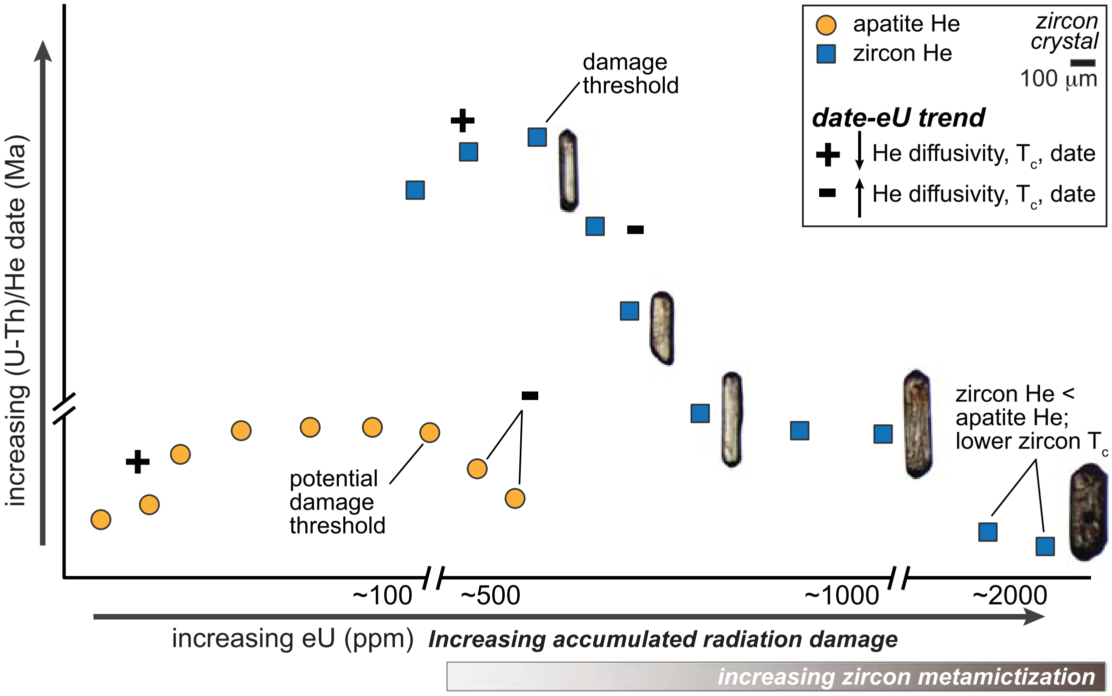

Figure 3.10 Patterns of relative individual apatite and zircon (U–Th)/He dates as a function of relative effective U concentration (eU), where eU is a proxy for radiation damage. This figure assumes that all aliquots experienced the same thermal history, which was that of slowly cooled bedrock. Damage in zircons with high eU values and high radiation damage is visible in the crystals. (Modified from Ault et al. 2019).

In apatite, radiation damage has a trapping effect where damages to the lattice structure obstruct diffusion pathways and reduce diffusion (Shuster and Farley 2009). This trapping causes diffusion to decrease while ^{4}He retentivity increases over time with radiation damage (Shuster et al. 2006; Flowers et al. 2007) possibly causing overestimated ages (Figure 3.10). At high eU values, a damage threshold is reached causing the size of damage sites to decrease, which decreases ^{4}He retentivity, T_c, and AHe ages (Figure 3.10) (Recanati et al. 2017; Ault et al. 2019). Damage in apatites is primarily a result of α-recoil (Willett et al. 2017). Experiments by Shuster and Farley (2009) revealed that increased radiation damage causes a higher E_a and $\ln(D_o/a^2)$ for diffusion in apatites resulting in a higher T_c, while annealing causes the opposite and a lower T_c (Figure 3.11).

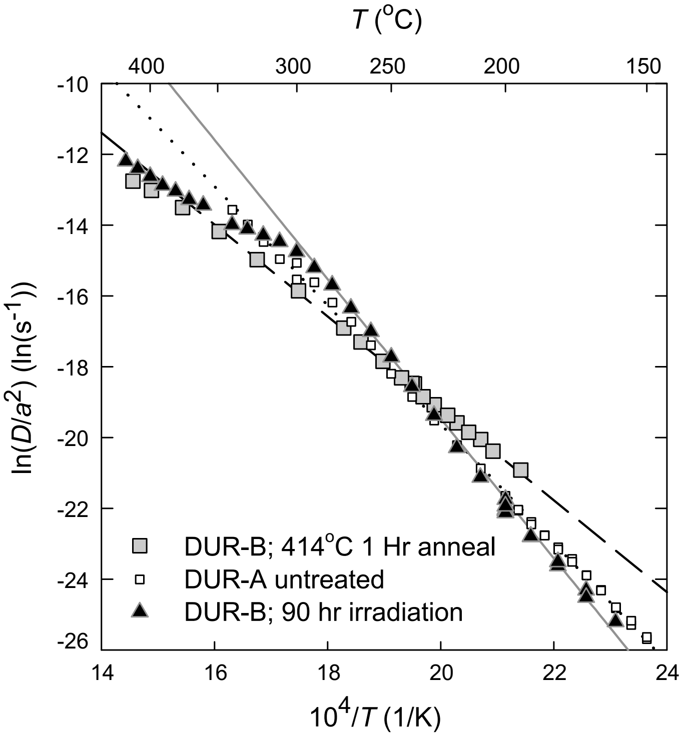

Figure 3.11 He diffusion Arrhenius plot for Durango apatite showing results from DUR-A (Farley 2000) as the control experiments without any time in the nuclear reactor or thermal annealing (white squares), DUR-B subjected to 90 h of neutron irradiation (triangles) and DUR-B subjected to 1 h of annealing at 414 °C (gray squares). Lines indicate helium diffusion kinetics, where the dashed line represents DUR-B 90hr irradiation diffusion kinetic, the dotted line represents DUR-A diffusion kinetic, and the full line represents DUR-B 414 °C 1 hr anneal diffusion kinetic. Neutron irradiation causes Arrhenius arrays to rotate clockwise, yielding higher closure temperatures, while annealing causes the reverse (Shuster and Farley 2009).

Existing models for interpreting (U-Th)/He ages use empirical models of apatite fission track (AFT) annealing (Flowers et al. 2009; Gautheron et al. 2009) to quantify the net effects of radiation damage (Willett et al. 2017), which assume that AFT annealing and α-recoil damage anneal at the same rate. According to measurements of optical properties (Ritter and Märk 1986), fission tracks anneal more readily than α-recoil damage. Previous diffusion models might overestimate the rate of damage annealing and underestimate the (U–Th)/He age (Figure 3.12) (Willett et al. 2017), such as the radiation damage accumulation and annealing model (RDAAM) that is incorporated into the *HeFTy* software used to extract thermal histories from our samples (Flowers et al. 2009). Willett et al. (2017) introduced a new α-damage annealing model (ADAM) to quantify an internally consistent and more direct relationship between α-recoil damage, annealing and He diffusivity (Figure 3.12), but this has not yet been incorporated into the *HeFTy* software.

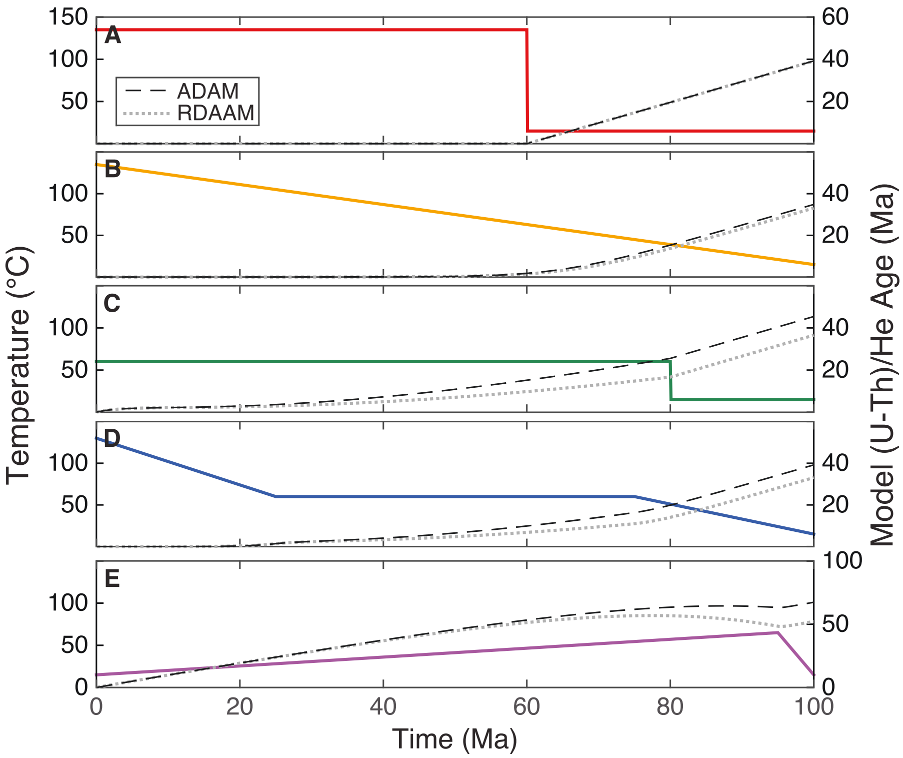

Figure 3.12 Comparing ages from ADAM (dashed line) to RDAAM (dotted line), against five temperature-time paths from Wolf et al (1998) (colored lines). Ages are nearly identical when temperature is mostly outside the HePRZ, as observed in graphs A and B. When there are long residence times in the HePRZ, the RDAAM underestimates ages compared to the ADAM (Willett et al. 2017).

3.10 ANALYTICAL PRODECURE

Samples were selected based on rock type likely to contain apatites and zircons (e.g. gneisses, tonalites) and location to complete four coast-perpendicular transects extending 32 – 132 km inland from the coastline. Transects extended inland to quantify the thermal evolution of the extension and rifting process and transects were spread out across the margin between the latitudes of Makkovik and Saglek, covering an area of ~61,750 km^2, to quantify the thermal evolution along strike of the margin. These samples were processed according to the (U-Th)/He dating analytical procedure, including three steps that are summarized in the following section: (1) crystal isolation and grain selection, (2) measurement of grain dimensions and preparation, or packing of selected grains, and (3) ^{4}He degassing, crystal dissolution, and parent (or solid) measurement (Figure 3.13).

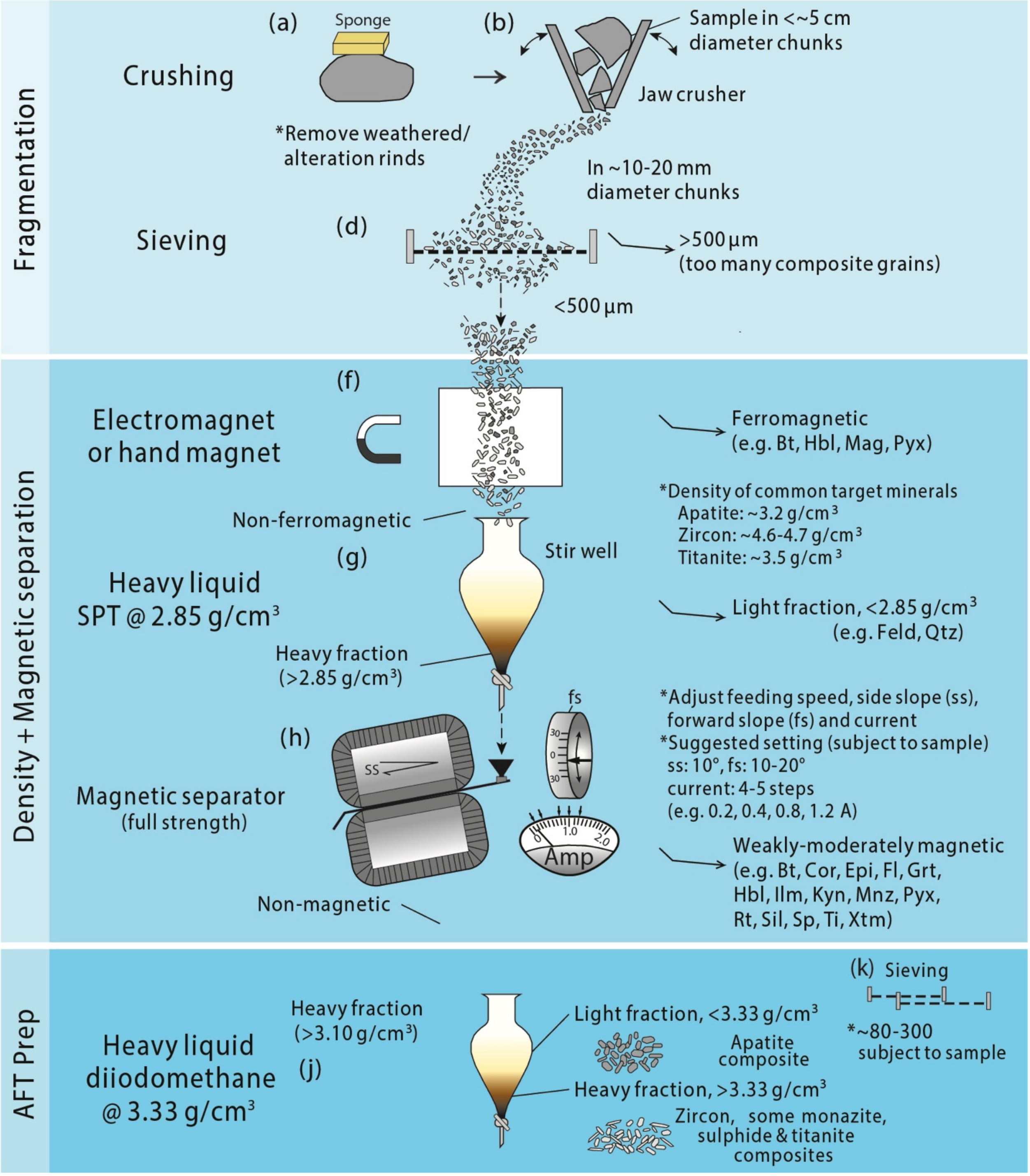

Figure 3.13 (U-Th)/He sample preparation flow chart including the steps required for the separation of minerals suitable for (U-Th)/He and AFT analysis (modified from Kohn et al. 2019).

3.10.1 CRYSTAL ISOLATION

The aim of crystal isolation is to extract datable zircon and apatite crystals from the rock mass. The process began with rock fragmentation using a hammer and a jaw crusher to crush the sample in gravel to sand-size particles then retrieve the >250 μm fraction through sieving. This sandy fraction was chemically cleaned using 10% acetic acid solution to remove carbonate particles, then a 3% hydrogen peroxide solution to remove clay minerals. The clean fraction was immersed in either lithium metatungstate (LMT), a heavy liquid with a density of 2.95 g/cm^3, or lithium heteropolytungstate (LST), a heavy liquid with a density of 2.8 g/cm^3, to separate the heavier minerals like apatites (3.16-3.22 g/cm^3) and zircon (3.9-4.8 g/cm^3) which sink, from the lighter minerals, such as quartz (2.65 g/cm^3) and feldspars (2.56 g/cm^3), which float. Once samples were dried, a hand magnet was used to remove heavy, magnetic grains. Nine samples collected along the Hopedale transect during the 2018 field season were processed as described at Dalhousie University, while 23 samples collected by the GSC during Operation Torngat (1967–1971) were processed by Overburden Drilling Management (ODM) in Ottawa. All samples were processed through a Frantz magnetic separator at intensities of 0.2, 0.4, 0.8, and 1.2 A to remove magnetically susceptible minerals including metallic oxides and some micas.

3.10.2 GRAIN SELECTION

Remaining heavy, non-magnetic fractions were inspected using a Nikon SMZ1500 stereoscopic microscope, under reflected, refracted and cross-polarized light to select suitable apatites and zircons for (U-Th)/He dating. Ideal apatite and zircon grains are wider than 70 μm, euhedral, transparent, and free of cracks and inclusions (Figure 3.14) (e.g. Reiners 2005). Euhedral grains were selected because they are consistent with geometries for α-particle ejection correction (described in section 3.5). Inclusions were avoided because they may contain solid radiogenic materials that likely produce α-particles, resulting in biased age. Inclusions can either be liquid or solid, and when solid, they are often composed of zircon. Therefore, zircon grains with inclusions were accepted if there were no other suitable grains, but apatite grains with inclusions were completely avoided because small zircon inclusions within the grain would have a high impact on data. Grains with fractures were discarded, as fractures act as a pathway for helium to diffuse out of the crystal during cooling, resulting in an underestimated age.

Grains from each sample were assessed using the same Nikon SMZ1500 DS-Fi2 transmitted light stereoscopic microscope, but at x106 magnification and under plane- and cross-polarized light. Out of the 32 samples analyzed, 27 contained suitable zircons and apatites. Five apatites and five zircons were selected for each sample. Each grain was photographed, and its length and width measured using imaging software NIS Elements version 4.10 (Figure 3.14). Grains were individually packed in 1 mm x 1 mm Platinum (Pt) foil tubes for protection from direct laser contact to prevent from shattering or uneven heating during degassing. Packets were placed in separate vials and labelled in preparation for dating.

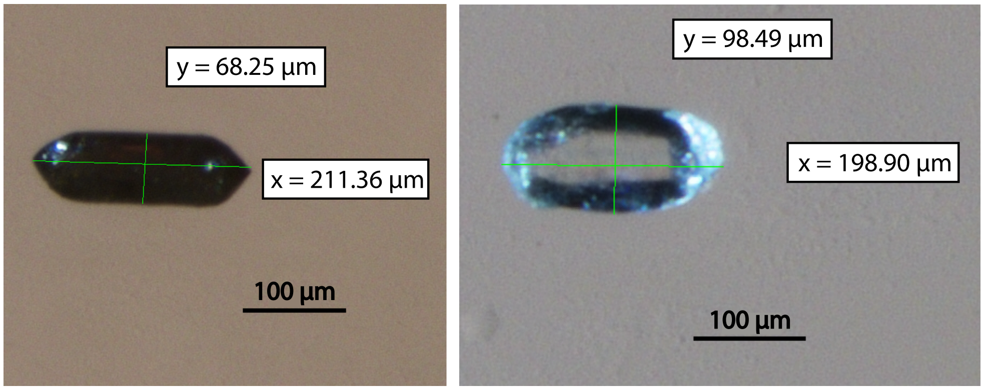

Figure 3.14 Example of zircon grain from sample 69FQ332 (left) and apatite grain from sample K0008 (right). Lengths (x) and widths (y) measured along green lines.

3.10.3 ISOTOPE EXTRACTION AND MEASUREMENT

The isotope extraction and measurement were carried out by Dr. Roman Kislitsyn at Dalhousie University. Parent and daughter isotopes were extracted in two phases. First, daughter products (^{4}He) were extracted at Dalhousie's Noble Gas Extraction Laboratory using an in house-built He extraction line with a 45 W diode laser and Pfeiffer Vacuum Prisma Pro quadrupole mass-spectrometer. Each grain, referred to as an aliquot, was unpacked, dissolved, and spiked (as described in section 3.10.3.2). Then, parent isotopes, (^{238}U, ^{235}U, ^{232}Th and ^{147}Sm) were measured using an iCAP Q inductively coupled plasma mass spectrometer (ICP-MS) at Dalhousie's Health and Environments Research Centre (HERC) Laboratory.

3.10.3.1 Laser Extraction and Measurement of Helium

^{4}He was extracted from five apatite grains and five zircon grains from each sample containing suitable grains for dating. Pt foil packets containing the grains were placed on a small planchet within a vacuum sealed chamber. The laser was directed at each grain in sequence, heating it to 1250 °C for 10 minutes (zircon) or 1050 °C for 5 minutes (apatite) to release the gases from the grains. A precisely measured aliquot ^{3}He spike was added to the gas and then the gas was frozen to 16 K using a cryotrap (or cryogenic pump). The gas was purified by heating it to 37 K to release the He while other active (heavier) gases remained frozen. The heated gas was directed to a quadrupole mass-spectrometer, which measured the ratio between ^{3}He and ^{4}He for each grain.

Measurements were made over 32 cycles, producing a mean ratio and a standard deviation. For zircon, this procedure was repeated to extract any ^{4}He remaining in the grain until the amount of He in the re-extraction was less than 1% of the total He extracted (usually 3–4 times). For apatites, there was only one re-extraction. For both apatites and zircons, measurement error typically ranges from 1.5–2% (1σ). The amount of ^{4}He from the grain was calculated using the measured ^{4}He/^{3}He ratio, the quantity of spike added, and the ratio of ^{4}He/^{3}He from calibrated ^{4}He standard. To ensure reproducibility and reliability of the data, samples were analyzed in groups of 36 with two Durango apatite standards or two Fish Canyon tuff zircon standards.

3.10.3.2 Extraction of U, Th, and Sm Isotopes

Measurement of parent isotopes ^{238}U, ^{235}U, ^{232}Th, and ^{147}Sm, involves dissolving grain in acidic solutions. Following ^{4}He extraction, metal packets were opened, and each sample was spiked with 100 μL of a solution containing 6.79 ng/g (ppb) ^{235}U, 3.77 ng/g ^{230}Th, and 34.51 ng/g

^{149}Sm. According to standard dissolution procedures, zircons were dissolved with the spike solution in high pressure dissolution vessels in concentrated HF and HNO_3 at 200 °C for 96 hours, while apatites were dissolved with the spike solution in 7N HNO_3 at 80 °C for 1.5 hours. Isotopic ratios between spike and sample were measured using iCAP Q ICP-MS and the amount of isotope was calculated based on the ratio as explained in section 3.10.3.3. Raw data were reduced using Helios software package (Kislitsyn 2020; 2008; 2007). To ensure analytical precision, spiked and acid blanks were analyzed alongside the samples.

3.10.3.3 Isotope Dilution Technique and Calculations

Isotope dilution technique involves comparing a specific isotope in a sample to a known isotopic ratio in a spike solution. For example, to measure the natural ratio of ^{238}U/^{235}U, a grain is dissolved and mixed with a spike solution containing a known ratio of ^{238}U/^{235}U prior to ICP-MS analysis. The quantity of the target isotope in a spiked solution is calculated using the following equation (Attendorn and Bowen 1998):

$$N_w = S_w \left(\frac{W_N}{W_s}\right)\left(\frac{Ab_S^A - R_M \times Ab_S^B}{R_M \times Ab_N^B - Ab_N^A}\right) \qquad \textbf{\textit{(3.16)}}$$

where N_w is the mass of the natural isotope *A* (the isotope of interest), S_w is the mass of spike isotope *B,* and W_N and W_s are the isotopic weights of the natural isotope and spike isotope respectively, Ab_S^A, Ab_S^B, Ab_N^B and Ab_N^A are the relative abundances of isotopes *A* and *B* in the spike and in nature, and R_M is the ratio of isotopes *A* and *B* acquired by the ICP-MS. The N_w value is divided by the mass of the grain being analyzed to find concentration, which is divided by the molar mass of the specific isotope of interest to calculate molar concentration.

3.11 (U-Th)/He RESULTS SUMMARY

In total, 135 ZHe and 135 AHe single-grain cooling ages were produced from 32 bedrock samples distributed along four transects extending inland from the coastline at the approximate latitudes of Saglek (~79 km length), Nain (~132 km length), Hopedale (~92 km length), and Makkovik (~32 km length), Newfoundland (Figure 3.15, Table 3.3). Five aliquots were dated for each sample yielding five single grain ages per samples, except for samples z69TA210 (Saglek transect), a69FQ335 (Nain transect) in which only four grains could be dated. ZHe single-grain ages range between 5.4 ± 0.03 Ma and 1612.7 ± 26.5 Ma and AHe between 18.0 ± 0.09 and 937.5 ± 3.32 Ma.

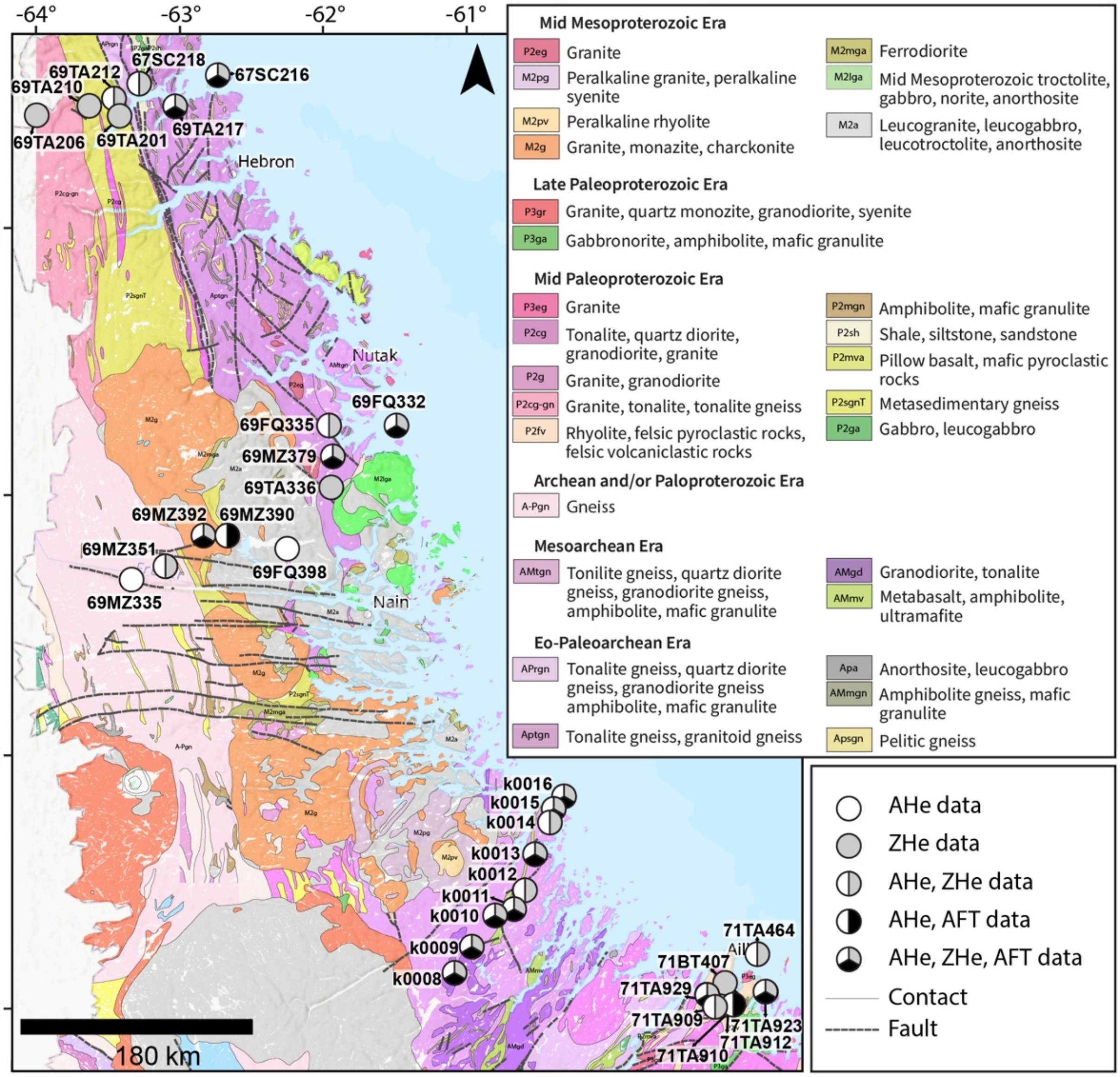

Figure 3.15 Geological map of the study area including symbols identifying sample locations and which type of data was obtained from each sample. (Geology: Geological Survey of Canada 2011).

Table 3.3 Sample list. Abbreviations are AHe, apatite (U-Th)/He; ZHe, zircon (U-Th)/He; AFT, apatite fission-track; Hnb, hornblende; Bio, biotite. The colour coding indicates the samples that have been dated (green) or not (grey) by the different thermochronological methods.

Transect Location	Sample Number	Latitude (°)	Longitude (°)	Lithology	Elevation (m)	AHe	ZHe	AFT
Saglek	67SC216	58.560891	-62.734905	Pegmatitic granite	16	🟩	🟩	🟩
	69TA217	58.445521	-63.03336	Garnet Gneiss	58	🟩	🟩	🟩
	67SC218	58.529892	-63.282755	Quartzites	615	🟩	🟩	⬛
	69TA212	58.47455	-63.460759	Mylonites	980	🟩	🟩	⬛
	69TA201	58.411542	-63.41939	Mylonites	610	⬛	🟩	⬛
	69TA210	58.448614	-63.631128	Mylonites	733	⬛	🟩	⬛
	69TA206	58.415302	-63.991759	Mylonites	877	⬛	🟩	⬛
Nain	69FQ332	57.265306	-61.488278	Granite	249	🟩	🟩	🟩
	69FQ335	57.263794	-61.957524	Migmatite Bio+Hnb	60	🟩	🟩	⬛
	69MZ379	57.149266	-61.932681	Migmatite Bio+Hnb	223	🟩	🟩	⬛
	69FQ398	56.796566	-62.249766	Diorite or Gabbro	502	🟩	⬛	⬛
	69MZ390	56.848991	-62.669949	Granodiorite	526	🟩	⬛	🟩
	69TA336	57.030891	-61.945188	Granite Bio	420	⬛	🟩	⬛
	69MZ392	56.846223	-62.831864	Granodiorite	534	🟩	🟩	🟩
	69MZ351	56.730363	-63.096312	Mylonitized granulite	536	🟩	🟩	⬛
	69MZ335	56.67772	-63.337447	Granitoid gneiss	512	🟩	⬛	⬛
Hopedale	k0016	55.842306	-60.324111	Migmatitic granodiorite	80	🟩	🟩	🟩
	k0015	55.792222	-60.395917	Granite	45	🟩	🟩	🟩
	k0014	55.740639	-60.419667	Gneiss	241	🟩	🟩	⬛
	k0013	55.611972	-60.525667	Migmatitic orthogneiss	84	🟩	🟩	🟩
	k0012	55.469583	-60.600083	Orthogneiss	162	🟩	🟩	⬛
	k0011	55.396222	-60.671333	Granite	231	🟩	🟩	🟩
	k0010	55.37075	-60.801556	Migmatitic orthogneiss	50	🟩	🟩	🟩
	k0009	55.248194	-60.963056	Granite or syeno-granite	117	🟩	🟩	🟩
	k0008	55.143722	-61.082111	Tonalite gneiss	317	🟩	🟩	🟩
Makkovik	71TA464	55.220033	-58.976276	Syenite	33	🟩	🟩	⬛
	71TA923	55.068319	-58.910698	Granite	4	🟩	🟩	🟩
	71BT407	55.101538	-59.196939	Granodiorite	0	⬛	🟩	⬛
	71TA910	55.033283	-59.170119	Granite Hnb	104	🟩	⬛	⬛
	71TA912	55.018116	-59.142955	Granodiorite Hnb	135	🟩	⬛	🟩
	71TA929	55.059172	-59.328118	Granite Hnb+Bio	163	🟩	🟩	🟩
	71TA909	55.011069	-59.275543	Granodiorite Hnb+Bio	193	🟩	🟩	⬛

3.12 SAGLEK TRANSECT: (U-Th)/He RESULTS

The Saglek transect consists of seven samples at the approximate latitude of Saglek, Newfoundland (58.474444°, -62.654167° at the Saglek Airport) (Figure 3.15). Samples were collected by the Geological Survey of Canada (GSC) between 1967 and 1971 during 'Opération Torngat', retrieved from the Taylor Collection of the GSC sample archives in Ottawa, (Ontario, Canada) and processed at the commercial facility Overburden Drilling Management in Ottawa for mineral separation. Samples were selected based on both the rock type (felsic igneous and metamorphic rocks which are generally fertile in apatite and zircon) and their location relative to the coastline to build coast-perpendicular transects. Selected rocks include pegmatitic granite, garnet gneiss, quartzite and mylonite. Geographically, the transect extends ~79 km inland from the coastline at sea level and samples range in elevation from 16 to 980 m above sea level (Figure 3.16).

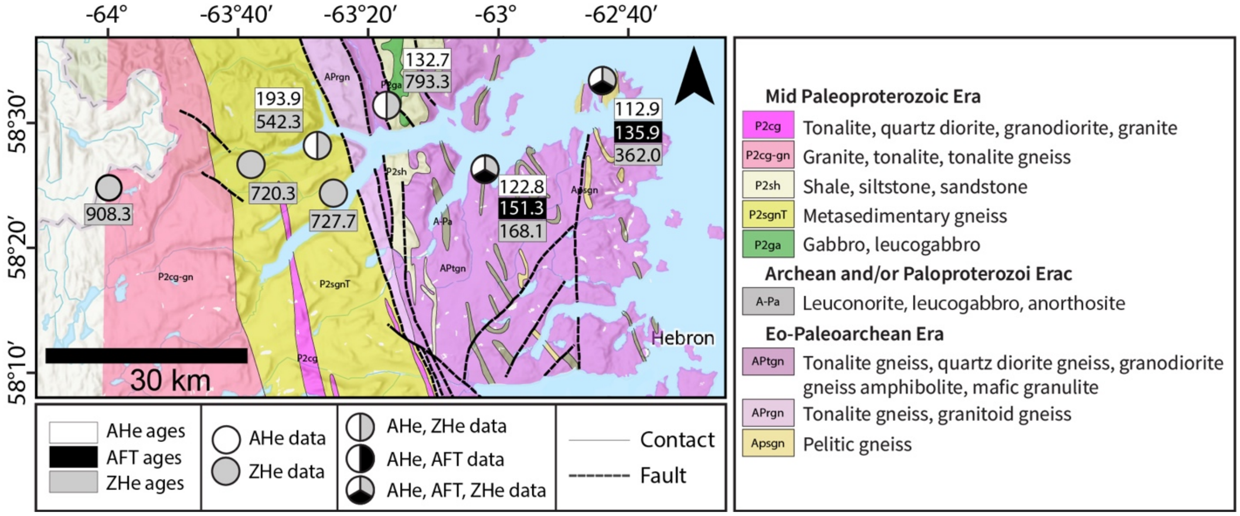

Figure 3.16 Regional geology, topography, sample locations and ages (including ZHe, AHe and AFT) along the Saglek transect (Geology: Geological Survey of Canada 2011).

3.12.1 SAGLEK TRANSECT: ZHe RESULTS

All seven samples collected for the Saglek transect contained suitable zircons to produce five aliquots, totaling 34 single grain ZHe cooling ages, as one aliquot (z69TA210-2) produced an unusable age with a negative value (Table 3.58). In this transect, ZHe ages range from 82.7 ± 0.4 Ma to 1612.7 ± 26.5 Ma. Each of the following paragraphs includes a description of the data for each sample, as well as analysis of which aliquots will be used to calculate the mean age of the sample and the error of the mean based on single-grain age dispersion. Mean age error was calculated according to the following equation:

$$Mean\ age\ error = \frac{STD\ of\ selected\ aliquots}{\sqrt{number\ of\ aliquots}} \tag{3.17}$$

Sample z67SC216

Sample z67SC216 is a pegmatitic granite, collected ~3.7 km from the coastline at an elevation of ~16 m above sea level (Figure 3.15). Zircons were very scarce in this sample. Aliquots range in age from 217.7 ± 1.05 Ma – 510.3 ± 2.37 Ma (Table 3.58, Table 3.4). Three aliquots are within 20% of the median, including aliquot 1, 4, and 5. Ages are unevenly dispersed between end members and have no obvious outliers (Table general results and your smaller table below). In all combinations of ages, there is overlap given the very large single grain ages standard deviation (STD) (Table 3.4). Column 1 (Table 3.4) with the largest STD yields a similar mean age to column 4 (Table 3.4). For this sample, the mean was plotted using column 4, as this column gave a mean age using at least 3 aliquots with the smallest standard deviation.

Table 3.4 Combinations of aliquot ages showing resulting mean ages, standard deviations (STDs) and error for sample z67SC216. The cells highlighted in green are the values used for this sample.

	1	2	3	4
Aliquot ages (Ma)	337.0	337.0	337.0	407.6
	510.3	217.7	217.7	341.3
	217.7	407.6	341.3	337.0
	407.6	341.3		
	341.3			
Mean age (Ma)	**362.8**	**325.9**	**298.6**	**361.9**
STD (Ma)	**107.2**	**79.0**	**70.2**	**39.6**
Mean age error (Ma)	**47.9**	**39.5**	**40.5**	**22.6**

Sample z69TA217

Sample z67SC217 is a garnet gneiss, collected ~23 km from the coastline at an elevation of ~58 m above sea level (Figure 3.15). Aliquots from this sample range in age from 82.7 ± 0.41 Ma –259.0 ± 1.25 Ma (Table 3.58, Table 3.5). z67SC217 has consistently young ages for each aliquot, where all ages are reset. Ages are evenly dispersed between end members (Table 5.6). Mean ages and STDs were calculated for sample z67SC217 using all aliquots (Table 3.5, column 1), the four youngest (Table 3.5, column 2), the four oldest (Table 3.5, column 3), the three youngest (Table 3.5, column 4) and the three oldest (Table 3.5, column 5). For these ages, dispersion is so homogeneous that the respective STDs are statistically similar and therefore, a mean age using the five aliquots is used for this sample.

Table 3.5 Combinations of aliquot ages showing resulting mean ages and standard deviations (STDs) for sample z69TA217. The cells highlighted in green are the values used for this sample.

	1	2	3	4	5
Aliquot Ages (Ma)	259	137.7	259	137.7	259
	137.7	203.7	137.7	157.2	203.7
	203.7	157.2	203.7	82.7	157.2
	157.2	82.7	157.2		
	82.7				
Mean Age (Ma)	**168.1**	**145.3**	**200.1**	**125.9**	**206.6**
STD (Ma)	**66.8**	**50.1**	**60.7**	**38.6**	**51**
Mean age error (Ma)	**29.9**	**25.1**	**30.4**	**22.3**	**29.4**

Sample z67SC218

Sample z67SC218 is a quartzite, collected ~36 km from the coastline at an elevation of ~615 m above sea level (Figure 3.15). Aliquots from this sample range in age from 564.8 ± 2.66 Ma –1096.3 ± 5.00 Ma (Table 3.58, Table 3.6). Ages are unevenly dispersed between end members and there are no obvious outliers. Three of the aliquots, aliquot 2, 4, and 5 can be grouped based on 20% above and below the median, while the highest and lowest end member should be discarded in calculations of the mean. For sample z67SC218, STD in column 4 is by far the lowest, while its mean age is comparable to that of column 1, which includes all aliquots (Table 3.6). Therefore, the mean age and STD from column 4 are used for this sample.

Table 3.6 Combinations of aliquot ages showing resulting mean ages, standard deviations (STDs) and error for sample z67SC218. The cells highlighted in green are the values used for this sample.

	1	2	3	4
Aliquot Ages (Ma)	564.8	564.8	810.2	810.2
	810.2	810.2	1096.3	762.2
	1096.3	762.2	762.2	807.6
	762.2	807.6	807.6	
	807.6			
Mean Age (Ma)	**808.2**	**736.2**	**889.6**	**793.3**
STD (Ma)	**190**	**116.4**	**180.6**	**27**
Mean age error (Ma)	**85.0**	**58.2**	**90.3**	**15.6**

Sample z69TA212

Sample z69TA212 is a mylonite, collected ~47 km from the coastline at an elevation of ~980 m above sea level (Figure 3.15). All zircons in this sample had their ends broken off. Aliquots range in age from 378.8 ± 7.96 Ma – 779.4 ± 7.38 Ma (Table 3.58, Table 3.7). Ages are unevenly dispersed between end members and there are no obvious outliers. Aliquots can be separated into two groups. The first group includes aliquots 1 and 5 (Table 3.7, column 3) and the second includes aliquots 2, 3, and 4 (Table 3.7, column 2), which are less obviously relatable, but ages here are relatively evenly distributed between end members 530.3 ± 2.64 Ma and 779.4 ± 7.38 Ma.

	1	2	3
Aliquot Ages (Ma)	397.9	530.3	397.9
	530.3	779.4	378.8
	779.4	625.3	
	625.3		
	378.8		
Mean Age (Ma)	**542.3**	**645**	**388.4**
STD (Ma)	**166.4**	**125.7**	**13.5**
Mean age error (Ma)	**74.4**	**72.6**	**9.5**

Table 3.7 Combinations of aliquot ages showing resulting mean ages, standard deviations (STDs) and error for sample z69TA212. The cells highlighted in green are the values used for this sample.

Sample z69TA201

Sample z69TA201 is a mylonite, collected ~46 km from the coastline at an elevation of ~610 m above sea level (Figure 3.15). Aliquots from this sample range in age from 618.4 ± 2.86 Ma – 836.4 ± 3.67 Ma (Table 3.58, Table 3.8). Ages in this sample are evenly distributed between the end members (Table 3.8) All aliquots are used in calculation of the mean age (Table 3.8).

Aliquot Ages (Ma)	768.9
	618.4
	669.4
	745.2
	836.4
Mean Age (Ma)	**727.6**
STD (Ma)	**85.4**
Mean age error (Ma)	**38.2**

Table 3.8 Aliquot ages showing resulting mean age, standard deviation (STD) and error for sample z69TA201. The cells highlighted in green are the values used for this sample.

Sample z69TA210

Sample z69TA210 is a mylonite, collected ~57 km from the coastline at an elevation of ~733 m above sea level (Figure 3.15). Aliquots from this sample range in age from 235.6 ± 2.30 Ma – 1612.7 ± 26.48 Ma (Table 3.58, Table 3.9). Aliquot number z69TA210-2 was not included in calculations, as there was an error in age measurement, giving an age of -1753232.6 Ma (Table 3.58). This sample has the largest age range compared to other samples in this transect. None of the ages fit into a range 20% above and below the median age and ages are not evenly dispersed between end members (Table 3.9). This sample will not be used further since it did not contain apatites.

Aliquot Ages (Ma)	349.6
	235.6
	1612.7
	683.4
Mean Age (Ma)	**720.3**
STD (Ma)	**624.5**
Mean age error (Ma)	**312.3**

Table 3.9 Aliquot ages showing resulting mean age, standard deviation (STD) and error for sample z69TA210.

Sample z69TA206

Sample z69TA206 is a mylonite, collected ~79 km from the coastline at an elevation of ~877 m above sea level (Figure 3.15). Aliquots from this sample range in age from 560.2 ± 2.62 Ma – 979.6 ± 4.45 Ma (Table 3.58, Table 3.10). Ages are unevenly dispersed between end members, but some aliquots are close enough in age to be grouped (Table 3.10). When the youngest age (aliquot 3) is discarded, the four remaining aliquots are well-grouped and range in age from 895.6 ± 3.97 Ma – 979.6 ± 4.45 Ma (Table 3.10). Mean age and STD obtained from those four aliquots is selected (Table 3.10).

	1	2
Aliquot Ages (Ma)	899.2	899.2
	895.6	895.6
	560.2	979.6
	979.6	858.7
	858.7	
Mean Age (Ma)	**838.7**	**908.3**
STD (Ma)	**161.8**	**50.9**
Mean age error (Ma)	**72.4**	**25.5**

Table 3.10 Combinations of aliquot ages showing resulting mean ages, standard deviations (STDs) and error for sample z69TA206. The cells highlighted in green are the values used for this sample.

3.12.2 SAGLEK TRANSECT: AHe RESULTS

Only four of the seven samples (67SC216, 67SC217, 67SC218, 69TA212) contained suitable apatites, each producing five aliquots, totaling 20 ages from this transect (Figure 3.16). AHe ages in this transect range from 63.8 ± 0.24 Ma – 355.4 ± 1.60 Ma. Sample a67SC218 has the highest range of measured grain ages, 63.8 ± 0.24 Ma – 355.4 ± 1.60 Ma, while sample a67SC216 has grain ages only ranging from 85.9 ± 0.36 Ma – 125.5 ± 0.54 Ma. Each of the following paragraphs includes a description of the data for each sample, as well as analysis of which aliquots will be used to calculate the mean age of the sample and the error of the mean based on single-grain age dispersion. Mean age error was calculated according to equation 3.17.

Sample a67SC216

Sample a67SC216 is a pegmatitic granite, collected ~4 km from the coastline at an elevation of ~16 m above sea level (Figure 3.15). Apatites in this samples were small and rounded. Aliquots range in age from 85.9 ± 0.36 Ma – 125.5 ± 0.54 Ma (Table 3.59, Table 3.11). Aliquot a67SC216-2 is an outlier within the group with an age of 85.9 ± 0.36 Ma, while the other four ages are well-grouped and range from 112.6 ± 0.48 Ma –125.5 ± 0.54 Ma. Although aliquot a67SC216-2 should be discarded from the mean, as it falls outside of the 20% rule, it does not greatly affect mean and STD values (Table 3.11). Therefore, it is worth keeping all of the aliquots for analyses.

	1	2
Aliquot Ages (Ma)	121.1	121.1
	85.9	119.2
	119.2	112.6
	112.6	125.5
	125.5	
Mean Age (Ma)	**112.9**	**119.6**
STD (Ma)	**15.8**	**5.4**
Mean age error (Ma)	**7.1**	**2.7**

Table 3.11 Combinations of aliquot ages showing resulting mean ages, standard deviations (STDs) and error for sample a67SC216. The cells highlighted in green are the values used for this sample.

Sample a69TA217

Sample a67SC217 is a garnet gneiss, collected ~23.4 km from the coastline at an elevation of ~58 m above sea level (Figure 3.15). This sample had many apatites with inclusions making it difficult to find appropriate grains for dating. Aliquots range in age from 112.9 ± 0.52 Ma – 192.4 ± 0.93 Ma (Table 3.59, Table 3.12). Three of the aliquots, aliquots 1, 2, and 5, are well-grouped ranging in age from 112.9 ± 0.52 Ma – 123.4 ± 0.58 Ma Ma. Aliquot 4, with an age of 192.4 ± 0.93 Ma is an outlier, although no abnormalities were observed in the grain photo (Appendix C). Mean and STD was plotted using values from column 2 (Table 3.12).

	1	2
Aliquot Ages (Ma)	112.9	112.9
	123.4	123.4
	140	140
	192.4	115
	115	
Mean Age (Ma)	**136.8**	**122.8**
STD (Ma)	**32.9**	**12.3**
Mean age error (Ma)	**14.7**	**6.2**

Table 3.12 Combinations of aliquot ages showing resulting mean ages, standard deviations (STDs) and error for sample a69TA217. The cells highlighted in green are the values used for this sample.

Sample a67SC218

Sample a67SC218 is a quartzite, collected ~36 km from the coastline at an elevation of ~615 m above sea level (Figure 3.15). Aliquots range in age from 63.8 ± 0.24 Ma – 355.4 ± 1.60 Ma (Table 3.59, Table 3.13). Aliquots 2–5 are relatively evenly distributed between end members 63.8 ± 0.24 Ma and 155.0 ± 0.59 Ma, while aliquot 1 is very far from this group with an age of 355.4 ± 1.60 Ma. None of the ages fit into 20% above or below the median age. Mean and STD was calculated for sample a67SC218 using all aliquots (Table 3.13, column 1), aliquots 2–4 removing the outlier, aliquot 1 (Table 3.13, column 2), the 3 youngest (Table 3.13, column 3), and the three oldest (Table 3.13, column 4). The mean obtained from the four aliquots (column 2) is within the range of the means with the three youngest or oldest aliquots (columns 3 and 4). Therefore, mean and STD was plotted using values from column 2.

Table 3.13 Combinations of aliquot ages showing resulting mean ages, standard deviations (STDs) and error for sample a67SC218. The cells highlighted in green are the values used for this sample.

	1	2	3	4
Aliquot Ages (Ma)	355.4	63.8	63.8	103.8
	63.8	103.8	103.8	155
	103.8	155	155	208.1
	155	208.1		
Aliquot Ages (Ma)	208.1			
Mean Age (Ma)	**177.2**	**132.7**	**107.6**	**155.6**
STD (Ma)	**113.4**	**62.6**	**45.7**	**52.1**
Mean age error (Ma)	**50.7**	**31.3**	**26.4**	**30.1**

Sample a69TA212

Sample a69TA212 is a mylonite, collected ~47 km from the coastline at an elevation of ~980 m above sea level (Figure 3.15). This sample had few apatites and it was difficult to pick any without inclusions. Aliquots range in age from 74.2 ± 00.29 Ma – 301.1 ± 1.26 Ma (Table 3.59, Table 3.14). Aliquots are not well grouped, none of the ages fit into 20% above or below the median age, ages are randomly dispersed between the end members and there is no reliable way to choose to keep or discard aliquots. This sample has the most consistently low [U]e values compared to the other samples in this transect.

Aliquot Ages (Ma)	284.7
	187.8
	74.2
	121.5
	301.1
Mean Age (Ma)	**193.9**
STD (Ma)	**99.2**
Mean age error (Ma)	**44.4**

Table 3.14 Aliquot ages showing resulting mean age, standard deviation (STD) and error for sample a69TA212. The cells highlighted in green are the values used for this sample.

3.13 NAIN TRANSECT: (U-Th)/He RESULTS

The Nain transect consists of nine samples at the approximate latitude of Nain, Newfoundland (56.542222, -61.692778). Samples were collected by the Geological Survey of Canada (GSC) between 1967 and 1971 during ‘Opération Torngat’. Samples were retrieved from the Taylor Collection of the GSC sample archives in Ottawa, (Ontario, Canada) and processed at the commercial facility Overburden Drilling Management in Ottawa for mineral separation. Samples were selected based on both the rock type (felsic igneous and metamorphic rocks which are generally fertile in apatite and zircon) and their location relative to the coastline; the aim was to build coast-perpendicular transects. Selected rocks include granite, migmatite, diorite or gabbro, granodiorite, granitoid gneiss, and mylonitized granulite. It is difficult to comment on the quality of the samples, as they were already crushed when they were received. Geographically, the transect extends 132.14 km inland from the coastline at sea level and samples range in elevation from 60 to 536 m above sea level.

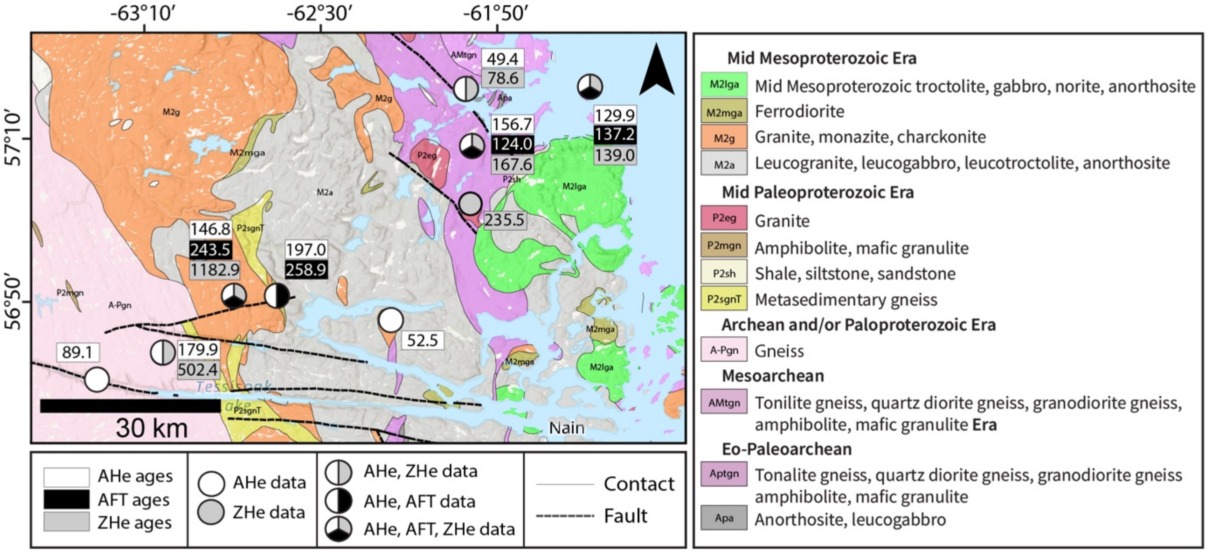

Figure 3.17 Regional geology, topography, sample locations and ages (including ZHe, AHe and AFT) along the Nain transect (Geology: Geological Survey of Canada 2011).

3.13.1 NAIN TRANSECT: ZHe RESULTS

Six of the nine samples (69FQ332, 69FQ335, 69MZ379, 69TA336, 69MZ392, 69MZ351) contained suitable zircons, each producing five aliquots, totaling 30 ZHe cooling ages for this transect. ZHe ages range from 55.4 ± 0.27 Ma–1340.6 ± 5.84 Ma (Figure 3.16). All of the samples have highly dispersed aliquot ages. Sample z69TA336 has the highest range of measured grain ages, 55.4 ± 0.27 Ma – 714.8 ± 3.18 Ma, while sample z69FQ332 has the lowest range 100.9 ± 0.48 Ma – 211.9 ± 0.96 Ma. Sample z69MZ392 has anomalously old ages compared to other samples in this transect (Figure 3.17). Each of the following paragraphs includes a description of the data for each sample, as well as analysis of which aliquots will be used to calculate the mean age of the sample and the error of the mean based on single-grain age dispersion. Mean age error was calculated according to equation 3.17.

Sample z69FQ332

Sample z69FQ332 is a granite, collected ~2 km from the coastline at an elevation of ~249 m above sea level (Figure 3.15). Aliquots from this sample range in age from 100.9 ± 0.48 Ma – 211.9 ± 0.96 Ma (Table 3.58, Table 3.15, Figure 3.16). This sample has consistently young ages where all grains ages are reset, compared to other samples in this transect. Ages are highly dispersed between end members. Aliquots 2, 3 and 5 fit into an age range 20% above and below the median age. Both end members, aliquot z69FQ332-1, the oldest age, should be discarded in calculations of the mean according to analysis in Table 3.15.

	1	2
Aliquot Ages (Ma)	211.9	156.1
	156.1	170.6
	170.6	100.9
	100.9	128.5
	128.5	
Mean Age (Ma)	**153.6**	**139**
STD (Ma)	**42.1**	**30.8**
Mean age error (Ma)	**18.8**	**15.4**

Table 3.15 Combinations of aliquot ages showing resulting mean ages, standard deviations (STDs) and error for sample z69FQ332. The cells highlighted in green are the values used for this sample.

Sample z69FQ335

Sample z69FQ335 is a biotite, hornblende migmatite, collected ~27 km from the coastline at an elevation of ~60 m above sea level (Figure 3.15). Aliquots range in age from 55.4

± 0.27 Ma – 554.1 ± 0.27 Ma (Table 3.58, Table 3.16, Figure 3.16) with aliquots 3 and 4 having anomalously young ages for this transect. Ages are highly and generally unevenly dispersed between end members with no obvious outliers. Aliquots 3, 4 and 5, with ages of 55.4 ± 0.27 Ma, 76.0 ± 0.37 Ma, and 104.5 ± 0.50 Ma respectively, are evenly dispersed from each other, while aliquots 1 and 2, with ages of 384.7 ± 1.88 Ma and 554.1 ± 2.63 Ma respectively, are much older. The youngest two aliquots 3 and 4 with ages of 55.4 ± 0.27 Ma and 76.0 ± 0.37 Ma respectively, could be grouped together, but there is no clear trend or other possible age grouping (Table 3.16). All ages should be used in calculations of the mean.

	1	2	1
Aliquot Ages (Ma)	384.7	55.4	55.4
	554.1	76	76
	55.4	104.5	
	76		
	104.5		
Mean Age (Ma)	**234.9**	**78.6**	**65.7**
STD (Ma)	**222.9**	**24.6**	**14.5**
Mean age error (Ma)	**99.7**	**14.2**	**10.3**

Table 3.16 Combinations of aliquot ages showing resulting mean ages, standard deviations (STDs) and error for sample z69FQ335. The cells highlighted in green are the values used for this sample.

Sample z69MZ379

Sample z69MZ379 is a biotite, hornblende migmatite, collected ~32 km from the coastline at an elevation of ~223 m above sea level (Figure 3.15). This sample was very small with abraded zircons. Aliquots range in age from 130.4 ± 0.64 Ma – 686.5 ± 3.35 Ma. Ages are highly and evenly dispersed between end members with no obvious outliers (Table 3.58, Table 3.17, Figure 3.16). The youngest two aliquots 4 and 5 are very close in age, with ages of 130.9 Ma and 130.4 Ma respectively. These aliquots could be grouped together, but otherwise there is no clear trend or other possible age grouping (Table 3.17). The three youngest ages should be used in calculations of the mean (Table 3.17).

	1	2
Aliquot Ages (Ma)	598.1	241.5
	686.5	130.9
	241.5	130.4
	130.9	
	130.4	
Mean Age (Ma)	**357.5**	**167.6**
STD (Ma)	**265.6**	**64**
Mean age error (Ma)	**118.8**	**37.0**

Table 3.17 Combinations of aliquot ages showing resulting mean ages, standard deviations (STDs) and error for sample z69MZ379. The cells highlighted in green are the values used for this sample.

Sample z69TA336

Sample z69TA336 is a biotite granite, collected ~39 km from the coastline at an elevation of ~420 m above sea level (Figure 3.15). This sample contained many euhedral zircons. Aliquots range in age from 55.5 ± 0.24 Ma – 714.8 ± 3.18 Ma (Table 3.58, Table 3.18, Figure 3.16). Ages are highly and unevenly dispersed between end members with only one sample fitting into an age range 20% above and below the median age. Aliquot 5 with an age of 714.8 ± 3.18 Ma is 439.6 Ma older than the other ages and is an outlier. This sample has the largest [U]e value of all the samples in this transect, belonging to aliquot z69TA336-4. For sample z69TA336, the oldest and youngest aliquot is removed to give the results in column 3 (Table 3.18), which contains at least three ages and the lowest STD.

	1	2	3
Aliquot Ages (Ma)	275.1	275.1	275.1
	250.4	250.4	250.4
	55.5	55.5	181.1
	181.1	181.1	
	714.8		
Mean Age (Ma)	**295.4**	**190.5**	**235.6**
STD (Ma)	**249.5**	**98.4**	**48.7**
Mean age error (Ma)	**111.6**	**49.2**	**28.1**

Table 3.18 Combinations of aliquot ages showing resulting mean ages, standard deviations (STDs) and error for sample z69TA336. The cells highlighted in green are the values used for this sample.

Sample z69MZ392

Sample z69MZ392 is a granodiorite, collected ~96 km from the coastline at an elevation of ~534 m above sea level (Figure 3.15). This sample contained many well-shaped, clear zircon grains. Aliquots have the most consistently old ages of all samples in this transect, ranging from 1057.4 ± 4.59 Ma – 1340.6 ± 5.84 Ma (Table 3.58, Table 3.19, Figure 3.16). This sample has anomalously low [U]e values compared to other samples in this transect. Ages are relatively well-grouped and yield a mean age of 1182.9 ± 56.8 Ma when all aliquots are included in the calculations of the mean (Table 3.19).

Aliquot Ages (Ma)	1340.6
	1159.9
	1070.3
	1286.4
	1057.4
Mean Age (Ma)	**1182.9**
STD (Ma)	**127**
Mean age error (Ma)	**56.8**

Table 3.19 Aliquot ages showing resulting mean age, standard deviation (STD) and error for sample z69MZ392. The cells highlighted in green are the values used for this sample.

Sample z69MZ351

Sample z69MZ351 is a mylonitized granulite, collected ~117 km from the coastline at an elevation of ~536 m above sea level (Figure 3.15). This sample was very small with abundant, but weathered zircons. Aliquots from this sample range in age from 265.3 ± 1.24 Ma – 749.3 ± 3.52 Ma (Table 3.58, Table 3.20, Figure 3.16). Ages are highly and relatively evenly dispersed between end members with only one aliquot fitting into an age range 20% above and below the median age. Aliquot 4 with an age of 749.3 ± 3.52 Ma could potentially be considered an outlier but is not greatly older than the second oldest age 557.0 ± 2.60 Ma (aliquot 3). Therefore, all aliquots should be included in calculations of the mean (Table 3.20).

Aliquot Ages (Ma)	404.9
	265.3
	557.0
	749.3
	535.3
Mean Age (Ma)	**502.4**
STD (Ma)	**180.8**
Mean age error (Ma)	**80.9**

Table 3.20 Aliquot ages showing resulting mean age, standard deviation (STD) and error for sample z69MZ351. The cells highlighted in green are the values used for this sample.

3.13.2 NAIN TRANSECT: AHe RESULTS

Eight of the nine samples (69FQ332, 69FQ335, 69MZ379, 69FQ398, 69MZ390, 69MZ392, 69MZ351, 69MZ335) contained suitable apatites, producing five aliquots per sample totaling 39 cooling ages, as one aliquot (a69FQ335-4) produced an unusable age with a negative value (Table 3.59). AHe ages range from 18.0 ± 0.09 Ma – 450.4 ± 1.74 Ma (Figure 3.17). Each of the following paragraphs includes a description of the data for each sample, as well as analysis of which aliquots will be used to calculate the mean age of the sample and the error of the mean based on single-grain age dispersion. Mean age error was calculated according to equation 3.17.

Sample a69FQ332

Sample a69FQ332 is a granite, collected ~2 km from the coastline at an elevation of ~249 m above sea level (Figure 3.15). Aliquots range in age from 123.6 ± 0.46 Ma – 422.3 ± 1.52 Ma (Table 3.59, Table 3.21, Figure 3.17). Ages are unevenly dispersed between end members (Table 3.21). If the oldest age (aliquot 3) is discarded, the new median age allows for the grouping of aliquots 1, 2, and 5, which range in age from 123.6 ± 0.46 Ma –141.0 ± 0.54 Ma, fitting into an age range 20% above and below the median age. Aliquot 4 has an age greater than 20% of the new median age, and therefore should also be discarded. Sample a69FQ332-3 and a69FQ332-4 should be discarded in calculations of the mean (Table 3.21, column 2).

	1	2	3
Aliquot Ages (Ma)	141	141	141
	123.6	123.6	123.6
	422.3	177.1	125.2
	177.1	125.2	
	125.2		
Mean Age (Ma)	**197.9**	**141.7**	**130**
STD (Ma)	**127.3**	**24.9**	**9.6**
Mean age error (Ma)	**56.9**	**12.5**	**5.5**

Table 3.21 Combinations of aliquot ages showing resulting mean ages, standard deviations (STDs) and error for sample a69FQ332. The cells highlighted in green are the values used for this sample.

Sample a69FQ335

Sample a69FQ335 is a biotite, hornblende migmatite, collected ~27 km from the coastline at an elevation of ~60 m above sea level (Figure 3.15). Many apatites in this sample had inclusions or fractures making it difficult to find appropriate grains. Aliquots are well-grouped and range in age from 42.7 ± 0.17 Ma – 54.2 ± 0.20 Ma (Table 3.59, Table 3.22, Figure 3.17). Aliquot number a69FQ335-4 was not included in calculations for this sample, as there was an error in age measurement, giving an age of -18766.4 Ma. All other aliquots are included in the calculation of the mean (Table 3.22).

Aliquot Ages (Ma)	54.2
	54
	46.5
	42.7
Mean Age (Ma)	**49.3**
STD (Ma)	**5.7**
Mean age error (Ma)	**3.3**

Table 3.22 Aliquot ages showing resulting mean age, standard deviation (STD) and error for sample a69FQ335. The cells highlighted in green are the values used for this sample.

Sample a69MZ379

Sample a69MZ379 is a biotite, hornblende migmatite, collected ~32 km from the coastline at an elevation of ~223 m above sea level (Figure 3.15). This sample's heavy fraction was very small; apatites were rare and had inclusions. Aliquots range in age from 18.0 ± 0.09 Ma – 318.1 ± 1.21 Ma (Table 3.59, Table 3.23, Figure 3.17) and ages are unevenly dispersed between end members. Aliquots 4 and 5, with ages of 23.1 ± 0.11 Ma and 18.0 ± 0.09 Ma respectively, can be grouped together, but otherwise there are no obvious age groupings as ages do not fit within 20% above or below the median age. Based on the age groupings, this sample was only partially reset making it impossible to pick a set of aliquots for a mean age calculation. Aliquot number a69MZ379-3 could be removed (Table 3.23, column 2), but a more accurate analysis would use two separate age groupings (Table 3.23, column 3 and 4).

Table 3.23 Combinations of aliquot ages showing resulting mean ages, standard deviations (STDs) and error for sample a69MZ379. The cells highlighted in green are the values used for this sample.

	1	2	3	4
Aliquot Ages (Ma)	182.1	182.1	182.1	23.1
	131.3	131.3	131.3	18
	318.1	23.1		
	23.1	18		
	18			
Mean Age (Ma)	**134.5**	**88.6**	**156.7**	**20.6**
STD (Ma)	**124.5**	**81.3**	**35.9**	**3.6**
Mean age error (Ma)	**55.7**	**40.7**	**20.7**	**2.5**

Sample a69FQ398

Sample a69FQ398 is either a diorite or gabbro, collected ~67 km from the coastline at an elevation of ~502 m above sea level (Figure 3.15). Apatites in this sample were either fractured, or too large in size to be acceptable for dating. Selected grains were all fractured. Aliquots from this sample range in age from 40.9 ± 0.18 Ma – 127.1 ± 0.55 Ma (Table 3.59, Table 3.24, Figure 3.17). Ages are unevenly dispersed between end members, but some aliquots are close enough in age to be grouped (Table 3.24). If the oldest aliquot 4 is discarded, the new median age allows for the grouping of aliquots 1, 2, and 5, which range in age from 40.9 ± 0.18 Ma – 62.8 ± 0.23 Ma, fitting into an age range 20% above and below the median age. Aliquot 3 has an age greater than 20% of the new median age, and therefore should also be discarded. Sample a69FQ398-3 and a69FQ398-4 should be discarded in calculations of the mean (Table 3.24, column 3).

Table 3.24 Combinations of aliquot ages showing resulting mean ages, standard deviations (STDs) and error for sample a69FQ398. The cells highlighted in green are the values used for this sample.

	1	2	3
Aliquot Ages (Ma)	40.9	40.9	40.9
	53.8	53.8	53.8
	91.5	91.5	62.8
	127.1	62.8	
Aliquot Ages (Ma)	62.8		
Mean Age (Ma)	**75.2**	**62.3**	**52.5**
STD (Ma)	**34.5**	**21.5**	**11**
Mean age error (Ma)	**15.4**	**10.8**	**6.4**

Sample a69MZ390

Sample a69MZ390 is a granodiorite collected ~87 km from the coastline at an elevation of ~526 m above sea level (Figure 3.15). Aliquots from this sample range in age from 149.3 ± 0.54 Ma – 418.7 ± 1.52 Ma (Table 3.59, Table 3.25, Figure 3.17). Aliquots are relatively evenly dispersed between end members, but the oldest age, aliquot 4 is an obvious outlier. STD is greatly reduced in mean calculations where aliquot 4 is discarded (Table 3.25, column 2).

	1	2
Aliquot Ages (Ma)	149.3	149.3
	269.6	269.6
	155.6	155.6
	418.7	213.4
	213.4	
Mean Age (Ma)	**241.3**	**197**
STD (Ma)	**110.5**	**56.3**
Mean age error (Ma)	**49.4171023**	**28.15**

Table 3.25 Combinations of aliquot ages showing resulting mean ages, standard deviations (STDs) and error for sample a69MZ390. The cells highlighted in green are the values used for this sample.

Sample a69MZ392

Sample a69MZ392 is a granodiorite, collected ~96 km from the coastline at an elevation of ~534 m above sea level (Figure 3.15). Aliquots from this sample range in age from 124.4 ± 0.50 Ma – 318.1 ± 1.23 Ma (Table 3.59, Table 3.26, Figure 3.17). Ages are unevenly dispersed between end members, but some aliquots are close enough in age to be grouped. If the oldest aliquot 4 is discarded, the new median age allows for the grouping of aliquots 1, 2, and 5, which range in age from 124.4 ± 0.50 Ma – 167.5 ± 0.64 Ma, fitting into an age range 20% above and below the median age. Remaining aliquots 3 and 4 are not close enough in age to be relatable. Samples a69MZ392-3 and a69MZ392-4 should be discarded in calculations of the mean (Table 3.26, column 3).

	1	2	3
Aliquot Ages (Ma)	124.4	124.4	124.4
	148.4	148.4	148.4
	214.4	214.4	167.5
	318.1	167.5	
	167.5		
Mean Age (Ma)	**194.5**	**163.6**	**146.7**
STD (Ma)	**76.6**	**38.1**	**21.6**
Mean age error (Ma)	**34.3**	**19.1**	**12.5**

Table 3.26 Combinations of aliquot ages showing resulting mean ages, standard deviations (STDs) and error for sample a69MZ392. The cells highlighted in green are the values used for this sample.

Sample a69MZ351

Sample a69MZ351 is a mylonitized granulite, collected ~117 km from the coastline at an elevation of ~536 m above sea level (Figure 3.15). This sample was small and contained few apatites. Aliquots range in age from 81.0 ± 0.38 Ma – 280.8 ± 1.20 Ma (Table 3.59, Table 3.27, Figure 3.17). Ages are evenly dispersed between end members with no obvious outliers or groupings. All aliquots should be included in calculations of the mean (Table 3.27, column 1).

Table 3.27 Combinations of aliquot ages showing resulting mean ages, standard deviations (STDs) and error for sample a69MZ351. The cells highlighted in green are the values used for this sample.

	1	2	3	4	5
Aliquot Ages (Ma)	81	130.8	280.8	130.8	81
	130.8	280.8	240.2	240.2	130.8
	280.8	240.2	166.7	166.7	166.7
	240.2	166.7			
	166.7				
Mean Age (Ma)	**179.9**	**204.6**	**229.2**	**179.2**	**126.1**
STD (Ma)	**80.9**	**68.2**	**57.8**	**55.8**	**43**
Mean age error (Ma)	**36.2**	**34.1**	**33.4**	**32.2**	**24.8**

Sample a69MZ335

Sample a69MZ335 is a granitoid gneiss, collected ~132 km from the coastline at an elevation of ~512 m above sea level (Figure 3.15). This sample contained many ideal apatites for dating. Aliquots range in age from 71.0 ± 0.30 Ma – 450.4 ± 1.74 Ma (Table 3.59, Table 3.28, Figure 3.17). Ages are unevenly dispersed between end members. Aliquots 1, 4 and 5 can be grouped together, with ages ranging from 71.0 ± 0.30 Ma – 100.8 ± 0.39 Ma, while aliquots 2 and 3 have ages far outside of this range with ages of 450.4 ± 1.74 Ma and 264.2 ± 1.12 Ma respectively (Table 4.26) and are discarded in the calculation of the mean (Table 3.28, column 2).

	1	2
Aliquot Ages (Ma)	95.5	95.5
	450.4	71
	264.2	100.8
	71	
	100.8	
Mean Age (Ma)	**196.4**	**89.1**
STD (Ma)	**161.4**	**15.9**
Mean age error (Ma)	**72.2**	**9.2**

Table 3.28 Combinations of aliquot ages showing resulting mean ages, standard deviations (STDs) and error for sample a69MZ335. The cells highlighted in green are the values used for this sample.

3.14 HOPEDALE TRANSECT: (U-Th)/He RESULTS

The Hopedale transect consists of nine samples at the approximate latitude of Hopedale, Newfoundland (55.484039, -60.203189). Samples were collected with the GSC during fieldwork from July 4th–26th 2018, in Labrador, Canada. Field sites were accessed by helicopter and pre-selected using GSC geological maps (Ermanovics 1992) to target specific rock types at locations extending landward from the coast to produce a coast-perpendicular transect at this latitude. In the field, the freshest and cleanest rock material at a site was targeted for collection, such that the samples were of high quality. Rock types vary, including migmatitic granodiorite, granite, gneiss, Migmatitic orthogneiss, orthogneiss, syeno-granite and tonalite gneiss (Table 3.3). Geographically, the transect extends 92 km inland from the coastline at sea level and samples range in elevation from 45 to 317 m above sea level.

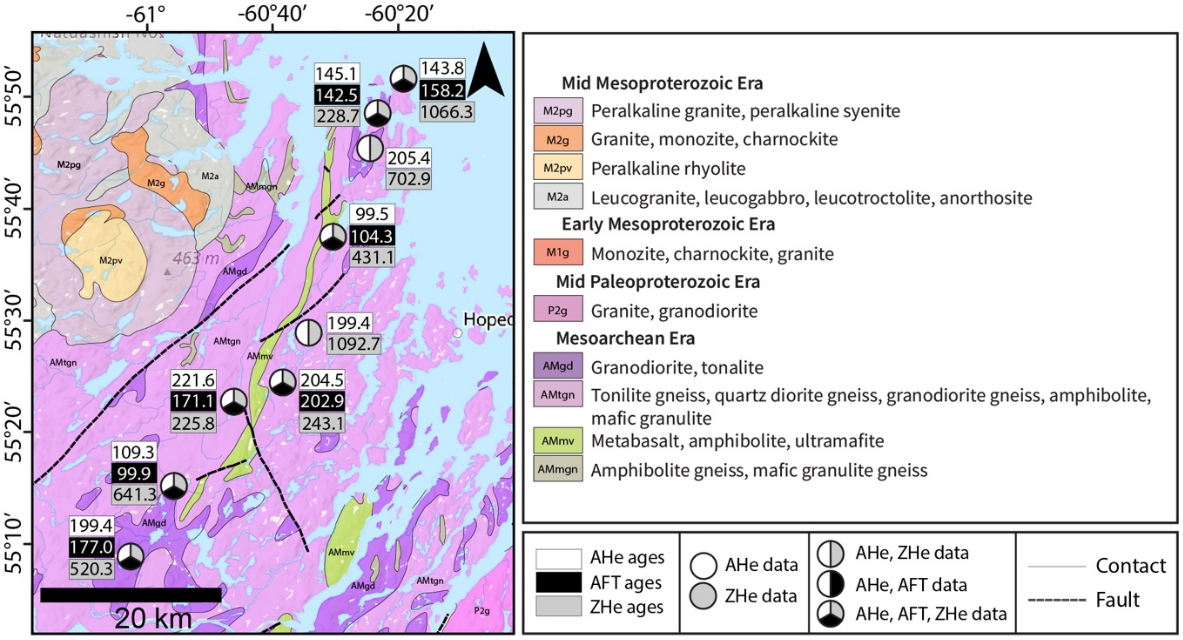

Figure 3.18 Regional geology, topography, sample locations and ages (including ZHe, AHe and AFT) along the Hopedale transect (Geology: Geological Survey of Canada 2011).

3.14.1 HOPEDALE TRANSECT: ZHe RESULTS

All nine samples contained suitable zircons, each producing five aliquots, totaling 45 cooling ages. ZHe ages from this transect range from 5.4 ± 0.03 Ma – 1380.6 ± 6.39 Ma. All of the samples have highly dispersed aliquot ages, but not all samples have equal amounts of dispersion. Each of the following paragraphs includes a description of the data for each sample, as well as analysis of which aliquots will be used to calculate the mean age of the sample and the error of the mean based on single-grain age dispersion. Mean age error was calculated according to equation 3.17.

Sample zk0016

Sample zk0016 is a migmatitic granodiorite, collected ~0.3 km from the coastline at an elevation of ~80 m above sea level (Figure 3.15). This sample contained large, clear zircons, as well as smaller cracked ones. Aliquots range in age from 432.1 ± 2.10 Ma – 1103.2 ± 5.34 Ma (Table 3.58, Table 3.29, Figure 3.18). Ages are unevenly dispersed between end members, but some aliquots are close enough in age to be grouped. If the youngest two aliquots 1 and 5 with ages of 715.9 ± 2.94 Ma and 432.1 ± 2.10 Ma respectively are discarded, aliquots 2–4, with an age range of 1046.1 ± 4.96 Ma –1103.2 ± 5.34 Ma can be grouped together yielding a mean age of 1066.4 Ma (Table 3.29, column 2).

	1	2
Aliquot Ages (Ma)	715.9	1046.1
	1046.1	1049.7
	1049.7	1103.2
	1103.2	
	432.1	
Mean Age (Ma)	**869.4**	**1066.4**
STD (Ma)	**288.6**	**32**
Mean age error (Ma)	**129.1**	**18.5**

Table 3.29 Combinations of aliquot ages showing resulting mean ages, standard deviations (STDs) and error for sample zk0016. The cells highlighted in green are the values used for this sample.

Sample zk0015

Sample zk0015 is a granite, collected ~7 km from the coastline at an elevation of ~45 m above sea level (Figure 3.15). This sample contained very few zircons making it difficult to select high quality grains. Aliquots range in age from 131.3 ± 0.64 Ma – 333.8 ± 1.66 Ma (Table 3.58, Table 3.30, Figure 3.18), the smallest age range in this transect. Ages are relatively evenly spaced between end members with no obvious outliers. All aliquots should be included in calculations of the mean (Table 3.30, column 1).

	1	2	3
Aliquot Ages (Ma)	149.9	333.8	149.9
	131.3	309	131.3
	333.8	219.4	219.4
	309		
	219.4		
Mean Age (Ma)	**228.7**	**287.4**	**166.8**
STD (Ma)	**91.2**	**60.2**	**46.4**
Mean age error (Ma)	**40.8**	**34.8**	**26.8**

Table 3.30 Combinations of aliquot ages showing resulting mean ages, standard deviations (STDs) and error for sample zk0015. The cells highlighted in green are the values used for this sample.

Sample zk0014

Sample zk0014 is a gneiss, collected ~13 km from the coastline at an elevation of ~241 m above sea level (Figure 3.15). Zircon grains in this sample were euhedral, but rare. Aliquots range in age from 369.9 ± 1.73 Ma – 1065.7 ± 5.09 Ma (Table 3.58, Table 3.31, 3.18), which is the largest age range in this transect. Ages are unevenly dispersed between end members and none of the ages fit into an age range 20% above and below the median age. Including all aliquots in the mean calculation yields such a large STD that the average age has little meaning (Table 3.31, column 1). There are two end-member possibilities (Table 3.31, column 2 and 3) that might be useful for determining cooling path after being compared with AFT data. Otherwise, the mean and STD values used for plotting will be those from column 1.

	1	2	3
Aliquot Ages (Ma)	1017	1017	369.9
	369.9	1065.7	428.3
	428.3		
	1065.7		
	633.7		
Mean Age (Ma)	**702.9**	**1041.3**	**399.1**
STD (Ma)	**324.6**	**34.4**	**41.3**
Mean age error (Ma)	**145.2**	**24.3**	**29.2**

Table 3.31 Combinations of aliquot ages showing resulting mean ages, standard deviations (STDs) and error for sample zk0014. The cells highlighted in green are the values used for this sample.

Sample zk0013

Sample zk0013 is a migmatitic orthogneiss, collected ~29 km from the coastline at an elevation of ~84 m above sea level (Figure 3.15). Many of the zircons in this sample were broken and/or needle shaped and not ideal for dating. Aliquots range in age from 701.3 ± 3.17 Ma – 219.0 ± 0.96 Ma (Table 3.58, Table 3.32, Figure 3.18). Ages are highly and unevenly dispersed between end members, but some aliquots are close enough in age to be grouped. If the youngest and oldest ages, aliquots 1 and 5, are discarded, the other ages, aliquots 2–4, ranging in age from 363.4 ± 1.59 Ma – 479.5 ± 2.32 Ma fit into an age range 20% above and below the median age and yield a mean age of 431.0 Ma ± 34.9 Ma (Table 3.32, column 3).

	1	2	3
Aliquot Ages (Ma)	701.3	363.4	363.4
	363.4	450.3	450.3
	450.3	479.5	479.5
	479.5	219	
	219		
Mean Age (Ma)	**442.7**	**378**	**431**
STD (Ma)	**176.5**	**116.9**	**60.4**
Mean age error (Ma)	**78.9**	**58.5**	**34.9**

Table 3.32 Combinations of aliquot ages showing resulting mean ages, standard deviations (STDs) and error for sample zk0013. The cells highlighted in green are the values used for this sample.

Sample zk0012

Sample zk0012 is an orthogneiss, collected ~44.6 km from the coastline at an elevation of ~162 m above sea level (Figure 3.15). This sample's heavy fraction was rich in euhedral zircons. Aliquots range in age from 1033.4 ± 5.07 Ma – 1380.6 ± 6.39 Ma (Table 3.58, Table 3.33, Figure 3.18). Ages are relatively evenly dispersed between end members, except for the oldest age, which can be considered an outlier. If the oldest age, aliquot 5, is discarded, the remaining ages, aliquots 1–4, range in age from 1033.4 ± 5.07 Ma – 1167.1 ± 5.43 Ma, yielding a mean age of 1092.7 ± 29.6 Ma (Table 3.33, column 2). Although calculations using all aliquots versus using four aliquots (discarding ak0012-5) yield a comparable mean age (Table 3.33), calculations where ak0012-5 is discarded (Table 3.33, column 2) have a smaller STD. Therefore, mean and STD was plotted using values from column 2.

	1	2
Aliquot Ages (Ma)	1111	1111
	1059.1	1059.1
	1167.1	1167.1
	1033.4	1033.4
	1380.6	
Mean Age (Ma)	**1150.2**	**1092.7**
STD (Ma)	**138.6**	**59.2**
Mean age error (Ma)	**62.0**	**29.6**

Table 3.33 Combinations of aliquot ages showing resulting mean ages, standard deviations (STDs) and error for sample zk0012. The cells highlighted in green are the values used for this sample.

Sample zk0011

Sample zk0011 is a granite, collected ~54 km from the coastline at an elevation of ~231 m above sea level (Figure 3.15). Zircons from this sample were very small and needle-shaped. Aliquots range in age from 5.4 ± 0.03 Ma – 293.8 ± 1.40 Ma (Table 3.58, Table 3.34, Figure 3.18). This sample contains the youngest zircon age of all the samples. Ages are highly and unevenly dispersed between end members without any samples falling within an age range 20% above and below the median age. Although the youngest age, aliquot 4, is an obvious outlier, discarding it does not result in groupings for the remaining samples. Otherwise, aliquots 1 and 3 are close in age, with ages of 293.8 ± 1.40 Ma and 281.1 ± 1.31 Ma respectively, but there are no other age connections. The mean age that is calculated using the most aliquot ages with the lowest STD is column 2 (Table 3.34).

	1	2	3
Aliquot Ages (Ma)	293.8	293.8	293.8
	37.6	281.1	281.1
	281.1	154.5	
	5.4		
	154.5		
Mean Age (Ma)	**154.5**	**243.1**	**287.4**
STD (Ma)	**133.5**	**77**	**9**
Mean age error (Ma)	**59.7**	**44.5**	**6.4**

Table 3.34 Combinations of aliquot ages showing resulting mean ages, standard deviations (STDs) and error for sample zk0011. The cells highlighted in green are the values used for this sample.

Sample zk0010

Sample zk0010 is a migmatitic orthogneiss, collected ~61 km from the coastline at an elevation of ~50 m above sea level (Figure 3.15). This sample was rich in euhedral zircons. Aliquots range in age from 26.8 ± 0.13 Ma – 510.7 ± 2.47 Ma (Table 3.58, Table 3.35, Figure 3.18). Ages are unevenly dispersed between end members. The youngest two samples, aliquots 1 and 2 with ages of 26.8 ± 0.13 Ma and 35.7 ± 0.18 Ma respectively, are close in age and can be grouped together. Remaining samples, aliquots 3–5 are highly and evenly dispersed between end members 197.6 ± 0.97 Ma and 510.7 ± 2.47 Ma without obvious outliers and none of the ages fitting into an age range 20% above and below the median age for these aliquots.

Aliquot Ages (Ma)	26.8
	35.7
	510.7
	197.6
	358.1
Mean Age (Ma)	**225.8**
STD (Ma)	**209.2**
Mean age error (Ma)	**93.55708418**

Table 3.35 Aliquot ages showing resulting mean age, standard deviation (STD) and error for sample zk0010. The cells highlighted in green are the values used for this sample.

Sample zk0009

Sample zk0009 is a granite, or syeno-granite, collected ~78 km from the coastline at an elevation of ~117 m above sea level (Figure 3.15). This sample was rich in euhedral zircons. Aliquots range in age from 197.2 ± 0.96 Ma – 700.1 ± 3.43 Ma (Table 3.58, Table 3.36, Figure 3.18). Ages are highly and unevenly dispersed between end members with no obvious outliers. Three of the aliquots 1, 2 and 5, with ages ranging from 588.0 ± 2.88 Ma – 700.1 ± 3.43 Ma fit into an age range 20% above and below the median age. The two youngest ages, aliquots 3 and 4 with ages of 442.9 ± 2.15 Ma and 197.2 ± 0.96 Ma respectively, do not fit into this age range and cannot be grouped together. Although a 4 aliquots solution is acceptable for calculations of the mean age (Table 3.36, column 2) samples ak0009-3 and ak0009-4 should be discarded in calculations of the mean (Table 3.36, column 3) to provide the lowest STD.

Table 3.36 Combinations of aliquot ages showing resulting mean ages, standard deviations (STDs) and error for sample zk0009. The cells highlighted in green are the values used for this sample.

	1	2	3	4
Aliquot Ages (Ma)	635.7	635.7	635.7	442.9
	700.1	700.1	700.1	588
	442.9	442.9	588	635.7
	197.2	588		
	588			
Mean Age (Ma)	**512.8**	**591.7**	**641.3**	**555.5**
STD (Ma)	**200.2**	**109.3**	**56.3**	**100.4**
Mean age error (Ma)	**89.5**	**54.7**	**32.5**	**58.0**

Sample zk0008

Sample zk0008 is a tonalite gneiss, collected ~92 km from the coastline at an elevation of ~317 m above sea level (Figure 3.15). Aliquots range in age from 226.4 ± 1.12 Ma – 534.4 ± 2.58 Ma (Table 3.58, Table 3.37, Figure 3.18). Ages are highly and unevenly dispersed between end members. Three of the aliquots 2, 3 and 5, with ages ranging from 495.9 ± 2.26 Ma – 534.4 ± 2.58 Ma fit into an age range 20% above and below the median age. The two youngest ages, aliquots 1 and 4 with ages of 226.4 ± 1.12 Ma and 365.9 ± 1.76 Ma respectively, do not fit into this age range and cannot be grouped together. Samples ak0008-1 and ak0008-4 should be discarded in calculations of the mean (Table 3.37, column 3).

	1	2	3
Aliquot Ages (Ma)	226.4	534.4	534.4
	534.4	495.9	495.9
	495.9	365.9	530.6
	365.9	530.6	
	530.6		
Mean Age (Ma)	**430.6**	**481.7**	**520.3**
STD (Ma)	**133.1**	**79.1**	**21.2**
Mean age error (Ma)	**59.5**	**39.6**	**12.2**

Table 3.37 Combinations of aliquot ages showing resulting mean ages, standard deviations (STDs) and error for sample zk0008. The cells highlighted in green are the values used for this sample.

3.14.2 HOPEDALE TRANSECT: AHe RESULTS

All nine samples contained suitable apatites, each producing five aliquots totaling 45 cooling ages. AHe ages from this transect range from 24.8 ± 0.12 Ma – 423.3 ± 1.83 Ma. Many of the samples have dispersed aliquot ages, but not as dispersed as zircon ages. Sample ak0015 has the highest range of measured grain ages, 112.4 ± 0.42 Ma – 360.9 ± 1.37 Ma, while sample ak0011 has grain ages only ranging from 187.4 ± 0.80 Ma – 223.9 ± 0.86 Ma. Ages are generally reset except for a few ages older than 350 Ma in samples ak0015, ak0012 and ak0010 (Figure 3.18). Samples with notably low ages include ak0013-2 (52.0 ± 0.21 Ma) and ak0009-4 (24.8 ± 0.12 Ma) (Figure 3.18). Each of the following paragraphs includes a description of the data for each sample, as well as analysis of which aliquots will be used to calculate the mean age of the sample and the error of the mean based on single-grain age dispersion. Mean age error was calculated according to equation 3.17.

Sample ak0016

Sample ak0016 is a migmatitic granodiorite, collected ~0.3 km from the coastline at an elevation of ~80 m above sea level (Figure 3.15). Aliquots from this sample range in age from 116.9 ± 0.47 Ma – 159.1 ± 0.64 Ma (Table 3.59, Table 3.38, Figure 3.18). Ages are unevenly dispersed between end members, but some aliquots are close enough in age to be grouped. If the youngest age, aliquot 4, is discarded, the other ages, aliquots 1, 2, 3, and 5, ranging in age from 138.1 ± 0.54 Ma – 159.1 ± 0.64 Ma fit into an age range 20% above and below the median age. Sample ak0016-4 could be discarded in calculations of the mean (Table 3.38, column 2), but if all aliquots are included instead, the STD is low. Therefore, the mean age from column 1 (Table 3.38) was used for plotting and calculations.

	1	2
Aliquot Ages (Ma)	154.6	154.6
	138.1	138.1
	150.3	150.3
	116.9	159.1
	159.1	
Mean Age (Ma)	**143.8**	**150.5**
STD (Ma)	**17**	**9**
Mean age error (Ma)	**7.6**	**4.5**

Table 3.38 Combinations of aliquot ages showing resulting mean ages, standard deviations (STDs) and error for sample ak0016. The cells highlighted in green are the values used for this sample.

Sample ak0015

Sample ak0015 is a granite, collected ~7 km from the coastline at an elevation of ~45 m above sea level (Figure 3.15). Aliquots from this sample range in age from 112.4 ± 0.42 Ma – 360.9 ± 1.37 Ma (Table 3.59, Table 3.39, Figure 3.18). Ages are unevenly dispersed between end members (Table 3.38). If the oldest age, aliquot 4, is discarded, the new median age allows for the grouping of aliquots 1, 2, and 3, which range in age from 112.4 ± 0.42 Ma – 139.8 ± 0.53 Ma, fitting into an age range 20% above and below the median age. Aliquot 5 has an age greater than 20% of the new median age, and therefore should also be discarded. Samples ak0015-4 and ak0015-5 could be discarded in calculations of the mean (Table 3.39, column 3), but if aliquot 4 is not discarded columns 2 and 3 yield statistically similar results. Column two was selected for analyses because it includes more ages.

	1	2	3
Aliquot Ages (Ma)	139.8	139.8	139.8
	112.4	112.4	112.4
	138.8	138.8	138.8
	360.9	189.4	
	189.4		
Mean Age (Ma)	**188.2**	**145.1**	**130.3**
STD (Ma)	**100.4**	**32.1**	**15.5**
Mean age error (Ma)	**44.9**	**16.1**	**8.9**

Table 3.39 Combinations of aliquot ages showing resulting mean ages, standard deviations (STDs) and error for sample ak0015. The cells highlighted in green are the values used for this sample.

Sample ak0014

Sample ak0014 is a gneiss, collected ~13 km from the coastline at an elevation of ~241 m above sea level (Figure 3.15). Aliquots from this sample range in age from 182.8 ± 0.79 Ma – 227.6 ± 1.02 Ma (Table 3.59, Table 3.40, Figure 3.18). This sample has little dispersion, as ages for have an even distribution between the end members, with all ages fitting within an age range 20% above and below the median age. ~~A~~ll aliquots should be included in calculations of the mean and yield an age of 205.4 ± 8.0 Ma (Table 3.40).

Aliquot Ages (Ma)	194.1
	227.6
	182.8
	205.1
	217.4
Mean Age (Ma)	**205.4**
STD (Ma)	**17.9**
Mean age error (Ma)	**8.0**

Table 3.40 Aliquot ages showing resulting mean age, standard deviation (STD) and error for sample ak0014. The cells highlighted in green are the values used for this sample.

Sample ak0013

Sample ak0013 is a migmatitic orthogneiss, collected ~29 km from the coastline at an elevation of ~84 m above sea level (Figure 3.15). Aliquots from this sample range in age from 52.0 ± 0.21 Ma – 115.4 ± 0.44 Ma (Table 3.59, Table 3.41, Figure 3.18). Ages for this sample are unevenly dispersed between end members, but some aliquots are close enough in age to be grouped. If the youngest age, aliquot 2, is discarded, the other ages, aliquots 1, 3-5, ranging in age from 91.8 ± 0.37 Ma – 115.4 ± 0.44 Ma fit into an age range 20% above and below the median age. If the oldest end member, aliquot 5, is also discarded, ages are grouped even more tightly, ranging from 91.8 ± 0.37 Ma – 98.6 ± 0.37 Ma. Sample ak0013-5 should be discarded in calculations of the mean (Table 3.41), although a four grains solution is comparable. Therefore, column 2 (Table 3.41) was used in calculations and plotting.

	1	2	3
Aliquot Ages (Ma)	91.8	91.8	91.8
	52	92.3	92.3
	92.3	98.6	98.6
	98.6	115.4	
	115.4		
Mean Age (Ma)	**90**	**99.5**	**94.2**
STD (Ma)	**23.3**	**11**	**3.8**
Mean age error (Ma)	**10.4**	**5.5**	**2.2**

Table 3.41 Combinations of aliquot ages showing resulting mean ages, standard deviations (STDs) and error for sample ak0013. The cells highlighted in green are the values used for this sample.

Sample ak0012

Sample ak0012 is an orthogneiss, collected ~45 km from the coastline at an elevation of ~162 m above sea level (Figure 3.15). Aliquots from this sample range in age from 152.4 ± 0.65 Ma – 390.7 ± 1.79 Ma (Table 3.59, Table 3.42, Figure 3.18). Ages are unevenly dispersed between end members and show no obvious outliers or groups, as none of the samples fit into an age range 20% above and below the median age. When comparing mean ages and STDs (Table 3.42), the four grains solution (column 2) includes more grains than columns 3 and 4, while having a smaller STD than column 1. Therefore, sample ak0012 yields a mean age of 199.4 ± 26.6.

Table 3.42 Combinations of aliquot ages showing resulting mean ages, standard deviations (STDs) and error for sample ak0012. The cells highlighted in green are the values used for this sample.

	1	2	3	4
Aliquot Ages (Ma)	219.1	219.1	219.1	160.6
	265.5	265.5	265.5	152.4
	160.6	160.6		
	390.7	152.4		
	152.4			
Mean Age (Ma)	**237.7**	**199.4**	**242.3**	**156.5**
STD (Ma)	**97.1**	**53.1**	**32.8**	**5.8**
Mean age error (Ma)	**43.4**	**26.6**	**23.2**	**4.1**

Sample ak0011

Sample ak0011 is a granite, collected ~54 km from the coastline at an elevation of ~231 m above sea level (Figure 3.15). Aliquots from this sample range in age from 187.4 ± 0.80 Ma – 223.9 ± 0.86 Ma (Table 3.59, Table 3.43, Figure 3.18). Ages are relatively evenly dispersed between end members and all of the ages fit into an age range 20% above and below the median age. All of the aliquots from this sample are used for calculating the mean and yield and mean age of 204.5 ± 6.2 (Table 3.43).

Aliquot Ages (Ma)	198.4
	201.5
	211.1
	187.4
	223.9
Mean Age (Ma)	**204.5**
STD (Ma)	**13.8**
Mean age error (Ma)	**6.2**

Table 3.43 Aliquot ages showing resulting mean age, standard deviation (STD) and error for sample ak0011. The cells highlighted in green are the values used for this sample.

Sample ak0010

Sample ak0010 is a migmatitic orthogneiss, collected ~61 km from the coastline at an elevation of ~50 m above sea level (Figure 3.15). Aliquots from this sample range in age from 203.8 ± 0.87 Ma – 423.3 ± 1.83 Ma (Table 3.59, Table 3.44, Figure 3.18). The oldest age, aliquot 3 is an outlier from otherwise well-grouped ages that fit into an age range 20% above and below the median age. Sample ak0010-3 is discarded and the mean age is 221.5 ± 10.6 (Table 3.44, column 2).

	1	2
Aliquot Ages (Ma)	203.8	203.8
	223.1	223.1
	423.3	208.4
	208.4	250.9
	250.9	
Mean Age (Ma)	**261.9**	**221.5**
STD (Ma)	**92.1**	**21.2**
Mean age error (Ma)	**41.2**	**10.6**

Table 3.44 Combinations of aliquot ages showing resulting mean ages, standard deviations (STDs) and error for sample ak0010. The cells highlighted in green are the values used for this sample.

Sample ak0009

Sample ak0009 is a granite or syeno-granite, collected ~78 km from the coastline at an elevation of ~117 m above sea level (Figure 3.15). Aliquots from this sample range in age from 24.8–187.4 Ma (Table 3.59, Table 3.45, Figure 3.15). Ages are unevenly dispersed between end members. If aliquots 3 and 4, the oldest and youngest ages, are discarded, the remaining ages, aliquots 1, 2 and 5 range in age from 100.4 ± 0.37 Ma – 124.2 ± 0.50 Ma, fitting into an age range 20% above and below the median age. Samples ak0009-3 and ak0009-4 were discarded and the mean age for this sample is 109.4 ± 7.4 Ma (Table 3.45, column 3).

	1	2	3
Aliquot Ages (Ma)	124.2	124.2	124.2
	103.4	103.4	103.4
	187.4	187.4	100.4
	24.8	100.4	
	100.4		
Mean Age (Ma)	**108**	**128.9**	**109.4**
STD (Ma)	**58.2**	**40.4**	**12.9**
Mean age error (Ma)	**26.0**	**20.2**	**7.4**

Table 3.45 Combinations of aliquot ages showing resulting mean ages, standard deviations (STDs) and error for sample ak0009. The cells highlighted in green are the values used for this sample.

Sample ak0008

Sample ak0008 is a tonalite gneiss, collected ~92 km from the coastline at an elevation of ~317 m above sea level (Figure 3.15). Aliquots from this sample range in age from 132.8 ± 0.57 Ma – 223.4 ± 1.00 Ma (Table 3.59, Table 3.46, Figure 3.18). If the youngest age, aliquot 1, is discarded, the new median age allows for the grouping of aliquots 2–5, which range in age from 172.7 ± 0.79 Ma – 223.4 ± 1.00 Ma, fitting into an age range 20% above and below the median age. Sample ak0008-1 was discarded and the mean age is 199.4 ± 12.7 Ma (Table 3.46, column 2).

	1	2
Aliquot Ages (Ma)	132.8	223.4
	223.4	218.6
	218.6	183
	183	172.7
	172.7	
Mean Age (Ma)	**186.1**	**199.4**
STD (Ma)	**37**	**25.4**
Mean age error (Ma)	**16.5**	**12.7**

Table 3.46 Combinations of aliquot ages showing resulting mean ages, standard deviations (STDs) and error for sample ak0008. The cells highlighted in green are the values used for this sample.

3.15 MAKKOVIK TRANSECT: (U-Th)/He RESULTS

The Makkovik transect consists of seven samples at the approximate latitude of Makkovik, Newfoundland (55.077222, -59.187778). Samples were collected by the GSC between 1967 and 1971 during ‘Opération Torngat’. Samples were retrieved from the Taylor Collection of the GSC sample archives in Ottawa (Ontario, Canada) and processed at Overburden Drilling Management in Ottawa for mineral separation. Samples were selected based on both the rock type (felsic igneous and metamorphic rocks which are generally fertile in apatite and zircon) and their location relative to the coastline; the aim was to build coast-perpendicular transects. Selected rocks include syenite, granite, granodiorite and possibly arkose. Geographically, the transect extends 32 km inland from the coastline at sea level and samples range in elevation from 0 to 193 m above sea level (Figure 3.19).

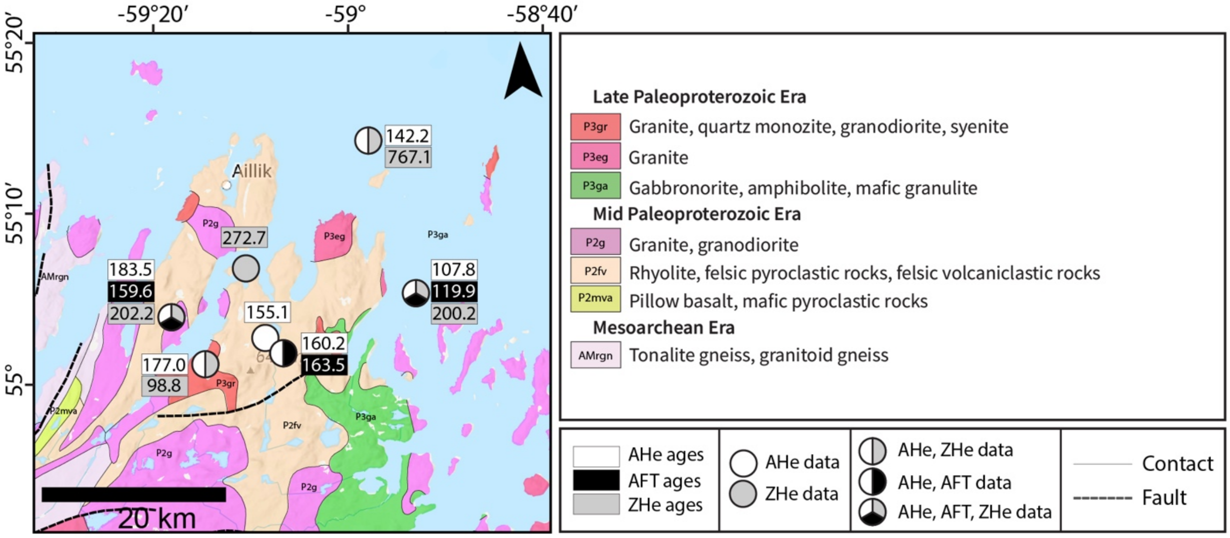

Figure 3.19 Regional geology, topography, sample locations and ages (including ZHe, AHe and AFT) along the Makkovik transect (Geology: Geological Survey of Canada 2011).

3.15.1 MAKKOVIK TRANSECT: ZHe RESULTS

Five of the seven samples (71TA464, 71TA923, 71BT407, 71TA929, 71TA909) contained suitable zircons, each producing five aliquots, totaling 25 cooling ages. ZHe ages in this transect range from 21.2 ± 0.09 Ma – 839.2 ± 3.90 Ma (Table 3.58, Figure 3.19). All of the samples have highly dispersed aliquot ages, but not all samples have equal amounts of dispersion. Sample z71TA923 has the highest range of measured grain ages, 172.9 ± 0.81 Ma – 471.7 ± 2.25 Ma, while sample z71TA909 has grain ages only ranging from 21.1 ± 0.09 Ma – 117.1 ± 0.54 Ma. Each of the following paragraphs includes a description of the data for each sample, as well as analysis of which aliquots will be used to calculate the mean age of the sample and the error of the mean based on single-grain age dispersion. Mean age error was calculated according to equation 3.17.

Sample z71TA464

Sample z71TA464 is a syenite, collected ~2 km from the coastline at an elevation of ~33 m above sea level (Figure 3.15). Aliquots from this sample range in age from 593.3 ± 2.80 Ma – 839.2 ± 3.90 Ma (Table 3.58, Table 3.47, Figure 3.19). Ages are unevenly dispersed between end members, but most aliquots are close enough in age to be grouped. If the youngest age, aliquot 3, is discarded, the other ages, aliquots 1, 2, 4, and 5 ranging in age from 658.6 ± 3.10 Ma –

800.4 ± 3.77 Ma fit into an age range 20% above and below the median age and can be grouped together. Sample z71TA464-3 was discarded in the calculation of the mean (Table 3.47, column 4), and the mean age is 743.0 ± 37.4 Ma.

Table 3.47 Combinations of aliquot ages showing resulting mean ages, standard deviations (STDs) and error for sample z71TA464. The cells highlighted in green are the values used for this sample.

	1	2	3	4
Aliquot Ages (Ma)	800.4	658.6	800.4	800.4
	658.6	593.3	770.1	658.6
	593.3	770.1	839.2	770.1
	770.1			839.2
	839.2			
Mean Age (Ma)	**732.3**	**674**	**803.2**	**743**
STD (Ma)	**102.8**	**89.4**	**34.6**	**74.7**
Mean age error (Ma)	**46.0**	**51.6**	**20.0**	**37.4**

Sample z71TA923

Sample z71TA923 is a granite, collected ~12 km from the coastline at an elevation of ~4 m above sea level (Figure 3.15). Aliquots from this sample range in age from 172.9 ± 0.81 Ma – 471.7 ± 2.25 Ma (Table 3.58, Table 3.48, Figure 3.19). Ages are unevenly dispersed between end members, but most aliquots are close enough in age to be grouped. If the oldest age, aliquot 2, is discarded, the other ages, aliquots 1, 3, 4, and 5 range in age from 172.9 ± 0.81 Ma – 228.5 ± 1.08 Ma, fit into a range 20% above and below the median age and can be grouped together. Sample z71TA923-2 is discarded and the mean age for this sample is 200.2 ± 11.4 Ma (Table 3.48, column 2).

	1	2
Aliquot Ages (Ma) Aliquot Ages (Ma	228.5	228.5
	471.7	201.7
	201.7	197.6
	197.6	172.9
	172.9	
Mean Age (Ma)	**254.5**	**200.2**
STD (Ma)	**123**	**22.7**
Mean age error (Ma)	**55.0**	**11.4**

Table 3.48 Combinations of aliquot ages showing resulting mean ages, standard deviations (STDs) and error for sample z71TA923. The cells highlighted in green are the values used for this sample.

Sample z71BT407

Sample z71BT407 is a granodiorite, collected ~21 km from the coastline at an elevation of ~0 m above sea level (Figure 3.15). Grains chosen from this sample for dating were not ideal, as the sample was very small with few zircons. Ages from this sample range in age from 44.6 ± 0.19 Ma – 357.7 ± 1.60 Ma (Table 3.58, Table 3.49, Figure 3.19). Aliquots are relatively evenly dispersed between end members with no obvious outliers and only one aliquot fitting into an age range 20% above and below the median age (Table 3.49). In calculations of the mean age and STD (Table 3.49), column 2, where the youngest age was removed, has a mean age that is comparable to all others, but an STD that is lower than in column 1 in which all aliquots are taken into account. Therefore, the mean age chosen for this sample is the one obtained in column 2; 272.7 ± 33.6 Ma.

Table 3.49 Combinations of aliquot ages showing resulting mean ages, standard deviations (STDs) and error for sample z71BT407. The cells highlighted in green are the values used for this sample.

	1	2	3	4
Aliquot Ages (Ma)	357.7	357.7	357.7	284.7
	44.6	284.7	284.7	197.3
	284.7	251	251	251
	197.3	197.3		
	251			
Mean Age (Ma)	**227.1**	**272.7**	**297.8**	**244.3**
STD (Ma)	**117.4**	**67.1**	**54.5**	**44.1**
Mean age error (Ma)	**52.5**	**33.6**	**31.5**	**25.5**

Sample z71TA929

Sample z71TA929 is a hornblende, biotite granite, collected ~31 km from the coastline at an elevation of ~163 m above sea level (Figure 3.15). Aliquots from this sample range in age from 68.1 ± 0.31 Ma – 249.9 ± 1.10 Ma (Table 3.58, Table 3.50, Figure 3.19) and ages are relatively evenly dispersed between end members. The youngest age, aliquot 3 is a possible outlier. If that aliquot is discarded, this sample could be broken into two groups consisting of (1) aliquots 2 and 4 with ages of 167.0 ± 0.77 Ma and 150.5 ± 0.70 Ma respectively, and (2) aliquots 1 and 5 with ages of 241.3 ± 1.11 Ma and 249.9 ± 1.10 Ma respectively. A four aliquots solution (Table 3.50, column 2) uses the most aliquot ages with the lowest STD. Therefore, mean age and STD from column 2 selected.

Table 3.50 Combinations of aliquot ages showing resulting mean ages, standard deviations (STDs) and error for sample z71TA929. The cells highlighted in green are the values used for this sample.

	1	2	3	4	5
Aliquot Ages (Ma)	241.3	241.3	241.3	241.3	167
	167	167	167	249.9	150.5
	68.1	150.5	249.9		
	150.5	249.9			
	249.9				
Mean Age (Ma)	**175.4**	**202.2**	**219.4**	**245.6**	**158.8**
STD (Ma)	**74.3**	**50.7**	**45.6**	**6.1**	**11.7**
Mean age error (Ma)	**33.2**	**25.4**	**26.3**	**4.3**	**8.3**

Sample z71TA909

Sample z71TA909 is a hornblende, biotite granodiorite, collected ~32 km from the coastline at an elevation of ~193 m above sea level (Figure 3.15). Aliquots from this sample range in age from 21.1 ± 0.09 Ma – 117.1 ± 0.54 Ma (Table 3.58, Table 3.51, Figure 3.19) and ages are relatively evenly dispersed between end members. The oldest age, aliquot 2 is a possible outlier. If that aliquot is discarded, this sample could be broken into two groups consisting of (1) aliquots 3 and 5 with ages of 21.1 ± 0.09 Ma and 38.6 ± 0.18 Ma respectively, and (2) aliquots 1 and 4 with ages of 97.3 ± 0.44 Ma and 82.1 ± 0.39 Ma respectively. An acceptable mean age for plotting and calculating is the solution from Table 3.51, column 2.

	1	2
Aliquot Ages (Ma)	97.3	97.3
	117.1	117.1
	21.1	82.1
	82.1	
	38.6	
Mean Age (Ma)	**71.3**	**98.9**
STD (Ma)	**40.3**	**17.6**
Mean age error (Ma)	**18.0**	**10.2**

Table 3.51 Combinations of aliquot ages showing resulting mean ages, standard deviations (STDs) and error for sample z71TA909. The cells highlighted in green are the values used for this sample.

3.15.2 MAKKOVIK TRANSECT: AHe RESULTS

Six of the seven samples (71TA464, 71TA923, 71TA910, 71TA912, 71TA929, 71TA909) contained suitable apatites, each producing five aliquots totaling 30 cooling ages. AHe ages range from 92.6 ± 0.33 Ma – 937.5 ± 3.32 Ma. Samples in this transect are the least dispersed of all apatite transects. Almost all of the grains are reset and generally fall between 100 and 300 Ma, except for sample a71TA910-5 with an age of 937.5 Ma (Figure 3.19). Each of the following paragraphs includes a description of the data for each sample, as well as analysis of which aliquots will be used to calculate the mean age of the sample and the error of the mean based on single-grain age dispersion. Mean age error was calculated according to equation 3.17.

Sample a71TA464

Sample a71TA464 is a syenite, collected ~2 km from the coastline at an elevation of ~33 m above sea level (Figure 3.15). Aliquots from this sample range in age from 92.6 ± 0.33 Ma – 147.1 ± 0.54 Ma (Table 3.59, Table 3.52, Figure 3.19). Aliquot a71TA464-4 is an outlier within the group with an age of 92.6 ± 0.33 Ma. If this aliquot were discarded, aliquots 1, 2, 3, and 5, ranging in age from 137.4 ± 0.53 Ma – 147.1 ± 0.54 Ma fit into an age range 20% above and below the median age. Sample a71TA464-4 should be discarded in calculations of the mean (Table 3.52, column 2).

	1	2
Aliquot Ages (Ma)	147.1	147.1
	137.4	137.4
	145.5	145.5
	92.6	138.6
	138.6	
Mean Age (Ma)	**132.2**	**142.1**
STD (Ma)	**22.6**	**4.8**
Mean age error (Ma)	**10.1**	**2.4**

Table 3.52 Combinations of aliquot ages showing resulting mean ages, standard deviations (STDs) and error for sample a71TA464. The cells highlighted in green are the values used for this sample.

Sample a71TA923

Sample a71TA923 is a granite, collected ~12 km from the coastline at an elevation of ~4 m above sea level (Figure 3.15). Aliquots from this sample range in age from 103.8 ± 0.38 Ma – 272.4 ± 0.99 Ma (Table 3.59, Table 3.53, Figure 3.19). The oldest age, aliquot a71TA923-1 with an age of 272.4 ± 0.99 Ma, is an outlier within the group. If this aliquot were discarded, aliquots 2–5, ranging in age from 103.8 ± 0.38 Ma – 116.1 ± 0.42 Ma fit into an age range 20% above and below the median age and group together well. Sample a71TA923-1 was discarded and we obtained a mean age of 109.9 ± 3.1 Ma (Table 3.53, column 2).

	1	2
Aliquot Ages (Ma)	272.4	116.1
	116.1	113.9
	113.9	103.8
	103.8	105.6
	105.6	
Mean Age (Ma)	**142.4**	**109.9**
STD (Ma)	**72.9**	**6.1**
Mean age error (Ma)	**32.6**	**3.1**

Table 3.53 Combinations of aliquot ages showing resulting mean ages, standard deviations (STDs) and error for sample a71TA923. The cells highlighted in green are the values used for this sample.

Sample a71TA910

Sample a71TA910 is a hornblende granite, collected ~26 km from the coastline at an elevation of ~104 m above sea level (Figure 3.15). This sample contained only few apatites. Aliquots from this sample range in age from 150.6 ± 0.54 Ma – 937.5 ± 3.32 Ma (Table 3.59, Table 3.54). Ages are highly and unevenly dispersed between end members. Aliquot 5 with an age of 937.5 ± 3.32 Ma is an obvious outlier, as it is 714.8 Ma older than the next oldest sample. Aliquots 1–3, ranging in age from 150.6 ± 0.54 Ma – 161.9 ± 0.57 Ma, fit into an age range 20% above and below the median age and can be grouped together. Aliquot 4 lies outside of this range and should not be included in the grouping. A mean age of 155.1 ± 3.4 Ma was obtained for this sample (Table 3.54, column 3).

	1	2	3
Aliquot Ages (Ma)	150.6	150.6	150.6
	161.9	161.9	161.9
	152.9	152.9	152.9
	222.7	222.7	
	937.5		
Mean Age (Ma)	**325.1**	**172**	**155.1**
STD (Ma)	**343.6**	**34.1**	**5.9**
Mean age error (Ma)	**153.7**	**17.1**	**3.4**

Table 3.54 Combinations of aliquot ages showing resulting mean ages, standard deviations (STDs) and error for sample a71TA910. The cells highlighted in green are the values used for this sample.

Sample a71TA912

Sample a71TA912 is a hornblende granodiorite, collected ~26 km from the coastline at an elevation of ~135 m above sea level (Figure 3.15). In this sample, most of the euhedral apatites had inclusions. AHe ages have the second lowest dispersion of all samples in all transects, with an age range of 153.7 ± 0.62 Ma – 167.7 ± 0.66 Ma (Table 3.59, Table 3.55, Figure 3.19). All of the aliquots from this sample are used for calculating the mean (Table 3.55).

Aliquot Ages (Ma)	153.7
	156.5
	167.7
	157.4
	165.5
Mean Age (Ma)	**160.2**
STD (Ma)	**6.1**
Mean age error (Ma)	**2.7**

Table 3.55 Aliquot ages showing resulting mean age, standard deviation (STD) and error for sample a71TA912. The cells highlighted in green are the values used for this sample.

Sample a71TA929

Sample a71TA929 is a hornblende, biotite granite, collected ~31 km from the coastline at an elevation of ~163 m above sea level (Figure 3.15). There were many apatites in this sample with inclusions. Ages from this sample range in age from 134.6 ± 0.49 Ma – 249.0 ± 0.90 Ma (Table 3.59, Table 3.56, Figure 3.19). Aliquots are relatively evenly dispersed between end members with no obvious outliers and only one aliquot fitting into an age range 20% above and below the median age. All of the aliquots from this sample were used for calculating the mean (Table 3.56).

	1	2
Aliquot Ages (Ma)	143.9	143.9
	249	191.4
	191.4	198.5
	198.5	134.6
	134.6	
Mean Age (Ma)	**183.5**	**167.1**
STD (Ma)	**46.2**	**32.5**
Mean age error (Ma)	**20.7**	**16.3**

Table 3.56 Combinations of aliquot ages showing resulting mean ages, standard deviations (STDs) and error for sample a71TA929. The cells highlighted in green are the values used for this sample.

Sample a71TA909

Sample a71TA909 is a hornblende, biotite granodiorite, collected ~32 km from the coastline at an elevation of ~193 m above sea level (Figure 3.15). There were few apatites in this sample to choose from. Aliquots from this sample range in age from 124.3 ± 0.45 Ma – 336.5 ± 1.25 Ma (Table 3.59, Table 3.57, Figure 3.19). Ages are unevenly dispersed between end members, but some aliquots are close enough in age to be grouped. Aliquots 1, 4, and 5, ranging in age from 165.3 ± 0.59 Ma – 198.0 ± 0.71 Ma, fit into an age range 20% above and below the median age. The youngest and oldest ages in this sample, aliquots 2 and 3 do not fit into this range and were discarded yielding a mean of 177.0 Ma ± 10.6 Ma for this sample (Table 3.57).

	1	2
Aliquot Ages (Ma)	198	198
	124.3	165.3
	336.5	167.7
	165.3	
	167.7	
Mean Age (Ma)	**198.4**	**177**
STD (Ma)	**81.6**	**18.3**
Mean age error (Ma)	**36.5**	**10.6**

Table 3.57 Combinations of aliquot ages showing resulting mean ages, standard deviations (STDs) and error for sample a71TA909. The cells highlighted in green are the values used for this sample.

3.16 (U-Th)/He RESULTS: RAW DATA TABLES

Table 3.58 Reduced ZHe data. Abbreviations are err, error; Ft, α-ejection correction; ESR, effective spherical ratio (of the grain).

Transect	Sample	Mineral	Corrected age, Ma	err., Ma	U (ppm)	Th (ppm)	147Sm (ppm)	eU	Th/U	He (nmol/g)	mass (ug)	Ft	ESR	Raw Age, Ma	err., Ma
Saglek	z67SC216-1	zircon	337.0	1.55	269.5	105.0	6.7	293.8	0.39	351.3	1.62	0.64	31.28	217.11	1.55
Saglek	z67SC216-2	zircon	510.3	2.37	95.2	31.6	2.5	102.5	0.33	237.5	10.78	0.81	61.43	412.19	2.37
Saglek	z67SC216-3	zircon	217.7	1.05	750.4	116.4	14.1	777.3	0.16	690.5	4.92	0.75	44.74	162.28	1.05
Saglek	z67SC216-4	zircon	407.6	1.90	279.1	86.0	9.4	299.0	0.31	467.8	2.82	0.69	36.73	282.28	1.90
Saglek	z67SC216-5	zircon	341.3	1.55	268.6	116.9	11.3	295.5	0.44	384.0	2.77	0.69	36.67	235.44	1.55
Saglek	z69TA217-1	zircon	259.0	1.25	492.2	73.2	8.7	509.1	0.15	574.3	9.24	0.79	55.75	205.19	1.25
Saglek	z69TA217-2	zircon	137.7	0.67	402.8	52.5	16.8	415.0	0.13	235.4	4.66	0.76	46.97	104.24	0.67
Saglek	z69TA217-3	zircon	203.7	0.96	522.8	146.6	28.4	556.7	0.28	486.7	8.68	0.78	53.96	159.66	0.96
Saglek	z69TA217-4	zircon	157.2	0.76	568.0	69.8	26.8	584.2	0.12	391.7	8.62	0.78	52.89	122.96	0.76
Saglek	z69TA217-5	zircon	82.7	0.41	823.5	62.6	23.3	838.1	0.08	287.3	6.18	0.76	48.37	63.27	0.41
Saglek	z67SC218-1	zircon	564.8	2.66	75.7	19.8	3.4	80.3	0.26	162.6	1.37	0.64	30.70	362.22	2.66
Saglek	z67SC218-2	zircon	810.2	3.43	107.6	90.7	7.1	128.5	0.84	396.9	2.02	0.67	34.75	542.33	3.43
Saglek	z67SC218-3	zircon	1096.3	5.00	51.2	21.4	1.1	56.1	0.42	274.8	5.19	0.75	47.31	826.47	5.00
Saglek	z67SC218-4	zircon	762.2	3.53	115.3	39.6	9.5	124.5	0.34	368.5	2.05	0.68	35.48	520.09	3.53
Saglek	z67SC218-5	zircon	807.6	3.76	124.2	39.9	3.3	133.4	0.32	345.8	0.73	0.57	24.77	458.72	3.76
Saglek	z69TA212-1	zircon	397.9	8.12	0.02	0.02	0.00	0.02	1.02	0.04	28.50	0.85	80.70	337.17	8.12
Saglek	z69TA212-2	zircon	530.3	2.64	2.29	0.06	0.09	2.30	0.03	6.14	57.06	0.89	105.59	470.93	2.64
Saglek	z69TA212-3	zircon	779.4	7.38	0.04	0.01	0.47	0.04	0.34	0.17	39.62	0.86	88.71	673.54	7.38
Saglek	z69TA212-4	zircon	625.3	29.12	0.01	0.01	0.00	0.01	0.75	0.03	30.28	0.86	86.11	536.30	29.12
Saglek	z69TA212-5	zircon	378.8	7.96	0.02	0.03	0.00	0.02	2.03	0.04	25.15	0.84	80.19	319.59	7.96

***Table 3.58* (cont'd)** Reduced ZHe data.

Transect	Sample	Mineral	Corrected age, Ma	err., Ma	U (ppm)	Th (ppm)	147Sm (ppm)	eU	Th/U	He (nmol/g)	mass (ug)	Ft	ESR	Raw Age, Ma	err., Ma
Saglek	z69TA201-1	zircon	768.9	3.57	220.4	73.3	5.3	237.3	0.33	766.9	4.01	0.73	43.31	564.75	3.57
Saglek	z69TA201-2	zircon	618.4	2.86	195.9	69.3	9.0	211.9	0.35	583.8	6.97	0.79	54.86	486.14	2.86
Saglek	z69TA201-3	zircon	669.4	3.31	14.3	0.7	0.5	14.4	0.05	42.2	5.17	0.77	49.15	514.63	3.31
Saglek	z69TA201-4	zircon	745.2	3.19	119.9	91.5	4.5	141.0	0.76	474.1	7.60	0.79	56.45	587.06	3.19
Saglek	z69TA201-5	zircon	836.4	3.67	71.0	44.2	2.2	81.2	0.62	319.0	10.09	0.81	63.53	678.30	3.67
Saglek	z69TA210-1	zircon	349.6	6.76	0.01	0.06	0.09	0.03	5.39	0.0	22.69	0.84	77.43	292.11	6.76
Saglek	z69TA210-3	zircon	235.6	2.30	0.04	0.04	0.10	0.05	1.14	0.1	27.46	0.85	83.97	200.86	2.30
Saglek	z69TA210-4	zircon	1612.7	26.48	0.02	0.03	0.12	0.03	1.27	0.2	28.03	0.86	87.39	1383.18	26.48
Saglek	z69TA210-5	zircon	683.4	3.13	124.8	50.1	2.0	136.3	0.40	427.1	8.87	0.80	60.16	548.91	3.13
Saglek	z69TA206-1	zircon	899.2	4.02	127.0	66.5	2.3	142.3	0.52	546.1	4.57	0.74	44.37	663.30	4.02
Saglek	z69TA206-2	zircon	895.6	3.97	111.9	63.1	0.7	126.5	0.56	476.2	3.49	0.73	42.69	651.87	3.97
Saglek	z69TA206-3	zircon	560.2	2.62	459.3	133.9	2.3	490.1	0.29	1174.2	5.40	0.76	48.18	425.62	2.62
Saglek	z69TA206-4	zircon	979.6	4.45	162.0	70.8	1.6	178.3	0.44	724.1	3.17	0.71	39.96	698.27	4.45
Saglek	z69TA206-5	zircon	858.7	3.65	123.2	99.5	4.0	146.1	0.81	527.3	3.90	0.73	43.59	627.30	3.65
Nain	z67SC216-1	zircon	337.0	1.55	269.5	105.0	6.7	293.8	0.39	351.3	1.62	0.64	31.28	217.11	1.55
Nain	z67SC216-2	zircon	510.3	2.37	95.2	31.6	2.5	102.5	0.33	237.5	10.78	0.81	61.43	412.19	2.37
Nain	z67SC216-3	zircon	217.7	1.05	750.4	116.4	14.1	777.3	0.16	690.5	4.92	0.75	44.74	162.28	1.05
Nain	z67SC216-4	zircon	407.6	1.90	279.1	86.0	9.4	299.0	0.31	467.8	2.82	0.69	36.73	282.28	1.90
Nain	z67SC216-5	zircon	341.3	1.55	268.6	116.9	11.3	295.5	0.44	384.0	2.77	0.69	36.67	235.44	1.55

***Table 3.58* (cont'd)** Reduced ZHe data.

Transect	Sample	Mineral	Corrected age, Ma	err., Ma	U (ppm)	Th (ppm)	147Sm (ppm)	eU	Th/U	He (nmol/g)	mass (ug)	Ft	ESR	Raw Age, Ma	err., Ma
Nain	z69FQ332-1	zircon	211.9	0.96	623.7	270.9	75.3	686.4	0.43	587.4	4.58	0.74	44.07	156.20	0.96
Nain	z69FQ332-2	zircon	156.1	0.69	707.8	396.3	58.4	799.3	0.56	458.4	2.33	0.67	34.82	105.13	0.69
Nain	z69FQ332-3	zircon	170.6	0.80	685.8	191.6	17.8	730.0	0.28	453.2	1.84	0.67	33.56	113.89	0.80
Nain	z69FQ332-4	zircon	100.9	0.48	410.4	92.7	59.2	432.0	0.23	166.6	2.75	0.70	38.02	71.01	0.48
Nain	z69FQ332-5	zircon	128.5	0.59	526.1	186.1	51.5	569.2	0.35	278.4	2.44	0.70	37.79	89.87	0.59
Nain	z69FQ335-1	zircon	384.7	1.88	318.6	34.5	13.2	326.6	0.11	539.9	6.29	0.77	50.73	297.78	1.88
Nain	z69FQ335-2	zircon	554.1	2.63	249.1	59.0	22.4	262.8	0.24	606.9	4.57	0.74	44.27	410.83	2.63
Nain	z69FQ335-3	zircon	55.4	0.27	595.2	23.1	31.4	600.7	0.04	141.7	6.89	0.79	53.78	43.63	0.27
Nain	z69FQ335-4	zircon	76.0	0.37	551.1	65.0	21.1	566.2	0.12	168.7	3.17	0.72	40.80	55.02	0.37
Nain	z69FQ335-5	zircon	104.5	0.50	520.1	117.7	54.9	547.5	0.23	214.0	2.45	0.69	36.04	71.99	0.50
Nain	z69MZ379-1	zircon	598.1	2.89	342.1	50.9	1.7	353.9	0.15	912.1	5.73	0.76	48.28	456.21	2.89
Nain	z69MZ379-2	zircon	686.5	3.35	146.8	16.0	1.9	150.5	0.11	452.3	5.73	0.77	49.30	527.26	3.35
Nain	z69MZ379-3	zircon	241.5	1.14	434.5	103.7	7.3	458.4	0.24	422.8	2.57	0.70	37.15	168.36	1.14
Nain	z69MZ379-4	zircon	130.9	0.65	666.2	36.3	2.8	674.6	0.05	387.4	10.16	0.81	59.50	105.55	0.65
Nain	z69MZ379-5	zircon	130.4	0.64	676.8	53.0	13.6	689.1	0.08	345.2	2.86	0.71	38.00	92.19	0.64
Nain	z69TA336-1	zircon	275.1	1.14	557.8	566.6	23.4	688.3	1.02	868.3	19.93	0.83	72.11	228.40	1.14
Nain	z69TA336-2	zircon	250.4	1.06	366.6	305.0	31.7	437.0	0.83	495.8	17.72	0.82	68.28	205.89	1.06
Nain	z69TA336-3	zircon	55.5	0.24	698.2	560.5	74.9	827.6	0.80	185.9	5.04	0.75	46.37	41.36	0.24
Nain	z69TA336-4	zircon	181.1	0.82	934.2	425.5	23.3	1032.3	0.46	847.9	16.18	0.83	69.83	150.04	0.82
Nain	z69TA336-5	zircon	714.8	3.18	187.4	102.1	17.1	211.0	0.54	701.9	13.02	0.81	63.84	580.76	3.18

***Table 3.58* (cont'd)** Reduced ZHe data.

Transect	Sample	Mineral	Corrected age, Ma	err., Ma	U (ppm)	Th (ppm)	147Sm (ppm)	eU	Th/U	He (nmol/g)	mass (ug)	Ft	ESR	Raw Age, Ma	err., Ma
Nain	z69MZ392-1	zircon	1340.6	5.84	26.1	17.4	1.2	30.2	0.67	181.3	4.77	0.74	45.18	992.60	5.84
Nain	z69MZ392-2	zircon	1159.9	5.12	21.1	12.5	0.7	24.0	0.59	129.8	9.04	0.78	53.83	904.31	5.12
Nain	z69MZ392-3	zircon	1070.3	4.59	16.0	12.7	1.2	18.9	0.79	84.8	3.61	0.71	40.85	764.54	4.59
Nain	z69MZ392-4	zircon	1286.4	5.51	46.1	35.4	2.1	54.3	0.77	305.1	4.93	0.73	43.22	937.43	5.51
Nain	z69MZ392-5	zircon	1057.4	4.59	17.1	11.9	2.2	19.9	0.69	91.6	5.08	0.74	45.48	784.28	4.59
Nain	z69MZ351-1	zircon	404.9	1.88	285.8	91.6	9.4	307.0	0.32	515.6	4.37	0.75	45.59	302.39	1.88
Nain	z69MZ351-2	zircon	265.3	1.24	541.6	158.7	7.9	578.2	0.29	615.2	3.68	0.73	42.40	193.68	1.24
Nain	z69MZ351-3	zircon	557.0	2.60	250.5	73.8	6.8	267.5	0.29	650.7	6.37	0.78	51.84	431.88	2.60
Nain	z69MZ351-4	zircon	749.3	3.52	313.2	88.0	3.8	333.5	0.28	1058.3	3.84	0.74	44.34	555.25	3.52
Nain	z69MZ351-5	zircon	535.3	2.43	276.7	124.2	9.6	305.3	0.45	673.9	3.69	0.74	43.72	393.49	2.43
Hopedale	zk0016-1	zircon	715.9	2.94	117.8	125.7	7.8	146.8	1.07	501.4	18.99	0.83	73.63	596.50	2.94
Hopedale	zk0016-2	zircon	1046.1	4.96	55.6	13.0	1.2	58.6	0.23	318.0	29.93	0.86	87.54	903.24	4.96
Hopedale	zk0016-3	zircon	1049.7	5.09	61.2	7.9	1.1	63.1	0.13	338.8	23.60	0.85	79.70	894.27	5.09
Hopedale	zk0016-4	zircon	1103.2	5.34	110.0	16.1	2.6	113.7	0.15	586.6	7.18	0.78	53.01	863.16	5.34
Hopedale	zk0016-5	zircon	432.1	2.10	260.3	31.7	17.9	267.7	0.12	517.9	9.46	0.80	58.60	346.65	2.10
Hopedale	zk0015-1	zircon	149.9	0.74	608.9	31.6	11.5	616.2	0.05	394.2	7.44	0.78	52.85	117.43	0.74
Hopedale	zk0015-2	zircon	131.3	0.64	471.4	59.6	13.1	485.2	0.13	257.0	4.52	0.74	43.92	97.41	0.64
Hopedale	zk0015-3	zircon	333.8	1.66	336.2	14.1	8.7	339.5	0.04	483.9	4.89	0.77	50.03	257.89	1.66
Hopedale	zk0015-4	zircon	309.0	1.49	385.9	59.4	24.8	399.7	0.15	485.1	2.86	0.71	39.21	220.40	1.49
Hopedale	zk0015-5	zircon	219.4	1.05	482.6	89.9	52.6	503.5	0.19	456.9	4.90	0.76	46.81	165.66	1.05

***Table 3.58* (cont'd)** Reduced ZHe data.

Transect	Sample	Mineral	Corrected age, Ma	err., Ma	U (ppm)	Th (ppm)	147Sm (ppm)	eU	Th/U	He (nmol/g)	mass (ug)	Ft	ESR	Raw Age, Ma	err., Ma
Hopedale	zk0014-1	zircon	1017.0	4.73	63.0	20.4	8.5	67.7	0.32	321.3	7.45	0.79	55.80	803.25	4.73
Hopedale	zk0014-2	zircon	369.9	1.73	351.6	103.2	87.1	375.8	0.29	549.3	3.84	0.71	39.74	264.00	1.73
Hopedale	zk0014-3	zircon	428.3	2.07	317.8	47.8	46.5	329.1	0.15	562.3	3.40	0.72	39.91	307.42	2.07
Hopedale	zk0014-4	zircon	1065.7	5.09	91.8	18.2	6.8	96.0	0.20	448.5	4.52	0.74	44.32	791.14	5.09
Hopedale	zk0014-5	zircon	633.7	2.99	206.8	54.1	22.6	219.3	0.26	626.6	9.62	0.79	56.61	502.86	2.99
Hopedale	zk0013-1	zircon	701.3	3.17	233.5	109.2	15.0	258.7	0.47	835.3	14.53	0.81	61.01	564.58	3.17
Hopedale	zk0013-2	zircon	363.4	1.59	204.1	133.8	9.5	234.9	0.66	361.2	7.81	0.76	49.91	277.30	1.59
Hopedale	zk0013-3	zircon	450.3	2.09	360.5	118.4	14.0	387.9	0.33	714.6	4.44	0.73	43.28	330.69	2.09
Hopedale	zk0013-4	zircon	479.5	2.32	266.8	43.3	11.4	276.8	0.16	522.3	2.37	0.71	38.13	338.41	2.32
Hopedale	zk0013-5	zircon	219.0	0.96	383.1	238.3	18.8	438.1	0.62	398.7	8.14	0.76	48.55	165.89	0.96
Hopedale	zk0012-1	zircon	1111.0	5.24	47.5	12.0	1.2	50.3	0.25	258.0	6.73	0.77	51.33	859.85	5.24
Hopedale	zk0012-2	zircon	1059.1	5.14	30.9	4.1	0.5	31.9	0.13	164.0	9.82	0.81	62.12	860.56	5.14
Hopedale	zk0012-3	zircon	1167.1	5.43	31.2	10.2	1.2	33.5	0.33	200.9	19.43	0.84	76.52	984.79	5.43
Hopedale	zk0012-4	zircon	1033.4	5.07	58.3	5.5	1.5	59.6	0.09	277.1	5.44	0.76	47.76	786.94	5.07
Hopedale	zk0012-5	zircon	1380.6	6.39	89.2	31.6	3.2	96.5	0.35	624.9	7.07	0.76	48.94	1052.40	6.39
Hopedale	zk0011-1	zircon	293.8	1.40	367.3	82.7	76.6	386.8	0.23	454.1	4.24	0.73	41.46	213.23	1.40
Hopedale	zk0011-2	zircon	37.6	0.19	651.4	6.7	11.5	653.0	0.01	96.6	3.52	0.73	41.07	27.39	0.19
Hopedale	zk0011-3	zircon	281.1	1.31	824.4	264.0	20.7	885.3	0.32	989.8	3.17	0.72	41.34	203.30	1.31
Hopedale	zk0011-4	zircon	5.4	0.03	2654.5	8.3	5.9	2656.5	0.00	66.8	34.44	0.86	86.56	4.67	0.03
Hopedale	zk0011-5	zircon	154.5	0.71	360.6	127.5	99.1	390.5	0.35	233.4	2.95	0.71	39.18	109.57	0.71

Table 3.58 **(cont'd)** Reduced ZHe data.

Transect	Sample	Mineral	Corrected age, Ma	err., Ma	U (ppm)	Th (ppm)	147Sm (ppm)	eU	Th/U	He (nmol/g)	mass (ug)	Ft	ESR	Raw Age, Ma	err., Ma
Hopedale	zk0010-1	zircon	26.8	0.13	1182.3	106.6	2.9	1206.8	0.09	145.3	15.19	0.83	68.99	22.30	0.13
Hopedale	zk0010-2	zircon	35.7	0.18	564.5	36.3	3.6	572.9	0.06	83.9	4.86	0.76	47.05	27.13	0.18
Hopedale	zk0010-3	zircon	510.7	2.47	217.3	29.8	4.5	224.2	0.14	491.9	5.87	0.77	48.98	391.21	2.47
Hopedale	zk0010-4	zircon	197.6	0.97	553.9	48.4	4.2	565.0	0.09	451.2	4.14	0.74	43.40	146.17	0.97
Hopedale	zk0010-5	zircon	358.1	1.77	332.7	18.3	2.2	336.9	0.05	491.5	3.67	0.74	42.71	263.84	1.77
Hopedale	zk009-1	zircon	635.7	3.08	173.8	22.6	12.9	179.0	0.13	485.1	5.61	0.75	45.98	478.17	3.08
Hopedale	zk009-2	zircon	700.1	3.43	158.5	15.2	126.9	162.6	0.10	482.2	4.13	0.74	43.86	519.60	3.43
Hopedale	zk009-3	zircon	442.9	2.15	154.0	18.2	23.0	158.3	0.12	293.5	4.18	0.75	45.66	332.61	2.15
Hopedale	zk009-4	zircon	197.2	0.96	263.7	36.3	56.6	272.4	0.14	210.8	2.95	0.72	39.87	141.60	0.96
Hopedale	zk009-5	zircon	588.0	2.88	131.4	12.4	24.2	134.4	0.09	325.6	3.28	0.73	41.89	429.95	2.88
Hopedale	zk008-1	zircon	226.4	1.12	713.4	30.0	9.6	720.4	0.04	702.5	8.25	0.79	53.44	177.97	1.12
Hopedale	zk008-2	zircon	534.4	2.58	169.9	25.3	6.1	175.8	0.15	411.7	6.24	0.78	52.23	416.50	2.58
Hopedale	zk008-3	zircon	495.9	2.26	150.2	63.3	4.3	164.8	0.42	335.3	3.66	0.73	43.43	363.88	2.26
Hopedale	zk008-4	zircon	365.9	1.76	148.3	26.1	8.3	154.4	0.18	256.7	12.18	0.82	64.57	299.53	1.76
Hopedale	zk008-5	zircon	530.6	2.57	145.5	21.3	11.6	150.4	0.15	360.0	10.40	0.80	58.33	424.93	2.57
Makkovik	z71TA464-1	zircon	800.4	3.77	48.4	13.1	4.8	51.4	0.27	190.5	10.25	0.80	58.95	641.14	3.77
Makkovik	z71TA464-2	zircon	658.6	3.10	49.0	13.1	5.6	52.1	0.27	144.8	4.98	0.74	44.93	490.20	3.10
Makkovik	z71TA464-3	zircon	593.3	2.80	137.5	35.1	22.8	145.6	0.26	328.8	2.07	0.68	34.67	401.98	2.80
Makkovik	z71TA464-4	zircon	770.1	3.59	54.7	16.8	10.9	58.6	0.31	186.4	3.63	0.72	41.10	556.04	3.59
Makkovik	z71TA464-5	zircon	839.2	3.90	34.5	11.3	4.3	37.1	0.33	141.1	8.53	0.78	53.96	657.16	3.90

***Table 3.58* (cont'd)** Reduced ZHe data.

Transect	Sample	Mineral	Corrected age, Ma	err., Ma	U (ppm)	Th (ppm)	147Sm (ppm)	eU	Th/U	He (nmol/g)	mass (ug)	Ft	ESR	Raw Age, Ma	err., Ma
Makkovik	z71TA923-1	zircon	228.5	1.08	367.2	91.2	35.3	388.4	0.25	329.9	2.90	0.68	34.87	155.20	1.08
Makkovik	z71TA923-2	zircon	471.7	2.25	697.5	149.8	35.4	732.1	0.21	1103.5	1.24	0.58	25.20	272.23	2.25
Makkovik	z71TA923-3	zircon	201.7	0.97	411.5	76.2	15.7	429.1	0.19	335.6	2.89	0.71	38.76	143.12	0.97
Makkovik	z71TA923-4	zircon	197.6	0.94	941.1	188.0	100.6	984.9	0.20	762.6	3.99	0.72	39.91	141.66	0.94
Makkovik	z71TA923-5	zircon	172.9	0.81	427.1	118.9	22.1	454.6	0.28	291.4	2.33	0.68	35.00	117.54	0.81
Makkovik	z71BT407-1	zircon	357.7	1.60	221.2	118.9	51.8	248.8	0.54	351.0	3.07	0.71	40.15	254.93	1.60
Makkovik	z71BT407-2	zircon	44.6	0.19	1047.5	986.9	32.6	1274.9	0.94	211.5	2.11	0.68	36.82	30.57	0.19
Makkovik	z71BT407-3	zircon	284.7	1.24	368.5	244.9	55.9	425.2	0.66	519.4	7.47	0.78	53.51	221.43	1.24
Makkovik	z71BT407-4	zircon	197.3	0.90	375.3	147.2	42.3	409.4	0.39	349.4	7.50	0.79	56.06	155.85	0.90
Makkovik	z71BT407-5	zircon	251.0	1.17	378.7	128.9	97.9	408.9	0.34	390.4	2.50	0.69	36.88	174.00	1.17
Makkovik	z71TA929-1	zircon	241.3	1.11	423.7	158.5	38.8	460.4	0.37	453.6	4.47	0.74	45.19	179.50	1.11
Makkovik	z71TA929-2	zircon	167.0	0.77	622.2	214.8	71.8	672.0	0.35	491.5	12.29	0.80	59.40	133.84	0.77
Makkovik	z71TA929-3	zircon	68.1	0.31	948.3	365.7	59.6	1032.8	0.39	280.3	3.80	0.74	43.55	50.05	0.31
Makkovik	z71TA929-4	zircon	150.5	0.70	408.2	141.3	71.2	441.1	0.35	260.4	3.10	0.72	40.74	108.26	0.70
Makkovik	z71TA929-5	zircon	249.9	1.10	367.7	215.6	38.1	417.6	0.59	425.6	4.61	0.74	45.31	185.44	1.10
Makkovik	z71TA909-1	zircon	97.3	0.44	716.4	312.1	18.3	788.3	0.44	336.0	9.65	0.81	60.92	78.38	0.44
Makkovik	z71TA909-2	zircon	117.1	0.54	1000.4	407.5	25.5	1094.3	0.41	549.7	9.44	0.79	55.52	92.28	0.54
Makkovik	z71TA909-3	zircon	21.1	0.09	2404.1	1333.3	97.5	2711.5	0.55	239.2	6.41	0.77	52.14	16.30	0.09
Makkovik	z71TA909-4	zircon	82.1	0.39	1165.9	251.9	22.2	1224.0	0.22	403.4	3.81	0.74	43.95	60.77	0.39
Makkovik	z71TA909-5	zircon	38.6	0.18	1301.3	561.9	69.3	1431.0	0.43	220.1	3.53	0.74	43.73	28.41	0.18

Table 3.59 Reduced AHe data. Abbreviations are err, error; Ft, α-ejection correction; ESR, effective spherical ratio (of the grain).

Transect	Sample	Mineral	Corrected age, Ma	err., Ma	U (ppm)	Th (ppm)	147Sm (ppm)	eU	Th/U	He (nmol/g)	mass (ug)	Ft	ESR	Raw Age, Ma	err., Ma
Saglek	a67SC216-1	apatite	121.1	0.56	22.3	7.5	45.5	24.2	0.34	11.4	3.10	0.71	50.40	85.89	0.56
Saglek	a67SC216-2	apatite	85.9	0.36	12.0	11.7	22.5	14.8	0.98	5.0	3.76	0.72	54.29	61.78	0.36
Saglek	a67SC216-3	apatite	119.2	0.52	16.8	10.3	38.4	19.4	0.62	9.0	3.41	0.71	52.37	85.17	0.52
Saglek	a67SC216-4	apatite	112.6	0.48	18.2	16.0	41.8	22.1	0.88	8.5	1.36	0.62	38.78	70.05	0.48
Saglek	a67SC216-5	apatite	125.5	0.54	17.6	13.0	49.8	20.9	0.74	9.5	2.04	0.66	43.85	83.20	0.54
Saglek	a69TA217-1	apatite	112.9	0.52	16.9	5.7	237.9	19.4	0.34	8.9	3.81	0.71	51.40	80.67	0.52
Saglek	a69TA217-2	apatite	123.4	0.58	10.2	2.5	264.4	12.1	0.25	6.9	10.01	0.79	72.11	97.81	0.58
Saglek	a69TA217-3	apatite	140.0	0.63	10.0	5.2	295.5	12.6	0.52	7.4	3.36	0.71	51.32	99.51	0.63
Saglek	a69TA217-4	apatite	192.4	0.93	20.0	3.5	246.5	22.1	0.17	18.6	6.47	0.77	65.09	148.82	0.93
Saglek	a69TA217-5	apatite	115.0	0.47	9.6	12.2	341.3	14.1	1.28	5.8	1.36	0.61	37.73	70.00	0.47
Saglek	a67SC218-1	apatite	355.4	1.60	10.3	5.2	27.9	11.6	0.51	17.9	6.99	0.78	67.59	275.64	1.60
Saglek	a67SC218-2	apatite	63.8	0.24	10.2	20.5	29.8	15.1	2.01	3.9	4.61	0.73	58.58	46.78	0.24
Saglek	a67SC218-3	apatite	103.8	0.45	17.9	11.9	40.3	20.8	0.66	7.8	1.92	0.66	42.83	68.19	0.45
Saglek	a67SC218-4	apatite	155.0	0.59	18.0	34.1	40.2	26.1	1.89	13.8	1.46	0.62	39.48	96.02	0.59
Saglek	a67SC218-5	apatite	208.1	0.81	8.5	14.2	101.7	12.3	1.66	8.8	1.37	0.61	38.62	127.63	0.81
Saglek	a69TA212-1	apatite	284.7	1.23	2.4	1.8	142.5	3.5	0.75	5.0	10.79	0.80	76.22	226.95	1.23
Saglek	a69TA212-2	apatite	187.8	0.83	4.6	3.1	148.7	6.1	0.67	5.0	5.57	0.75	59.50	139.98	0.83
Saglek	a69TA212-3	apatite	74.2	0.29	1.5	3.9	217.1	3.5	2.64	1.2	4.71	0.73	58.34	54.12	0.29
Saglek	a69TA212-4	apatite	121.5	0.47	1.9	4.4	148.9	3.6	2.38	1.9	3.85	0.70	52.47	85.39	0.47
Saglek	a69TA212-5	apatite	301.1	1.26	2.8	3.1	200.6	4.5	1.13	6.2	5.35	0.73	56.74	219.63	1.26

Table 3.59 (cont'd) Reduced AHe data.

Transect	Sample	Mineral	Corrected age, Ma	err., Ma	U (ppm)	Th (ppm)	147Sm (ppm)	eU	Th/U	He (nmol/g)	mass (ug)	Ft	ESR	Raw Age, Ma	err., Ma
Nain	a69FQ332-1	apatite	141.0	0.54	5.3	48.5	134.5	17.1	9.13	10.9	1.36	0.59	37.22	82.87	0.54
Nain	a69FQ332-2	apatite	123.6	0.46	3.1	22.5	41.1	8.5	7.26	14.7	3.64	0.69	50.74	84.92	0.46
Nain	a69FQ332-3	apatite	422.3	1.52	14.5	82.2	158.8	34.3	5.65	123.3	2.34	0.64	43.85	272.32	1.52
Nain	a69FQ332-4	apatite	177.1	0.64	4.3	27.2	196.5	11.5	6.37	43.7	5.04	0.73	60.04	129.68	0.64
Nain	a69FQ332-5	apatite	125.2	0.49	2.3	20.9	142.9	7.8	9.12	9.4	2.49	0.66	46.16	82.48	0.49
Nain	a69FQ335-1	apatite	54.2	0.20	3.7	8.3	255.0	6.8	2.28	4.3	2.80	0.68	48.47	36.90	0.20
Nain	a69FQ335-2	apatite	54.0	0.21	2.6	5.5	304.9	5.4	2.12	4.0	3.28	0.65	43.38	35.05	0.21
Nain	a69FQ335-3	apatite	46.5	0.17	2.8	9.4	185.0	5.9	3.42	2.6	2.40	0.67	46.63	31.00	0.17
Nain	a69FQ335-5	apatite	42.7	0.17	2.3	17.7	176.8	7.2	7.79	1.5	1.37	0.59	37.17	25.08	0.17
Nain	a69MZ379-1	apatite	182.1	0.81	13.3	7.2	137.1	15.6	0.54	11.7	4.14	0.73	55.24	132.73	0.81
Nain	a69MZ379-2	apatite	131.3	0.53	8.4	11.3	78.2	11.4	1.35	5.4	1.77	0.65	43.10	85.48	0.53
Nain	a69MZ379-3	apatite	318.1	1.21	11.4	20.0	86.0	16.5	1.75	22.3	6.84	0.76	65.25	241.43	1.21
Nain	a69MZ379-4	apatite	23.1	0.11	0.4	6.0	145.7	2.5	14.11	0.3	3.04	0.68	49.38	15.64	0.11
Nain	a69MZ379-5	apatite	18.0	0.09	0.4	8.7	166.7	3.2	21.91	0.2	2.10	0.64	44.12	11.58	0.09
Nain	a69FQ398-1	apatite	40.9	0.18	0.4	3.0	278.8	2.4	8.52	0.5	4.82	0.71	56.09	29.20	0.18
Nain	a69FQ398-2	apatite	53.8	0.21	0.2	1.5	268.5	1.9	7.22	0.7	17.86	0.81	87.70	43.70	0.21
Nain	a69FQ398-3	apatite	91.5	0.38	0.2	1.5	259.9	1.8	8.41	1.1	14.05	0.80	80.46	72.80	0.38
Nain	a69FQ398-4	apatite	127.1	0.55	0.2	1.7	328.9	2.2	9.11	1.7	10.05	0.75	63.71	94.73	0.55
Nain	a69FQ398-5	apatite	62.8	0.23	0.5	1.9	348.3	2.7	3.77	1.0	17.12	0.80	81.78	50.27	0.23

Table 3.59 (cont'd) Reduced AHe data.

Transect	Sample	Mineral	Corrected age, Ma	err., Ma	U (ppm)	Th (ppm)	147Sm (ppm)	eU	Th/U	He (nmol/g)	mass (ug)	Ft	ESR	Raw Age, Ma	err., Ma
Nain	a69MZ390-1	apatite	149.3	0.54	1.6	9.3	236.5	4.9	5.81	3.5	6.93	0.75	63.33	111.27	0.54
Nain	a69MZ390-2	apatite	269.6	0.96	1.5	8.1	136.7	4.0	5.39	5.4	17.87	0.81	84.50	217.20	0.96
Nain	a69MZ390-3	apatite	155.6	0.57	1.9	11.9	216.4	5.8	6.12	4.2	7.99	0.76	66.57	117.74	0.57
Nain	a69MZ390-4	apatite	418.7	1.52	1.9	12.1	243.1	5.9	6.41	11.9	9.28	0.77	71.23	322.97	1.52
Nain	a69MZ390-5	apatite	213.4	0.80	1.8	13.6	259.5	6.2	7.57	5.9	4.08	0.71	54.42	150.69	0.80
Nain	a69MZ392-1	apatite	124.4	0.50	1.4	15.3	400.4	6.9	11.24	3.7	2.72	0.67	47.94	83.23	0.50
Nain	a69MZ392-2	apatite	148.4	0.56	4.6	39.9	741.2	17.5	8.65	11.1	3.21	0.68	50.27	101.45	0.56
Nain	a69MZ392-3	apatite	214.4	0.80	4.3	34.5	433.0	14.4	8.10	14.4	8.79	0.77	71.42	165.30	0.80
Nain	a69MZ392-4	apatite	318.1	1.23	5.4	52.1	818.6	21.4	9.74	24.0	1.34	0.57	35.27	180.64	1.23
Nain	a69MZ392-5	apatite	167.5	0.64	5.5	50.7	831.9	21.3	9.21	14.3	2.43	0.65	44.53	108.42	0.64
Nain	a69MZ351-1	apatite	81.0	0.38	1.7	24.8	22.3	7.5	14.36	1.8	0.69	0.52	31.34	42.19	0.38
Nain	a69MZ351-2	apatite	130.8	0.51	1.9	16.4	28.0	5.8	8.81	2.8	2.34	0.66	46.54	86.46	0.51
Nain	a69MZ351-3	apatite	280.8	1.20	29.6	24.1	322.7	36.8	0.81	39.2	2.25	0.67	45.41	188.75	1.20
Nain	a69MZ351-4	apatite	240.2	0.88	17.3	41.7	185.0	27.8	2.41	23.3	1.38	0.62	39.89	149.01	0.88
Nain	a69MZ351-5	apatite	166.7	0.65	2.0	18.7	31.5	6.4	9.56	4.1	2.65	0.68	49.33	113.03	0.65
Nain	a69MZ335-1	apatite	95.5	0.37	3.5	26.6	31.3	9.8	7.65	2.8	1.04	0.55	33.42	52.41	0.37
Nain	a69MZ335-2	apatite	450.4	1.74	2.2	18.7	29.1	6.6	8.61	10.6	2.07	0.63	42.15	283.84	1.74
Nain	a69MZ335-3	apatite	264.2	1.12	2.0	21.1	19.3	7.0	10.34	5.7	0.92	0.55	33.53	144.94	1.12
Nain	a69MZ335-4	apatite	71.0	0.30	1.1	14.2	26.5	4.5	13.06	1.1	1.86	0.63	41.78	44.43	0.30
Nain	a69MZ335-5	apatite	100.8	0.39	2.2	15.6	26.9	6.0	7.00	2.1	1.58	0.61	39.65	61.58	0.39

Table 3.59 (cont'd) Reduced AHe data.

Transect	Sample	Mineral	Corrected age, Ma	err., Ma	U (ppm)	Th (ppm)	147Sm (ppm)	eU	Th/U	He (nmol/g)	mass (ug)	Ft	ESR	Raw Age, Ma	err., Ma
Hopedale	ak0016-1	apatite	154.6	0.60	1.1	1.9	5.4	1.6	1.66	1.1	12.64	0.80	79.98	123.87	0.60
Hopedale	ak0016-2	apatite	138.1	0.54	3.3	6.1	10.5	4.7	1.86	2.4	2.73	0.67	47.03	93.13	0.54
Hopedale	ak0016-3	apatite	150.3	0.59	1.3	8.9	6.6	3.4	6.84	1.8	2.11	0.64	43.26	96.14	0.59
Hopedale	ak0016-4	apatite	116.9	0.47	3.2	3.9	19.7	4.2	1.21	2.0	4.72	0.74	58.29	85.94	0.47
Hopedale	ak0016-5	apatite	159.1	0.64	4.1	5.6	10.4	5.4	1.39	3.4	3.83	0.72	55.24	114.70	0.64
Hopedale	ak0015-1	apatite	139.8	0.53	2.8	8.1	161.7	5.5	2.88	3.0	2.23	0.65	43.82	90.72	0.53
Hopedale	ak0015-2	apatite	112.4	0.42	3.9	12.0	66.0	7.0	3.12	2.7	1.57	0.61	38.59	68.23	0.42
Hopedale	ak0015-3	apatite	138.8	0.52	4.3	13.1	63.8	7.7	3.04	3.6	1.36	0.60	37.72	83.21	0.52
Hopedale	ak0015-4	apatite	360.9	1.37	4.9	15.4	71.3	8.8	3.17	10.0	1.06	0.56	33.85	202.04	1.37
Hopedale	ak0015-5	apatite	189.4	0.73	4.7	11.6	196.4	8.3	2.49	5.4	1.23	0.58	35.65	110.08	0.73
Hopedale	ak0014-1	apatite	194.1	0.87	7.3	4.1	44.4	8.4	0.56	6.8	4.80	0.75	59.20	144.68	0.87
Hopedale	ak0014-2	apatite	227.6	1.02	12.2	6.6	49.4	14.0	0.54	12.8	4.56	0.72	54.33	164.98	1.02
Hopedale	ak0014-3	apatite	182.8	0.79	7.8	5.4	34.6	9.2	0.70	6.6	4.04	0.71	52.11	130.13	0.79
Hopedale	ak0014-4	apatite	205.1	0.83	7.6	10.1	35.8	10.1	1.33	7.2	1.57	0.62	39.66	128.12	0.83
Hopedale	ak0014-5	apatite	217.4	0.93	13.9	10.8	59.2	16.7	0.78	13.6	2.45	0.68	45.85	146.86	0.93
Hopedale	ak0013-1	apatite	91.8	0.37	2.0	6.9	19.2	3.7	3.40	1.2	1.80	0.63	40.88	57.40	0.37
Hopedale	ak0013-2	apatite	52.0	0.21	0.9	7.5	11.9	2.7	8.55	0.5	2.48	0.64	43.02	33.09	0.21
Hopedale	ak0013-3	apatite	92.3	0.35	1.6	8.1	15.2	3.6	4.97	1.2	2.75	0.64	43.06	59.05	0.35
Hopedale	ak0013-4	apatite	98.6	0.37	1.9	7.8	16.2	3.7	4.19	1.3	2.41	0.64	42.98	63.13	0.37
Hopedale	ak0013-5	apatite	115.4	0.44	2.4	9.9	14.4	4.8	4.07	1.9	1.80	0.62	39.86	71.06	0.44

Table 3.59 (cont'd) Reduced AHe data.

Transect	Sample	Mineral	Corrected age, Ma	err., Ma	U (ppm)	Th (ppm)	147Sm (ppm)	eU	Th/U	He (nmol/g)	mass (ug)	Ft	ESR	Raw Age, Ma	err., Ma
Hopedale	ak0012-1	apatite	219.1	1.06	28.1	4.4	39.8	29.3	0.16	25.8	3.77	0.73	54.14	160.33	1.06
Hopedale	ak0012-2	apatite	265.5	1.13	11.9	10.2	27.9	14.3	0.86	12.5	1.29	0.60	35.94	158.36	1.13
Hopedale	ak0012-3	apatite	160.6	0.71	13.9	8.4	26.2	15.9	0.61	9.3	1.88	0.66	43.19	106.03	0.71
Hopedale	ak0012-4	apatite	390.7	1.79	15.3	6.6	32.5	17.0	0.43	25.0	2.30	0.68	45.58	265.37	1.79
Hopedale	ak0012-5	apatite	152.4	0.65	15.9	13.2	26.7	19.1	0.83	9.4	1.21	0.59	35.42	90.20	0.65
Hopedale	ak0011-1	apatite	198.4	0.86	10.6	7.5	62.4	12.6	0.71	9.3	2.32	0.67	44.83	132.87	0.86
Hopedale	ak0011-2	apatite	201.5	0.82	6.6	8.5	39.8	8.8	1.29	6.2	1.69	0.63	40.84	127.85	0.82
Hopedale	ak0011-3	apatite	211.1	0.87	9.7	10.2	53.3	12.3	1.05	9.2	1.93	0.64	41.01	134.70	0.87
Hopedale	ak0011-4	apatite	187.4	0.80	7.7	6.2	52.4	9.4	0.81	6.6	2.50	0.68	45.93	126.62	0.80
Hopedale	ak0011-5	apatite	223.9	0.86	3.1	6.7	14.1	4.7	2.15	4.0	2.75	0.68	48.84	153.15	0.86
Hopedale	ak0010-1	apatite	203.8	0.87	8.5	6.7	102.8	10.5	0.80	8.6	3.44	0.71	51.98	144.74	0.87
Hopedale	ak0010-2	apatite	223.1	0.99	15.2	8.6	110.1	17.7	0.56	15.6	3.51	0.71	50.88	157.81	0.99
Hopedale	ak0010-3	apatite	423.3	1.83	11.6	8.5	105.9	14.1	0.73	23.9	3.20	0.70	50.55	297.71	1.83
Hopedale	ak0010-4	apatite	208.4	0.91	8.6	5.6	75.2	10.3	0.65	8.6	3.51	0.72	52.83	149.24	0.91
Hopedale	ak0010-5	apatite	250.9	1.14	20.2	8.5	106.8	22.7	0.42	23.2	4.21	0.73	55.65	183.83	1.14
Hopedale	ak0009-1	apatite	124.2	0.50	0.6	1.3	8.3	1.0	2.11	0.5	12.33	0.80	79.96	99.31	0.50
Hopedale	ak0009-2	apatite	103.4	0.42	4.6	6.6	59.0	6.4	1.46	2.5	3.02	0.69	48.47	70.88	0.42
Hopedale	ak0009-3	apatite	187.4	0.75	4.0	12.9	57.2	7.3	3.23	4.6	1.38	0.60	38.05	112.78	0.75
Hopedale	ak0009-4	apatite	24.8	0.12	0.5	9.0	7.3	2.6	17.70	0.2	2.08	0.65	44.72	16.02	0.12
Hopedale	ak0009-5	apatite	100.4	0.37	3.5	13.0	106.0	7.0	3.74	2.7	2.21	0.66	46.20	66.63	0.37

Table 3.59 (cont'd) Reduced AHe data.

Transect	Sample	Mineral	Corrected age, Ma	err., Ma	U (ppm)	Th (ppm)	147Sm (ppm)	eU	Th/U	He (nmol/g)	mass (ug)	Ft	ESR	Raw Age, Ma	err., Ma
Hopedale	ak0008-1	apatite	132.8	0.57	4.7	4.1	50.4	5.8	0.88	3.2	3.94	0.72	55.20	96.28	0.57
Hopedale	ak0008-2	apatite	223.4	1.00	10.1	5.4	35.2	11.5	0.53	10.2	3.88	0.72	52.67	160.17	1.00
Hopedale	ak0008-3	apatite	218.6	0.93	16.3	13.3	83.6	19.7	0.82	16.8	3.21	0.70	50.07	152.99	0.93
Hopedale	ak0008-4	apatite	183.0	0.82	5.8	3.2	35.2	6.7	0.54	5.2	5.93	0.76	62.37	138.63	0.82
Hopedale	ak0008-5	apatite	172.7	0.79	4.9	2.2	63.1	5.7	0.46	4.4	8.50	0.78	67.89	134.20	0.79
Makkovik	a71TA464-1	apatite	147.1	0.54	18.6	54.7	859.7	35.5	2.94	17.5	1.20	0.57	34.49	83.48	0.54
Makkovik	a71TA464-2	apatite	137.4	0.52	14.6	29.3	555.9	24.1	2.01	11.6	1.41	0.60	37.01	82.01	0.52
Makkovik	a71TA464-3	apatite	145.5	0.54	26.4	59.7	709.9	43.7	2.26	20.7	1.07	0.57	34.09	82.32	0.54
Makkovik	a71TA464-4	apatite	92.6	0.33	7.9	29.5	573.8	17.6	3.72	6.1	1.61	0.62	40.70	57.72	0.33
Makkovik	a71TA464-5	apatite	138.6	0.51	16.5	43.6	534.2	29.2	2.65	14.3	1.74	0.61	38.65	84.41	0.51
Makkovik	a71TA923-1	apatite	272.4	0.99	10.5	27.2	348.1	18.5	2.58	74.9	3.70	0.69	49.85	187.43	0.99
Makkovik	a71TA923-2	apatite	116.1	0.42	5.3	18.7	234.6	10.8	3.53	7.9	1.77	0.61	39.16	70.93	0.42
Makkovik	a71TA923-3	apatite	113.9	0.40	7.8	27.9	386.2	16.1	3.59	29.1	3.81	0.70	53.35	80.28	0.40
Makkovik	a71TA923-4	apatite	103.8	0.38	3.2	14.1	170.6	7.3	4.47	4.9	1.77	0.62	41.02	64.86	0.38
Makkovik	a71TA923-5	apatite	105.6	0.39	7.2	34.0	355.4	16.8	4.75	5.3	0.93	0.56	33.92	58.83	0.39
Makkovik	a71TA910-1	apatite	150.6	0.54	32.3	118.4	481.9	62.0	3.67	118.4	3.22	0.70	52.34	105.33	0.54
Makkovik	a71TA910-2	apatite	161.9	0.57	45.1	184.3	477.9	90.0	4.08	130.8	2.42	0.66	46.32	107.41	0.57
Makkovik	a71TA910-3	apatite	152.9	0.54	32.7	131.6	426.2	65.2	4.02	43.8	1.30	0.60	38.58	92.49	0.54
Makkovik	a71TA910-4	apatite	222.7	0.79	16.9	79.1	232.7	36.3	4.69	38.8	1.40	0.61	39.37	135.99	0.79
Makkovik	a71TA910-5	apatite	937.5	3.32	45.5	173.4	452.0	87.6	3.81	433.4	1.49	0.61	39.54	575.28	3.32

Table 3.59 (cont'd) Reduced AHe data.

Transect	Sample	Mineral	Corrected age, Ma	err., Ma	U (ppm)	Th (ppm)	147Sm (ppm)	eU	Th/U	He (nmol/g)	mass (ug)	Ft	ESR	Raw Age, Ma	err., Ma
Makkovik	a71TA912-1	apatite	153.7	0.62	28.8	36.4	58.6	37.5	1.26	57.1	2.69	0.67	45.66	102.88	0.62
Makkovik	a71TA912-2	apatite	156.5	0.60	17.0	28.8	32.3	23.8	1.69	49.9	3.48	0.70	51.04	109.30	0.60
Makkovik	a71TA912-3	apatite	167.7	0.66	28.4	40.1	45.6	37.8	1.41	125.4	5.03	0.72	54.16	120.02	0.66
Makkovik	a71TA912-4	apatite	157.4	0.62	22.9	30.7	43.4	30.1	1.34	45.7	2.62	0.67	45.86	105.47	0.62
Makkovik	a71TA912-5	apatite	165.5	0.66	30.9	41.0	57.9	40.6	1.33	60.0	2.43	0.67	45.71	110.71	0.66
Makkovik	a71TA929-1	apatite	143.9	0.54	10.7	23.6	188.6	17.0	2.22	15.0	1.73	0.63	40.57	90.20	0.54
Makkovik	a71TA929-2	apatite	249.0	0.90	20.6	60.2	380.4	36.4	2.91	66.9	2.03	0.64	42.54	159.29	0.90
Makkovik	a71TA929-3	apatite	191.4	0.70	23.8	56.7	316.5	38.4	2.38	25.9	1.10	0.57	34.37	108.77	0.70
Makkovik	a71TA929-4	apatite	198.5	0.73	51.0	110.8	535.4	79.2	2.17	55.9	1.12	0.57	33.99	112.19	0.73
Makkovik	a71TA929-5	apatite	134.6	0.49	18.7	48.2	322.6	31.4	2.58	14.3	1.52	0.60	37.55	80.69	0.49
Makkovik	a71TA909-1	apatite	198.0	0.71	11.7	36.2	253.9	21.3	3.09	18.9	1.33	0.59	36.91	117.16	0.71
Makkovik	a71TA909-2	apatite	124.3	0.45	6.4	33.0	134.4	14.7	5.15	14.9	2.22	0.65	44.81	81.03	0.45
Makkovik	a71TA909-3	apatite	336.5	1.25	2.5	16.6	22.4	6.4	6.71	19.4	2.42	0.66	46.90	223.65	1.25
Makkovik	a71TA909-4	apatite	165.3	0.59	43.8	130.6	463.6	76.2	2.98	35.1	0.92	0.54	32.23	89.56	0.59
Makkovik	a71TA909-5	apatite	167.7	0.60	16.2	57.8	327.8	31.2	3.57	24.5	1.41	0.59	36.70	98.67	0.60

3.17 TECHNIQUES USED FOR ASSESSING AGES

A general '20% above and below the median' rule was established for consistency when assessing the quality of the data to address dispersion and decide which datum should be discarded. 20% was used to prepare for the modelling software, where we used ages that fell into a maximum error of 20% above and below the raw age. To use this rule for assessing (U-Th)/He ages, the median age value for the sample was calculated, then ages 20% above and 20% below that age were calculated. Ages lying outside of 20% above and below the median were considered outliers. In some cases where there were obvious outliers (for example, a69FQ332), this outlier was removed, and a new median calculated to assess whether or not remaining ages would fit into the 20% above and below the median. Samples that had low dispersion (for example, a71TA912) were highlighted as candidates for AFT dating to determine more detail and a higher resolution cooling path, while samples that had multiple groupings of closely related ages were also highlighted as candidates for AFT dating (for example, a69FQ332), to determine if the AFT age is compatible with the grouped aliquots. For calculation of the mean, it is best to select a mean age using at least 3 aliquots (when available) with the smallest standard deviation. For each sample, all aliquots were analyzed in Excel to assess how mean and standard deviation (STD) would change with the different combinations of aliquots. These calculations are included below in each sample description.

"Distance from the coastline" measurements were collected using Google Earth Pro. The coastline was identified using the Borders and Labels, Coastlines option under Layers in the left side panel. Using the Ruler function, a perpendicular line was drawn from the coastline border to the sample that was furthest inland. Each sample's distance from the coastline was determined along this red line by drawing perpendicular lines branching out to each sample, then measuring the distance from the coastline to where the blue and red lines intersect.

3.18 SINGLE-GRAIN (U-Th)/He AGES DISPERSION

In our dataset, single-grain (U-Th)/He ages dispersion is observed for aliquots of a same sample. Literature focused on characterizing (U-Th-Sm)/He datasets with large amounts of scatter (e.g., Ault et al. 2019; Flowers et al. 2009; Gautheron et al. 2009; Guenthner et al. 2013; Shuster et al. 2006), provides insight into possible causes of dispersion. To investigate the reasons that might be influencing dispersion, single-aliquot corrected ZHe and AHe ages were plotted against a number of variables including parent nuclide concentration (effective Uranium, eU), grain size (Effective Spherical Ratio), grain geometry (aspect ratio). The only variable that showed relationships was eU, which is discussed below.

3.18.1 AGE COMPARED WITH PARENT NUCLIDE CONCENTRATION

Parent nuclide concentration, or effective U concentration (where $[U]e = U + 0.235 \times Th + 0.005 \times Sm$)(Gastil et al. 1967) was compared to ZHe ages and AHe ages in (Figure 3.20 and 3.21). eU is used as a proxy for radiation damage within the grain because cumulative damage is a function of initial U and Th content (Ault et al. 2018). The relationship of ZHe age to eU ($y = -0.7557x + 756.78$, $R^2 = 0.4106$) is negative and opposite to the relationship of AHe age to eU ($y = 0.052x + 7.3215$, $R^2 = 0.113$), which is positive (Figures 3.20, 3.21). This is expected in zircon with high eU contents (~400 – 10,000 ppm) (Ault et al. 2018; Guenthner et al. 2013), as radiation damage reduces the ^{4}He retentivity of the crystal lattice (Reiners 2005), such that a higher eU value results in increased ^{4}He diffusivity, an increase in daughter product loss and therefore, younger ages. Conversely, radiation damage in apatite obstructs diffusion pathways and reduces diffusion (Shuster and Farley 2009) such that a higher eU value results in increased ^{4}He retention, increased daughter products retention compared to parent isotopes and therefore, older ages.

The overall trend for ZHe age compared to eU is negative, as eU values decrease with increasing age (Figure 3.20). When plotting ZHe single-grain corrected ages against eU for each transect separately, eU values tend to get consistently lower northwards (Figures 3.22 – 3.29). The Makkovik transect, which is located furthest south, has the highest eU value of 2711.5 ppm (sample z71TA909) corresponding to the lowest age sample as well (21.1 Ma). The Saglek transect, which is located furthest north, has the lowest eU value of 0.01 ppm (sample z69TA212). The range of eU values within each transect also varies from south to north, as the Makkovik transect has the highest range of eU values (37.1–2711.5 ppm), while the Saglek transect has the lowest range (0.01–838.1 ppm). This is because the Makkovik samples are richer in U content on average than the Saglek samples (see Table 3.58).

eU versus all AHe ages generally has a positive relationship (Figure 3.21). The Makkovik transect has the highest eU value of 90.0 ppm (sample a71TA910), while the Hopedale transect has the lowest eU value of 1.0 ppm (sample ak0009). The Makkovik transect also has the highest range in eU values (6.4–90.0 ppm), while the Saglek transect has the lowest range (3.5–26.1 ppm). In all transects, for apatites, eU values are low and there is less variation compared to zircon of the same samples because zircons have higher eU content and require higher temperatures to anneal radiation damage (Ault et al. 2018).

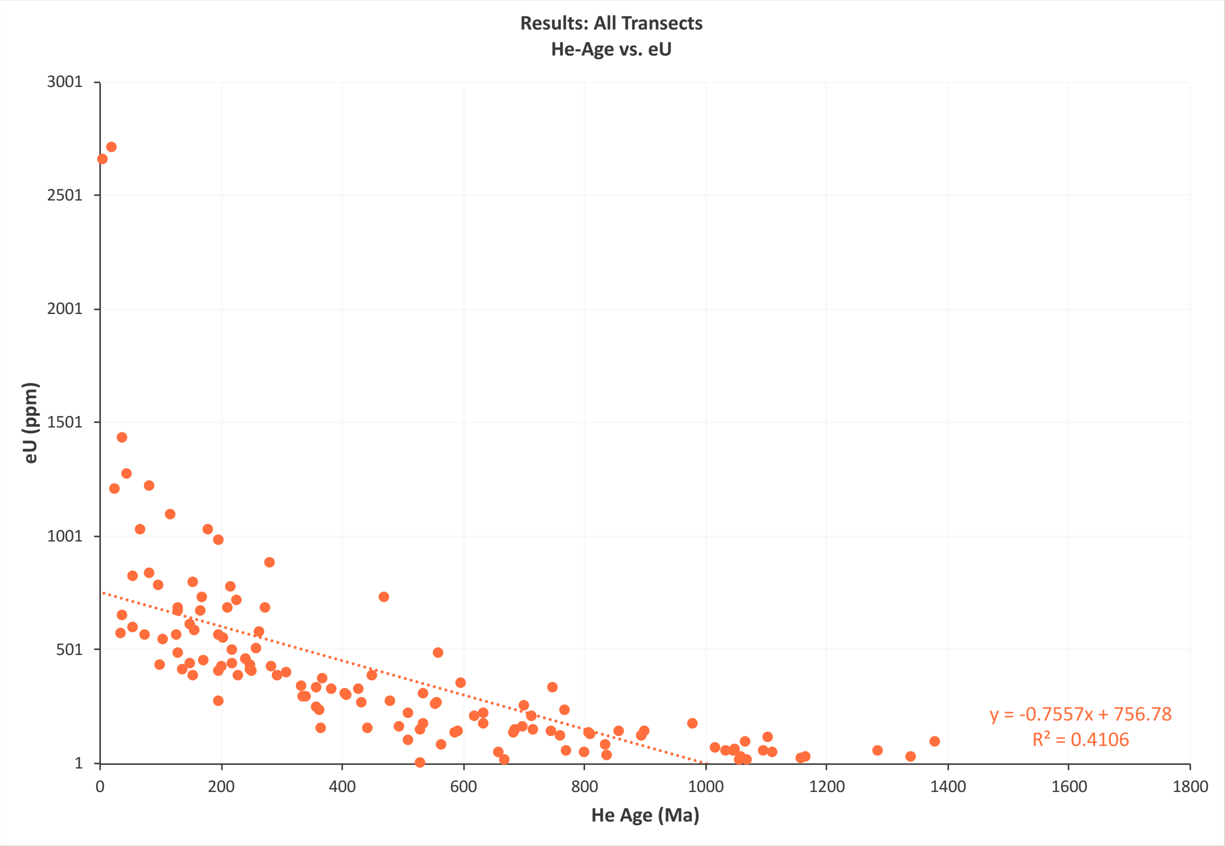

Figure 3.20 Results from ZHe analyses comparing all ages to total eU (ppm).

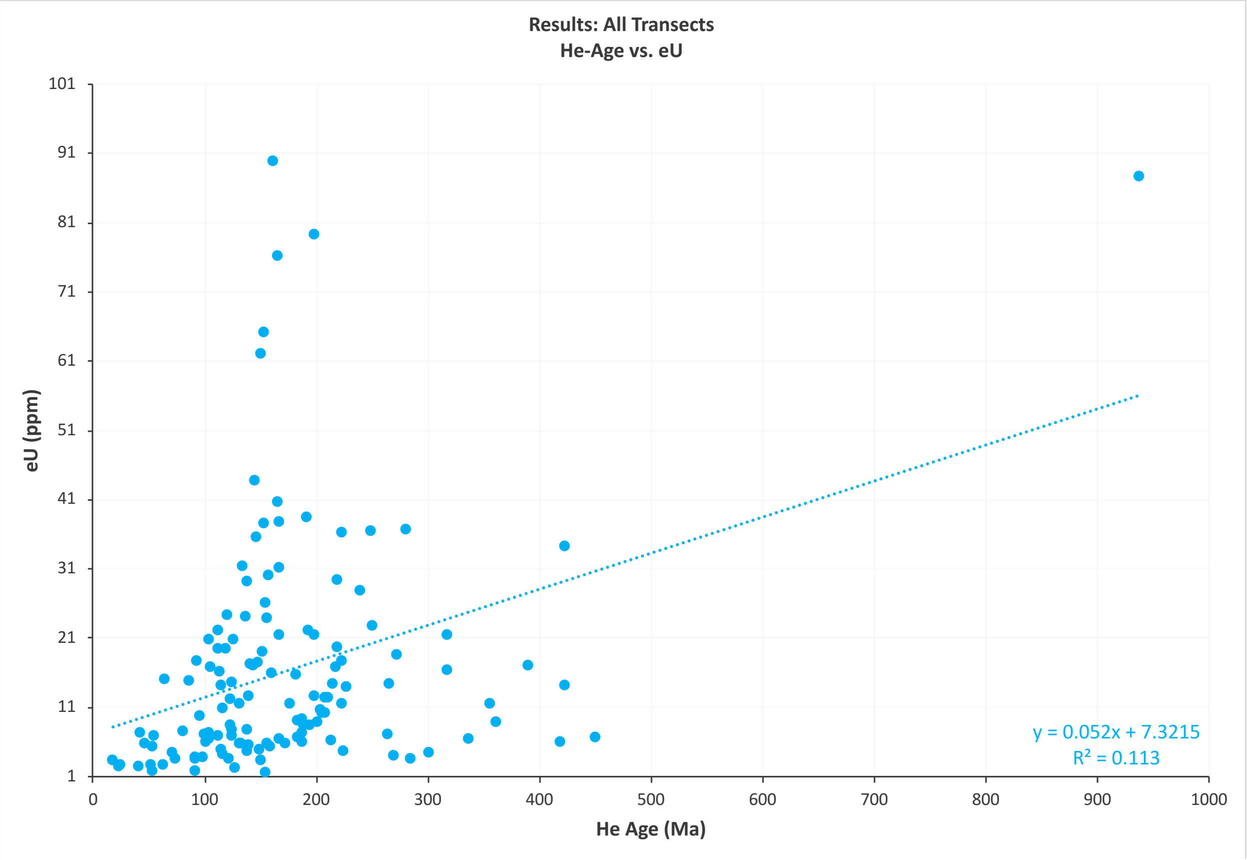

Figure 3.21 Results from AHe analyses comparing all ages to total eU (ppm).

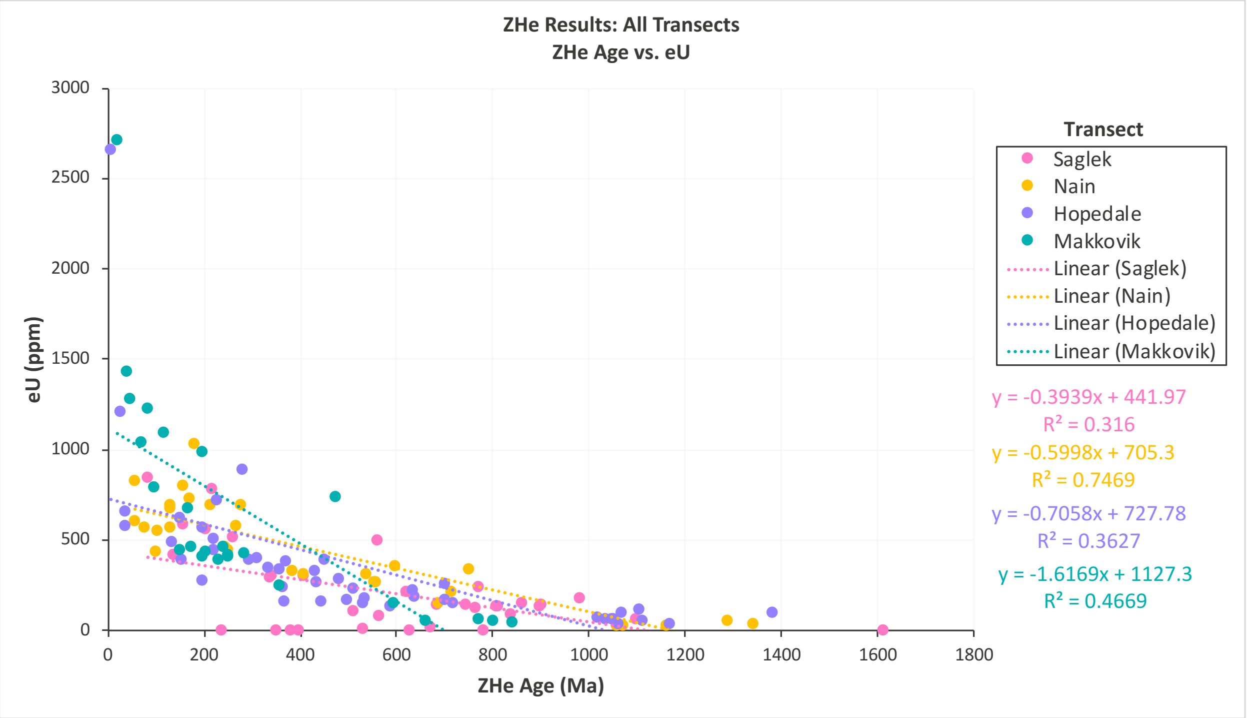

Figure 3.22 Results from ZHe analyses comparing separate transects' ZHe ages to eU (ppm).

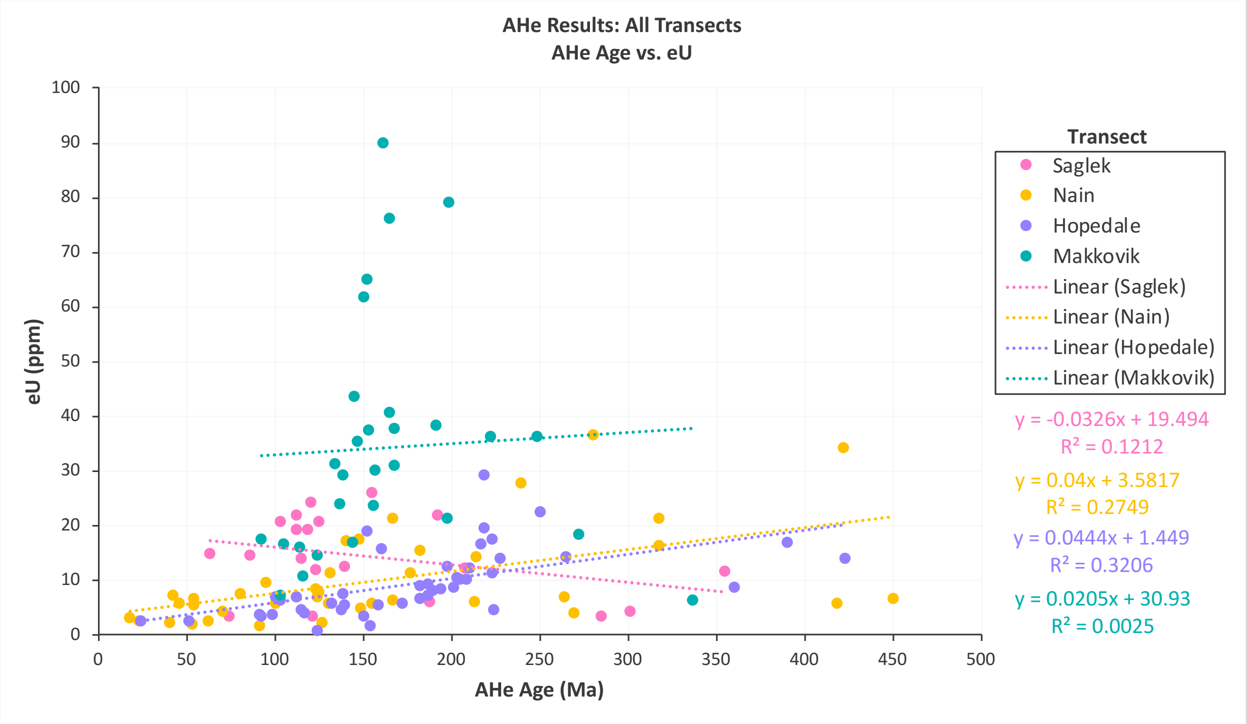

Figure 3.23 Results from AHe analyses comparing separate transects' AHe ages to eU (ppm), where outlier a71TA910 was removed.

In the Saglek transect, parent nuclide concentration varies greatly as it is low in some samples and high in others. eU in sample z69TA212 ranges from 0.01–2.30 ppm, whereas eU in sample z69TA217 ranges from 415.0–838.1 ppm. Figure 3.22 shows that Saglek samples with the greatest eU values (z67SC216, z69TA217) have younger ages (<200 Ma), but ages older than ~200 Ma do not show a distinct trend regarding eU, ZHe age, and distance. There is less variation of eU within the apatite samples than in the zircon samples, where sample a69TA212 has the lowest values for eU, ranging from 3.5–6.1 ppm, and sample a67SC218 has the highest values for eU, ranging from 12.3–26.1 ppm (Figure 3.23). Sample a69TA212 stands out with high age dispersion and the largest STD, as well as the lowest eU values for both AHe and ZHe data.

In the Nain transect, Parent nuclide concentration varies from sample to sample. eU is low in sample z69MZ392 compared to other samples in this transect, ranging from 18.9–54.3 ppm. The highest [U]e value occurs in sample z69TA336, which has a range of 211.0–1032.3 ppm (Figure 3.22). The plot shows a trend that generally increases with distance from the coastline, except for sample z69TA336. For the apatite ages, sample a69FQ398 has the lowest values for eU, ranging from 8.1–2.7 ppm, and sample a69MZ351 has the highest values for eU, ranging from 5.8–36.8 ppm (Figure 3.23).

In the Hopedale transect, parent nuclide concentration for ZHe varies greatly, but it is high in all samples. eU values range from 31.9–2656.5 ppm, where sample zk0012 has the lowest range in values for eU, 31.9–96.5 ppm, and sample ak0011 has the highest values for eU, ranging from 386.8–2656.5 ppm (Figure 3.22). eU values for apatite in Hopedale range from 1.0–29.3 ppm, where sample ak0013 has the lowest range in values for eU, 2.7–4.8 ppm, and sample ak0008 has the highest values for eU, ranging from 5.7–19.7 ppm. There is no pattern relating location relative to coastline and eU versus age, as all samples overlap each other (Figure 3.23).

In the Makkovik transect, parent nuclide concentration varies greatly within each sample and between samples. In the zircon samples, eU is lowest in sample z71TA464, ranging from 37.1–145.6 ppm, and highest in sample z71TA909, ranging from 788.3–2711.5 ppm (Figure 3.22). In the apatite samples, a71TA909 has the lowest values for eU, ranging from 6.4–76.2 ppm, and sample a71TA910 has the highest values for eU, ranging from 36.3–90.0 ppm. There is little trend connecting age and eU to location relative to the coastline, as all samples overlap each other in the plot (Figure 3.23).

3.19 AGE COMPARED WITH DISTANCE FROM THE COASTLINE

Arithmetic mean age of each sample was compared to horizontal distance along the transects from the coastline (transects are perpendicular to the coastline) (Figures 3.24 – 3.27). There is a more representative correlation between age and physiography when plotting the mean ages than when plotting all aliquot ages. X-axes are scaled to the longest transect (Nain, 140 km) and y-axes are scaled to the oldest ages (also Nain, 1182 ± 127 Ma). Overall, there are no progressive variations from one transect to another in the North-South direction. There are no consistent east-west age trends (e.g. younging or aging away from the coast), except for

Saglek, where ages generally increase with distance from the coastline. Once consistency is that mean AHe ages are all younger than ~200 Ma.

Along the Saglek transect, ZHe ages are < 400 Ma nearer to the coastline, then > 400 Ma further than ~35 km from the coastline. Mean AHe ages slightly increase with distance, but all remain younger than ~200 Ma (Figure 3.24). Along the Nain transect, a few of the ZHe and AHe ages actually overlap, or are very similar nearest to the coastline. ZHe ages nearer to the coastline are < ~250 Ma and furthest from the coastline, ages are > 400 Ma. All AHe ages occur between 0 – ~200 Ma (Figure 3.25). The Hopedale transect does not show any apparent trend regarding both AHe and ZHe versus distance from the coastline, although all AHe ages are > ~250 Ma (Figure 3.26). Makkovik ZHe ages do not show any distinct trends with distance, but AHe ages remain relatively consistent between ~100 – 200 Ma (Figure 3.27).

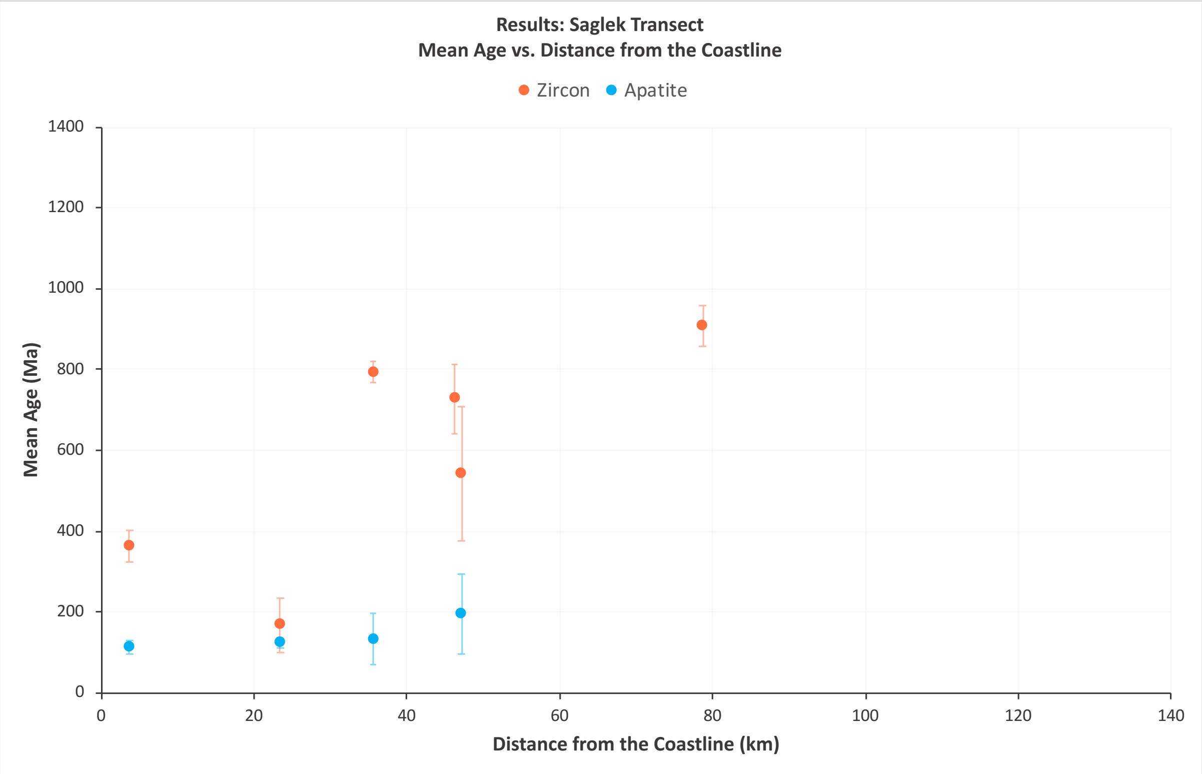

Figure 3.24 Results from ZHe and AHe analyses comparing mean ages from the Saglek transect to their sample's perpendicular distance from the coastline. This plot does not include sample z69TA210 because this sample was too dispersed to calculate a meaningful average and will not be used in defining a cooling path.

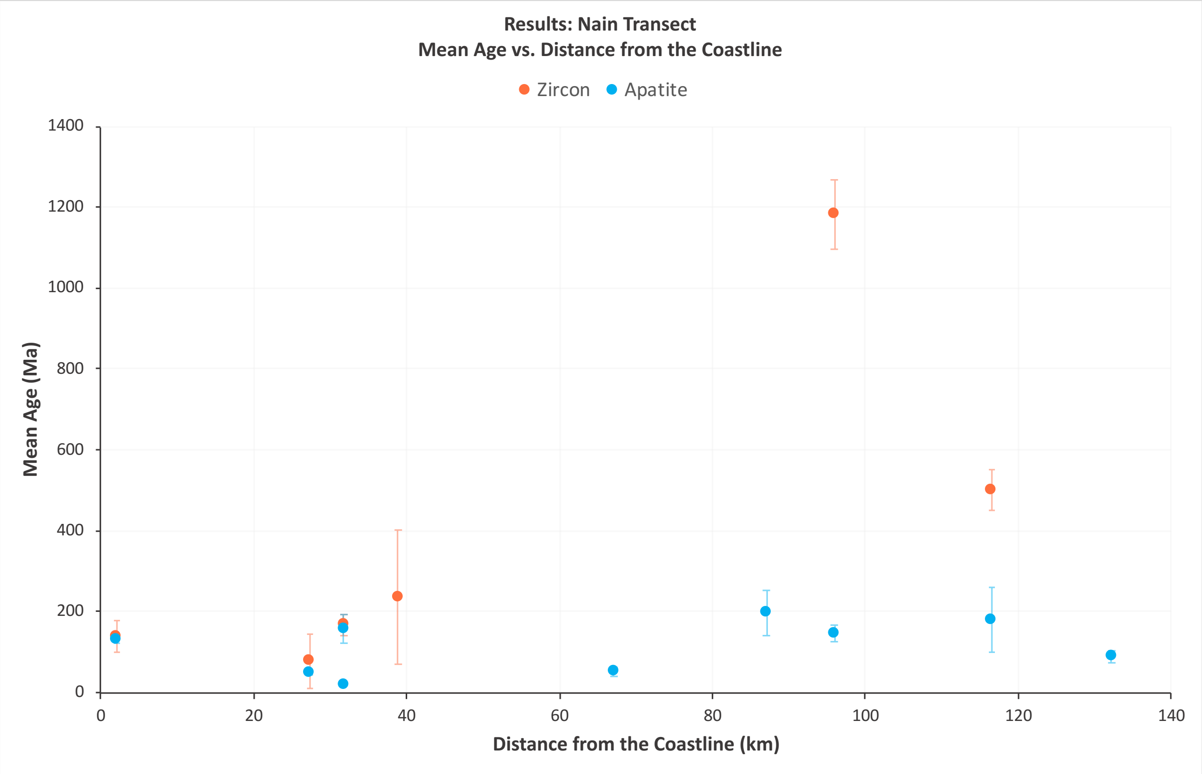

Figure 3.25 Results from ZHe and AHe analyses comparing mean ages from the Nain transect to their sample's perpendicular distance from the coastline.

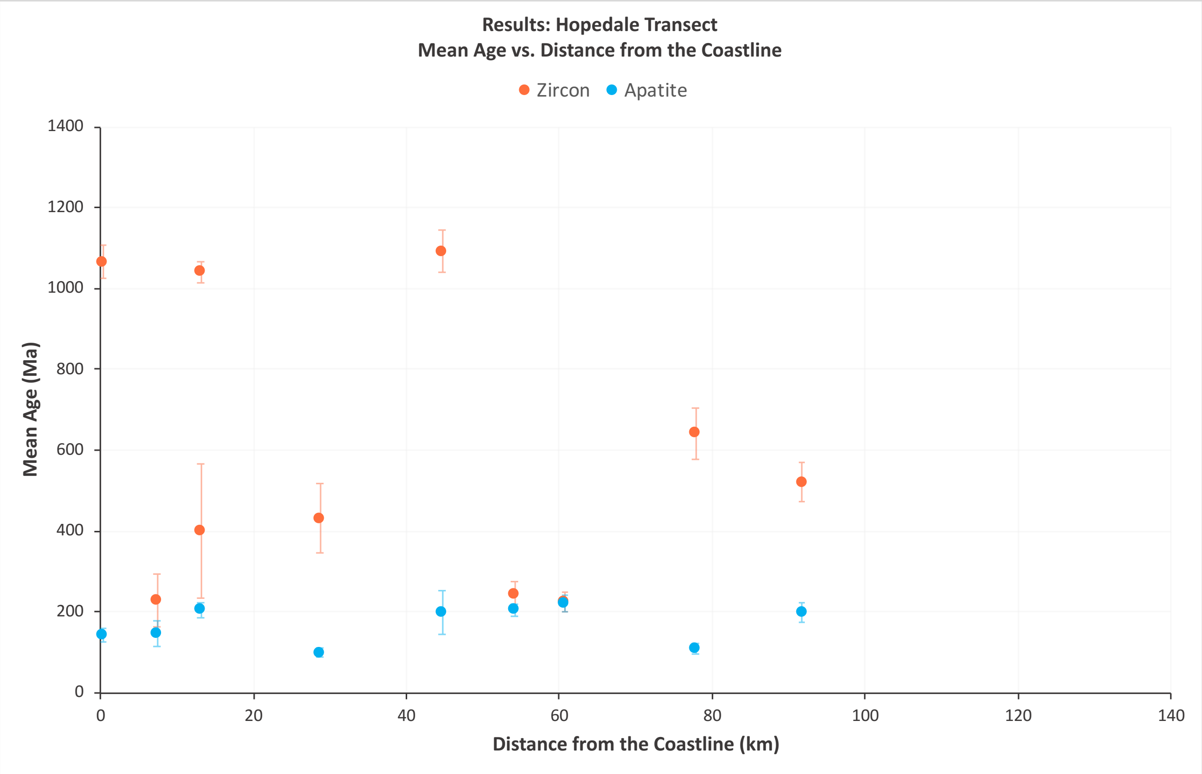

Figure 3.26 Results from ZHe and AHe analyses comparing mean ages from the Hopedale transect to their sample's perpendicular distance from the coastline.

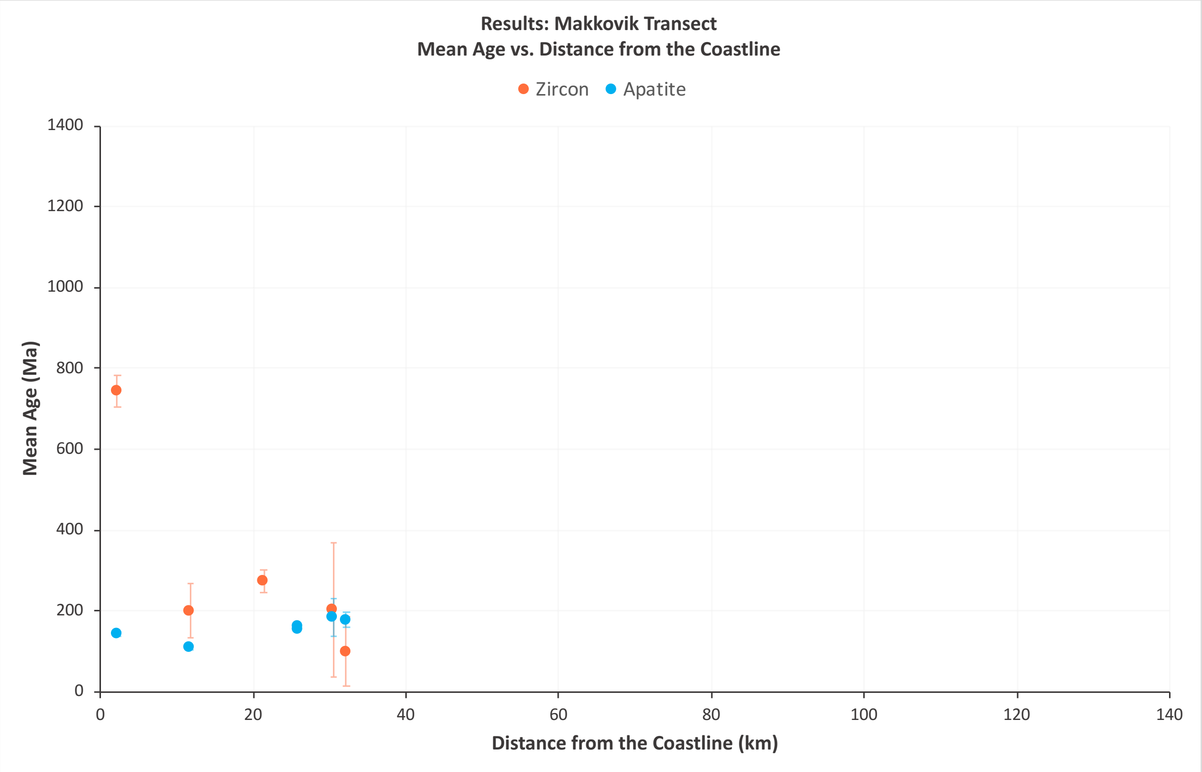

Figure 3.27 Results from ZHe and AHe analyses comparing mean ages from the Makkovik transect to their sample's perpendicular distance from the coastline.

CHAPTER 4: APATITE FISSION TRACK DATING - THEORY, METHODS AND RESULTS

4.1 INTRODUCTION TO APATITE FISSION TRACK (AFT) THERMOCHRONOLOGY

4.1.1 WHAT IS AFT?

Fission track (FT) thermochronology is a radiometric dating method based on the spontaneous nuclear fission of ^{238}U, most abundant uranium isotope in nature (Table 4.1), which causes physical damages or “fission-tracks” in the crystal lattice (e.g. Figure 4.1) that accumulate once the mineral has cooled in the crust (e.g. Donelick et al. 2005, Tagami and O’Sullivan 2005). Apatite fission track (AFT) dating has a T_c of 110 ± 10 °C (Gleadow and Duddy 1981), which is valuable for studying long-term landscape evolution; the timing and rate of tectonic events (Donelick et al. 2005); and the exhumation history of crustal rocks (Hurford 2019), as well as the evolution of sedimentary basins; hydrocarbon generation; ore mineralization; and the absolute age of volcanic deposits (Donelick et al. 2005). Although spontaneous fission also occurs in ^{234}U, ^{235}U and ^{232}Th, these isotopes do not produce significant numbers of natural tracks compared to ^{238}U because either their spontaneous fission half-lives are too long, or their abundances are too low (Table 4.1) (Hurford 2019).

Table 4.1 Isotope information, where (α) indicates alpha-decay series, (s.f.) indicates spontaneous fission decay (Donelick et al. 2005 and references therein).

Isotope	Abundance (%)	Half-Life (yr)	Decay Constant (yr^{-1})	Thermal-Neutron Capture Cross-Section (σ) ($10^{-24} cm^2$)
^{232}Th	100.0000	1.41×10^{10} (α)	4.916 x 10-11 (α)	7.4
^{234}U	0.0057	2.47×10^{5} (α)	2.806×10^{-6} (α)	100
^{235}U	0.7200	0.7038×10^{9} (α)	9.8485×10^{-10} (α)	580
^{238}U	99.2743	4.468×10^{9} (α) $\sim 1.3 \times 10^{16}$ (s.f.)	1.55125×10^{-10} (α) $\sim 7.5 \times 10^{-17}$ (s.f.)	2.7

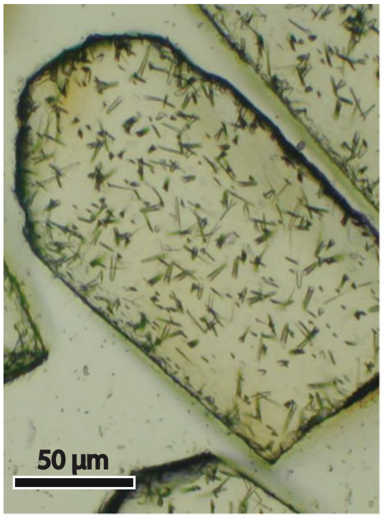

Figure 4.1 A photo of etched spontaneous ^{238}U fission tracks in an apatite grain from Tioga ash bed, Pennsylvania, USA, etched 5 M HNO3 at 20 ° C for 20 seconds (after Hurford 2019).

Each track is produced by the spontaneous fission of a single ^{238}U atom. In the External Detector Method (EDM) that is used at Dalhousie (Section 4.4), the amount of parent ^{238}U in the apatite is indirectly measured by irradiating the sample with low-energy neutrons to induce fission of the less abundant ^{235}U isotope and reveal a second generation of induced tracks in a detector held against the mineral (Hurford 2019). Under the assumption that the atomic ratio $[^{235}U]/[^{238}U]$ of natural uranium is constant in nature, the ratio of spontaneous-to-induced tracks is measured by comparing atoms decayed by fission to the total uranium remaining (Hurford 2019). The cooling age, or the time that fission tracks have been accumulating in the mineral, is calculated using this spontaneous-to-induced track ratio and the rate of spontaneous fission decay (Hurford 2019).

4.1.2 FISSION AND FORMATION OF FISSION TRACKS

Fission is a type of radioactive decay, where the nucleus of a radioactive, unstable element, such as ^{238}U, splits into two positively charged fragment nuclei including a lighter (Lt) fragment and a heavier (Hv) fragment, along with 2-3 neutrons (Gallagher et al. 1998). This process is described in the “ion spike explosion model” (Figure 4.2) (Fleischer et al. 1965a, 1975), where 170 MeV out of ~210 MeV of energy created by the fission reaction is transferred to the fragments in the form of kinetic energy, which allow the two positively charged nuclei to repel each other in opposite directions from the reaction site (Figure 4.4(b)). The fragment nuclei ionize atoms along their repulsive paths by stripping atoms of electrons. The resulting cations are displaced from their original positions due to coulomb repulsion and cluster to create fission tracks (Figure 4.4(c)) (Fleischer et al. 1975). As the fragment nuclei interact with the host lattice, they gradually lose their kinetic energy and eventually come to a stop (Tagami and O’Sullivan 2005). Tracks form randomly oriented within the three-dimensional crystal (Gallagher et. al 1998). As long as there is parent ^{238}U in a grain, fission tracks will form continuously at a rate determined by ^{238}U concentration (Donelick et al. 2005).

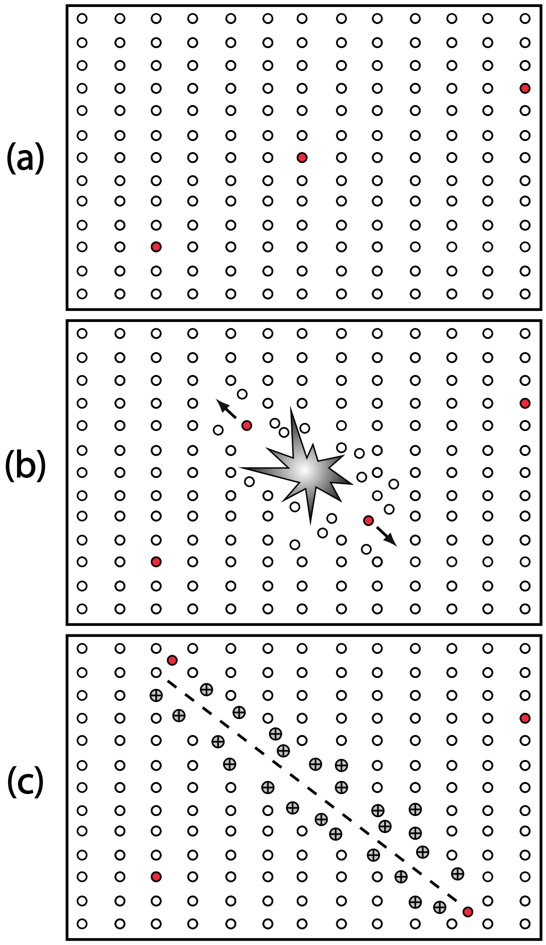

Figure 4.2 Ion spike model from Fleischer et al. (1965), showing how parent atoms are randomly dispersed within a crystal lattice (a), then undergo spontaneous fission, releasing energy and dividing into two positively charged fragment nuclei which repel each other (b), ionizing atoms along their repulsion paths (c) before coming to a stop in the crystal lattice (modified from Fleischer et al. 1965).

Tracks generally have a cylindrical shape that is linear and continuous, with an approximately uniform diameter of 6–10 nm (in apatite) along most of their length, except at its ends where the track tapers (Figure 4.3) (Tagami and O’Sullivan 2005). Fresh fission tracks are ~16 µm long in apatite (Reiners and Brandon 2006). Tracks are composed of amorphous material within the crystalline matrix and show a sharp transition at amorphous-crystalline boundary (Tagami and O'Sullivan 2005). Fission tracks counted for dating purposes are those that intersect the polished surface of the grain and are visible under reflected light as etch pits and under refracted light as truncated tracks (Figure 4.3). The confined fission tracks that are used for track length analysis and in which the thermal history of the sample is recorded, are those located below the surface of a polished grain, oriented sub-horizontally (Gleadow et al. 1986).

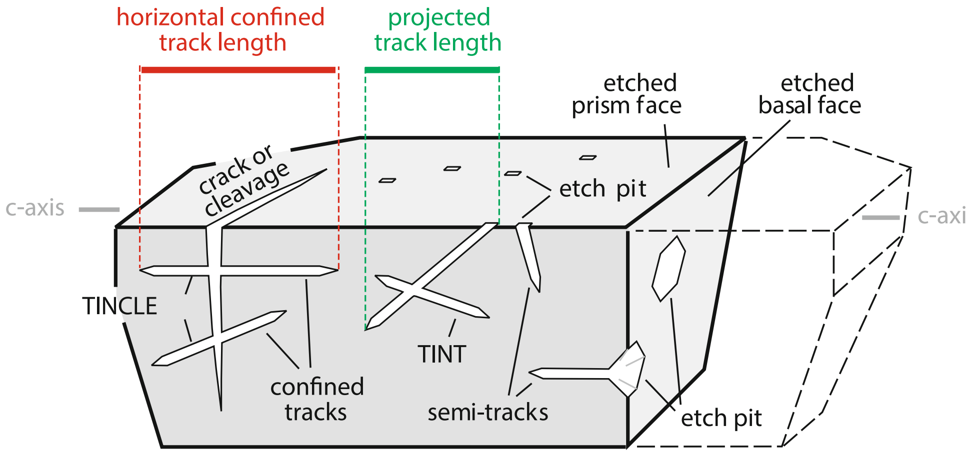

Figure 4.3 Schematic diagram from Hurford (2019) showing confined and semi-confined fission tracks in a polished, etched apatite crystal, as well as etch pits where vertical tracks are cross cut but the polished surface of the grain. Acronyms are: TINT, Track-IN-Track fission tracks; TINCLE, Track-IN-CLEavage fission tracks; and TINDEF, Track-IN-DEFect or fluid or soluble mineral inclusion fission tracks.

4.2 FISSION TRACK ANNEALING AND PARTIAL ANNEALING ZONE (PAZ)

Fission track annealing is the process by which spontaneous tracks heal or fade (Hurford 2019) due to thermally activated diffusion (Fleischer et al 1975, Tagami and O'Sullivan. 2005), where an ordered crystalline matrix progressively replaces the amorphous and disordered fission track (Paul and Fitzgerald 1992; Paul 1993). The rate of annealing and resulting grain age primarily depends on temperature and time (Figure 4.4) (Ketcham 2009; Fleischer et al. 1975; Gleadow et al. 1986; Donelick et al. 2005; Hurford 2019). The partial annealing zone (PAZ), similar to the HePRZ discussed in Chapter 3, is the range of temperatures or depths where fission tracks form but are only partially annealed due to thermally controlled diffusion, and as a result shorten over geological time (Figure 4.5). For the AFT thermochronometric system, this temperature range between ~60–110 °C (e.g., Gleadow et al. 1986; Green et al. 1989; Ketcham et al. 2009; Tagami and O'Sullivan 2005). At temperatures > ~110 °C, the system is 'open', where fission tracks form and anneal instantaneously, and at temperatures < ~60 °C, fission tracks are effectively stable, annealing at very slow rates (e.g., Fitzgerald and Gleadow 1990).

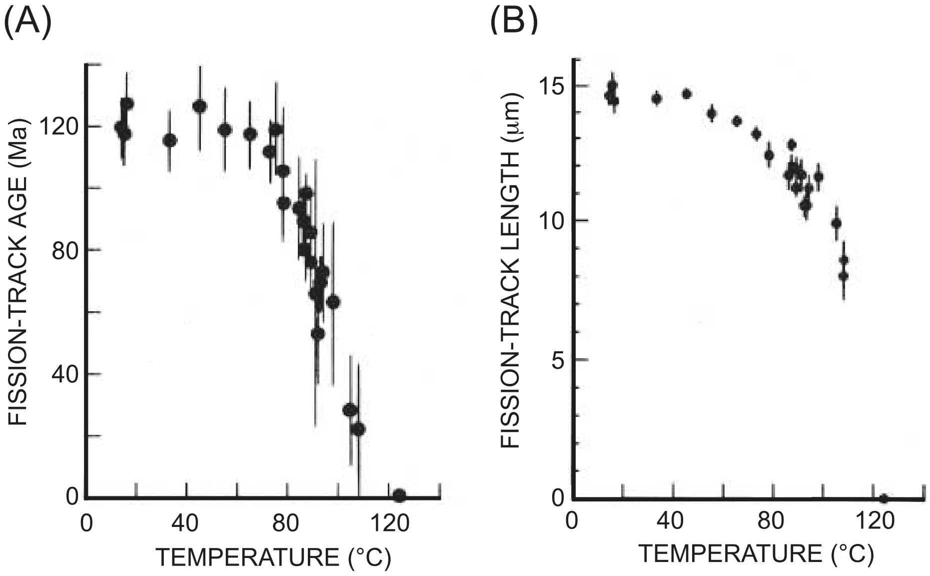

Figure 4.4 The effect of temperature on fission-track age (A) and length (B) in apatites from borehole samples from the Otway Basin, Australia, showing how tracks anneal and shorten as a function of temperature, specifically in the temperature range of ~60–120 °C. Error bars are ± 2σ (Tagami and O'Sullivan 2005 after Green et al. 1989a).

Other factors affecting annealing are the composition of the apatite crystal and the orientation of the fission-track. The chemical formula for apatite is $CA_5(PO_4)_3[F,Cl,OH]$ (Deer et al. 1969), where F^{-1}, Cl^{-1}, and OH^{-1} substitute for one another producing the end-member compositions fluorapatite, chlorapatite, and hydroxyapatite, respectively (Donelick et al. 2005). Annealing may be affected by the degree of mixing on the halogen site of the crystal which is typically occupied by F, Cl, or OH depending on the end member composition of the crystal Carlson et al. 1999). The rate of annealing is decreased when there is significant substitution for Ca by other cations, such as Fe and Mn, and even Sr, Ce, La, and Na, and significant substitution for P by Si, S, and C (Donelick et al. 2005, Carlson et al. 1999). Retentivity of fission tracks is increased by end member substitutions of Cl and OH (Donelick et al. 2005, Carlson et al. 1999). Annealing rate is affected by the orientation of the fission tracks, where tracks parallel to the c-axis of a crystal will anneal more slowly than tracks oriented at high angles to the c-axis (Donelick 1999; Green and Durrani 1977).

4.2.1 ANNEALING KINETIC PARAMETERS

Fission tracks immediately begin to spontaneously heal or anneal once they are formed (e.g., Donelick et al. 1990). Fission-track annealing kinetics can be correlated with measurable parameters referred to as kinetic parameters. Kinetic parameters allow for grouping apatite grains according to their kinetic response, which is essential for plotting and modelling ages (Donelick et al. 2005). The two most studied and commonly applied kinetic parameters that are effective for 90% of all apatite grains likely to be encountered include D_{par} and Cl wt%, but for a complete list of parameters, refer to Donelick et al. (2005). The kinetic parameter Cl wt% involves using electron probe microanalysis (EPMA) to obtain chemical composition data of the halogen site in an apatite grain, then using Cl wt% to determine the annealing rate. Although this method is effective it will not be discussed further, as the D_{par} method is used at Dalhousie.

The kinetic parameter D_{par} is defined as the average length of FT etch pits measured parallel to the crystallographic c-axis (Kohn et al. 2019). D_{par} values are calculated from a minimum of four etch pit measurements (Donelick et al. 2005). The most common apatite grains are those with low D_{par} values of ≤1.75 µm (for apatite grains etched for 20 s in 5.5 M HNO_3 at 21 °C) are considered fast-annealing and are typical near-end-member calcian-fluorapatites (Donelick et al. 2005; Carlson et al. 1999). Apatite grains high D_{par} values of >1.75 µm (for apatite grains etched for 20 s in 5.5 M HNO_3 at 21 °C) anneal more slowly in general, but with exceptions (Donelick et al. 2005; Carlson et al. 1999). These types of apatite grains are common, but less so than apatite grains with low D_{par} values. Although chemical composition is likely important, the factors controlling D_{par} in apatite are unclear (Donelick et al. 2005). Some parameters that may be important to concentration and type of crystallographic imperfections in apatite include accumulated α-particle damage, crystallization age, temperature of formation, and deformation history (Donelick et al. 2005).

4.2.2 TRACK LENGTHS DISTRIBUTION

Younger fission tracks have only experienced part of the integrated time-temperature history of older fission tracks in the same apatite crystal, meaning that older fission tracks have experienced more partial annealing and may be significantly shorter than younger tracks (Donelick et al. 2005). The overall distribution of confined fission-track lengths can be used for quantitative modelling of a mineral or rock's thermal history to identify the amount of time spent in the PAZ and the style of the cooling process (Figure 4.5) (e.g. Gallagher et al. 1998, Donelick et al. 2005).

In a scenario of rapid cooling (Figure 4.5, Curve 1, distribution 1), the measured age is approximately the formation age and the track lengths distribution would be dominated by long tracks with a mean of ~14 µm and have a narrow, steep peak (Donelick et al. 2005; Hurford 2019; Wagner 1972). In a scenario of slow cooling (Figure 4.5, Curve 2, distribution 2), stability is reached sometime after formation where older tracks are partially annealed and younger tracks are not (Donelick et al. 2005; Hurford 2019; Wagner 1972). The resulting track lengths distribution would appear broader, with mean track lengths of ~12– 13 µm. In this case, the resulting age would be younger than the rapid cooling scenario, as tracks have been annealed and less of them intersect the crystal surface. A mixed age (Figure 4.5, Curve 3, distribution 3) results when previously cooled samples are reheated, as existing tracks are partially annealed according to time and temperature experienced in the PAZ. A second family of tracks are recorded when the sample re-enters the stability zone and apatites have a mixed track length distribution that may be bimodal (Hurford 2019, from Wagner 1972). A reset age (Figure 4.5, Curve 4, distribution 4) is obtained when a crystal in the stability zone is reheated and returns to the unstable zone where existing tracks anneal such that the AFT age relates to the time of re-cooling (Hurford 2019, from Wagner 1972). The track lengths distribution for a reset age may appear bimodal or have distributions that resemble rapid or slow cooling.

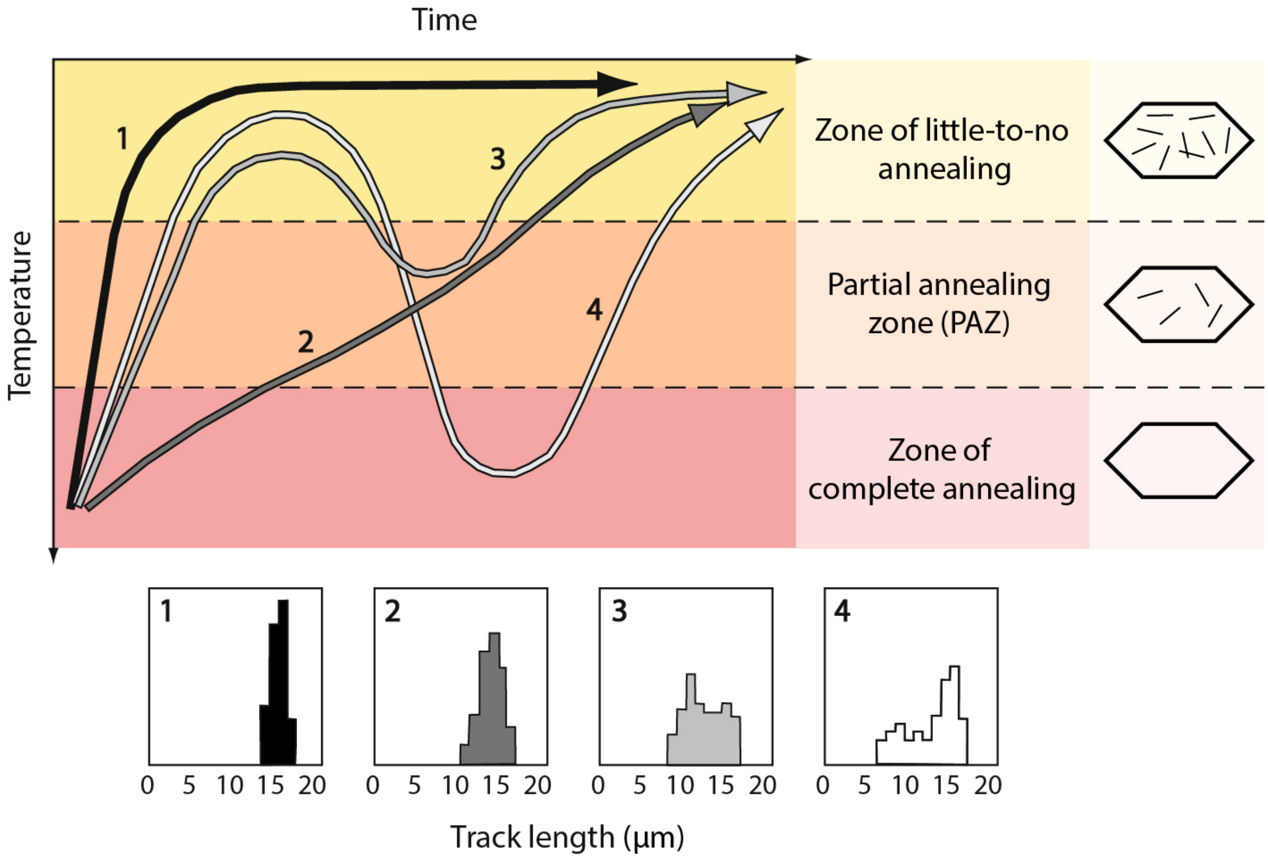

Figure 4.5 Different scenarios for cooling and their associated confined track lengths distributions (modified after Hurford 2019; Naeser 1979; and Wagner 1979). Curve 1, track lengths distribution 1: rapid cooling scenario; measured age is approximately formation age; track lengths distribution has a narrow peak. Curve 2, track lengths distribution 2: slow cooling scenario; older tracks are partially annealed while younger tracks are not; track lengths distribution is broader. Curve 3, track lengths distribution 3: mixed age scenario; previously cooled samples are reheated, existing tracks are partially annealed and a second family of tracks are recorded when the sample re-enters the stability zone; track lengths distribution shows mixed lengths and may be bimodal. Curve 4, track lengths distribution 4: reset age scenario; a crystal in the stability zone is reheated, existing tracks anneal, AFT age relates to time of re-cooling; track lengths distribution may appear bimodal or have distributions resembling scenario 1 or 2.

4.3 AGE CALCULATIONS

AFT age calculation equation stems from the standard radiometric age equation 3.1 ($\frac{\mathrm{d}N_p}{\mathrm{d}t} = -\lambda N_p$), which requires an estimated relative abundance of the parent, ^{238}U, and daughter product, fission tracks. Daughters represented by fission tracks per unit volume are counted on the surface of a mineral grain (Gallagher et al. 1998). Parent ^{238}U concentration is indirectly quantified by irradiating apatite grains with low-energy thermal neutrons to induce fission in ^{235}U, an isotope that has a much larger thermal neutron capture cross-section than ^{238}U, producing tracks that are counted to estimate the amount of ^{238}U according to the known and constant ratio of ^{235}U/^{238}U in nature (e.g. Gallagher et al. 1998). Accordingly, the fission track age equation is (Price and Walker 1963; Naeser 1967):

$$t = \frac{1}{\lambda_D} ln\left(1 + \left(\frac{\lambda_D}{\lambda_f}\right)\left(\frac{\rho_s}{\rho_i}\right) gI\sigma\phi\right) \quad \textbf{\textit{(4.1)}}$$

where *t* is the fission-track age, λ_D is the α-decay constant of ^{238}U = 1.55125 x 10^{-10} yr^{-1}, λ_f is the fission decay constant of ^{238}U = 7.5 10^{-17} yr^{-1}, σ is the thermal-neutron fission cross-section for ^{235}U (5.80 x 10^{-22} cm^{-2}), *I* is ^{235}U/^{238}U isotopic ratio (7.253 x 10^{-3}), *g* is a geometry factor (= 0.5 for the EDM), ρ_s is spontaneous fission-track density (cm^{-2}), ρ_i is induced fission-track density (cm^{-2}), and ϕ is thermal neutron fluence, ca. 10^{-15} (cm^{-2}s^{-1}) (Hurford 2019). The thermal neutron fluence, referred to as just 'fluence', is defined as the density of thermal neutrons hitting a sample (e.g. Hurford 2019). Fluence is found by irradiating a uranium-doped dosimeter glass and counting the resulting induced tracks in the dosimeter (Hurford 2019 and referenced therein). The induced track density, ρ_d, is used to calculate the fluence, ϕ, according to the following equation (Fleischer et al. 1975; Hurford and Green 1981a):

$$\phi = B\rho_d \quad \textbf{\textit{(4.2)}}$$

where *B*, is a calibration constant that is specific to the dosimeter used.

4.3.1 ZETA AND FT CALIBRATION

Zeta, ζ, is a proportionality factor used for calibrating the FT dating system, proposed by Fleischer and Hart in 1972 (Hurford 2019). The form of this equation used in the lab at Dalhousie is from Dumitru (2000):

$$t_{std} = (1/\lambda_t)\{ln[1 + (g\,\rho_s/\rho_i)\lambda_t\zeta\rho_d]\} \quad \textbf{\textit{(4.3)}}$$

where λ_t is the total decay constant of ^{238}U (1.551×10^{-10} yr^{-1}), *a* is the thermal neutron capture cross-sectional area of ^{235}U (584.25×10^{-24} $cm^2 neutron^{-1}$, which is a measure of how likely a thermal neutron in the reactor is to induce fission of a ^{235}U nucleus and ζ for a specific dosimeter glass is evaluated against a mineral standard with known age, t_{std}, (Hurford 2019; 1990), such as Durango Apatite from Cerro de Mercado open-pit iron mine, Durango City, Mexico (31.4 ± 0.5 Ma) (Green 1985) and Fish Canyon Tuff Apatites from La Garita Caldera, southwest Colorado, USA (27.8 ± 0.2 Ma) (Hurford and Hammerschmidt 1985). ζ is calculated according to the following equation (Dumitru 2000):

$$\zeta = (1/\lambda_t)[exp(t_{std}\lambda_t) - 1][\rho_i/g\rho_s](1/\rho_d) \qquad \textbf{\textit{(4.4)}}$$

4.3.2 ERROR REPORTING

Since FT thermochronometry is dependent on the experience and technique of the person counting, reproducibility of results must be demonstrated. It is recommended for experienced operators to establish their calibration by making 5 measurements per mineral phase over a minimum of 3 irradiations (Hurford 2019). The standard deviation, σ, of a track count, *N*, is approximated using the following equation (Hurford 1990; Naeser et al. 1979):

$$\sigma(N) = N^{0.5} \qquad \textbf{\textit{(4.5)}}$$

Equation 4.5 can be applied to spontaneous, induced, and dosimeter track densities. Error for a calculated age, *t*, is evaluated according to the following ‘conventional error analysis’ equation (Donelick et al. 2005):

$$\sigma_i = \left[\frac{1}{N_{s,i}} + \frac{1}{N_{i,i}} + \frac{1}{N_d} + \left(\frac{\sigma_\zeta}{\zeta}\right)^2\right]^{1/2} \qquad \textbf{\textit{(4.6)}}$$

where N_s is the sum of spontaneous tracks counted in all grains, N_i is the sum of all induced tracks counted in all grains, and N_d is the sum of all tracks counted in the dosimeter glass.

4.4 EXTERNAL DETECTOR METHOD (EDM)

The External Detector Method (EDM) (Fleischer et al. 1964b; Naeser and Dodge 1969) is used almost exclusively for FT dating (Hurford 2019) and is the analysis method used by Dalhousie University and the majority of the laboratories worldwide. To prepare apatite grains for EDM, an internal surface of the grain is exposed by polishing (Figure 4.6(b)) and chemical etching (Figure 4.6(c)) to expose spontaneous tracks (Gallagher et al. 1998; Hurford and Carter 1991). The external detector, usually a uranium-free muscovite slab, is held against the grain mount during irradiation (Figure 4.6(d)), where the sample is irradiated with low-energy thermal neutrons (Figure 4.6(e)) in a nuclear reactor to induce fission in ^{235}U (Gallagher et al. 1998). Fission in ^{235}U can be induced without affecting fission in other U and Th isotopes because it has a high thermal neutron capture surface (Donelick et al. 2005). During fission, the induced tracks near the surface of the grain impact the mica detector producing a mirror image of the original grain (Figure 4.6(f)) (Gallagher et al. 1998). Following irradiation, the sample is returned to the lab and the mica detector is chemically etched to reveal the induced tracks (Gallagher et al. 1998). Induced tracks are counted on the mica to determine the amount of ^{235}U-daughter product, which is used to estimate the concentration of ^{238}U-parent through the known ^{238}U/^{235}U ratio (Fleischer et al. 1975).

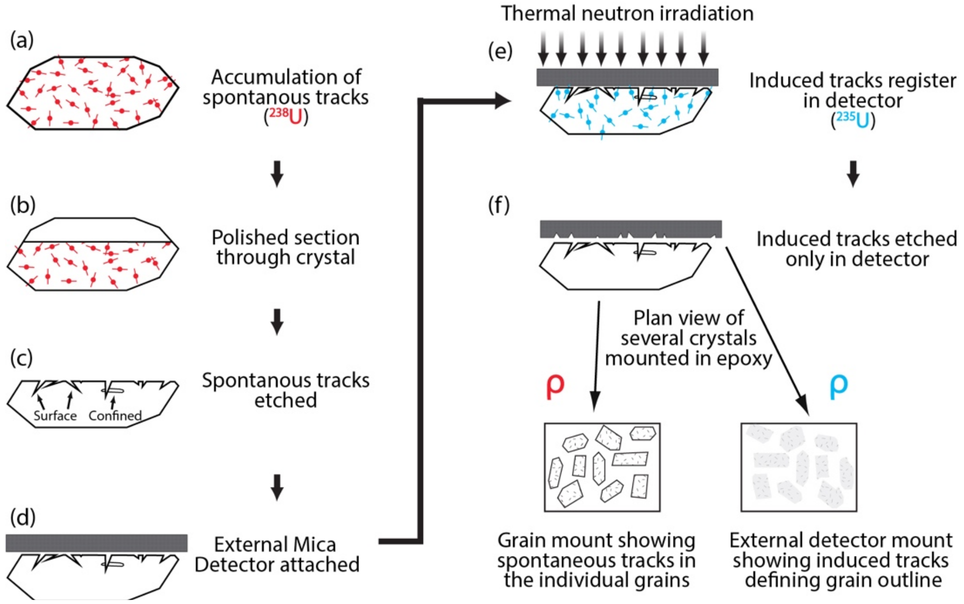

Figure 4.6 Procedures involved in the External Detector Method (EDM) (modified from Gallagher et al. 1998 and Hurford and Carter 1991).

4.5 SUMMARIZED ANALYTICAL PRODECURE

4.5.1 SAMPLE PREPARATION FOR AFT

Sample preparation was conducted in the Fission Track Laboratory at Dalhousie University. Samples followed the procedure of section 3.9.1 Crystal Isolation, where each sample was crushed, chemically cleaned, immersed in LMT or LST heavy liquid, and processed through a Frantz magnetic separator. After grains were picked for (U-Th)/He dating, the remaining heavy fraction of each sample was assessed for AFT. Samples underwent any combination of the following steps to concentrate the apatite grains: 1) micro-sieving using mesh coarseness of 75 μm, 104 μm, and 180 μm, depending on which grain size needed to be isolated for the given sample; 2) immersion in diiodomethane (MI, ρ~3.2 g/cm^3), a second heavy liquid, to separate out zircons and concentrate the apatites; and 3) hand cleaning under a Nikon DS-Fi2 transmitted light stereoscopic microscope to manually separate out apatites in samples that were too small for micro-sieving or MI.

4.5.2 MOUNTING, POLISHING, ETCHING AND PACKING

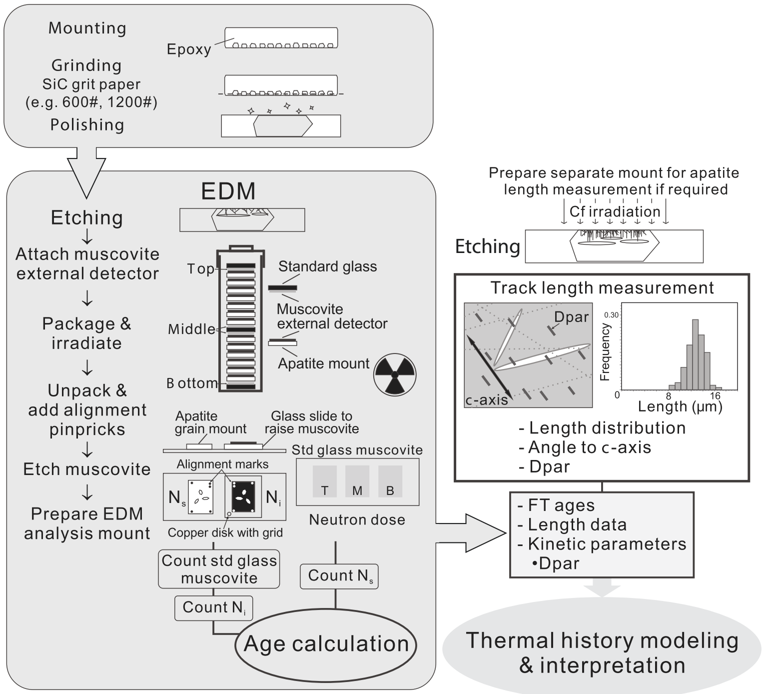

Figure 4.7 Methods for preparing grains and collecting data for fission-track analysis according to the EDM method. Measurement of track lengths and a kinetic indicator in apatite, either Dpar or Cl, where Dpar is measured parallel to the crystallographic c-axis. On grain mount: N_s = spontaneous fission tracks counted on grain mount; N_i= induced fission tracks counted on mica detector; ρ_s = the spontaneous fission-track density (tracks/cm^{-2}) calculated from N_s (modified from Kohn et al. 2019).

The mounting technique used at Dalhousie University is the epoxy-on-glass method (rather than the epoxy-only method, Figure 4.7). For each sample, a standard petrographic glass slide (~1 x 2 in) was cut in half using a diamond pen and a piece of double-sided tape (~1 x 1.5 cm) was applied to the ½ slide. A second petrographic glass slide was prepared by carving the sample name into the slide using the diamond pen. Stacks of 4 pieces of post-it note paper were cut into thin strips and one strip of stacked post-it paper was placed on the ½ slide on either side of the double sided tape. The top layer of the double-sided tape was removed so that the sticky side was exposed and the labelled slide was placed resting on post-it strips over the ½ slide and tape with the sample number facing up. 10 g of resin to 1.7 g of hardener were measured using an ultraprecision balance and mixed very thoroughly for 60 seconds. The resin-hardener mixture was placed in an oven at 35 °C for 10-15 minutes for bubbles to escape before working with the resin. Working one sample at a time, the labelled slide was removed, and grains were sprinkled on the tape. 2-3 drops of epoxy were applied to the centre of the tape using a pick, then spread over the tape square to cover the grains. The labelled slide was returned to its position over the ½ slide, smoothing the resin down (Figure 4.8 A). When all samples on a tray were completed, the tray was placed in an oven at 35 °C for ~12 hours to cure.

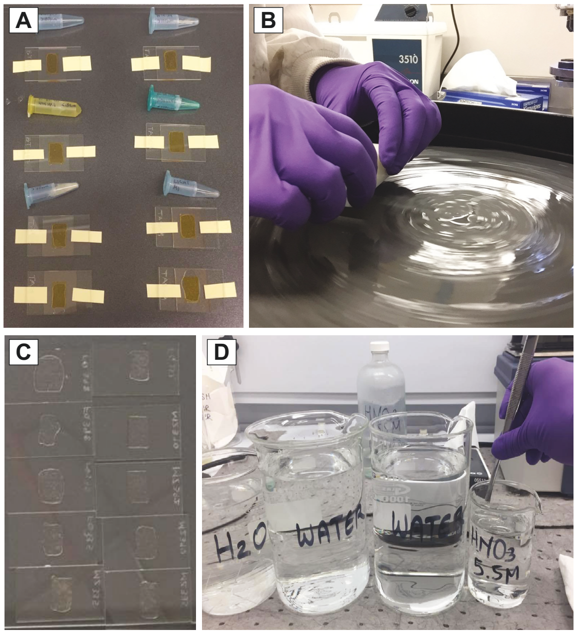

Figure 4.8 A: Apatite grain mounts prepared with double-sided tape, grains, epoxy, and post-it pieces, ready to cure in the oven. B: Polishing apatite grain mounts to open the grains and expose the fission tracks. C: Grain mounts polished and ready for etching. D: Beakers prepared for the etching process with HNO_3 5.5 mol.

To prepare the mounts for polishing, the ½ slide was removed from the epoxy using a scalpel as a lever to expose the grains at the surface of the mount. Polishing occurs in several steps to achieve a very smooth surface. Step 1 involves grinding using glycerine and silica carbide grinding paper at 600/P1200 grit on an automated grinder to open the grains by removing the upper surface, such that the grain is opened in half lengthwise (Figure 4.8 B). Step 2 involves polishing the mounts using 3 μm diamond suspension and a synthetic woven polishing cloth on the automated grinder. Step 3 involves polishing the mount using 0.3 μm suspension composed of alumina powder and water and a porous neoprene cloth on the automated grinder. To avoid contamination, the automated grinder is thoroughly cleaned with distilled water between steps and mounts are thoroughly cleaned between steps by placing each mount in an individual beaker in an ultrasound bath filled with water for 10 minutes, then rinsing each mount with soap and water. When polishing is complete, mounts are placed on a tray in the oven at 30°C for ~12 hours.

Each mount was etched using HNO_3 5.5 mol for 20.0 s (± 0.5 s) at 21 °C (±1 °C) following the standardized procedure described in Donelick et al. (2005), then rinsed thoroughly using distilled water and ethyl alcohol and returned to the oven to dry (Figure 4.8 D). Mounts were broken down to a smaller size using a diamond pen to be loaded into polyethylene tubes. The sample number was carved into the now smaller mount, as well as a mica slab (external detector), which was taped onto each mount using scotch Magic Tape. Slides were packed into a standard polyethylene tube to be sent to the reactor for irradiation at the reactor at the Oregon State University Radiation Center in Corvallis, Oregon, USA. A parameter required for EDM is an accurate value of the intensity of the flux of thermal neutrons during irradiation. To achieve this, U-doped CN_5 dosimetry glasses prepared with a mica slab detector tightly taped to it, are placed at the top, middle, and bottom of the sample stack in the tube. Induced tracks near the surface of the glass impact the mica detector, allowing the calculation of the intensity of the neutron flux through the stack of samples during irradiation.

4.5.3 CALIBRATION AND COUNTING

AFT counting was conducted by Dr. Isabelle Coutand in the Fission-Track Lab at Dalhousie University. The analyst must first establish their calibration by making 5 measurements per mineral phase over at least 3 irradiations (Hurford 2019). The operator used a Zeta factor of 370.6 ± 5.0 (cm^2/yr track). For the EDM, the following three track densities must be counted: spontaneous (ρ_s), induced (ρ_i) and standard glass (ρ_d) (Kohn et al. 2018). Tracks were counted using a Zeiss Axioplan petrographic microscope at 1000 x magnification or higher, using both transmitted and reflected light. For measuring track density, a grain and an area of that grain (or mica detector, or standard glass) was selected for counting (Donelick et al. 2005) based on the following criteria: tracks are randomly oriented and uniformly distributed, and etch pits are parallel to indicate a proper c-axis orientation of the polished surface (Donelick et al. 2005). The analyst systematically scanned across eyepiece grid squares, such that each track was included in the measurement only once. If possible, at least 20 grains were counted, and the results were combined to give an age for the sample.

4.6 RESULTS FROM AFT DATING

Below are summarized results from AFT dating.

Table 4.2 List of variables used in AFT dating and referenced in table 4.3 AFT results.

Zeta	370.6
Zeta error	5
Decay k	1.55 E-10
RhoD	(varies for each sample)
ND	6139
Area	8.985065 E-7 cm^2
Ns	number of spontaneous tracks counted
ρs	density of spontaneous tracks
Ni	number of induced tracks counted
ρi	density of induced tracks on mica
Nd	number of tracks counted in the dosimetry glass
ρd	density of tracks on dosimetry glass
MTL	Mean Track Length
X^2 test	(P > 5%) is a pass on the X^2 test
Dpar	Two to four Dpar measurements were averaged from each analysed crystal when available; when several track lengths were taken in the same grain, two to four Dpar measurements were made too. The Dpar values are the mean of those 4 Dpar values.
U	average U concentration (ppm) of grains used for age calculation

Table 4.3 Summary of AFT results including all samples from all transects that were usable for AFT dating. For a list defining all variables, see table 4.2. Results where there is 'xx' were unattainable.

Sample Number	Number of grains	Spontaneous Track Density rs x 10^6 cm^{-2} (Ns)	Induced Track Density ri x 10^6 cm^{-2} (Ni)	Dosimeter Track Density rd x 10^6 cm^{-2} (Nd)	P(c^2) (%)	Central Age ± 1s (Ma)	U (ppm)	Confined Track-Lengths (TL)	MTL (c-Axis Not Corrected) mm ± STD	Dpars mm	Dpar STD mm	Comments
K8	10	0.3798 (266)	0.4254 (298)	1.0852 (8425)	99	177.0 ± 15.2	6	70	13.09 ± 1.97	2.57	0.12	
K9	18	xxxx (591)	xxxx (1187)	1.0908 (8425)	40	99.9 ± 5.3	13	41	13.72 ± 1.49	2.56	0.18	
K10	15	1.2207 (855)	1.4305 (1002)	1.0964 (8425)	76	171.1 ± 8.4	19	xx	xx	2.20	0.15	
K11	12	0.7533 (322)	0.7463 (319)	1.1020 (8425)	77	202.9 ± 16.4	9	37	13.22 ± 1.36	2.74	0.25	
K12	xx	xx	xx	1.1076 (8425)	xx	xxx	xx	xx	xx	xx	xx	
K13	12	0.1408 (129)	0.2762 (253)	1.1133 (8425)	94	104.3 ± 11.4	3	xx	xx	2.50	0.20	
K14	xx	xx	xx	1.1189 (8425)	xx	xxx	xx	xx	xx	xx	xx	10 grains were dated - very dispersed, huge errors - AFT age is younger than AHe
K15	13	0.5178 (451)	0.6991 (609)	1.1245 (8425)	56	142.5 ± 9.8	8	xx	xx	1.96	0.12	
K16	21	0.5740 (799)	0.7465 (1039)	1.1301 (8425)	76	158.2 ± 8.1	9	62	13.15 ± 1.23	2.22	0.20	
TA912	9	xxxx (1021)	xxx (1304)	1.1413 (8425)	98	163.5 ± 7.3		87	13.81 ± 1.28	3.75	0.25	
TA923	14	0.2506 (185)	0.4403 (325)	1.1470 (8425)	88	119.9 ± 11.2	5	xx	xx	2.39	0.33	
TA929	13	0.7815 (426)	1.0329 (563)	1.1526 (8425)	51	159.6 ± 10.6	12	xx	xx	2.35	0.20	
TA212	xx	xx	xx	1.1582 (8425)	xx	xxx	xx	xx	xx	xx	xx	
TA217	14	1.3434 (1181)	1.8973 (1668)	1.1638 (8425)	32	151.3 ± 6.6	22	101	12.70 ± 1.46	2.20	0.15	
SC216	10	1.2463 (310)	1.9659 (489)	1.1694 (8425)	90	135.9 ± 10.1	24	17	13.48 ± 1.54	2.80	0.46	
FQ332	14	0.5621 (426)	0.8827 (669)	1.1750 (8425)	60	137.2 ± 8.8	11	17	13.31 ± 2.01	2.21	0.19	
FQ335	xx	xx	xx	1.1807 (8425)	xx	xxx	xx	xx	xx	xx	xx	Ages dispersed - not usable
FQ398	xx	xx	xx	1.1919 (8425)	xx	xxx	xx	xx	xx	xx	xx	No Uranium - Not datable
MZ335	xx	xx	xx	1.2155 (8425)	xx	xxx	xx	xx	xx	xx	xx	Ages dispersed - not usable
MZ351	xx	xx	xx	1.2403 (8425)	xx	xxx	xx	xx	xx	xx	xx	Few grains - super high track density - not countable but probably old
MZ379	10	1.1558 (274)	2.1639 (513)	1.2651 (8425)	92	124.0 ± 9.5	23	60	12.76 ± 1.82	2.82	0.44	
MZ390	11	0.4281 (346)	0.3873 (313)	1.2899 (8425)	91	258.9 ± 20.7	4	26	11.20 ± 2.34	2.28	0.44	
MZ392	12	1.0509 (604)	0.7256 (417)	1.3146 (8425)	13	243.5 ± 22.7	7	55	11.45 ± 2.16	xx	xx	

CHAPTER 5: MODELLING METHODS AND RESULTS

5.1 INTRODUCTION TO THERMAL MODELLING

The forward thermal modeling approach assumes a particular starting point and pre-determined time-temperature history to predict how a given instance of a system will evolve over time to the end condition, such as the surface temperature (Ketcham 2005). Forward modelling predicts how a given instance of a system will evolve over time, producing data that can be compared with measured observations (Ketcham 2005). Inverse modelling uses input data, including the measured ages and temperature-time constraints, to construct time-temperature paths that would produce those final results (Ketcham 2005). Inverse models are based on a theoretical diffusion, or annealing model and an algorithm, which continuously calculates the model evolution over the time-temperature path. Inverse thermal modeling produces tens to hundreds of thousand forward models, or temperature-time (T-t) paths, that are consistent with input parameters. The program searches through these candidate thermal histories using a Monte Carlo approach to evaluate the paths, while the software keeps track of each path tested and reports the set of paths that pass the statistical criteria. While the reliability of the model depends on the quality of the input data and constraints (Ketcham 2005), the thermal history that best matches the input data is selected from the models.

5.2 *HeFTy* SOFTWARE

HeFTy (Ketcham 2005) is a thermal modelling software used to calculate the thermal history of a rock sample, from multiple thermochronometers data, through a multi-step process which includes forward and inverse modelling. The version of *HeFTy* used for this study is version 1.9.3, build 1.9.3.74, which can derive cooling histories from multiple sources from individual samples, including AHe, ZHe and AFT, using a Monte Carlo search.

5.2.1 INPUT DATA PREPARATION

Thermochronological input data in the models were carefully reviewed and selected (c.f. Chapter 3). Samples were not modeled if they only had results from one thermochronometer. Setting up the models includes: inputting age data; defining temperature-time (T-t) constraints based on the thermochronological ages obtained and what is known from independent geological constraints; defining characteristics of half-segments between T-t constraints; and select the most recent diffusion (AHe, ZHe), or annealing (AFT) models used for each thermochronometer.

5.2.2 AHe AND ZHe DATA AND INPUT FOR THIS STUDY

(U-Th)/He data were entered aliquot per aliquot using their uncorrected ages, ESR, and composition of U, Th and Sm. Data input is separated into (1) Model Parameters, which identify the options for published theoretical diffusion models (2) Data, including measured ages and grain size, or ESR, and (3) Composition of the grain that was dated. Data input is exactly the same for AHe as for ZHe, except for the calibration chosen in Model Parameters, which allows the software to differentiate an apatite grain from a zircon grain based on the selected diffusion model.

The *model parameters* selected were the latest diffusion models published for AHe and ZHe and embedded in the code, including the Guenthner et al. 2013 calibration for zircon and the Flowers et al. (2009) radiation damage accumulation and annealing model (RDAAM) calibration for apatite. The *grain radius* is used to define diffusion and was input using the grain's ESR value from the sample's data table. *Abraded* was set to 0 μm because samples were not abraded. "Good" *Precision*, was selected in order to keep the model running quickly. Under *Stopping distances*, "Ketcham et al. 2011" was selected because it is the most recent iteration of values, giving the most accurate α-ejection calculation. For *Alpha calculation*, "Ejection" was selected to illustrate the effects of alpha stopping distances on model predictions (Ketcham 2011) (Figure 5.1). In the Data window, the input value for *Measured age (uncorrected)* was the aliquot's raw age (Ma) value from the sample's data table. The *$\pm(1\sigma)$* error was input based on methods discussed below. For *Age to report*, “Corrected” was selected so the age reported by the model was corrected for α-ejection. In (3) Composition, the values for U, Th, and Sm (ppm) were input using the corresponding composition values for the grain in the sample’s data table (Figure 5.1).

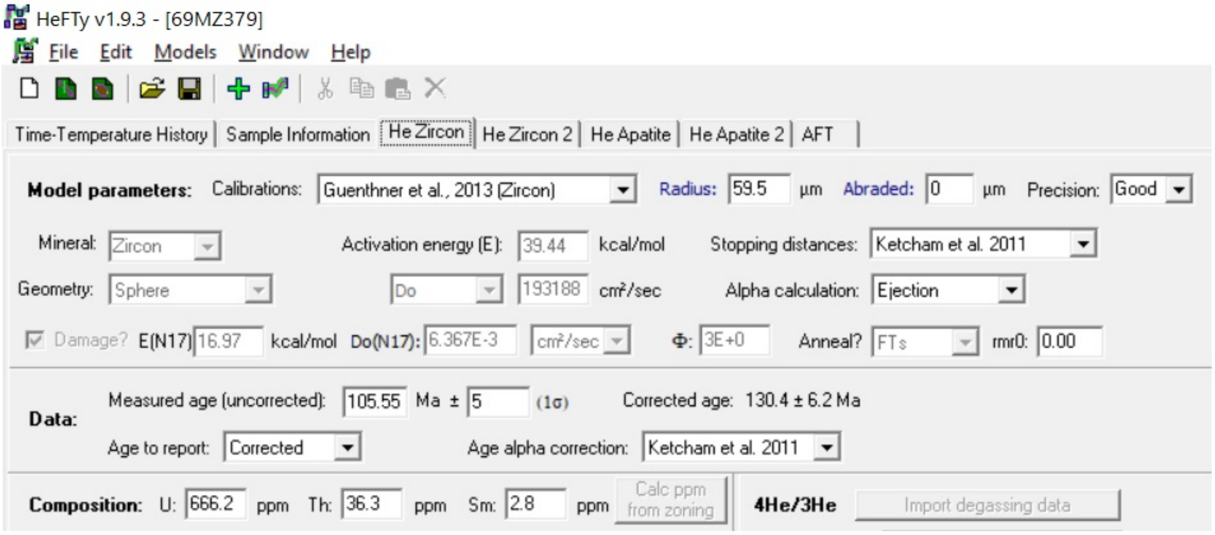

Model parameters: Calibrations: Guenthner et al., 2013 (Zircon) Radius: 59.5 μm Abraded: 0 μm Precision: Good

Mineral: Zircon Activation energy (E): 39.44 kcal/mol Stopping distances: Ketcham et al. 2011

Geometry: Sphere Do 193188 cm²/sec Alpha calculation: Ejection

☑ Damage? E(N17) 16.97 kcal/mol Do(N17): 6.367E-3 cm²/sec Φ: 3E+0 Anneal? FTs rmr0: 0.00

Data: Measured age (uncorrected): 105.55 Ma ± 5 (1σ) Corrected age: 130.4 ± 6.2 Ma

Age to report: Corrected Age alpha correction: Ketcham et al. 2011

Composition: U: 666.2 ppm Th: 36.3 ppm Sm: 2.8 ppm

Figure 5.1 Example of data input in *HeFTy* for ZHe data from sample 69MZ379. AHe data input is very similar, only differing in the calibration model chosen (for AHe, the model used is Flowers et al. 2009 RDAAM (Apatite)).

5.2.2.1 ERROR

Input aliquot ages must overlap, within errors, for *HeFty* to find T-t paths solutions. For most of our (U-Th-Sm)/He samples, this is not the case because analytical errors obtained from raw data are very small. Therefore, we needed to increase the single-grain age error for each aliquot of a given sample to overlap with the other aliquots’ ages. We have used errors of up to 20% of the aliquots’ raw ages in order to be able to include the most aliquots possible in each model (those that we had selected and grouped together in the previous chapter). There are some exceptions to this 20% value to allow the inclusion of more aliquots, including sample 69MZ351 (AHe 25%), K0015 (AHe 25%), K0012 (AHe 25%), 69FQ335 (ZHe 40%, AHe 30%) because ages are very young (only 38 – 76 Ma) and 69MZ379 (AHe 40%) because ages are very young (15 – 20 Ma).

5.2.3 AFT DATA AND INPUT FOR THIS STUDY

AFT data were input using measured ages and track lengths. Annealing model and parameters data settings were selected as follows. For *Annealing model*, “Ketcham et al., 2007” was selected because it is the most recent annealing model. For *C-axis projection*, “Ketcham et al. 2007, 5.5M” was selected because we follow the apatite etching protocol using HNO_3 at 5.5 M to reveal the tracks as described in Ketcham et al. (2007). The *Model c-axis projected lengths* box was checked to generate track length histograms using c-axis projection, a method that estimates the length of each track as if it were oriented parallel to the c-axis (Ketcham 2011). Since samples did not need additional irradiation to reveal confined track lengths, the *Used Cf Irradiation* box was not checked. For *Default initial mean track length*, “From Dpar μm” was selected so that the initial length estimate would be generated for each length measurement based on the corresponding Dpar kinetic parameter value (Ketcham 2011). For *Length reduction in standard*, the default value of 0.893 was used, which represents the ratio of spontaneous track length to induced track length in Durango apatite, the standard used for calibration (Ketcham 2011). The kinetic parameter used to distinguish different populations was Dpar, which is the mean diameter of fission-track etch pits parallel to the crystallographic c-axis within each apatite grain (e.g., Donelick, 1993; Donelick, 1995).

In the Length Data section, default values and options were used, including ^{a}*Len*: 1, ^{a}*Dpar*: 1, *Calibration mode*: KCH 2015, and Goodness of Fit or *GOF method*: Kuiper’s Statistic. The GOF method determines which function is used to compare model results to measured length histograms, where the Kuiper’s statistic (Press et al. 1992) option equalizes sensitivity between the median and tails (Ketcham 2011). Data for *Length* (of each fission track in μm), *Angle* (of each track to the C-axis), and *Dpar (μm)* were input from the measured data in the sample’s data table. The value used for *Lo (μm)*, which is the assumed unannealed, or initial length of a fission track, was input for each track according to the *Default initial track length* value of 16.10 (Ketcham 2011). *Lc (μm)*, the C-axis projected length of the fission track, is calculated by *HeFTy* after a correction using the angle between the measured track and the C-axis and the Dpar value of the grain.

In the Age Data section, the options that were selected and input are as follows. For *Zeta mode*, Traditional was selected, representing the traditional zeta calibration method (Hurford and Green 1983) for determining fission-track age which requires values for zeta (ζ), uncertainty in zeta ($\sigma(\zeta)$), measured fission-track density in a standard dosimeter glass (ρ_d), and total number of tracks measured in the glass (N_d). The values used for these variables are: ζ = 370.6, because it is the operator's (Dr. I. Coutand) calibration factor; for $\sigma(\zeta)$ = 5, ρ_d and N_d were reported as per values from the data table. For *Uncertainty mode*, 95% +/- was selected, representing asymmetric uncertainties with a 95% confidence limit (Ketcham 2011). Data for N_s (spontaneous track counts) and N_i (induced track counts), *Age (Ma)* and *Dpar (μm)* were input from the measured data in the sample's data table (Figure 5.2).

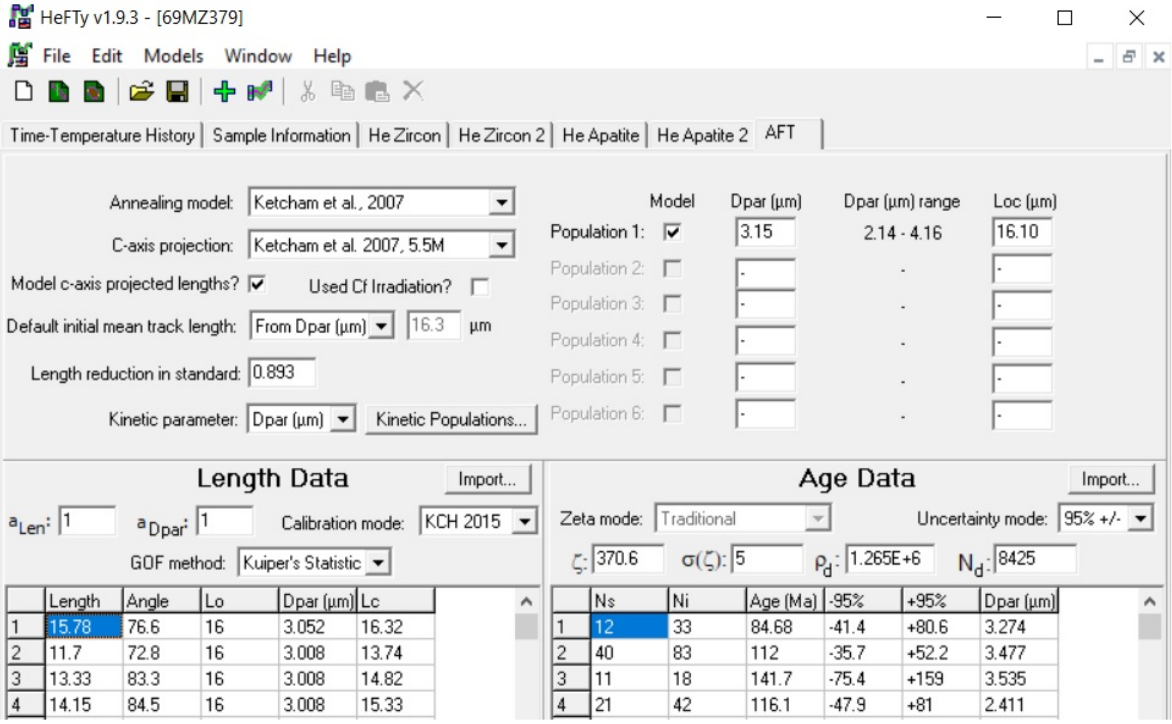

Annealing model: Ketcham et al., 2007
C-axis projection: Ketcham et al. 2007, 5.5M
Model c-axis projected lengths? ☑ Used Cf Irradiation? ☐
Default initial mean track length: From Dpar (μm) 16.3 μm
Length reduction in standard: 0.893
Kinetic parameter: Dpar (μm)

	Model	Dpar (μm)	Dpar (μm) range	Loc (μm)
Population 1:	☑	3.15	2.14 - 4.16	16.10
Population 2:	☐	-	-	-
Population 3:	☐	-	-	-
Population 4:	☐	-	-	-
Population 5:	☐	-	-	-
Population 6:	☐	-	-	-

Length Data

a_{Len}: 1 a_{Dpar}: 1 Calibration mode: KCH 2015
GOF method: Kuiper's Statistic

	Length	Angle	Lo	Dpar (μm)	Lc
1	15.78	76.6	16	3.052	16.32
2	11.7	72.8	16	3.008	13.74
3	13.33	83.3	16	3.008	14.82
4	14.15	84.5	16	3.008	15.33

Age Data

Zeta mode: Traditional Uncertainty mode: 95% +/-
ζ: 370.6 $\sigma(\zeta)$: 5 ρ_d: 1.265E+6 N_d: 8425

	Ns	Ni	Age (Ma)	-95%	+95%	Dpar (μm)
1	12	33	84.68	-41.4	+80.6	3.274
2	40	83	112	-35.7	+52.2	3.477
3	11	18	141.7	-75.4	+159	3.535
4	21	42	116.1	-47.9	+81	2.411

Figure 5.2 Example of data input in *HeFTy* for AFT data from sample 69MZ379.

5.2.4 CONSTRAINTS, HALF SEGMENTS, SEARCH METHODS

Constraints are represented by time-temperature regions that the thermal history must pass through. They are used to help direct the model by narrowing its search. Constraints are drawn on the model as time-temperature boxes where the initial temperature condition greater than the upper limit of the PAZ/PRZ such that a total ^{4}He diffusion or annealing of fission tracks (Ketcham 2005) is assumed at the start of the run. Temperature parameters remained consistent for each sample, including [40-80] °C for AHe, [100-140] °C for AFT, and [160-200] °C for ZHe to include the approximate temperatures of the HePRZ or PAZ and [0] °C for the temperature at which the sample was collected, or present-day temperature (Environment Canada 2020). The age parameters were adjusted depending on the aliquots chosen for each sample, except for surface temperature, which was always was set to 0 °C at 0 Ma (Figure 5.3).

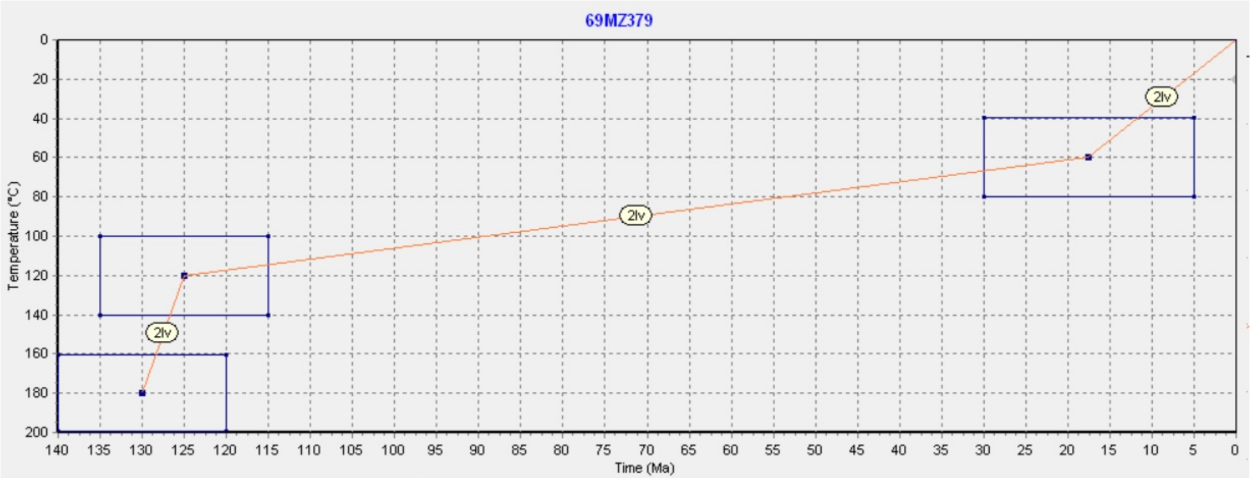

Figure 5.3 Example of constraint boxes (blue boxes) drawn for sample 69MZ379 according to age data and temperature parameters which are determined according to the PAZ/PRZ and remain the same for each sample, including [0] °C for present-day temperature, [40-80] °C for AHe, [100-140] °C for AFT, and [160-200] °C for ZHe.

Half segments were adjusted to define how the T-t path would be interpolated by *HeFTy* between two constraints (Ketcham 2011). All half segments were set to the code *2Iv*, where “2” is the number of times the segment is halved by introducing new nodal points that allow a change of slope; “I”, which stands for intermediate, determines the randomizer that generates the interpolating node points and path segments, intermediate meaning that the path is less prone to sudden changes, for example, in the case of fast sedimentation and basin subsidence; and “v” indicates that the path is monotonic-variable, which means that the constraints can be connected by either heating or cooling paths (compared to monotonic-consistent, where paths have a heating- or cooling-only direction) (Ketcham 2011).

Models were run using a Monte Carlo search method. A Monte Carlo approach generates and evaluates tens of thousands of independent time-temperature paths (Ketcham 2005), while the software records each path tested and reports the paths that pass the statistical criteria being used. A "Good" fit is one that corresponds to a value of ≥ 0.50, meaning that the path is supported by the data. An "Acceptable" fit is one that corresponds to a value of ≥ 0.05, indicating that the model has not failed the null hypothesis test meaning that the path is not ruled out by the data. Results were recorded in a data table including ages used, different modelling attempts for each sample, and constraints used. See Appendix D for tables.

5.2.5 PROBLEM SOLVING: AFT DATA CHALLENGES

Four of the samples' models did not work with both AFT and AHe data. For these samples, the AHe ages were used with a constraint box to guide the model through the AFT partial annealing temperature range. This occurred only in samples where AFT ages were very close to AHe ages and/or where AFT track lengths were relatively long (> 13 microns) indicating fast cooling, including the following samples: k0016, where the AFT central age is 158.2 ± 8.10 Ma, mean track length is 13.15 μm, and AHe ages used in the model range from 150.3 – 159.1 Ma; k0011, where the AFT central age is 202.9 ± 16.40 Ma, mean track length is 13.22 μm, and AHe ages used in the model range from 187.4 – 201.5 Ma; 71TA912, where the AFT central age is 163.70 ± 7.30 Ma, mean track length is 13.81 μm, and AHe ages used in the model range from 153.7 – 157.4 Ma; and 69MZ392, where the AFT central age is 243.5 ± 22.7 Ma and mean track length is 11.45 μm.

5.3 INVERSION CONTSTRAINTS AND THERMAL MODELLING RESULTS

Table 5.1 Saglek transect inversion constraints and thermal modelling results. Abbreviations: T, temperature, t, time.

Sample	1st constraint		2nd constraint		3rd constraint		Model	Accept-able fits	Good fits
	T (°C)	t (Ma)	T (°C)	t (Ma)	T (°C)	t (Ma)	runs		
67SC216	160-180	310-370	100-140	125-145	40-80	100-130	50,000	430	0
67SC217-1	160-180	130-180	100-140	130-160	40-80	90-130	50,000	62	0
67SC217-2	160-180	200-250	100-140	150-180	40-80	95-125	50,000	429	2
67SC217-3	160-180	150-190	100-140	150-170	40-80	90-125	50,000	165	1
67SC218 - 4	160-180	730-840	40-80	150-200	-	-	20,000	802	99
67SC218 - 5	160-180	730-840	40-80	100-150	-	-	20,000	938	148
69TA212 - 3	160-180	360-400	40-80	250-290	-	-	10,000	5,564	456
69TA212 - 4	160-180	500-635	40-80	250-290	-	-	50,000	686	0

Table 5.2 Nain transect inversion constraints and thermal modelling results. Abbreviations: T, temperature, t, time.

Sample	1st constraint		2nd constraint		3rd constraint		Model	Accept-able fits	Good fits
	T (°C)	t (Ma)	T (°C)	t (Ma)	T (°C)	t (Ma)	runs		
69FQ332 - 3	160-180	140-190	100-140	135-175	40-80	110-140	20,000	3,599	8
69FQ335 - 2	160-180	40-90	40-80	20-70	-	-	20,000	8,304	9,266
69MZ379	160-180	120-140	100-140	115-135	40-80	05-30	20,000	1,144	313
69MZ390 - 2	100-140	240-280	40-80	115-165	-	-	50,000	56	0
69MZ392	160-180	1010-1150	100-140	225-265	40-80	110-170	50,000	413	0

Table 5.2 (***Cont'd)*** Nain transect inversion constraints and thermal modelling results. Abbreviations: T, temperature, t, time

Sample	1st constraint		2nd constraint		3rd constraint		Model	Accept-able fits	Good fits
	T (°C)	t (Ma)	T (°C)	t (Ma)	T (°C)	t (Ma)	runs		
69MZ351 - 1	160-180	510-570	40-80	110-180	-	-	20,000	1,439	417
69MZ351 - 2	160-180	510-570	40-80	210-290	-	-	20,000	2,162	578

Table 5.3 Hopedale transect inversion constraints and thermal modelling results. Abbreviations: T, temperature, t, time.

Sample	1st constraint		2nd constraint		3rd constraint		Model	Accept-able fits	Good fits
	T (°C)	t (Ma)	T (°C)	t (Ma)	T (°C)	t (Ma)	runs		
k0016	160-180	1000-1110	100-140	130-190	40-80	115-185	50,000	1,514	83
k0015 - 1	160-180	280-360	100-140	130-180	40-80	85-160	20,000	1,013	171
k0014 - 2	160-180	970-1060	40-80	165-240	-	-	20,000	1,811	383
k0014 - 4	160-180	350-450	40-80	165-240	-	-	20,000	8,199	6,422
k0013	160-180	430-500	100-140	85-125	40-80	65-115	50,000	250	6
k0012 - 1	160-180	980-1170	40-80	195-280	-	-	20,000	2,926	254
k0012 - 2	160-180	980-1170	40-80	120-185	-	-	20,000	1,304	168
k0011	160-180	260-310	100-140	130-220	40-80	160-215	10,000	1,648	174
k0009 - 2	160-180	560-170	100-140	80-140	40-80	75-120	50,000	775	0
k0008 - 4	160-180	470-550	100-140	160-200	40-80	145-200	50,000	712	0

Table 5.4 Makkovik transect inversion constraints and thermal modelling results. Abbreviations: T, temperature, t, time.

Sample	1st constraint		2nd constraint		3rd constraint		Model	Accept-able fits	Good fits
	T (°C)	t (Ma)	T (°C)	t (Ma)	T (°C)	t (Ma)	runs		
71TA464 - 1	160-180	740-840	40-80	105-150	-	-	50,000	527	94
71TA464 - 2	160-180	570-150	40-80	105-150	-	-	20,000	1,307	209
71TA923	160-180	150-220	100-140	100-140	40-80	75-125	10,000	3,172	926
71TA912	100-140	145-185	40-80	130-180	-	-	10,000	3,870	1,883
71TA929	160-180	220-270	100-140	100-160	40-80	140-180	10,000	1,268	155

5.4 AFT THERMAL MODELLING RESULTS

Table 5.5 Saglek transect AFT best-fit thermal modelling results. Abbreviations: MTL, mean track length, GOF, goodness of fit, OT, oldest track, SD, standard deviation.

Samplea	Best-fit AFT age				Best-fit MTLproj			Notes
	Modelled	Measured ± 1σ	GOF	OT age	Modelled ± SD	Measured ± SD	GOF	
67SC216	144.0	135.9 ± 10.0	0.4	175.0	15.16 ± 1.2	13.48 ± 1.54	0.2	
67SC217-1	147.0	151.3 ± 6.6	0.6	163.0	14.60 ± 0.94	12.70 ± 1.46	0.1	
67SC217-2	151.0	151.3 ± 6.6	1.0	177.0	14.47 ± 0.99	12.70 ± 1.46	0.3	
67SC217-3	153.0	151.3 ± 6.6	0.8	169.0	14.58 ± 0.82	12.70 ± 1.46	0.2	
67SC218 - 4	-	-	-	-	-	-	-	No AFT data
67SC218 - 5	-	-	-	-	-	-	-	No AFT data
69TA212 - 3	-	-	-	-	-	-	-	No AFT data
69TA212 - 4	-	-	-	-	-	-	-	No AFT data

Table 5.6 Nain transect AFT best-fit thermal modelling results. Abbreviations: MTL, mean track length, GOF, goodness of fit, OT, oldest track, SD, standard deviation.

Sample	Best-fit AFT age				Best-fit MTLproj			Notes
	Modelled	Measured ± 1σ	GOF	OT age	Modelled ± SD	Measured ± SD	GOF	
69FQ332 - 3	150.0	137.2 ± 8.8	0.2	160.0	15.02 ± 0.78	13.31 ± 2.01	0.2	-
69FQ335 - 2	-	-	-	-	-	-	-	No AFT data
69MZ379	110.0	124.0 ± 9.5	0.2	133.0	14.33 ± 1.21	12.76 ± 1.82	1.0	-
69MZ390 - 2	230.0	258.9 ± 20.7	0.1	276.0	14.23 ± 1.37	11.20 ± 2.34	0.1	-
69MZ392	-	-	-	-	-	-	-	Model does not run with AFT data
69MZ351 - 1	-	-	-	-	-	-	-	No AFT data
69MZ351 - 2	-	-	-	-	-	-	-	No AFT data

Table 5.7 Hopedale transect AFT best-fit thermal modelling results. Abbreviations: MTL, mean track length, GOF, goodness of fit, OT, oldest track, SD, standard deviation, TL, track length.

Sample	Best-fit AFT age				Best-fit MTLproj			Notes
	Modelled	Measured ± 1σ	GOF	OT age	Modelled ± SD	Measured ± SD	GOF	
k0016	-	-	-	-	-	-	-	Model does not run with AFT data
k0015 - 1	155.0	142.5 ± 9.8	0.8	167.0	-	-	-	No TL data
k0014 - 2	-	-	-	-	-	-	-	No AFT data
k0014 - 4	-	-	-	-	-	-	-	No AFT data

Table 5.7 Cont'd Hopedale transect AFT best-fit thermal modelling results. Abbreviations: MTL, mean track length, GOF, goodness of fit, OT, oldest track, SD, standard deviation, TL, track length.

Sample	Best-fit AFT age				Best-fit MTLproj			Notes
	Modelled	Measured ± 1σ	GOF	OT age	Modelled ± SD	Measured ± SD	GOF	
k0013	120.0	104.3 ± 11.40	0.2	150.0	-	-	-	No TL data
k0012 - 1	-	-	-	-	-	-	-	No AFT data
k0012 - 2	-	-	-	-	-	-	-	No AFT data
k0011	-	-	-	-	-	-	-	Model does not run with AFT data
k0009 - 2	106	99.9 ± 5.30	0.27	112	14.75 ± 0.98	13.72 ± 1.49	0.31	-
k0008 - 4	197	177 ± 15.20	0.21	254	14.79 ± 1.26	13.09 ± 1.97	0.17	-

Table 5.8 Makkovik transect AFT best-fit thermal modelling results. Abbreviations: MTL, mean track length, GOF, goodness of fit, OT, oldest track, SD, standard deviation, TL, track length.

Sample	Best-fit AFT age				Best-fit MTLproj			Notes
	Modelled	Measured ± 1σ	GOF	OT age	Modelled ± SD	Measured ± SD	GOF	
71TA464 - 1	-	-	-	-	-	-	-	No AFT data
71TA464 - 2	-	-	-	-	-	-	-	No AFT data
71TA923	118	119.9 ± 11.20	0.9	131	-	-	-	No TL data
71TA912	-	-	-	-	-	-	-	Model does not run with TL data
71TA929	159	159.6 ± 10.60	0.98	171	-	-	-	No TL data

5.5 SAGLEK TRANSECT: MODELLING RESULTS AND COOLING HISTORIES

Trends in tendency of cooling history based on *HeFTy* models show that samples 67SC216, 67SC217 and 67SC218 each demonstrated a Mesozoic cooling event beginning between 174 – 125 Ma (Figure 5.8). All samples, except 67SC212 furthest inland, displayed a period of stagnancy prior to the Mesozoic cooling event, where rate of cooling ranged from 0.06 – 0.09 °C/Ma (Table 5.9), but this period ranged in its starting time from 317.52 – 668.29 Ma. The two samples closest to the coastline, including 67SC216 and 67SC217, displayed a Cenozoic episode of cooling ranging from ~30 – 50 Ma (Figure 5.8). Otherwise, there is no distinct east-west trend regarding the timing of Mesozoic cooling.

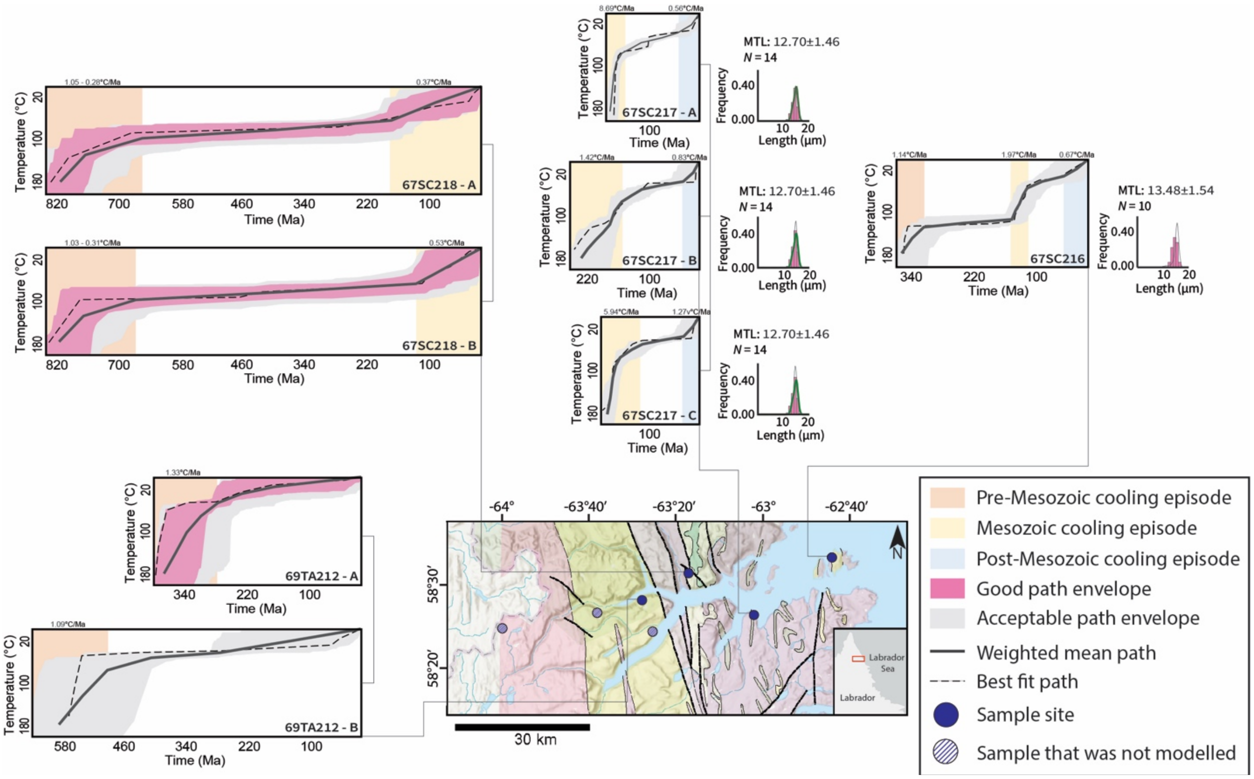

Figure 5.4 Saglek transect geological map showing cooling histories for modelled samples, including 67SC216, 67SC217, 67SC218 and 69TA212.

5.5.1 SAGLEK TRANSECT: INDIVIDUAL SAMPLE HISTORIES

- **67SC216**: This sample's cooling path shows an initial pulse of cooling at an average rate of 1.14 °C/Ma from 360.63 – 317.52 Ma, followed by a period of stagnation. There is another pulse of cooling from 147.20 – 117.68 Ma, at an average rate of 1.97 °C/Ma, which slows to 0.31 °C/Ma before another small pulse of cooling at a rate of 0.67 °C/Ma beginning at 46.40 Ma.
- **67SC217**: This sample had three possible solutions for cooling history. 67SC217-A and B are very similar except at the start, as 67SC217-A began cooling at 172.58 Ma and 67SC217-B began cooling at 229.0 Ma. Both models begin following a similar cooling path at ~170 Ma, when cooling began to slow until a final pulse of cooling at ~30 – 40 Ma. 67SC217-C began cooling earlier at 813.09 Ma, cooling at an average rate of 3.44 °C/Ma before cooling stagnated at 655.42 Ma until a final pulse of cooling at 174.12 Ma at a rate of 1.27 °C/Ma.
- **67SC218**: This sample had two possible solutions for cooling history. Both solutions follow a comparable path with an initial cooling rate of ~1°C/Ma from 813.08 – 655.42 Ma, followed by a period of stagnation. Both cooling paths display a period of cooling during the Mesozoic Era at an average rate of 0.37 – 0.53 °C/Ma, where 67SC218-A begins cooling at 174.13 Ma, but 67SC218-B begins cooling at 125.08 Ma.
- **67SC212**: This sample had two possible solutions for cooling history, both following the same trend where an initial pulse of cooling tapers off. 69TA212-A begins cooling at 381.16 Ma at a rate of 1.33 °C/Ma, which begins tapering off at 276.74 Ma to a rate of 0.22 °C/Ma. 69TA212-B begins cooling earlier at 584.16 Ma at a rate of 1.09 °C/Ma, which begins tapering off at 490.66 Ma to a rate of 0.17 °C/Ma.

Table 5.9 Saglek transect cooling rates, where age values represent the time intervals between which cooling rates were calculated.

Sample	Initial				Cooling rate (°C/Ma)					Final
	Age (ma)	Rate	Age (ma)	Rate	Age (ma)	Rate	Age (ma)	Rate	Age (ma)	Rate
67SC216	360.63 317.52	1.14	317.52 147.20	0.09	147.20 117.68	1.97	117.68 46.40	0.31	46.40 0.0	0.67
67SC217 - A	172.58 149.56	8.69	149.56 112.53	1.57	112.53 41.42	0.26	-	-	41.42 0.0	0.56
67SC217 - B	229.0 173.10	1.42	173.10 111.07	0.58	111.07 30.90	0.19	-	-	30.90 0.0	0.83
67SC217 - C	813.09 765.56	5.94	765.56 655.42	0.95	655.42 174.12	0.17	-	-	174.12 0.0	1.27
67SC218 - A	813.09 765.56	1.05	765.56 96.09	0.28	96.09 174.13	0.07	-	-	174.13 0.0	0.37
67SC218 - B	815.95 768.63	1.03	768.63 96.72	0.31	96.72 125.08	0.06	-	-	125.08 0.0	0.53
69TA212 - A	381.16 276.74	1.33	-	-	-	-	-	-	276.74 0.0	0.22
69TA212 - B	584.16 490.66	1.09	-	-	-	-	-	-	490.66 0.0	0.17

5.6 NAIN TRANSECT: MODELLING RESULTS AND COOLING HISTORIES

Trends in the tendency of cooling history within samples from this transect show that four of the six samples, including 69FQ332, 69MZ379, 69MZ390 and 69FQ351 demonstrated a Mesozoic cooling event beginning between 172.81 – 135.72 Ma (Figure 5.9). Of the two remaining samples, 69FQ335 was reset and cooled after this event at 65.99 Ma, while 69MZ392 had an increase in cooling rate beginning at 243.56 Ma. Samples located closest to the coastline, including 69FQ332, 69FQ335, and 69FQ379, were fully reset during the Mesozoic or Cenozoic Eras. Zircon cooling for samples 69FQ332 and 69FQ379 began at 172.81 Ma and 135.72 Ma, respectively. Sample 69FQ335 was fully reset during the Cenozoic Era, as cooling started at 65.99 Ma (Figure 5.9). Further west from the coastline, samples 69MZ390, 69MZ392 and 69FQ351 show a pulse of cooling occurring between 243.56 – 273.09 Ma. The two samples furthest inland from the coastline, 69MZ392 and 69FQ351, have the oldest and un-reset ages of all the samples, where 69MZ392 zircons cooled at 1111.35 Ma and 69FQ351 zircons cooled at ~555 Ma.

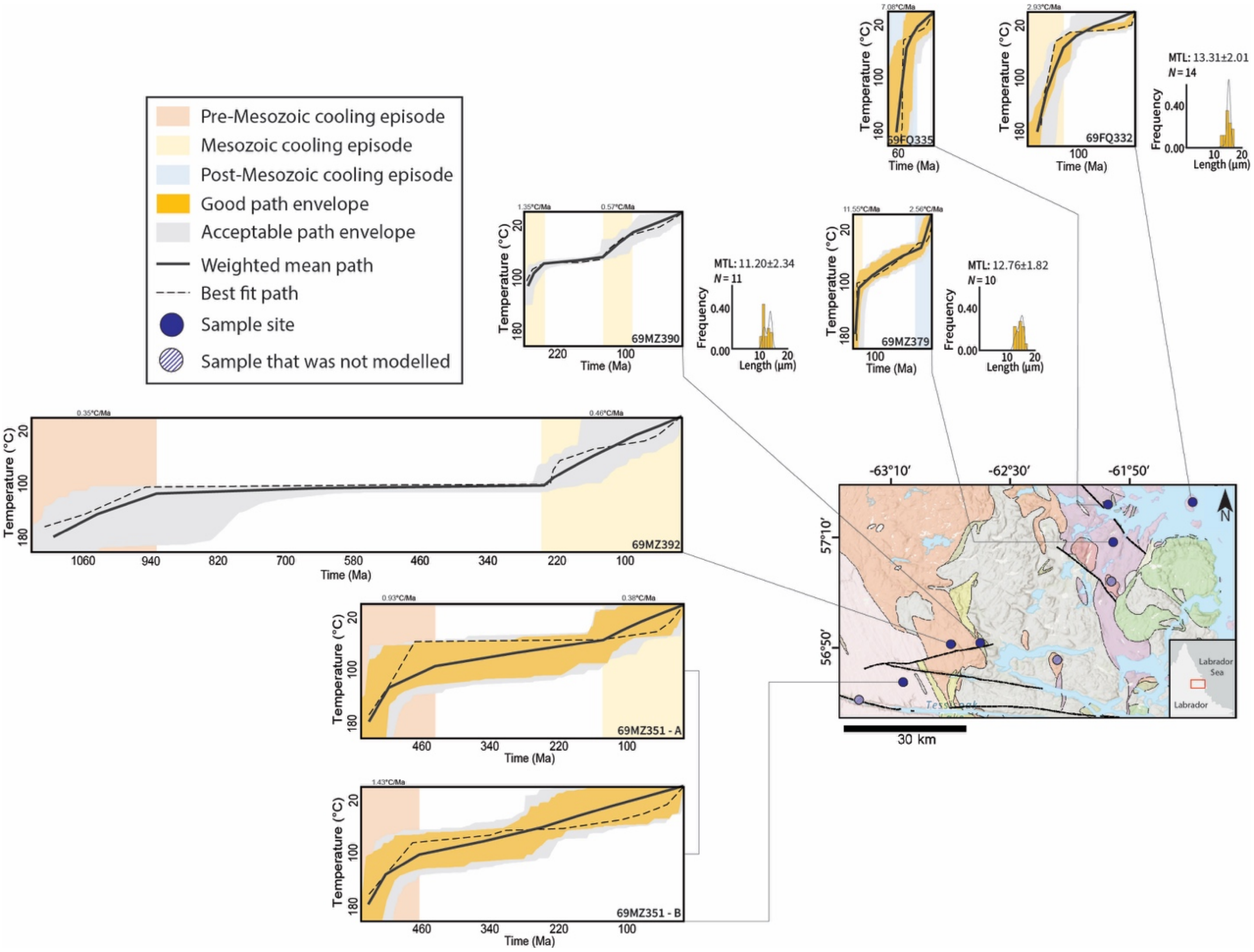

Figure 5.5 Nain transect geological map showing cooling histories for modelled samples, including 69FQ332, 69FQ335, 69MZ379, 69MZ390, 69MZ392 and 69MZ351.

5.6.1 NAIN TRANSECT: INDIVIDUAL SAMPLE HISTORIES

- **69FQ332**: The model shows that even zircon ages were reset where cooling began at 172.81 Ma, cooling at an average rate of 2.93 °C/Ma until 126.76 Ma, where the rate changed to 0.5 °C/Ma
- **69FQ335**: The model shows that even zircon ages are were reset where cooling began at ~65.99 Ma indicating a heating event at the start of the Cenozoic. The sample cooled quickly at first, at an average rate of 7.08 °C/Ma, then cooling slowed to 1.36 °C/Ma at 39.25 Ma.
- **69MZ379**: This model shows rapid cooling (11.55 °C/Ma) between 135.72 Ma and 129.69 Ma, then a pulse of slow cooling before a second, notable episode of cooling at 2.56 °C/Ma, beginning at 19.09 Ma.

- **69MZ390**: This model shows an initial phase of cooling from 273.09 – 245.53 Ma, then a period of stagnation until 140.63 Ma, when cooling rate increases to 0.57 °C/Ma.
- **69MZ392**: Initial cooling beginning at 1111.35 Ma at a rate of 0.35 °C/Ma, then a period of stagnation between 929,.48 - 243.56 Ma, when cooling rate increases to 0.46 °C/Ma.
- **69FQ351**: This sample had two possible solutions for cooling history. Both solutions include a cooling episode between ~555 – 520 Ma. Solution A, (69FQ351-A) shows slow cooling (0.13 °C/Ma) following the initial event, then a pulse of still relatively slow (0.39 °C/Ma) Mesozoic cooling beginning at 109.93 Ma, whereas Solution B (69FQ351-B) cooled consistently at an average rate of 0.27 °C/Ma following the event that caused zircon to cool.

Table 5.10 Nain transect cooling rates, where age values represent the time intervals between which cooling rates were calculated.

Sample	Initial		Cooling rate (°C/Ma)			Final
	Age (Ma)	Rate	Age (Ma)	Rate	Age (Ma)	Rate
69FQ332	172.81	2.93	-	-	126.76	0.50
	126.76				0.0	
69FQ335	65.99	7.08	-	-	48.20	1.36
	48.20				0.0	
69MZ379	135.72	11.55	129.69	0.56	19.09	2.56
	129.69		19.09		0.0	
69MZ390	273.09	1.35	245.53	0.09	140.63	0.57
	245.53		140.63		0.0	
69MZ392	111.35	0.35	929.48	0.02	243.56	0.46
	929.48		243.56		0.0	
69MZ351 - A	556.84	0.93	439.40	0.13	142.64	0.38
	439.40		142.64		0.0	
69MZ351 - B	577.81	1.43	-	-	466.95	0.26
	466.95				0.0	

5.7 HOPEDALE TRANSECT: MODELLING RESULTS AND COOLING HISTORIES

The general tendency of cooling within samples from this transect (with exceptions) includes a pre-Mesozoic cooling event, then a period of stagnancy throughout the Paleozoic and early Mesozoic Eras, followed by rapid cooling in the Mesozoic Era and then cooling slows throughout the end of the Mesozoic and into the Cenozoic Eras. No samples were fully reset by any events after the Paleozoic Era and many of the cooling paths begin with cooling events in the Precambrian Era including k0016, k0014-A, k0012 A and B, and k0009 (Figure 5.10). The period of stagnancy is identified in samples k0016, k0015, k0014-A, k0012-A and B, k0009 and k0008 by cooling rates ranging from 0.03 – 0.09 °C/Ma (except sample k0015, where the stagnant period occurred at a rate of 0.14 °C/Ma) (Table 5.11). The timing of onset of this period ranged from 888.26 – 290.78 Ma. The steep, Mesozoic cooling event is exhibited by every sample except k0014-B, where onset ranges from 205.73 – 111.71 Ma (Figure 5.10). There are no distinct east-west trends regarding distance from the coastline.

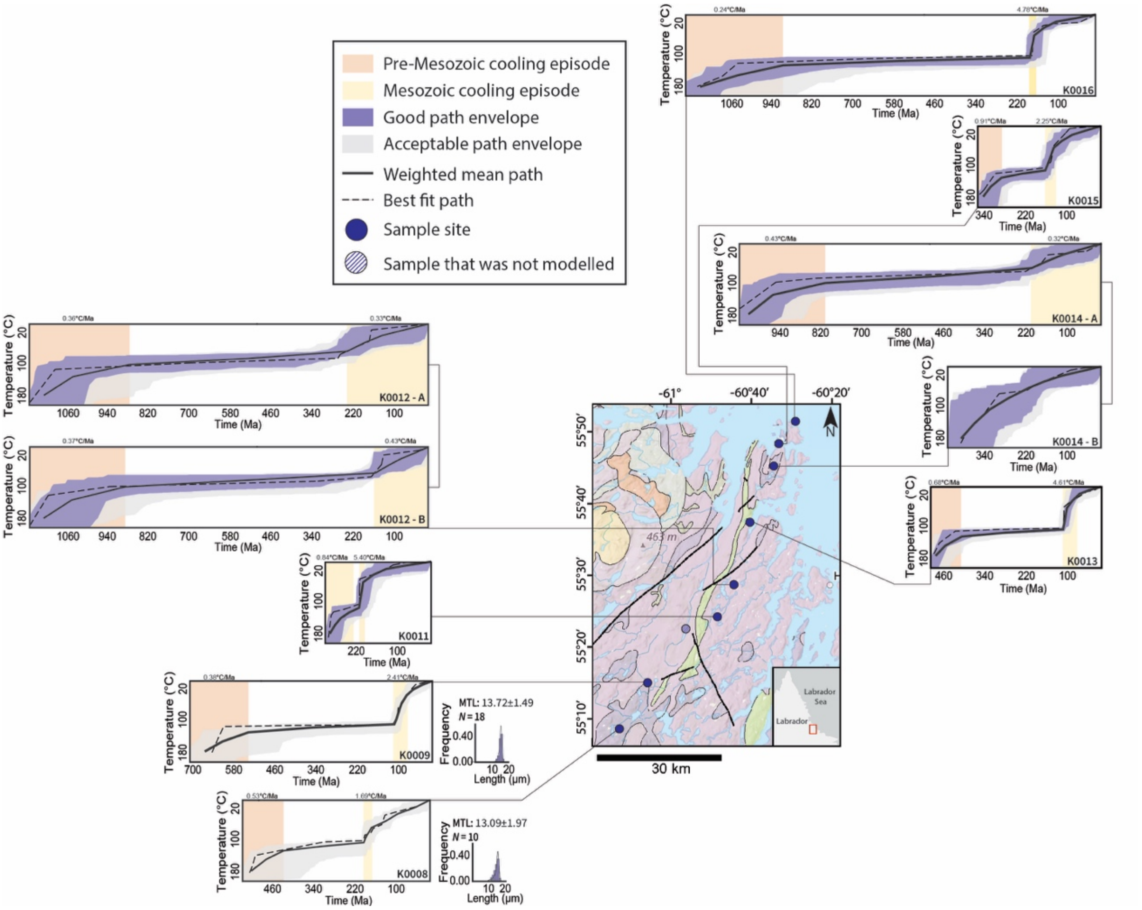

Figure 5.6 Hopedale transect geological map showing cooling histories for modelled samples, including k0016, k0015, k0014, k0013, k0012, k0011, k0009, and k0008.

5.7.1 HOPEDALE TRANSECT: INDIVIDUAL SAMPLE HISTORIES

- **K0016**: The Precambrian cooling event for this sample was recorded beginning at 1071.59 Ma, cooling at a rate of 0.24 °C/Ma until a period of stagnancy, which started at

846.68 Ma. A pulse of rapid cooling at an average rate of 4.78 °C/Ma occurred between 178.60 – 167.20 Ma, before cooling slowed to 0.45 °C/Ma by 142.17 Ma.

- **K0015**: The initial cooling episode for sample k0015 occurred from 344.5 – 290.79 Ma, at a rate of 0.91 °C/Ma. This sample also experienced a stagnant period of little cooling until 162.64 – 138.17 Ma when cooling rate increased to 2.25 °C/Ma, before slowing to 0.49 °C/Ma by 114.43 Ma.
- **K0014**: This sample had two possible solutions for cooling history. K0014-A displayed a cooling history comparable to all other samples in this transect. There was an initial cooling period from 1031.95 Ma to 808.26 Ma, then a period of stagnancy before a second cooling period beginning at 205.73 Ma and cooling at an average rate of 0.43 °C/Ma. K0014-B shows a cooling history where all samples were reset and started cooling at 411.70 Ma, then cooled approximately consistently at a rate of 0.49 °C/Ma until it was at the surface.
- **K0013**: The initial cooling episode for sample k0013 occurred from 485.75 – 408.79 Ma, at a rate of 0.68 °C/Ma. This sample experienced a stagnant period of little cooling until 111.71 – 100.05 Ma, when cooling rate increased to 4.61 °C/Ma, before slowing to 0.76 °C/Ma by 84.42 Ma.
- **K0012**: This sample had two possible solutions for cooling history, which are very similar until the Mesozoic cooling episode. Both cooling paths show cooling from ~1125 – 880 Ma at an average rate of ~0.4 °C/Ma, then a stagnant period of little cooling. K0012-A begins cooling again at 239.37 Ma, then cools consistently until surface temperatures, while k0012-B begins cooling again at 156.36 Ma, then cools consistently until surface temperatures.
- **K0011**: This sample did not experience any stagnant period, but this sample was completely reset compared to other samples in this transect. The initial cooling episode for sample k0009 occurred from 297.23 – 211.23 Ma, at a rate of 0.84 °C/Ma. Then, cooling increased rapidly to 5.40 °C/Ma until 199.64 Ma, when cooling rate slowed to 0.39 °C/Ma, cooling consistently until surface temperatures.

- **K0009**: The initial cooling episode for sample k0009 occurred from 667.21 – 539.25 Ma, at a rate of 0.38 °C/Ma. This sample experienced a stagnant period of little cooling until 112.23 – 90.60 Ma, when cooling rate increased to 2.41 °C/Ma, before slowing to 0.85 °C/Ma by 56.00 Ma.
- **K0008**: The initial cooling episode for sample k0013 occurred from 524.17 – 429.05 Ma, at a rate of 0.53 °C/Ma. This sample experienced a stagnant period of little cooling until 194.62 – 172.19 Ma, when cooling rate increased to 1.69 °C/Ma, before slowing to 0.40 °C/Ma by 130.27 Ma.

Table 5.11 Hopedale transect cooling rates, where age values represent the time intervals between which cooling rates were calculated.

Sample	Initial			Cooling rate (°C/Ma)				Final
	Age (Ma)	Rate	Age (Ma)	Rate	Age (Ma)	Rate	Age (Ma)	Rate
k0016	1071.59	0.24	846.68	0.03	178.60	4.78	167.20	0.45
	846.68		178.60		167.20		0.0	
k0015	344.52	0.91	290.78	0.14	162.64	2.25	138.17	0.49
	290.78		162.64		138.17		0.0	
k0014 - A	1031.95	0.43	808.26	0.06	-	-	205.73	0.32
	808.26		205.73				0.0	
k0014 - B	-	-	-	-	-	-	411.70	0.49
							0.0	
k0013	485.75	0.68	408.79	0.06	111.70	4.61	100.05	0.76
	408.79		111.70		100.05		0.0	
k0012 - A	1125.89	0.36	875.67	0.05	-	-	239.37	0.33
	875.67		239.37				0.0	
k0012 - B	1128.44	0.37	888.26	0.04	-	-	156.36	0.43
	888.26		156.36				0.0	
k0011	297.23	0.84	-	-	211.22	5.40	199.64	0.39
	211.22				199.64		0.0	
k0009	667.21	0.38	539.25	0.05	112.23	2.41	90.60	0.85
	539.25		112.23		90.60		0.0	
k0008	524.17	0.53	429.05	0.09	194.62	1.69	172.19	0.40
	429.05		194.62		172.19		0.0	

5.8 MAKKOVIK TRANSECT: MODELLING RESULTS AND COOLING HISTORIES

All of the cooling paths for samples in this transect exhibit a pulse of rapid cooling during the Mesozoic Era, where the timing of onset ranges from 165.27 – 125.79 Ma (Figure 5.11). The two samples furthest inland, including 71TA923 and 71TA929, show very similar cooling paths, where cooling begins between 200 – 300 Ma, then rate increases during that Mesozoic cooling episode, before cooling rate slows and remains consistent until surface temperatures.

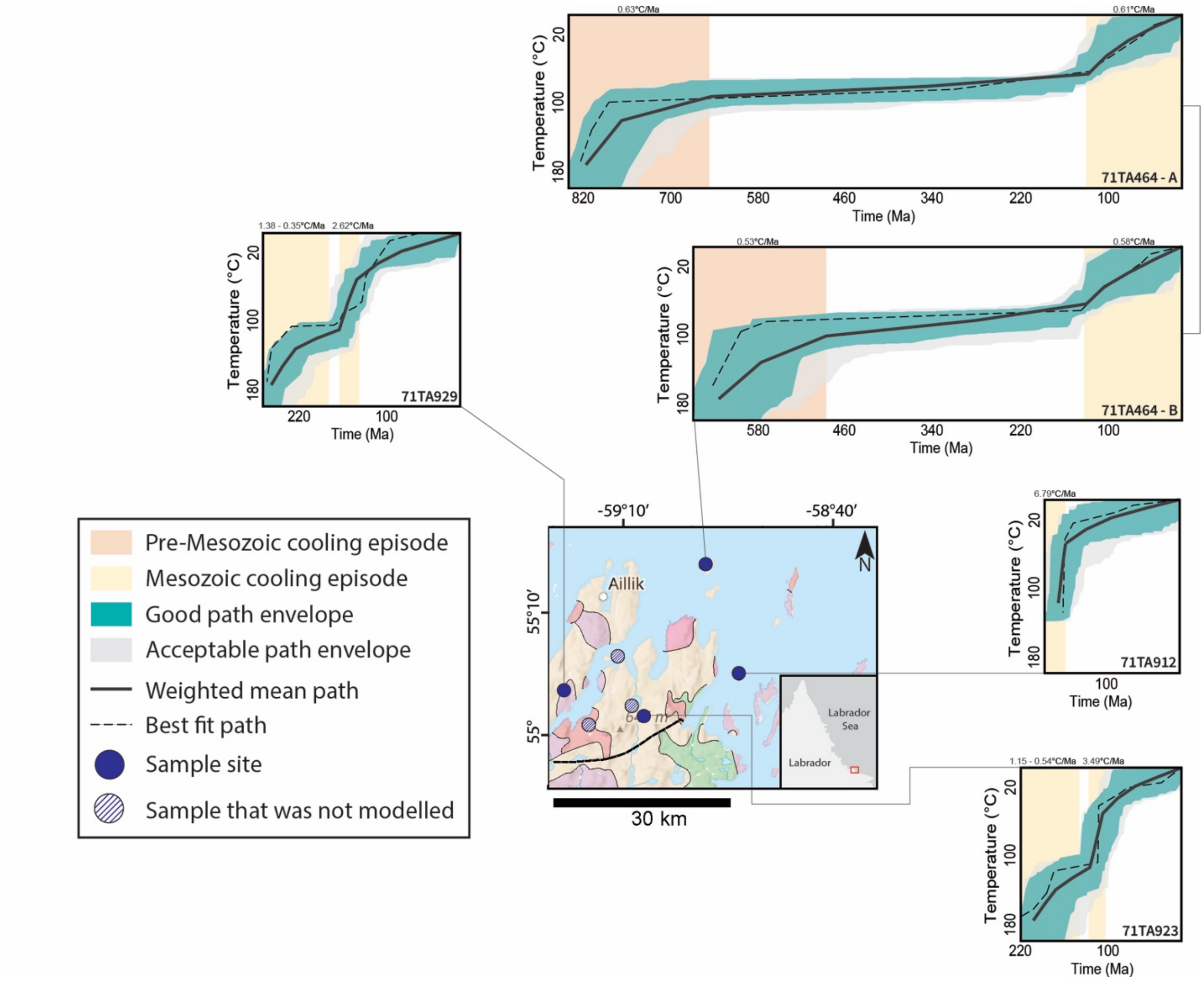

Figure 5.7 Makkovik transect geological map showing cooling histories for modelled samples, including 71TA464, 71TA912, 71TA923 and 71TA929.

5.8.1 MAKKOVIK TRANSECT: INDIVIDUAL SAMPLE HISTORIES

- **71TA464**: This sample has the oldest cooling history where zircon ages were not reset after the Precambrian Era. There are two possible solutions for cooling history, which differ only in their pre-Mesozoic cooling paths. 71TA464-A shows an initial cooling episode from 817.38 – 645.28 Ma, at a rate of 0.63 °C/Ma, followed by a stagnant period of little cooling until 129.29 Ma. 71TA464-B shows an initial cooling episode from

635.56 – 488.38 Ma, at a rate of 0.53 °C/Ma, followed by a stagnant period of little cooling until 131.10 Ma. At this time (~130 Ma), both samples have an increase in cooling rate to ~0.6 Ma.

- **71TA912**: Cooling history begins with rapid cooling at a rate of 6.69 °C/Ma from 166.76 – 156.70 Ma, before cooling slows to 0.40 °C/Ma by 128.60 Ma.
- **71TA923**: An initial cooling episode for sample 71TA923 occurred from 203.56 – 125.79 Ma, at a rate of 1.15 – 0.54 °C/Ma, when cooling increased rapidly to 3.49 °C/Ma until 107.89 Ma, when cooling rate slowed to 0.59 °C/Ma, cooling consistently until surface temperatures. This cooling pattern is comparable to k0011.
- **71TA929**: The cooling path for 71TA929 resembles that of 71TA923. An initial cooling episode occurred from 258.69 – 165.27 Ma, at a rate of 1.38 – 0.35 °C/Ma, when cooling increased rapidly to 2.62 °C/Ma until 142.81 Ma, when cooling rate slowed to 0.46 °C/Ma, cooling consistently until surface temperatures.

Table 5.12 Makkovik transect cooling rates, where age values represent the time intervals between which cooling rates were calculated.

Sample	Initial		Cooling rate (°C/Ma)				Final	
	Age (Ma)	Rate	Age (Ma)	Rate	Age (Ma)	Rate	Age (Ma)	Rate
71TA464 - A	817.38	0.63	645.28	0.05	-	-	129.29	0.61
	645.28		129.29				0.0	
71TA464 - B	635.56	0.53	488.38	0.10	-	-	131.10	0.58
	488.38		131.10				0.0	
71TA923	203.56	1.15	172.58	0.54	125.79	3.49	107.89	0.59
	172.58		125.79		107.89		0.0	
71TA912	166.76	6.79	-	-	-	-	156.70	0.40
	156.70						0.0	
71TA929	258.69	1.38	227.17	0.35	165.27	2.62	142.81	0.46
	227.17		165.27		142.81		0.0	

5.9 MODELLING RESULTS SUMMARY

In general, the models record a few notable cooling episodes and follow similar cooling paths, which include a Paleozoic or Precambrian cooling event (Figure 5.4), followed by a period of stagnancy where there was very little cooling at rates of less than 0.1 °C/Ma, then an abrupt cooling event initiating the Mesozoic Era (Figure 5.4), which slows in the late Mesozoic and into the Cenozoic. Many of the samples were only partially reset before Mesozoic events, as ZHe cooling reflects Paleozoic and even Precambrian ages. There is a Mid-Late Proterozoic event occurring between 800 – 1200 Ma recorded in Hopedale samples (k0016, k0014, k0012) and inland Nain (60MZ392), and sporadic cooling events between 400 – 800 Ma in each of the transects.

Mesozoic cooling events are either short and rapid before cooling slows and remains consistent throughout the Cenozoic, or long and consistent where cooling begins at 100 – 250 Ma (Figure 5.4) and steadily persists throughout the Cenozoic. The onset of the short, rapid cooling events occurred between 211.23 – 111.71 Ma, lasting an average of ~25 Ma. All transects display both types of Mesozoic cooling (Figure 5.4). In general, the onset of this cooling pulse gets younger to the north.

Four samples close to the coastline in the more northern transects of Saglek and Nain (67SC216, 67SC217, 69FQ335, 69MZ379) have a small cooling event that occurs in the Cenozoic, initiating between ~19 – 66 Ma (Figure 5.4) and cooling at a rate of 0.4 – 1.27 °C/Ma. Within 20 km from the coastline, the onset of cooling ranges from ~150 – 200 Ma (Figure 5.4). There are no other apparent east-west or north-south trends throughout all the transects.

Some of the samples had multiple possible groupings of ages. For example, sample 69MZ351 was modelled twice while keeping ZHe ages the same but grouping AHe ages 280.8 and 240.2 Ma in one model, then AHe ages 130.8 and 166.7 Ma in another models. Samples like this, including 67SC217, 67SC218, 69MZ351, k0014, k0012 and 71TA464, had multiple possible modelling solutions, all of which are displayed in Figures 5.4 – 5.11 and Tables 5.1 – 5.12.

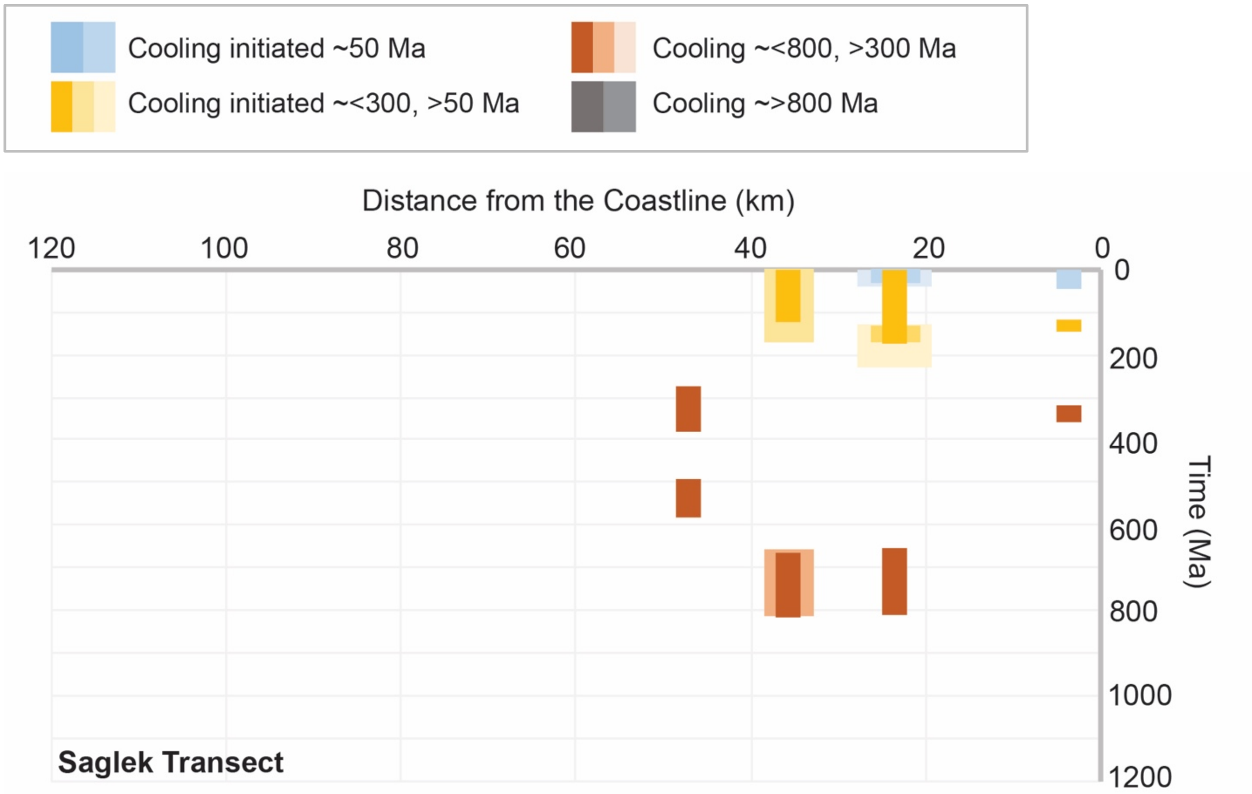

Figure 5.8 Cooling episodes extracted from the cooling paths of samples from the Saglek Transect, showing the timespan of each cooling period (y-axis) compared to the sample's distance from the coastline (x-axis). Different shades of the same colour indicate different solutions for a sample that was modelled multiple times using different age groupings. The colour in front (darkest shade) is option A, then behind is option B, and furthest in the back (lightest shade) is option C.

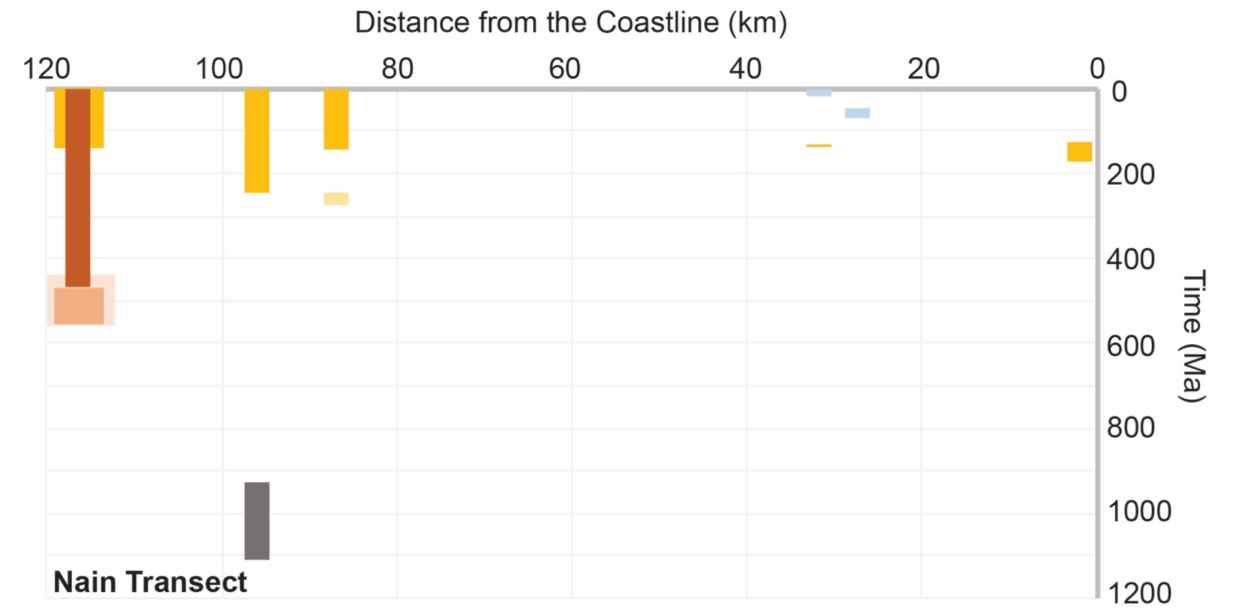

Figure 5.9 Cooling episodes extracted from the cooling paths of samples from the Nain Transect, showing the timespan of each cooling period (y-axis) compared to the sample's distance from the coastline (x-axis). Different shades of the same colour indicate different solutions for a sample that was modelled multiple times using different

age groupings. The colour in front (darkest shade) is option A, then behind is option B, and furthest in the back (lightest shade) is option C. See figure 5.8 for legend.

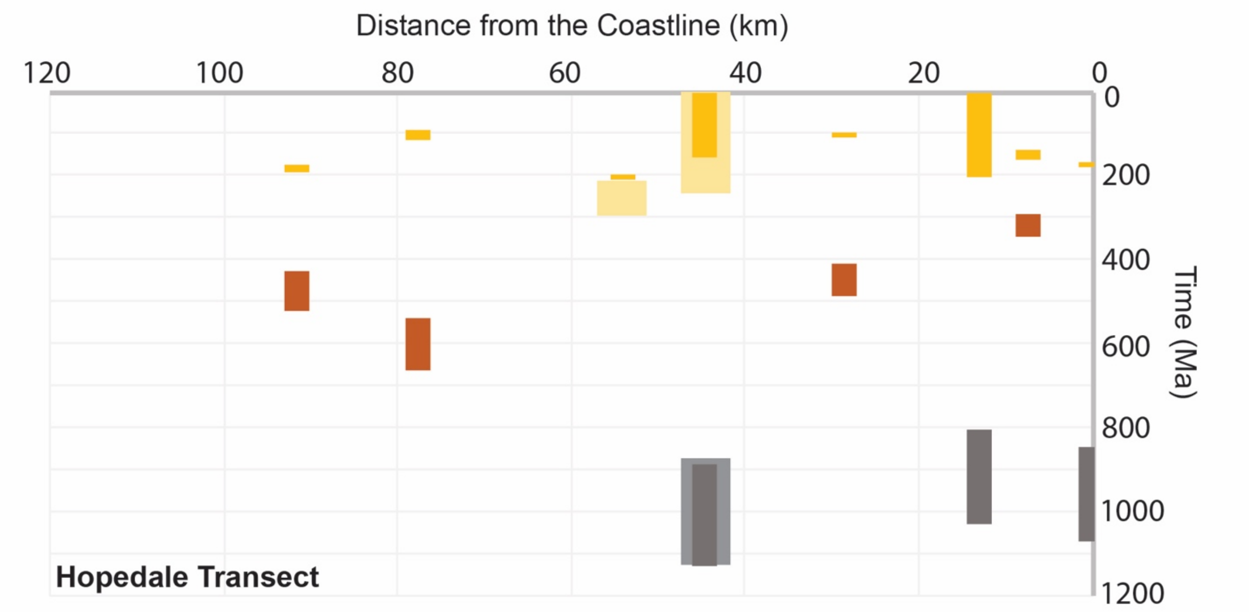

Figure 5.10 Cooling episodes extracted from the cooling paths of samples from the Hopedale Transect, showing the timespan of each cooling period (y-axis) compared to the sample's distance from the coastline (x-axis). Different shades of the same colour indicate different solutions for a sample that was modelled multiple times using different age groupings. The colour in front (darkest shade) is option A, then behind is option B, and furthest in the back (lightest shade) is option C. See figure 5.8 for legend.

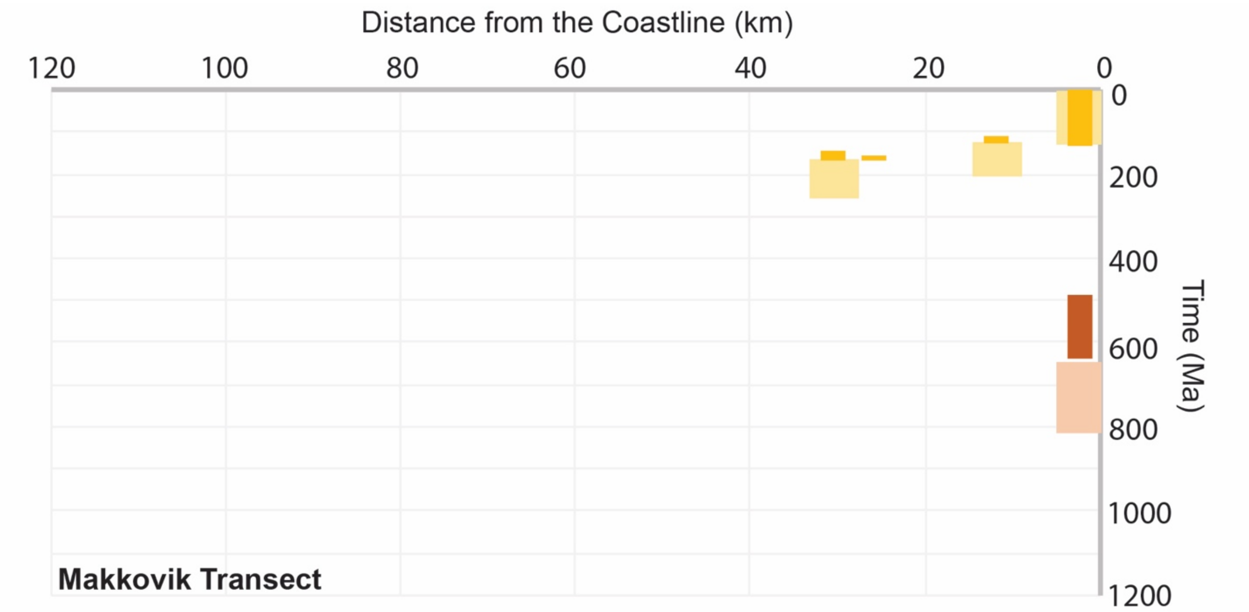

Figure 5.11 Cooling episodes extracted from the cooling paths of samples from the Makkovik Transect, showing the timespan of each cooling period (y-axis) compared to the sample's distance from the coastline (x-axis). Different shades of the same colour indicate different solutions for a sample that was modelled multiple times using different age groupings. The colour in front (darkest shade) is option A, then behind is option B, and furthest in the back (lightest shade) is option C. See figure 5.8 for legend.

CHAPTER 6: DISCUSSION AND CONCLUSIONS

The objective of this study was to present the thermal history of the upper continental crust during Mesozoic rifting and post-rift processes along the Labrador margin using low-temperature thermochronology including AHe, AFT and ZHe dating methods. The intention is to answer questions regarding timing of onset and duration of rifting, spatial and temporal distribution of nucleation and propagation of seafloor spreading, zonation of the magma-poor and magma-rich margin, episodes of erosion, transport of sediments to offshore basins, and landscape evolution.

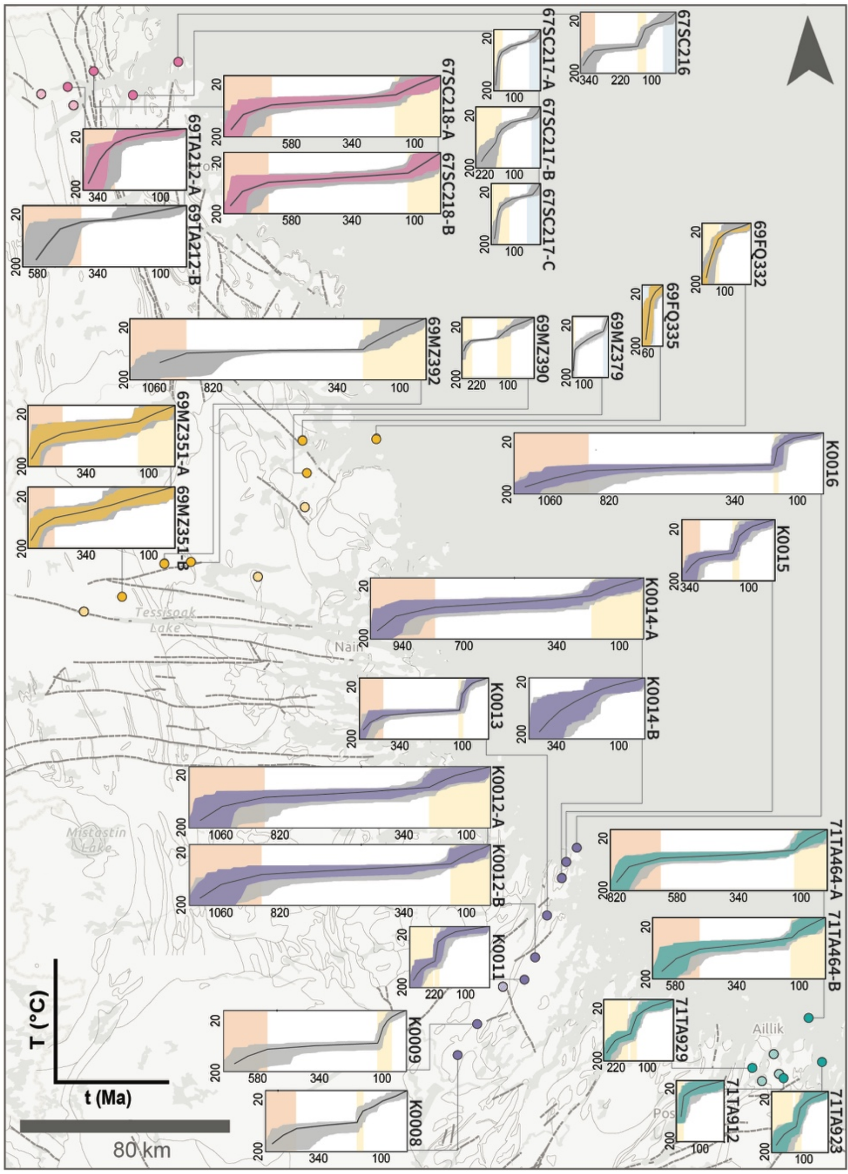

Figure 6.1 Summary of transects along the Labrador margin including the Saglek transect (pink), Nain transect (yellow), Hopedale transect (purple) and Makkovik transect (turquoise) and their resulting temperature-time paths from *HeFTy* modelling. Different cooling episodes are indicated by shading (see legend).

6.1 INTERPRETATIONS OF COOLING PATHS

The most common cooling path observed in samples from all transects included a period of rapid cooling in the Mesozoic era, initiating between 211.23 – 111.71 Ma lasting an average of ~25 Ma then slowing and remaining at a consistent rate until present (e.g. Figure 6.1 sample K0016). Based on the geometry of these cooling paths, samples from the Labrador margin are likely representative of the footwall of normal faulting (Stockli 2005) resulting from extension within the proximal domain of the rift (Malusá and Fitzgerald 2019). The inflections in the cooling paths at this time represent the initiation of faulting (Stockli 2005) which would have occurred at the base of the rapid increase in the T-t path (Campani et al. 2010). Thermal relaxation of elevated isotherms follows the exhumation pulse (Malusá and Fitzgerald 2019), which may account for the slowed and consistent cooling that follows rapid cooling in the T-t paths.

Periods of rapid cooling recorded by samples from the Saglek transect can be compared to a model from Centeno (2005), produced using AHe data from a vertical transect from Mt. D'Iberville near the Nachvak Fiord north of Saglek. Centeno's model produced comparable cooling paths where all T-t paths converge at a period of rapid cooling between ~140 – 150 Ma (Figure 2.8 Background section 2.2.3). This timing is younger than the periods of rapid cooling recorded by samples from the Saglek transect in this study and occurs over a shorter period of time. Discrepancies between the two studies may result because T-t in the Centeno (2005) are from one thermochronometer, whereas T-t paths in this study include AFT, which has a higher closure temperature compared to AHe.

Another common cooling path observed in samples from all transects includes the onset of cooling beginning between 100 – 150 Ma, then remaining at a consistent rate throughout the rest of the Mesozoic and Cenozoic eras (e.g. Figure 6.1 sample 69MZ392). This type of cooling is comparable to continuous monotonic cooling paths reported by Japsen et al. (2006) in Greenland, which are representative of long-term exhumation. This type of cooling path can result from a scenario where rapid cooling is short-lived because fast displacement stops shortly after it starts (Campani et al. 2010). This type of cooling may also be accounted for by progressive cooling by a period of erosion, as the onset of this cooling pattern occurs within a time during the rifting process of subsidence and sedimentation as described by Larsen et al. (2009).

A proximal margin thermal regime is more likely controlled by exhumation due to erosion than processes involving a rising asthenosphere in the distal margin (Malusá and Fitzgerald 2019). An accelerated cooling rate is a representative response to the onset of major normal faulting and extensional exhumation (Campani et al. 2010; Stockli 2005). Rapid cooling is likely associated with advection of footwall (U–Th)/He and AFT closure isotherms (Ehlers et al. 2005) during rapid exhumation (>0.3 km/Myr, Gleadow and Brown 2000), leading to a progressive elevation of the isothermal surfaces, which results in a temporary increase in the near-surface geothermal gradient (Figure 6.2) (Malusá and Fitzgerald 2019).

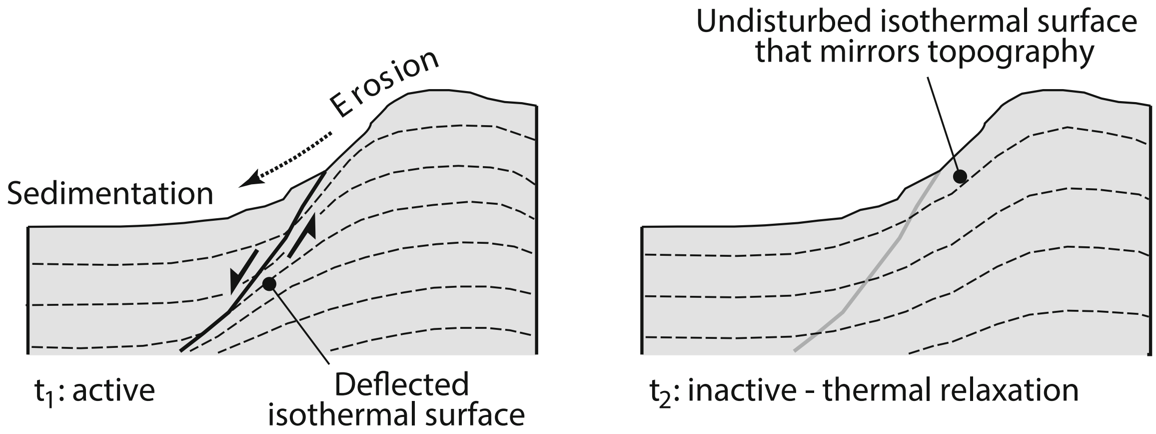

Figure 6.2 Advection of footwall isotherms during rapid exhumation, leading to temporary elevation of the isothermal surfaces and increase in the near-surface geothermal gradient (t_1). Thermal relaxation of these isotherms follows the exhumation pulse (t_2) (Malusá and Fitzgerald 2019).

Temperature-time paths show a long period of stagnancy following initial cooling of zircon grains (e.g. Figure 6.1, samples 67SC218, 69MZ392, K0016, 71TA464). The relationship between ZHe age and uranium concentration (eU) can be used to estimate exhumation histories (Guenthner 2019). The negative relationship between eU and ZHe age observed in samples from Labrador indicates that samples spent a long time in the PRZ. For example, the scenario outlined by Guenthner et al. (2013) of early cooling followed by prolonged time in the

PRZ at low temperatures (e.g. 180 °C) and then subsequent late cooling, crystal defects caused by radiation damage outpace annealing (Guenthner et al. 2013). The resulting eU-age relationship has a negative correlation, as observed in data from transects, even at relatively low eU concentrations (Guenthner et al. 2013).

Many of the ZHe ages recorded by samples in all transects have not been reset by Mesozoic rifting, maintaining ages between ~400 – 1100 Ma (Figure 6.1). In the northern transects (Saglek and Nain), unreset zircons are more common in the samples located further from the coastline, but the oldest unreset ages (> 1000 Ma) occur either inland (e.g. ~95 km from the coastline in the Nain transect) or further south in the Hopedale and Makkovik transects (Figure 6.1). Asthenospheric upwelling in the distal margin following the thinning phase of rifting causes isotherms to form a bell shape, where they converge in the distal margin and fan out into the proximal margin (Figure 6.3) (Malusá and Fitzgerald 2019; Malusá et al. 2016). Depending on the distance from the rift axis and crustal level of the sample during asthenospheric upwelling, different thermochronometric systems may be affected differently. It is possible that zircon samples were not reset, as they were likely already closer to the surface in the proximal domain of the rift where the impact of heating is minor, affecting temperatures of 110 – 70 °C, which would reset AHe and in some cases AFT (Malusá and Fitzgerald 2019).

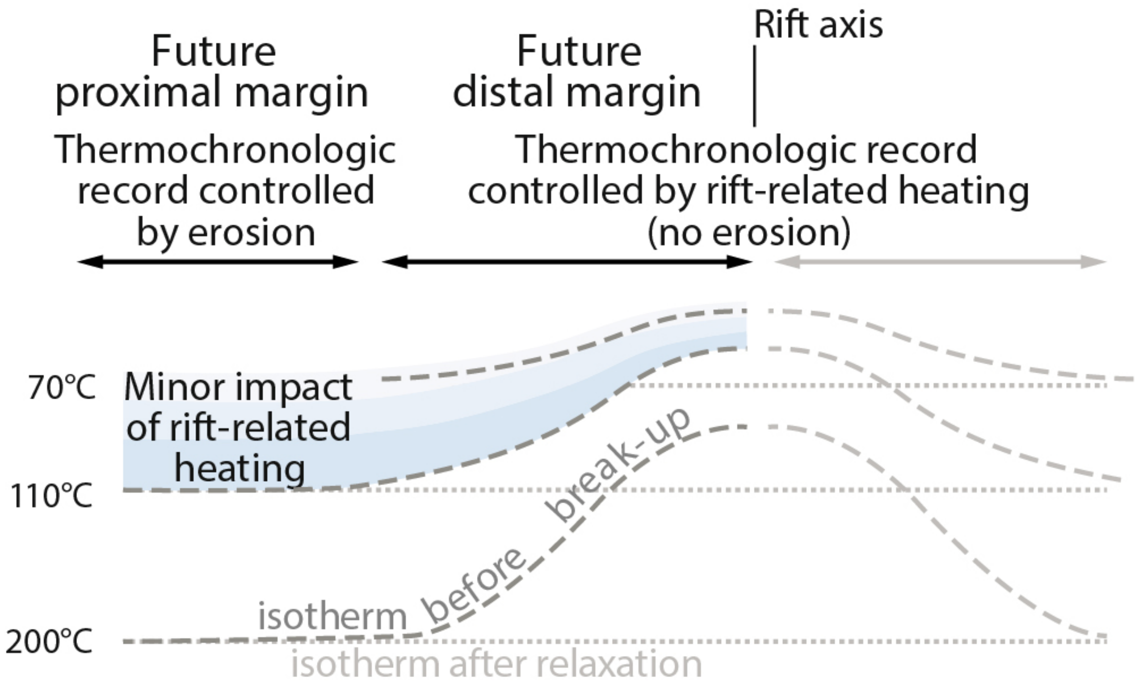

Figure 6.3 Asthenospheric upwelling in the distal margin causing isotherms to form a 'bell-shape', where isotherms fan out into the proximal margin affecting samples that are close to the distal margin (after Malusá and Fitzgerald 2019; Malusá et al. 2016).

After continental breakup, isotherms that formed the bell shape undergo thermal relaxation and flatten out (Malusá and Fitzgerald 2019). This can cause a type of cooling to occur without rock uplift or displacement of overburden. Rather, cooling results from the change in position of an isotherm. It is unlikely that the Mesozoic ages observed from the Labrador coast, at least in the southern transects, are a result of thermal relaxation because their ages (e.g. 100 – 250 Ma) are much older than that of breakup (e.g. 66 – 63 Ma according to C27, the oldest undisputed anomaly; Chalmers and Larsen 1995). It is possible though, that young ages recorded in the northern transects (e.g. ~30 – 66 Ma) do represent relaxation of isotherms, as breakup may have occurred closer to the modern Labrador coastline in the north (e.g. north of Nain) than in the south, where breakup occurred closer to the modern Greenland margin. Seismic reflection data from deep crustal profiles shows an asymmetric rift where a reversal in the asymmetry occurs part way through the rift (Keen et al. 2012; 2018). For example, along the southern margin, thinned crust off the coast of Labrador is much wider than in Greenland, but further north, the opposite is true. Therefore, the 'bell-shape' from asthenospheric upwelling may have been closer to the Labrador margin in the north, having more of an impact on samples close to the modern coastline than in the south, whereby AFT ages in the young profiles may represent extension-related faulting, while AHe ages represent thermal relaxation (Malusá and Fitzgerald 2019).

Other possible causes for Cenozoic cooling observed in the Saglek and Nain transects include differential erosion of the rift flank, tectonic uplift associated with the Proto-Icelandic plume, or decreasing surface temperatures in the Late Cenozoic influencing modelling (Jess et al. 2019). Rift flank uplift and erosion is more likely in Saglek and Nain transects than southern transects, as topography is more comparable to that of Greenland, with higher elevations and fjords. Early Paleocene ages (66 Ma, Jess et al. 2019) from the Cumberland Peninsula, Baffin Island (just north of Labrador), which are comparable to ages of ~45 – 66 from the Saglek and Nain transects, indicate differential erosion of the rift flank and denudation across the landscape, where thermal histories from across the margin outline continuous cooling throughout the Cenozoic Era. Cooling at 66 Ma in the Nain transect may also correspond to tectonic uplift prior to 61 Ma (Japsen et al. 2006) associated with flood basalts and the arrival of the Proto-Icelandic plume in the Davis Strait, which occurred ~61.6 – 59.2 Ma (Dickie et al. 2011). Otherwise, young ages between 30 – 45 Ma from the Saglek transect could be an artefact of modelling, as they are not specifically constrained by AHe ages. Climatic cooling at high latitudes is considered to have occurred at the Eocene–Oligocene boundary (e.g. 33 Ma) with the onset of glaciation occurring across northeast Canada in the Miocene and surface temperatures decreasing 10–20 °C in the late Cenozoic (Jess et al. 2019 and references therein). Since the present-day temperature was set to 0°C for thermal modelling, a significant decrease in surface temperature after a sample cooled above the PAZ and HePRZ would present itself in thermal models (Jess et al. 2019). Although this may be true for samples from the Saglek transect, young samples from the Nain transect are constrained by actual AHe ages at the time of Cenozoic cooling.

Unreset zircon ages of ~400 – 600 Ma might have recorded post-intrusion cooling from widespread and recurrent magmatism. Tappe et al. (2009) reported ages of 610 – 550 Ma from Cabonatite provinces in Sarfartoq, Greenland, a time when the craton would have still been connected to Labrador. Related carbonatite dykes dated using ^{40}Ar/^{39}Ar in Aillik Bay, Labrador produced similar ages (~141 – 142 Ma, ^{40}Ar/^{39}Ar phlogopite, Tappe et al. 2009). It is hypothesized that widespread, recurrent magmatism at this time may have modified the integrity of the cratonic mantle, allowing stretching and thinning to remove the cratonic lithosphere (Tappet et al. 2007), creating a weakness from which Mesozoic rifting could initiate. Old ages will not be discussed further, as the focus of this study is Mesozoic rifting.

The timing of onset of rifting generally youngs to the north, as the initiation of cooling episodes in the two northern transects occurs between 175 – 65 Ma (with exceptions), while initiation of cooling episodes in the two southern transects occurs between 297 – 130 Ma (with exceptions). A younging to the north trend is also observed in dyke swarms in west Greenland when ages of emplacement ranged from ~28 – 186 Ma (^{40}Ar/^{39}Ar whole rock and plagioclase, Rb-Sr phlogopite and whole rock, and U-Pb), with Paleogene ages occurring north of Uummannaq Fjord and Triassic-Cretaceous ages generally occurring south of Uummannaq Fjord (Figure 2.6 Background section 2.2.2) (Larsen et al. 2009). AHe data from the Torngat Orogen and Ungava Peninsula regions on the northern tip of Labrador (Centeno 2005) are younger than data from Saglek to Makkovik, showing ages at the coastline near the Nachvak Fiord ranging from 100 – 150 Ma and further north near the Kangalaksiorvik Fiord ~80 – 130 Ma. Even further north of Labrador AHe and AFT data from the Cumberland Peninsula record a syn-rift phase between 120 – 0 Ma (Jess et al. 2019; McGregor et al. 2013). South of the study area, igneous rocks from the Atlantic margin along Nova Scotia and Newfoundland related to rifting and opening between North America and Europe include alkaline and tholeiitic volcanic and intrusive igneous rocks ranging in age from 247–140 Ma (Larsen et al. 2009 and references therein), which are even slightly older than ages from the Labrador margin marking the onset of extension. Northward younging of data appearing in cooling ages recorded between Makkovik and Saglek may be attributed to diachronous rift propagation and rift-related cooling from south to north along the axis of the Labrador Sea.

6.2 COOLING PATHS FROM THE LABRADOR MARGIN WITHIN THE CONTEXT OF THE LABRADOR SEA RIFT

Many of the cooling episodes observed between Saglek and Makkovik are likely associated with the start of extension, according to aillikite, alnöite and carbonatite dykes dated 223 – 150 Ma (Rb-Sr phlogopite and whole rock and U-Pb dating) associated with generation of small volumes of magma at great depths (Larsen et al. 2009; Tappe et al. 2009) and carbonatite sheets ranging from ~158 – 155 Ma (U-Pb dating of baddeleyite and pyrochlore) considered a distal effect of rift initiation (Tappe et al. 2009). Cooling events initiated between 230 – 220 Ma and 160 – 150 Ma were a result of rock uplift and exhumation, according to AFT analyses from West Greenland between Nuussuaq and Itilleq (Japsen et al. 2006). In all transects from the Labrador margin, in almost all samples, the initial pulse of Mesozoic cooling began within this timeframe and even slightly older (up to ~300 Ma). AFT and AHe data, especially in the Hopedale and Makkovik transects and inland in Saglek and Nain transects exhibit mean cooling ages that correspond with this time. Cooling pulses initiating before the onset of initial extension with late Paleozoic–early Mesozoic dates (~250 Ma) may instead be a result of exhumation of central Laurentia (Jess et al. 2019).

A period where extension rate increased began at ~150 Ma, which is interpreted from Rb-Sr phlogopite and U-Pb ages and compositions of monchiquite dykes from Greenland (Larsen et al. 2009). Although this was not specifically observed in T-t paths from Saglek to Makkovik transects, mean AHe ages in the Hopedale and Makkovik transects and inland in the Nain transect contain cooling ages of ~150 Ma. Increased extension may correlate to rapid cooling observed in the Mt. D'Iberville vertical transect between 140 – 150 Ma (Centeno 2005). Following increased extension, regional rifting between Labrador and Greenland occurred between 140 – 133 Ma, which is interpreted from $^{40}Ar/^{39}Ar$ whole rock ages and compositions of basaltic alkaline to enriched tholeiitic dykes representative of large degrees of melting at shallower depths from both Greenland (Larsen et al. 2009) and Labrador (Tappe et al. 2007). This event was recorded by the Alexis Formation in the Hopedale basin, containing basaltic volcanic rocks emplaced between 140 – 120 Ma (Dickie et al. 2011 and references therein) and captured in T-t paths from all transects from the Labrador margin where a cooling event initiated between ~130 – 145 Ma.

Sedimentation in offshore basins can indicate the transfer of mass from the footwall of a fault to the hanging wall (Stockli 2005). The low-angle detachment fault model of rifting expressed in Labrador involves a period of exhumation that is associated with increased erosion in the footwall (Campani et al. 2010), which is reflected in sedimentation in the Hopedale and Saglek basins. Deposition of the Bjarni and Markland Formations in the Hopedale Basin (and the Kitsissut sequence offshore Greenland) is associated with Mesozoic rifting between 130 – 120 Ma, then again with renewed extension between 100 – 65 Ma (Larsen et al. 2009). Rapid cooling initiating at ~125 Ma in the Makkovik and Saglek transects, along with mean AHe and AFT cooling ages in samples located near the coastline in all transects is likely associated with this erosive event. Younger rapid cooling events that occur between ~110 – 90 Ma observed within T-t paths from the Hopedale transect are likely associated with renewed extension and sedimentation, according to evidences from offshore large-scale growth faulting during the Cenomanian (100 – 93.3 Ma) and structural inversions of Bjarni sediments during what is described as a fairly localized phase of rock uplift (Dickie et al. 2011). Cooling observed in the Saglek transect between ~30 – 45 Ma, although this may be a relic of modelling, could indicate the end of seafloor spreading at ~33 Ma (Srivastava 1978). A period of rock uplift beginning between 36 and 30 Ma, subsequent to the cessation of sea-floor spreading in the Labrador Sea (Chalmers and Pulvertaft 2001) is indicated by an unconformity at the top of the Kenamu Formation, which is overlain by the Mokami Formation (~30 – 10 Ma, McWhae et al. 1980). The onset of cooling at 19 Ma in the Nain transect correlates to the upper Mokami member, which is composed of coarse-grained quartz and igneous clasts as evidence for a period of post-uplift deposition along coastal Labrador in the Late Oligocene to early Miocene (Balkwill et al. 1990).

6.3 CONCLUSIONS

New apatite and zircon (U-Th)/He and apatite fission track data from 32 samples collected along four transects across northern Labrador from Makkovik to Saglek provide cooling ages ranging from 18.0 – 937.5Ma (AHe), 99.9 – 258.9 Ma (AFT), and 5.4 – 1612.75 Ma (ZHe). AHe and AFT data are comparable to studies from Greenland (e.g. Japsen et al. 2009, 2006; Larsen et al. 2009; Tappe et al. 2009, 2007) and the Torngat mountains (Centeno 2005), which showed ages younging to the north, indicating that rifting evolved spatially and temporally from south to north. Most ZHe ages are older than 400 Ma and are associated with events predating Mesozoic rifting.

Suitable T-t paths modeled using *HeFTy* software indicated that the Labrador margin experienced episodes of rapid rock uplift, mostly initiating between 211.23 – 111.71 Ma, and also slow, continuous cooling initiating between 100 – 150 Ma. There were instances of cooling initiating between 19 – 66 Ma, but only in northern transects at latitudes of Saglek and Nain. Cooling path geometries suggest that cooling occurred due to extension, rock uplift and exhumation in the footwall of normal-faults in the proximal domain of the rift. Mesozoic cooling initiating between 250 – 150 Ma is likely associated with early extension, while younger cooling initiating between 130 – 100 Ma is associated with erosion of the footwalls and sedimentation into offshore basins. Paleocene ages in the north result from thermal relaxation of isotherms related to continental breakup and seafloor spreading, whereas Eocene and younger cooling events are associated with cessation of seafloor spreading and deposition into offshore basins.

REFERENCES

Anthony, J.W., Bideaux, R.A. Bladh, K.W., and Nichols, M.C. 1995. Handbook of Mineralogy. Chantilly, VA, US: Mineralogical Society of America. ISBN 978-0962209710.

Ault, A.K., Gautheron, C., and King, G.E. 2019. Innovations in (U-Th)/He, fission track, and trapped charge thermochronometry with applications to earthquakes, weathering, surface-mantle connections, and the growth and decay of mountains. Tectonics. **38**. DOI: 10.1029/2018TC005312

Balkwill, H.R., McMillan, N.J. 1990. Mesozoic-Cenozoic geology of the Labrador shelf, chapter 7 (Part1). In: Keen, M.J., Williams, G.L. (Eds.), Geology of the Continental Margin of Eastern Canada, Geology of Canada, no.2, pp. 31–85 (Geological Survey of Canada).

Beaumont, C., Fullsack, P., and Hamilton, J. 1994. Styles of crustal deformation in compressional orogens caused by subduction of the underlying lithosphere. Tectonophysics. **232**(1-4): 119–132. https://doi.org/10.1016/0040-1951(94)90079-5.

Bernet, M. and Garver, J.I. 2005. Fission-track analysis of detrital zircon: techniques, interpretations and applications. Reviews in Mineralogy Geochemistry. 58: 205–238. DOI: 10.1515/9781501509575-010

Bertotti, G., Seward, D., Wijbrans, J., ter Voorde, M., Hurford, A. 1999. Crustal thermal regime prior to, during, and after rifting; a geochronological modeling study of the Mesozoic South Alpine rifted margin. Tectonics **18**(2): 185-200.

Braun, J. (2018). A review of numerical modeling studies of passive margin escarpments leading to a new analytical expression for the rate of escarpment migration velocity. *Gondwana Research, 53*, 209–224.

Braun, J., van der Beek, P., and Batt, G. (2006). *Quantitative thermochronology: numerical methods for the interpretation of thermochronological data.* New York, NY. Cambridge University Press.

Bridgwater, D., and Schiotte, L. 1990. The Archean gneiss complex of northern Labrador; a review of current results, ideas and problems. Bulletin of the Geological Society of Denmark. **39**: 153–166.

Brune, S. Heine, C., Pérez-Gussinyé, M., and Sobolev, S.V. 2014. Rift migration explains continental margin asymmetry and crustal hyper-extension. Nature Communications. DOI: 10.1038/ncomms5014.

Buchan, K.L., Mortensen, J.K., Card, K.D., and Percival, J.A. 1998. Paleomagnetism and U-Pb geochronology of diabase dyke swarms of Minto block, Superior Province, Quebec, Canada. Canadian Journal of Earth Sciences. **35**: 1054–1069.

Campani, M., Herman, F., and Mancktelow, N. 2010. Two- and three-dimensional thermal modeling of a low-angle detachment: exhumation history of the Simplon Fault Zone, central Alps. Journal of Geophysical Research. **115**(B10420). DOI: 10.1029/2009JB007036.

Carlson, W.D., Donelick, R.A., and Ketcham, R.A. 1999. Variability of apatite fission-track annealing kinetics: I. experimental results. American Mineralogist. **84**: 1213–1223.

Centeno, J.P. 2005. Exhumation and incision history of the Torngat Mountains, northern Labrador and Quebec, Canada, using apatite (U-Th)/He thermochronology. M.Sc. thesis, Department of Geology, University of Kansas, Lawrence, KS.

Chalmers, J. A. 1997. The continental margin off southern Greenland: Along-strike transition from an amagmatic to a volcanic margin. Journal of the Geological Society. **154**(3): 571–576. https://doi.org/10.1144/gsjgs.154.3.0571.

Chalmers, J.A., and Laursen, K.H. 1995. Labrador Sea: the extent of continental and oceanic crust and timing of the onset of seafloor spreading. Marine and Petroleum Geology. **12**(2): 205–217.

Chalmers, J.A. and Pulvertaft, T.C.R. 2001. Development of the continental margins of the Labrador Sea: a review. Geological Society, London, Special Publications. **187**: 77–105. https://doi.org/10.1144/GSL.SP.2001.187.01.05.

Chenin, P., Manatschal, G., Picazo, S., Müntener, O., Karner, G., Johnson, C., and Ulrich, M. 2017. Influence of the architecture of magma-poor hyperextended rifted margins on orogens produced by the closure of narrow versus wide oceans. Geosphere. **13**(2): 1–18. DOI:10.1130 /GES01363.1.

Cherniak, D.J., and Watson, E.B. 2003. Diffusion in zircon. Reviews in Mineralogy & Geochemistry. **53**(1): 113–143. DOI: 10.2113/0530113.

Cherniak, D.J., Watson, E.B., and Thomas, J.B. 2009. Diffusion of helium in zircon and apatite. Chemical Geology. **268**: 155–166.

Cherniak, D.J. 2010. Diffusion in accessory minerals: zircon, titanite, apatite, monazite, and xenotime. Reviews in Mineralogy & Geochemistry. **72**: 827–869. DOI: 10.2138/rmg.2010.72.18

Chian, D., Keen, C., Reid, I., and Louden, K.E. 1995. Evolution of nonvolcanic rifted margins: new results from the conjugate margins of the Labrador Sea. Geology. **23**: 589–592.

Clarke, D.B., and Beutel, E.K. 2019. Davis Strait Paleocene Picrites: Products of a Plume or Plates? Earth-Science Reviews. **206**: 102770. https://doi.org/10.1016/j.earscirev.2019.01.012.

Clerc, C., Jolivet, L., and Ringenbach, J.C. 2015. Ductile extensional shear zones in the lower crust of a passive margin. Earth and Planetary Science Letters. **431**: 1–7. https://doi.org/10.1016/j.epsl.2015.08.038

Clerc, C., Ringenbach, J.C., Jolivet, L., and Ballard, J.F. 2018. Rifted margins: ductile deformation, boudinage, continentward-dipping normal faults and the role of the weak lower crust. Gondwana Research. **53**: 20–40.

Clowes, R.M. 2010. Initiation, development, and benefits of Lithoprobe – shaping the direction of Earth science research in Canada and beyond. Canadian Journal of Earth Sciences. **47**: 291–314. doi:10.1139/E09-074

Connelly, J.N., and Ryan, B. 1994. Late Archean and Proterozoic events in the central Nain craton. In Eastern Canadian Shield Onshore-Offshore Transect (ECSOOT), Report of the 1993 Transect Meeting. Compiled by R.J. Wardle and J. Hall. The University of British Columbia, Lithoprobe Secretariat, Report 36, pp. 53-61.

Cooperdock, E.H.G., Ketcham, R.A., and Stockli, D.F. 2019. Resolving the effects of 2-D versus 3-D grain measurements on apatite (U-Th)/He age data and reproducibility. Geochronology. **1**(1): 17–41.

Corrigan, D., Wodicka, N., McFarlance, C., Lafrance, I., van Rooyen, D., Bandyayera, D., and Bilodeau, C. 2018. Lithospheric framework of the Core Zone, Southeastern Churchill Province, Canada. Geoscience Canada. **45**: 1–24. https://doi.org/10.12789/geocanj.2018.45.128.

Costantini, J.M., Trocellier, P., Haussy, J., and Grob, J.-J. 2002. Nuclear reaction analysis of helium diffusion in britholite. Nucl. Instrum. Methods. **B195**: 400–407.

Dam, G., Pedersen, G.K., Sønderholm, M., Midtgaard, H.H., Larsen, L.M., Nøhr-Hansen, H., and Pedersen, A.K. 2009. Lithostratigraphy of the Cretaceous-Paleocene Nuussuaq Group, Nuussaq Basin, West Greenland. Geological Survey of Denmark and Greenland Bulletin. **19.**

Deer, W.A., Howie, R.A., and Zussman, J. 1969. An Introduction to the Rock-forming Minerals. John Wiley and Sons, New York.

Delescluse, M., Funck, T., Dehler, S.A., Louden, K.E., and Watremez, L. 2015. The oceanic crustal structure at the extinct, slow to ultraslow Labrador Sea spreading center. Journal of Geophysical Research: Solid Earth. **120**: 5249–5272.

DeSilva, N.R. 1999. Sedimentary basins and petroleum systems offshore Newfoundland and Labrador, *in* Fleet, A.J., and Boldy, S.A.R., eds., Petroleum Geology of Northwest Europe:

Proceedings of the 5th Conference on the Petroleum Geology of Northwest Europe: Geological Society of London Petroleum Geology Conference Series, v. 1, p. 501–516. DOI: 10.1144 /0050501.

Dick, H.J.B., Lin, J., and Schouten, H. 2003. An ultraslow-spreading class of ocean ridge. Nature. **426**(6965): 405–412.

Dickie, K., Keen, C.E., Williams, G.L., Dehler, S.A. 2011. Tectonostratigraphic evolution of the Labrador margin, Atlantic Canada. Marine and Petroleum Geology. **28**: 1663–1675.

Dodson, M.H. 1973. Closure temperature in cooling geochronological and petrological systems. Contributions to Mineralogy and Petrology. **40**: 259–274.

Donelick, R.A. 1991. Crystallographic orientation dependence of mean etchable fission track length in apatite: an empirical model and experimental observations. American Mineralogist. **76**: 83–91.

Donelick, R.A., O'Sullivan, P.B., and Ketcham, R. A. 2005. Apatite fission track analysis. Reviews in Mineralogy and Geochemistry. 58: 49-94.

Doré, T. and Lundin, E. 2015. Hyperextended continental margins–Knowns and unknowns. Geology. **43**: 95–96.

Dumitru, T.A. 2000. Fission-track geochronology. In: Noller JS, Sowers JM, Lettis, WR (eds) Quaternary geochronology: methods and applications. American Geophysical Union Reference Shelf 4, Washington, DC, American Geophysical Union, pp 131–155.
Ehlers, T.A., Armstrong, P.A., and Chapman, D.S. 2001. Normal fault thermal regimes and the interpretation of low-temperature thermochronometers. Physics of the Earth and Planetary Interiors. **126**: 179–194.

Ehlers, T.A., and Farley, K.A. 2003. Apatite (U-Th)/He thermochronometry: methods and applications to problems in tectonic and surface processes. Earth and Planetary Science Letters. **206**(1-2): 1–14.

Ehlers, T.A., Willett, S.D., Armstrong, P.A., and Chapman, D.S. 2002. Exhumation of the central Wasatch Mountains, Utah: 2. Thermo-kinematic model of exhumation, erosion, and thermochronometer interpretation. Journal of Geophysical Research. **108**(B3).
DOI: 10.1029/2001JB001723

Eldholm, O., and Sundvor, E. 1979. Geological events during the early formation of a passive margin. Tectonophysics. **59**: 233–237. DOI: 10.1016/0040-1951(79)90047-7.

Emproto., C., Alvarez, A., Anderkin, C., and Rakovan, J. 2020. The crystallinity of apatite in contact with metamict pyrochlore from the Silver Crater Mine, ON, Canada. Minerals. **10**(3). DOI: 10.3390/min10030244

Environment Canada. 2020. Meteorological Service of Canada. Canadian Climate Normals. 1981-2010 Climate Normals & Averages. Accessed from https://climate.weather.gc.ca/climate_normals/index_e.html.

Ermanovics, I.F. 1992. Geology, Central Hopedale Block, Labrador, Newfoundland. Geological Survey of Canada, Map.

Ermanovics, I. 1993. Geology of Hopedale block, southern Nain province, and the adjacent Proterozoic terranes, Labrador, Newfoundland. Geological Survey of Canada Memoir 431.

Farley, K.A. 2000. Helium diffusion from apatite: general behaviour as illustrated by Durango fluorapatite. Journal of Geophysical Research. **105**(B2): 2903–2014.

Farley, K.A. 2002. (U-Th)/He dating; Techniques, calibrations, and applications. Noble Gases in Geochemimstry and Cosmochemistry, Reviews in Mineralogy & Geochemistry. **47**: 819–844.

Farley, K.A., Wolf, R.A., and Silver, L.T. 1996. The effects of long alpha-stopping distances on (U-Th)/He ages. Geochimica et Cosmochimica Acta. 60**(21)**: 4223–4229.

Fitzgerald, P., and Gleadow, A.J.W. 1990. New approaches in fission track geochronology as a tectonic tool: Examples from the Transantarctic Mountains. Nuclear Tracks and Radiation Measurements. **17**: 351–357.

Fleischer, R.L., Price, P.B., and Walker, R.M. 1964b. Fission track ages of zircons. Geophysical Research Letters. **69**: 4885–4888.

Fleischer, R.L., Price, P.B., and Walker, R.M. 1975. Nuclear tracks in solids. University of California Press, Berkeley, 605pp.

Flowers, R.M., Ketcham, R.A., Shuster, D.L., and Farley, K.A. 2009. **Apatite (U–Th)/He thermochronometry using a radiation damage accumulation and annealing model**. Geochimica Cosmochimica Acta. 73(8): 2347–2365.

Flowers, R., Shuster, D., Wernicke, B., Farley, K., 2007. Radiation damage control on apatite (U–Th)/He dates from the Grand Canyon region, Colorado Plateau. Geology, 35 (5), 447–450.

Friedlander, G., Kennedy, J.W., Macias, E.S., Miller, J.M. 1981. Nuclear and Radiochemisty. John Wiley and Sons, New York.

Funck, T. and Louden, K.E. 1998. Wide angle seismic imaging of pristine Archean crust in the Nain Province, Labrador. Canadian Journal of Earth Sciences. **35**: 672–685.

Funck, T., Louden, K.E., and Reid, I.D. 2001. Crustal structure of the Grenville Province in southeastern Labrador from refraction seismic data: evidence for a high-velocity lower crustal wedge. Canadian Journal of Earth Sciences. **38**: 1463–1478.
Gaina, C., Roest, W.R. and Müller, R.D. 2002. Late Cretaceous-Cenozoic deformation of northeast Asia. Earth and Planetary Science Letters. **197**(3-4): 273–286. https://doi.org/10.1016/S0012-821X(02)00499-5.

Galbraith, R.F. 1981. On statistical models for fission track counts. Mathematical Geology. **13**: 471–488.

Galbraith, R.F. 1990. The radial plot: graphical assessment of spread in ages. Nuclear Tracks and Radiation Measurements. **17**: 207–214.

Galbraith, R.F., Roberts, R.G., Laslett, G.M., Yoshida, H., and Olley, J.M. 1999. Optical dating of single and multiple grains of quartz from Jinmium rock shelter, northern Australia: Part I, experimental design and statistical models. Archaeometry. **41**(2): 339–364.

Gallagher, K. 2012. Transdimensional inverse thermal history modeling for quantitative thermochronology. Journal of Geophysical Research Solid Earth. **117**: (B2).

Gallagher, K., Brown, R., and Johnson, C. 1998. Fission track analysis and its applications to geological problems. Annual Review of Earth and Planetary Sciences. **26**(1): 519–572.

Gastil, R.G.m DeLisle, M., and Morgan, J.R. 1967. Some effects of progressive metamorphism on zircons. Geological Society of America Bulletin. **78**(7): 879–906.

Gautheron, C., Tassan-Got, L., Barbarand, J., and Pagel, M. 2009**. Effect of α-damage annealing on apatite (U–Th)/He thermochronology.** Chemical Geology. **266**(3–4): 157–170.

Geological map of the Arctic. 2011. Arctic Circumpolar bedrock - Geological Survey of Canada - Natural Resources Canada. Geological Survey of Canada, "A" Series Map 2159A, 2011; 9 sheets; 1 DVD, doi:10.4095/287868.

Gleadow, A.J.W., Belton, D.X., Kohn, B.P., and Brown, R.W. 2002. Fission track dating of phosphate minerals and the thermochronology of apatite. Reviews in Mineralogy & Geochemistry. **48**: 579–630.

Gleadow, J.W., and Brown, R.W. 2000. Fission track thermochronology and the long-term denudational response to tectonics. Geomorphology and Global Tectonics. 57–75.

Gleadow, A.J.W., and Duddy, I.R. 1981. A natural long-term annealing experiment for apatite. Nuclear Tracks. **5**: 169–174.

Gleadow, A.J.W., Duddy, I.R., Green, P.F., and Lovering, J.F. 1986. Confined fission track lengths in apatite: a diagnostic tool for thermal history analysis. Contributions to Mineral and Petrology. **94**: 405–415.

Gleadow, A.J.W and Fitzgerald, P.G. 1987. Uplift history and structure of the Transantarctic Mountains: new evidence from fission track dating of basement apatites in the Dry Valleys area, southern Victoria Land. Earth and Planetary Science Letters. **82**: 1–14.

Gouiza, M. and Paton, D.A. 2019. The role of inherited lithospheric heterogeneities in defining the crustal architecture of rifted margins and the magmatic budget during continental breakup. Geochemistry, Geophysics, Geosystems. **20**: 1836–1853. https://doi.org/10.1029/2018GC007808.

Gosset, L.G., Damlencourt, J.F., Renault, O., Rouchon, D., Holliger, Ph., Ermolieff, A., Trimaille, I., Ganem, J.J., Martin, F., and Séméria. 2002. Interface and material characterization of thin Al_2O_3 layers deposited by ALD using TMA/H_2O. Journal of Non-Crystalline Solids. **303**(1): 17–23. https://doi.org/10.1016/S0022-3093(02)00958-4.

Gower, C.F., Hall, J., Kilfoil, G.J., Quinlan, G.M. and Wardle, R.J. 1997. Roots of the Labradorian orogen in the Grenville Province in southeast Labrador: evidence from marine deep-seismic reflection data. Tectonics. **16**(5): 795–809. https://doi.org/10.1029/97TC01284.

Gower, C.F., Schärer, U., and Heaman, L.M. 1992. The Labradorian orogeny in the Grenville Province, eastern Labrador, Canada. Canadian Journal of Earth Sciences. **29**: 1944–1957.

Green, P.F. 1981b. A new look at statistics in fission track dating. Nuclear Tracks. **5**: 77–86.

Green, P.F. 1985. Comparison of zeta calibration baselines for fission track dating of apatite, zircon and sphene. Chemical Geology (Isotope Geoscience Section). **58**: 1–22.

Green, P.F., Duddy, I.R., Laslett, G.M., Hegarty, K.A., Gleadow, A.J.W., and Lovering, J.F. 1989. Thermal annealing of fission tracks in apatite 4: quantitative modeling techniques and extension to geological timescales. Chemical Geology (Isotope Geoscience Section). **79**:155–182.

Green, P.F., Lidmar-Bergström, K., Japsen, P., Bonow, J.M., and Chalmers, J.A. 2013. Stratigraphic landscape analysis, thermochronology and the episodic development of elevated, passive continental margins. Geological Survey of Denmark and Greenland Bulletin. **30**.

Green, P.F., and Durrani, S.A. 1977. Annealing studies of tracks in crystals. Nuclear Track Detection. **1**: 33–39.

Groch, M.W. 1998. Radioactive decay. Imaging & Therapeutic Technology. **8**(5): 1247–1256.

Guenthner, W.R., Reiners, P.W., Ketcham, R.A., Nasalda, L., and Geister, G. 2013. Helium diffusion in natural zircon: radiation damage, anisotropy, and the interpretation of zircon (U-Th)/He thermochronology. American Journal of Science. **313**: 145–198. DOI: 10.2475/03.2013.01.
Guenthner, W.R. 2019. Implementation of an alpha damage annealing model of zircon (U-Th)/He thermochronology with comparison to a zircon fission track annealing model. Geochemistry, Geophysics, Geosystems. **22**: e2019GC008757. https://doi. org/10.1029/2019GC008757.

Hall, J., Wardle, R.J., Gower, C.F., Kerr, A., Coflin, K., Keen, C.E., and Carroll, P. 1995 Proterozoic orogens of the northeastern Canadian Shield: new information from the Lithoprobe ECSOOT crustal reflection seismic survey. Canadian Journal of Earth Sciences. **32**: 1119–1131.

Hall, J., Louden, K.E., Funck, T., and Deemer, S. 2002. Geophysical characteristics of the continental crust along the Lithoprobe Eastern Canadian Shield Onshore-Offshore Transect (ECSOOT): a review. Canadian Journal of Earth Sciences. **39**: 569–587. DOI: 10.1139/E02-005

Hamilton, M.A., Ryan, A.B., Emslie, R.F, and Ermanovics, I. 1998. Identification of Paleoproterozoic anorthositic and monzonitic rocks in the vicinity of the Mesoproterozoic Nain Plutonic Suite, Labrador: U-Pb evidence. In Current research, part F. Radiometric age and isotopic studies: Report 11. Geological Survey of Canada, Report 1998-F, pp. 23-40.

Hammer, P.T.C., Clowes, R.M., Cook, F.A., van der Velden, A.J., and Vasudevan, K. 2010. The Lithoprobe trans-continental lithospheric cross sections: imaging the internal structure of the North American continent. Canadian Journal of Earth Sciences. **47**(5): 821 – 857. doi:10.1139/E10-036.

Hinchey, A.M., Rayner, N., and Davis, W.J. 2020. Episodic Paleoproterozoic crustal growth preserved in the Aillik Domain, Makkovik Province, Labrador. Precambrian Research. **337**(105526). https://doi.org/10.1016/j.precamres.2019.105526.

Hourigan, J.K., Reiners, P.W., and Brandon, M.T. 2005. U-Th zonation dependent alpha-ejection in (U-Th)/He chronometry. Geochemica et Cosmochimica Acta. **69**(13): 3349–3365.

House, M.A., Wernicke, B.P., Farley, K.A., and Dumitru, T.A. 1997. Cenozoic thermal evolution of the central Sierra Nevada, California, from (U– Th)/He thermochronometry. Earth and Planetary Scientific Letters. **151**: 167–179.

House, M.A., Wernicke, B.P., and Farley, K.A. 1998. Dating topography of the Sierra Nevada, California, using apatite (U–Th)/He ages. Nature. **396**: 66–69. https://doi.org/10.1038/23926.

Huismans, R., and Beaumont, C. 2011. Depth-dependent extension, two-stage breakup and cratonic underplating at rifted margins. Nature. **473**: 74–78. DOI: 10.1038/nature09988.

Hurford, A.J. 2019. An historical perspective on fission-track thermochronology (Chapter 1). In: Malusà MG, Fitzgerald PG (eds) Fission-track thermochronology and its application to geology. Springer, Berlin.

Hurford, A.J. 1990. Standardization of fission-track dating calibration: recommendation by the Fission Track Working Group of the I.U.G. S. Subcommission on Geochronology. Chemical Geology (Isotope Geoscience Section). **80**: 171–178.

Hurford, A.J., and Carter, A. 1991. The role of fission track dating in discrimination of provenance. In: Developments in Sedimentary Provenance Studies. Morton AC, Todd SP, Haughton PDW (eds) Geological Society Special Publication. **57**: 67–78.

Hurford, A.J., and Green, P.F. 1981a. A reappraisal of neutron dosimetry and ^{238}U kf values in fission-track dating. Nuclear Tracks. **5**: 53–61.

Hurford, A.J., and Green, P.F. 1983. The zeta age calibration of fission-track dating. Isotope Geoscience. **1**: 285–317.

Hurford, A.J., and Hammerschmidt, K. 1985. ^{40}Ar-^{39}Ar and K-Ar dating of the Bishop and Fish Canyon tuffs: calibration ages for fission-track dating standards. Chemical Geology (Isotope Geoscience Section). **58**: 23–32.

Isnard, H., Parent, M., Bardoux, M., David, J., Gariepy, C., and Stevenson, R.K. 1998. U-Pb, Sm-Nd and Pb-Pb isotope geochemistry of the high-grade gneiss assemblages along the southern shore of Ungava Bay. In Eastern Canadian Shield Onshore-Offshore Transect (ECSOOT), Report of the 1998 Transect Meeting. Compiled by R.J. Wardle and J. Hall. The University of British Columbia, Lithoprobe Secretariat, Report 68, pp. 67-77.

James, D.T., and Dunning, G.R. 2000. U-Pb geochronological constraints for Paleoproterozoic evolution of the Core Zone, southeastern Churchill Province, northeastern Laurentia. Precambrian Research. **103**: 31–54.

Japsen, P., Bonow, J.M., Green, P.F., Chalmers, J.A., and Lidmar-Bergström, K. 2006. Elevated, passive continental margins: Long-term hights or Neogene uplifts? New evidence from West Greenland. Earth and Planetary Science Letters. **248**: 330–339.

Japsen, P., Bonow, J.M., Green, P.F., Chalmers, J.A., and Lidmar-Bergström, K. 2009. Formation, uplift and dissection of planation surfaces at passive continental margins – a new approach. Earth Surface Processes and Landforms. **34**: 683–699.

Japsen, P. Green, P.F., Bonow, J.M., Nielsen, T.F.D., and Chalmers, J.A. 2014. From volcanic plains to glaciated peaks: burial, uplift and exhumation history of southern East Greenland after opening of the NE Atlantic. *Global and Planetary Change, 116*, 91–114.

Japsen, P., Green, P.F., Bonow, J.M., Hinchey, A.M., and Wilton, D.H.C. 2016. Burial and exhumation history of the Labrador-Newfoundland margin: first observations. Geological Survey of Denmark and Greenland Bulletin. **35**: 91–94.

Jeong, Y.J., Lee, S., Ju Kim, S., Je Jo, H., Yi, K., and Chang-sik Cheong, A. 2018. U–Th isotopic microanalysis of zircon reference materials and KBSI working standards. Journal of Analytical Science and Technology. **9**(16).

Jess, S., Stephenson, R., Nielsen, S.B., and Brown, R. 2019. The source of topography across the Cumberland Peninsula, Baffin Island, Arctic Canada: differential exhumation of a North Atlantic rift flank. Journal of the Geological Society. **176**; 1093–1106. https://doi.org/10.1144/jgs2018-211.

Karl, M., Glasmacher, U.A., Kollenz, S., Franco-Magalhaes, A.O.B., Stockli, D.F., and Hackspacher, P.C. 2013. Evolution of the South Atlantic passive continental margin in southern Brazil derived from zircon and apatite (U-Th-Sm)/He and fission-track data. Tectonophysics. **604**: 224–244.

Keen, C.E. 1978. Thermal history and subsidence of rifted continental margins – evidence from wells on the Nova Scotian and Labrador shelves. Canadian Journal of Earth Sciences. **16**: 505–522.

Keen, C.E., Courtney, R.C., Dehler, S.A. and Williamson, M.C. 1994. Decompression melting at rifted margins: comparison of model predictions with the distribution of igneous rocks on the eastern Canadian margin. Earth and Planetary Science Letters. **121**: 403–416.

Keen, C.E., Dickie, K., and Dafoe, L.T. 2018. Structural characteristics of the ocean-continent transition along the rifted continental margin, offshore central Labrador. Marine and Petroleum Geology. **89**: 443–463.

Keen, C.E., Dickie, K., and Dafoe, L.T. 2018. Structural evolution of the rifted margin off northern Labrador: the role of hyperextension and magmatism. Tectonics. **37**: 1955–1972.

Keen, C.E., Dickie, K., and Dehler, S.A. 2012. The volcanic margins of the northern Labrador Sea: insights to the rifting process. Tectonics. **31**. TC1011, doi: 10.1029/2011TC002985

Kerr, A., Hall, J., Wardle, R.J., Gower, C.F., and Ryan, B. 1997. New reflections on the structure and evolution of the Makkovikian–Ketilidian Orogen in Labrador and southern Greenland. Tectonics. **16**: 942–965.

Kerr, A., Ryan, B., Gower, C.F., and Wardle, R.J. 1996. Makkovik Province: extension of the Ketilidian Mobile Belt in mainland North America. **112**: 115–177. https://doi.org/10.1144/GSL.SP.1996.112.01.09.

Ketcham, R.A. 2005. Forward and inverse modeling of low-temperature thermochronometry data. Reviews in Mineralogy & Geochemistry. **58**: 275–314. DOI: 10.2138/rmg.2005.58.11

Ketcham, R. A. 2011. HeFTy Version 1.7.0: Manual.

Ketcham, R. A., Donelick, R. A., Balestrieri, M. L., and Zattin, M. 2009. Reproducibility of apatite fission-track length data and thermal history reconstruction. Earth and Planetary Science Letters. **284**: 504–515.

Ketcham, R.A., Donelick, D.A., and Carlson, W.D. 1999. **Variability of apatite fission-track annealing kinetics: III. Extrapolation to geologic time scales.** Am. Mineral. **84**: 1235–1255.

Ketcham, R.A., Gautheron, C., and Tassan-Got, L. 2011. Accounting for long alpha-particle stopping distances in (U–Th–Sm)/He geochronology: Refinement of the baseline case. Geochemica et Cosmochemica Acts. 75(24): 7779–7791.

Ketcham, R.A., Mora, A., and Parra, M. 2016. Deciphering exhumation and burial history with multi-sample down-well thermochronometric inverse modelling. Basin Research. **30**: 48–64.

Ketchum, J.W.F, Culshaw, N.G., and Barr, S.M. 2002. Anatomy and orogenic history of a Paleoproterozoic accretionary belt: the Makkovik Province, Labrador, Canada. Canadian Journal of Earth Sciences. **39**(5): 711–730.

Kerr, A., Krogh, T.E., Corfu, F., Scharer, U., Gandhi, S.S., and Kwok, Y.Y. 1992. Episodic early Proterozoic granitoid plutonism in the Makkovik Province, Labrador: U-Pb geochronological data and geological implications. Canadian Journal of Earth Sciences. **29**: 1166- 1179.

Kohn, B., Chung, L., and Gleadow, A. 2018. Fission-track analysis: field collection, sample preparation and data acquisition (Chapter 2). In: Malusà MG, Fitzgerald PG (eds) Fission-track thermochronology and its application to geology. Springer, Berlin.

Kossert, K., Jörg, G., Nähle, O., and Lierse v. Gostomski, C. 2009. High-precision measurement of the half-life of ^{147}Sm. Applied Radiation and Isotopes **67**(9): 1702–1706. doi.org/10.1016/j.apradiso.2009.03.013

Larsen, L. M., Heaman, L. M., Creaser, R. A., Duncan, R. A., Frei, R., and Hutchison, M. 2009. Tectonomagmatic events during stretching and basin formation in the Labrador Sea and the Davis Strait: Evidence from age and composition of Mesozoic to Palaeogene dyke swarms in west Greenland. Journal of the Geological Society. **166**(6). 999–1012. https://doi.org/10.1144/0016-76492009-038.

Laslett, G.M., Green, P.F., Duddy, I.R., and Gleadow, A.J.W. 1987. Thermal annealing of fission tracks in apatite 2: a quantitative analysis. Chemical Geology (Isotope Geoscience Section). **65**: 1–15.

Lavier, L.L., and Manatschal, G. 2006. A mechanism to thin the continental lithosphere at magma-poor margins. Nature. **440**: 324–328. DOI: 10.1038/nature04608.

Le Guerroué, E., Jermannaud, P., Filleadeau, P.Y., Perez-Drago, G., Chenet, P., Gillis, E., Montevecchi, N., and Wright, R. 2018. Play elements of the Chidley Basin, Offshore Newfoundland and Labrador Canada. 80th EAGE Conference and Exhibition 2018, Copenhagen. DOI:10.3997/2214-4609.201801082.

Liao, J., and Gerya, T. 2014. From continental rifting to seafloor spreading: insight from 3D thermo-mechanical modelling. Gondwana Research. **28**: 1329–1343. DOI: 10.1016/j.gr.2014.11.004

Lippolt, H.J., Leitz, M., Wernicke, R.S., and Hagedorn, B. 1994. (U-Th)/He dating of apatite: experience with samples from different geochemical environments. Chemical Geology. **112**: 179–191.

Lisker, F., Ventura, B., and Glasmacher, U.A. 2009. Apatite thermochronology in modern geology. Thermochronological Methods: From Palaeotemperature Constraints to Landscape Evolution Models. Geological Society, London, Special Publications. **324**: 1–23. DOI: 10.1144/SP324.1

Lister, G.S., Etheridge, M.A., and Symonds, P.A. 1986. Detachment faulting and the evolution of passive continental margins. Geology. **14**: 891–892. doi:10.1130/0091-7613(1986)14.

Louden, K.E., and Fan, J. 1998. Crustal structures of Grenville, Makkovik, and southern Nain provinces along the Lithoprobe ECSOOT Transect: regional seismic reftraction and gravity models and their tectonic implications. Canadian Journal of Earth Sciences. **35**(5): 583 – 601.

Louis, B. 2015. Late Cenozoic upper-crustal cooling history of the Shuswap Metamorphic Complex, southern Canadian Cordillera, British Columbia: New insights from low-temperature multi-thermochronometry and inverse thermal modelling. M.Sc. thesis, Department of Earth Sciences, Dalhousie University, Halifax, N.S.

Malusà, M.G., Danišík, M., and Kuhlemann, J. 2016. Tracking the Adriatic-slab travel beneath the Tethyan margin of Corsica-Sardinia by low-temperature thermochronometry. Gondwana Research. **31**: 135–149.

Malusà, G.M. and Fitzgerald, P.G. 2019. Fission-track thermochronology and its applications to geology. Springer, Cham, Switzerland.

Malusà M.G., Fitzgerald P.G. (2019) Application of Thermochronology to Geologic Problems: Bedrock and Detrital Approaches. In: Malusà M., Fitzgerald P. (eds) Fission-Track Thermochronology and its Application to Geology. Springer Textbooks in Earth Sciences, Geography and Environment. Springer, Cham. https://doi.org/10.1007/978-3-319-89421-8_10.

Manatschal, G. 2004. New models for evolution of magma-poor rifted margins based on a review of data and concepts from West Iberia and the Alps. International Journal of Earth Sciences. **93**: 432–466. DOI 10.1007/s00531-004-0394-7.
Mancktelow, N.S., and Grasemann, B. 1997. Time-dependent effects of heat advection and topography on cooling histories during erosion. Tectonophysics. **270**: 167-195.

Mann, P., Gahagan, L., and Gordon, M.B. 2003. Tectonic setting of the world's giant oil and gas fields. AAPG Memoir. **78** (78): 15–105.

McGregor, E.D., Nielsen, S.B., Stephenson, R.A., Petersen, K.D., and MacDonald, D.I.M. 2013. Long-term exhumation of a Palaeoproterozoic orogen and the role of pre-existing heterogeneous thermal crustal properties: a fission-trach study of SE Baffin Island. Journal of the Geological Society, London. **170**: 877–891.

McIntyre, G.A., Brooks, C., Compston, W., and Turek, A. 1966. The statistical assessment of Rb-Sr isochrons. Journal of Geophysical Research. **71**: 5459–5468.

McKenzie, D. 1978. Some remarks on the development of sedimentary basins. Earth and Planetary Science Letters. **40**: 25–32. doi:10.1016/0012-821X(78)90071-7.

Meesters, A.G.C.A., and Dunai, T.J. 2005. A noniterative solution of the (U-Th)/He age equation. Geochemistry, Geophysics, Geosystems. **6**(4).

Meesters, A. G. C. A, and Dunai, T. J. 2002. Solving the production-diffusion equation for finite diffusion domains of various shapes: Part II. Application to cases with α-ejection and nonhomogeneous distribution of the source. Chemical Geology. **186**(1–2): 57–73. http://dx.doi.org/10.1016/S0009- 2541(01)00423-5

Miro, S., Studer, F., Costantini, J.-M., Haussy, J., Trouslard, P., and Grob, J.-J. 2006. Effect of composition on helium diffusion in fluoroapatites investigated with nuclear reaction analysis. J. Nucl. Mater. **355**: 1–9.

Miro, S., Studer, F., Costantini, J.-M., Berger, P., Haussy, J., Trouslard, P., and Grob, J.-J. 2007. Effect of gold ion irradiation on helium migration in fluoroapatites investigated with nuclear reaction analysis. J. Nucl. Mater. **362**: 445–450.

Mohn, G., Manatschal, G., Beltrando, M., Masini, E., and Kusznir, N. 2012. Necking of continental crust in magma-poor rifted margins: evidence from the fossil Alpine Tethys margins. Tectonics. **31**: TC1012. DOI:10.1029/2011TC002961.

Naeser, C.W. 1967. The use of apatite and sphene for fission track age determinations. Bulletin of the Geological Society of America. **78**: 1523–1526.

Naeser, C.W., and Dodge, F.C.W. 1969. Fission-track ages of accessory minerals from granitic rocks of the central Sierra Nevada Batholith, California. Bulletin of the Geological Society of America. **80**: 2201–2212.

Nasdala, L., Hanchar, J.M., Kronz, A., Whitehouse, M.J., 2004. Long-term stability of alpha particle damage in natural zircon. Chem. Geol. 220, 83–103.

Nicolaysen, L. 1961. Graphic interpretation of discordant age measurements on metamorphic rocks. Annals of the New York Academy of Sciences. **91**(1): 198–206.

Nunn, G.A.G., Heaman, L.M., and Krogh, T.E. 1990. U-Pb geochronological evidence for Archean crust in the continuation of the Rae Province (eastern Churchill Province), Grenville Front Tectonic Zone, Labrador. Geoscience Canada. **17**: 259–265.

Nyberg, B., Helland-Hansen, W., Gawthorpe, R.L., Sandbakken, P., Haug Eide, C., Sømme, T., Hadler-Jacobson, F., and Leiknes, S. 2018. Revisiting morphological relationships of modern source-to-sink segments as a first-order approach to scale ancient sedimentary systems. Sedimentary Geology. **373**: 111–133.

Oakey, G.N., and Chalmers, J.A. 2012. A new model for the Paleogene motion of Greenland relative to North America: Plate reconstructions of the Davis Strait and Nares Strait Regions between Canada and Greenland. Journal of Geophysical Research. **117**.

Oelkers, E.H., and Montel, J.M. 2008. Phosphates and nuclear waste storage. Elements. **4**(2): 113–116. DOI: 10.2113/GSELEMENTS.4.2.113

O'Neil, J., Carlson, R.W., Francis, D., and Stevenson, R.K. 2008. Neodymium-142 evidence for Hadean mafic crust. Science. **321**(5897): 1828–1831. doi:10.1126/science.1161925

Ouchani, S., Dran, J.-C., and Chaumont, J. 1998. Exfoliation and diffusion following helium ion implantation in fluorapatite: implications for radiochronology and radioactive waste disposal. Appl. Geochem. **13**: 707–714.

Paul, T.A. 1993. Transmission electron microscopy investigation of unetched fission tracks in fluorapatite—physical process of annealing. Nuclear Tracks and Radiation Measurements. **21**: 507–511.

Paul, T.A., and Fitzgerald, P.G. 1992. Transmission electron microscopic investigation of fission tracks in fluorapatite. American Mineralogist. **77**: 336–344.

Peace, A.L., Foulger, G.R., Schiffer, C., McCaffrey, K.J.W. 2017. Evolution of Labrador Sea–Baffin Bay: Plate or plume processes? Geoscience Canada. **44**: 91–102.

Peace, A., McCaffrey, K., Imber, J., Phethean, J., Nowell, G., Gerdes, K., and Dempsey, E. 2016. An evaluation of the Labrador Sea: Implications for rifting and passive margin asymmetry. Geosphere. 12**(6)**: 1701–1724.

Pérez-Gussinyé, M., Morgan, J. P., Reston, T. J., and Ranero, C. R. 2006. The rift to drift transition at non-volcanic margins: insights from numerical modelling. Earth and Planetary Science Letters. **244**: 458–473. DOI: 10.1016/j.epsl.2006.01.059.

Péron-Pinvidic, G., and Manatschal, G. 2019. Rifted margins: state of the art and future challenges. Frontiers in Earth Science. https://doi.org/10.3389/feart.2019.00218.

Péron-Pinvidic, G., and Manatschal, G. 2009. The final rifting evolution at deep magma-poor passive margins from Iberia-Newfoundland: a new point of view. International Journal of Earth Sciences. **98**: 1581–1597. DOI 10.1007/s00531-008-0337-9.

Péron-Pinvidic, G., Manatschal, G., and Osmundsen, P.T. 2013. Structural comparison of archetypal Atlantic rifted margins: a review of observations and concepts. Marine and Petroleum Geology. **43**: 21–47. doi.org/10.1016/j.marpetgeo.2013.02.002

Price, P.B., and Walker, R.M. 1963. Fossil tracks of charged particles in mica and the age of minerals. Journal of Geophysical Research. **68**:4847–4862.

Ranero, C. R., and Perez-Gussinye, M. 2010. Sequential faulting explains the asymmetry and extension discrepancy of conjugate margins. Nature. **468**: 294–297. DOI: 10.1038/nature09520.

Recanati, A. Gautheron, C., Barbarand, J., Missenard, Y., Pinna-Jamme, R., Tassan-Got, L., Carter, A., Douville, E., Bordier, L., Pagel, M., and Gallagher, K. 2017. Helium trapping in apatite damage: insights from (U-Th-Sm)/He dating of different granitoid lithologies. Chemical Geology. **420**: 116–131.

Reiners, P.W. 2005. Zircon (U-Th)/He thermochronometry. Reviews in Mineralogy & Geochemistry. **58**: 151–179.

Reiners, P.W., Brady, R., Farley, K.A., Fryxell, J.E., Wernicke, B., Lux, D., 2000. Helium and argon thermochronometry of the Gold Butte Block, South Virgin Mountains, Nevada. Earth and Planetary Science Letters. **178**: 315–326.

Reiners, P.W., and Brandon, M.T. 2006. Using thermochronology to understand orogenic erosion. The Annual Review of Earth and Planetary Science. **34**: 419–66.

Reiners, P.W., Ehlers, T.A., and Zeitler P.K. 2005. Past, present, and future of thermochronology. Reviews in Mineralogy & Geochemistry. **58**: 1–18.

Reiners, P.W., and Farley, K.A. 2001. Influence of crystal size on apatite (U– Th)/He thermochronology: an example from the Bighorn Mountains, Wyoming. Earth and Planetary Science Letters. **188**(3): 413–420.

Reiners, P.W., and Farley, K.A. 1999. Helium diffusion and (U–Th)/He thermochronometry of titanite. Geochimica Cosmochimica Acta. **63**(22): 3845–3859.

Reiners, P.W., Farley, K., and Hickes, H. 2002. He diffusion and (U–Th)/He thermochronometry of zircon: Initial results from Fish Canyon Tuff and Gold Butte, Nevada. Tectonophysics. **349**: 297–308.

Reiners, P.W., and Shuster, D.L. 2009. Thermochronology and landscape evolution. Physics Today. **62**: 31–36.

Reston, T. J. (2005). Polyphase faulting during the development of the west Galicia rifted margin. Earth and Planetary Science Letters. **237**: 561–576. DOI: 10.1016/j.epsl.2005.06.019.

Rios, S., Salje, E.K.H., Zhang, M., and Ewing, R.C. 2000. Amorphization in zircon: evidence for direct impact damage. Journal of Physics: Condensed Matter. **12**(11): 2401–2412.

Ritter, W. and Märk, T.D. 1986. **Radiation damage and its annealing in apatite.** Nuclear Instruments and Methods in Physics Research. **814**: 314–322.

Roest, W.R., and Srivastava, S.P. 1989. Sea-floor spreading in the Labrador Sea: a new reconstruction. Geology. **17**: 1000–1003.

Rowley, D.B. and Lottes, A.L. 1988. Plate-kinematic reconstructions of the North Atlantic and Arctic: late Jurassic to present. Tectonophysics. **155**(1-4): 73–120. https://doi.org/10.1016/0040-1951(88)90261-2.

Rutherford, E. and Soddy, F. 1902a. The cause and nature of radioactivity – part i. The London, Edinburgh, and Dublin Philosophical Magazine and Journal of Science. **4**(21):370–396.

Rutherford, E. and Soddy, F. 1902b. The cause and nature of radioactivity – part ii. The London, Edinburgh, and Dublin Philosophical Magazine and Journal of Science. **4**(23):569–585, 1902b.

Ryan, B. 2000. The Nain-Churchill boundary and the Nain Plutonic Suite: a regional perspective on the geologic setting of the Voisey's Bay Ni-Cu-Co deposit. Economic Geology. **95**(4): 703–724. https://doi.org/10.2113/gsecongeo.95.4.703**.**

Ryan, B. (compiler), Krogh, T.E., Heaman, L., Scharer, U., Philippe, S., and Oliver, G. 1991. On recent geochronological studies in the Nain Province, Churchill Province and Nain Plutonic Suite, north-central Labrador. In Current research. Geological Survey, Newfoundland Department of Mines and Energy, Report 91-1, pp. 257-261.

Schiffer, C., Doré, A.G., Foulger, G.R., Franke, D., Geoffroy, L., Gernigon, L., Holdsworth, B., Kusznir, N., Lundin, E., McCaffrey, K., Peace, A.L., Petersen, K.D., Phillips, T.B., Stephenson, R., Stoker, M.S., and Welford, J.K. 2020. Structural inheritance in the North Atlantic. Earth-Science Reviews. **206**: 102975. https://doi.org/10.1016/j.earscirev.2019.102975.

Scott, R.J., Foster, D.A., and Lister, G.S. 1998. Tectonic implications of rapid cooling of denuded lower plate rocks from the Buckskin-Rawhide metamorphic core complex, west-central Arizona. Geological Society of America Bulletin. **110**: 588–614.

Seton, M., Müller, R.D., Zahirovic, S., Gaina, C., Torsvik, T., Shephard, G., Talsma, A., Gurnis, M., Tuner, M., Maus, S., and Chandler, M. 2012. Global continental and ocean basin reconstructions since 200 Ma. Earth-Science Reviews. **113**: 212–270.

Shuster, D.L., and Farley, K.A. 2004. ^{4}He/^{3}He thermochronometry. Earth Planet. Sci. Lett. **217**: 1–17.

Shuster, D.L., and Farley, K.A. 2005a. ^{4}He/^{3}He thermochronometry; theory, practice, and potential complications. In: Reiners, P.W., Ehlers, T.A. (Eds.), Low-temperature Thermochronology: Techniques, Interpretations, and Applications. Reviews in Mineralogy and Geochemistry, vol. 58. Mineralogical Society of America and Geochemical Society, Washington, DC, pp. 181–203.

Shuster, D.L., and Farley, K.A. 2005b. Diffusion kinetics of proton-induced Ne-21, He-3, and He-4 in quartz. Geochim. Cosmochim. Acta **69**: 2349–2359.

Shuster, D.L., and Farley, K.A. 2009. Influence of artificial radiation damage and thermal annealing on helium diffusion kinetics in apatite. Geochemica et Cosmochimica Acta. **73**: 183–196. doi:10.1016/j.gca.2008.10.013

Shuster, D.L., Farley, K.A., Sisterson, J.M., Burnett, D.S., 2003. Quantifying the diffusion kinetics and spatial distribution of radiogenic 4He in minerals containing protoninduced 3He. Earth Planet. Sci. Lett. **217**: 19–32.

Shuster, D.L., Flowers, R.M., Farley, K.A., 2006. The influence of natural radiation damage on helium diffusion kinetics in apatite. Earth Planet. Sci. Lett. **249**: 148–161.

Spiegel, C., Kohn, B.P., Belton, D. Berner, Z., and Gleadow, A. 2009. Apatite (U-Th-Sm)/He thermochronology of rapidly cooled samples: the effect of He implantation. Earth and Planetary Science Letters. **285**(1-2): 105–114.

Spiegel, C., Kohn, B.P., Raza, A., Rainer, T., and Gleadow, A.J.W. 2007. The effect of long-term low temperature exposure on apatite fission track stability: A natural annealing experiment in the deep ocean. Geochimica Cosmochimica Acta. **71**: 4512–4537

Srivastava, S.P. 1978. Evolution of the Labrador Sea and its bearing on the early evolution of the North Atlantic. Geophysical Journal International. **52**: 313–357.

Srivastava, S.P., and Roest, W.R. 1995. Nature of Thin Crust Across the Southwest Greenland Margin and its Bearing on the Location of the Ocean-Continent Boundary. In: Banda E., Torné M., Talwani M. (eds) Rifted Ocean-Continent Boundaries. NATO ASI Series (Series C: Mathematical and Physical Sciences), vol 463. Springer, Dordrecht. https://doi.org/10.1007/978-94-011-0043-4_6

Srivastava, S.P., and Roest, W.R. 1999. Extent of oceanic crust in the Labrador Sea. Marine and Petroleum Geology. **16**: 65–84.

Stanley, J.R., and Flowers, R.M. 2016. Dating kimberlite emplacement with zircon and perovskite (U-Th)/He geochronology. Geochemistry, Geophysics, Geosystems. **17**: 4517–4533.

Steiger, R.H. and Jäger, E. 1977. Subcomission on geochronology: convention on the use of decay constants in geo- and cosmochronology. Earth and Planetary Science Letters. **36**: 359–362.

Stockli, D.F. 2005. Application of low-temperature thermochronometry to extensional tectonic settings. Reviews in Mineralogy & Geochemistry. **58**: 411–448. DOI: 10.2138/rmg.2005.58.16.

Stockli, D. F. and Wolfe, M. R. 2009. Zircon (U-Th)/He thermochronometry in the KTB drill hole, Germany - Implications for He diffusion in zircon. American Geophysical Union, Fall Meeting 2009, abstract #V52C-05.

Stockli, D.F., Farley, K.A., and Dumitru, T.A. 2000. **Calibration of the (U-Th)/He thermochronometer on an exhumed fault block, White Mountains, California.** **G**eology. **28**(11): 983–986.

Storey, M., Duncan, R.A., Pedersen, A.K., Larsen, L.M., Larsen, H.C. 1998. ^{40}Ar/^{39}Ar geochronology of the West Greenland Tertiary volcanic province. Earth and Planetary Science Letters. **160**: 569–586.

Tagami, T., and O'Sullivan, P.B. 2005. Fundamentals of fission-track thermochronology. Reviews in Mineralogy & Geochemistry. **58**: 19–47.

Tappe, S., Foley, S. F., Stracke, A., Romer, R. L., Kjarsgaard, B. A., Heaman, L. M., and Joyce, N. 2007. Craton reactivation on the Labrador Sea margins: 40Ar/39Ar age and Sr–Nd–Hf–Pb isotope constraints from alkaline and carbonatite intrusives. Earth and Planetary Science Letters. **256**(3-4): 433–454. https://doi.org/10.1016/j.epsl.2007.01.036.

Tappe, S., Steenfelt, A., Heaman, L.M., and Simonetti, A. 2009. The newly discovered Jurassic Tikiusaaq carbonatite-aillikite occurrence, West Greenland, and some remarks on carbonatite-kimberlite relationships. Lithos. **1125**: 385–399. DOI:10.1016/j.lithos.2009.03.002.

Tollo, R.P., Corriveau, L., McLelland, J., and Bartholomew, M.J. 2004. Proterozoic tectonic evolution of the Grenville orogen in North America: An introduction. Geological Society of America Memoir. **197**: 1–18. ISBN 978-0-8137-1197-3.

Trachenko, K., Dove, M.T., and Salje, E.K.H. 2002. Structural changes in zircon under alpha-decay irradiation. Physical Review B. **65**(18).

Trocellier, P., Gosset, D., Simeone, D., Costantini, J.M., Deschanels, X., Roudil, D., Serruys, Y., Grynszpan, R., Saudé, S., and Beauvy, M. 2003a. Application of nuclear reaction geometry for 3He depth profiling in nuclear ceramics. Nucl. Instrum. Methods. **B206**: 1077–1082.

Trocellier, P., Gosset, D., Simeone, D., Costantini, J.-M., Deschanels, X., Roudil, D., Serruys, Y., Grynszpan, R., Saudé, S., and Beauvy, M. 2003b. 3He thermal diffusion coefficient measurement in crystalline ceramics by NRA depth profiling. Nucl. Instrum. Methods. **B210**: 507–512.

Umpleby, D. 1979. Geology of the Labrador Shelf: Geological Survey of Canada Paper. **34**: 79-13.

van der Pluijm, B., and Marshak, S. 2003. Earth structure: An introduction to structural geology and tectonics. W. W. Norton & Company, New York, NY.

van Wijk, J.W. and Cloetingh, S.A.P.L. 2002. Basin migration caused by slow lithospheric extension. Earth and Planetary Science Letters. **198**: 275-288.

Vermeesch, P. 2008. Three new ways to calculate average (U–Th)/He ages. Chemical Geology. 249**(3)**: 339–347.

Vermeesch, P. 2010. HelioPlot, and the treatment of overdispersed (U-Th-Sm)/He data. Chemical Geology. **271**(3–4): 108–111. doi.org/10.1016/ j.chemgeo.2010.01.002.

Vermeesch, P. 2018. IsoplotR: a free and open toolbox for geochronology. Geoscience Frontiers. **9**: 1479–1493. doi.org/10.1016/j.gsf.2018.04.001

Wagner GA, Reimer GM (1972) Fission track tectonics: the tectonic interpretation of fission track ages. Earth and Planetary Science Letters. **14**: 263–268.

Wagner, G.A., Reimer, G.M., Carpenter, B.S., Faul, H., Van den Linden, R., and Gijbels, R. 1975. The spontaneous fission rate of ^{238}U and fission track dating. Geochimica et Cosmochimica Acta. **39**: 1279–1286.

Wardle, R.J., James, D.T., Scott, D.J., and Hall, J. 2002. The southeastern Churchill Province: synthesis of a Paleoproterozoic transpressional orogen. Canadian Journal of Earth Sciences, 39(5): 639–663. doi:10.1139/e02-004

Watt, W.S. 1969. The coast-parallel dike swarm of southwest Greenland in relation to the opening of the Labrador Sea. Canadian Journal of Earth Sciences. **6**: 1320–1321.
Wildman, M., Cogné, N., & Beucher, R. (2018). Fission-Track Thermochronology Applied to the Evolution of Passive Continental Margins. *Geography and Environment,* 351-371.

Wernicke, B. 1981. Low-angle normal faults in the Basin and Range Province: Nappe tectonics in an extending orogen. Nature. **291**: 645–648. DOI: 10.1038/291645a0.

Wernicke, B. 1985. Uniform-sense normal simple shear of the continental lithosphere. Canadian Journal of Earth Sciences. **22**: 108–125. DOI:10.1139/e85-009.

Wildman, M., Brown, R., Beucher, R., Persano, C., Stuart, F., Gallagher, K., Schwanethal, J., and Carter, A. 2016. The chronology and tectonic style of landscape evolution along the elevated Atlantic continental margin of South Africa resolved by joint apatite fission track and (U-Th-Sm)/He thermochronology. Tectonics. **35**: 511–545. DOI:10.1002/2015TC004042.

Willett, C.D., Fox, M., Shuster, D.L. 2017. A helium-based model for the effects of radiation damage annealing on helium diffusion kinetics in apatite. Earth and Planetary Science Letters. **447**: 195–204. https://doi.org/10.1016/j.epsl.2017.07.047.

Wolf, R.A., Farley, K.A., and Kass, D.M. 1998. Modeling of the temperature sensitivity of the apatite (U–Th)/He thermochronometer, Chemical Geology. **148**(1–2): 105–114.

Wolf, R.A., Farley, K.A., and Silver, L.T. 1996. Helium diffusion and low temperature thermochronometry of apatite. Geochimica Cosmochimica Acta **60**: 4231–4240.

Wolfe, M.R., and Stockli, D.F. 2010. Zircon (U–Th)/He thermochronometry in the KTB drill hole, Germany, and its implications for bulk He diffusion kinetics in zircon. Earth and Planetary Science Letters 295 (2010) 69–82.

Wu, L., Shi, G., Danišík, M., Zhang, Z., Wang, Y., and Wang, F. 2019. MK-1 apatite: a new potential reference material for (U-Th)/He dating. Geostandards and Geoanalytical Research. **43**(2).

Yamada R., Tagami T., Nishimura S., and Ito H. 1995. Annealing kinetics of fission tracks in zircon: An experimental study. Chem. Geol. 122, 249–258.

York, D. 1966. Least-squares fitting of a straight line. Canadian Journal of Physics. **44**(5): 1079–1086.

Zeitler, P., Herczeg, A., McDougall, I., and Honda, M. 1987. U–Th-He dating of apatite: a potential thermochronometer. Geochimica Cosmochimica Acta. **51**(10): 2865–2868.

APPENDIX A: Field methods and field notes

Fieldwork for this project was conducted with the Geological Survey of Canada (GSC) from July 4th–26th 2018, in Labrador, Canada. The field camp was based out of Hopedale, Labrador. Field sites were accessed by helicopter. Sample sites selected for the 2018 field season for this project were based on ideal rock type for thermochronology and strategic location. Specific GPS coordinates were selected as prospective field sites by comparing Google Earth Pro to GSC maps made by Ermanovics (1992) to target specific rock types, such as gneisses and tonalites, which contain apatite and zircon crystals used in AHe and ZHe thermochronology (Kohn et al., 2019 in Malusa and Fitzgerald, 2019). In the field, 1-3 kg of rock was collected per sample, plus a hand sample and a sample to be made into a thin section.

17 samples were collected in total. 6 samples were collected an average of 46 km apart from each other in a coastline-parallel transect, spanning ~174 km with northernmost sample located at 56.755560, -61.776530 and the southernmost sample located at 55.467139, -60.210862. This transect was used in the undergraduate honours thesis of Sarima Vahrenkamp, but not in this M.Sc. study. 11 samples were collected an average of ~13 km apart from each other in a coastline-perpendicular transect, spanning 112 km from a sample located at 55.842306, -60.324111 on the coast to a sample at 55.190889, -61.681167 inland.

Other samples used for this project are from the Taylor Collection in the GSC sample archives. These samples were collected by the GSC between 1967 and 1971 during "Opération Torngat". This part of the dataset comprises 3 coast-perpendicular transects at the latitudes of Saglek, Nain, and Makkovik consisting of 28 samples in total. Samples were chosen by Dr.

Coutand according to rock type, considering which rock types are most likely to carry apatite and zircon grains.

FIELD NOTES

Station: 18CXAK0006 (not used in this study)
Date: July 14, 2018
Location: 55.190882, -61.681176
Lithology: Gabbro anorthosite
Mineralogy: Ca-rich feldspar (Labradorite >5 cm), biotite, pyroxene, coarse grained, all euhedral crystals
Structures: N/A
Photo:

Station: 18CXAK0007 (not used in this study)
Date: July 14, 2018
Location: 55.11585267, -61.40472
Lithology: Amphibolite gneiss, no separated banding
Mineralogy: Quartz, K-feldspar, amphibole, fine grained, equigranular
Structures: Slight foliation oriented 223° – 062°
Photo:

Station: 18CXAK0008 (referred to as sample K0008)
Date: July 14, 2018
Location: 55.1437175, -61.08210583
Lithology: Tonalite gneiss
Mineralogy: K-feldspar, quartz
Structures: N/A
Photo:

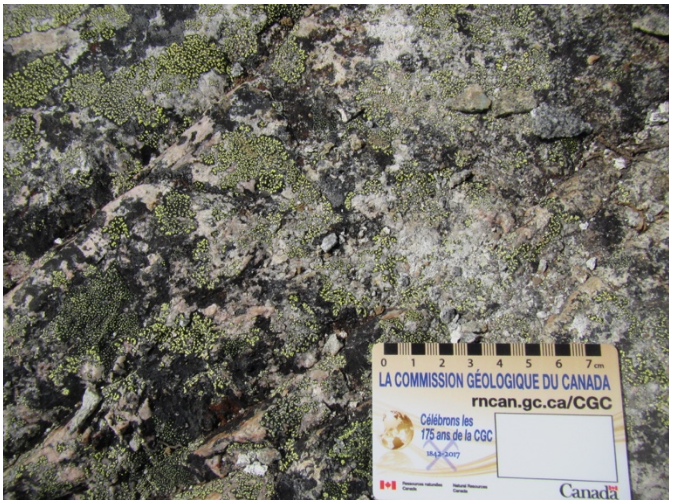

Station: 18CXAK0009 (referred to as sample K0009)
Date: July 14, 2018
Location: 55.2481815, -60.9630495
Lithology: Granite, or syeno-granite
Mineralogy: K-feldspar, possibly chlorite
Structures: N/A
Photo:

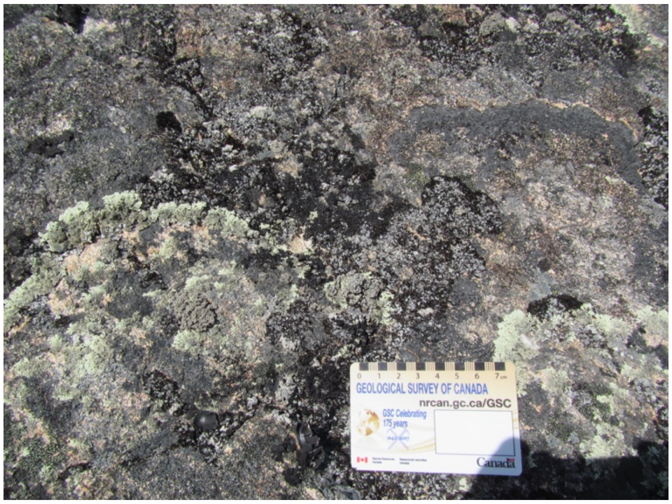

Station: 18CXAK0010 (referred to as sample K0010)
Date: July 15, 2018
Location: 55.370751167, -60.801542667
Lithology: Migmatitic orthogneiss (intermediate composition with some mafic and felsic end members)
Mineralogy: Quartz, K-feldspar, some plagioclase, biotite? Amphibole? Fine-grained.
Structures: Foliation banding oriented 040° – 220°, leucosome veins trnasposed
Photo:

Station: 18CXAK0011 (referred to as sample K0011)
Date: July 15, 2018
Location: 55.3962075, -60.67132483
Lithology: Quartz-K feldspar-biotite granite to orthogneiss. Very heterogenous outcrop (e.g. gneiss next to granite, next to pegmatite), isotriopic (no fabric)
Mineralogy: Quartz, k-feldspar (in pegmatite), biotite, some medium to fine grained, some pegmatite

Structures: N/A
Photo:

Station: 18CXAK0012 (referred to as sample K0012)
Date: July 15, 2018
Location: 55.469593833, -60.6000881667
Lithology: Mafic-intermediate migmatitic orthogneiss, tonalitic components, granite (ranges in composition)
Mineralogy: K-feldspar, plagioclase, biotite, amphibole, quartz
Structures: Quartz veins, foliation (also refolded), folds (both large and small scale)
Photo:

Station: 18CXAK0013 (referred to as sample K0013)
Date: July 15, 2018
Location: 55.61196433, -60.525673667
Lithology: intermediate-mafic migmatitic orthogneiss (grey rock, no K-feldspar)

Mineralogy: Plagioclase, amphibole (hornblende), quartz (veins), biotite
Structures: Folded quartz veins, veins up to 1 m wide, cross cutting relationships
Photo:

Station: 18CXAK0014 (referred to as sample K0014)
Date: July 17, 2018
Location: 55.74064733, -60.419617833
Lithology: melted pegmatite, metagranite (metaplutonic/gneiss), granodiorite with pegmatitic layers in some places
Mineralogy: K-feldspar, quartz, chlorite? Allanite, epidote
Structures: Gneissic foliation, diatexis
Photo:

Station: 18CXAK0015 (referred to as sample K0015)
Date: July 17, 2018
Location: 55.79223, -60.39590667

Lithology: Granite, metaplutonic, very heterogeneous outcrop (changes from pegmatite to gneiss)
Mineralogy: Coarse grained, very quartz-rich, biotite, K-feldspar
Structures: Foliation, compositional banding
Photo:

Station: 18CXAK0016 (rederred to as sample K0016)
Date: July 17, 2018
Location: 55.84231033, -60.3241091667
Lithology: Migmatitic granodiorite, partial melting in-situ, gneissosity – transposed leucosome
Mineralogy: Quartz, biotite, feldspar, chlorite
Structures: Quartz veins, mafic dykes
Photo:

APPENDIX B: Calculations used in *Helios* software

Helios software was written by Dr. Roman Kislitsyn to approximate the *t* variable in the Age Equations using Taylor Series Expansion. It was initially written in VBA for Excel in 2007, then revised for Visual Basic .Net in 2008, and is now being working to a database that is integrated in Helios (2020). The calculations are as follows (personal communication, Dr. Roman Kislitsyn, July 24, 2020):

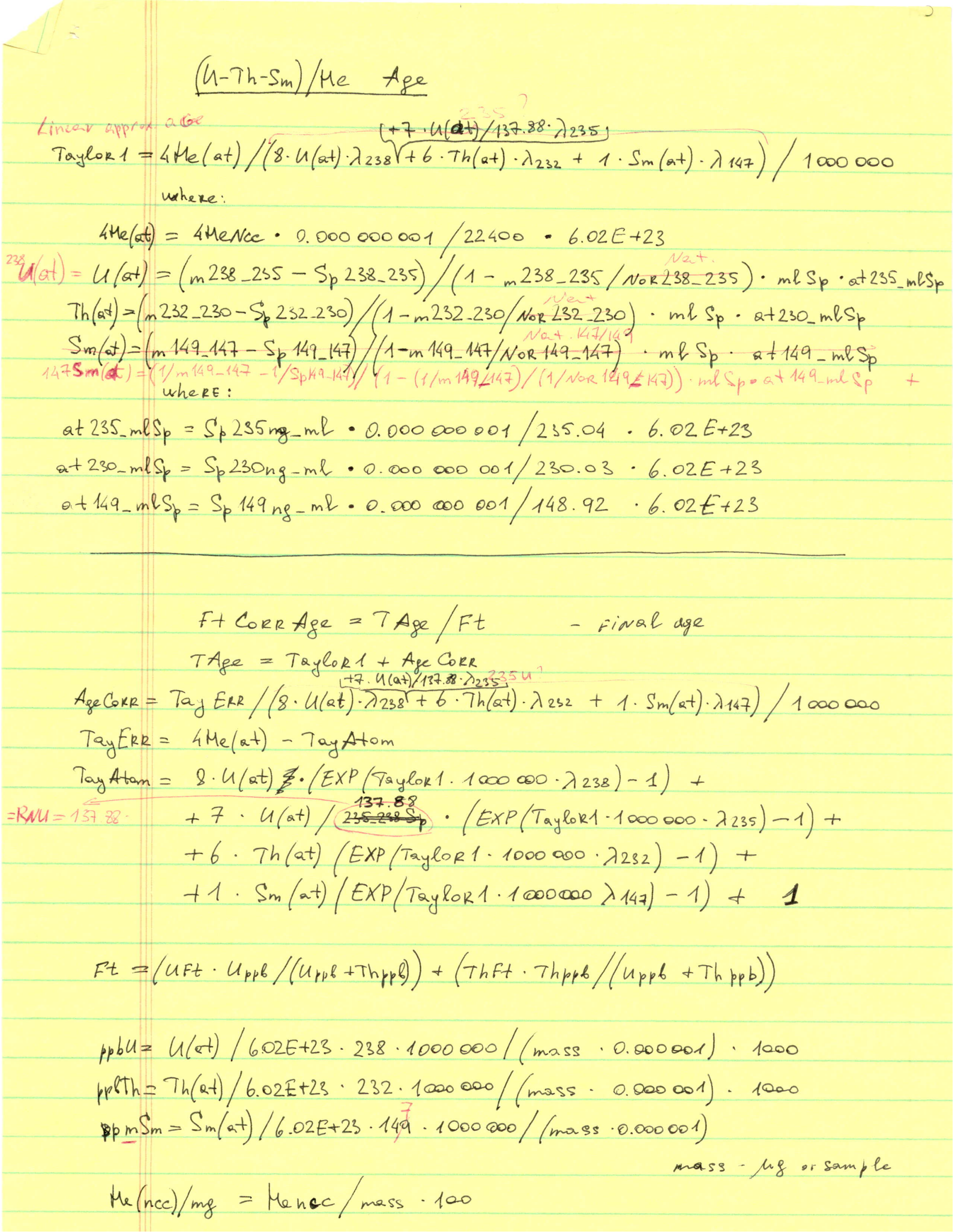

(U-Th-Sm)/He Age

Linear approx. age

235 ?

(+7 · U(at) / 137.88 · λ_{235})

Taylor1 = 4He(at) / (8 · U(at) · λ_{238} + 6 · Th(at) · λ_{232} + 1 · Sm(at) · λ_{147}) / 1 000 000

where:

4He(at) = 4HeNcc · 0.000 000 001 / 22400 · 6.02E+23

^{238}U(at) = U(at) = (m238_235 − Sp 238_235) / (1 − m238_235 / Nat. NoR 238_235) · ml Sp · at235_mlSp

Th(at) = (m232_230 − Sp 232_230) / (1 − m232_230 / Nat NoR 232_230) · ml Sp · at230_mlSp

Nat. 147/149

~~Sm(at) = (m149_147 − Sp 149_147) / (1 − m149_147 / NoR 149_147) · ml Sp · at149_mlSp~~

147Sm(at) = (1/m149_147 − 1/Sp149_147) / (1 − (1/m149_147) / (1/NoR 149_147)) · ml Sp · at149_ml Sp +

where:

at235_mlSp = Sp235ng_ml · 0.000 000 001 / 235.04 · 6.02E+23

at230_mlSp = Sp230ng_ml · 0.000 000 001 / 230.03 · 6.02E+23

at149_mlSp = Sp149ng_ml · 0.000 000 001 / 148.92 · 6.02E+23

Ft Corr Age = TAge / Ft — final age

TAge = Taylor1 + Age Corr

+7 · U(at) / 137.88 · λ_{235} 235U ?

AgeCorr = Tay Err / (8 · U(at) · λ_{238} + 6 · Th(at) · λ_{232} + 1 · Sm(at) · λ_{147}) / 1 000 000

TayErr = 4He(at) − TayAtom

TayAtom = 8 · U(at) ~~3~~ · (EXP(Taylor1 · 1 000 000 · λ_{238}) − 1) +

=RNU = 137.88

+ 7 · U(at) / 137.88 ~~235_238 Sp~~ · (EXP(Taylor1 · 1 000 000 · λ_{235}) − 1) +

+ 6 · Th(at) (EXP(Taylor1 · 1000 000 · λ_{232}) − 1) +

+ 1 · Sm(at) (EXP(Taylor1 · 1000000 λ_{147}) − 1) + 1

Ft = (UFt · U_{ppb} / (U_{ppb} + Th_{ppb})) + (ThFt · Th_{ppb} / (U_{ppb} + Th_{ppb}))

ppbU = U(at) / 6.02E+23 · 238 · 1000 000 / (mass · 0.000 001) · 1000

ppbTh = Th(at) / 6.02E+23 · 232 · 1000 000 / (mass · 0.000 001) · 1000

ppmSm = Sm(at) / 6.02E+23 · 14~~9~~7 · 1000 000 / (mass · 0.000 001)

mass - µg or sample

He(ncc)/mg = Hencc / mass · 100

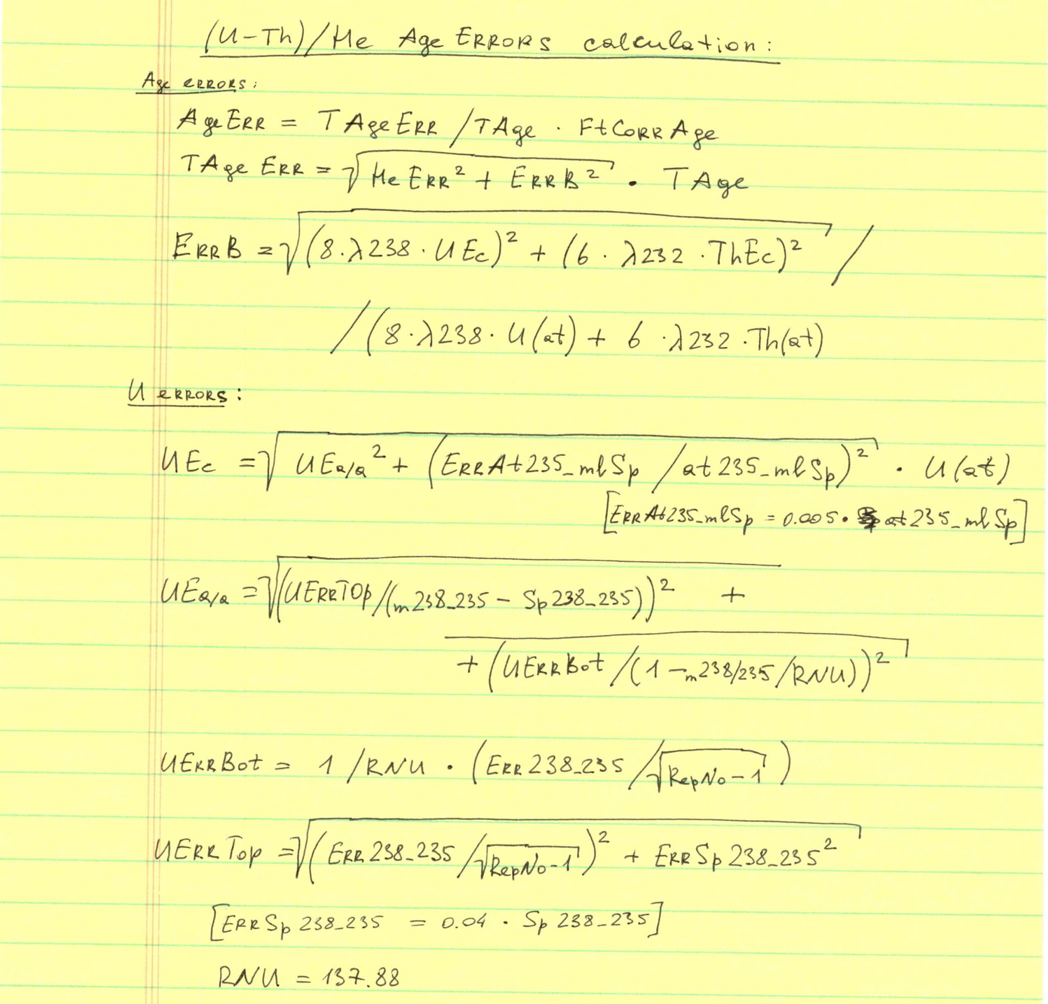

(U-Th)/He Age Errors calculation:

Age errors:

$$\text{AgeErr} = \text{TAgeErr} / \text{TAge} \cdot \text{FtCorrAge}$$

$$\text{TAgeErr} = \sqrt{\text{HeErr}^2 + \text{ErrB}^2} \cdot \text{TAge}$$

$$\text{ErrB} = \sqrt{(8 \cdot \lambda 238 \cdot \text{UEc})^2 + (6 \cdot \lambda 232 \cdot \text{ThEc})^2} \, / \, / (8 \cdot \lambda 238 \cdot \text{U(at)} + 6 \cdot \lambda 232 \cdot \text{Th(at)})$$

U errors:

$$\text{UEc} = \sqrt{\text{UE}_{a/a}{}^2 + (\text{ErrAt235\_mlSp} / \text{at235\_mlSp})^2} \cdot \text{U(at)}$$

$$[\text{ErrAt235\_mlSp} = 0.005 \cdot \text{at235\_mlSp}]$$

$$\text{UE}_{a/a} = \sqrt{(\text{UErrTop} / (\text{m238\_235} - \text{Sp238\_235}))^2 + + (\text{UErrBot} / (1 - \text{m238/235} / \text{RNU}))^2}$$

$$\text{UErrBot} = 1 / \text{RNU} \cdot \left(\text{Err238\_235} / \sqrt{\text{RepNo} - 1}\right)$$

$$\text{UErrTop} = \sqrt{\left(\text{Err238\_235} / \sqrt{\text{RepNo} - 1}\right)^2 + \text{ErrSp238\_235}^2}$$

$$[\text{ErrSp238\_235} = 0.04 \cdot \text{Sp238\_235}]$$

$$\text{RNU} = 137.88$$

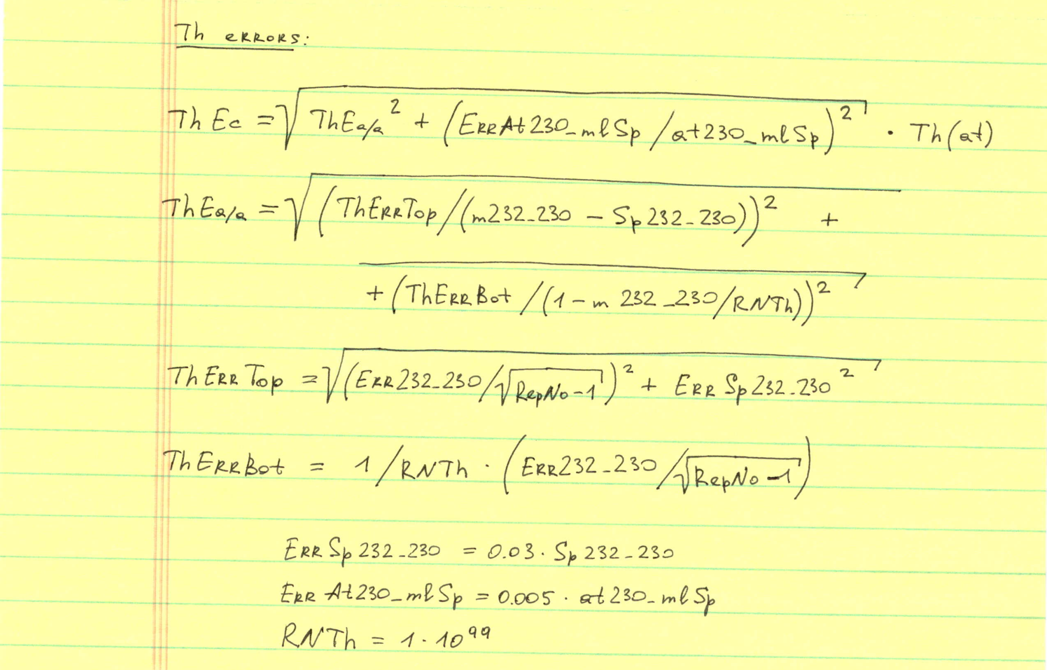

Th errors:

$$\text{ThEc} = \sqrt{\text{ThE}_{a/a}{}^2 + (\text{ErrAt230\_mlSp} / \text{at230\_mlSp})^2} \cdot \text{Th(at)}$$

$$\text{ThE}_{a/a} = \sqrt{(\text{ThErrTop} / (\text{m232\_230} - \text{Sp232\_230}))^2 + + (\text{ThErrBot} / (1 - \text{m232\_230} / \text{RNTh}))^2}$$

$$\text{ThErrTop} = \sqrt{\left(\text{Err232\_230} / \sqrt{\text{RepNo} - 1}\right)^2 + \text{ErrSp232\_230}^2}$$

$$\text{ThErrBot} = 1 / \text{RNTh} \cdot \left(\text{Err232\_230} / \sqrt{\text{RepNo} - 1}\right)$$

$$\text{ErrSp232\_230} = 0.03 \cdot \text{Sp232\_230}$$

$$\text{ErrAt230\_mlSp} = 0.005 \cdot \text{at230\_mlSp}$$

$$\text{RNTh} = 1 \cdot 10^{99}$$

APPENDIX C: Grain photos and measurements

Saglek Transect			
Zircon samples			
Sample ID		**Measurements (µm)**	**Photo**
z67SC216	1	Length = 148.30 Width = 48.53	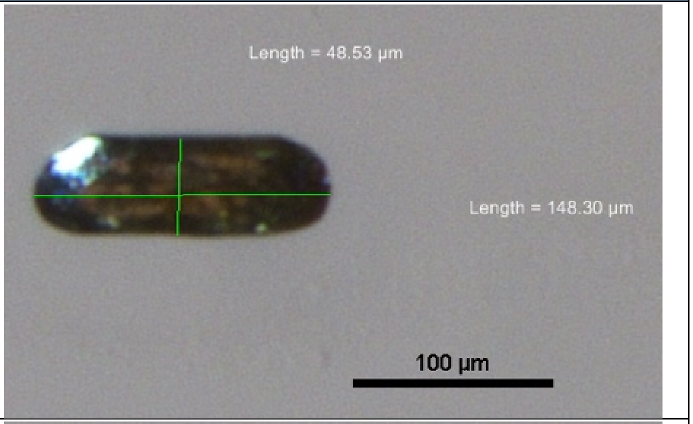
	2	Length = 236.04 Width = 99.1	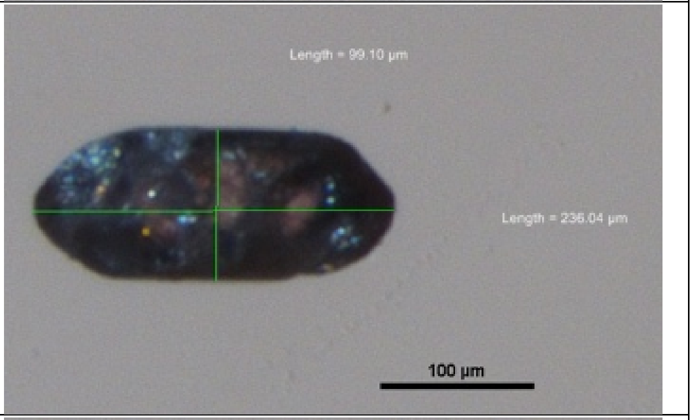
	3	Length = 223.04 Width = 68.87	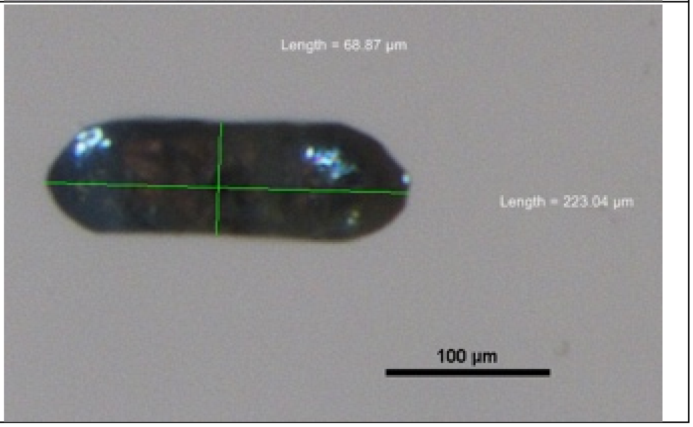

	4	Length = 193.03 Width = 56.09	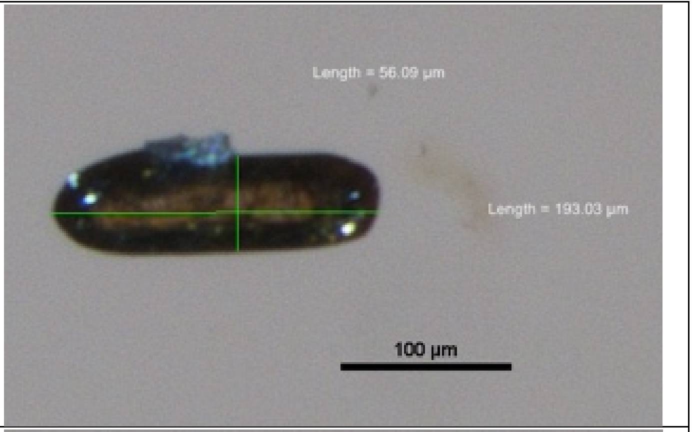
	5	Length = 188.91 Width = 56.16	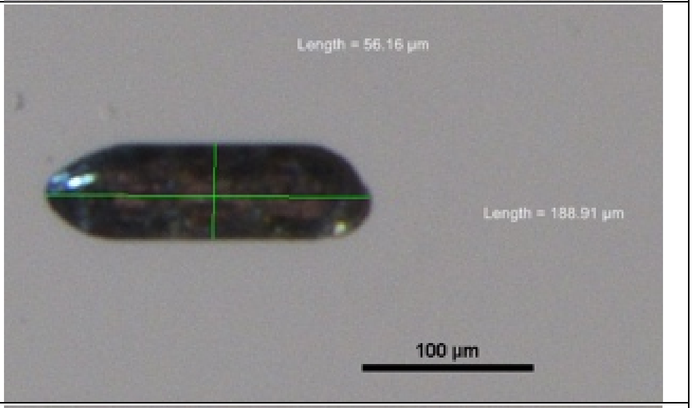
z69TA217	1	Length = 266.32 Width = 86.39	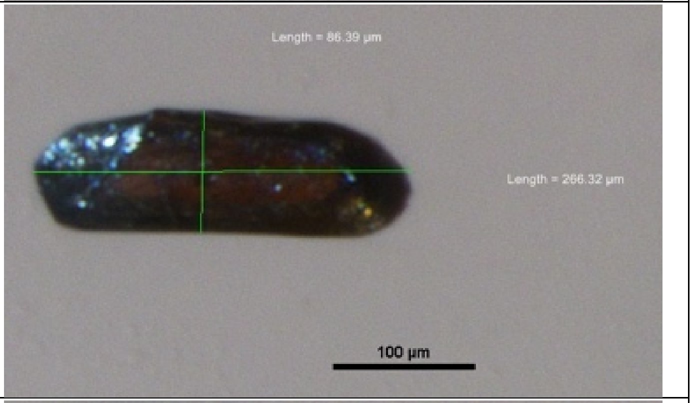
	2	Length = 169.98 Width = 76.76	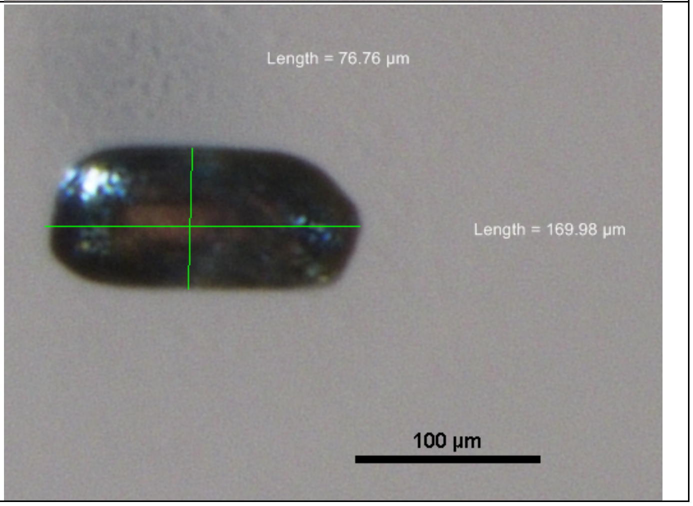

	3	Length = 271.14 Width = 82.95	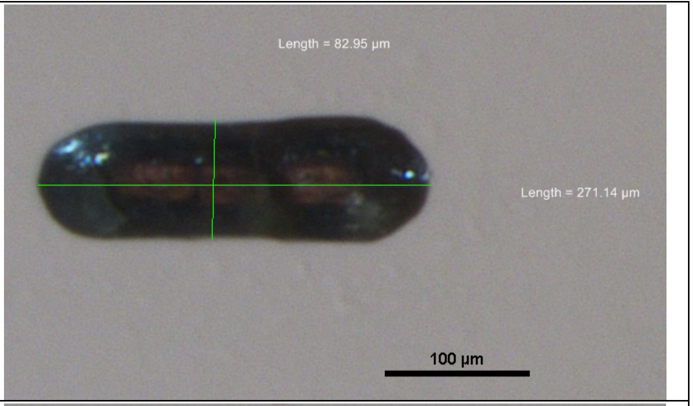
	4	Length = 286.6 Width = 80.42	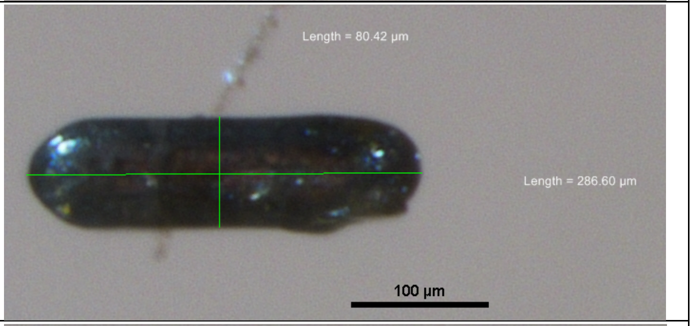
	5	Length = 239.48 Width = 74.52	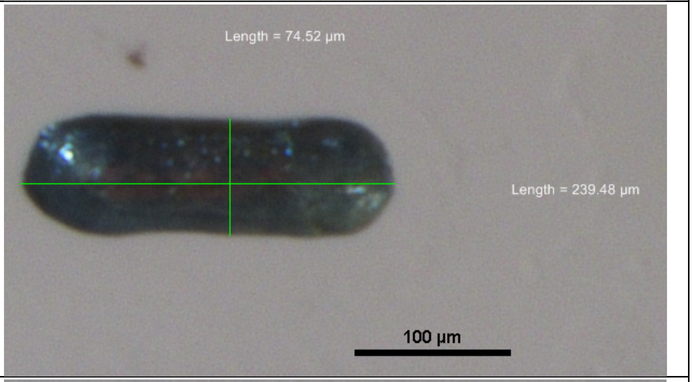
z67SC218	1	Length = 121.81 Width = 49.20	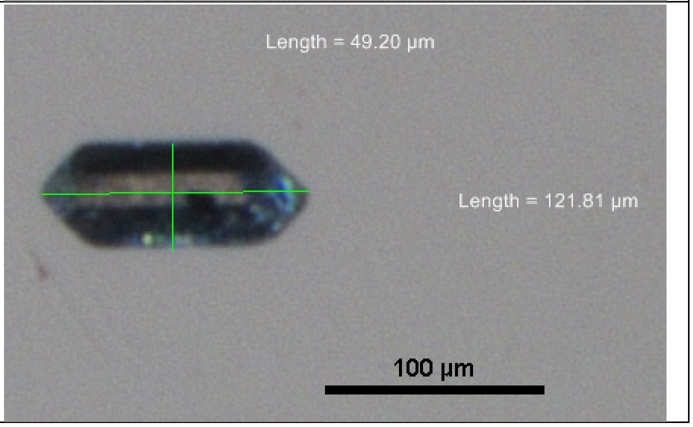

	2	Length = 141.42 Width = 55.41	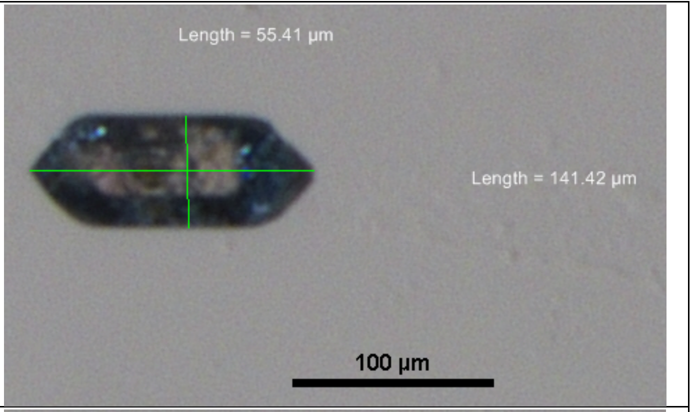
	3	Length = 198.19 Width = 75.02	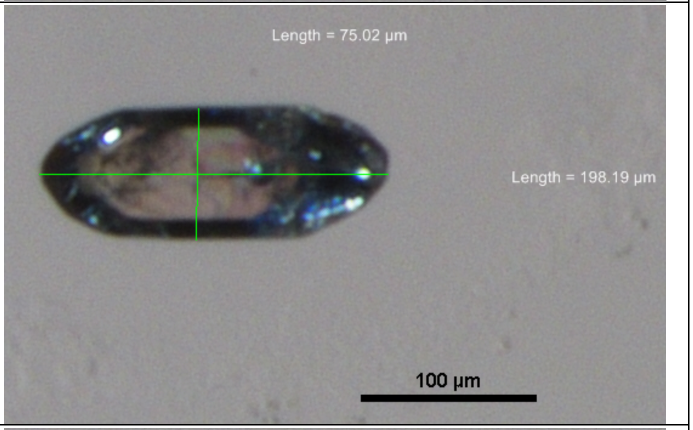
	4	Length = 133.85 Width =57.46	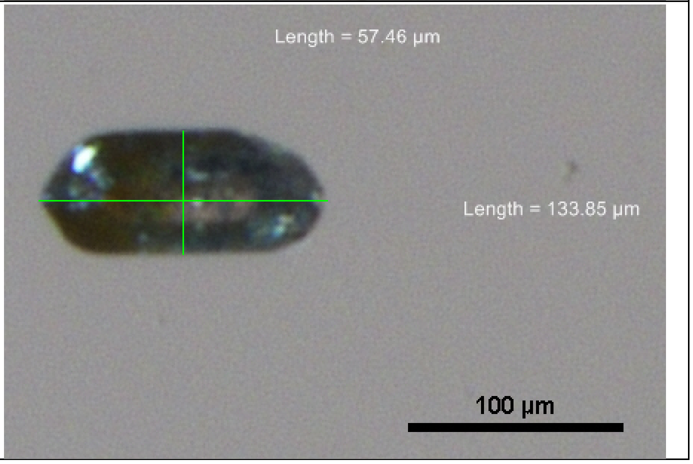

	5	Length = 99.78 Width = 39.57	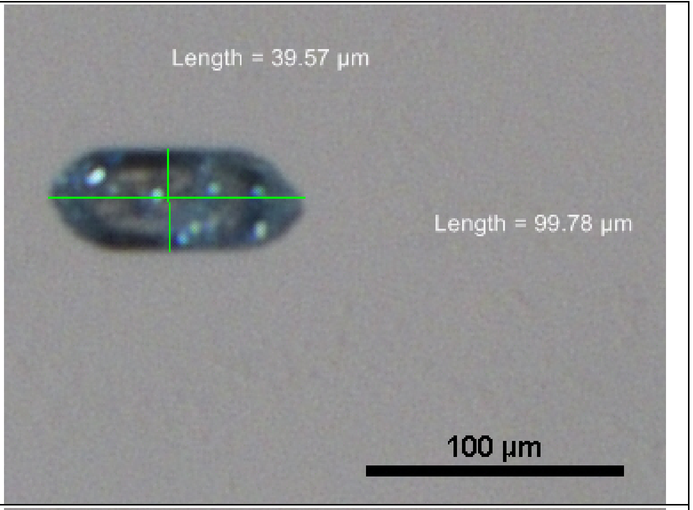
z69TA212	1	Length = 395.01 Width = 124.56	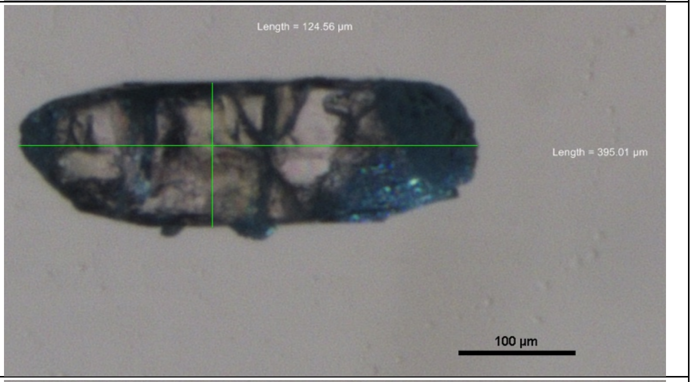
	2	Length = 434.93 Width = 167.97	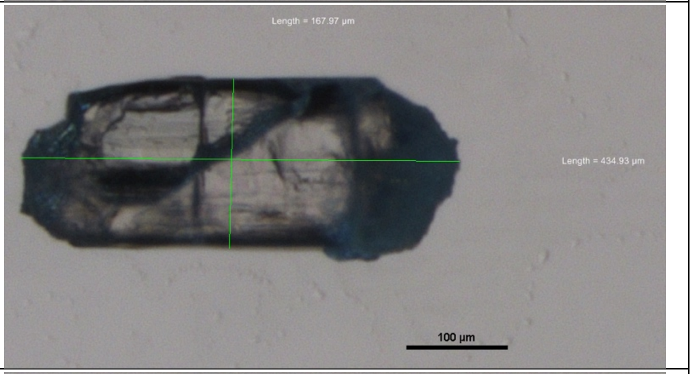
	3	Length = 463.48 Width = 135.58	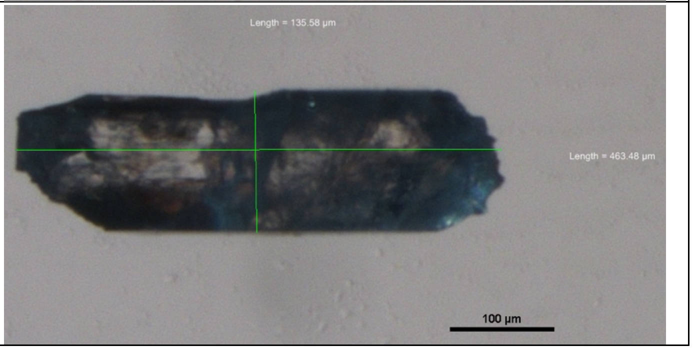

	4	Length = 342.02 Width = 137.98	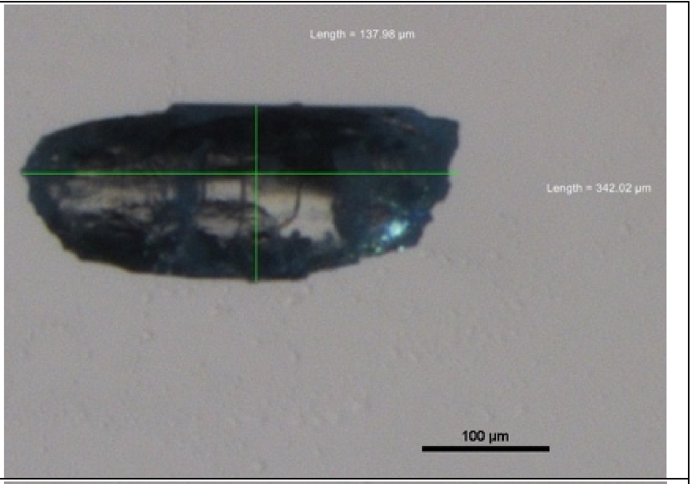
	5	Length = 333.76 Width = 127.31	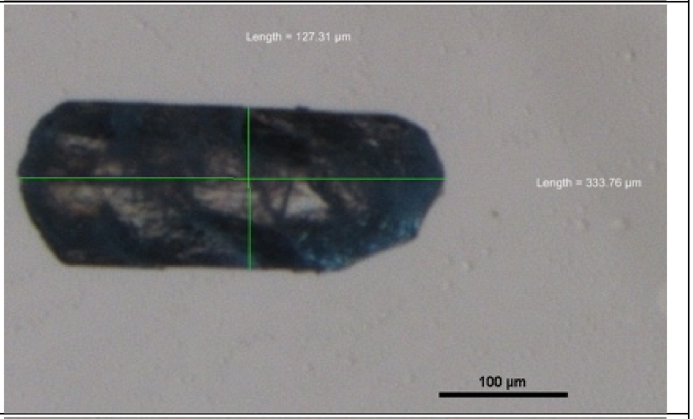
z69TA201	1	Length = 183.77 Width = 68.51	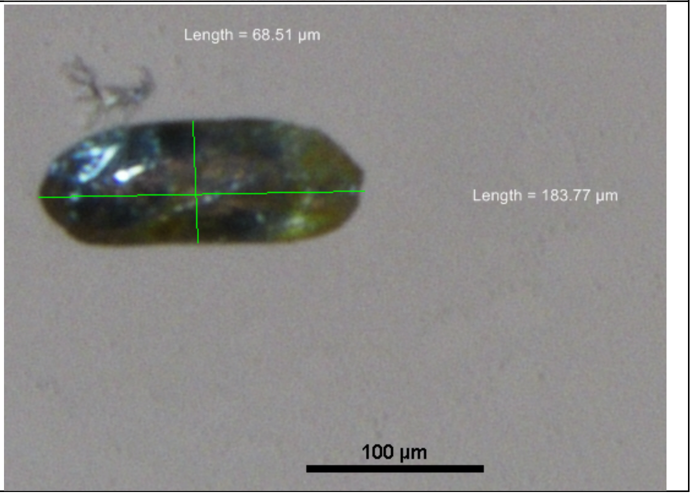

	2	Length = 175.90 Width = 92.34	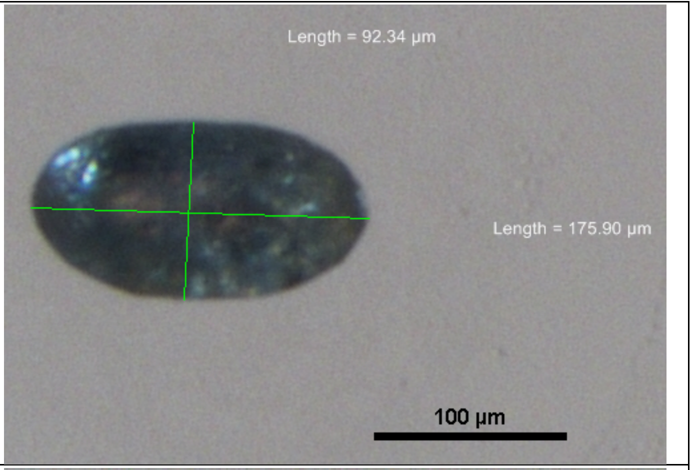
	3	Length = 167.32 Width = 81.50	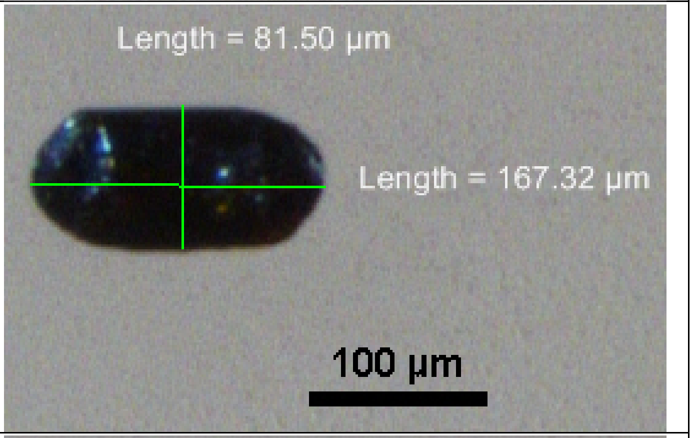
	4	Length = 181.33 Width = 94.97	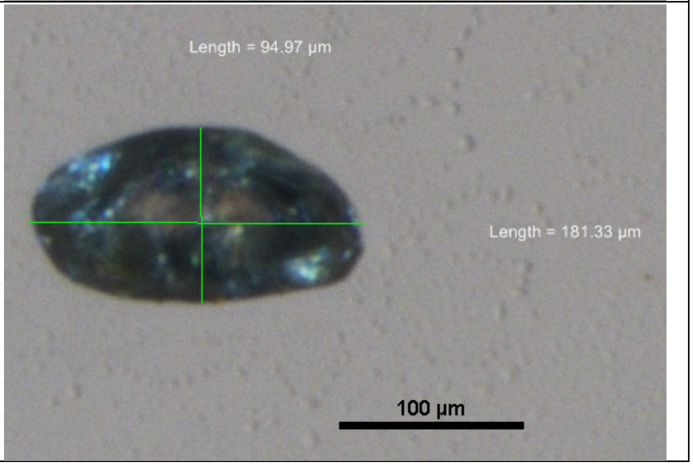

<table>
<tr><td></td><td>5</td><td>Length = 171.35
Width = 112.52</td><td>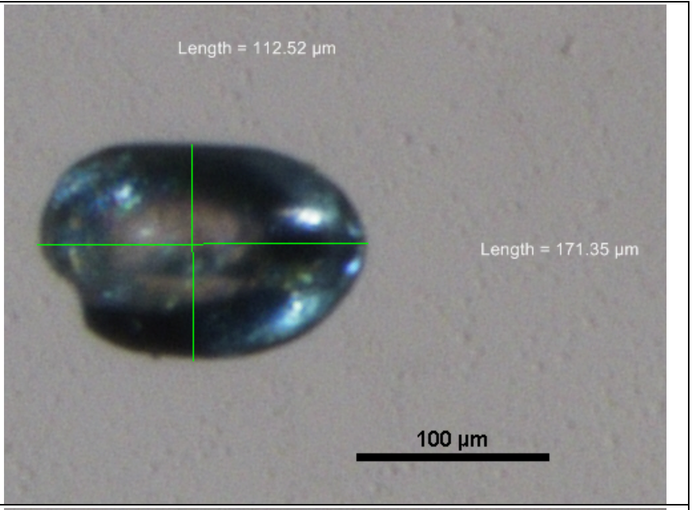
</td></tr>
<tr><td rowspan="3">z69TA210</td><td>1</td><td>Length = 323.44
Width = 122.84</td><td>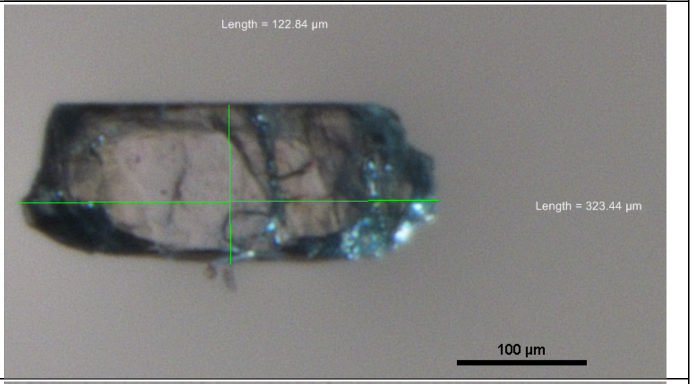
</td></tr>
<tr><td>2</td><td>Length = 307.62
Width = 83.61</td><td>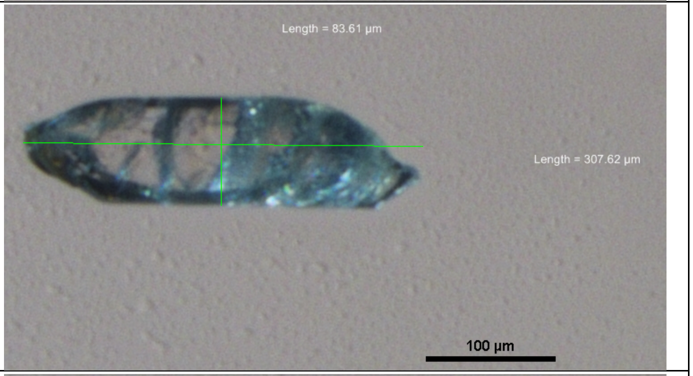
</td></tr>
<tr><td>3</td><td>Length = 321.06
Width = 135.61</td><td>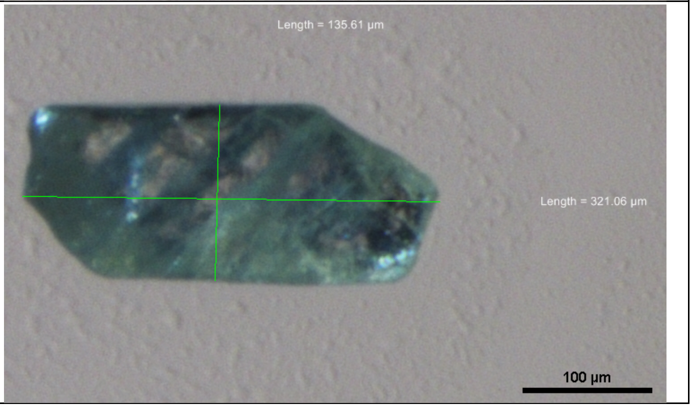
</td></tr>
</table>

	4	Length = 276.65 Width = 147.61	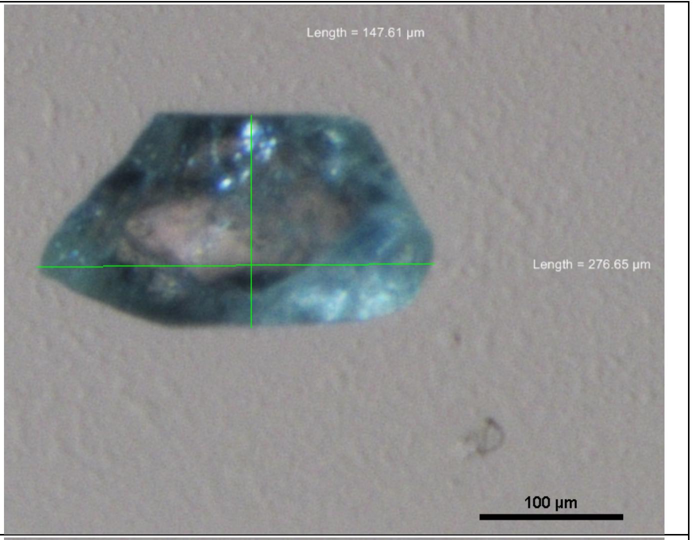
	5	Length = 177.89 Width = 103.57	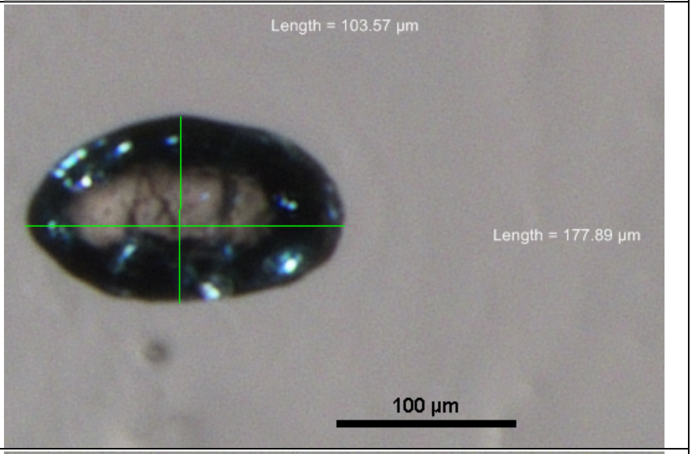
z69TA206	1	Length = 205.65 Width = 69.09	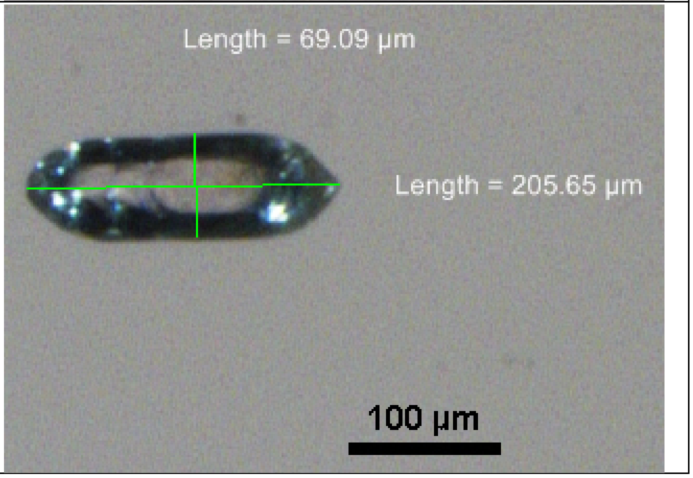

	2	Length = 153.82 Width = 69.85	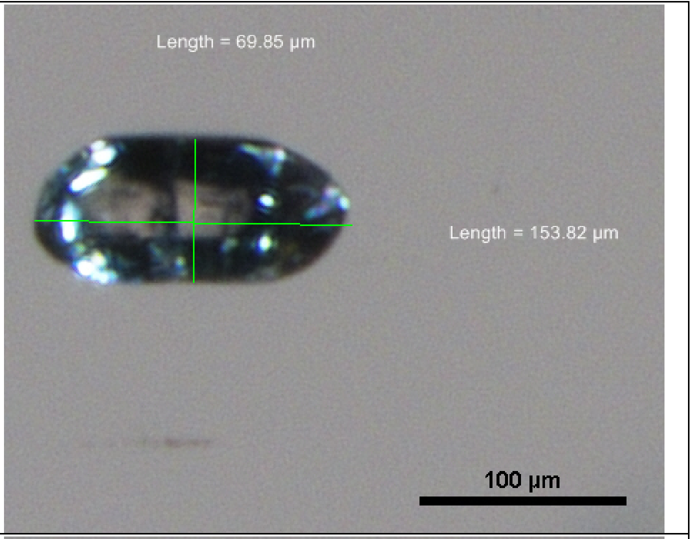
	3	Length = 196.89 Width = 76.77	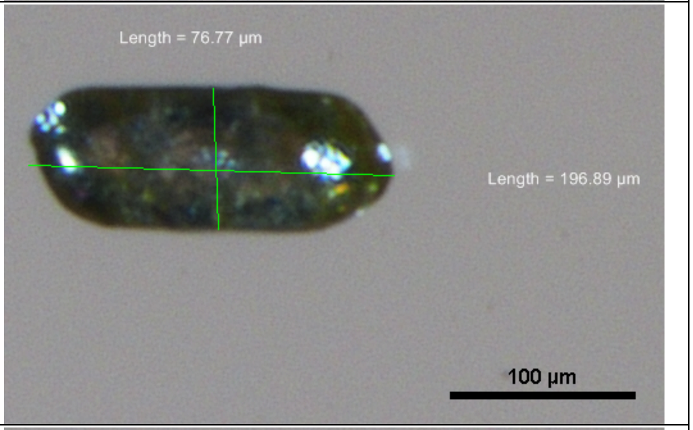
	4	Length = 171.49 Width = 63.08	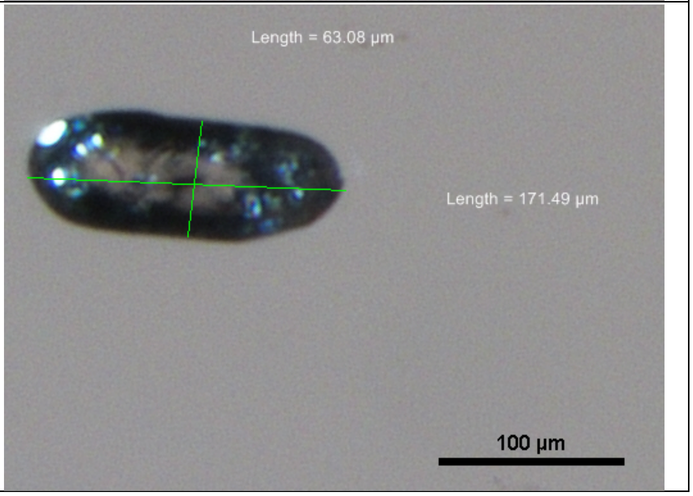

	5	Length = 171.43 Width = 69.99	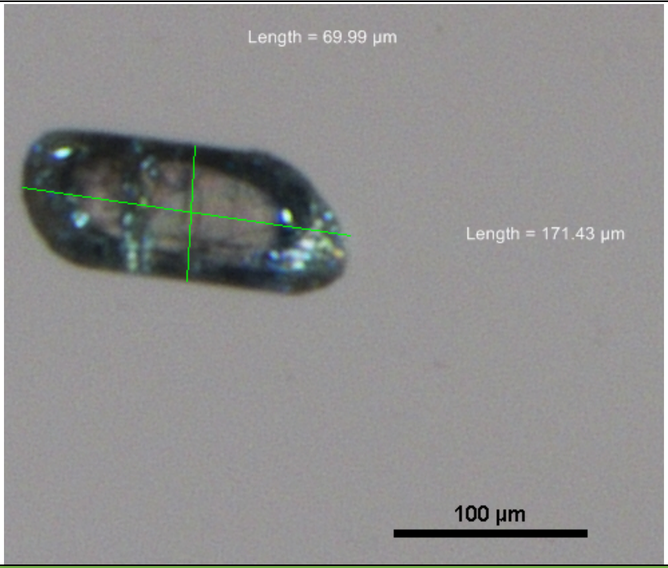
Apatite Samples			
Sample ID		Measurements (µm)	Photo
a67SC216	1	Length = 158.97 Width = 98.41	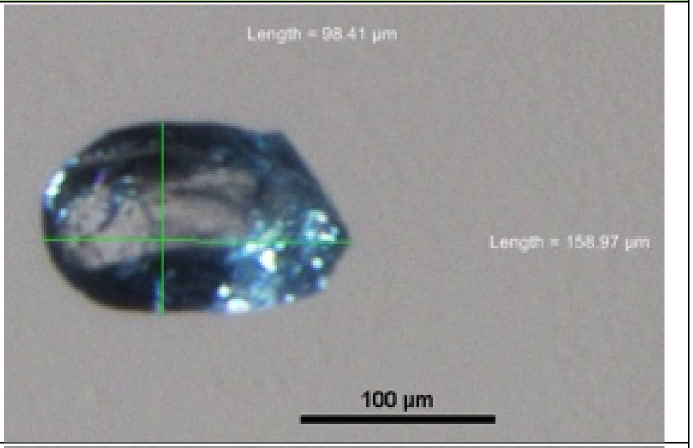
	2	Length = 160.00 Width = 108.04	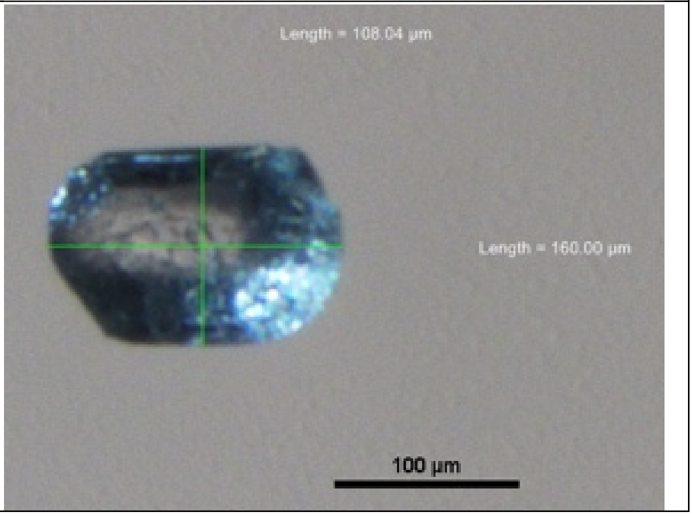

	3	Length = 157.59 Width = 103.60	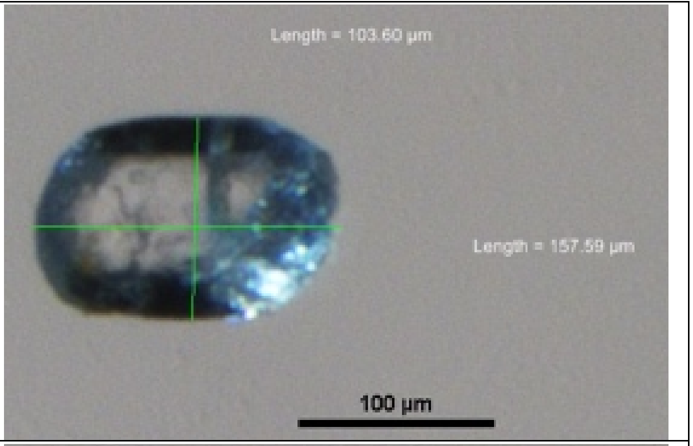
	4	Length = 111.48 Width = 77.76	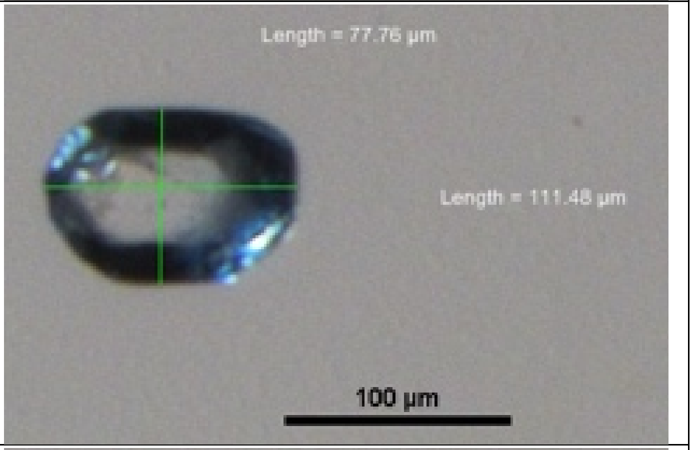
	5	Length = 137.98 Width = 85.68	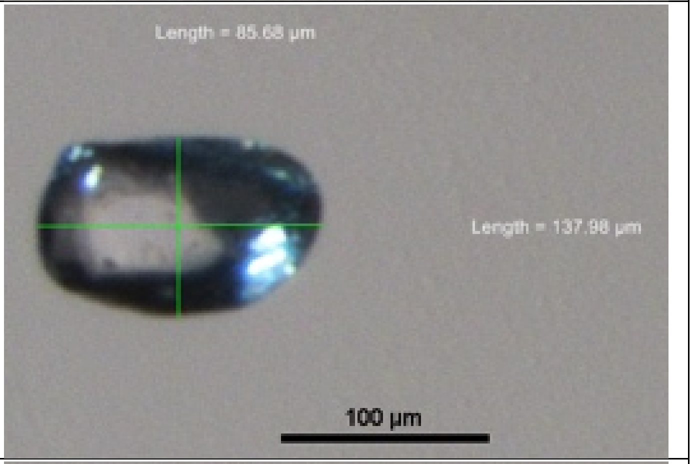
a69TA217	1	Length = 212.79 Width = 94.34	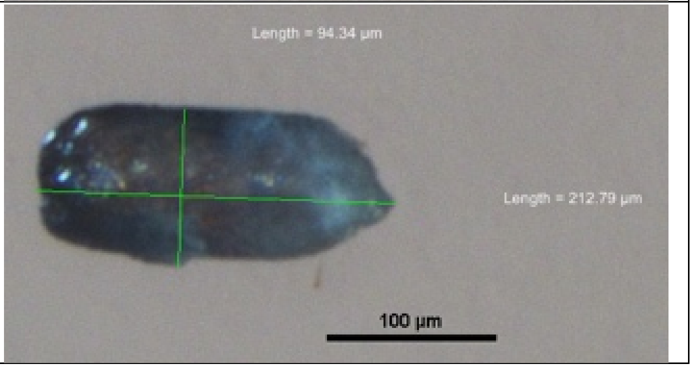

	2	Length = 273.99 Width = 134.68	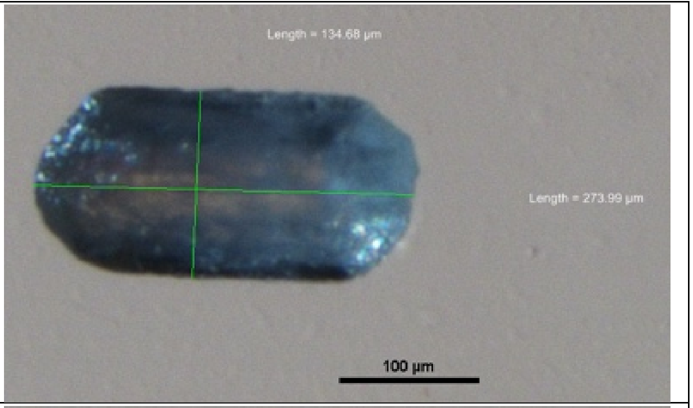
	3	Length = 171.01 Width = 98.79	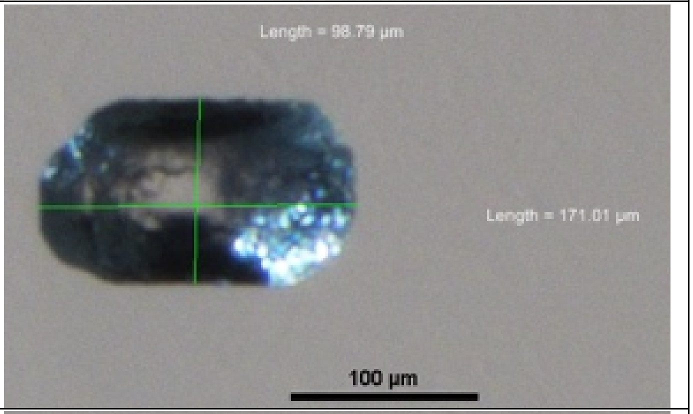
	4	Length = 190.62 Width = 129.79	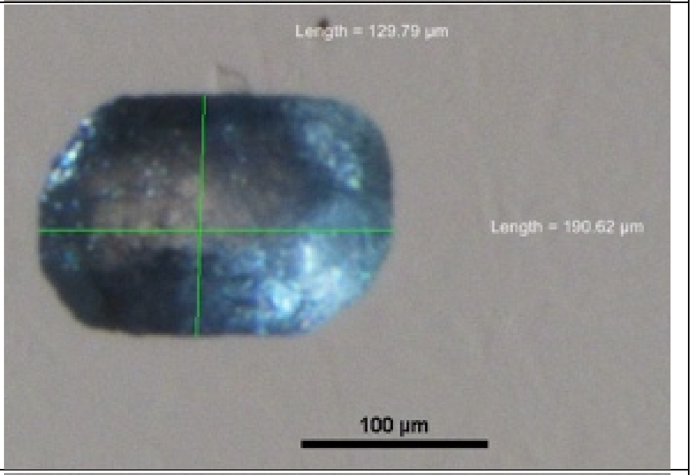
	5	Length = 131.10 Width = 71.91	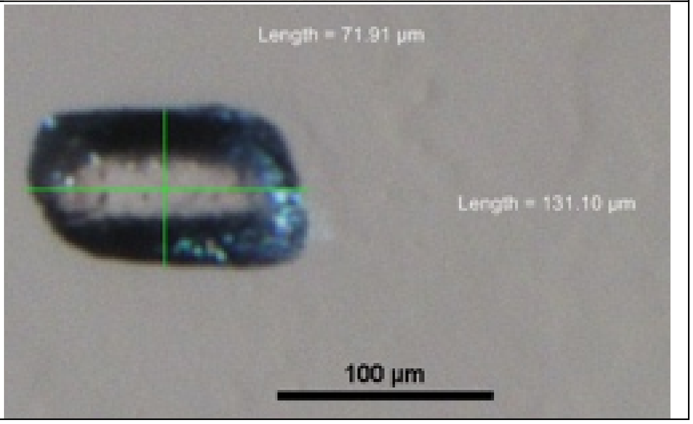

a69TA218	1	Length = 180.65 Width = 138.67	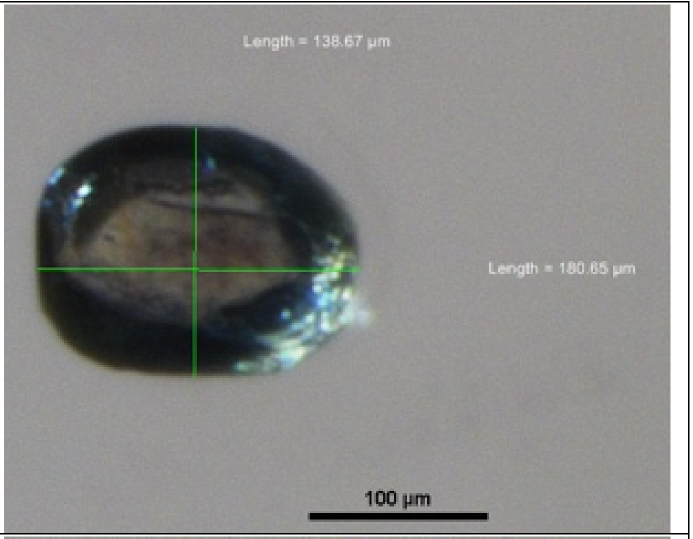
	2	Length = 162.51 Width = 118.76	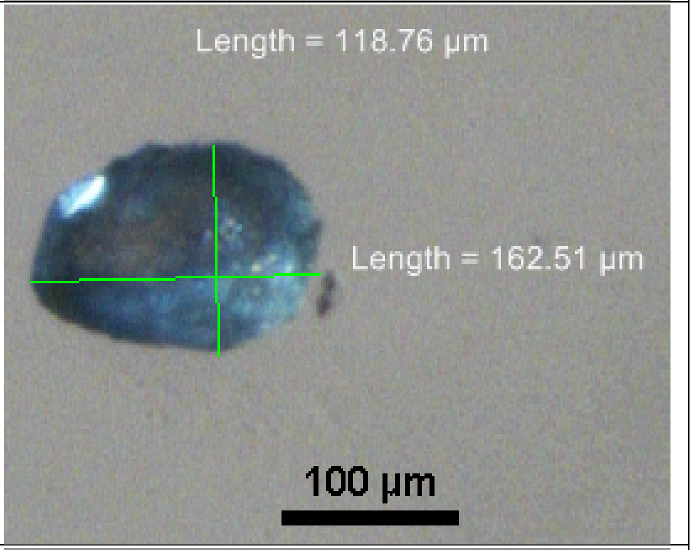
	3	Length = 137.29 Width = 83.28	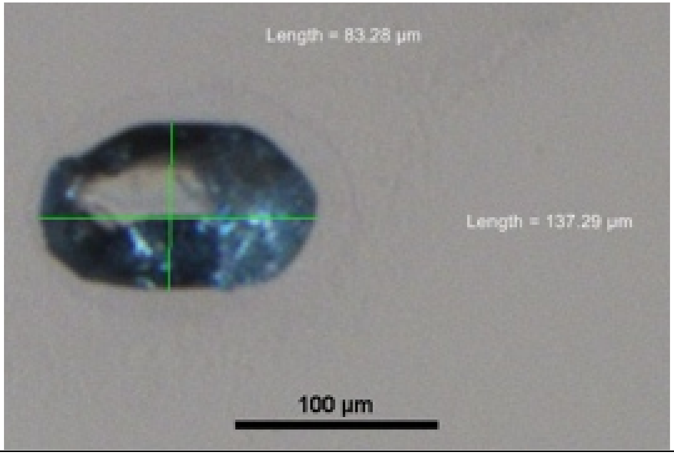

	4	Length = 118.31 Width = 78.20	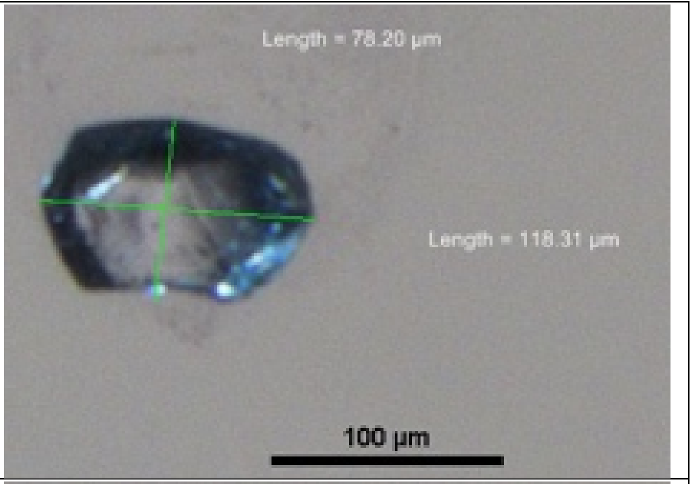
	5	Length = 116.68 Width = 76.32	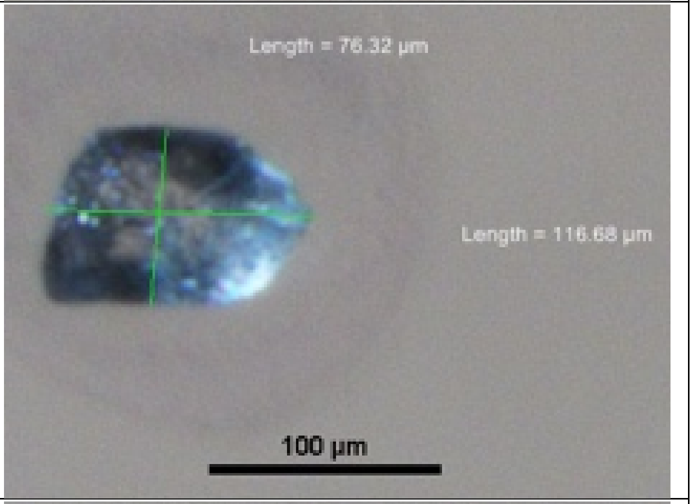
a96TA212	1	Length = 243.63 Width = 148.31	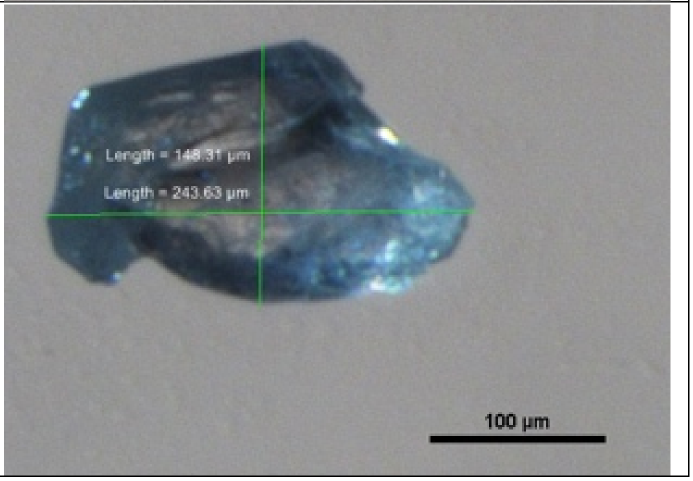

	2	Length = 222.30 Width = 111.52	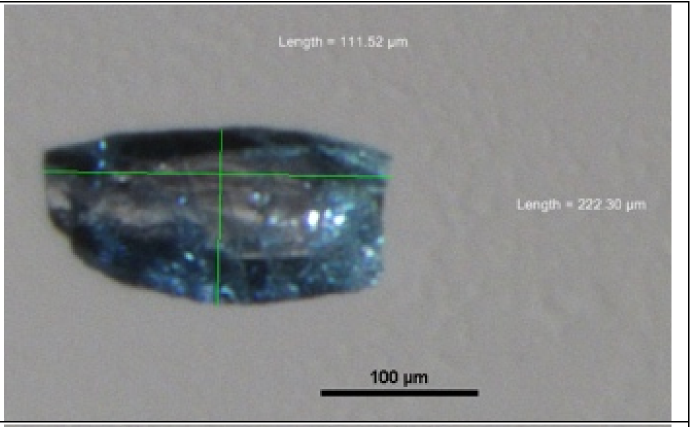
	3	Length = 175.86 Width = 115.35	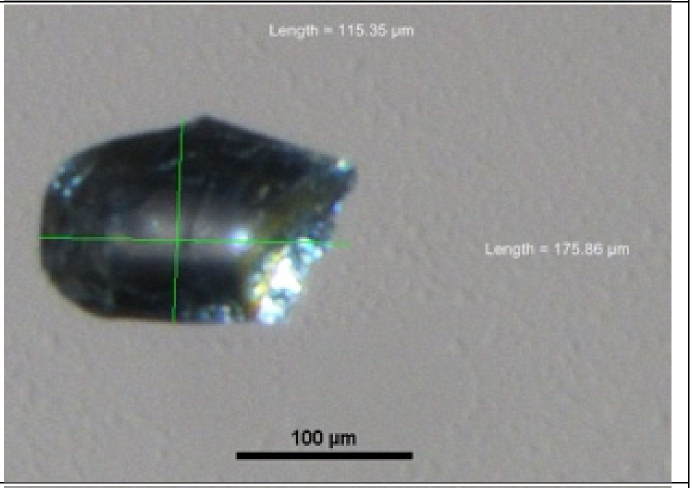
	4	Length = 198.56 Width = 98.09	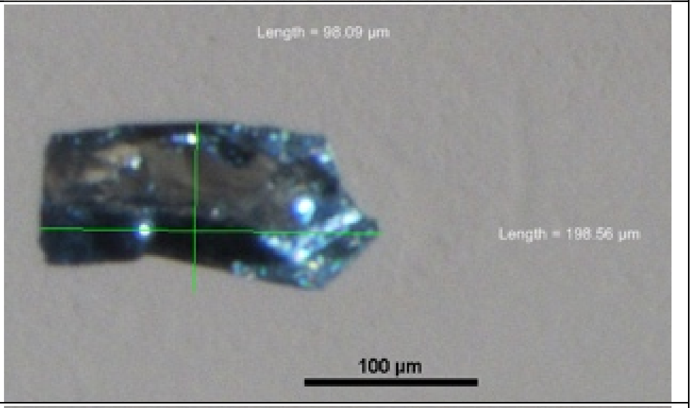
	5	Length = 250.87 Width = 102.90	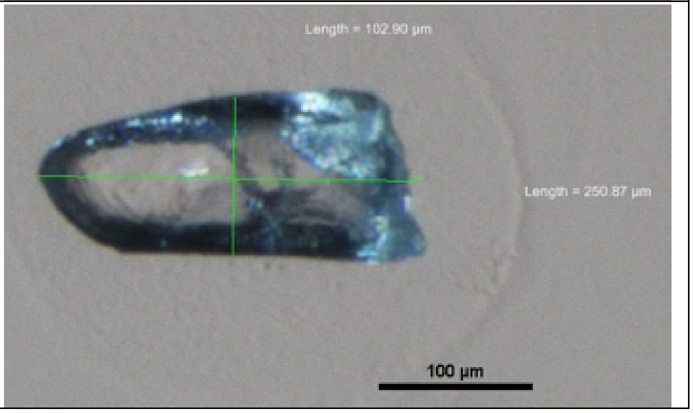

Nain Transect			
Zircon samples			
Sample ID		**Measurements (µm)**	**Photo**
z69FQ332	1	Length = 211.36 Width = 68.25	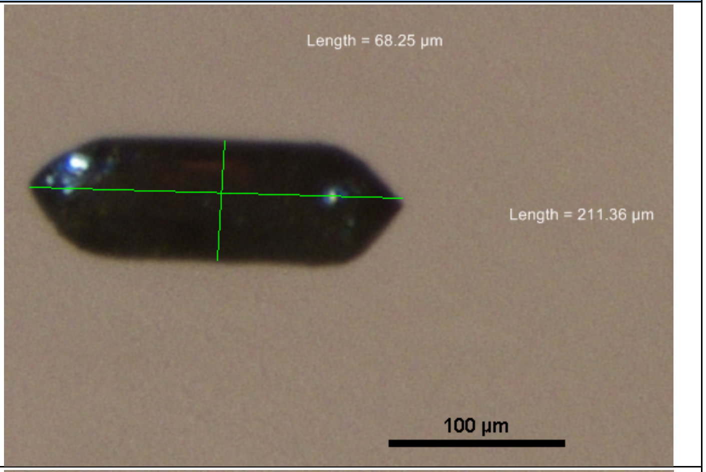
	2	Length = 174.90 Width = 53.53	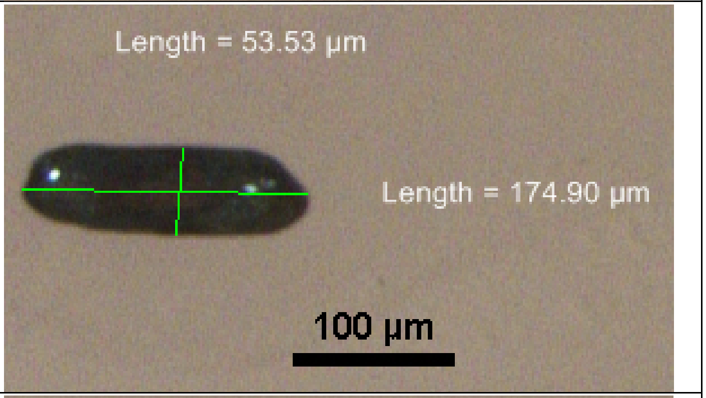
	3	Length = 138.67 Width = 53.36	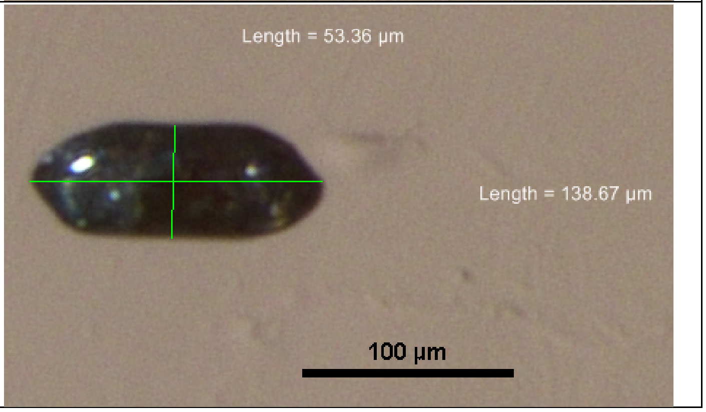

	4	Length = 165.04 Width = 59.90	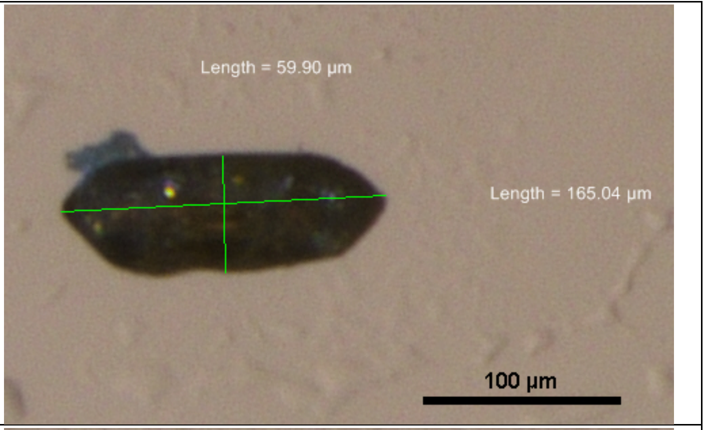
	5	Length = 138.24 Width = 61.62	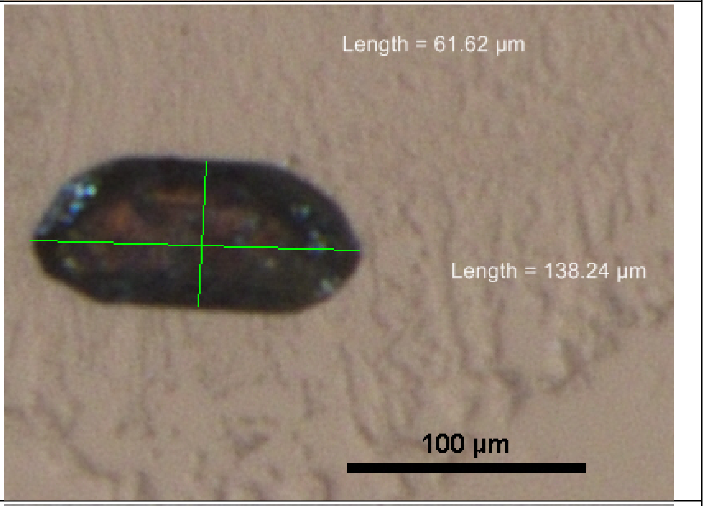
z69FQ335	1	Length = 206.80 Width = 80.86	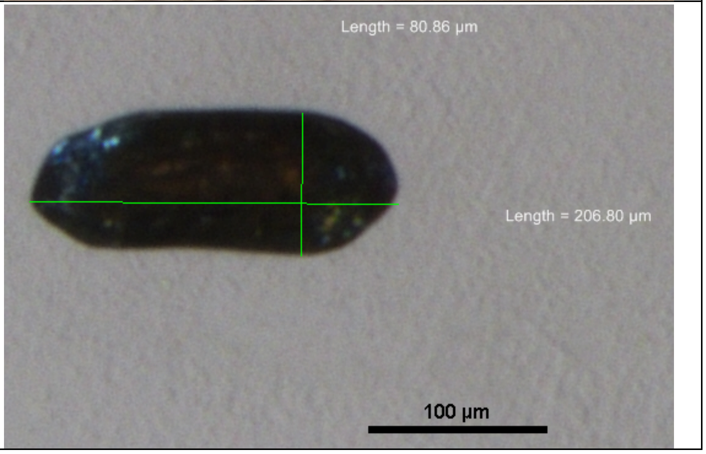

	2	Length = 207.49 Width = 68.82	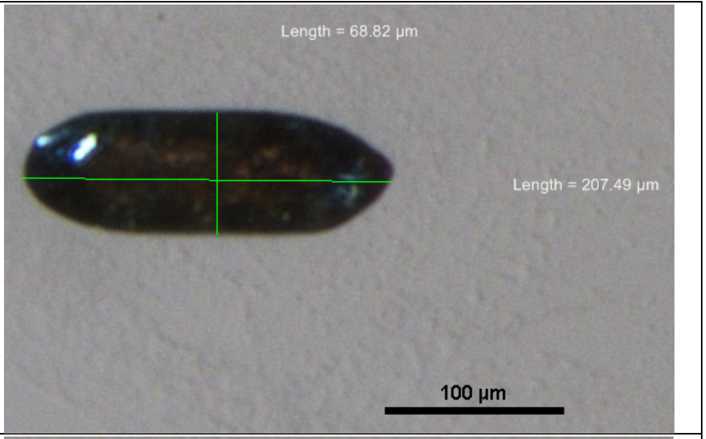
	3	Length = 189.59 Width = 88.43	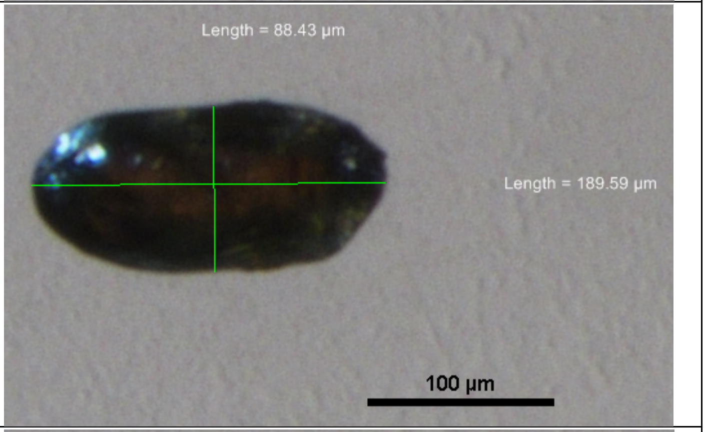
	4	Length = 157.94 Width = 65.72	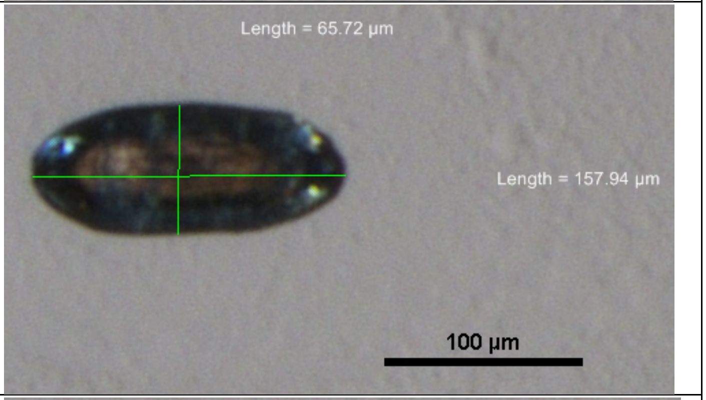
	5	Length = 167.57 Width = 56.09	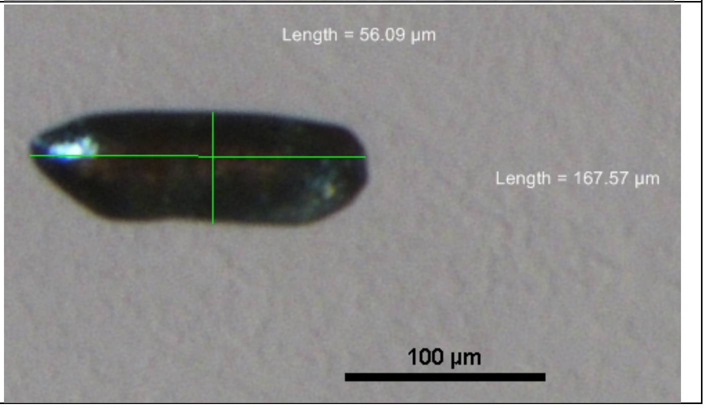

z69MZ379	1	Length = 215.05 Width = 75.71	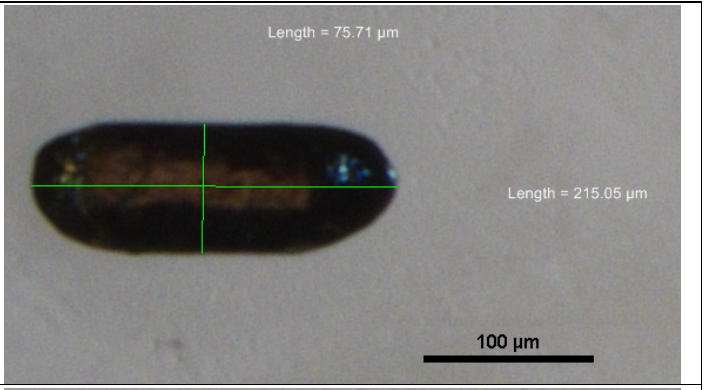
	2	Length = 198.31 Width = 78.80	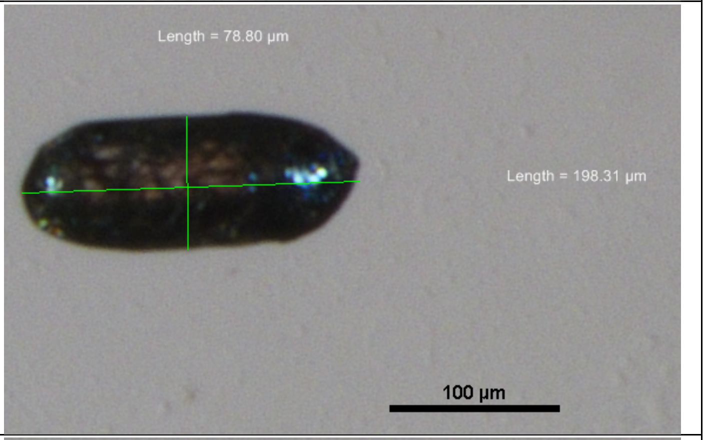
	3	Length = 161.38 Width = 58.51	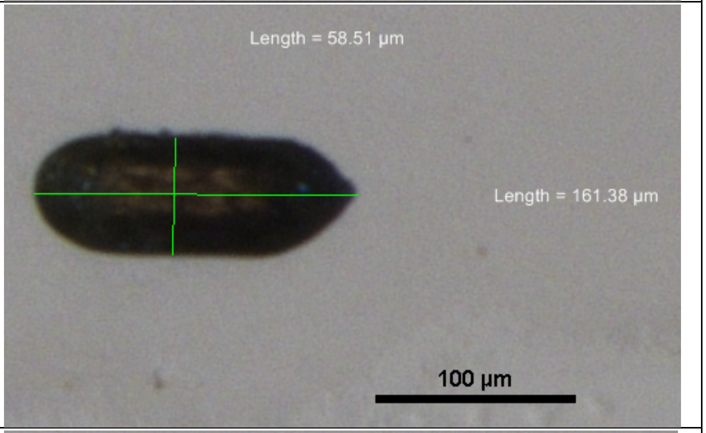
	4	Length = 243.03 Width = 94.80	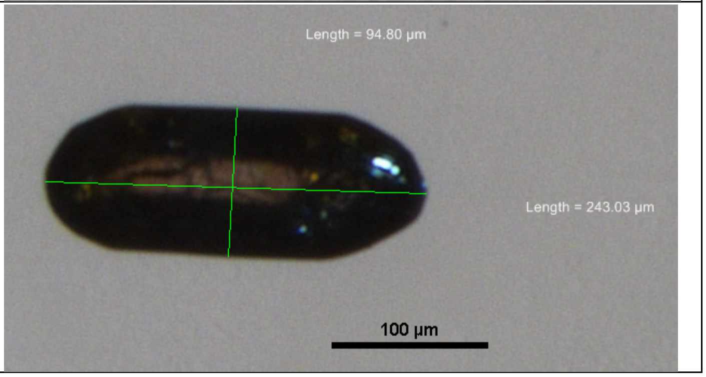

	5	Length = 174.84 Width = 59.26	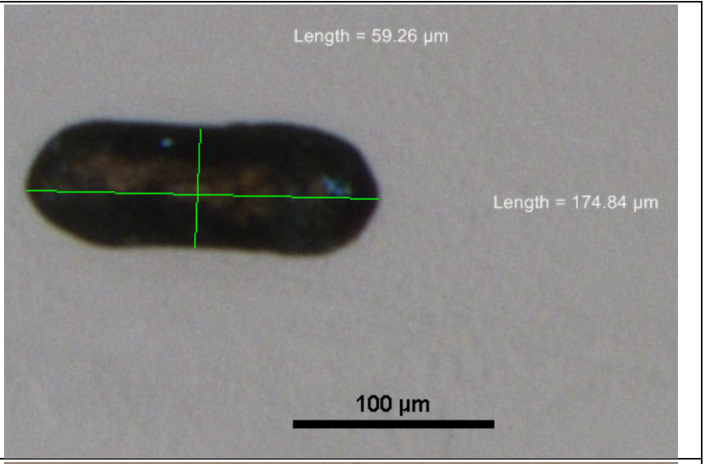
z69TA336	1	Length = 342.72 Width = 111.84	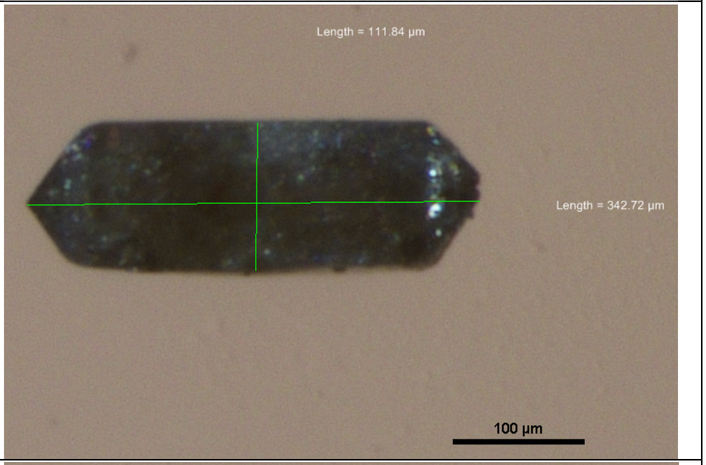
	2	Length = 347.09 Width = 104.78	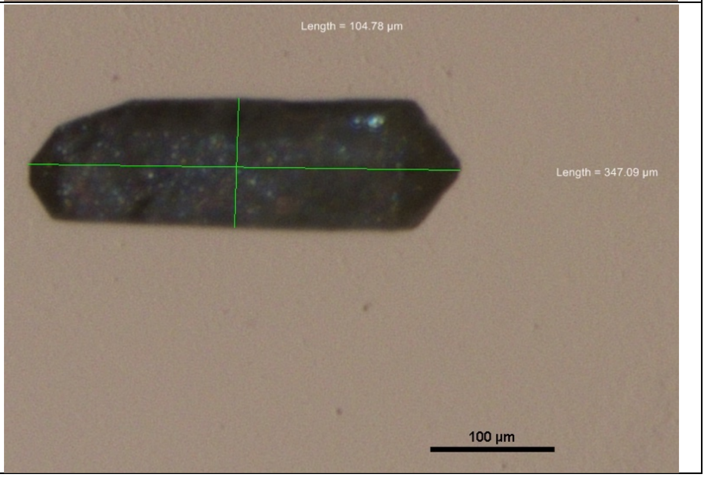

	3	Length = 204.36 Width = 72.84	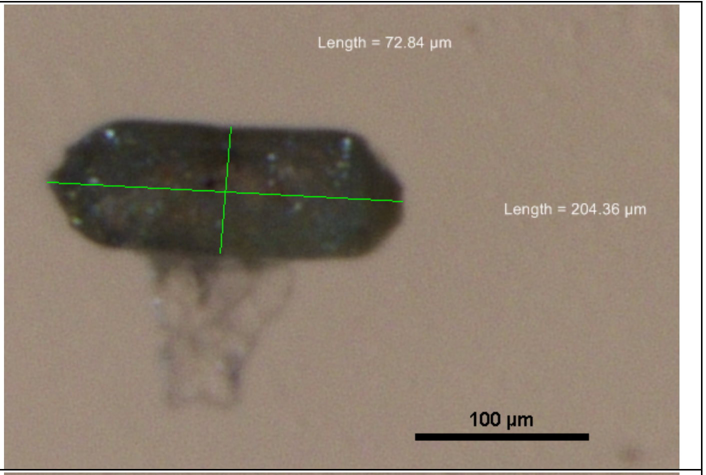
	4	Length = 278.38 Width = 111.81	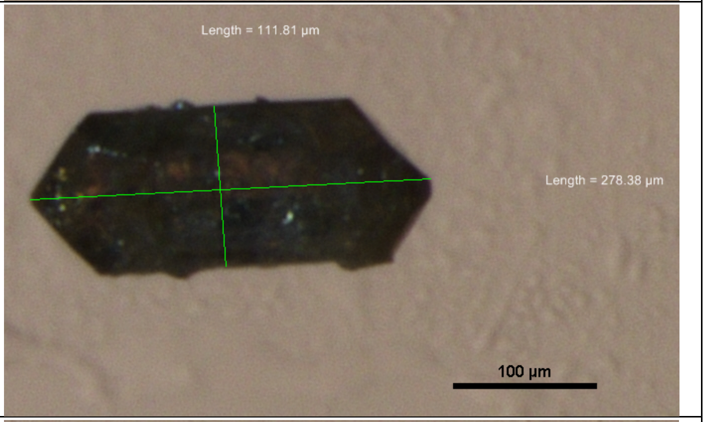
	5	Length = 276.77 Width = 100.59	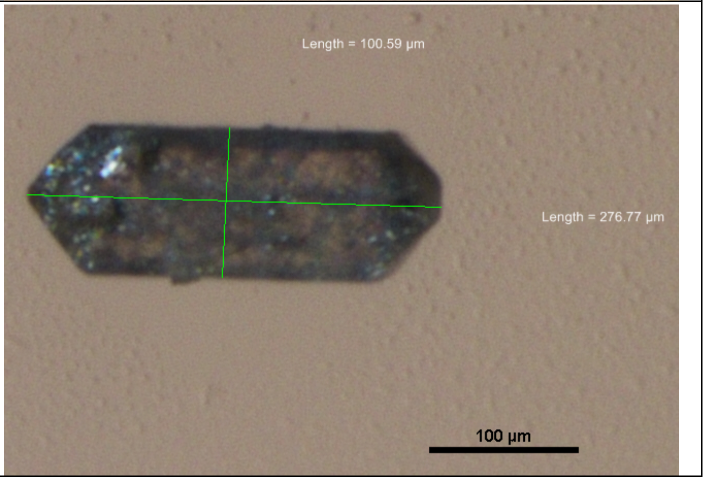

z69MZ392	1	Length = 205.99 Width = 70.56	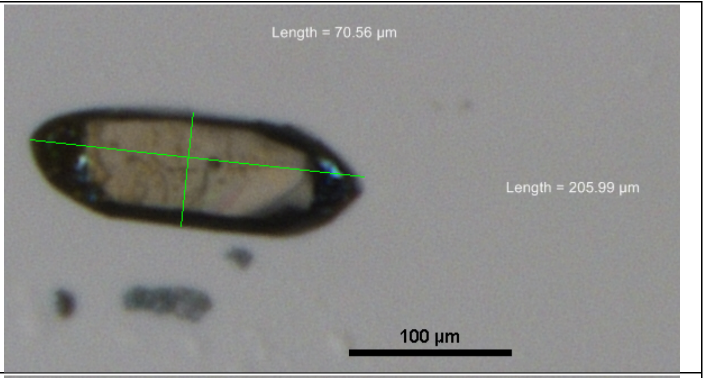
	2	Length = 289.55 Width = 81.92	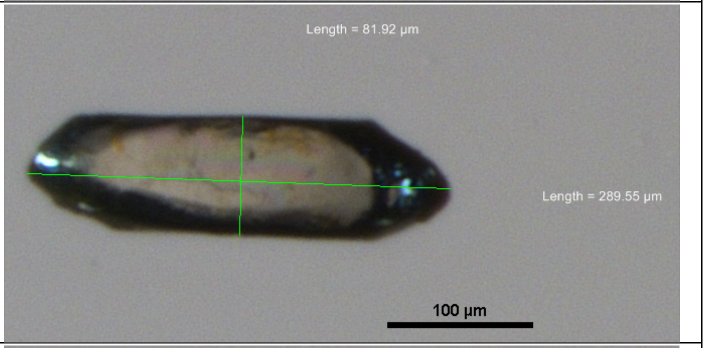
	3	Length = 193.39 Width = 63.40	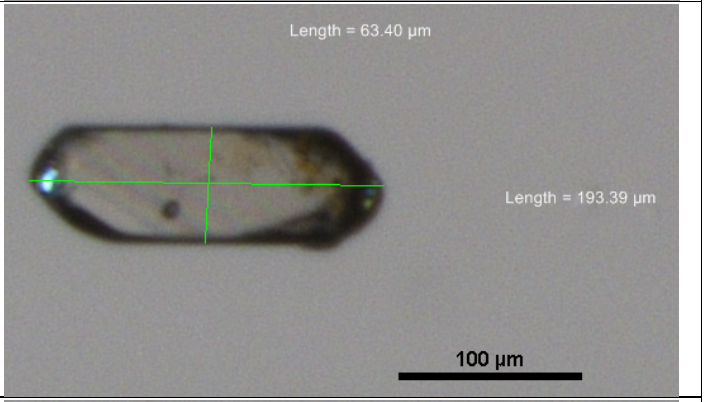
	4	Length = 249.92 Width = 65.14	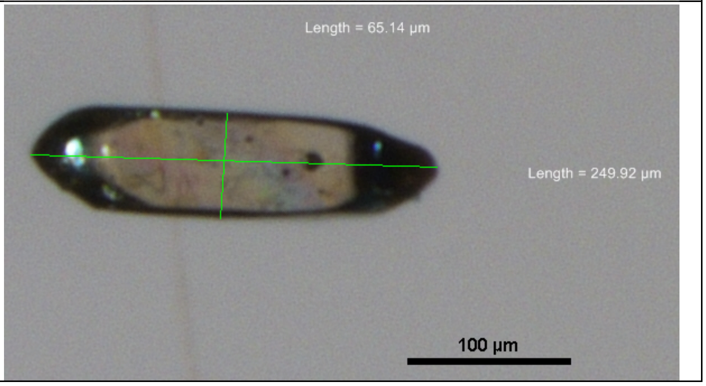

	5	Length = 220.99 Width = 70.29	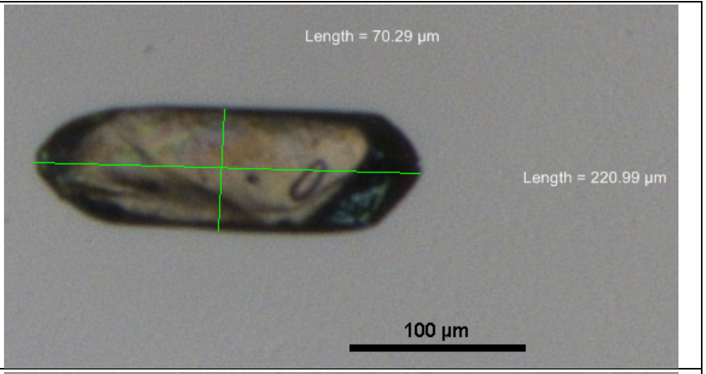
z69MZ351	1	Length = 172.99 Width = 73.74	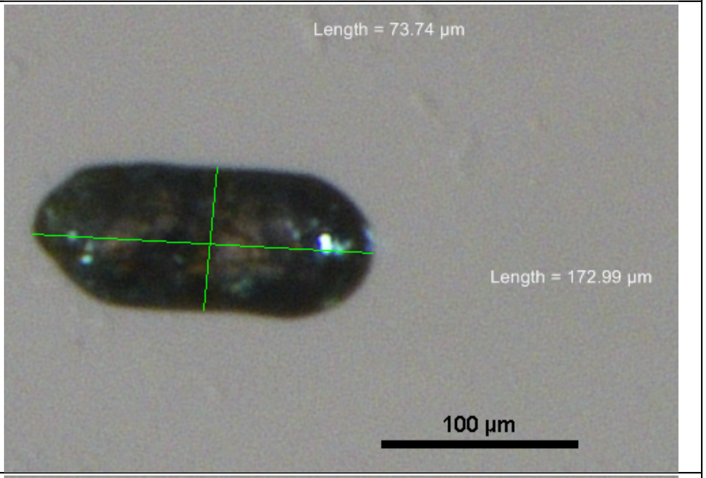
	2	Length = 173.34 Width = 67.55	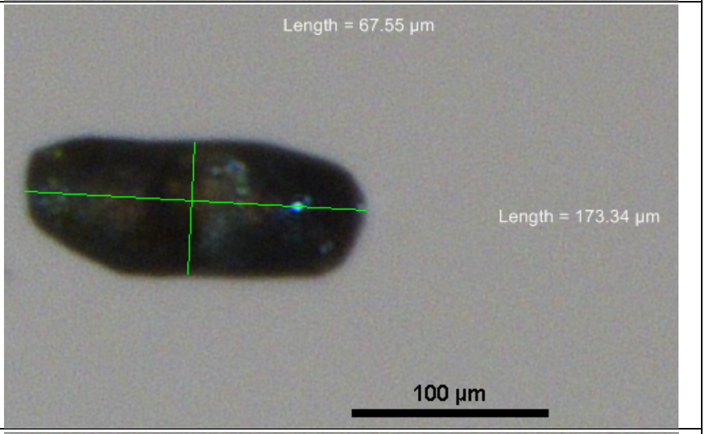
	3	Length = 193.45 Width = 84.16	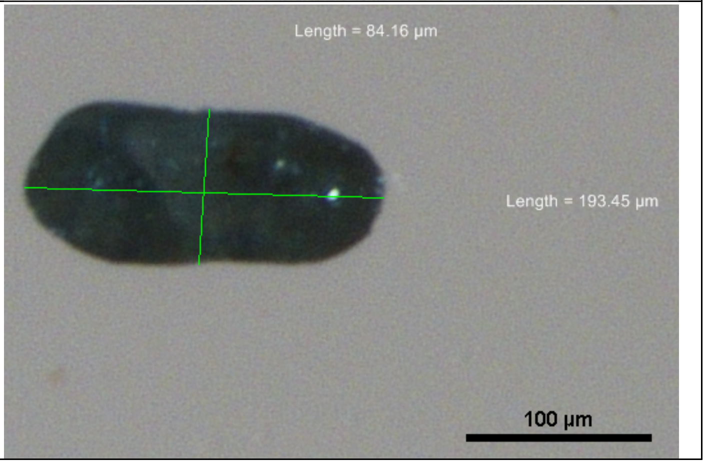

	4	Length = 154.91 Width = 73.06	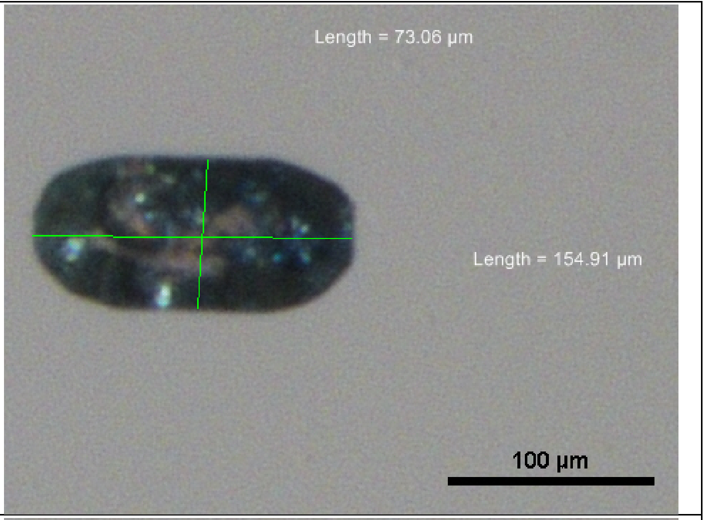
	5	Length = 153.49 Width = 71.95	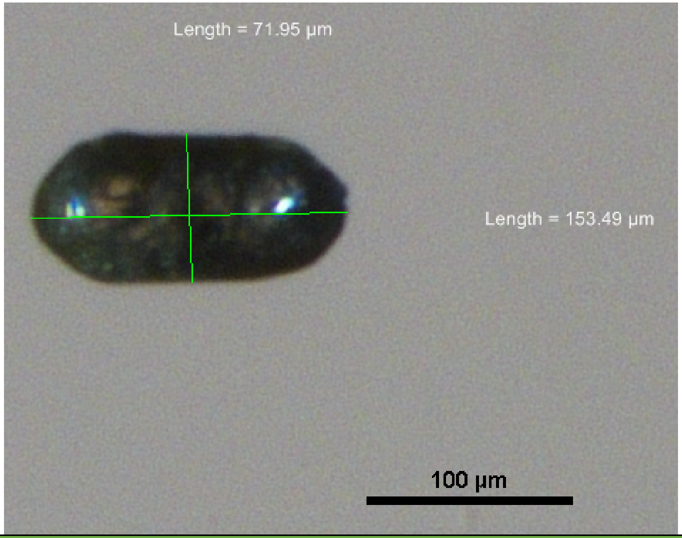
Apatite Samples			
Sample ID		**Measurements (µm)**	**Photo**
a69FQ332	1	Length = 138.32 Width = 69.85	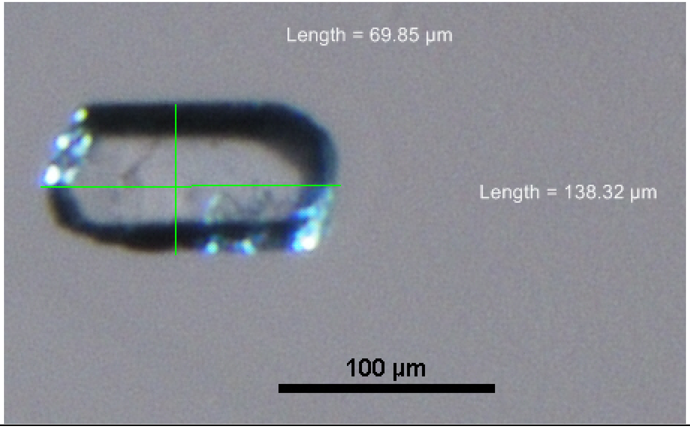

	2	Length = 207.28 Width = 93.38	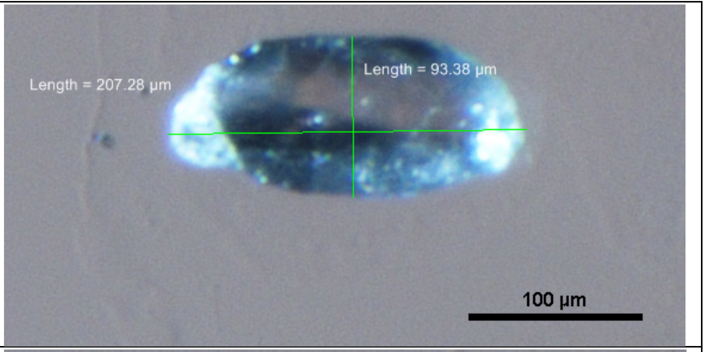
	3	Length = 178.26 Width = 80.78	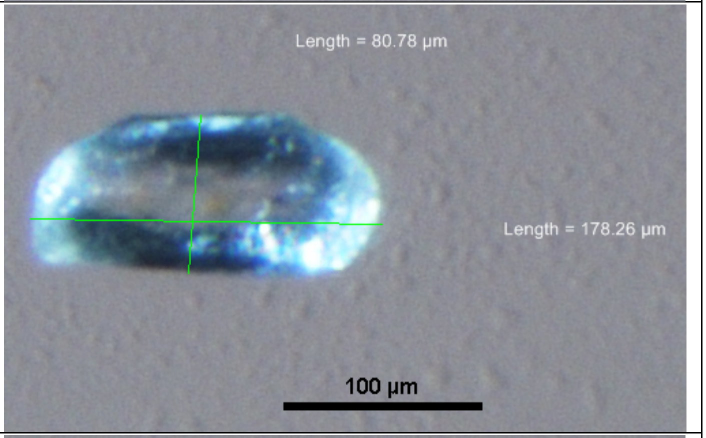
	4	Length = 173.07 Width = 120.28	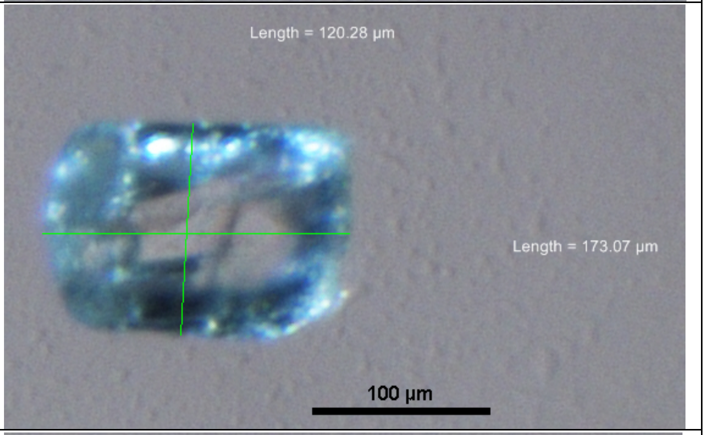
	5	Length = 159.31 Width = 88.11	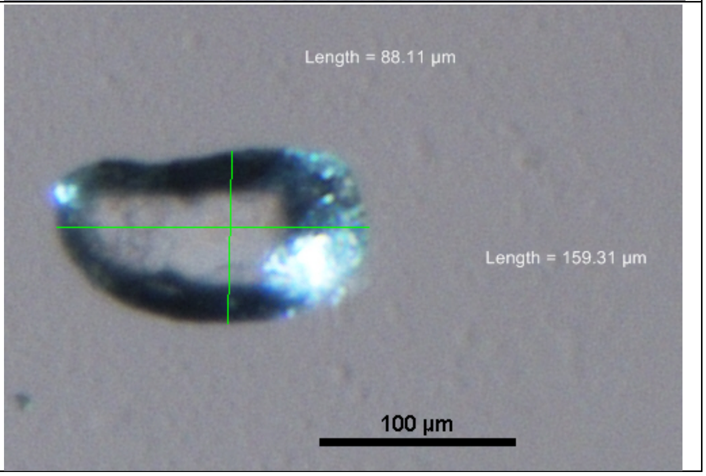

a69FQ335	1	Length = 157.31 Width = 93.94	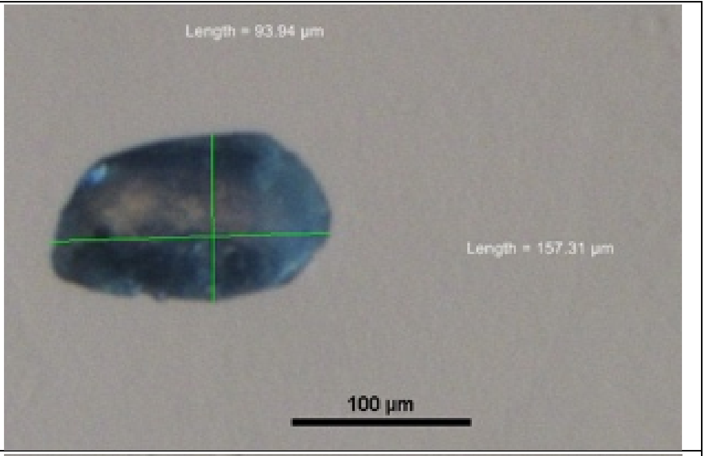
	2	Length = 297.30 Width = 74.00	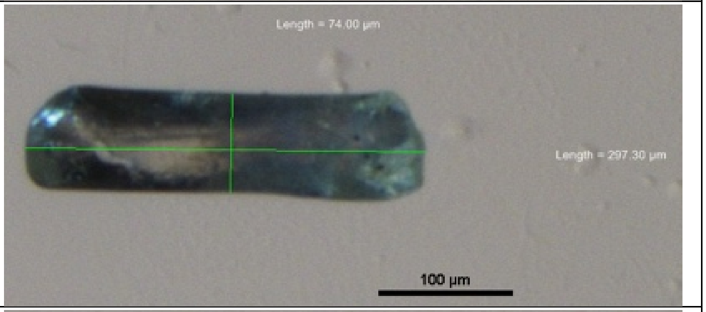
	3	Length = 140.41 Width = 92.23	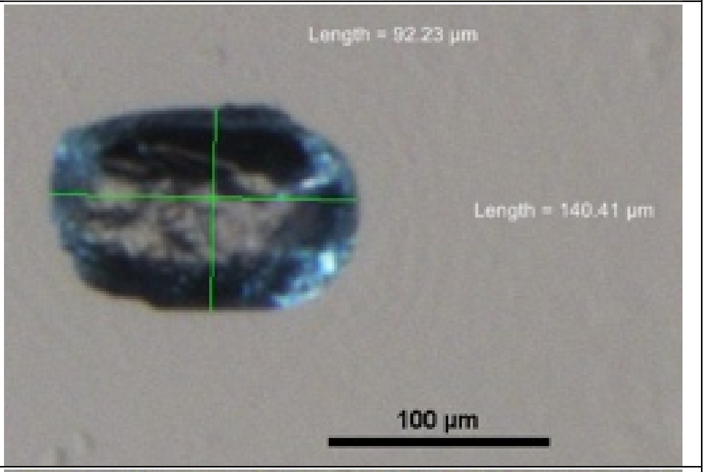
	4	Length = 152.22 Width = 65.34	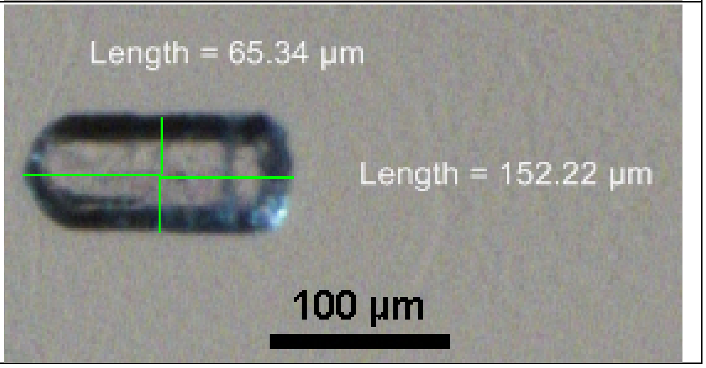

	5	Length = 140.39 Width = 69.51	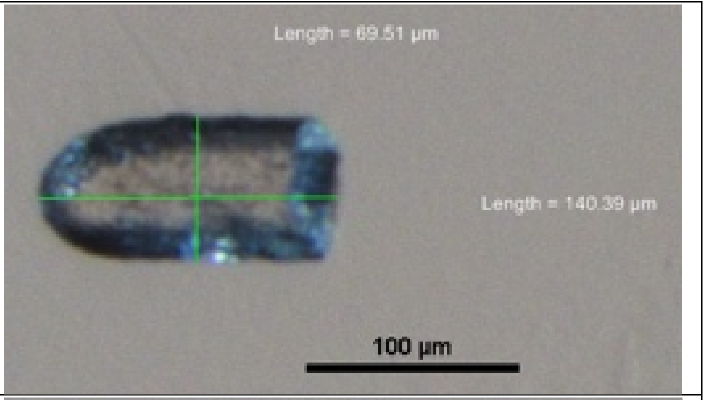
a69MZ379	1	Length = 179.62 Width = 107.02	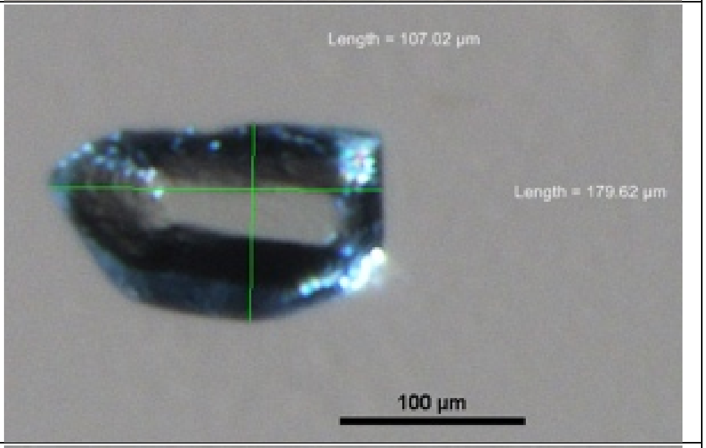
	2	Length = 105.63 Width = 91.18	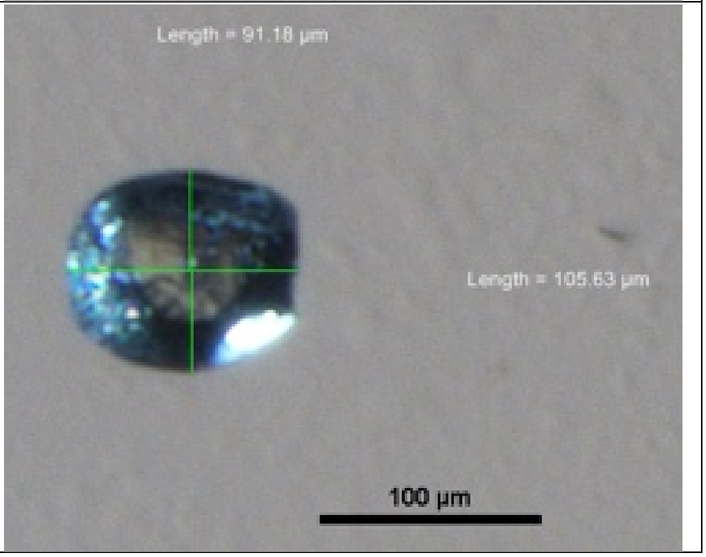

	3	Length = 212.99 Width = 126.28	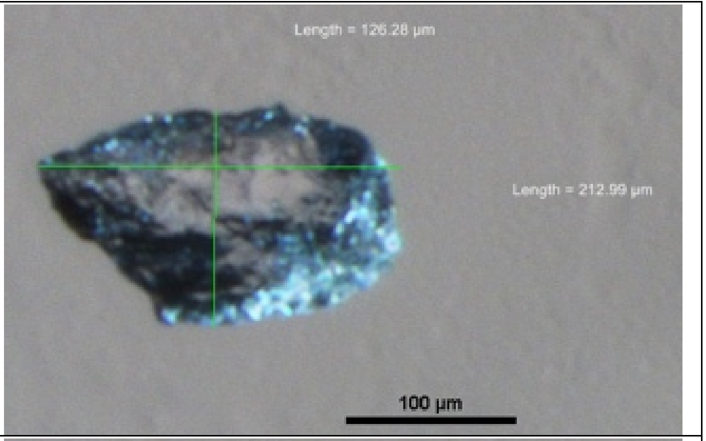
	4	Length = 169.13 Width = 94.42	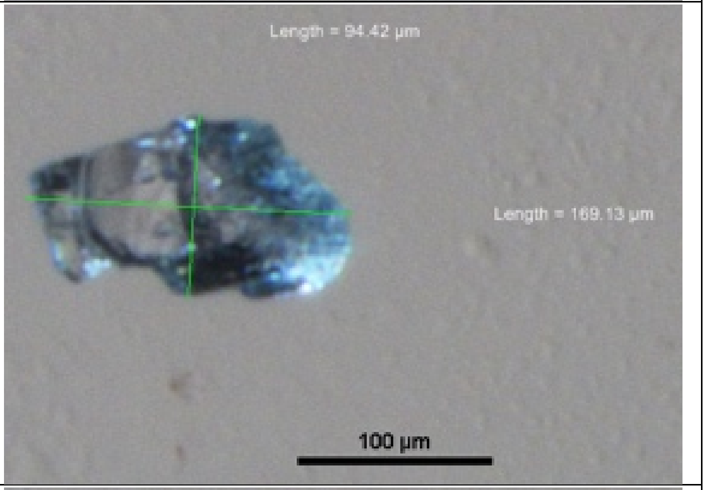
	5	Length = 142.11 Width = 85.69	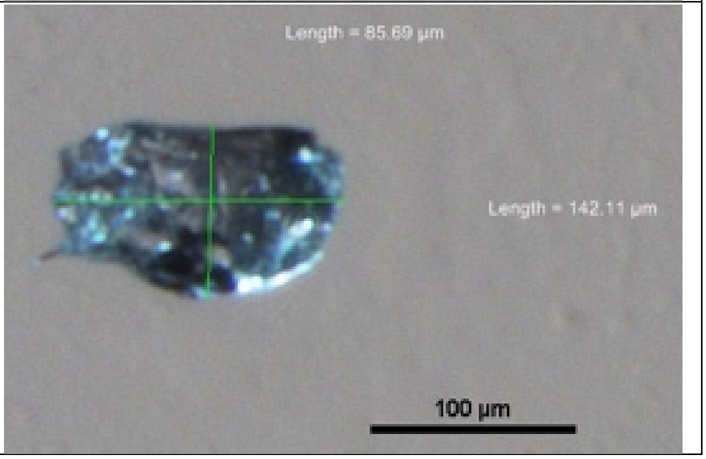

a69FQ398	1	Length = 221.59 Width = 103.92	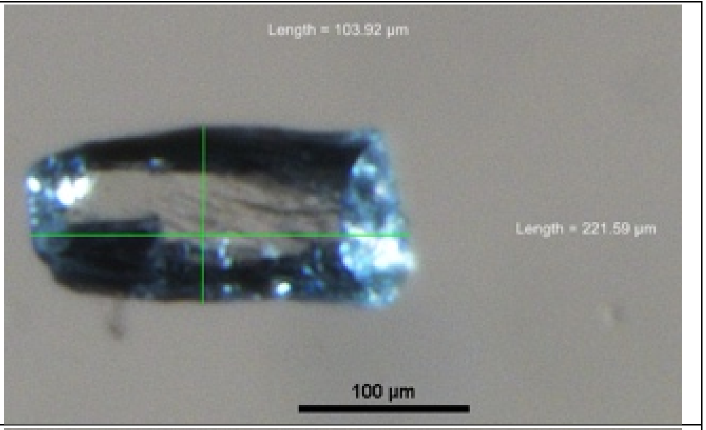
	2	Length = 328.71 Width = 164.28	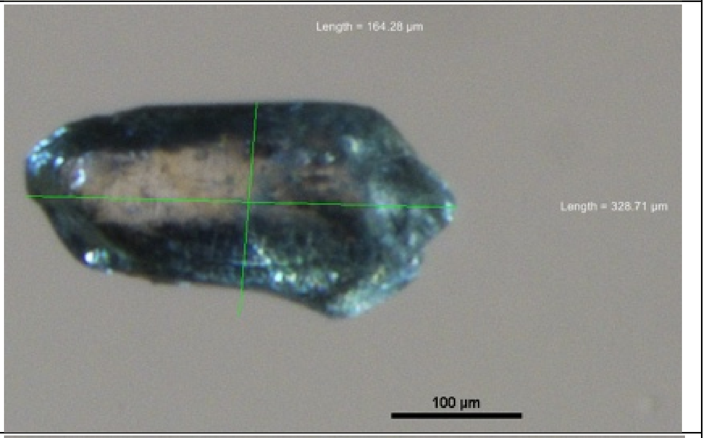
	3	Length = 311.40 Width = 149.69	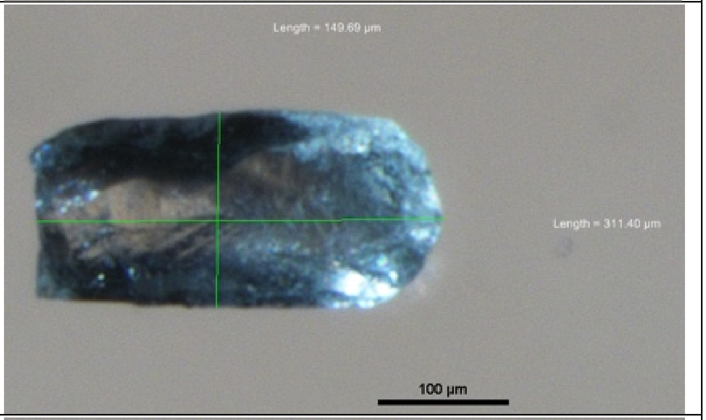
	4	Length = 418.80 Width = 109.18	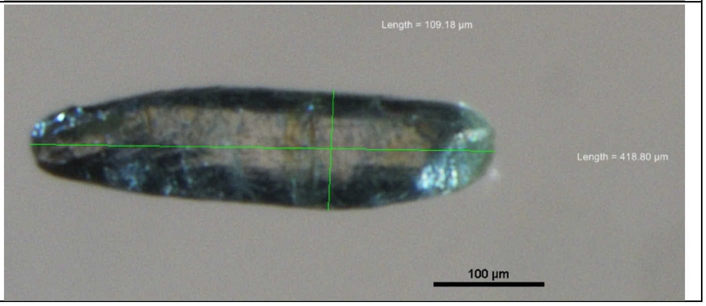

	5	Length = 399.67 Width = 145.84	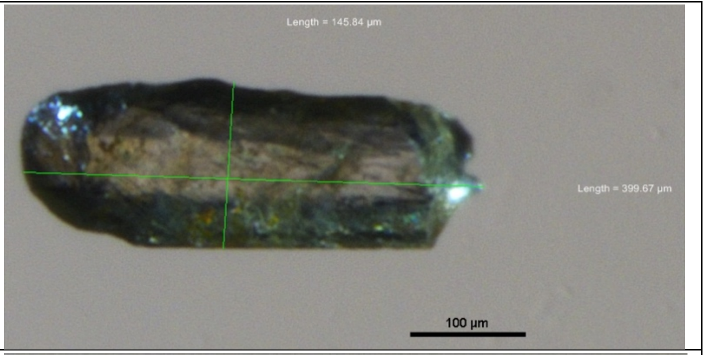
a69MZ390	1	Length = 250.15 Width = 117.33	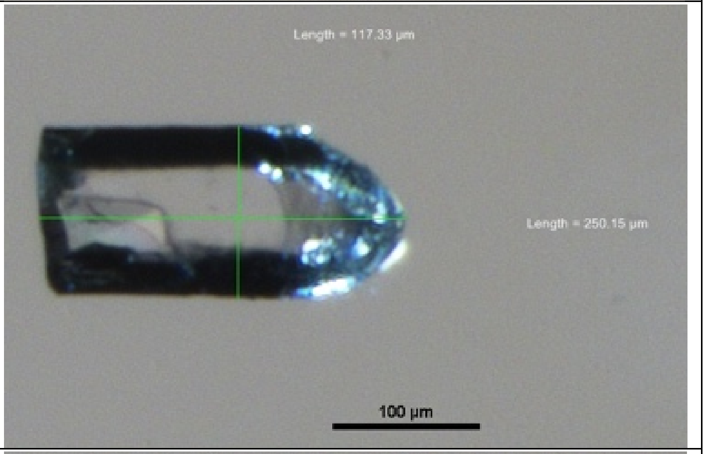
	2	Length = 380.27 Width = 152.77	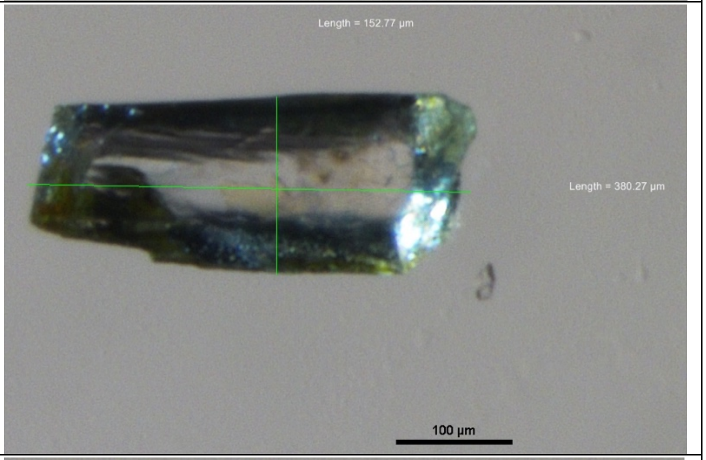
	3	Length = 259.47 Width = 123.68	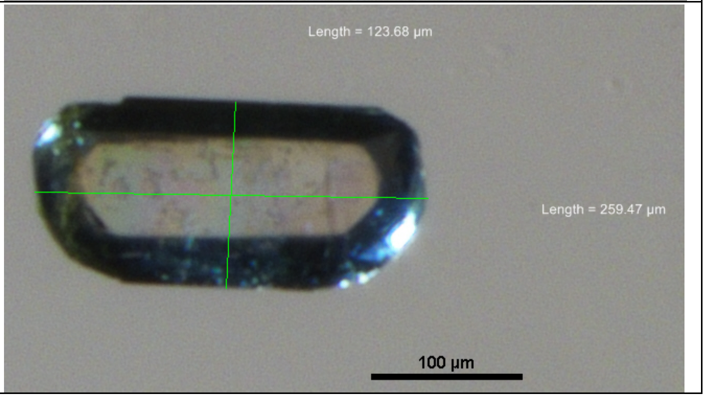

	4	Length = 252.71 Width = 135.07	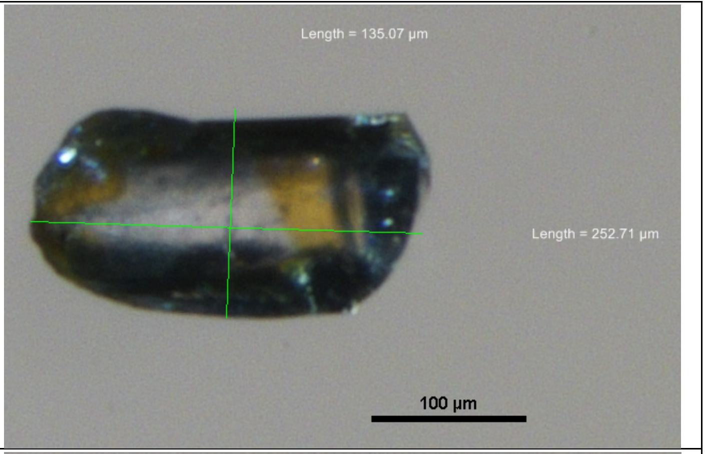
	5	Length = 187.53 Width = 103.91	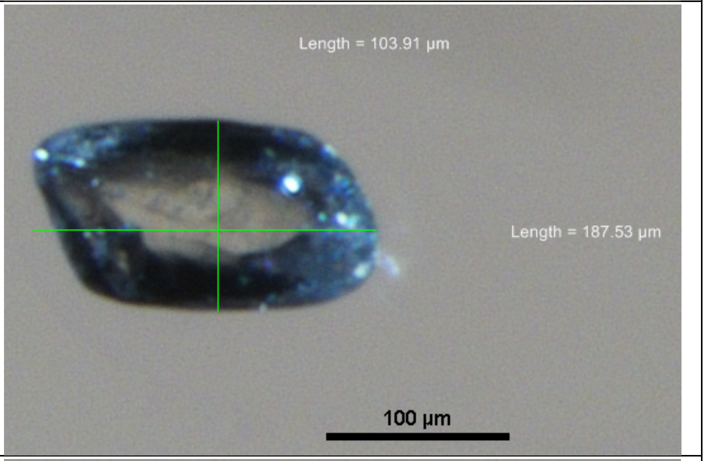
a69MZ392	1	Length = 157.93 Width = 92.56	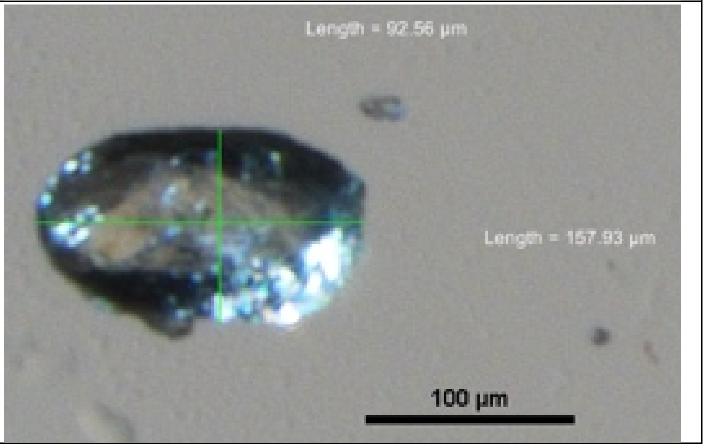

	2	Length = 173.07 Width = 96.00	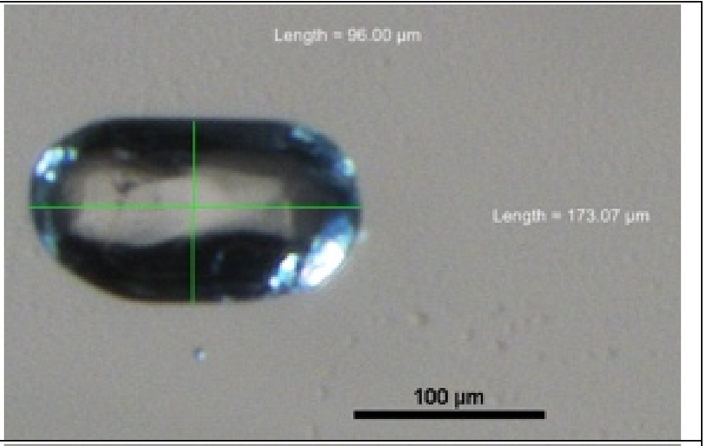
	3	Length = 139.76 Width = 223.53	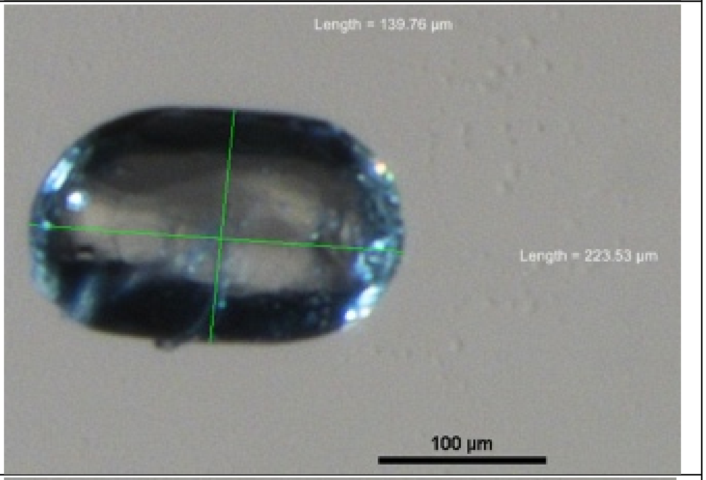
	4	Length = 165.50 Width = 63.31	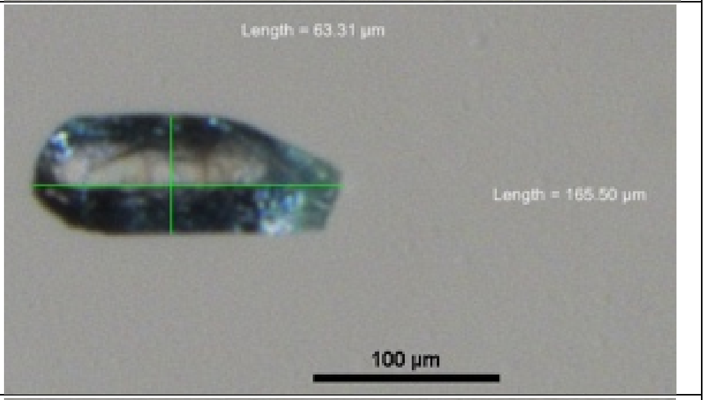
	5	Length = 178.58 Width = 82.24	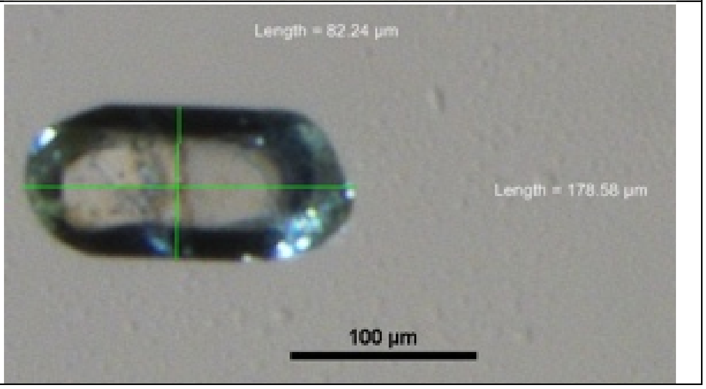

a69MZ351	1	Length = 80.86 Width = 65.09	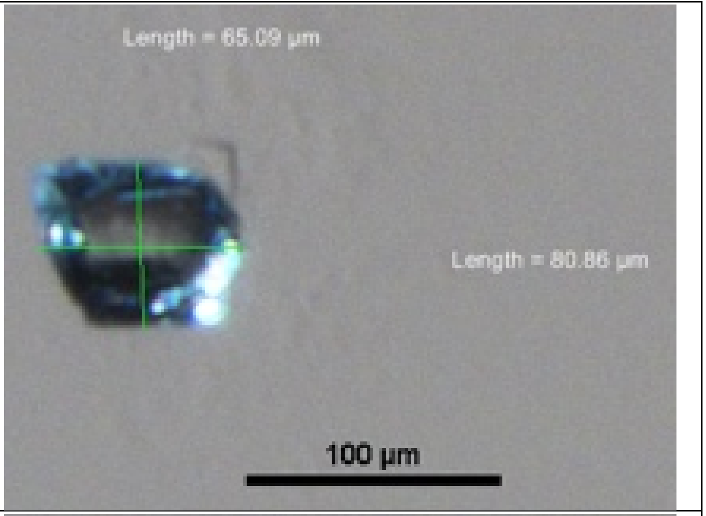
	2	Length = 132.48 Width = 93.60	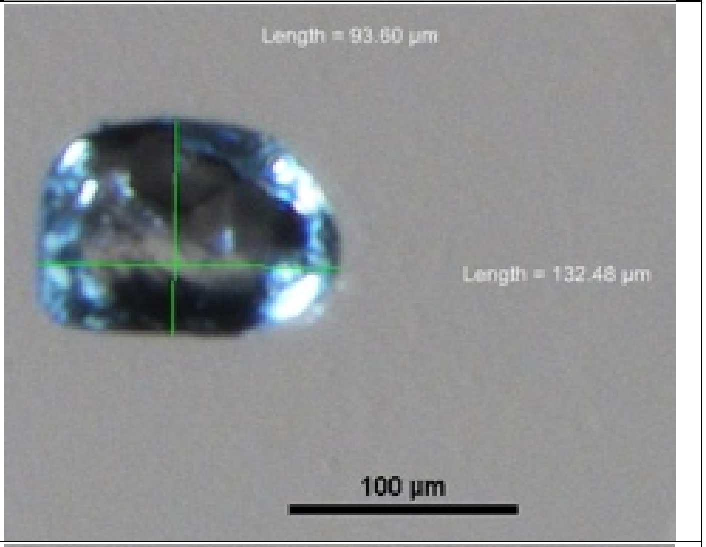
	3	Length = 140.34 Width = 89.16	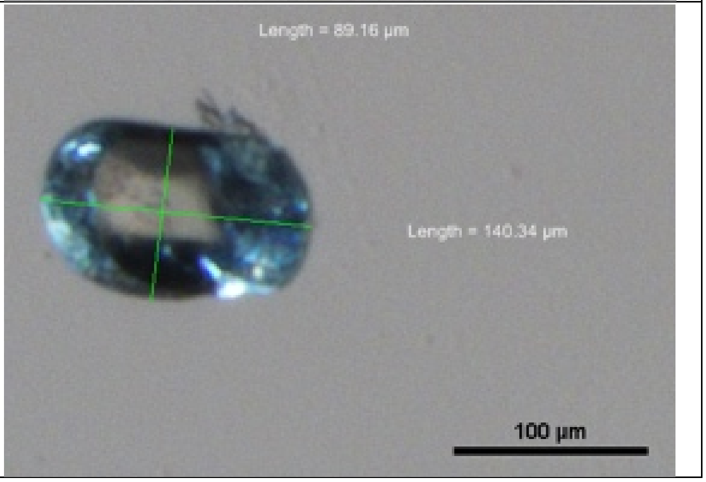

	4	Length = 86.64 Width = 91.38	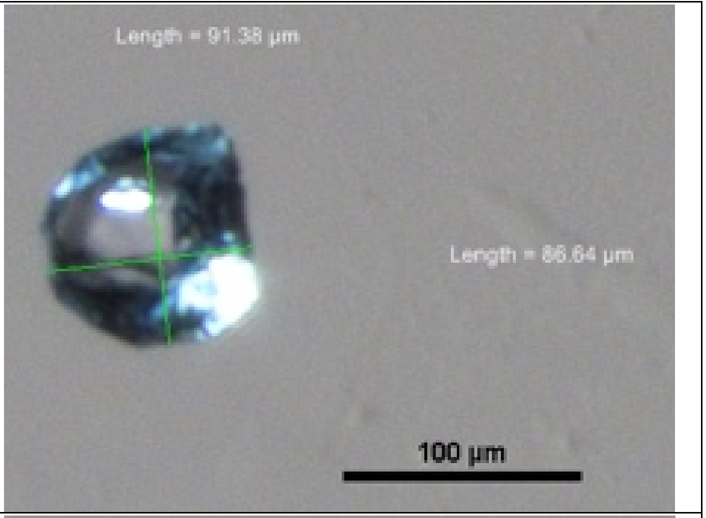
	5	Length = 121.12 Width = 104.29	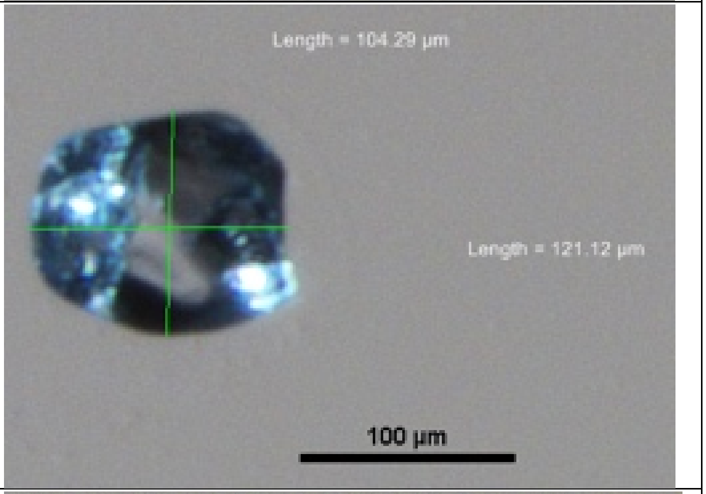
a69MZ335	1	Length = 135.57 Width = 61.59	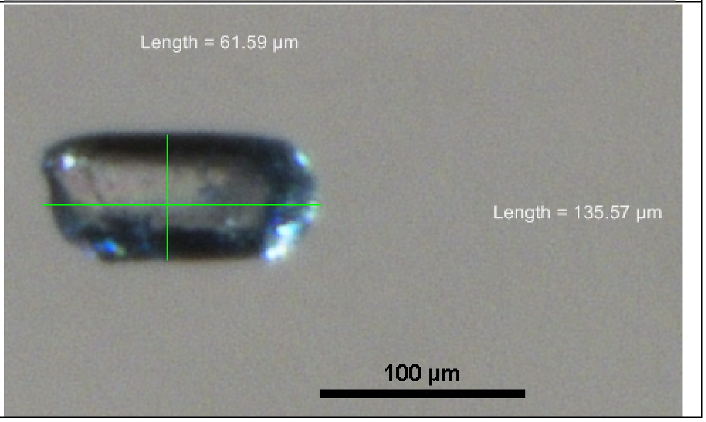

	2	Length = 169.98 Width = 77.77	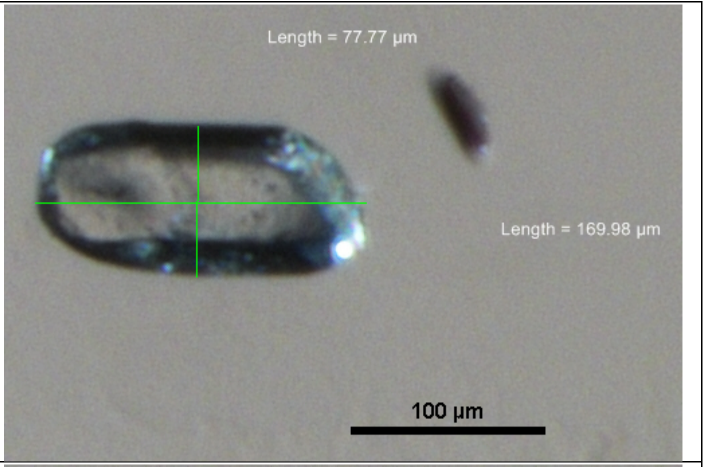
	3	Length = 106.32 Width = 65.38	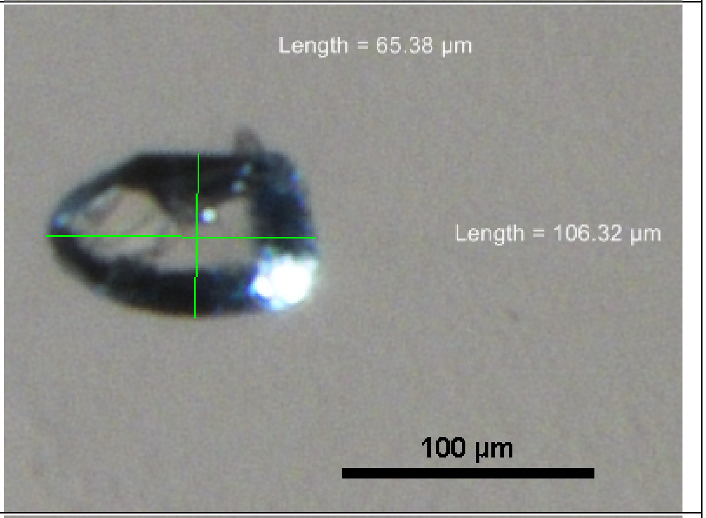
	4	Length = 146.24 Width = 79.48	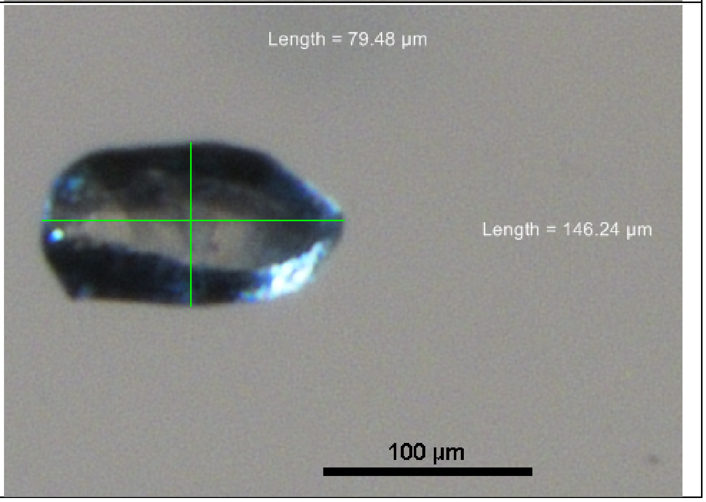

	5	Length = 136.60 Width = 75.71	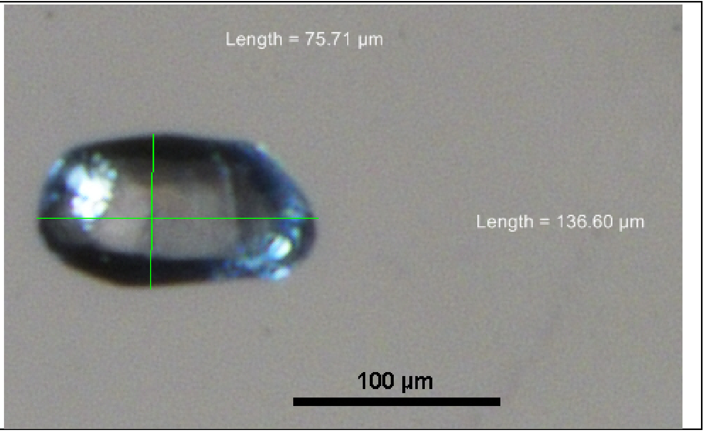

Hopedale Transect			
Zircon samples			
Sample ID		**Measurements (µm)**	**Photo**
zK0016	1	Length = 294.01 Width = 117.85	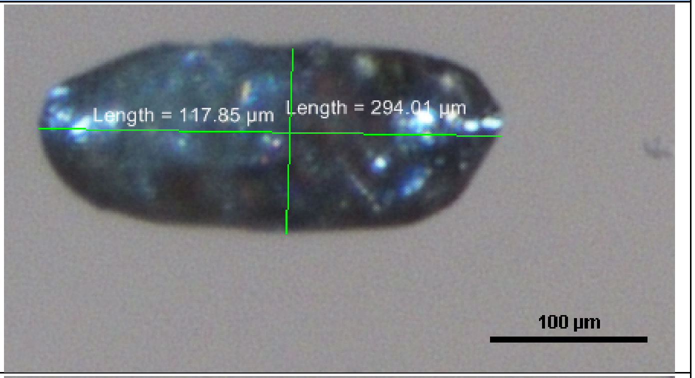
	2	Length = 312.40 Width = 143.53	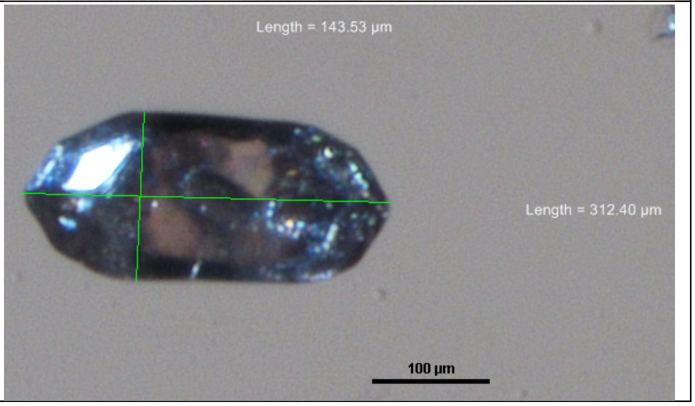

	3	Length = 307.52 Width = 128.46	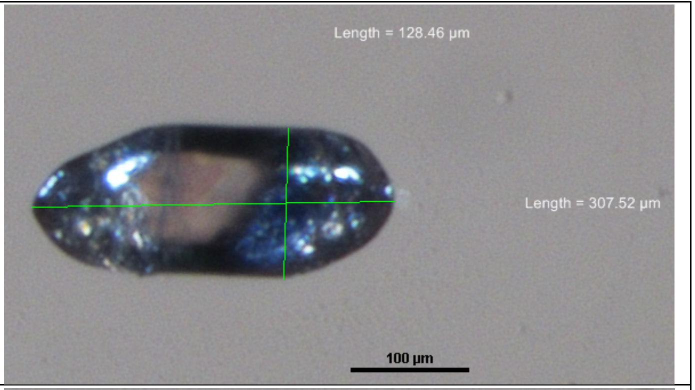
	4	Length = 216.26 Width = 84.49	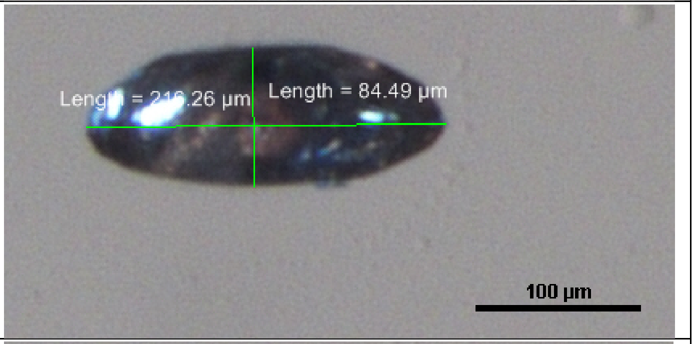
	5	Length = 229.31 Width = 94.18	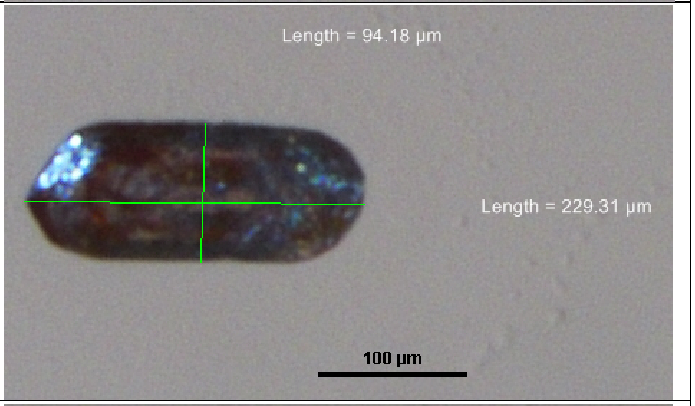
zK0015	1	Length = 231.71 Width = 83.10	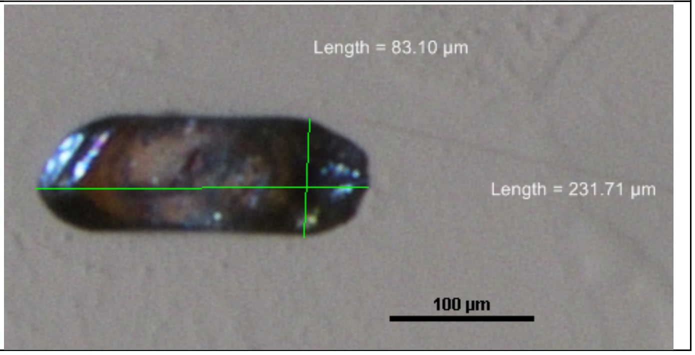

	2	Length = 209.59 Width = 68.07	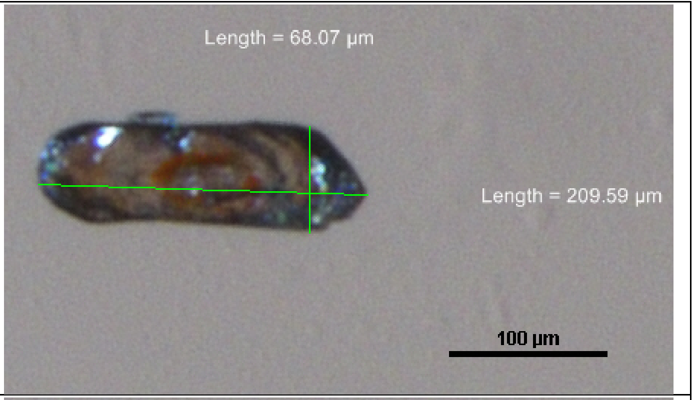
	3	Length = 131.78 Width = 89.32	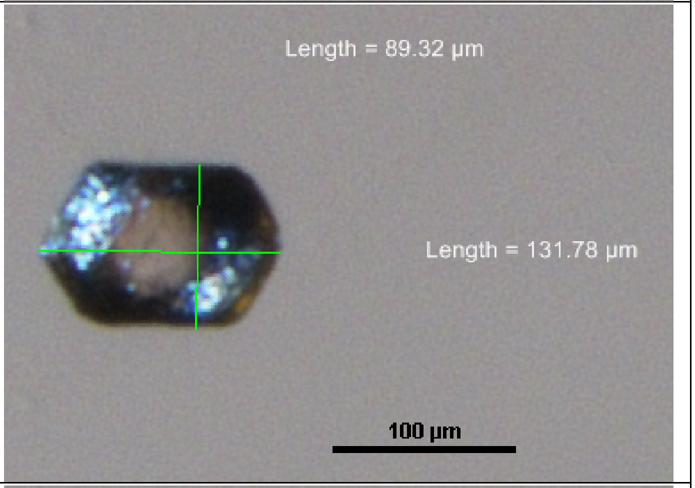
	4	Length = 155.60 Width = 62.84	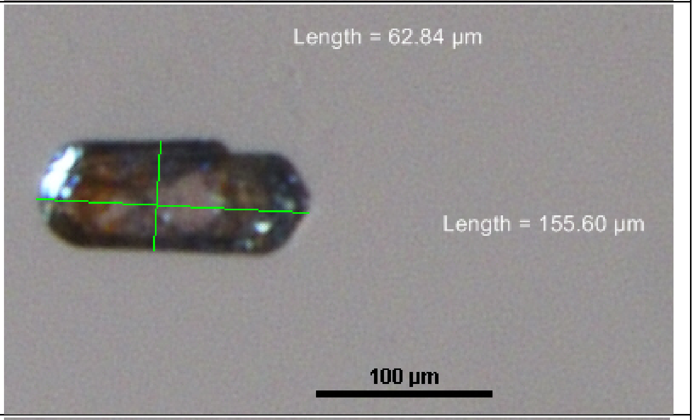
	5	Length = 188.27 Width = 74.82	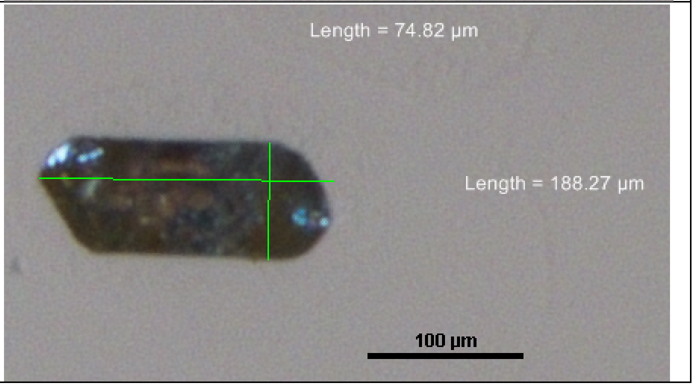

zK0014	1	Length = 184.43 Width = 93.19	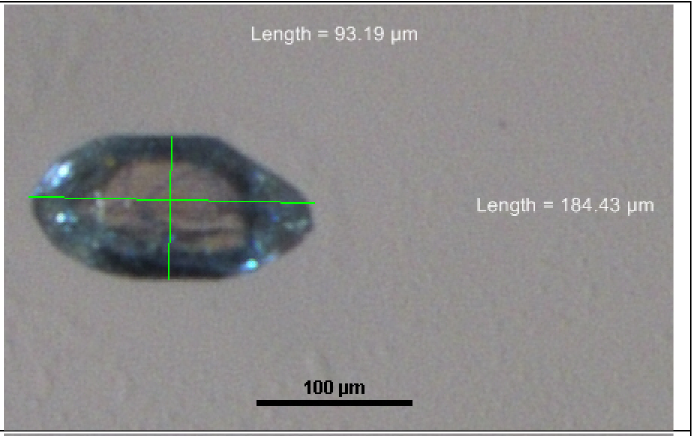
	2	Length = 230.27 Width = 59.87	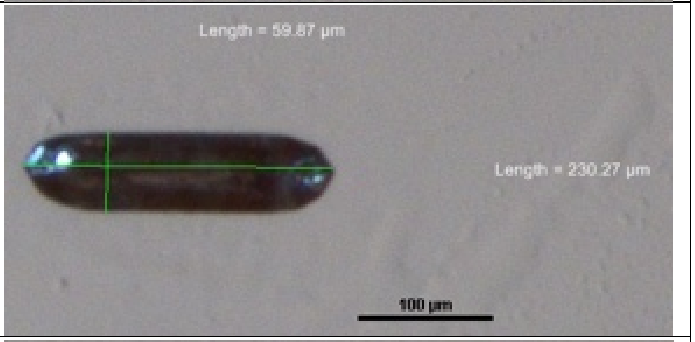
	3	Length = 191.64 Width = 61.79	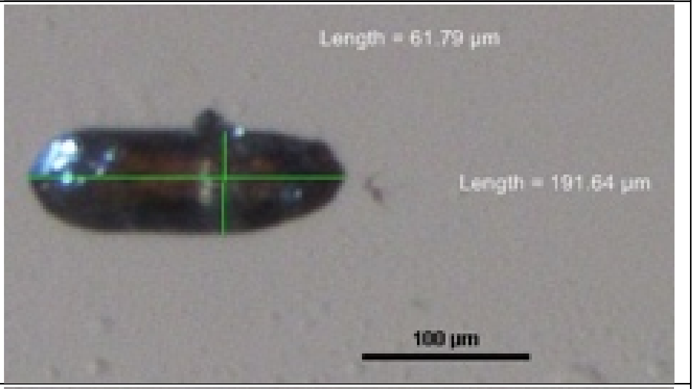
	4	Length = 203.26 Width = 69.14	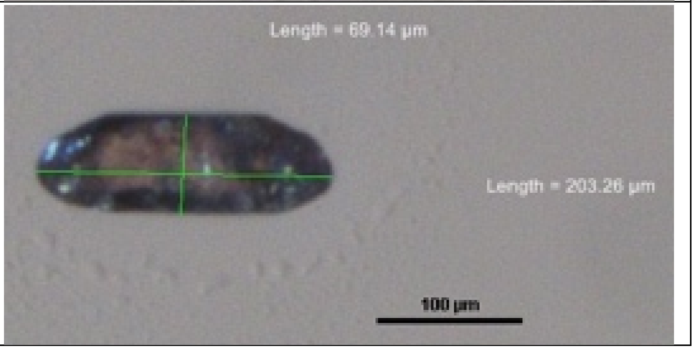

	5	Length = 267.96 Width = 87.86	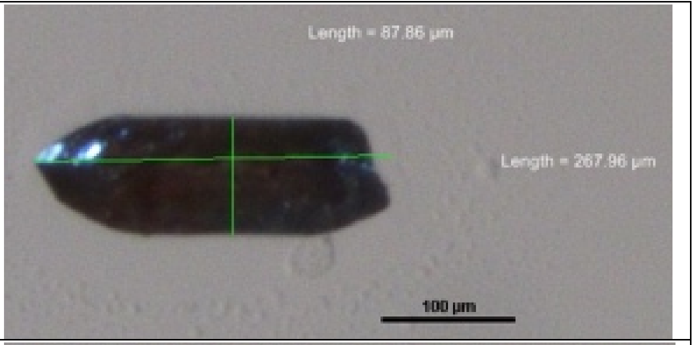
zK0013	1	Length = 375.56 Width = 91.23	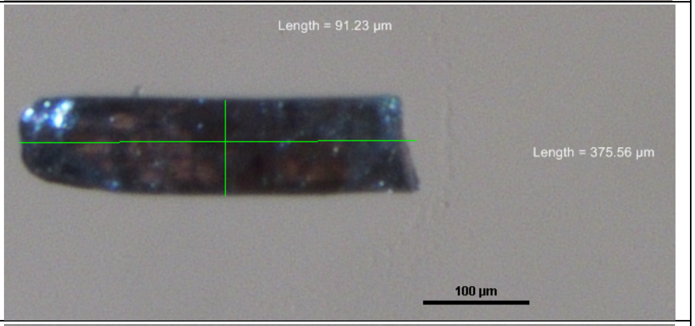
	2	Length = 299.77 Width = 74.86	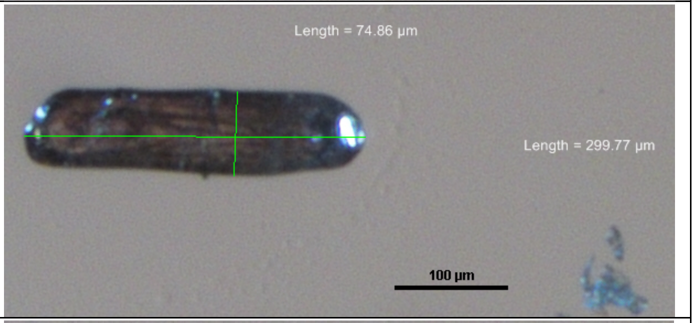
	3	Length = 214.85 Width = 66.66	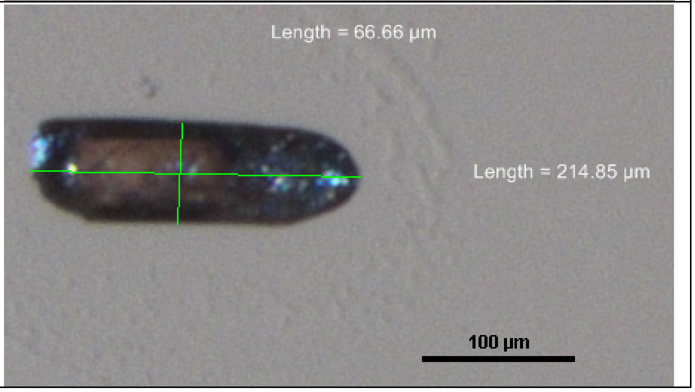

	4	Length = 125.51 Width = 63.76	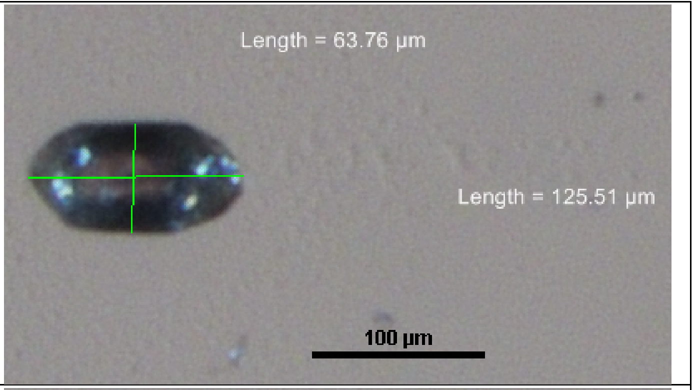
	5	Length = 342.31 Width = 71.50	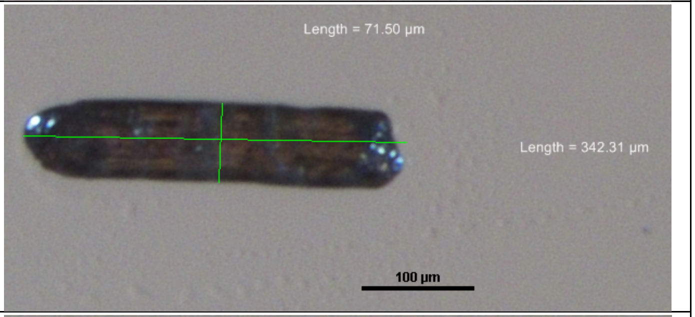
zK0012	1	Length = 220.37 Width = 81.02	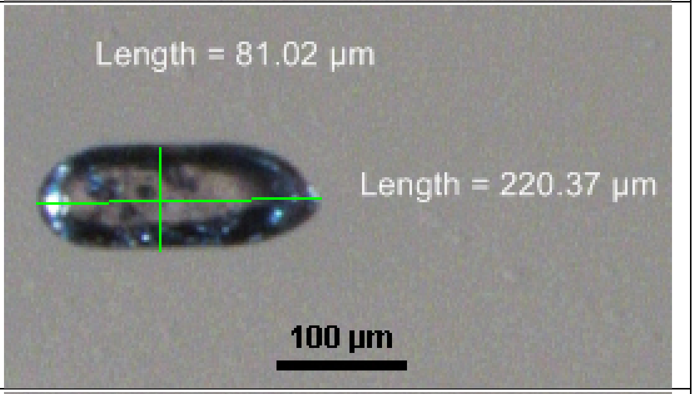
	2	Length = 185.79 Width = 106.59	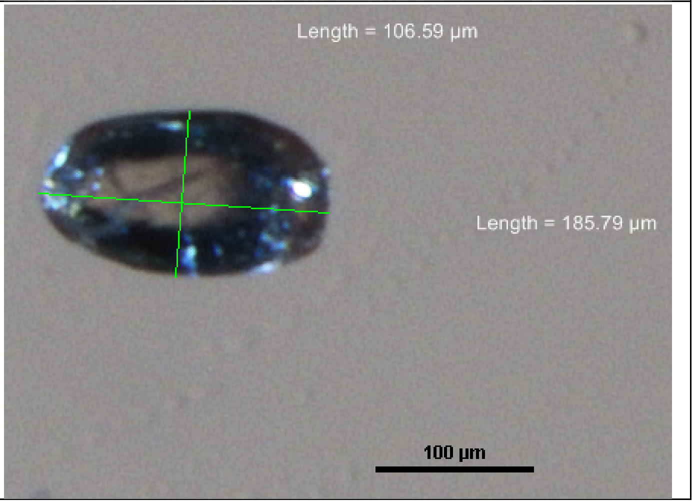

	3	Length = 258.84 Width = 127.07	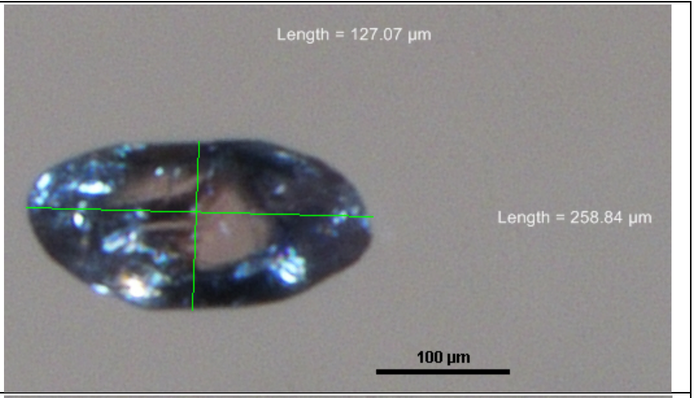
	4	Length = 206.12 Width = 75.31	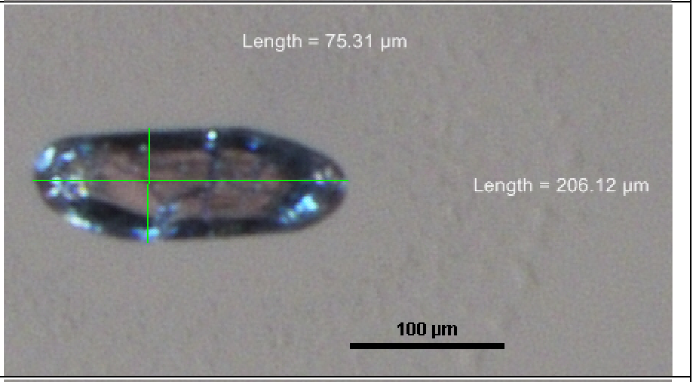
	5	Length = 278.07 Width = 73.93	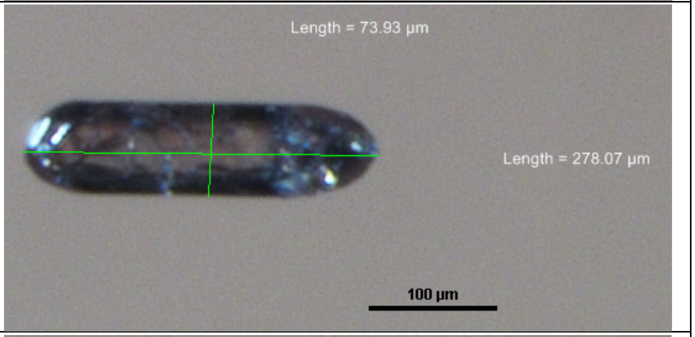
zK0011	1	Length = 231.71 Width = 62.76	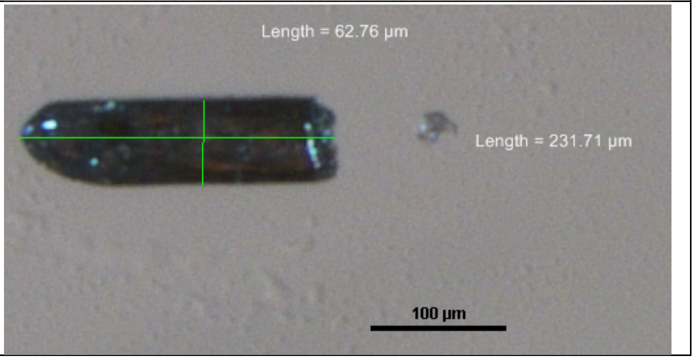

	2	Length = 182.49 Width = 64.43	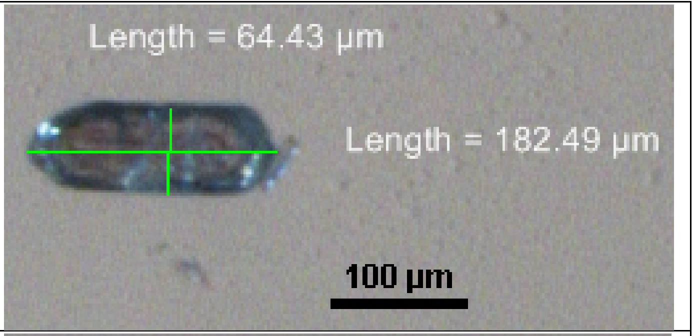
	3	Length = 149.17 Width = 67.61	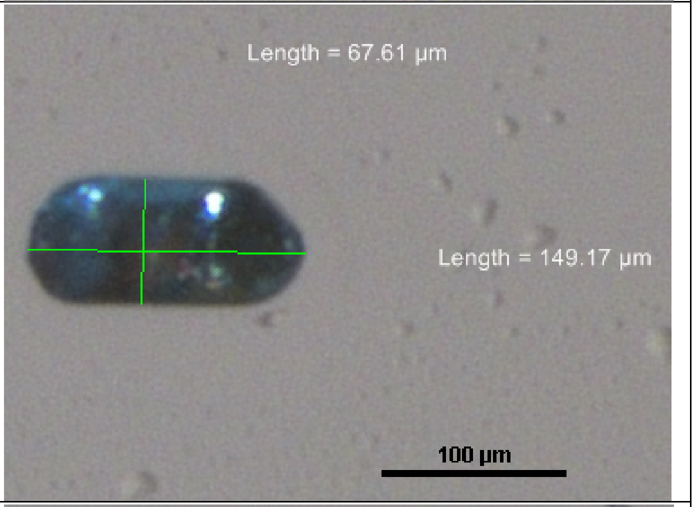
	4	Length = 410.80 Width = 134.27	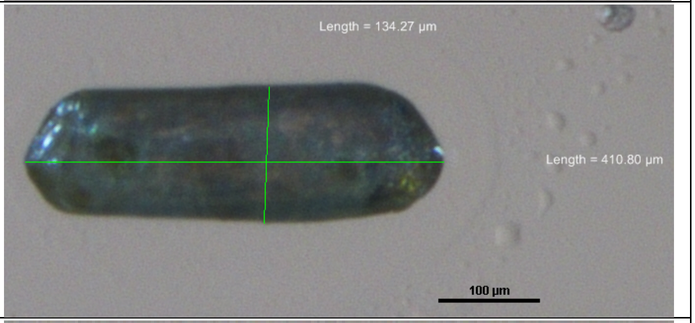
	5	Length = 164.31 Width = 62.11	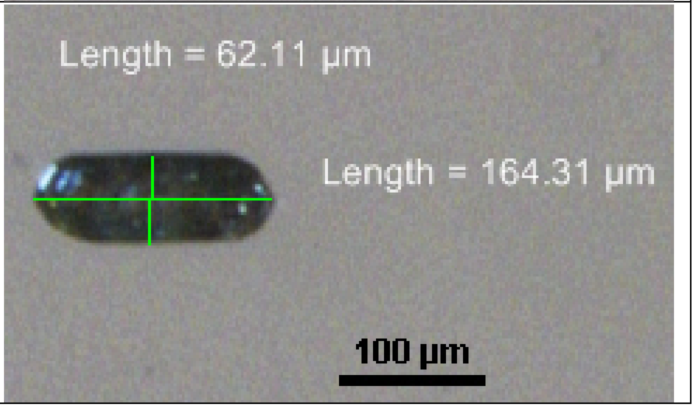

zK0010	1	Length = 262.68 Width = 111.52	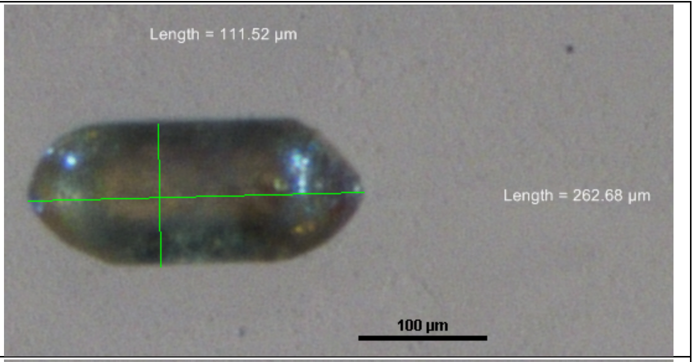
	2	Length = 182.05 Width = 75.80	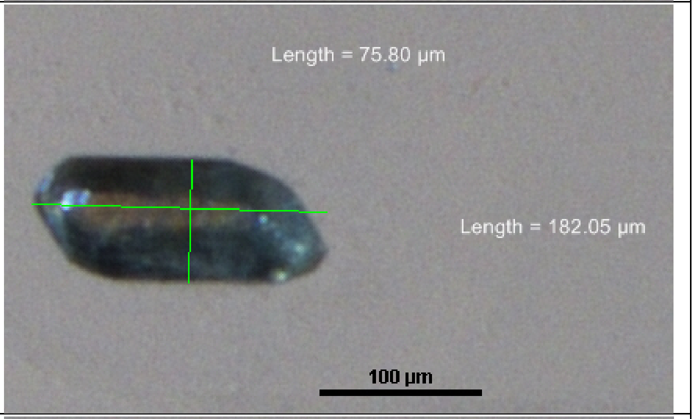
	3	Length = 211.43 Width = 77.24	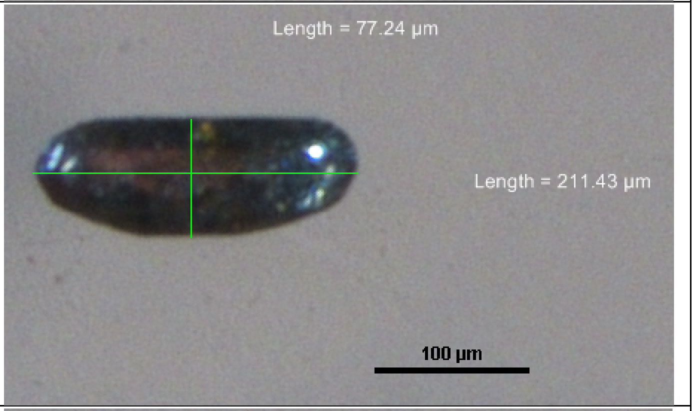
	4	Length = 191.64 Width = 68.15	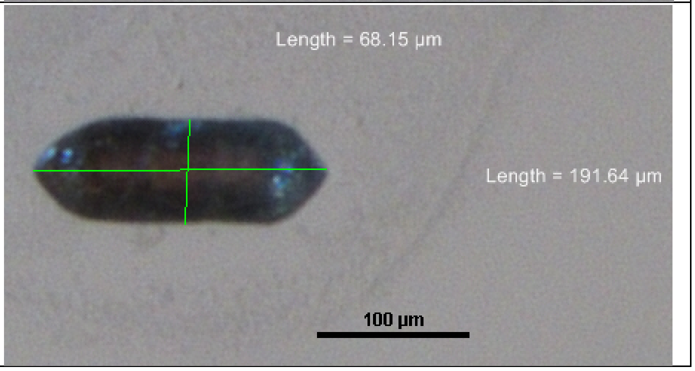

	5	Length = 167.99 Width = 68.56	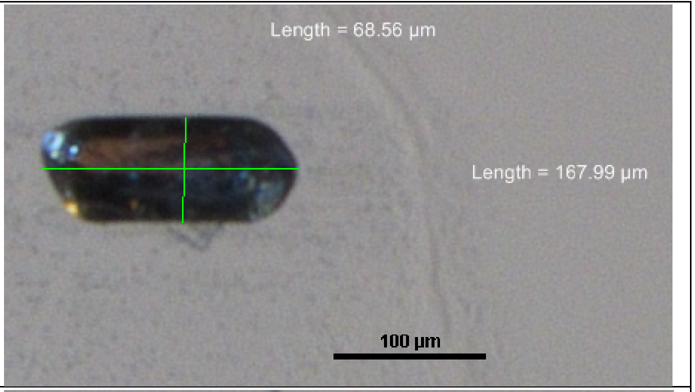
zK0009	1	Length = 246.20 Width = 70.02	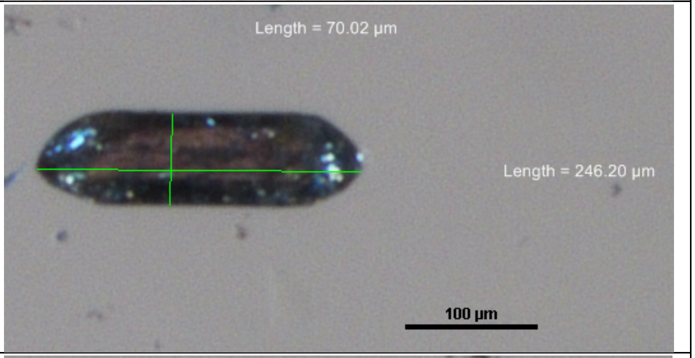
	2	Length = 183.92 Width = 69.53	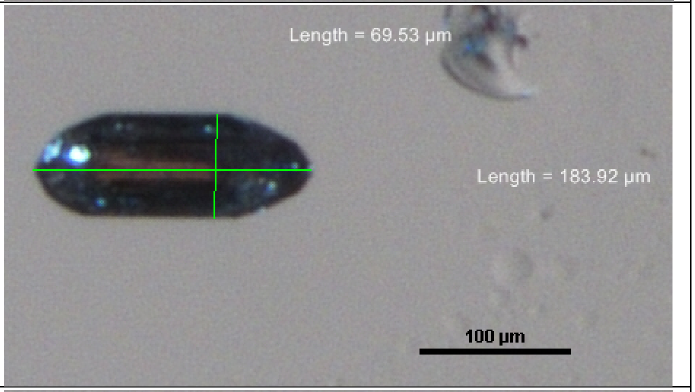
	3	Length = 158.34 Width = 75.36	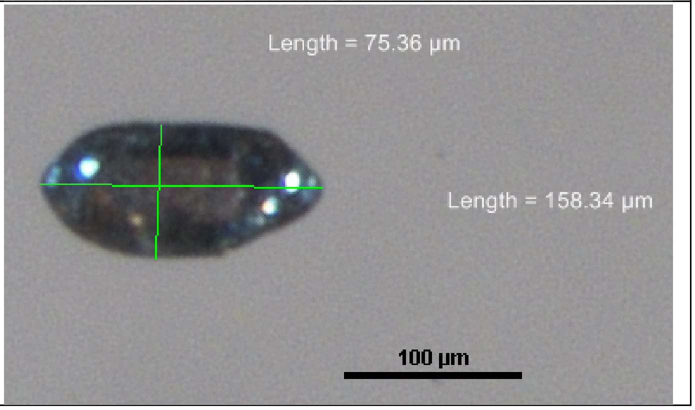

	4	Length = 153.10 Width = 64.32	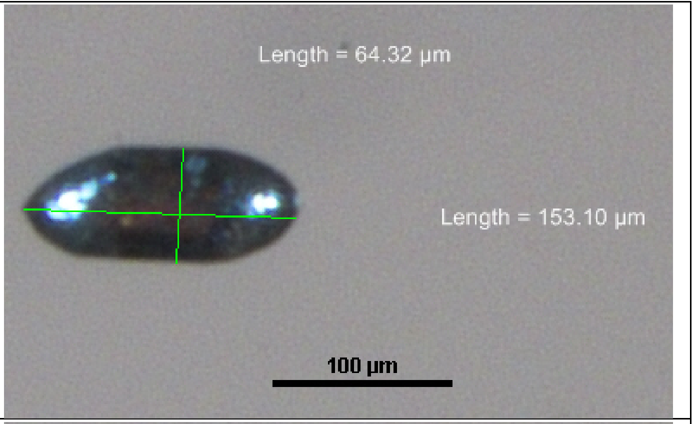
	5	Length = 149.64 Width = 68.66	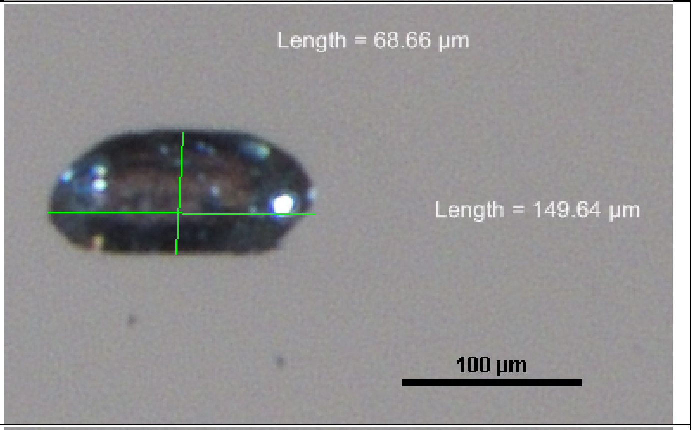
zK0008	1	Length = 260.53 Width = 82.54	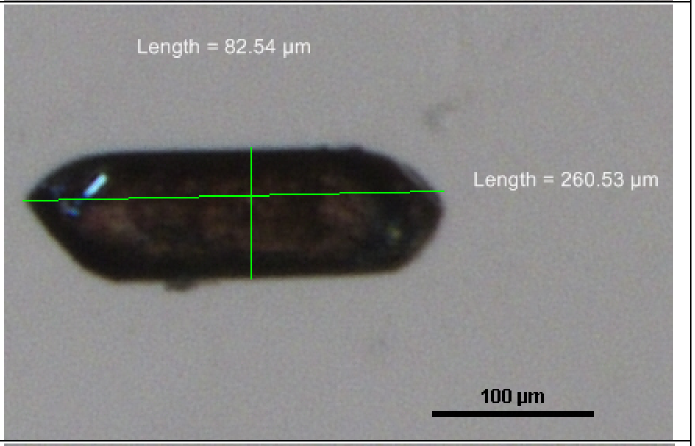
	2	Length = 180.22 Width = 86.32	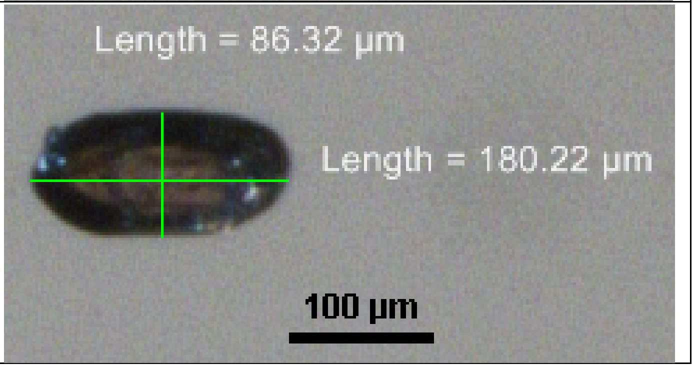

	3	Length = 155.24 Width = 71.18	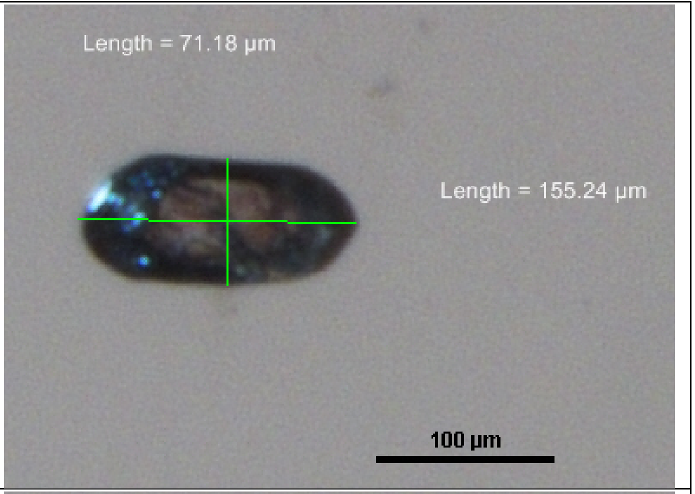
	4	Length = 236.25 Width = 105.28	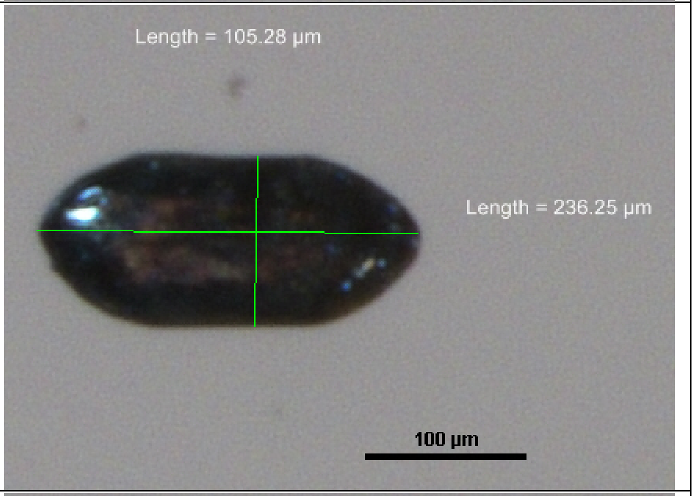
	5	Length = 271.46 Width = 90.77	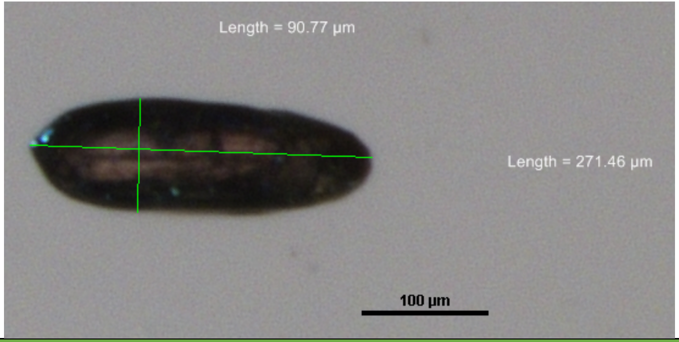
Apatite Samples			
Sample ID		**Measurements (µm)**	**Photo**

aK0016	1	Length = 263.08 Width = 154.49	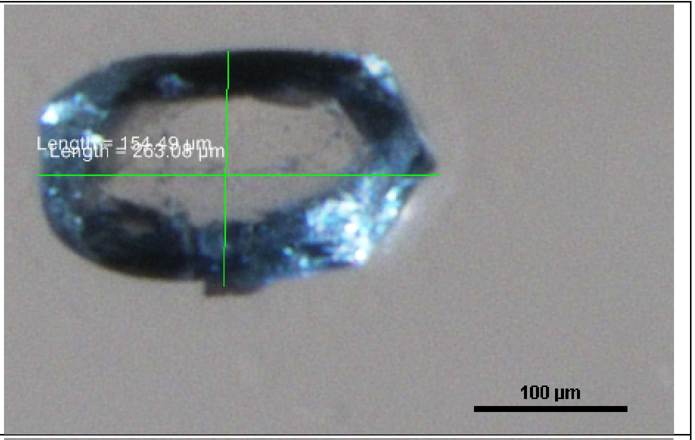
	2	Length = 173.82 Width = 88.36	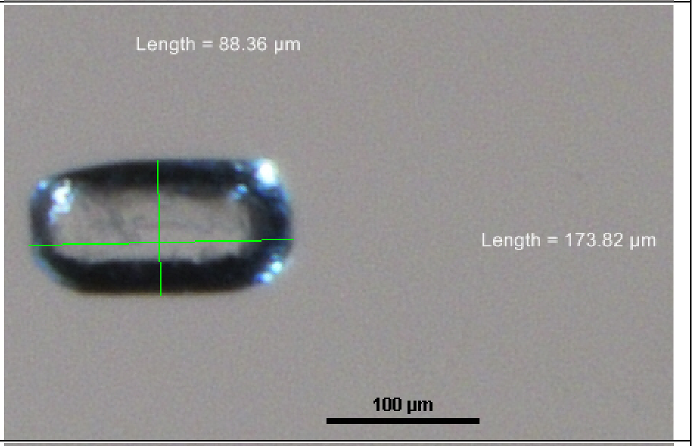
	3	Length = 157.37 Width = 81.58	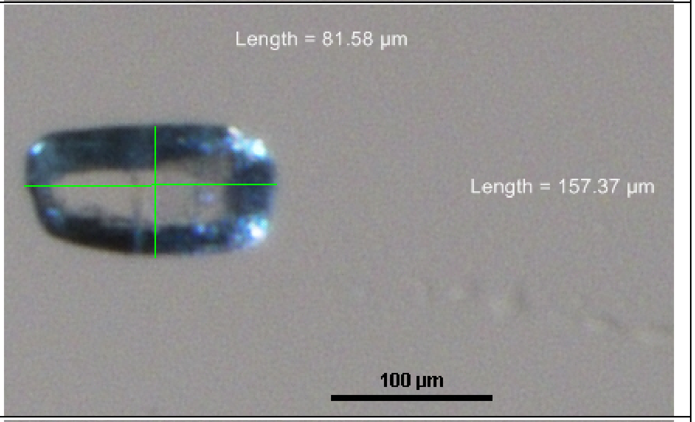
	4	Length = 177.66 Width = 114.89	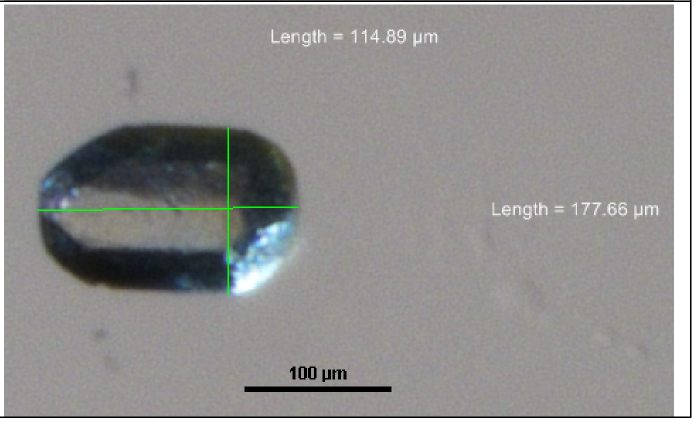

	5	Length = 149.17 Width = 112.96	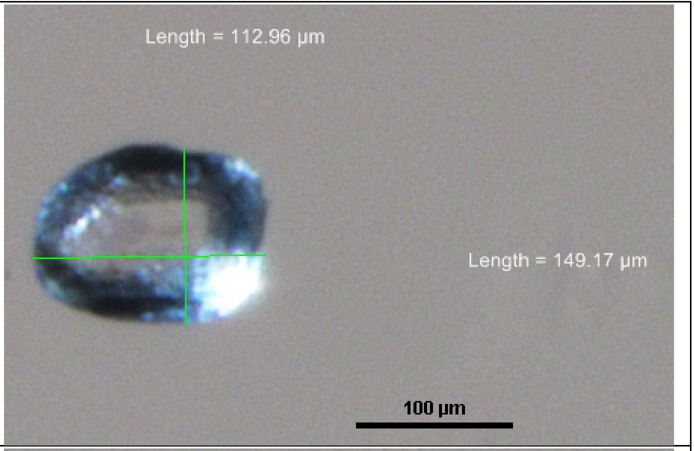
aK0015	1	Length = 164.17 Width = 82.09	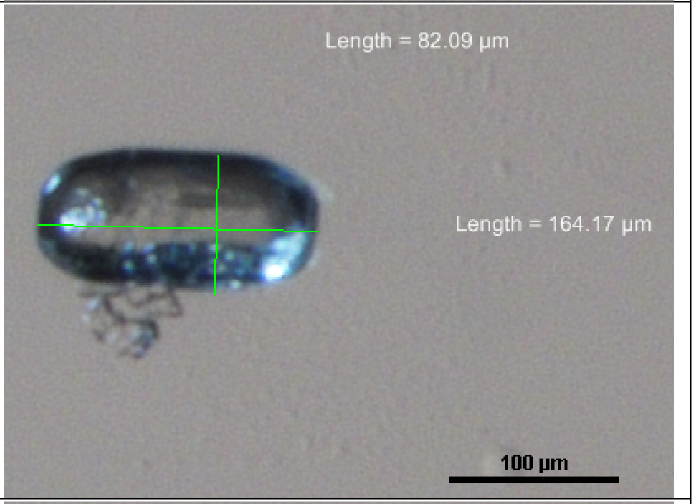
	2	Length = 153.03 Width = 71.44	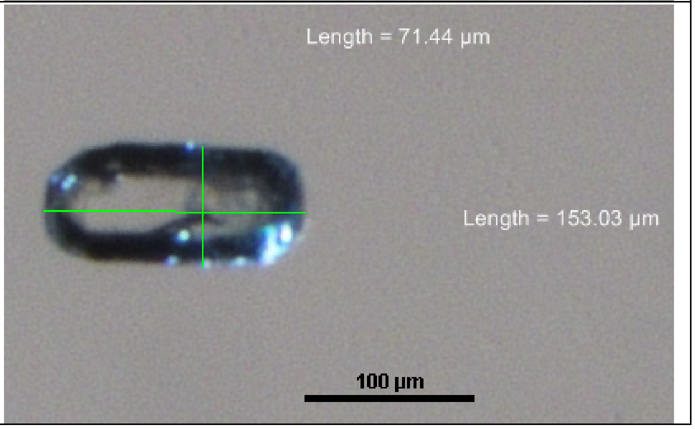

	3	Length = 130.42 Width = 71.97	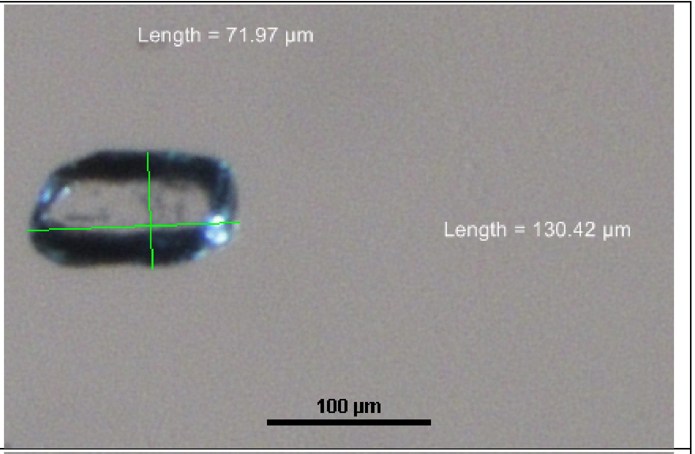
	4	Length = 133.25 Width = 62.75	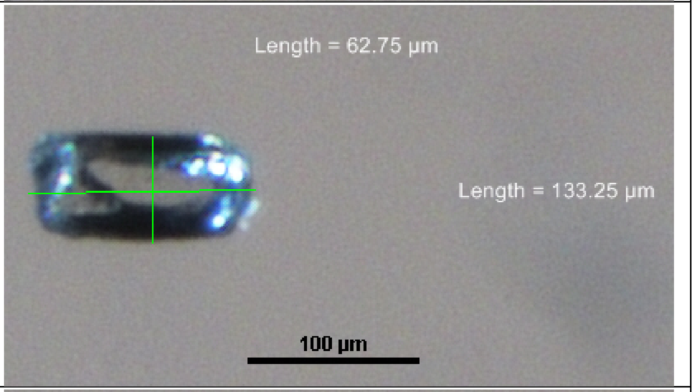
	5	Length = 140.02 Width = 66.13	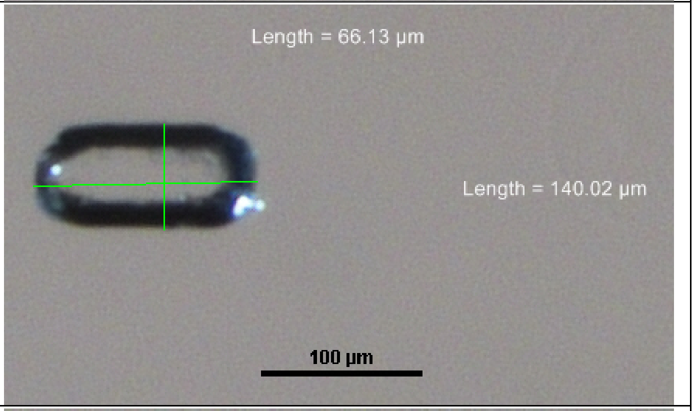
aK0014	1	Length = 168.18 Width = 119.12	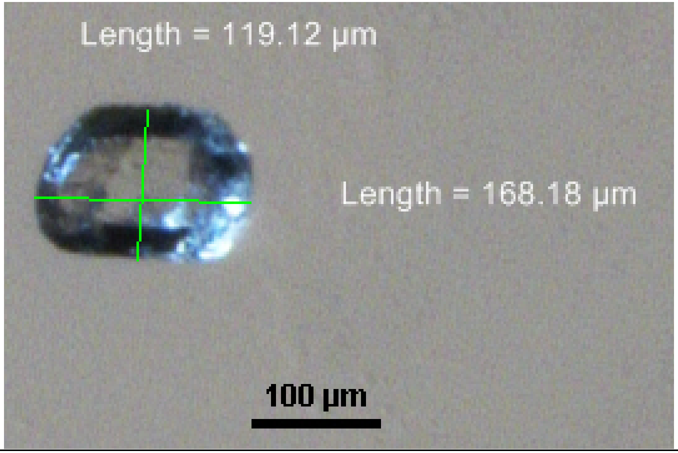

	2	Length = 228.37 Width = 99.44	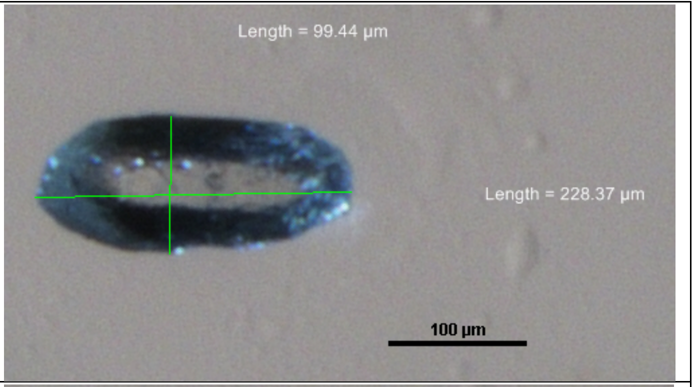
	3	Length = 221.64 Width = 95.17	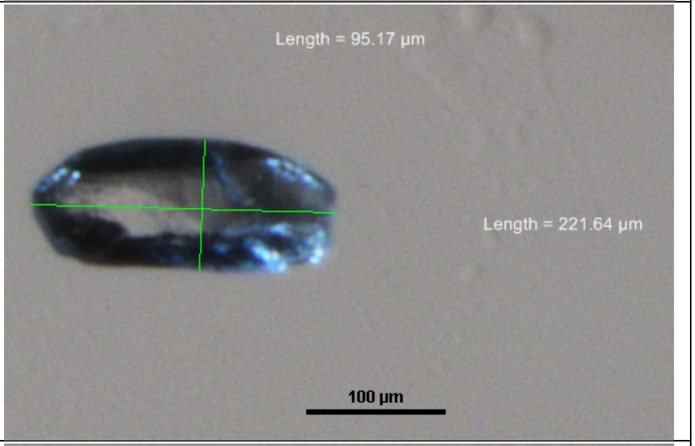
	4	Length = 136.15 Width = 75.79	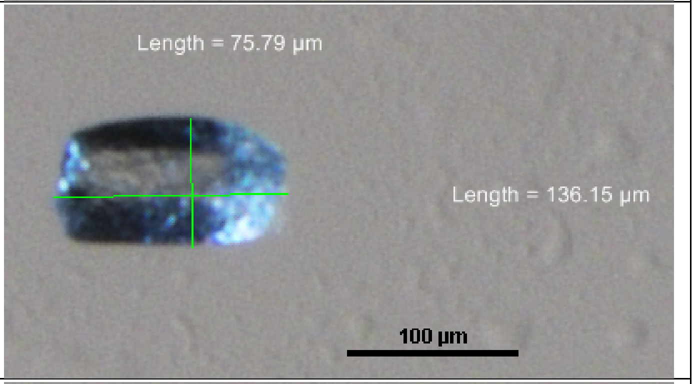
	5	Length = 159.32 Width = 87.37	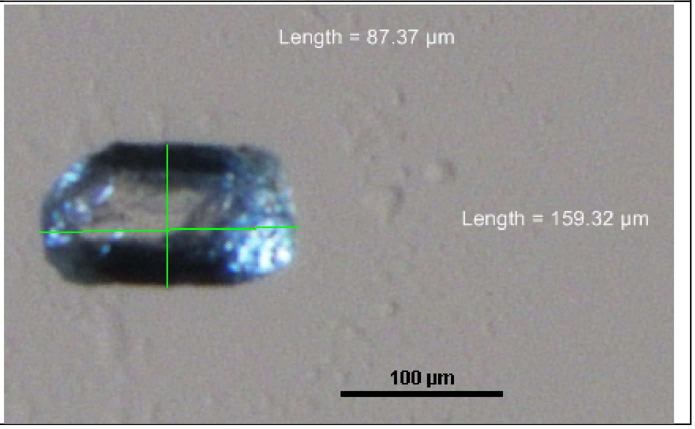

aK0013	1	Length = 151.58 Width = 76.75	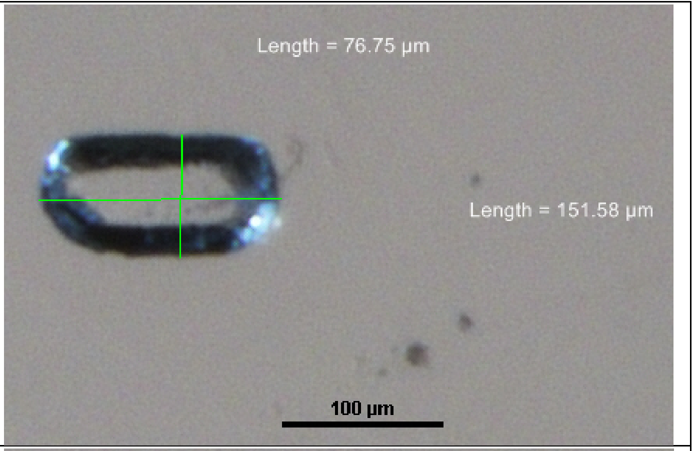
	2	Length = 209.50 Width = 76.75	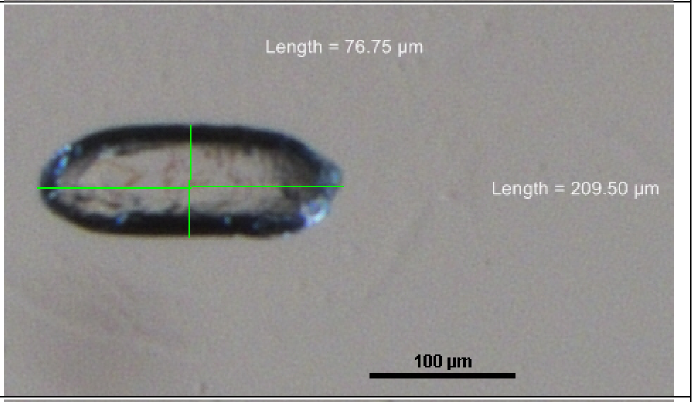
	3	Length = 240.45 Width = 75.31	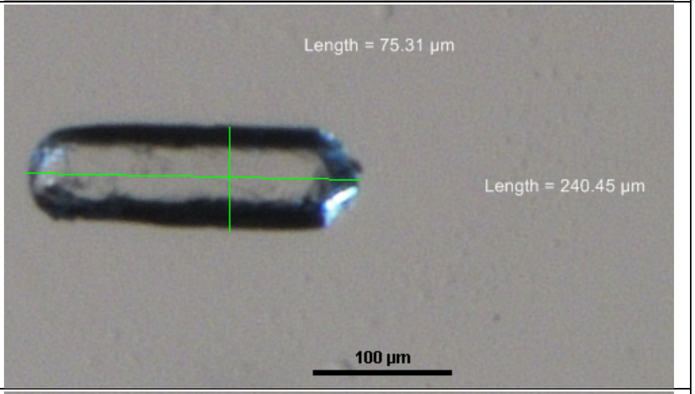
	4	Length = 200.33 Width = 77.24	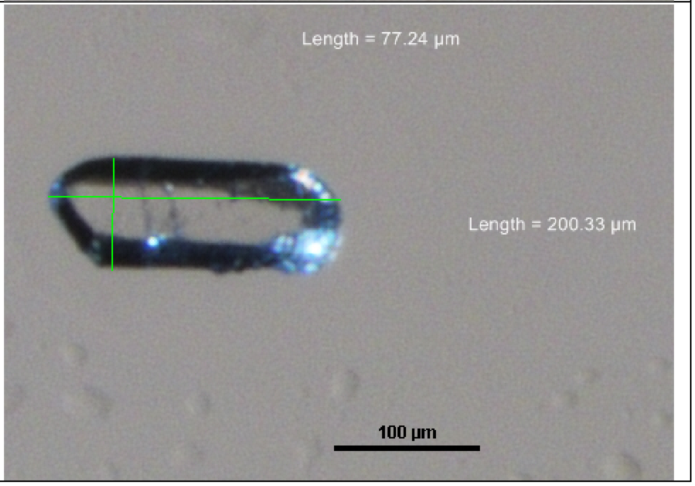

	5	Length = 167.99 Width = 72.92	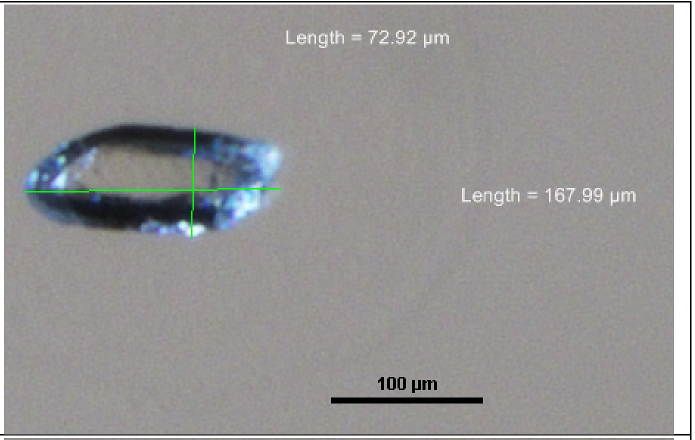
aK0012	1	Length = 164.05 Width = 106.90	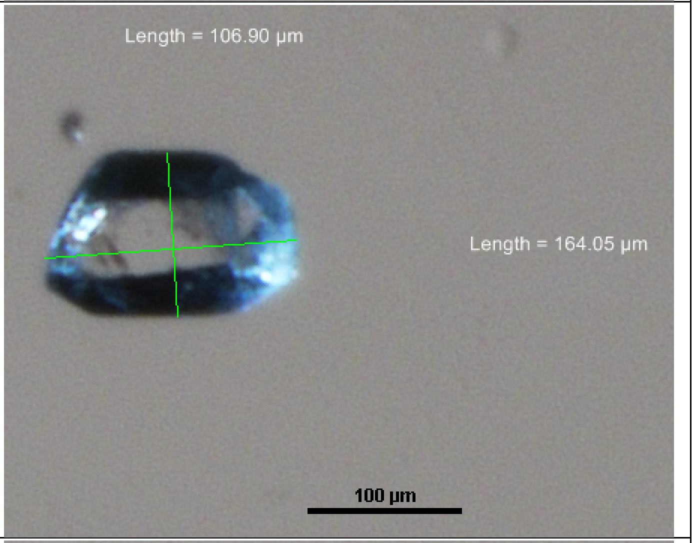
	2	Length = 146.76 Width = 66.15	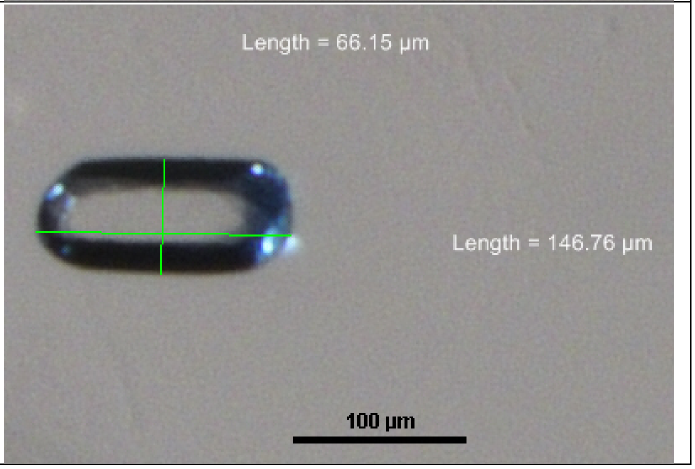

	3	Length = 125.03 Width = 86.41	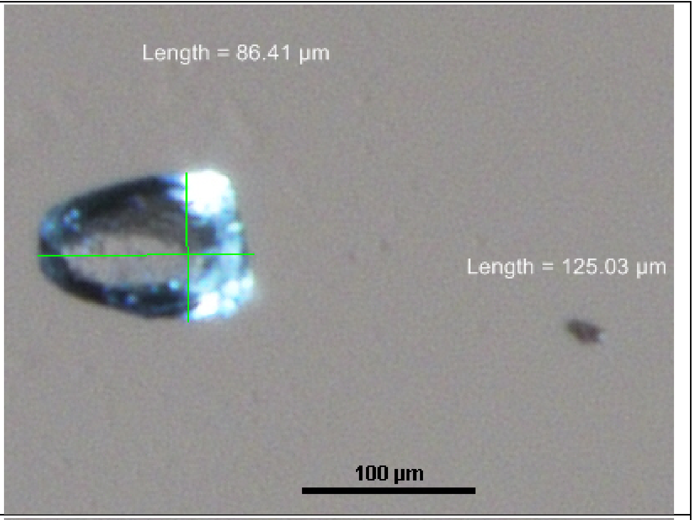
	4	Length = 144.82 Width = 88.82	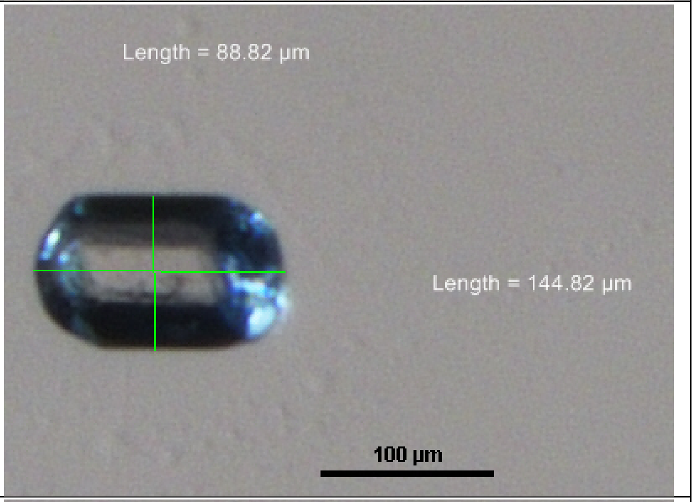
	5	Length = 139.51 Width = 65.65	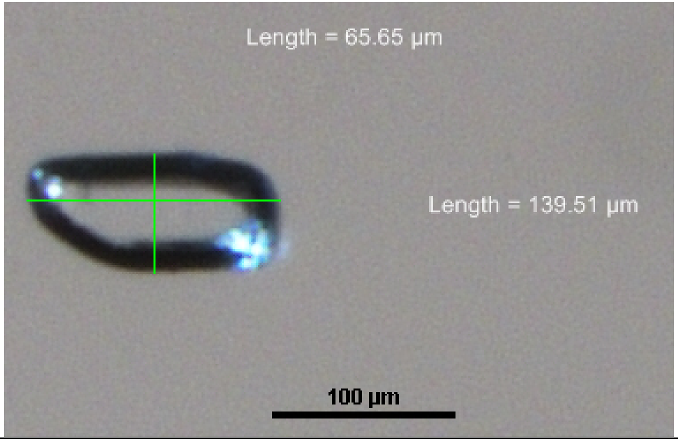

aK0011	1	Length = 159.30 Width = 84.98	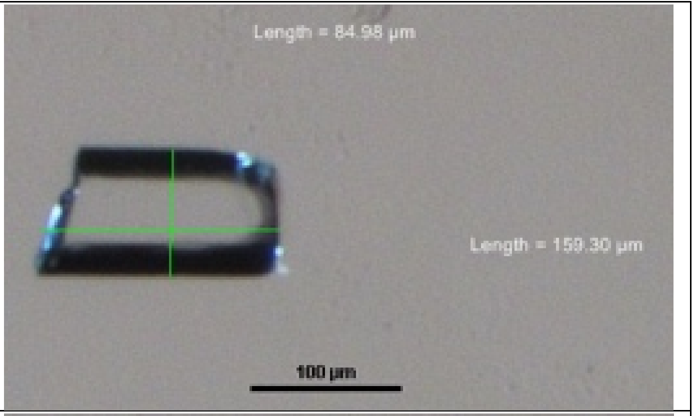
	2	Length = 135.65 Width = 78.68	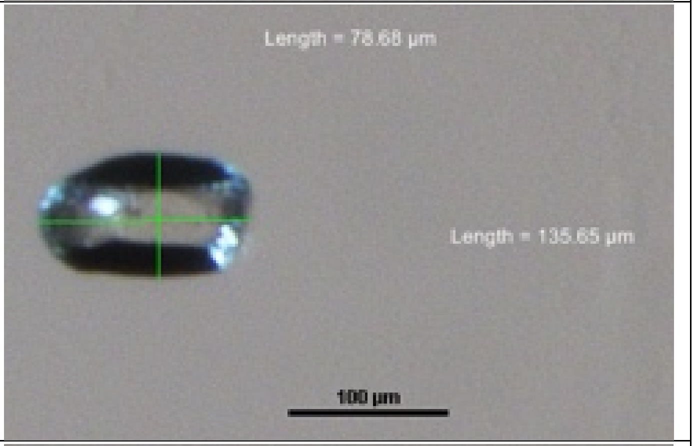
	3	Length = 169.44 Width = 75.30	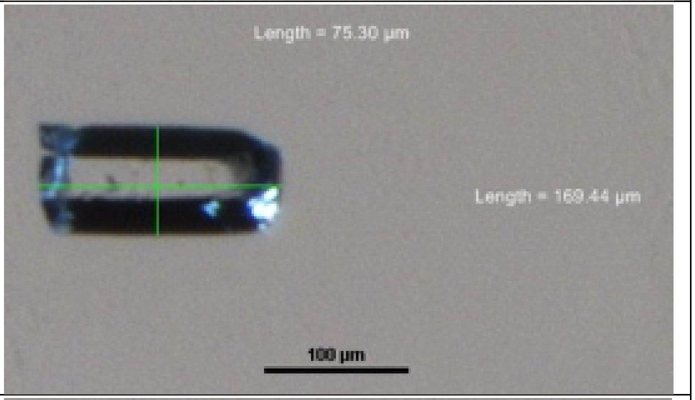
	4	Length = 164.61 Width = 86.89	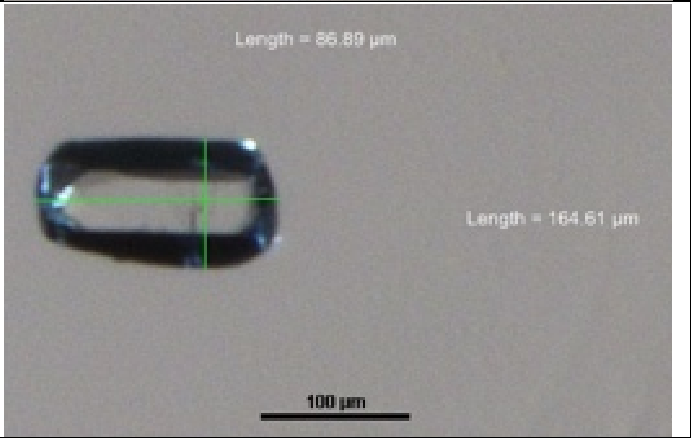

	5	Length = 144.84 Width = 97.03	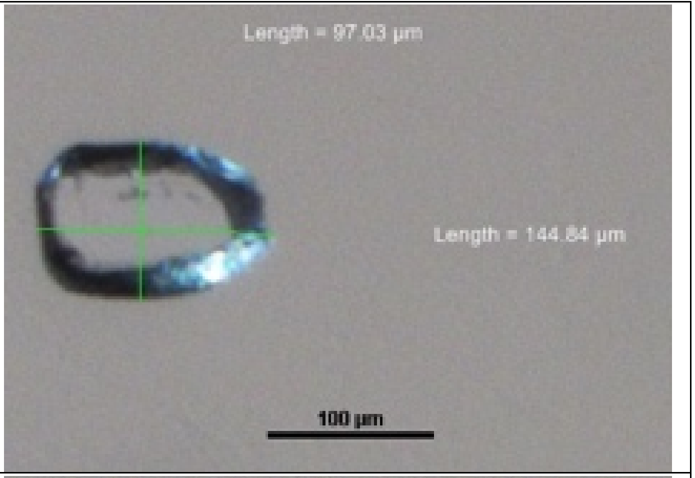
aK0010	1	Length = 167.57 Width = 100.91	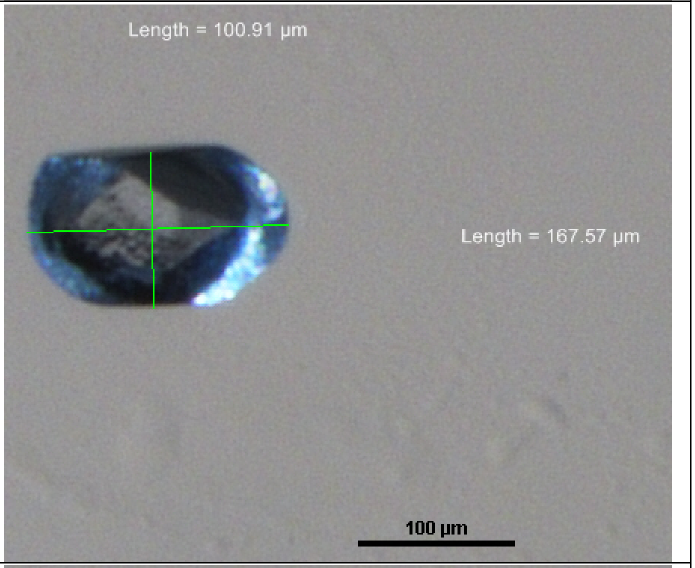
	2	Length = 192.61 Width = 95.10	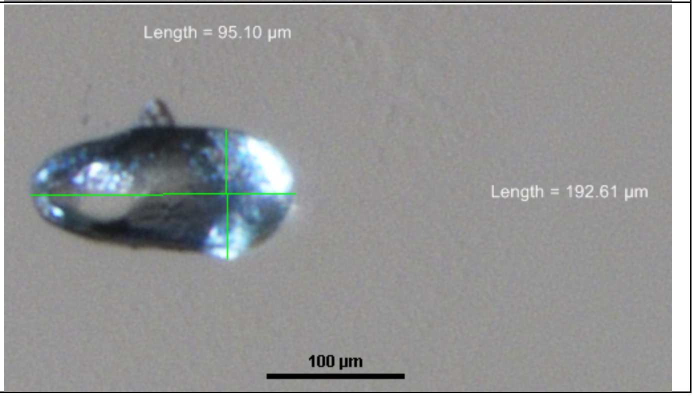

	3	Length = 167.02 Width = 97.53	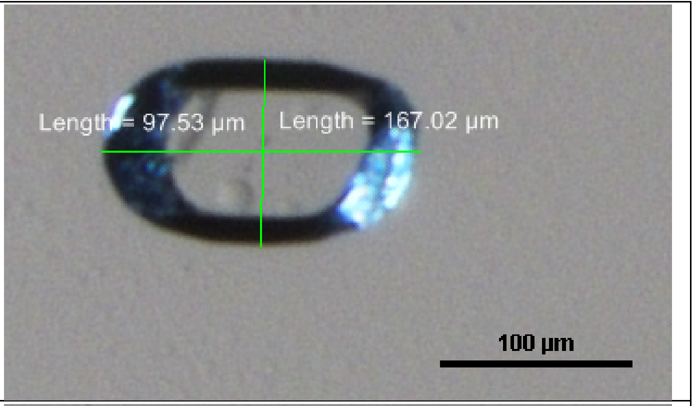
	4	Length = 160.27 Width = 104.27	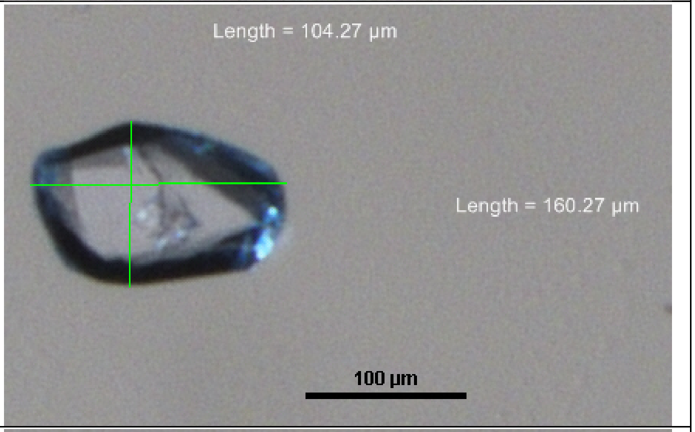
	5	Length = 178.61 Width = 108.17	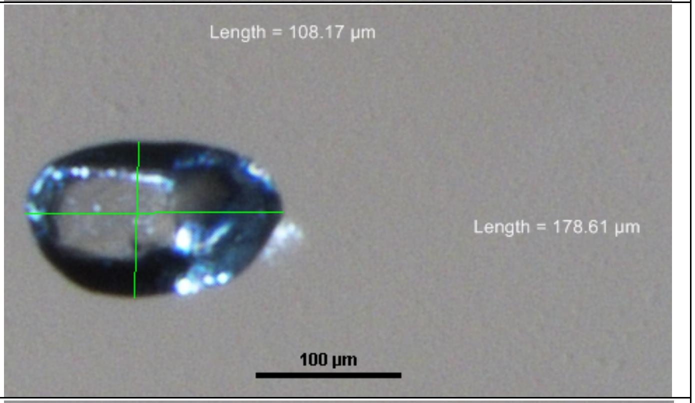
aK0009	1	Length = 250.07 Width = 156.49	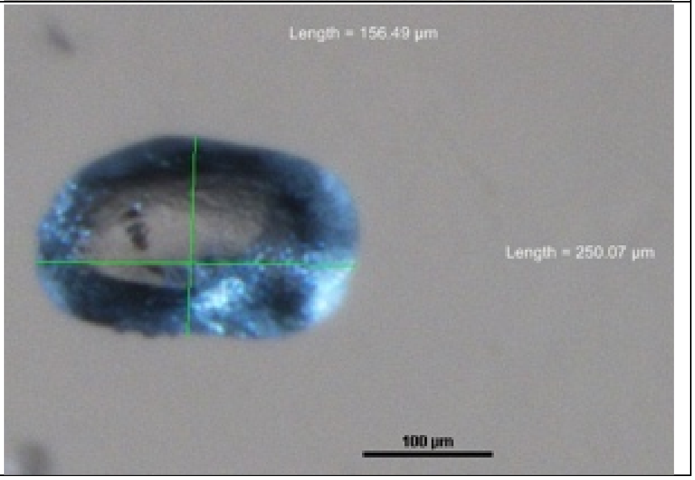

	2	Length = 181.99 Width = 90.76	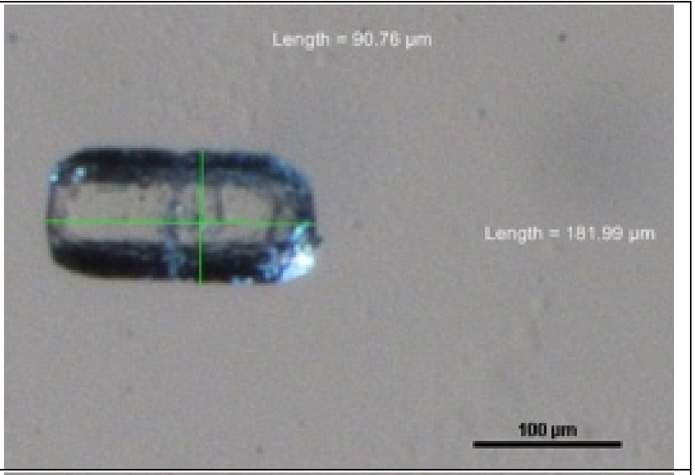
	3	Length = 129.38 Width = 72.89	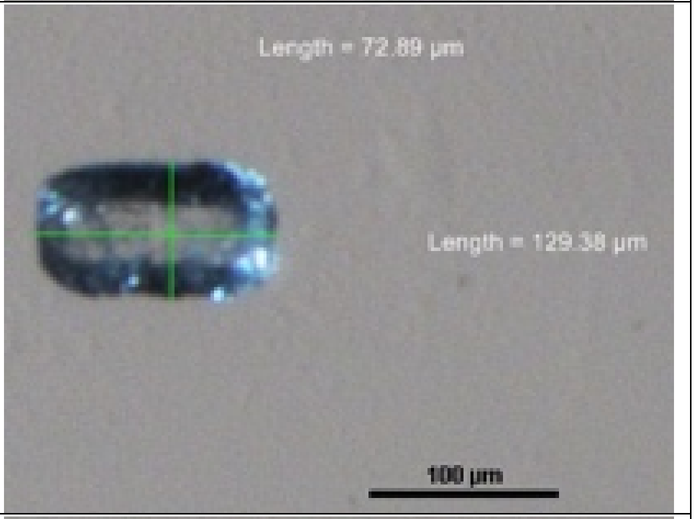
	4	Length = 127.92 Width = 89.79	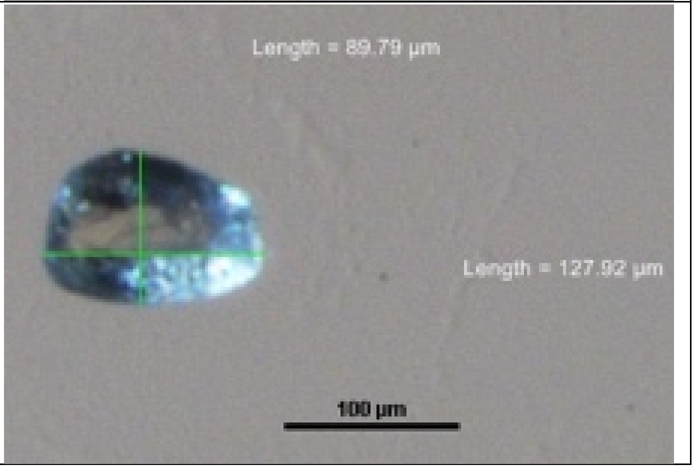

	5	Length = 118.75 Width = 96.07	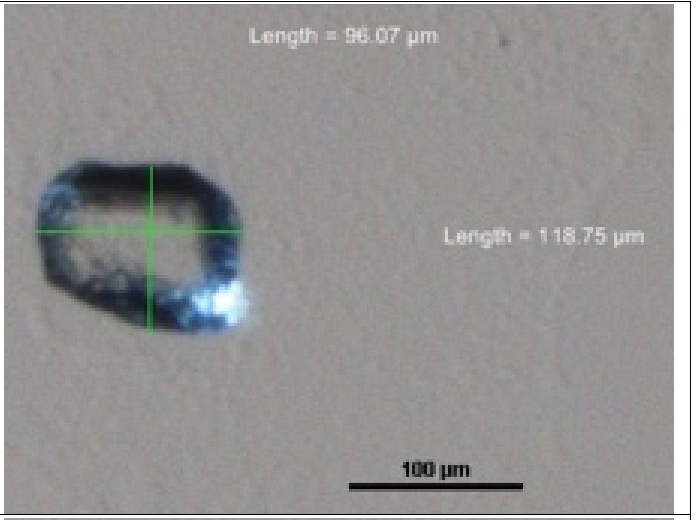
aK0008	1	Length = 110.06 Width = 161.72	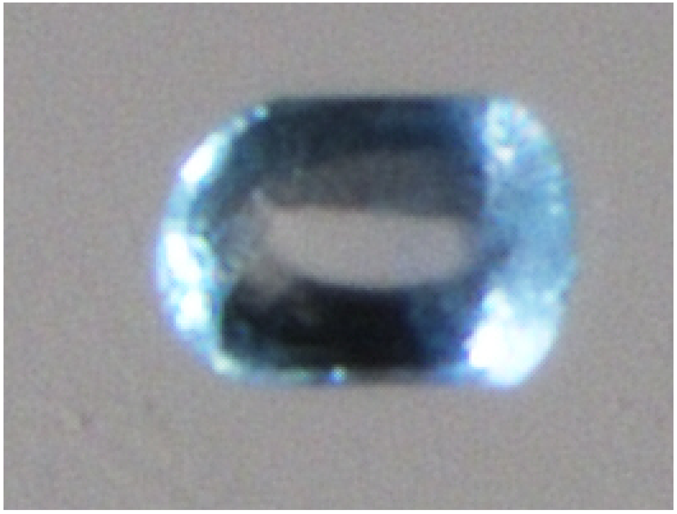 **Note: did not take photo with measurements on it for this grain.
	2	Length = 198.90 Width = 98.49	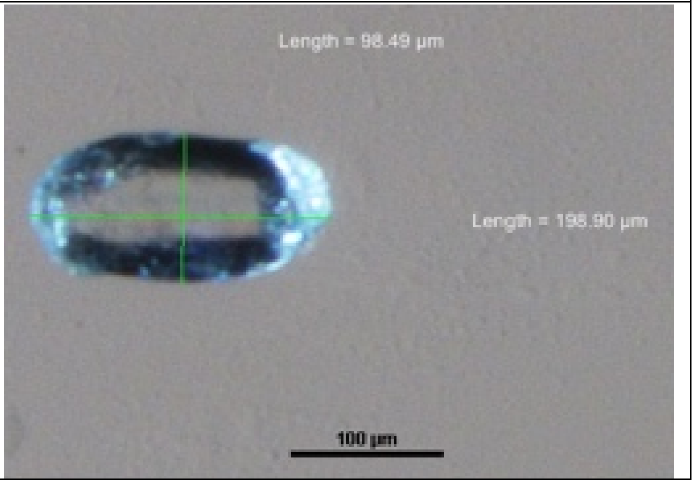

	3	Length = 176.19 Width = 95.13	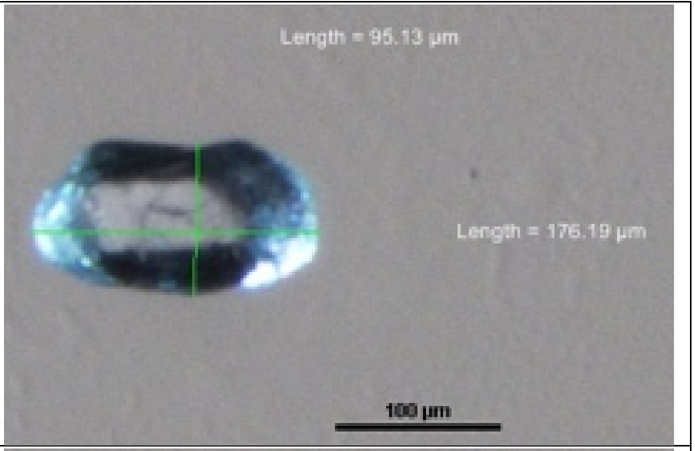
	4	Length = 200.40 Width = 121.20	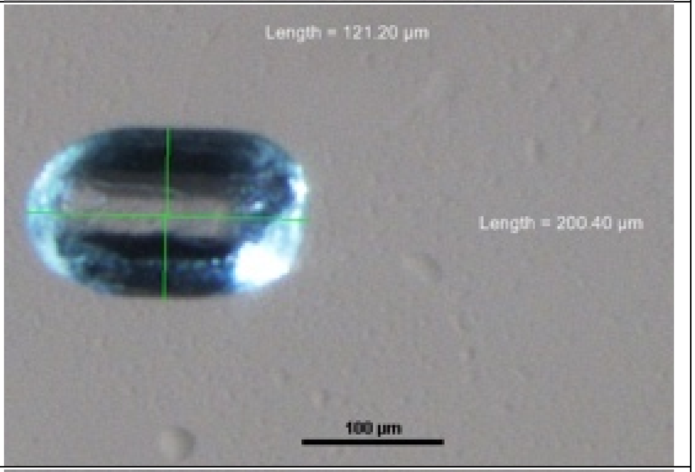
	5	Length = 266.04 Width = 125.99	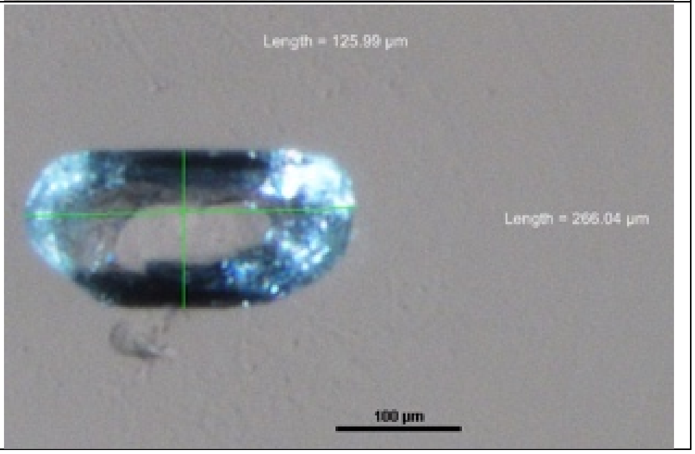

Makkovik Transect			
Zircon samples			
Sample ID		**Measurements (µm)**	**Photo**
z71TA464	1	Length = 255.32 Width = 92.90	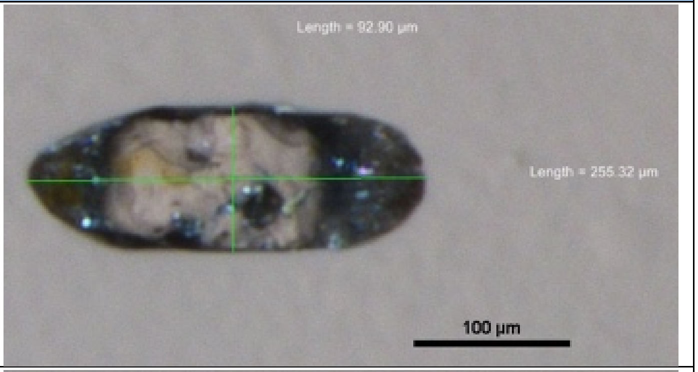
	2	Length = 223.65 Width = 69.17	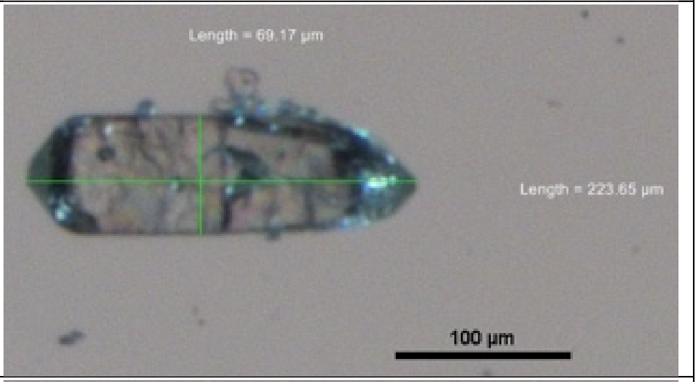
	3	Length = 148.99 Width = 54.71	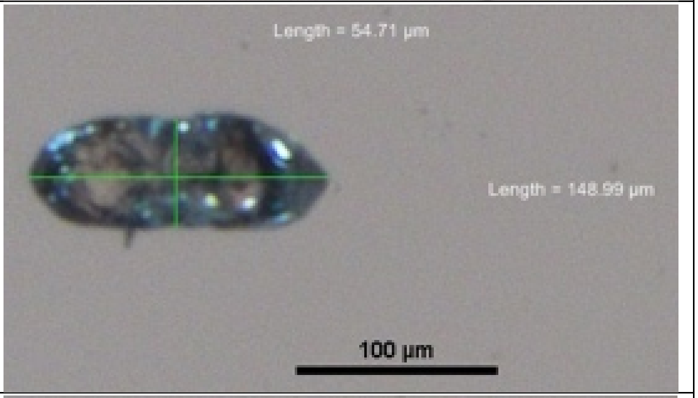
	4	Length = 190.28 Width = 64.01	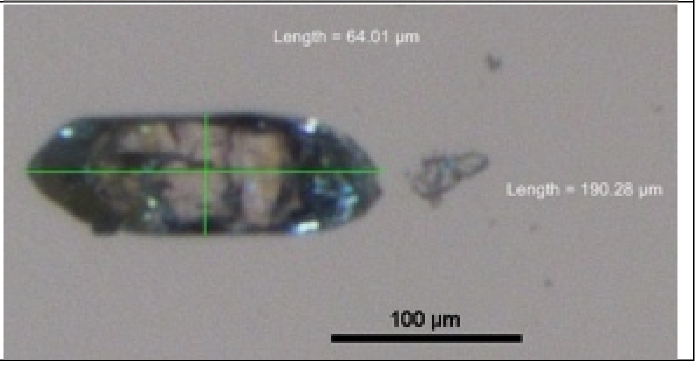

	5	Length = 264.60 Width = 83.27	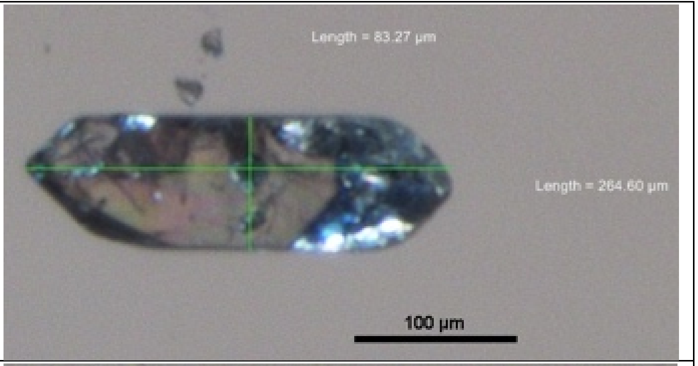
z71TA923	1	Length = 234.32 Width = 51.61	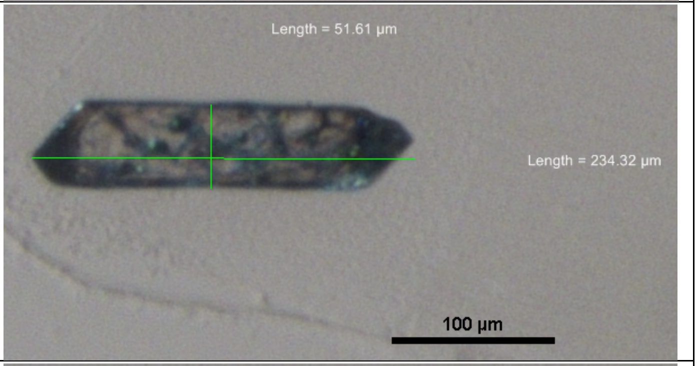
	2	Length = 197.54 Width = 36.72	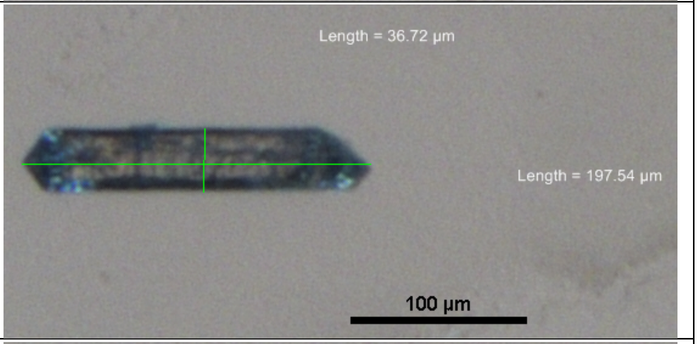
	3	Length = 165.50 Width = 61.25	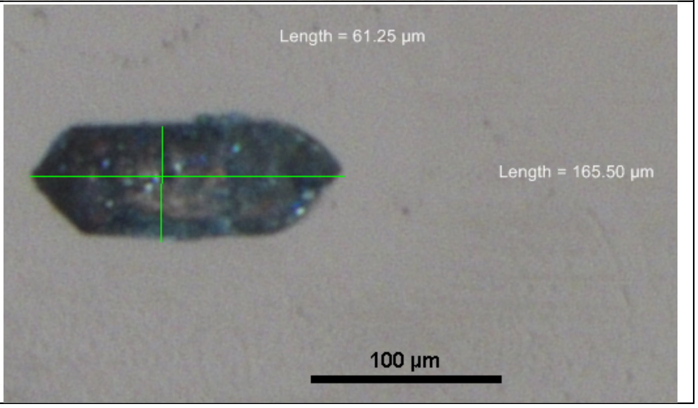

	4	Length = 239.53 Width = 59.87	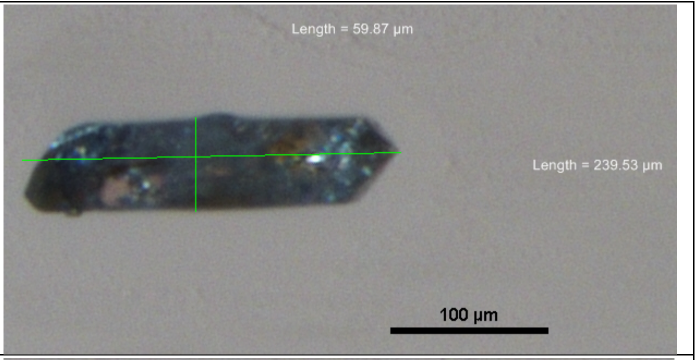
	5	Length = 171.37 Width = 54.03	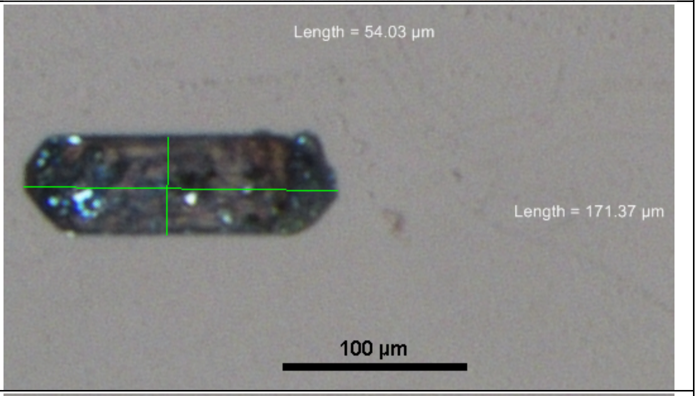
z71BT407	1	Length = 159.31 Width = 64.34	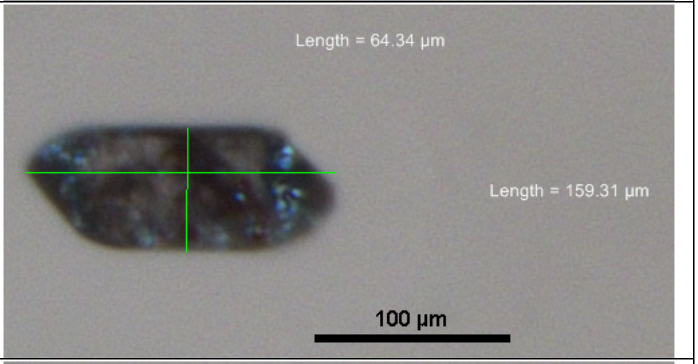
	2	Length = 118.37 Width = 61.93	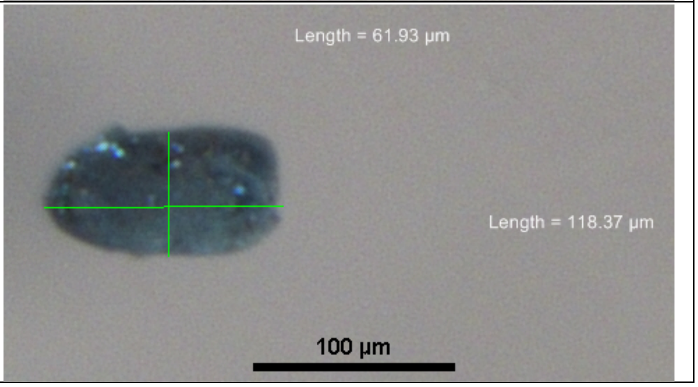

	3	Length = 222.28 Width = 84.99	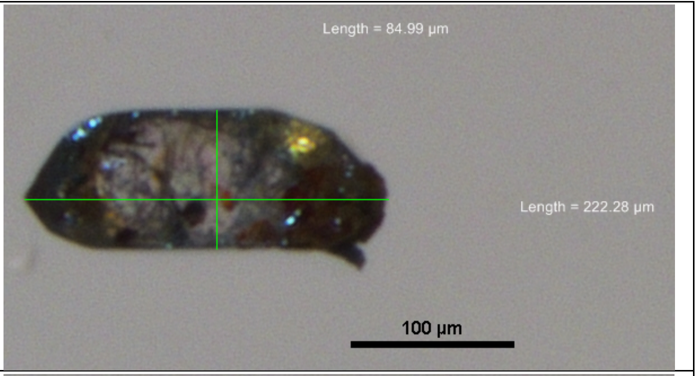
	4	Length = 182.71 Width = 93.96	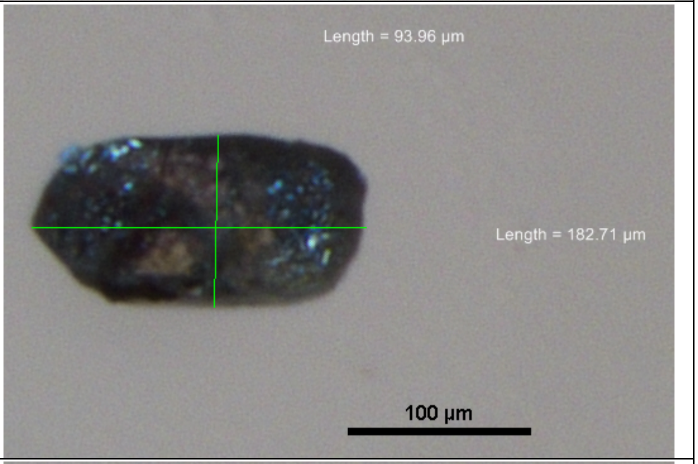
	5	Length = 159.31 Width = 58.15	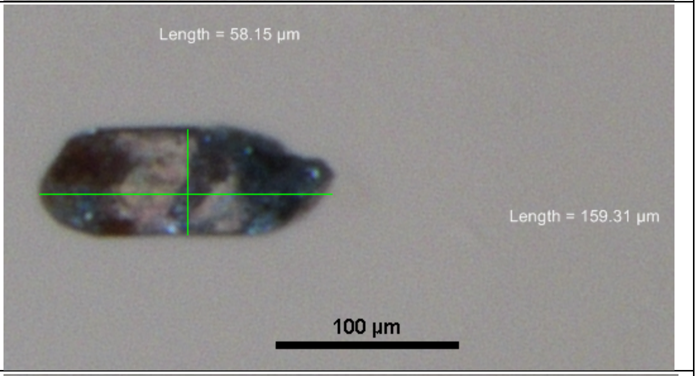
z71TA929	1	Length = 185.82 Width = 71.92	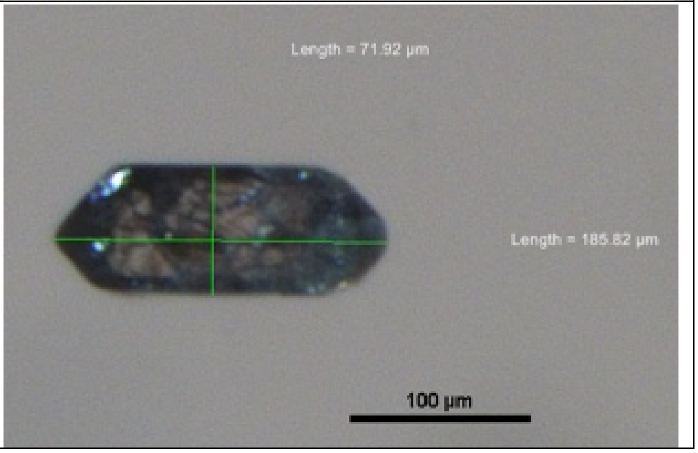

	2	Length = 324.83 Width = 90.20	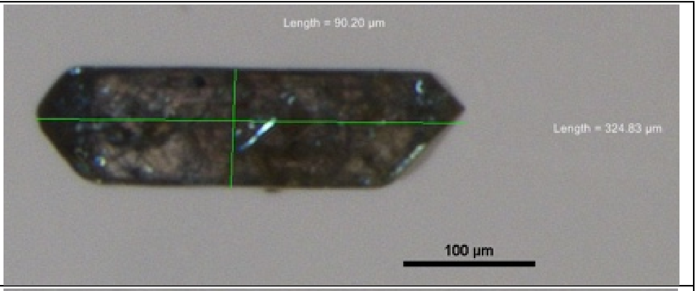
	3	Length = 164.13 Width = 70.55	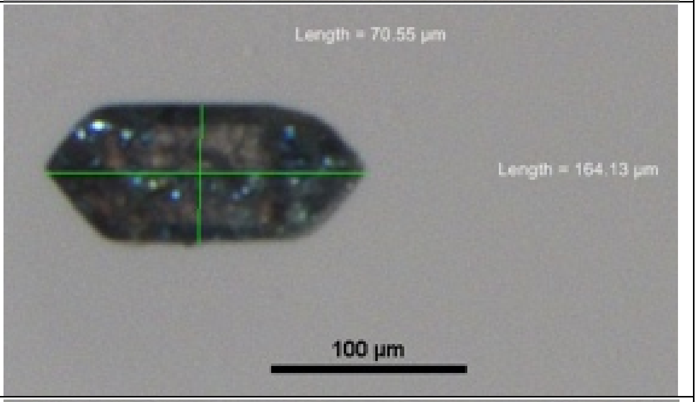
	4	Length = 152.78 Width = 66.07	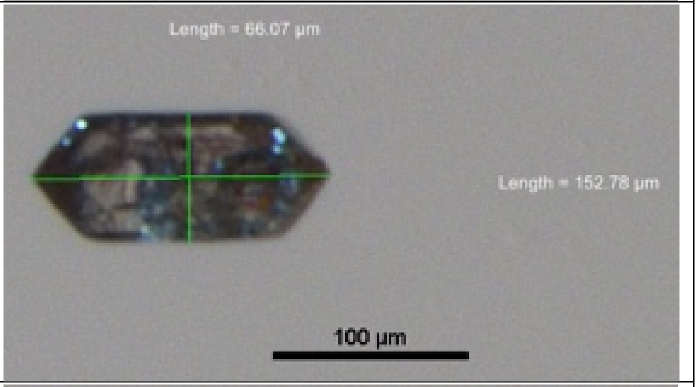
	5	Length = 193.72 Width = 71.57	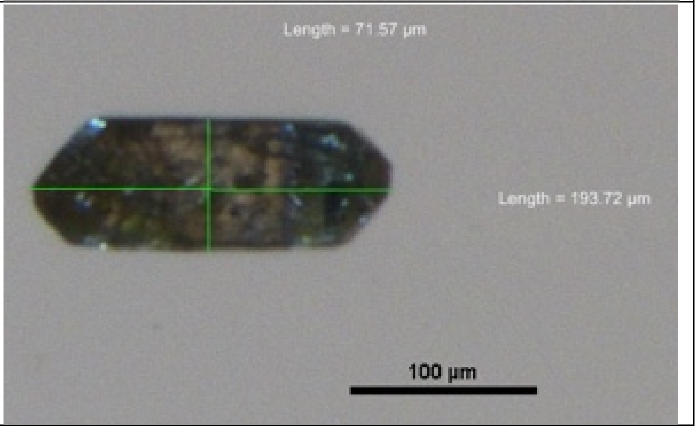

z71TA909	1	Length = 199.30 Width = 102.02	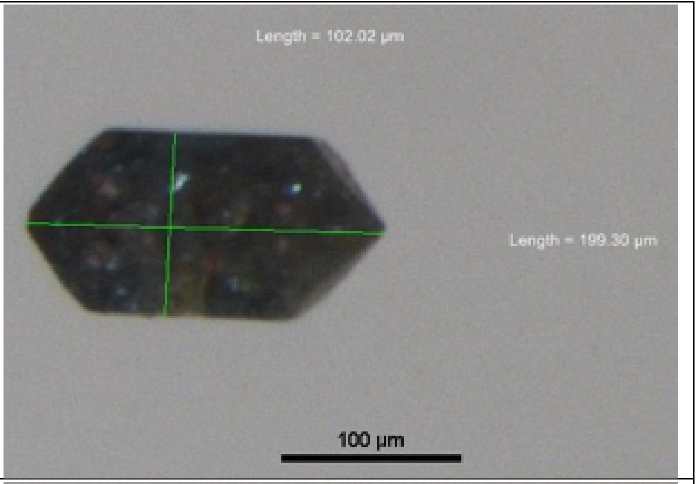
	2	Length = 278.71 Width = 85.36	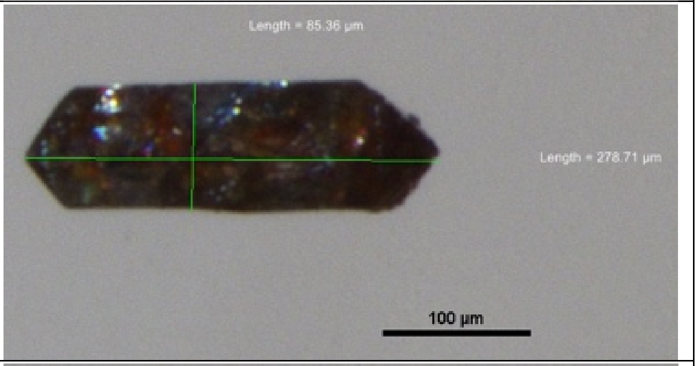
	3	Length = 190.97 Width = 84.99	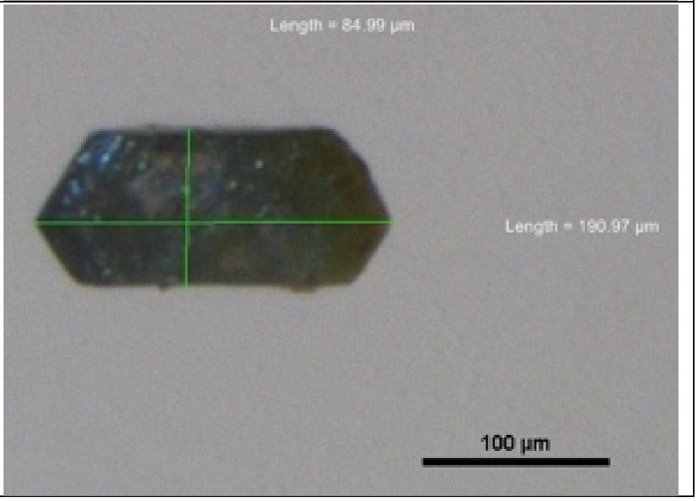

	4	Length = 158.29 Width = 71.91	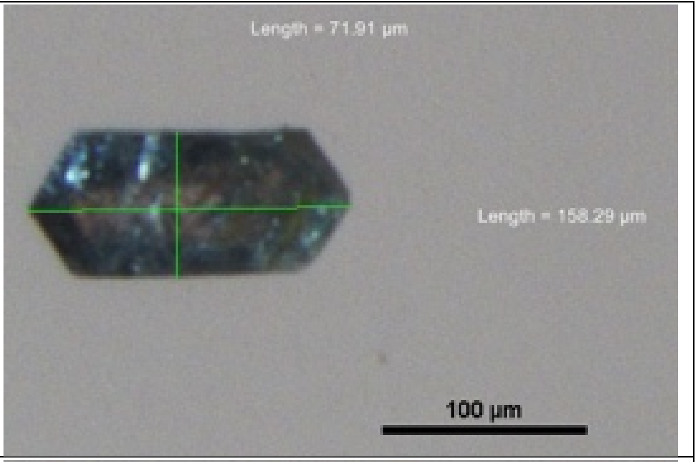
	5	Length = 140.04 Width = 73.63	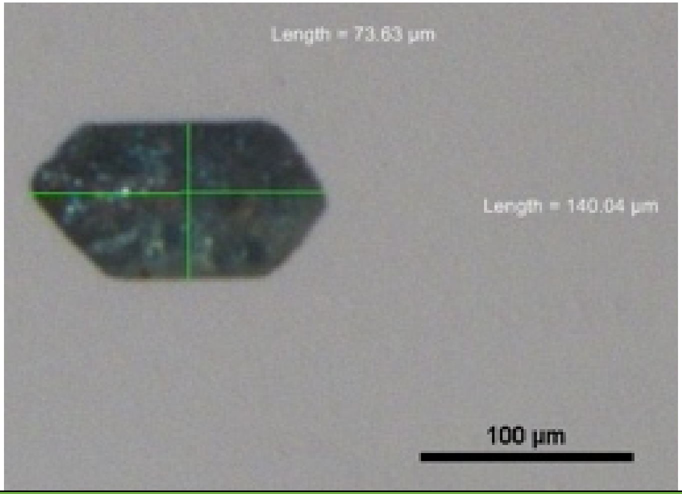
Apatite Samples			
Sample ID		Measurements (µm)	Photo
a71TA464	1	Length = 151.40 Width = 62.63	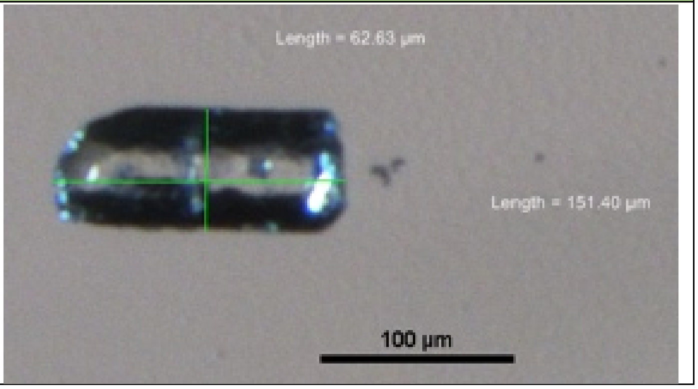

	2	Length = 151.06 Width = 68.13	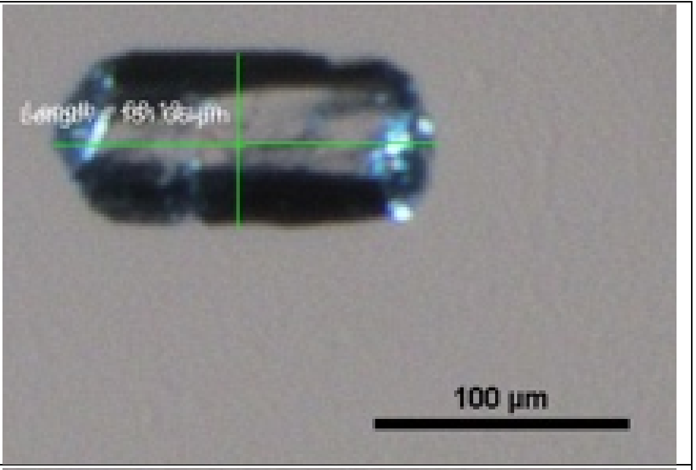
	3	Length = 132.86 Width = 63.33	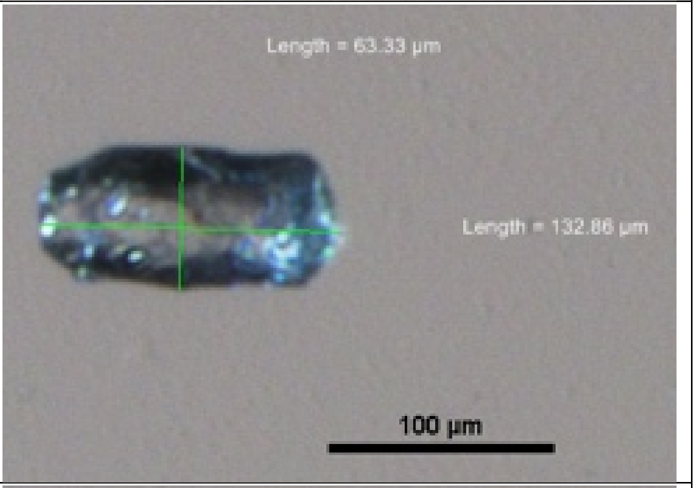
	4	Length = 124.24 Width = 80.20	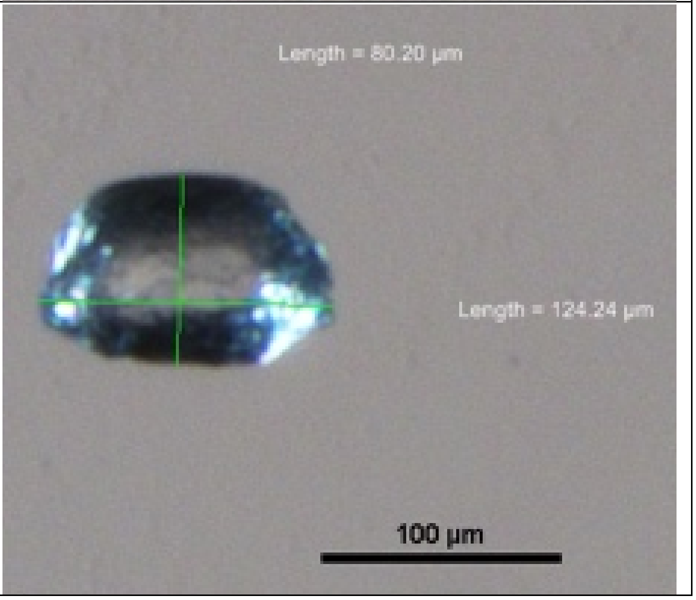

	5	Length = 177.96 Width = 69.59	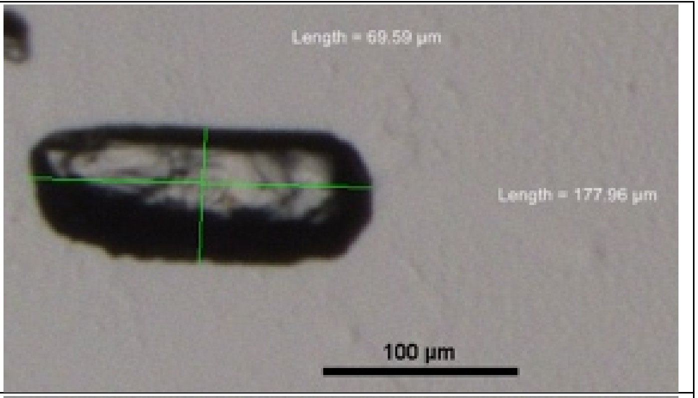
a71TA923	1	Length = 227.18 Width = 89.92	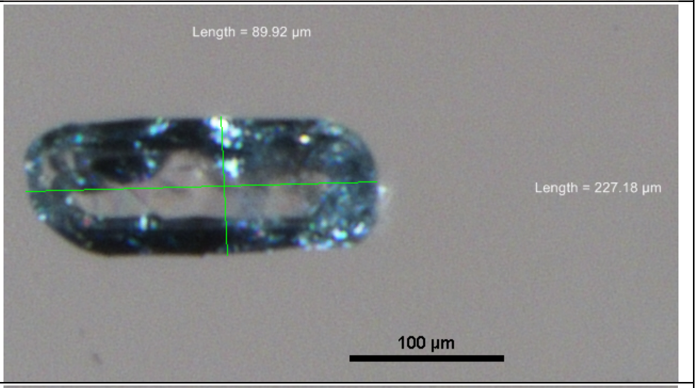
	2	Length = 175.14 Width = 70.88	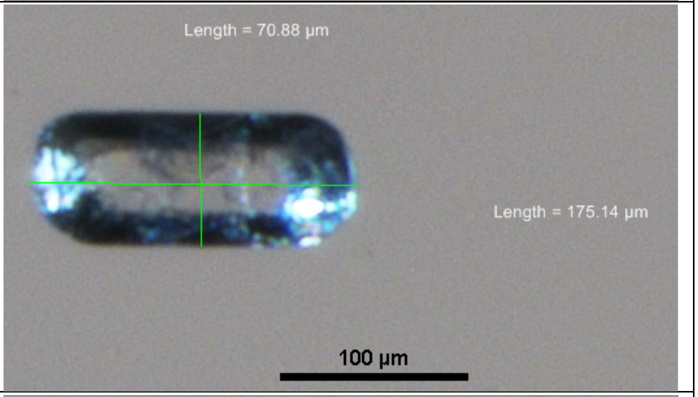
	3	Length = 181.33 Width = 102.20	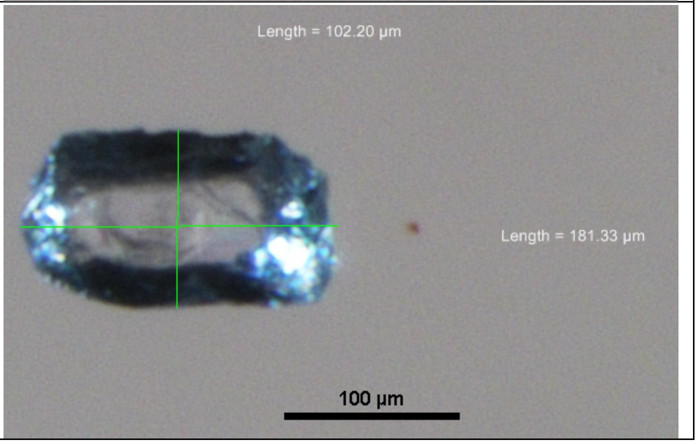

	4	Length = 145.56 Width = 77.78	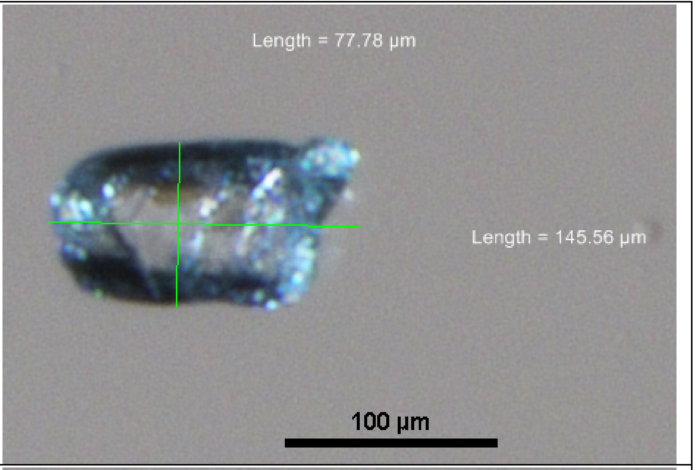
	5	Length = 101.95 Width = 67.13	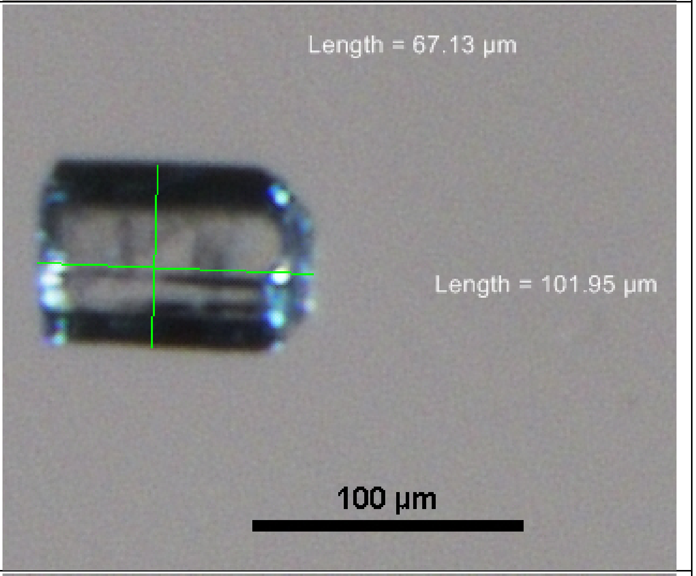
a71TA910	1	Length = 136.27 Width = 108.36	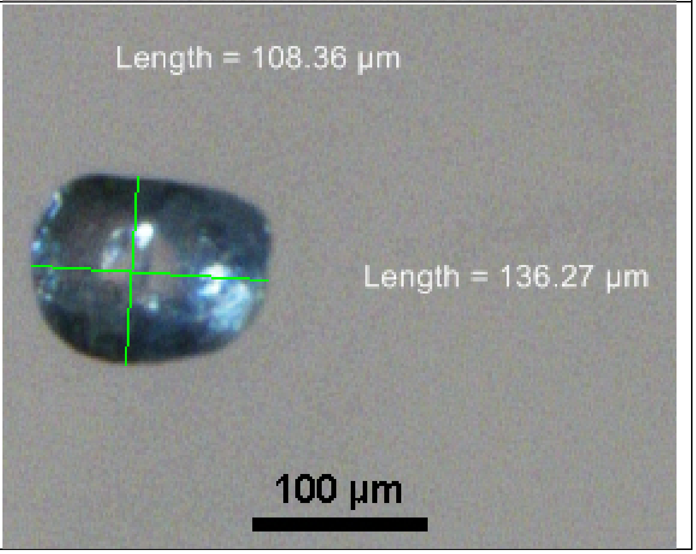

	2	Length = 147.91 Width = 90.15	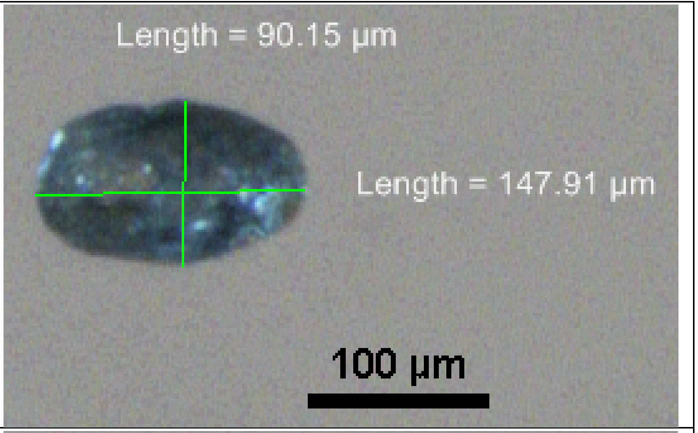
	3	Length = 101.85 Width = 79.48	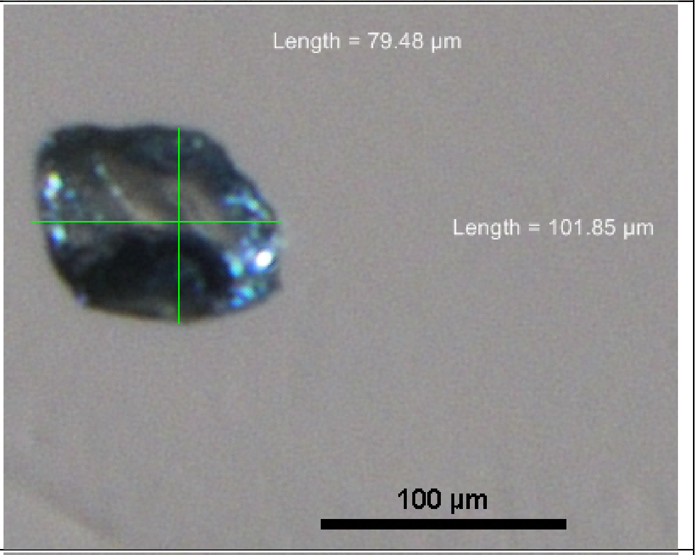
	4	Length = 109.08 Width = 79.83	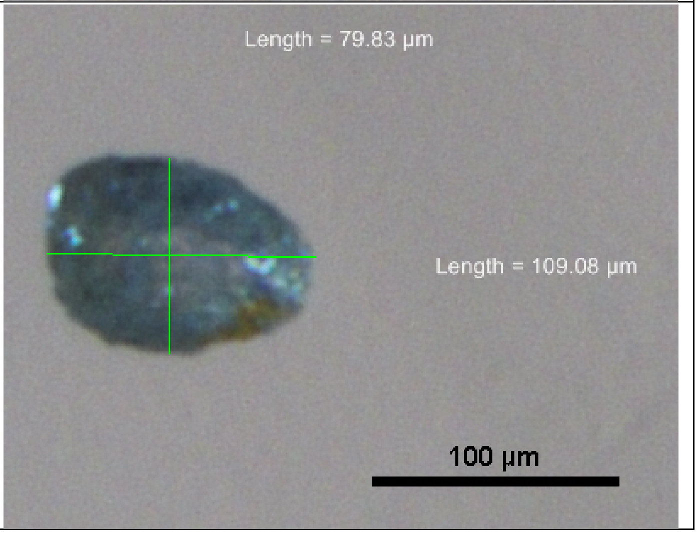

	5	Length = 123.53 Width = 77.42	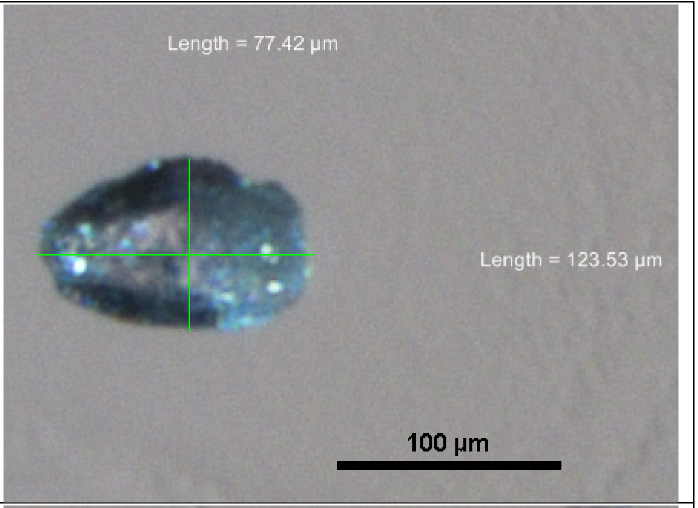
a71TA912	1	Length = 191.31 Width = 83.62	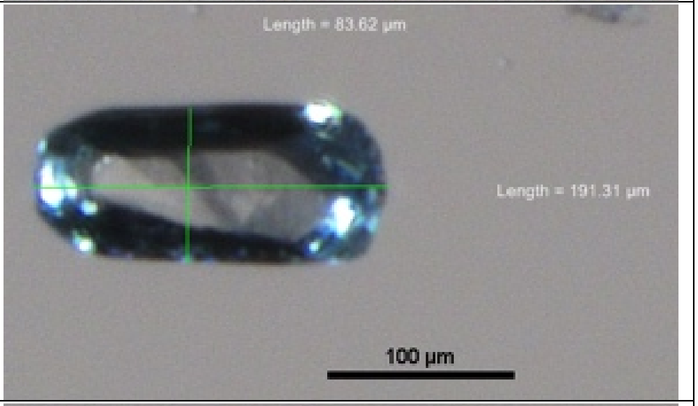
	2	Length = 187.53 Width = 96.03	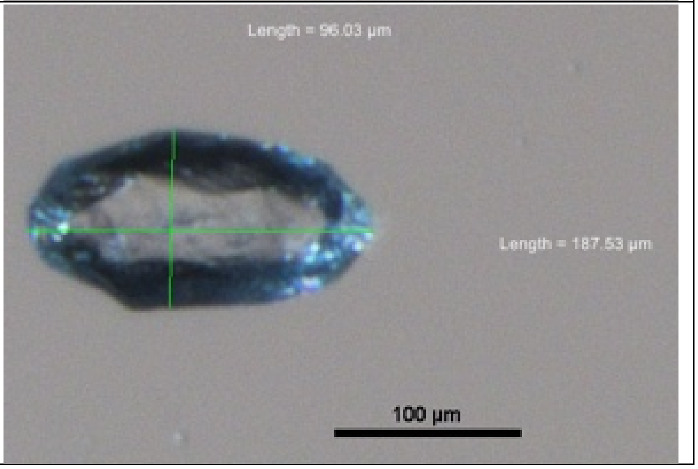

	3	Length = 269.07 Width = 96.34	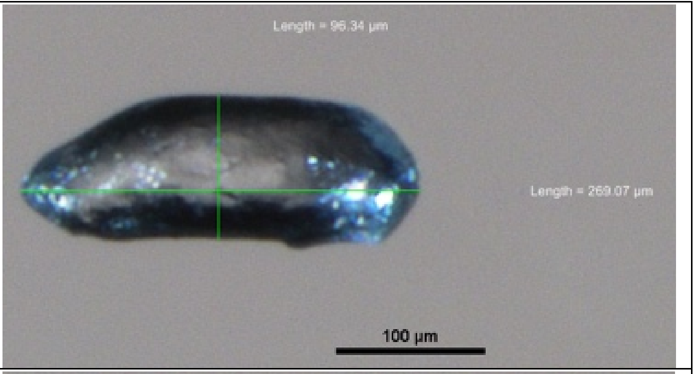
	4	Length = 179.53 Width = 85.12	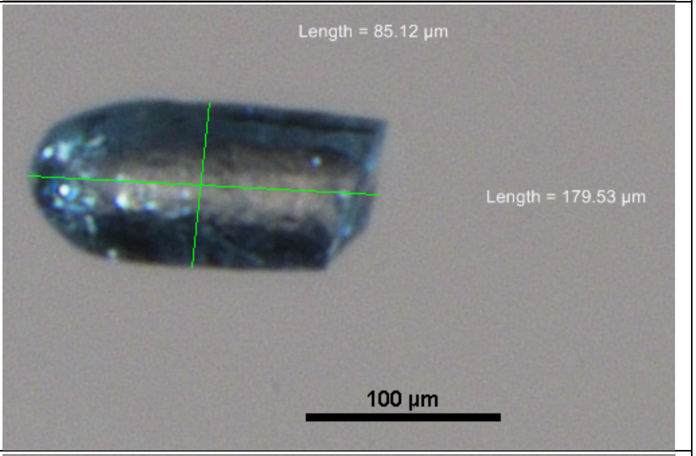
	5	Length = 159.02 Width = 87.08	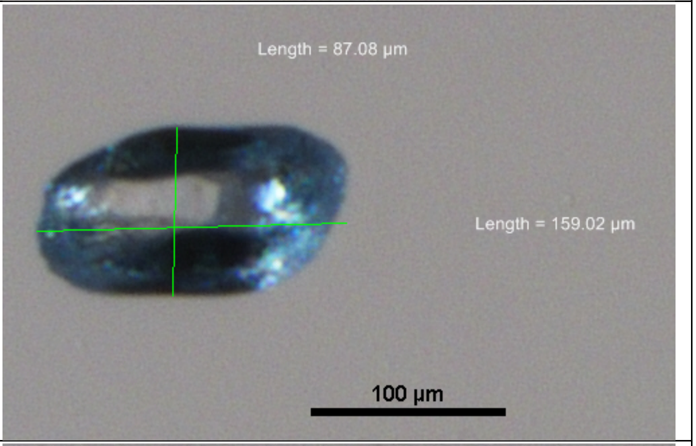
a71TA929	1	Length = 145.56 Width = 76.74	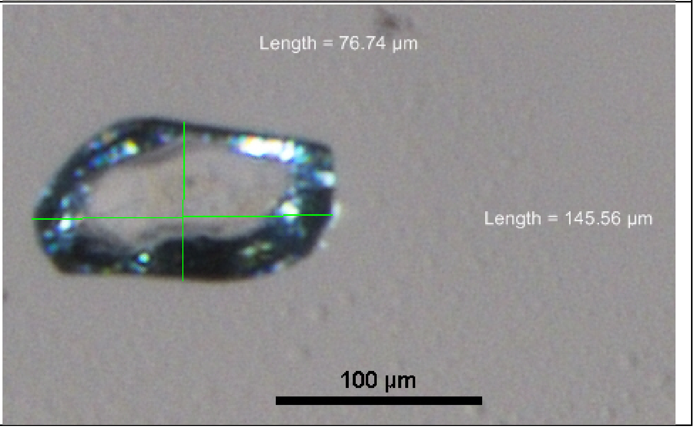

	2	Length = 157.93 Width = 79.84	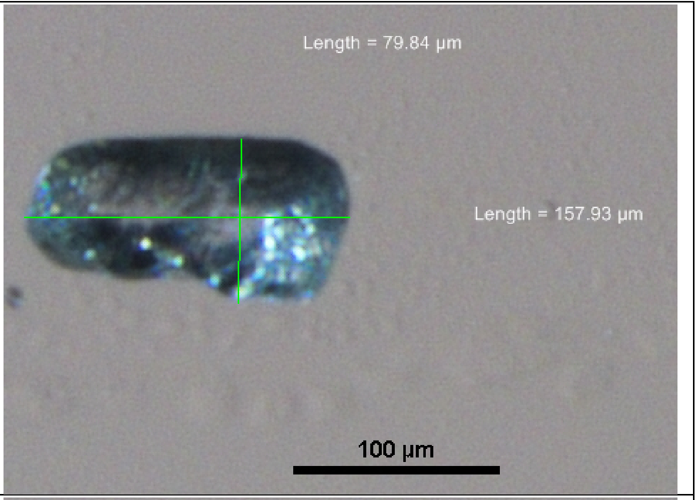
	3	Length = 134.92 Width = 63.75	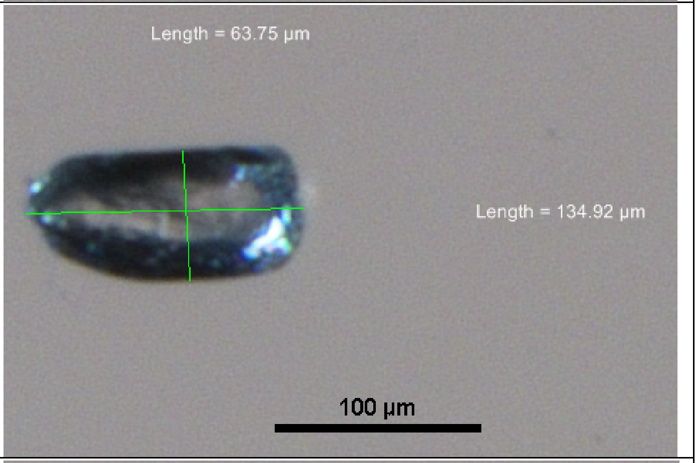
	4	Length = 144.67 Width = 62.07	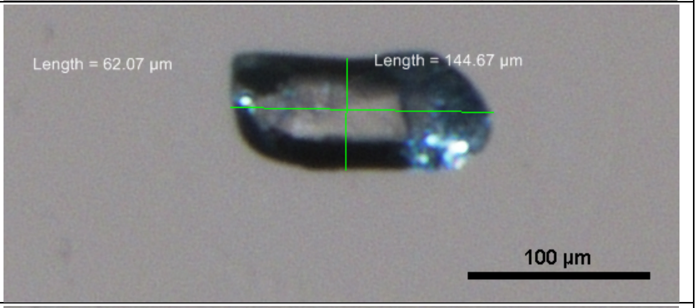
	5	Length = 161.05 Width = 68.47	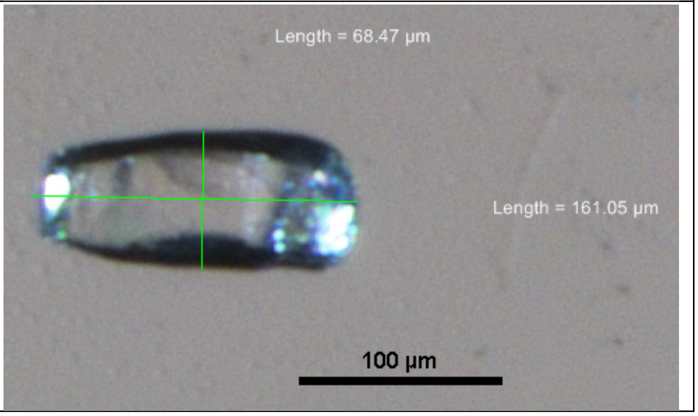

a71TA909	1	Length = 137.24 Width = 69.26	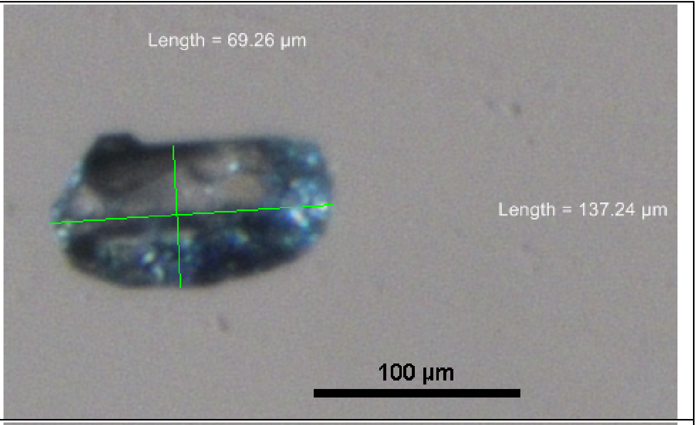
	2	Length = 146.27 Width = 86.73	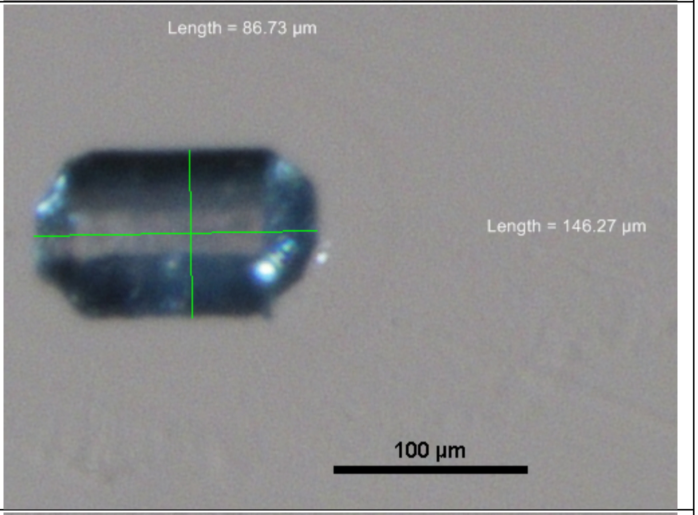
	3	Length = 136.95 Width = 93.59	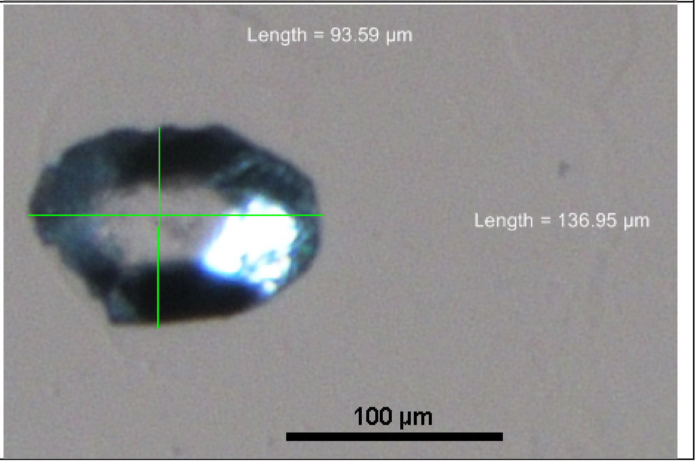

	4	Length = 129.04 Width = 59.55	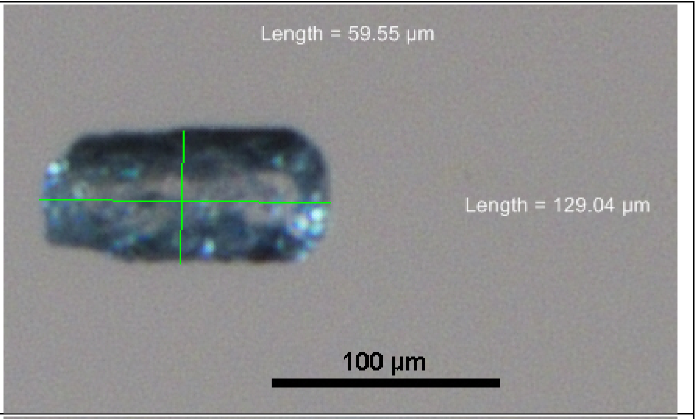
	5	Length = 155.18 Width = 67.10	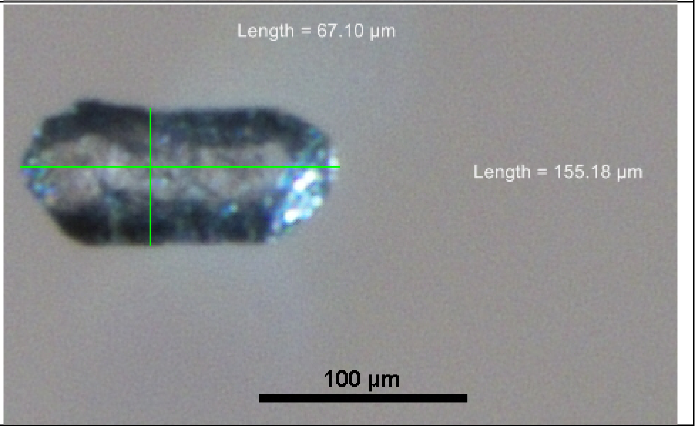

APPENDIX D: Error and constraint calculations for modelling

D.1 SAGLEK TRANSECT ERROR AND CONSTRAINTS

Sample	Attempt	Dating Method	Sigma 1 % error	Ages Used	Error	Constraint	Notes
67SC216	x	Zhe	5%	340	17.3	330-350	
				341.4	17.4		
		Ahe	10%	118	5.5	100-130	This is the issue here (need higher error) **can run 50000 models here. Check with ISA before long runs **Must fix table values to match what we changed in HeFTy
				115.9	5.4		
				121.8	5.4		
		AFT	x	135.9	10	125-145	
	x	Zhe	x	340	17.3	330-350	
				341.4	17.4		
		Ahe	x	118	5.5	100-140	
				115.9	5.4		
				121.8	5.4		
		AFT		135.9	10	120-150	
	1	Zhe	10%	340.5	31.4	310-370	
				341.4	34.8		
		Ahe	20%	118	24.8	100-130	
				115.9	24.5		
				121.8	23.4		
		AFT		135.9	10	110-170	
67SC217	1	Zhe	15%	137.6	21.1	130-180	**Do more runs: Use the 2 oldest aliquots
				156.5	22.9		
		Ahe	15%	108	16.1	90-130	Use mean of 3 oldest Use mean of 4 oldest
				117.7	18.1		
				104.4	16.4		
		AFT		151.3	6.6	130-160	
	2 (2 oldest)	Zhe	20%	229.9	45.4	200-250	Mean of the 2 oldest ages (203 and 257)
		Ahe	15%	108	16.1	95-125	
				117.7	18.1		
				104.4	16.4		
		AFT		151.3	6.6	150-180	
	3 (2 second oldest)	Zhe	20%	170.4	33.6	150-190	Mean of the 2 second oldest ages (203 and 157)
		Ahe	15%	108	16.1	90-125	
				117.7	18.1		

				104.4	16.4		
		AFT		151.3	6.6	150-170	
67SC218	1	Zhe	10%	800.1	80	730-840	DONE*try with Ahe ages 103 and 155 - Error too high
				754.8	75.5		
				821.6	80.6		
		Ahe	50%	150.5	75.2	90-160	
				101	50.4		
	2	Zhe	10%	800.1	80	730-840	Error too high
				754.8	75.5		
				821.6	80.6		
		Ahe	70%	62	43.8	50-110	
				101.4	71.4		
	3	Zhe	10%	800.1	80	730-840	DONE*try with Ahe ages 155 and 208 - Error too high
				754.8	75.5		
				821.6	80.6		
		Ahe	40%	197.5	78.9	140-210	
				150.5	59.6		
	4	Zhe	10%	800.1	80	730-840	DONE*Mean of Ahe ages 155 and 208
				754.8	75.5		
				821.6	80.6		
		Ahe	20%	174.8	34.4	150-200	
	5	Zhe	10%	800.1	80	730-840	DONE*Mean of Ahe ages 103 and 155
				754.8	75.5		
				821.6	80.6		
		Ahe	20%	125	70	100-150	
69TA212	1	Zhe	10%	392.6	39.6	360-400	
				373.5	37.4		
		Ahe	70%	65.7	54.7	50-120	This error is pretty bad
				109.5	98.8		
	2	Zhe	10%	392.6	39.6	360-400	
				373.5	37.4		
		Ahe	60%	109.5	65.4	110-190	
				176.1	105.7		
	3	Zhe	20%	392.6	39.6	360-400	
				373.5	37.4		
		Ahe	20%	265.5	12.9	250-290	
				272.5	13.6		
	4	Zhe	20%	616.3	123	500-635	
				524.1	104.6		
		Ahe	20%	265.5	39.5	250-290	
				272.5	40.9		

69TA201							Only Zhe data. Did not model.
69TA210							Only Zhe data. Did not model.
69TA206							Only Zhe data. Did not model.

D.2 NAIN TRANSECT ERROR AND CONSTRAINTS

Sample	Attempt	Dating Method	Sigma 1 % error	Ages Used	Error	Constraint	Notes
69FQ332	1	ZHe	40%	129.1	51.7	140-190	DONE**FIX THIS, then do 20000 runs. (must put back what is in this table)
				157.3	62.9		
				172.5	69.7		
		AHe	5%	120.2	5.7	105-140	
				117.8	5.7		
		AFT		137.2	8.8	130-170	
	2	ZHe	15%	157.3	23.9	140-190	**See results yielded in Modelling Table document Difficult to decide 1 or 2 because 1 has some good fits but 2 has way more acceptable, although no good DONE*Increase error to 20% for Zhe and 10% for AHe DONE*If result is not that different, keep what I have and run 20,000 models
				172.5	25.8		
		AHe	5%	120.2	5.7	110-140	
				117.8	5.7		
		AFT		137.2	8.8	135-175	
	3	ZHe	20%	157.3	31.4	140-190	
				172.5	34.8		
		AHe	10%	120.2	11.3	110-140	
				117.8	11.4		
		AFT		137.2	8.8	135-175	
69FQ335	1	Zhe	100%	55.4	55.8	35-135	
				76.5	76.4		
				105.6	105.6		
		Ahe	30%	48.8	14.5	20-70	
				46.3	14.5		
				42.2	12.3		
				38.9	12.4		
	2	Zhe	40%	55.4	21.6	40-90	I think #2 is better because #1 has 100% error for Zhe. Isabelle, please confirm that
				76.5	30.6		

							this is bad (e.g. is it 100% error or is it the sigma value DONE*Run with smaller constraint boxes (if find solutions, make boxes closer to your actual data)
		Ahe	30%	48.8	14.5	20-70	Although error on Zhe is still large, we find good solutions so we use it!
				46.3	14.5		
				42.2	12.3		
				38.9	12.4		
	3	Zhe	40%	55.4	21.6	40-90	I think this one is best (bc of Ahe error). I don’t know how to reduce error in Zhe
				76.5	30.6		
		Ahe	15%	48.8	14.5	20-70	
				46.3	14.5		
				42.2	12.3		
69MZ379	1	Zhe	5%	130.4	6.2	120-140	**Error is only this high for apatite because ages are very young. DONE*Run 20,000
				131.6	7.1		
		Ahe	40%	20.2	6.5	005-030	
				15.7	6.8		
		AFT		124	9.5	115-135	
69FQ398							Only Zhe data. Did not model.
69MZ390	1	AHe	45%	135.8	61	115-215	**Error too high, try with average for 4 youngest ages Average of 4 youngest Ahe ages Average of 3 youngest ages **Tried 269, 213, error was greater than 40% Produced no results
				144.1	63.6		
				193.3	87		
		AFT	x	258.9	20.7	240-280	
	2	AHe	20%	135.8	13.4	115-165	
				144.1	14.7		
		AFT	x	258.9	20.7	240-280	
	3	AHe	20%	181.5	36.5	160-200	
		AFT	x	258.9	20.7	240-280	
	4	AHe	20%	157	31	140-180	
		AFT	x	258.9	20.7	240-280	
	5	AHe	20%	222.7	44.8	200-240	
		AFT	x	258.9	20.7	240-280	
69TA336							Only Zhe data. Did not model.
69MZ392	1	Zhe	10%	1129.9	112.4	1010-1150	
				1045.2	103.9		
				1032	102.6		
		Ahe	40%	108.2	42.9	90-170	
				133.3	53.9		
				149.3	59.2		

	2	Zhe	20%	1129.9	112.4	1010-1150	**This one is better, must wait for AFT data **Added AFT data, the model did not produce any acceptable or good results **Checked all the data, raised the error to 20% for Ahe and Zhe, still no results **Increased the constraint boxes, still no results
				1045.2	103.9		
				1032	102.6		
		Ahe	20%	133.3	19.7	100-200	
				149.3	22		
		AFT	x	243.5	22.7	225-265	
69MZ351	1	Zhe	5%	550	28	510-570	*Error for Ahe is a little too high **Use both in thesis** DONE*do 20000 runs for both
				529.7	26.9		
		Ahe	25%	127.4	38.3	110-180	
				162.4	48.8		
	2	Zhe	5%	550	28	510-570	
				529.7	26.9		
		Ahe	20%	267.2	53.8	210-290	
				229.3	46.2		
69MZ335							**Only Ahe data

D.3 HOPEDALE TRANSECT ERROR AND CONSTRAINTS

Sample	Attempt	Dating Method	Sigma 1 % error	Ages Used	Error	Constraint	Notes
k0016	1	ZHe	20%	1025.7	102.2	1000-1110	**Missing AFT data (length, angle, Dpar) Not getting great results here… increased the error (Zhe from 10% to 20%, Ahe, 5% to 10% **Added AFT data, got no results
				1028.6	102.4		
				1078.3	107.4		
		AHe	10%	150.3	7.3	115-185	
				147.3	7.7		
				154.2	8.1		
		AFT	x	158.2	8.1	130-190	
	2	ZHe	20%	1025.7	102.2		This run is similar to attempt 1. I will use attempt 1 because it uses more data
				1028.6	102.4		
		AHe	10%	150.3	7.3	115-185	
				147.3	7.7		
				154.2	8.1		
		AFT	x	158.2	8.1	130-190	
k0015	1	ZHe	10%	332.2	33.5	280-360	**Missing AFT data (length, angle, Dpar)
				309.4	30.9		
		AHe	25%	126.6	32.1	85-160	
				106.8	26.6		
				132.3	33.4		

		AFT	x	142.5	9.8	130-180	
	2	ZHe	10%	332.2	33.5	280-360	**Attempt without Ahe 106.8 age to reduce the error Probably this one (according to error) - check with Isa **Did not have measureable confined track lengths data. Dataset is complete as is (not AFT data to add)
				309.4	30.9		
		AHe	10%	126.6	12.6	110-155	
				132.3	12.7		
		AFT	x	142.5	9.8	135-185	
k0014	1	ZHe	10%	994.3	99	970-1060	
				1042.9	104.1		
		AHe	20%	187.6	37.6	155-230	
				197.4	40.1		
				209.7	41.4		
				176.7	35.3		
	2	ZHe	10%	994.3	99	970-1060	Must use both DONE*Run 20,000 times
				1042.9	104.1		
		AHe	20%	187.6	37.6	165-240	
				220.4	44.1		
				197.4	40.1		
				209.7	41.4		
	3	ZHe	10%	368.9	74.1	350-450	
				427.2	84.8		
		AHe	20%	187.6	37.6	155-230	
				197.4	40.1		
				209.7	41.4		
				176.7	35.3		
	4	ZHe	10%	368.9	74.1	350-450	Must use both DONE*Run 20,000 times
				427.2	84.8		
		AHe	20%	187.6	37.6	165-240	
				220.4	44.1		
				197.4	40.1		
				209.7	41.4		
k0013	1	ZHe	10%	447.1	44.6	430-500	**Missing AFT data (length, angle, Dpar) **Did not have measureable confined track lengths data. Dataset is complete as is (not AFT data to add)
				478.6	48.1		
		AHe	15%	88.5	13.9	65-115	
				89.6	13.7		
				95.5	13.6		
		AFT	x	104.3	11.4	85-125	
k0012	1	ZHe	15%	1084.8	162.7	980-1170	**Ahe error is too high
				1036.6	155.4		
				1140.5	171.4		
				1012.4	151.8		

		AHe	25%	214.3	53.5	195-280	
				257.5	65		
	2	ZHe	15%	1084.8	162.7	980-1170	
				1036.6	155.4		
				1140.5	171.4		
				1012.4	151.8		
		AHe	10%	156.1	16.2	120-185	
				148.7	14.8		
	3	ZHe	15%	1084.8	162.7	980-1120	
				1036.6	155.4		
				1012.4	151.8		
		AHe	10%	156.1	16.2	120-185	
				148.7	14.8		
k0011	1	ZHe	10%	293.2	28.9	260-310	**Missing AFT data (length, angle, Dpar) **Added AFT data, got no results
				280.6	27.6		
		Ahe	15%	191	28.7	160-215	
				193.6	28.8		
				180.1	27		
		AFT		202.9	16.4	180-220	
k0010	1	Zhe	50%	505.7	253.4	340-525	This sample is totally all over the place: Really young Zhe ages Ahe ages older than AFT Zhe and Ahe data
				357.6	178.9		
		Ahe	25%	194.5	48.4	175-260	
				214.6	53		
				200.1	49.6		
				242.5	60.7		
	2	Zhe	20%	432.8	87.2	410-450	AHe and avg Zhe data
		Ahe	25%	194.5	48.4	175-260	
				214.6	53		
				200.1	49.6		
				242.5	60.7		
	3	Zhe	20%	432.8	87.2	410-450	
		AFT	x	171.1	8.4	150-190	
k0009	1	Zhe	20%	628.5	126.2	560-710	DONE*Use the Zhe ages highlighted, then the Ahe 100 and 103 and the AFT age DONE (received missing data and input it)**Missing AFT angle data **This one is better
				691.2	138.4		
				583.5	116.7		
		Ahe	30%	120.6	36.4	65-125	
				98.6	29.2		
				94.6	28.4		
		AFT	x	99.9	5.3	80-125	
	2	Zhe	20%	628.5	126.2	560-710	This one has less error (below 30%!!)
				691.2	138.4		

				583.5	116.7		
		Ahe	15%	98.6	9.7	75-120	
				94.6	9.9		
		AFT	x	99.9	5.3	80-140	
k0008	1	ZHe	10%	528	53.2	470-550	DONE*Use ages highlighted in the modeling document Not getting great results for this one
				491.3	48.6		
				524.2	51.8		
		AHe	40%	127.4	51.6	110-200	
				177	70.2		
				166.1	66.8		
		AFT	x	177	15.2	160-200	
	2	ZHe	10%	528	53.2	470-550	
				491.3	48.6		
				524.2	51.8		
		AHe	10%	177	17.9	145-200	
				166.1	16.1		
		AFT	x	177	15.2	160-200	
	3	ZHe	20%	528	105.2	470-550	Same data as 1, increased error for Zhe
				491.3	98.6		
				524.2	104.9		
		AHe	40%	127.4	51.6	110-200	
				177	70.2		
				166.1	66.8		
		AFT	x	177	15.2	160-200	
	4	ZHe	20%	528	105.2	470-550	Same data as 2, increased error for Ahe and Zhe
				491.3	98.6		
				524.2	104.9		
		AHe	20%	177	35.8	145-200	
				166.1	330.5		
		AFT	x	177	15.2	160-200	

D.4 MAKKOVIK TRANSECT ERROR AND CONSTRAINTS

Sample	Attempt	Dating Method	Sigma 1 % error	Ages Used	Error	Constraint	Notes
71TA464	1	ZHe	10%	785.8	78.4	740-840	
				759.1	76.5		
				823.1	82.7		
		AHe	10%	132.3	12.7	105-150	
				124.7	12.2		

				134.2	13		
				127.9	12.1		
	2	ZHe	15%	650.3	98.2	570-670	This one had better results but slightly higher error and fewer data points.
				591.4	88.3		
		AHe	10%	132.3	12.7	105-150	
				124.7	12.2		
				134.2	13		
				127.9	12.1		
71TA923	1	ZHe	20%	202.5	39.6	150-220	**Missing AFT data (length, angle, Dpar) Yeilded good results, not going to mess with this one **Did not have measureable confined track lengths data. Dataset is complete as is (not AFT data to add)
				198.2	39.2		
				170.1	32.7		
		AHe	15%	106	15.8	75-125	
				95.2	14.7		
				96.3	14.7		
		AFT		119.9	11.2	100-140	
71BT407							**Only Zhe data
71TA910							**Only Ahe data
71TA912	1	Ahe	20%	149	14.5	130-180	help!! ***Ahe and AFT ages very close, TL are long (although avg is approx 13)
				151.9	15.3		
				162.7	16.3		
				152.6	15.9		
				160.4	15.9		
		AFT	x	163.5	7.3	145-185	
	2	Ahe	10%	149	14.5	130-170	
				151.9	15.3		
				152.6	15.9		
		AFT	x	163.5	7.3	145-185	
	3	Ahe	10%	149	14.5	130-170	***TRY THIS WITH INCREASED ERROR
				151.9	15.3		
				152.6	15.9		
		AFT	x	163.5	7.3	145-185	
71TA929	1	ZHe	10%	240.2	24.1	220-270	**Missing AFT data (length, angle, Dpar) **Did not have measureable confined track lengths data. Dataset is complete as is (not AFT data to add)
				248.5	25.5		
		AHe		135.8	13.6	100-160	
				127.2	12.6		
		AFT		159.6	10.6	140-180	
71TA909							Ahe ages older than Zhe

APPENDIX E: Modelling figures

E.1 SAGLEK TRANSECT MODELS

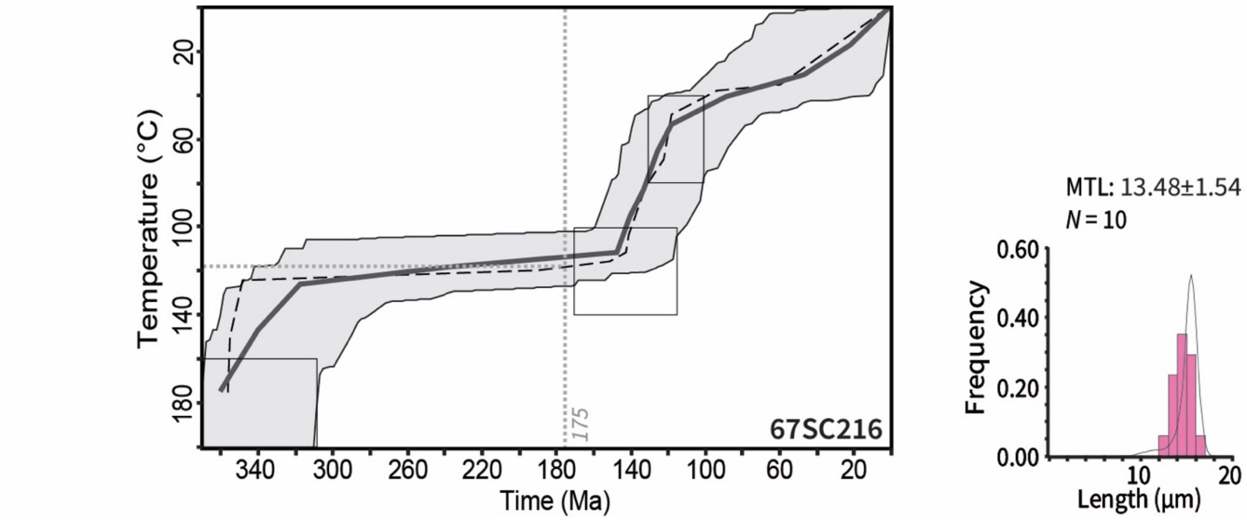

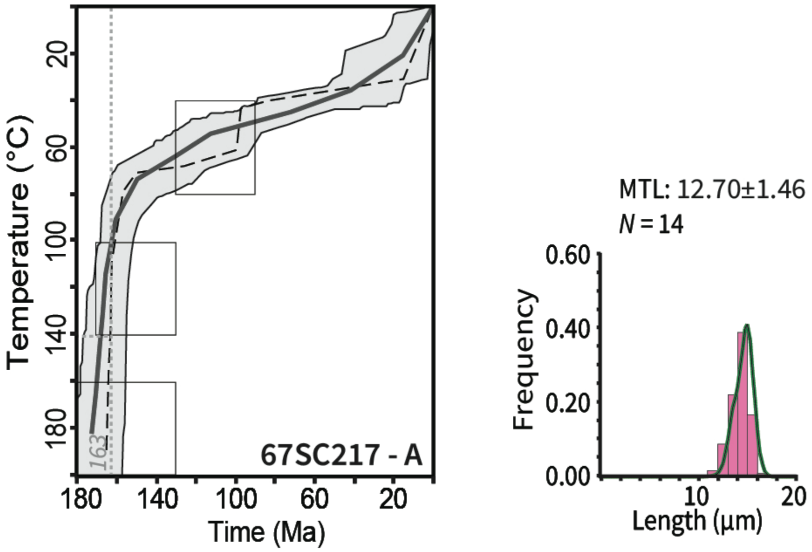

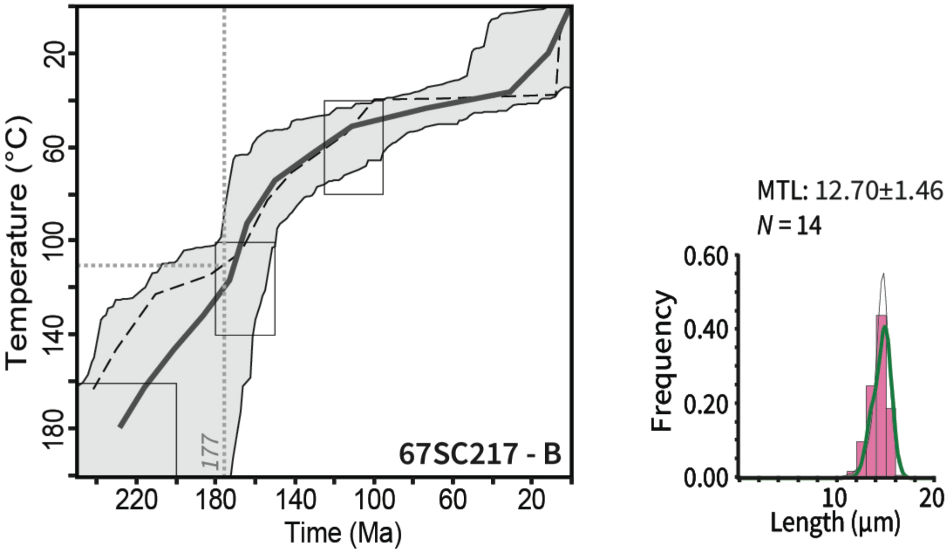
Temperature (°C)
20
60
100
140
180
177
67SC217 - B
220
180
140
100
60
20
Time (Ma)
MTL: 12.70±1.46
N = 14
Frequency
0.60
0.40
0.20
0.00
10
20
Length (µm)

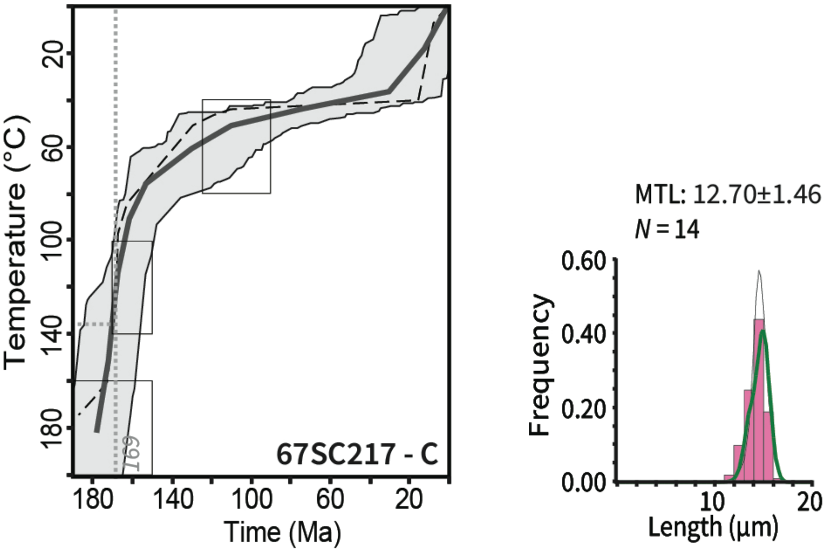
Temperature (°C)
20
60
100
140
180
169
67SC217 - C
180
140
100
60
20
Time (Ma)
MTL: 12.70±1.46
N = 14
Frequency
0.60
0.40
0.20
0.00
10
20
Length (µm)

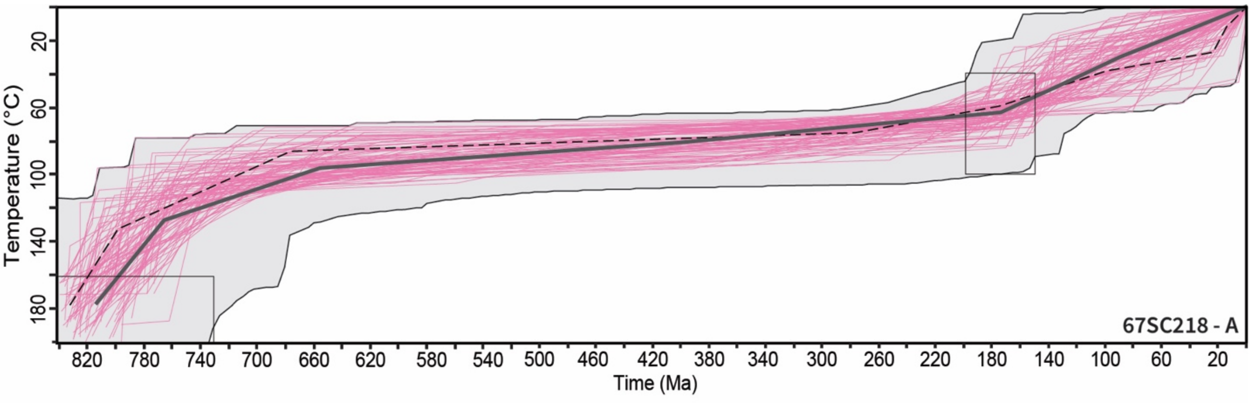
Temperature (°C)
20
60
100
140
180
67SC218 - A
820
780
740
700
660
620
580
540
500
460
420
380
340
300
260
220
180
140
100
60
20
Time (Ma)

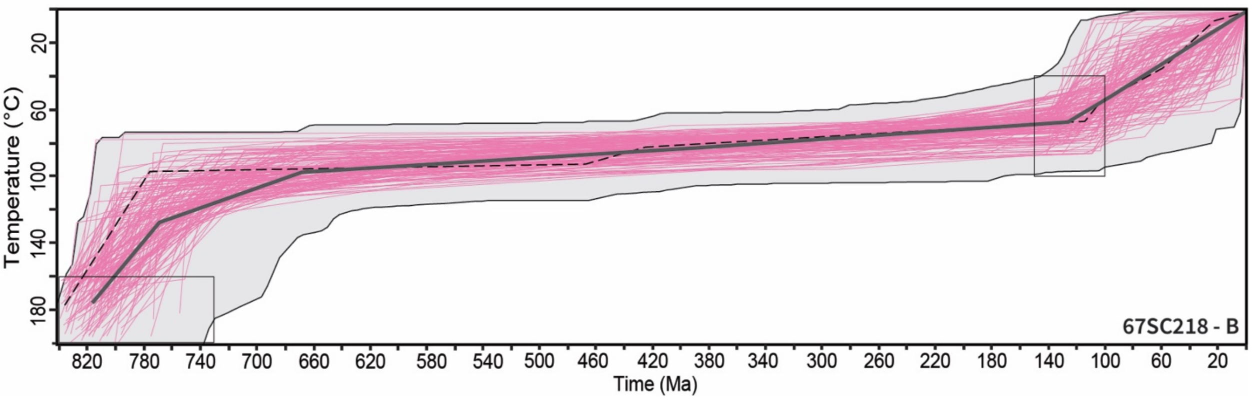
Temperature (°C)
20
60
100
140
180
820
780
740
700
660
620
580
540
500
460
420
380
340
300
260
220
180
140
100
60
20
Time (Ma)
67SC218 - B

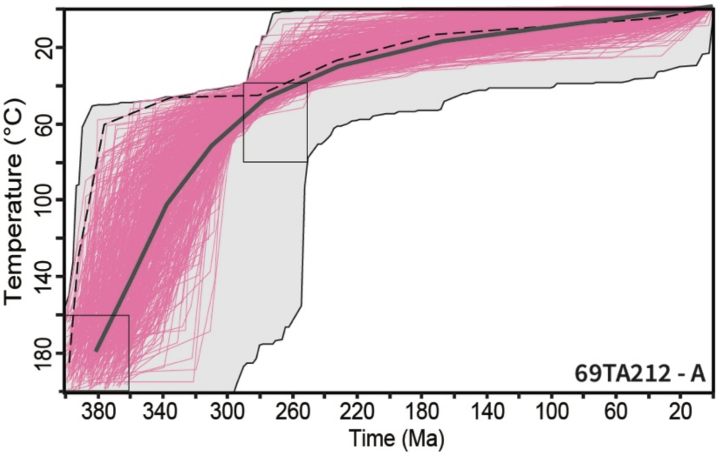
Temperature (°C)
20
60
100
140
180
380
340
300
260
220
180
140
100
60
20
Time (Ma)
69TA212 - A

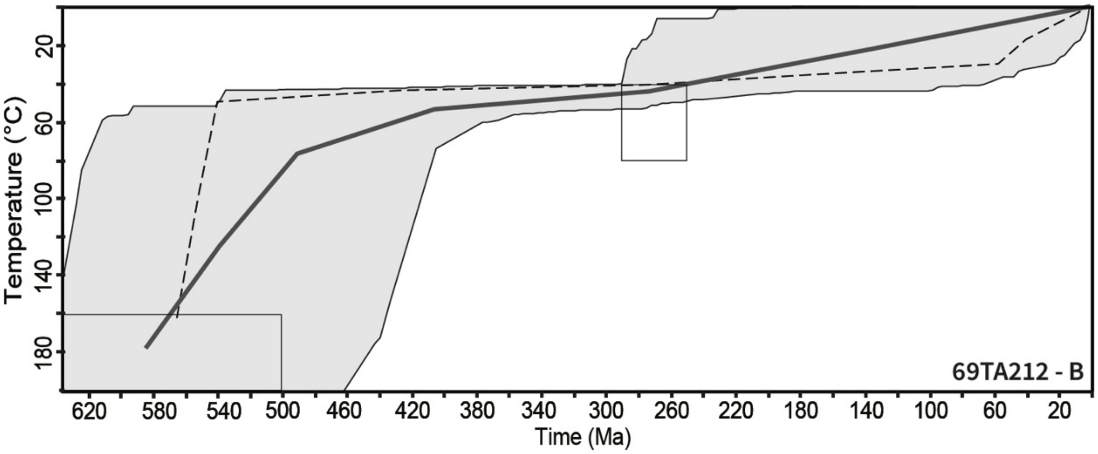
Temperature (°C)
20
60
100
140
180
620
580
540
500
460
420
380
340
300
260
220
180
140
100
60
20
Time (Ma)
69TA212 - B

E.2 NAIN TRANSECT MODELS

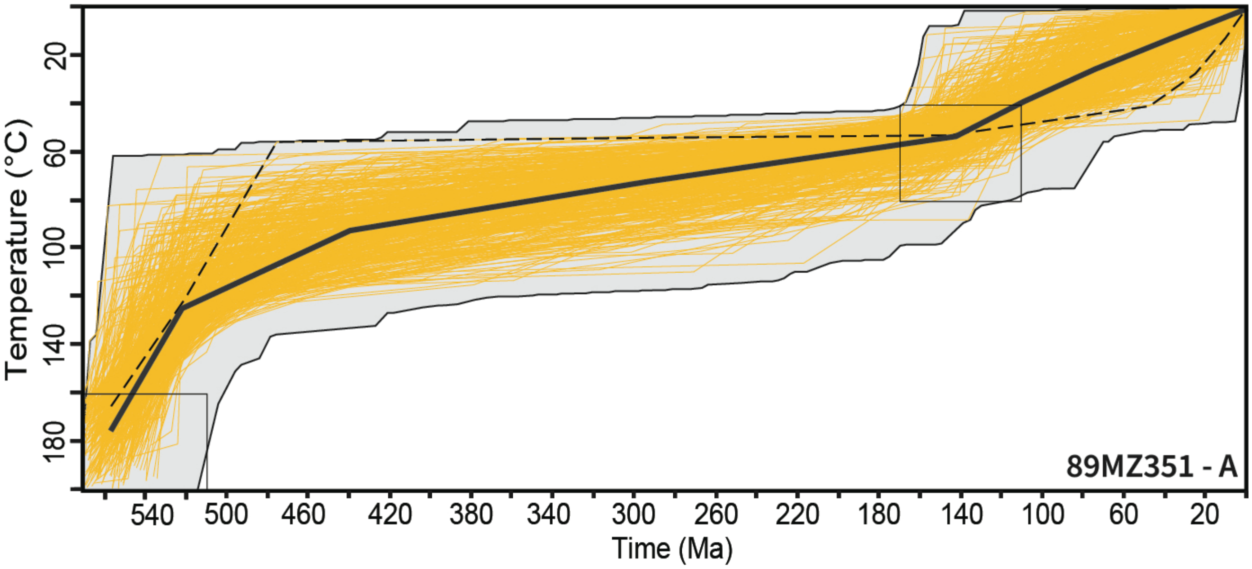

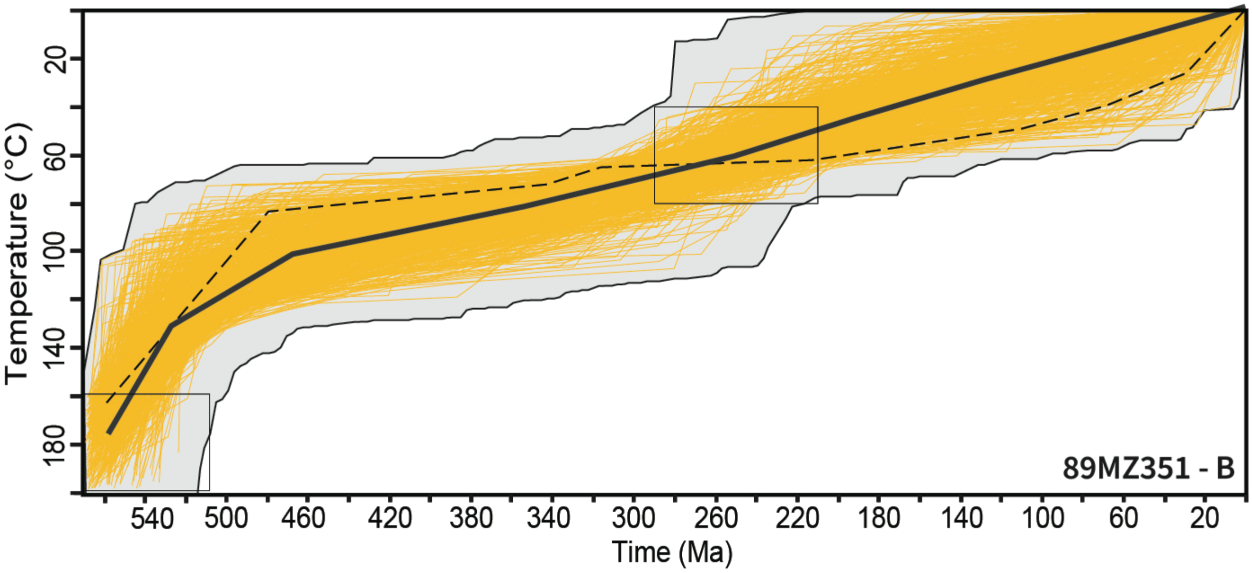

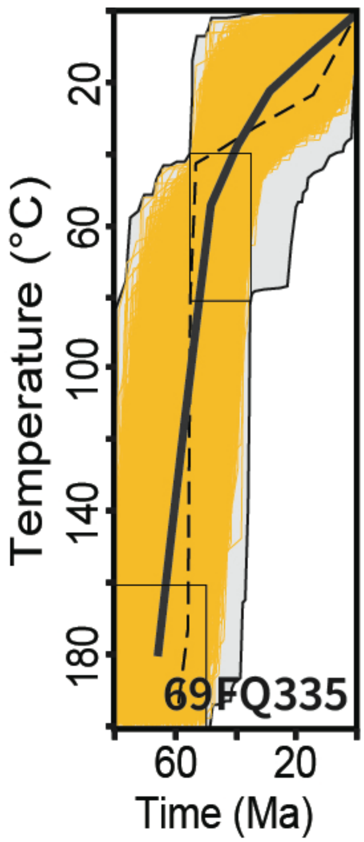
Temperature (°C)
20
60
100
140
180
69FQ335
60
20
Time (Ma)

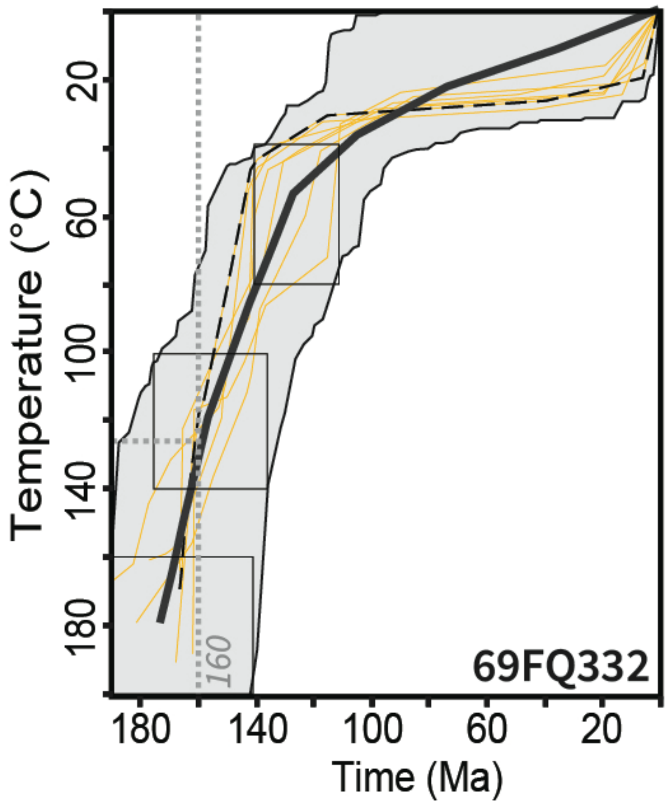
Temperature (°C)
20
60
100
140
180
160
69FQ332
180
140
100
60
20
Time (Ma)

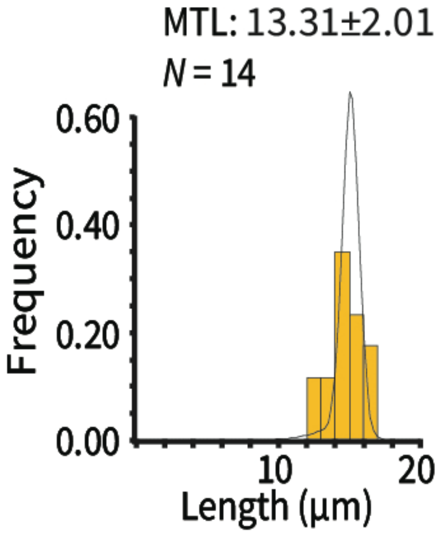
MTL: 13.31±2.01
N = 14
Frequency
0.60
0.40
0.20
0.00
10
20
Length (µm)

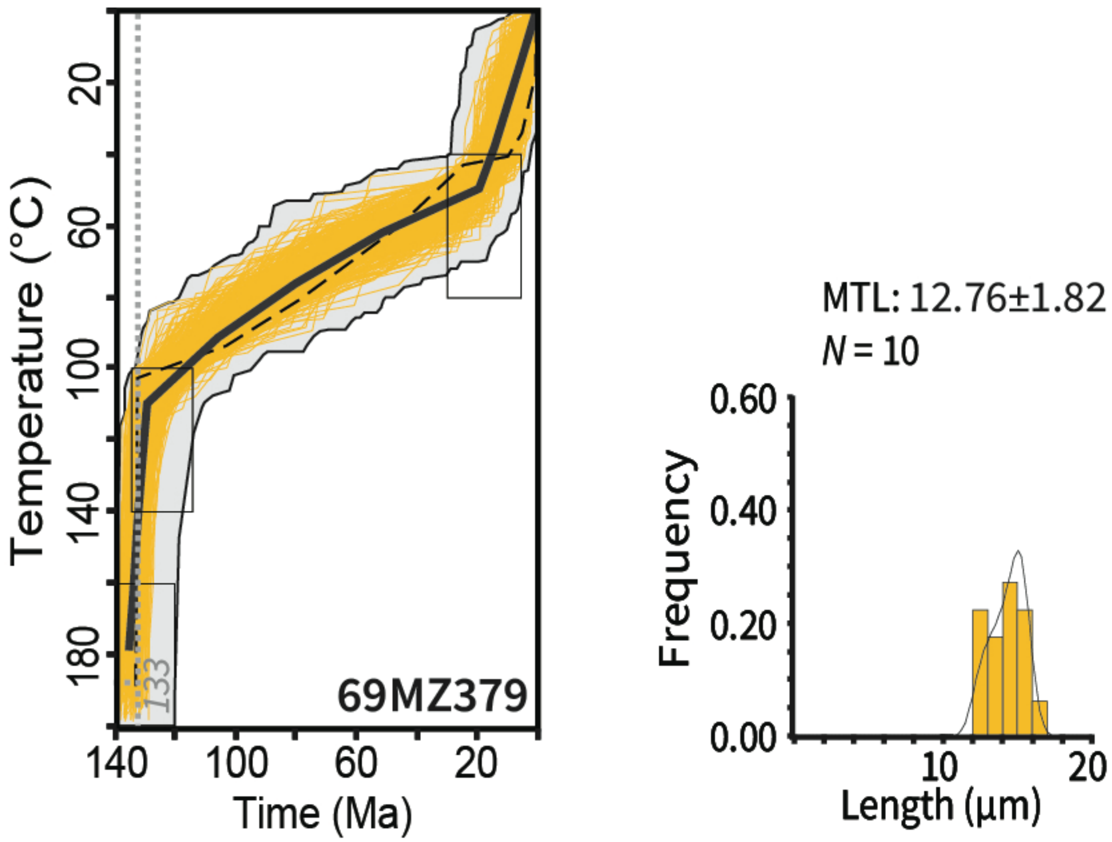
Temperature (°C)
20
60
100
140
180
133
69MZ379
140
100
60
20
Time (Ma)
MTL: 12.76±1.82
N = 10
Frequency
0.60
0.40
0.20
0.00
10
20
Length (µm)

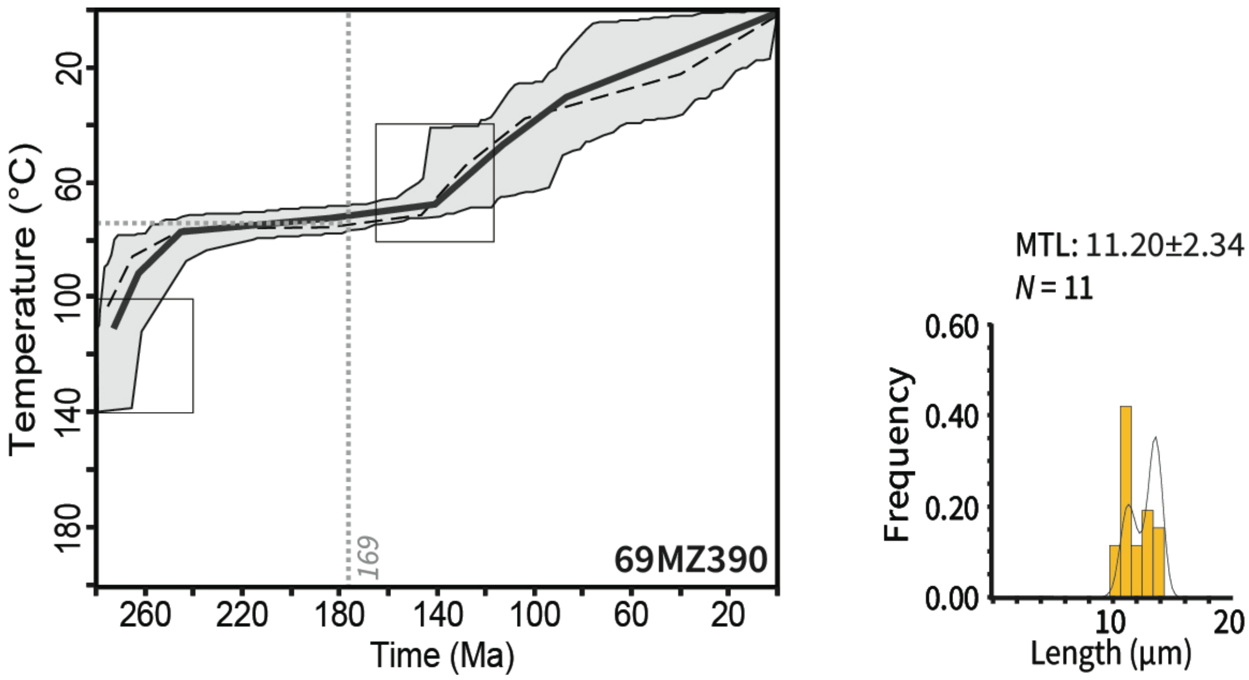
Temperature (°C)
20
60
100
140
180
169
69MZ390
260
220
180
140
100
60
20
Time (Ma)
MTL: 11.20±2.34
N = 11
Frequency
0.60
0.40
0.20
0.00
10
20
Length (µm)

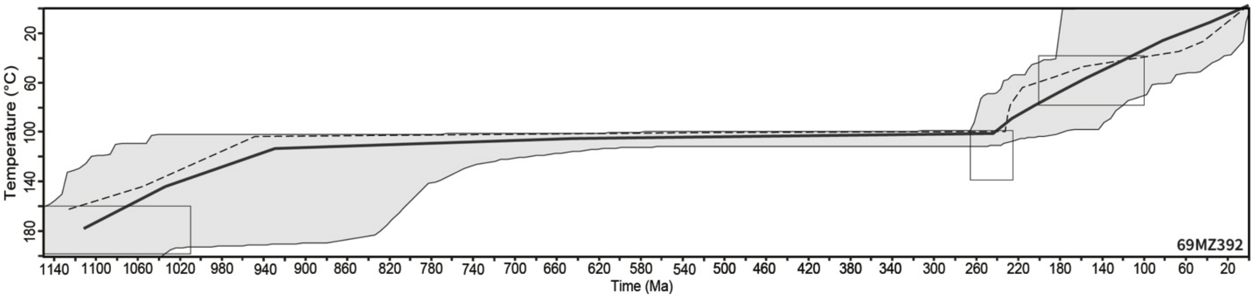

E.3 HOPEDALE TRANSECT MODELS

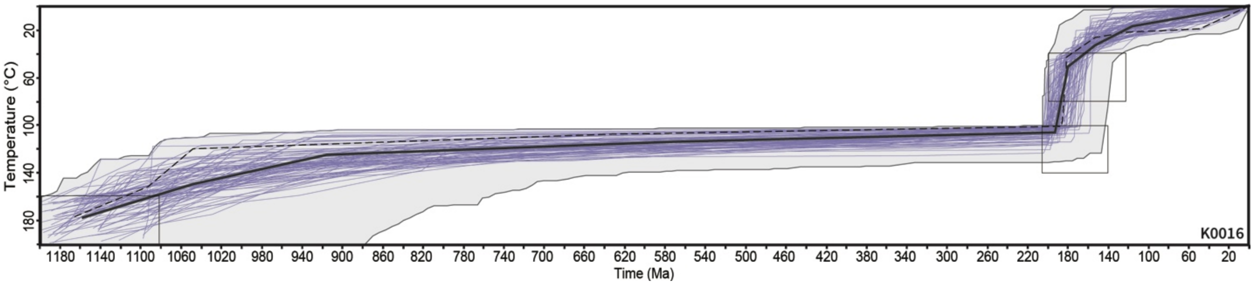

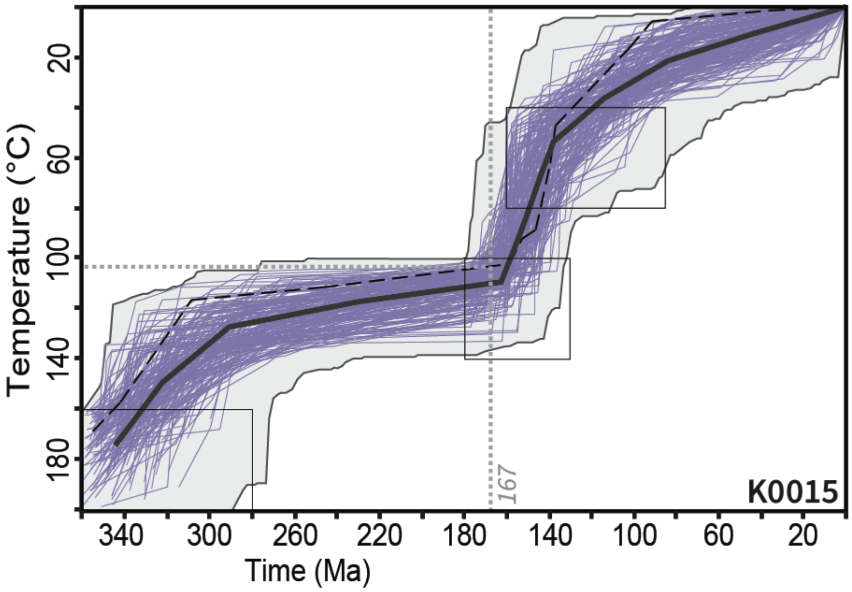

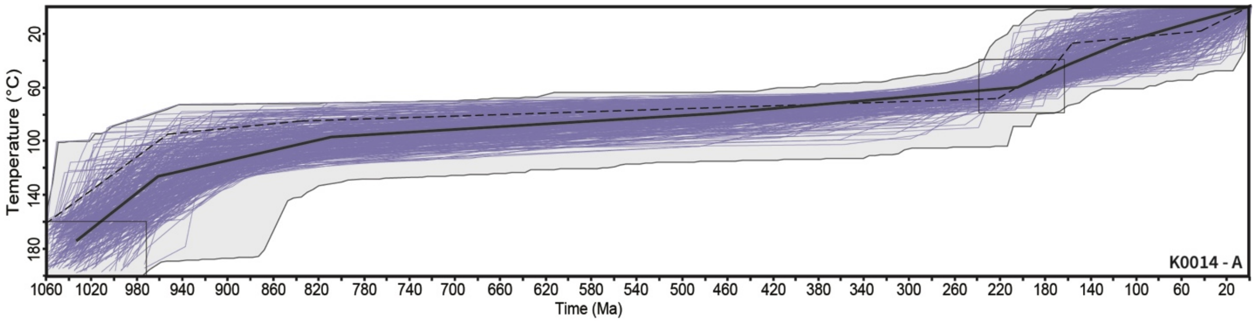
Temperature (°C)
20
60
100
140
180
Time (Ma)
1060 1020 980 940 900 860 820 780 740 700 660 620 580 540 500 460 420 380 340 300 260 220 180 140 100 60 20
K0014 - A

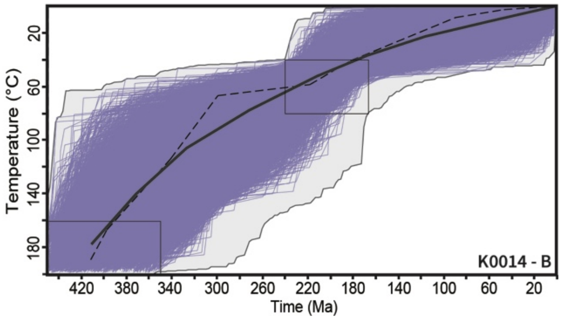
Temperature (°C)
20
60
100
140
180
Time (Ma)
420 380 340 300 260 220 180 140 100 60 20
K0014 - B

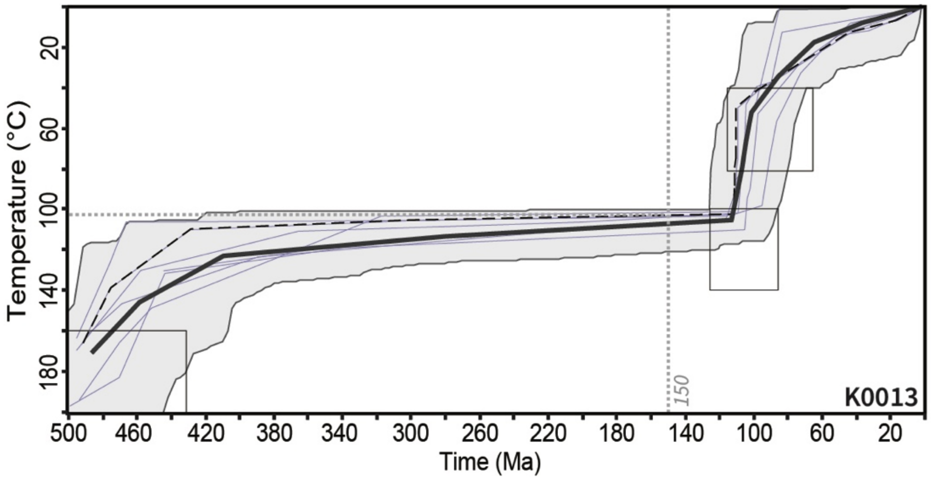
Temperature (°C)
20
60
100
140
180
Time (Ma)
500 460 420 380 340 300 260 220 180 140 100 60 20
150
K0013

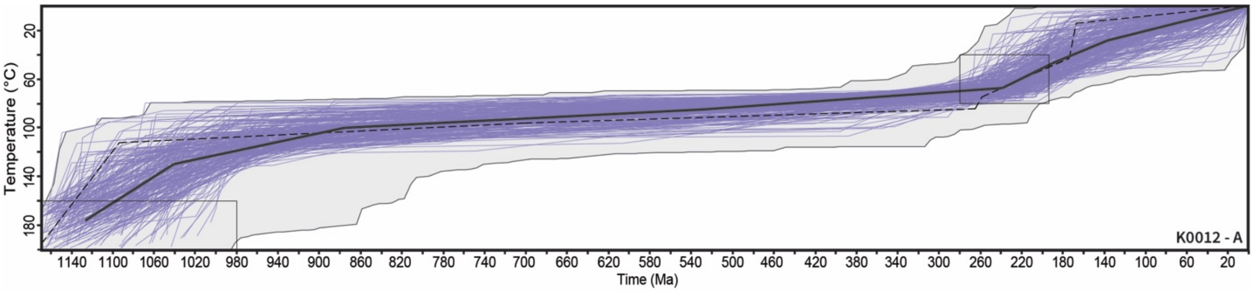
Temperature (°C)
20
60
100
140
180
K0012 - A
1140
1100
1060
1020
980
940
900
860
820
780
740
700
660
620
580
540
500
460
420
380
340
300
260
220
180
140
100
60
20
Time (Ma)

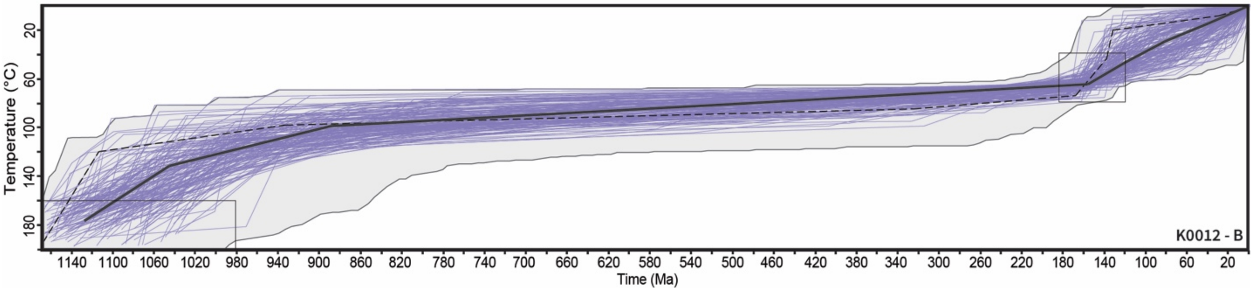
Temperature (°C)
20
60
100
140
180
K0012 - B
1140
1100
1060
1020
980
940
900
860
820
780
740
700
660
620
580
540
500
460
420
380
340
300
260
220
180
140
100
60
20
Time (Ma)

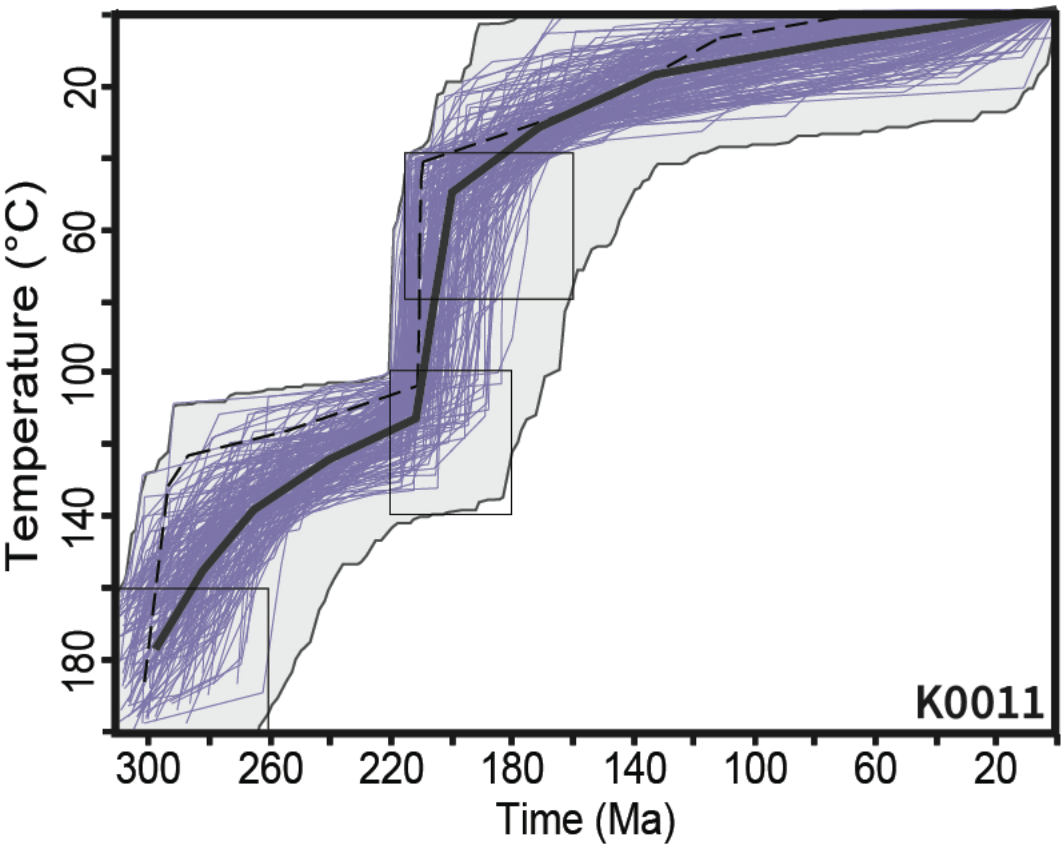
Temperature (°C)
20
60
100
140
180
K0011
300
260
220
180
140
100
60
20
Time (Ma)

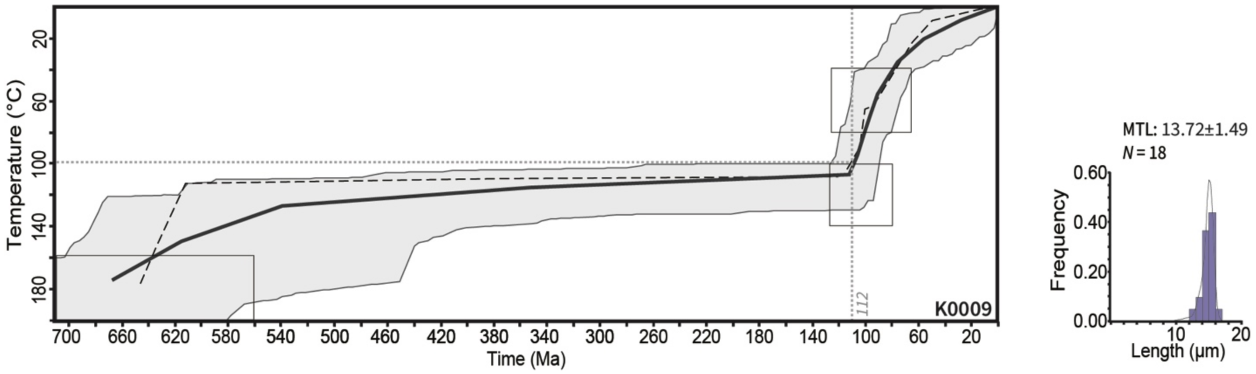

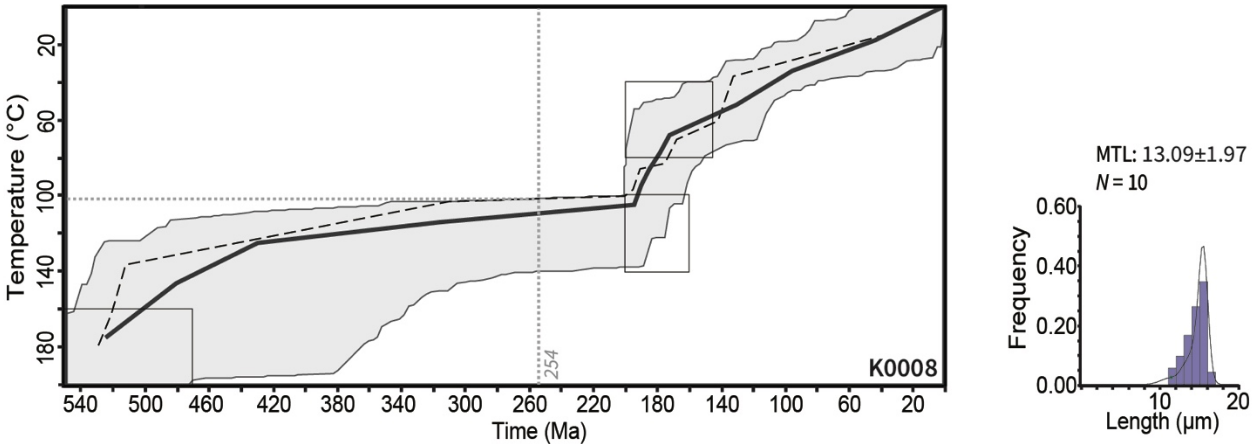

E.4 MAKKOVIK TRANSECT MODELS

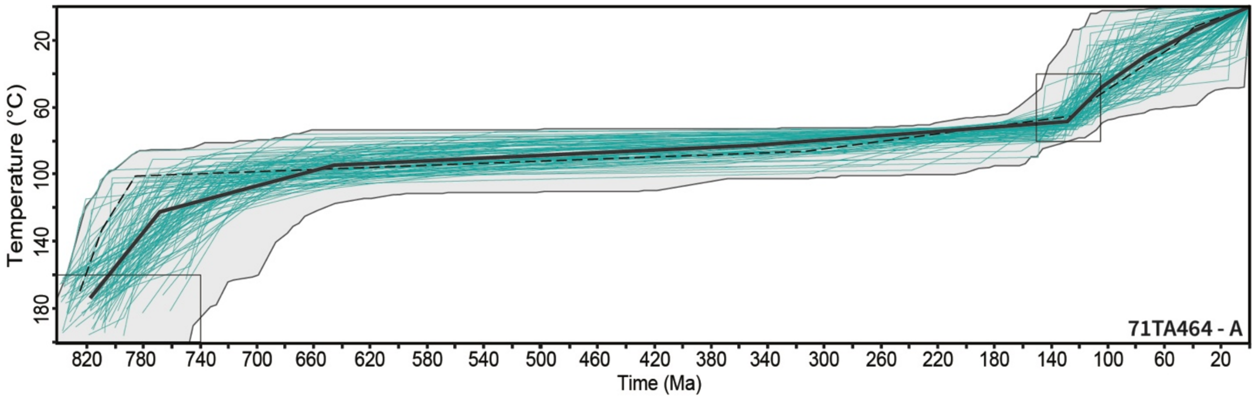

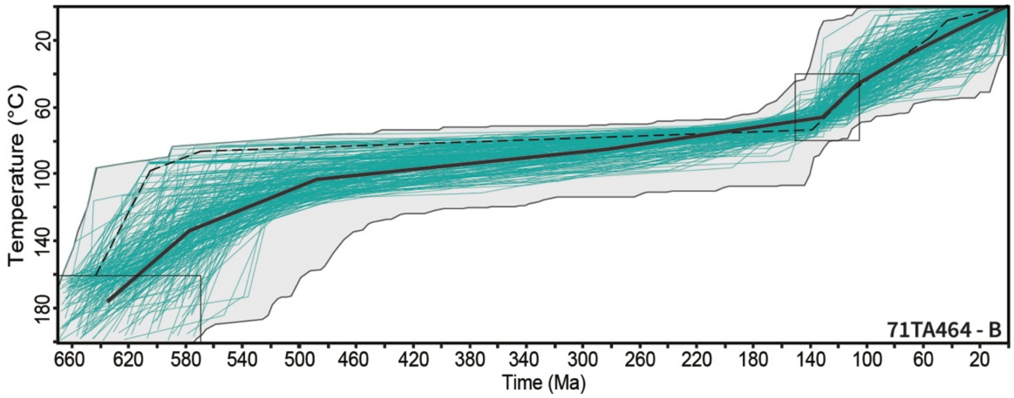
Temperature (°C)
20
60
100
140
180
71TA464 - B
660
620
580
540
500
460
420
380
340
300
260
220
180
140
100
60
20
Time (Ma)

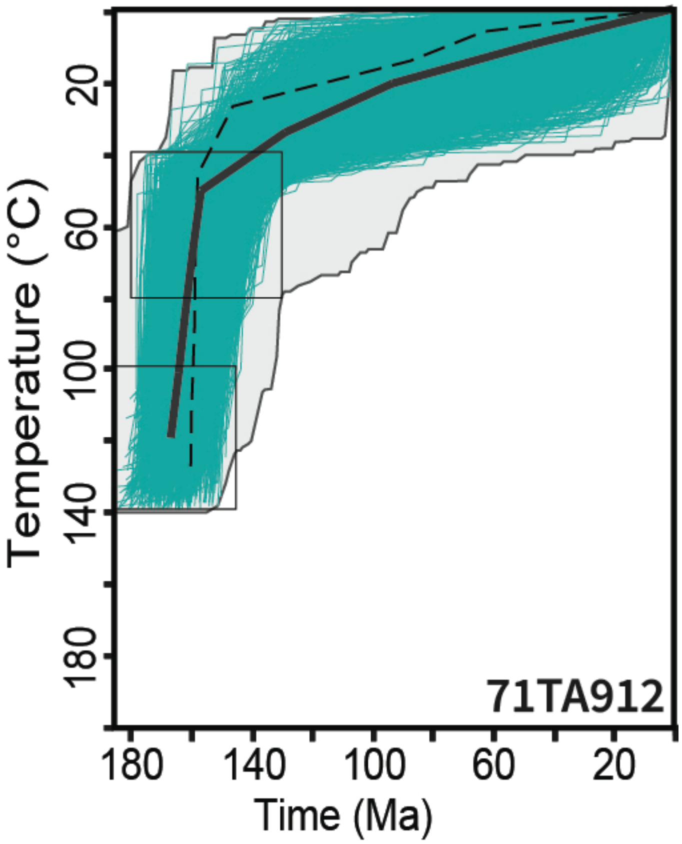
Temperature (°C)
20
60
100
140
180
71TA912
180
140
100
60
20
Time (Ma)

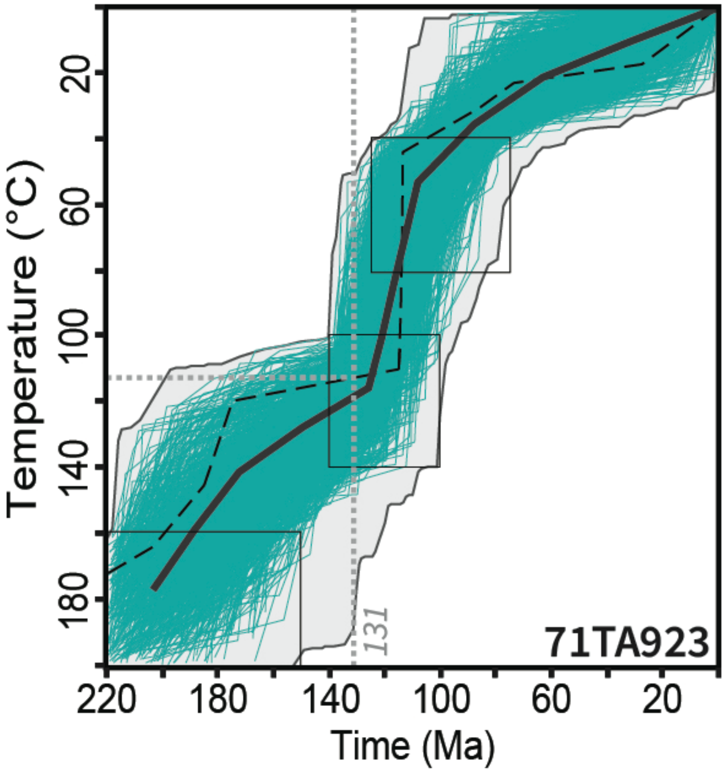
Temperature (°C)
20
60
100
140
180
Time (Ma)
220
180
140
100
60
20
131
71TA923

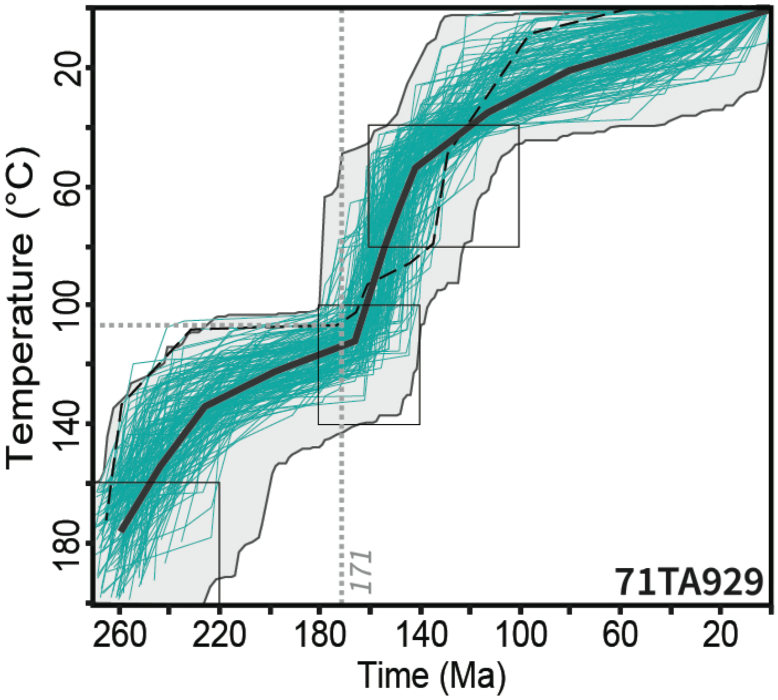
Temperature (°C)
20
60
100
140
180
Time (Ma)
260
220
180
140
100
60
20
171
71TA929

Thank you for reading!